METALS. SUPERCONDUCTORS

Phase segregation and crystallization in the amorphous alloy $Ni_{70}Mo_{10}P_{20}$

G. E. Abrosimova, A. S. Aronin, A. F. Gurov, I. I. Zver'kova, and E. Yu. Ignat'eva

Institute of Solid State Physics, Russian Academy of Sciences, 142432 Chernogolovka, Moscow District, Russia

(Submitted February 2, 1998)
Fiz. Tverd. Tela (St. Petersburg) **40**, 1577–1580 (September 1998)

Structural evolution of the amorphous alloy $Ni_{70}Mo_{10}P_{20}$ has been studied by x-ray diffraction, and by following transmission and high-resolution electron microscopy annealing both above and below the glass-transition temperature. When annealed above this temperature, the amorphous phase undergoes segregation into regions about 100 nm in size having different chemical composition. Diffraction from such samples produces diffuse rings, and the scattering vector corresponding to the maximum intensity varies from point to point within the interval of 4.88 to 4.78 nm^{-1}. When occurring between the glass-transition and crystallization temperatures, crystallization produces groups of nanocrystals, 20–30 nm in size, which are in direct contact with one another and form a polymorphic mechanism. The crystallization mechanism changes when the annealing temperature is brought below the glass-transition point. At these temperatures the amorphous matrix crystallizes entectically with formation of eutectic colonies. © *1998 American Institute of Physics.* [S1063-7834(98)00109-9]

Considerable interest is focused presently on bulk amorphous alloys, a new class of materials.[1,2] These alloys (mostly Zr based) have a complex chemical composition and possess a number of remarkable properties, in particular, a high elastic deformation energy, a large Young's modulus, and so on. This particular interest stems also from the fact that these materials can be obtained in bulk state, thus offering a possibility of realizing such attractive characteristics in a large volume. The glass-transition temperature T_g and the crystallization temperature T_x of these alloys differ considerably. Thus there exists a comparatively broad temperature interval within which they remain in the state of supercooled liquid, but where their properties vary sharply. It is difficult to understand what occurs with a bulk amorphous alloy within the temperature interval $T_g<T<T_x$, because these alloys are multicomponent. At the same time there exist alloys with $\Delta T=T_x-T_g>0$ of a simpler chemical composition, which have not yet been obtained in bulk state. Among such alloys is $Ni_{70}Mo_{10}P_{20}$, which has a high thermal stability for $T_g<T<T_x$, as well as a good corrosion resistance.[3]

This work uses a Ni–Mo–P alloy in an attempt to follow the evolution of the amorphous state during heating, with particular emphasis placed on its variations in the T_x-T_g interval. Investigation of the transformations occurring for $T_g<T<T_x$ is useful not only for understanding the transitions in bulk amorphous alloys but also provide new information on the processes taking place in the structure of an amorphous alloy in the interval between the glass transition and crystallization temperatures. Besides, they can shed light on the mechanism of crystallization, as well as on the structure and morphology of the forming crystal phases.

1. EXPERIMENTAL TECHNIQUES

The amorphous alloy $Ni_{70}Mo_{10}P_{20}$ was obtained in the form of a ribbon by quenching the melt onto a rapidly spinning disc. The ribbon was 1 mm wide and 40 μm thick. The structure was studied by diffraction techniques with a Siemens D-500 diffractometer (with Cu $K\alpha$ radiation) and JEM-100 CX and JEOL-4000 EX electron microscopes. The samples for the electron microscope studies were prepared by ion milling. The thermal properties were investigated with a Perkin-Elmer differential scanning calorimeter. The samples were heat treated in a resistance furnace and in the calorimeter, thus making it possible to measure the fraction of the transformation occurring during a heating or anneal. Microdiffraction measurements in the JEOL-4000 EX microscope were performed under conditions where the examined region did not exceed 15 nm in size. A more detailed description of the experiment will be given in the corresponding Sections.

2. EXPERIMENTAL RESULTS

As follows from the thermogram in Fig. 1, the glass-transition temperature T_g of the $Ni_{70}Mo_{10}P_{20}$ alloy under study is lower than the crystallization temperature T_x. The measurements were performed at a sample heating rate of 20 K/min. The temperature T_g is 430 °C, and $T_x=457$ °C. While the difference between the glass-transition and crystallization temperatures is not large, it is sufficient to carry out heat treatments for subsequent studies of the structure of the samples annealed in this temperature interval.

The samples were annealed for different times at temperatures both below and above the glass-transition point.

 © 1998 American Institute of Physics

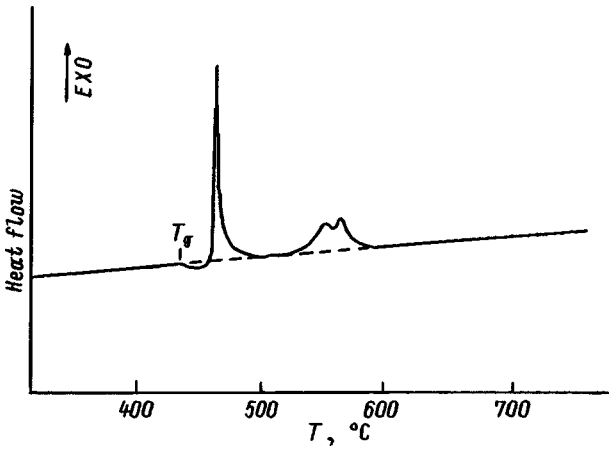

FIG. 1. Thermogram of the $Ni_{70}Mo_{10}P_{20}$ alloy.

The structure of the sample annealed at 400 °C for one hour is shown in Fig. 2. After this heat treatment the alloy is partially crystalline and contains an amorphous phase and crystalline eutectic colonies consisting of two phases. The amorphous matrix is seen in the photomicrograph to have uniform contrast without any features. Figure 3 presents the structure of a sample following a 20-min anneal at 435 °C. In contrast to the preceding case, this structure exhibits a clearly pronounced spotty contrast. One cannot exclude naturally the possibility that most of the contrast is due here to variations in the thickness of the sample, and that the thinner regions appear lighter. A question may arise, however, why after annealing in this temperature interval, the samples prepared for electron microscope measurements under exactly the same conditions should become thinned nonuniformly. One may suggest that this is due to different chemical composition of the milled regions.

The alloy begins to crystallize in the regions looking lighter in the photomicrographs. Here fcc crystals of the solid solution of Mo in Ni form, 20 to 30 nm in size. A characteristic feature of this structure is that these nanocrystals are in direct contact with one another, with no amorphous-phase zone in between. Figure 4a and 4b presents images of such regions obtained with small magnification and high resolution. Note that the crystallization occurred here before the sample thinning, and therefore the nonuniform distribution of crystals in the early stages of crystallization, namely, their appearance in the light regions, is not connected in any way with the sample thickness.

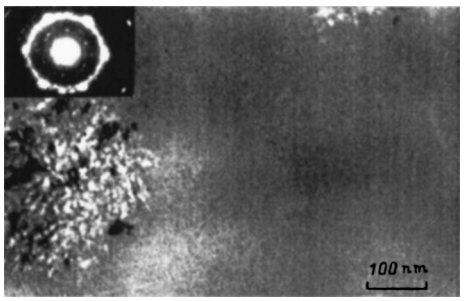

FIG. 2. Photomicrograph of a sample annealed at 400 °C for one hour.

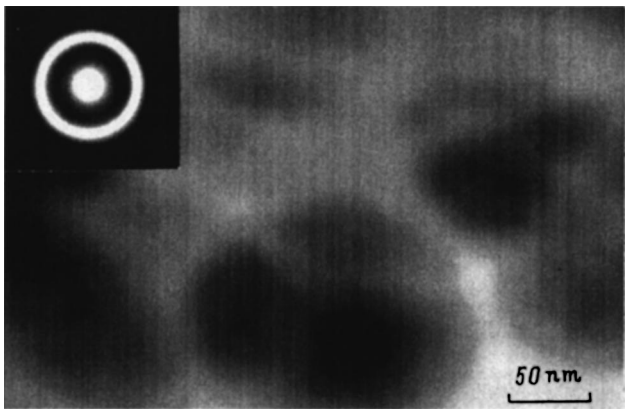

FIG. 3. Photomicrograph of a sample annealed at 435 °C for 20 min.

Special attempts were made at studying the structure of the sample with spotty contrast. It should be pointed out that such contrast appeared always in samples annealed in the temperature interval between T_g and T_x. The structure was studied using the microdiffraction patterns obtained from the sample regions with spotty contrast. The region of the sample responsible for the pattern was 15 nm in size. A series of patterns was obtained in identical diffraction conditions, which were carefully monitored. The patterns thus produced were subsequently digitized. The scattering (diffrac-

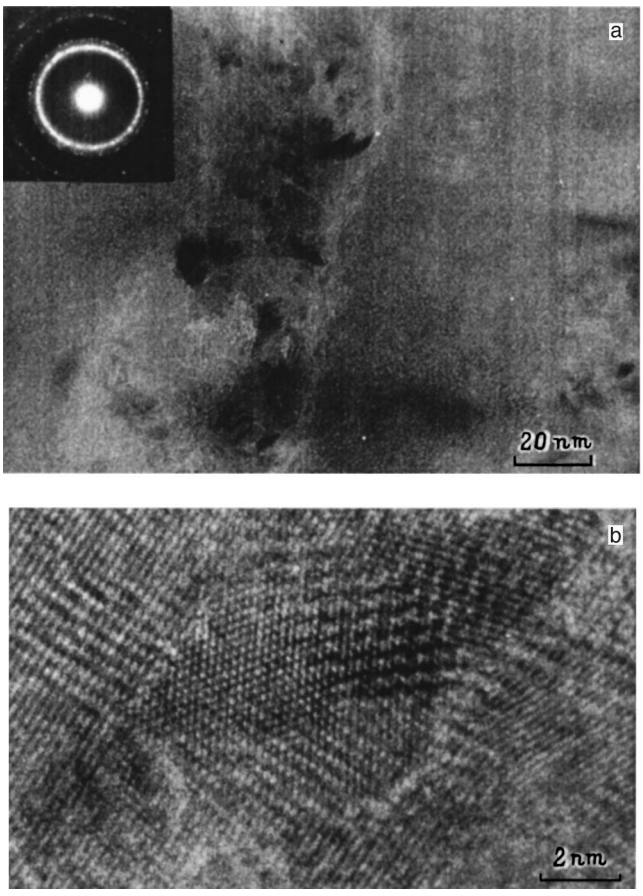

FIG. 4. Sample microstructure in the initial stages of crystallization (a bright-field image, b high-resolution image).

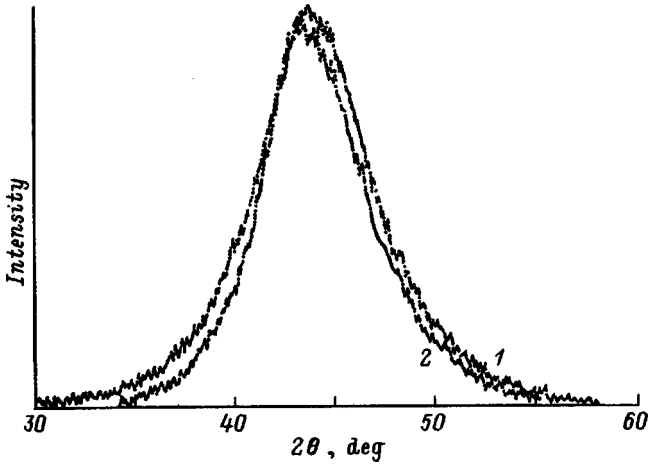

FIG. 5. X-ray diffraction patterns of (*1*) the initial sample and (*2*) the sample annealed at 435 °C.

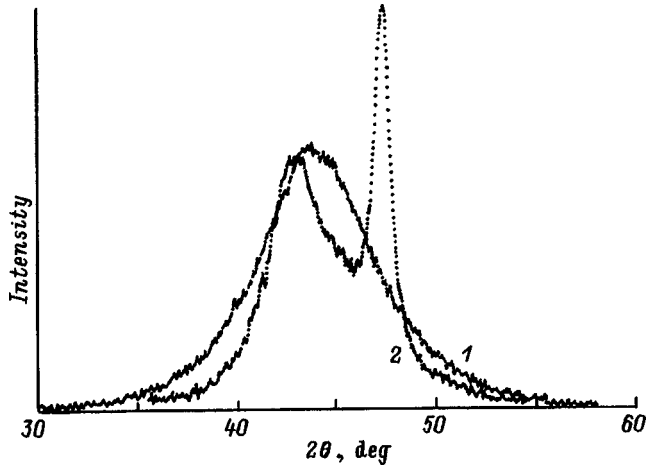

FIG. 6. X-ray diffraction patterns of (*1*) the initial sample and (*2*) the sample annealed at 435 °C for 55 min.

tion) vector corresponding to the maximum intensity of the main diffuse ring was measured using special image-processing computer codes.

It was found that the scattering vector corresponding to the maximum intensity of the diffuse halo from the amorphous phase varied from one region of the sample to another. The maximum change of the scattering vector S ($S = 2 \sin\theta/\lambda$, where θ is the scattering angle, and λ is the wavelength) was $0.1\ \text{nm}^{-1}$. Unfortunately, we cannot establish a one-to-one correspondence between a given value of the scattering vector and the contrast, because in some cases the different regions overlapped, and the scattering vectors had a continuous distribution. One can be certain, however, that the scattering vectors corresponding to the maxima in the diffuse ring intensity change in going from one region of the amorphous sample to another.

X-ray diffraction studies of the sample structure revealed similar changes in the diffraction pattern. Figure 5 shows the first diffuse maxima for the original (curve *1*) and annealed (curve *2*) samples. The position of the diffuse maximum of the original amorphous sample corresponds to $d = 0.205\ \text{nm}$ ($S = 4.88\ \text{nm}^{-1}$). Annealing distorts the shape of the diffuse maximum. An analysis of the shape of the maximum obtained on an annealed sample shows that it can be fitted by two Gaussians, although one can see that the observed diffraction pattern can be better described by a larger number of Gaussians, which implies that the sample can be characterized by a set of coordination spheres with continuously varying radii. This variation is revealed still better in the initial stages of crystallization (Fig. 6). Curve *1* in Fig. 6 is the same as in Fig. 5. Curve *2* in Fig. 6 was obtained for a sample annealed at 435 °C for 55 min. As the heat treatment becomes longer, the accuracy of fitting a maximum with only two Gaussians increases, and these maxima shift in opposite directions.

Crystallization starts with segregation of fcc crystals of the solid solution of Mo in Ni. As the fraction of the crystalline phase increases in the course of annealing, the shift of the left-hand diffuse maximum increases (up to $S = 4.78\ \text{nm}^{-1}$). The lattice parameter of the Ni-based solid solution is 0.358 nm.

3. DISCUSSION

The nature of the processes occurring in amorphous alloys within the $T_x - T_g$ temperature interval is fairly complex. It is known that physical properties change dramatically between the glass-transition and crystallization temperatures, viz. the viscosity decreases, and the diffusion-controlled processes are intensified. We showed[4] the Ni–Mo–P alloy to be very stable within this temperature interval. The crystallization activation energy is about 1000 kJ/mole,[4] which is higher than the corresponding figures for most amorphous alloys, 145–250 kJ/mole (Ref. 5). Hence some processes resulting in a decrease of the free energy of the alloy take place in it within this temperature interval. One of them could be segregation within the amorphous state into regions with different chemical composition and/or short-range order. This argument is supported by the following experimental data.

1) There are some processes within this temperature interval which give rise to the formation of regions about 100 nm in size producing different contrast in electron microscope images (Fig. 2). The scattering vector changes from one point on the sample to another from 4.88 to $4.78\ \text{nm}^{-1}$;

2) In some regions, annealing above the glass-transition temperature results in crystallization (with formation of Ni nanocrystals). These regions look lighter in electron microscope images. There is no transition amorphous-phase regions between the nanocrystals (Fig. 4b). Usually, the grains of the nanophase produced in nanocrystallization are distributed uniformly throughout the amorphous matrix, and nanocrystals are separated by regions with amorphous structure.[6] The existence of these amorphous regions is usually related to a change in their chemical composition in the course of crystallization and, thus, to an increase of their thermal stability.[7] The concentration redistribution may take place before the crystallization within the amorphous state, as well as as a result of the primary crystallization, where the composition of the as-formed crystals differs from that of the

matrix. Crystallization by the primary mechanism changes the composition of the remaining amorphous matrix. One may expect that the composition of the ''light'' regions corresponds to the solid solution of Mo in Ni, because while we witness here formation of several crystals, there is no amorphous matrix between the grains, and the nanocrystals contact directly one another. Obviously enough, these regions crystallize by the polymorphic mechanism, i.e. without any change in the chemical composition. Phosphorus practically does not dissolve in nickel,[8] and therefore it can be expected that crystallization of an fcc Ni-based solid solution will concentrate nearly all of the phosphorus in the amorphous matrix (outside the light regions). Estimation of the solid-solution composition from the lattice parameter of the fcc phase by Vegard's law yields ~ 12 at. % Mo in Ni. This value corresponds to the equilibrium solubility of Mo in Ni at the annealing temperature. As for the excess phosphorus, it most likely becomes redistributed within the ″dark″ contrast region before the onset of crystallization;

3) The mechanism of crystallization below the glass-transition temperature is different, namely, it involves eutectic crystallization with formation of colonies. In this case redistribution of components before the crystallization is insignificant or does not occur at all;

4) The distortion of the maximum in the x-ray diffraction patterns obtained before and in the initial stages of crystallization within the $T_g < T < T_x$ interval may also be connected with redistribution of the components in the course of heat treatment. One may expect that the phosphorus concentration in the amorphous matrix should grow, because it is practically insoluble in fcc Ni.

It should be pointed out that phase segregation within amorphous state of phosphorus alloys was observed earlier.[9] It was found[10] that phosphorus-rich regions have a higher thermal stability, and therefore amorphous regions enriched in phosphorus should crystallize later. The phase composition of these regions after crystallization is so far unclear requiring further studies to determine it.

Thus heat treatment of the amorphous $Ni_{70}Mo_{10}P_{20}$ alloy within the temperature interval between the glass-transition and crystallization temperatures produces segregation into regions about 100 nm in size having different chemical compositions. Crystallization within the $T_x - T_g$ interval starts with the formation of groups of nanocrystals of the Ni-based solid solution. These groups appear in regions which, after sample milling, look lighter in photomicrographs. The nanocrystals do not have amorphous-phase interfaces and are in direct contact with one another. These regions crystallize by polymorphic transitions. Annealing a sample below the glass-transition temperature results in a change of the crystallization mechanism and proceeds by the eutectic mechanism.

The authors are grateful to V. V. Molokanov for preparing the ribbons of the amorphous alloy.

Support of the Russian Fund for Fundamental Research (Grants 96-02-19582 and 97-02-17753) is gratefully acknowledged.

[1] L. Q. Xing and P. Ochina, Mater. Lett. **30**, 283 (1997).
[2] W. H. Wang, Q. Wei, and H. Y. Bai, Appl. Phys. Lett. **74**, 58 (1997).
[3] V. V. Molokanov, A. I. Shcherbakov, M. I. Petrzhik, T. N. Mikhailova, A. S. Aronin, and T. E. Andreeva, Prot. Metals **33**, 127 (1997).
[4] V. V. Molokanov, T. N. Mikhailova, I. A. Kliger, and M. I. Petrzhik, Mater. Sci. Eng., A **226–228**, 474 (1997).
[5] K. Suzuki, K. Fuzimori, and L. Hasimoto, *Amorphous Metals*, Metallurgiya, Moscow (1987), 328 pp.
[6] A. S. Aronin, G. E. Abrosimova, I. I. Zver'kova, Yu. V. Kir'janov, V. V. Molokanov, and M. I. Petrzhik, Mater. Sci. Eng., A **226–228**, 536 (1997).
[7] G. E. Abrosimova, A. S. Aronin, I. I. Zver'kova, A. F. Gurov, and Yu. V. Kir'yanov, Fiz. Tverd. Tela (St. Petersburg) **40**, 10 (1998) [Phys. Solid State **40**, 8 (1998)].
[8] M. Hansen and K. Anderko, *Constitution of Binary Alloys* [McGraw-Hill, New York, 1958; Metallurgizdat, Moscow, 1962, 1488 pp.].
[9] G. E. Abrosimova, A. S. Aronin, and L. V. Voropaeva, Metallofizika **11**, 3, 102 (1989).
[10] A. S. Aronin, S. A. Ivanov, and A. E. Yakshin, Fiz. Tverd. Tela (Leningrad) **33**, 2527 (1991) [Sov. Phys. Solid State **33**, 1427 (1991)].

Translated by G. Skrebtsov

Effect of thermal expansion on the elastic moduli and Debye temperature of paramagnetic lutetium

V. Yu. Bodryakov, A. A. Povzner, and O. G. Zelyukova

Ural State Technical University, 620002 Ekaterinburg, Russia
(Submitted February 2, 1998)
Fiz. Tverd. Tela (St. Petersburg) **40**, 1581–1584 (September 1998)

The temperature dependence of the Young's modulus E of paramagnetic lutetium has been studied. It has been shown that an important reason for the dependence $E(T)$ is thermal expansion of the crystal lattice, which also leads to a change in the Debye temperature Θ. The effect of this factor is also revealed in the thermodynamic properties of metals. In particular, we have shown that there is another contribution to variation of the total specific heat of lutetium, associated with the $\Theta(T)$ dependence and comparable with the electronic contribution. © *1998 American Institute of Physics.* [S1063-7834(98)00209-3]

Rare-earth $4f$ metals (REM) are distinguished by the anomalously strong effect of temperature and magnetic ordering on the elastic moduli of their crystal lattice.[1,2] However, the reasons for this dependence have not yet been elucidated. The temperature dependence of the elastic moduli of paramagnetic rare-earth metals have not been sufficiently examined. As a consequence, a generally accepted methodology for separating the nonmagnetic from the magnetic contributions to the elastic moduli of rare-earth metals has not yet been worked out.

Among the elements of the rare-earth series, paramagnetic lutetium possesses a completely filled shell in contrast to scandium and yttrium, where it is absent, and lanthanum, in which it is empty. Therefore, the paramagnetic state of lutetium is most similar to the paramagnetic phase of the magnetically ordered rare-earth $4f$ metals.

Ultrasound studies of the elastic constants of high-purity lutetium were reported in Ref. 3. On the basis of the data obtained there, calculations were performed, which made it possible to determine indirectly the average values of Young's modulus, the shear modulus, and the bulk modulus. However, reliable direct measurements of the elastic moduli of this metal are still lacking. The temperature dependence of the elastic moduli and related lattice characteristics (Debye temperature, lattice specific heat, etc.) has not yet been established.

In the present paper we report direct measurements of the temperature dependence of Young's modulus $E(T)$ in polycrystalline lutetium in the temperature interval 4.2–370 K. The measurements used the method of free bending vibrations of the sample, a thin rod, at frequencies in the acoustic range ($\sim$1 kHz). The measurement technique and preliminary results were described earlier in Ref. 4. The present measurements of the elastic modulus are shown in Fig. 1. The values of Young's modulus we measured exceed the values obtained in Ref. 3 by roughly 10%, which is comparable with their variation over the entire temperature interval measured.

For a theoretical description of the isothermal Young's modulus E_T we employed the well-known thermodynamic relation[5,6]

$$E_T=(\partial p/\partial u)_T, \tag{1}$$

where the pressure p caused by the uniaxial deformation is expressed in terms of the derivative of the free energy of the crystal lattice with respect to the volume

$$p=(\partial F/\partial V)_T, \tag{2}$$

and the uniaxial deformation u defines the relative change in the volume.

The free energy of the crystal lattice for one mode in the Debye approximation has the form[5]

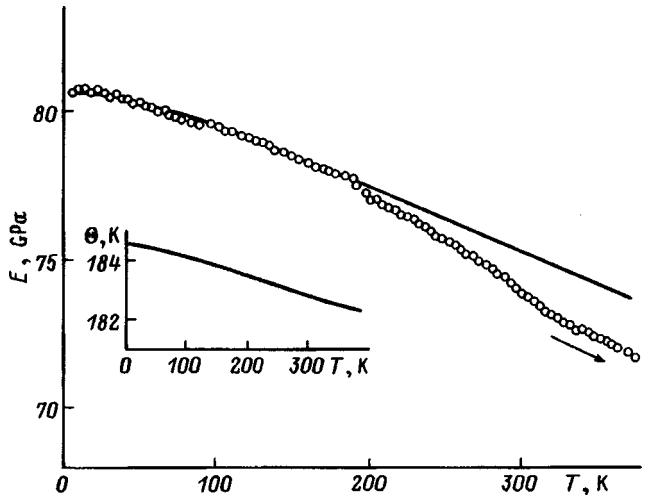

FIG. 1. Temperature dependence of Young's modulus $E(T)$ of lutetium. Solid line — theoretical calculation. Inset shows temperature dependence of the Debye temperature $\Theta(T)$ of lutetium.

 © 1998 American Institute of Physics

$$F(V,T)=F_0(V)+(9/8)R\Theta_0+3RTf(T/\Theta)+(1/2)\zeta T^2, \quad (3)$$

where $\Theta_0=\Theta(T=0)$ is the value of the Debye temperature near absolute zero, $F_0(V)$ is the temperature-independent part of F, R is the gas constant, ζ is the coefficient of the electronic specific heat,

$$f(x)=\ln(1-\exp(x))-(1/3)D(x), \quad (4)$$

$D(x)$ is the tabulated Debye function. Finding the pressure with the help of expression (2) and then expanding the expression so obtained near the equilibrium volume V_0 in the small variations of the volume associated with the additional elastic deformation u, we obtain an expression for the lattice part of the isothermal Young's modulus in the form

$$E_T=E_0-[3R\rho\gamma(1-2\sigma)/M]TD(T/\Theta). \quad (5)$$

In expression (5) we have introduced the following notation: $E_0=E_T\,(T=0)$ for the low-temperature limit of the Young's modulus, ρ for the density of the metal, σ for Poisson's coefficient, and M for the molar mass (atomic weight). The Grüneisen constant γ is equal to

$$\gamma=-(\partial\ln\Theta/\partial\ln V) \quad (6)$$

and reflects the degree of anharmonicity of the vibrations of the atoms of the crystal lattice. For typical metals, γ lies in the interval from one to three and is essentially constant over a wide range of intermediate temperatures.[7] According to the ultrasound data,[3] γ is essentially constant for lutetium and equal to unity to within better than 10% accuracy in the temperature interval from 30 to 300 K.

Thus, neglecting the very weak temperature dependence of ρ, γ, and σ, the temperature-dependent part of Young's modulus of paramagnetic lutetium turns out to be proportional to $TD(T/\Theta)$, i.e., it is proportional to the Debye energy of the crystal lattice. This fact, as was indicated earlier,[8] allows us within the limits of Debye model to indirectly interrelate two independently measured sets of physical characteristics of a given material: the thermodynamic and elastic characteristics. Note also that the expression [expression (8)] for the isothermal Young's modulus, which we obtained from general thermodynamic relations, has a form analogous to the expression obtained in Ref. 9 on the basis of the model of a solid body as a one-dimensional quantum ensemble of anharmonic oscillators.

The temperature dependence of the Young's modulus of lutetium, calculated on the basis of expression (5) (neglecting the difference between the isothermal and adiabatic elastic moduli), is plotted in Fig. 1 by the solid line. In the low-temperature region, almost up to 200 K, there is good agreement between the calculated and experimental values. This agreement breaks down with further increase in the temperature. This is attributable, as was shown in Ref. 4, to the presence of gaseous impurities in the metal.

It should also be noted that the existence of the electronic contribution E_e to the elastic modulus follows formally from relation (3)

$$E_e=(1/2)[\rho\gamma_e(1-2\sigma)/M]\zeta T^2,$$

where the electronic Grüneisen parameter

$$\gamma_e=(\partial\ln\zeta/\partial\ln V).$$

However, estimates show that in the case of paramagnetic lutetium this contribution is negligibly small in comparison with the effect of thermal expansion. Indeed, comparing these two contributions we find that we can neglect the electronic component of the elastic modulus provided $\zeta T/(3R)\ll 2D(x)(\gamma/\gamma_e)$. For lutetium and other rare-earth metals, $\zeta\sim 10^{-3}\,\mathrm{J\cdot K^{-2}\cdot mol^{-1}}$, and $\gamma/\gamma_e\sim 1$.[7,10] As the temperature is lowered, $D(x)$ falls abruptly, and already at the temperature of liquid helium the given contributions to the elastic modulus become comparable.

The traditional treatment of the Debye model of a solid body (see, e.g., Ref. 5) is based on a temperature-independent Debye temperature. However, as a consequence of thermal expansion this assumption quickly comes into contradiction both with the very definition of the Debye temperature (which is a function of the volume and, in a certain sense, the average speed of sound[5]) and with the experimentally determined fact of the constancy of the Grüneisen parameter [see Eq. (6)]. As will be shown below, although the temperature dependence $\Theta(V(T))$ for lutetium is comparatively weak, the contribution to the specific heat of the metal associated with the dependence $\Theta(V(T))$ is comparable with the electronic contribution and therefore should also be taken into account.

The temperature dependence of the Debye temperature for paramagnetic lutetium arising as a result of thermal expansion can be determined directly from the definition of the Grüneisen constant (6), which it is convenient to rewrite in the form

$$\partial\Theta/\Theta=-\gamma(\partial V/V).$$

Hence we immediately obtain that

$$\Theta=\Theta_0\exp\left(-\int_0^T\gamma\beta dT\right), \quad (7)$$

where $\beta=\beta(T)$ is the bulk thermal expansion coefficient . The argument of the exponential in Eq. (7) is usually small, so that the explicit form of the dependence $\Theta(V(T))$ can be represented in a form convenient for rough calculations

$$\Theta=\Theta_0[1-\gamma\Delta V/V], \quad (8)$$

where $\Delta V(T)/V(T)$ is the relative increment of the volume of the body when it is heated to the temperature T. The so-calculated temperature dependence of the Debye temperature of lutetium is shown in the inset to Fig. 1. The quantity Θ_0 and the thermal expansion data were taken from Ref. 3, which, however, did not calculate the dependence $\Theta(T)$. According to our calculations, the Debye temperature of lutetium decreases monotonically from 184.5 to 182.5 K as the sample is heated from helium temperatures to room temperature and beyond.

On the basis of expression (3) for the free energy as well as the familiar thermodynamic relations it is also possible to arrive at an expression for the molar specific heat of the metal [with the dependence $\Theta(V(T))$ taken into account]. This expression, taking the electronic contribution into account, has the form

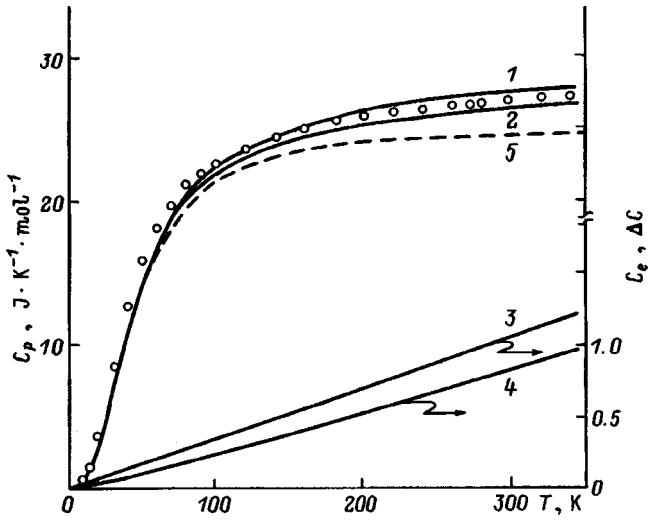

FIG. 2. Temperature dependence of the specific heat of lutetium. Points — experimental values of the isobaric specific heat $C_P(T)$ (Ref. 11): Solid lines are calculated curves [for $\Theta=\Theta(T)$]: *1* — $C_P(T)$ for $\zeta=9.5\,\mathrm{mJ}\cdot\mathrm{K}^{-2}\cdot\mathrm{mol}^{-1}$ according to Ref. 11, *2* — $C_P(T)$ according to Ref. 10, *3* — electronic specific heat $C_e(T)$. For curves *2* and *3* we adopted the value $\zeta=3.26\,\mathrm{mJ}\cdot\mathrm{K}^{-2}\cdot\mathrm{mol}^{-1}$. *4* — the contribution to the specific heat associated with thermal expansion, $\Delta C(T)$. The dashed line *5* (for $\Theta=\Theta_0=184.5\,\mathrm{K}$) is the specific heat at constant volume, $C_V(T)$.

$$C_p(T)=C_V(x)\left[1+x\frac{d\Theta}{dT}\right]^2-3RTxD(x)\frac{d^2\Theta}{dT^2}+\zeta T, \quad (9)$$

where we have introduced the notation

$$C_V(x)=3R[4D(x)-(3/x)/(\exp(1/x)-1)]. \quad (10)$$

Note that expression (10) formally coincides with the expression for the constant-volume Debye specific heat, which assumes $\Theta=\Theta_0=\mathrm{const}$.

Results of calculations of the specific heat $C_P(T)$ according to relation (9) are plotted in Fig. 2 by the solid lines and compared with experimental measurements.[11] It is necessary to point out that the authors of Ref. 11 found a substantially different value than that given in Ref. 10 for the electronic specific heat: $\zeta=3.26\,\mathrm{mJ}\cdot\mathrm{K}^{-2}\cdot\mathrm{mol}^{-1}$ (Ref. 10), $\zeta=9.5\,\mathrm{mJ}\cdot\mathrm{K}^{-2}\cdot\mathrm{mol}^{-1}$ (Ref. 11). Such a discrepancy cannot be explained by experimental errors and is connected in an essential way with the procedure for separating out the different contributions to the specific heat of the metal. This discrepancy again emphasizes the importance of taking a correct account of the effect of anharmonicity and, in particular, thermal expansion on the thermodynamic properties of materials. The solid lines plotting $C_P(T)$ thus correspond to two values of ζ: those from Ref. 10 and Ref. 11. It can be seen that for temperatures above 100 K the experimental points lie between the calculated curves. For temperatures below 100 K the experimental points lie somewhat above the calculated curves. Nevertheless, the agreement between the calculated and experimental data is completely satisfactory, considering that the calculated curves were constructed without benefit of any additional information about the specific heat of lutetium. We may add that the authors of Ref. 11 obtained a value of the Debye temperature $\Theta_0=166\,\mathrm{K}$ significantly different from the results[3] we used.

For comparison, the dashed line in Fig. 2 plots the temperature dependence of the standard constant-volume Debye specific heat $C_{V0}(T)$ for $\Theta=\Theta_0=184.5\,\mathrm{K}$ (Ref. 3). The lower part of Fig. 2 plots the temperature dependence of the electronic specific heat of lutetium $C_e(T)=\zeta T$ (for $\zeta=3.26\,\mathrm{mJ}\cdot\mathrm{K}^{-2}\cdot\mathrm{mol}^{-1}$, Ref. 10) and also the contribution $\Delta C(T)$ to the total specific heat of lutetium due to thermal expansion. The latter is calculated as the difference

$$\Delta C(T)=C_P(T)-C_{V0}(T)-C_e(T). \quad (11)$$

Thus, thermal expansion, due to the anharmonicity of the crystal lattice, has a noticeable effect on the elastic and thermodynamic properties of paramagnetic rare-earth metals. Taking this effect into account is of fundamental importance for understanding the temperature dependence of the elastic moduli not only for lutetium, but, obviously, also of other rare-earth metals in their paramagnetic phases. The effect of this anharmonicity on the Debye temperature and thus on the thermodynamic properties of rare-earth metals is also an important factor. As the treatment of the contributions to the specific heat of lutetium given here shows, this effect in the paramagnetic region can be comparable with the electronic contribution (Fig. 2). In the magnetically ordered region it is necessary to take this latter effect into account in order to correctly separate out the magnetic contribution to anomalies of the thermodynamic properties of rare-earth metals.

This work was partly supported by a grant from the Concourse Center for Fundamental Natural Sciences of the Russian Ministry of General and Professional Education (Project No. 95-0-7.2-165).

[1] K. P. Belov, *Magnetostrictive Phenomena and Their Technological Applications* [in Russian], Nauka, Science (1987), 242 pp.
[2] K. A. Gschneidner, Jr. and L. R. Eyring, *Physics and Chemistry of Rare Earths*, Vol. 1, *Metals*. (North Holland, Amsterdam, 1978)
[3] J. J. Tonnies, K. A. Gschneidner, Jr., and F. H. Spedding, J. Appl. Phys. **42**, 3275 (1971).
[4] V. Yu. Boryakov, Candidate's Dissertation, Moscow State Univ. (1995), 202 pp.
[5] L. D. Landau and E. M. Lifshitz, *Statistical Physics*, 3rd ed. [Pergamon Press, Oxford, 1980; Nauka, Moscow, 1976, Ch. 1, 584 pp.].
[6] L. D. Landau and E. M. Lifshitz, *Theory of Elasticity*, 2nd ed. (Pergamon Press, Oxford, 1970; Nauka, Moscow, 1987, 248 pp.].
[7] S. I. Novikova, *Thermal Expansion of Solids* [in Russian], Nauka, Moscow (1974), 292 pp.
[8] V. Yu. Bodriakov, Solid State Commun. **83**, 1053 (1992).
[9] S. C. Lakkad, J. Appl. Phys. **42**, 4277 (1971).
[10] V. E. Zinov'ev, *Thermal-Physical Properties of Metals at High Temperatures* [in Russian], Metallurgiya, Moscow (1989), 384 pp.
[11] L. D. Jennings, R. E. Miller, and F. H. Spedding, J. Chem. Phys. **33**, 1849 (1960).

Translated by Paul F. Schippnick

Amorphization of solids by fast neutrons

S. F. Dubinin, V. D. Parkhomenko, S. G. Teploukhov, and B. N. Goshchitskiĭ

Institute of Metal Physics, Urals Branch of the Russian Academy of Sciences, 620219 Ekaterinburg, Russia
(Submitted February 3, 1998)
Fiz. Tverd. Tela (St. Petersburg) **40**, 1584–1588 (September 1998)

The diffraction patterns of amorphous solids prepared in the traditional way and by fast neutron bombardment are systematized. It is found that the diffraction patterns of these two classes of materials are different. In the case of a single crystal of titanium nickelide we have demonstrated here for the first time that these radiation-modified solids belong to the class of amorphous materials of distortion type. © *1998 American Institute of Physics.* [S1063-7834(98)00309-8]

The first papers on the amorphization of solids by fast neutrons appeared more than ten years ago.[1,2] In these works it was found that the ferrogarnet $Y_3Fe_5O_{12}$ and the intermetallic compound V_2Zr with *C*-15 structure after bombardment by fast neutrons with a fluence of $\Phi = 2 \times 10^{20}\,\mathrm{cm}^{-2}$ lose their translational symmetry and go over to the amorphous state.

In the last 15 years, several types of materials amorphized by fast neutrons have become known.[3–5] As an example, Figs. 1b and 1c display x-ray and neutron diffraction patterns of an irradiated single crystal of titanium nickelide ($\Phi = 2.5 \times 10^{20}\,\mathrm{cm}^{-2}$, $T_{\mathrm{irr}} = 340\,\mathrm{K}$), measured at 300 K (Ref. 5). The scattering vectors $k_i (i = 1,2,3)$ corresponding to the peak intensities of the diffraction maxima in Fig. 1c are listed in Table I.

Table I also lists the experimental values of k_i for other amorphous materials of this class. It is noteworthy that the values of k_i for different materials differ substantially. This indicates a difference in the irradiated materials of the positional short-range order, which largely determines the diffraction pattern.

One particular feature of these diffraction patterns is distinctly revealed by comparing them with well-known x-ray diffraction patterns of amorphous materials in the literature, obtained by quenching from the liquid phase. In this regard, Fig. 1a shows the x-ray diffraction pattern of amorphous titanium nickelide amorphized in this way.[6] The diffuse peaks in this figure correspond to the scattering vector

$$k_1 = 3\ \text{Å}^{-1}, \quad k_2 = 5\ \text{Å}^{-1}. \tag{1}$$

As follows from Figs. 1a–1c, the experimental situation depends strongly on the means of preparation of the amorphous material.

It was noted long ago that this scattering vector is universal. This can be seen, for example, from Table II, which lists the scattering vectors of the diffuse maxima in the diffraction patterns of amorphous materials prepared by traditional methods.[6–8]

The diffraction patterns of classical amorphous materials have been quite reliably interpreted. It was found that their universal character is largely due to the similarity of the atomic short-range order of these materials in the amorphous and liquid states.[7]

It is specifically the absence of universality in the diffraction patterns of solids amorphized by fast neutrons (Table I) that constitutes their distinguishing feature. A determination of the specifics of the structural state of amorphous materials of the given class is the main goal of the present work.

To solve this problem, we chose a single crystal of the ordered binary alloy with a simple cubic lattice, β-$Ti_{49}Ni_{51}$. The structural state of irradiated titanium nickelide and information about its point defects were obtained from resis-

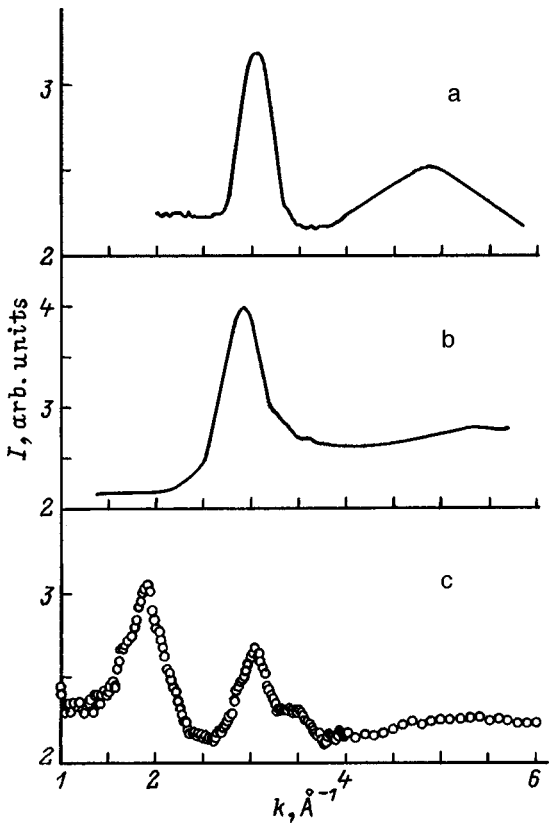

FIG. 1. a — X-ray diffraction pattern of amorphous titanium nickelide prepared by quenching from the liquid phase; b,c — x-ray and neutron diffraction patterns of amorphous titanium nickelide prepared by fast neutron bombardment.

 © 1998 American Institute of Physics

TABLE I. Scattering vectors of the diffuse maxima in the diffraction patterns of solids amorphized by fast neutrons.

Compound	Initial phase	k_1, Å^{-1}	k_2, Å^{-1}	k_3, Å^{-1}
V_2Zr, Ref. 2	*C*-15	2.5	3.6	4.2
Mo_3Si, Ref. 3	*A*-15	2.9	4.5	
$Gd_3Ga_5O_{12}$, Ref. 4	Garnet	2.2	3.8	
$Ti_{49}Ni_{51}$, Ref. 5	*B*2	1.9	3.0	3.5

TABLE II. Scattering vectors of the diffuse maxima in the diffraction patterns of materials amorphized by quenching from the liquid phase.

Material	Initial phase	k_1, Å^{-1}	k_2, Å^{-1}
Fe, Ref. 7	*A*2	3	5
NiTi, Ref. 6	*B*2	3	5
$Ni_{60}Nb_8$, Ref. 8	*R*	3	5

tivity data. Detailed information about the samples and the technique is contained in Ref. 9.

First, let us properly consider the structure of amorphous titanium nickelide, and then special features of amorphization of solids by fast neutrons.

The most characteristic feature of titanium nickelide amorphized by fast neutrons is that annealing of the irradiated alloy regenerates not only the initial crystal structure, but also the degree of perfection of the initial single crystal. This can be seen from Fig. 2, where the empty circles and dark squares represent respectively the (110) intensities of the Bragg reflection in the neutron diffraction patterns of the initial and annealed (after fast-neutron bombardment) samples.[1)] This fact is fundamental because it means that the positional near-range order of the amorphous phase has a direct relation to the *B*2 crystal phase (CP). In other words, a structural transition to the amorphous phase (AP) occurs under the action of fast neutrons according to the direct scheme CP→AP, not in the sequence CP→LP→AP, as in the case of quenching from the liquid phase (LP).

In this light, let us turn our attention to the neutron diffraction pattern of titanium nickelide in the amorphous state and compare it with the neutron diffraction patterns of polycrystalline $Ti_{49}Ni_{51}$. The necessary data are contained in Figs. 3a and 3b. As can be seen from these figures, the angular positions of the diffuse maxima approximately coincide with the Bragg reflections (100), (110), and (111) of the starting *B*2 phase. Here, the first and third maxima in Fig. 3a as well as the Bragg reflections (100) and (111) in Fig. 3b are superstructural. The origin of this superstructure is connected to the preservation in the amorphous phase of titanium nickelide of chemical short-range order. It is logical to assume that the intensities of the superstructure diffuse maxima in the diffraction pattern are proportional to the difference of the atomic scattering factors of nickel and titanium: $(f_{\mathrm{Ni}} - f_{\mathrm{Ti}})^2$. Thus, in the case of diffraction of thermal neutrons the superstructure should be clearly visible since the nuclear scattering amplitudes of nickel and titanium have different signs, and should be absent in the diffraction pattern since the atomic factors of Ni and Ti are positive and close to unity. This accords well with experiment [Figs. 1b and 1c].

Thus, only one diffuse maximum in Figs. 1b and 1c corresponding to $k=2.9$ Å^{-1} characterizes the positional short-range order in irradiated $Ti_{49}Ni_{51}$. This constitutes one more special feature of the diffraction pattern of amorphous titanium nickelide amorphized by fast neutrons. The absence in Fig. 1b of diffuse maxima in the region $k>3$ Å^{-1} is an indication of compact positional short-range order or, said differently, it is an indication that the arrangement of the atoms in the radiation-modified alloy is more uniform. In view of this, let us turn now to the radial distribution function of the atoms in such an alloy.

For isotropic systems the reduced radial distribution function has the form[10]

$$g(r)-1=\Omega/(2N\pi^2 r)\int [I(k)-1]\sin(kr)kdk. \qquad (2)$$

The function $g(r)$ is proportional to the mean number of atoms in a spherical shell with inner and outer radii r and $r+dr$. The quantity N/Ω in Eq. (2) is equal to the mean atomic density of the amorphous alloy, and $I(k)$ is a structure factor, which after subtracting out well-known corrections gives the experimental diffraction pattern. Results of our calculation of $g(r)$ are shown by the solid curve in Fig. 4. As can be seen from this figure, with increasing distance from the central atom ($r=0$) modulations of the atomic density decay rapidly and above $r=6$ Å $g(r)$ becomes constant and equal to its own mean value. For comparison, the dashed line in this figure plots the function $g(r)$ of titanium nickelide quenched from the liquid phase.[6] It can be seen that the

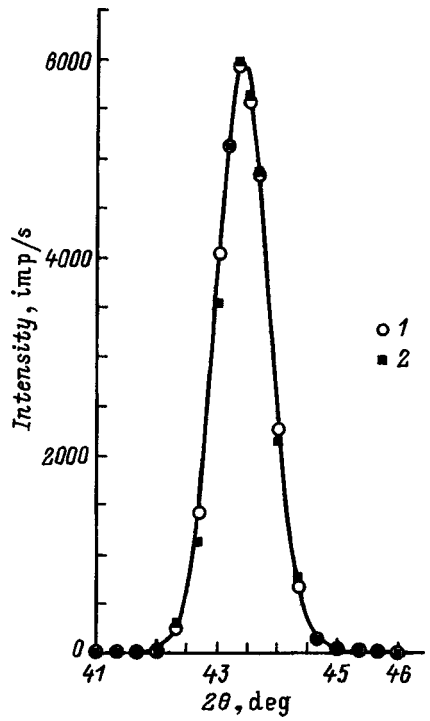

FIG. 2. Structural reflection (110) in the neutron diffraction pattern of titanium. *1* — before bombardment; *2* — after annealing a sample of the alloy amorphized by fast neutrons.

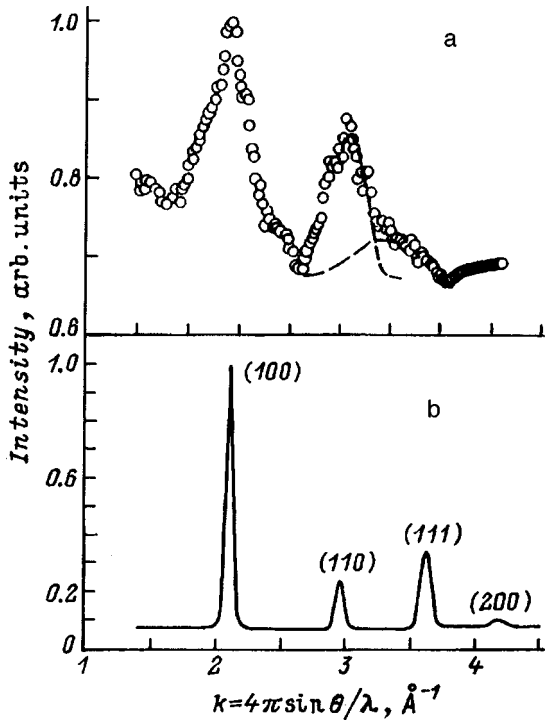

FIG. 3. Neutron diffraction patterns of titanium nickelide amorphized by fast neutrons (a), and of polycrystalline titanium nickelide (b).

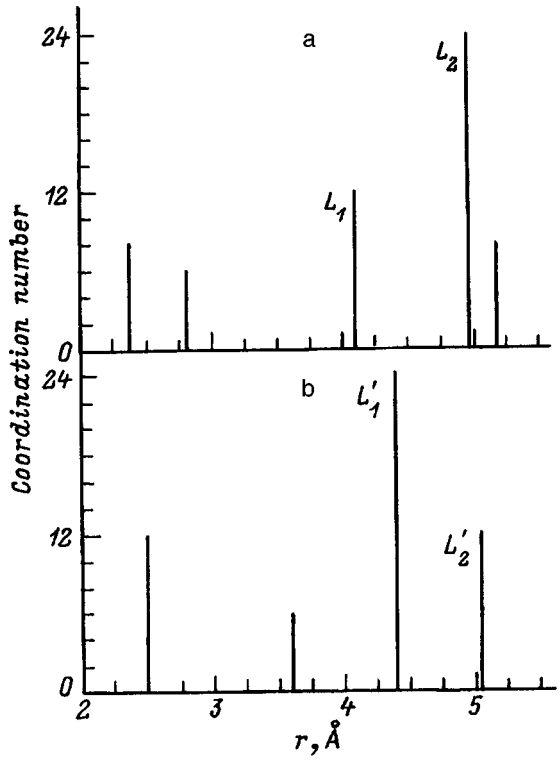

FIG. 5. Atomic filling functions of nearest coordination spheres of a *bcc* lattice (a) and a *fcc* lattice (b).

modulations of the dashed curve extend out to $r=10$ Å, i.e., the short-range order in the classical amorphous alloy is more extended.

One more important difference between these two functions in Fig. 4 is worthy of note. It shows up most distinctly in the structure of the second large modulation of $g(r)$, which includes within itself two maxima.[6] Their positions are marked by the arrows labeled L_1' and L_2' for the dashed curve and L_1 and L_2 for the solid curve. It is logical to assume that the heights of these maxima are proportional to the coordination numbers of crystalline lattices of the types responsible for the short-range order in the specific amorphous material. In the case in question, comparison must be made with the characteristic atomic distances of a *bcc* lattice, whereas to analyze the function $g(r)$ plotted in the figure by the dashed line, it is necessary to use atomic distances of close-packed lattices such as *fcc*.

The coordination numbers for *bcc* and *fcc* lattices are given in Figs. 5a and 5b, respectively. This figure plots the atomic distances and coordination numbers which we believe form the maximum in question. Their ratio qualitatively explains the magnitudes of the corresponding partial maxima in Fig. 4.

Let us summarize the first result of the present work pertaining to the structure of titanium nickelide amorphized by fast neutrons. First, this is that its positional short-range order corresponds to the initial $B2$ phase and not to a densely packed crystal structure (as is the case in an amorphous alloy obtained by the traditional means). Second, chemical short-range order is preserved in the amorphous phase. And finally, the positional short-range order of radiation-modified titanium nickelide is more compact.

Let us turn now to a discussion of the origin of the amorphization effect in irradiated titanium nickelide. Earlier it was shown[11] that the reason for amorphization is radiation defects which give rise to random displacements of the atoms from sites of the original cubic lattice. Let us consider here in more detail a qualitative model of fast-neutron-bombarded titanium nickelide, whose structure is stable over a wide temperature range.

In the case under consideration, radiation damage occurs according to the scheme $n^0 \rightarrow \text{PDA} \rightarrow \text{CAC}$, where n^0 is a fast neutron; PDA is an atom knocked out of a lattice site by the fast neutron and which it is customary to call a primary displaced atom; and CAC is the cascade of atomic collisions created by the PDA as it brakes in the crystal. Cross sections

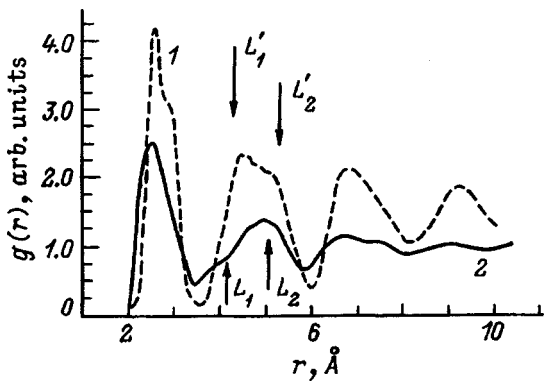

FIG. 4. Radial distribution functions of atoms in amorphous titanium nickelide. *1* — after quenching, *2* — after bombardment by fast neutrons.

of the indicated reactions are discussed in detail in Ref. 12.

According to experiment[11] it may be surmised that the amorphous phase is formed at the site of origination of the CAC in bulk $Ti_{49}Ni_{51}$. In connection with this, let us determine the mean volume of the CAC micro-region V. The relationship between V and the fraction of amorphous phase C in the sample ($T_{irr}=80$ K, $\Phi=1.5\times10^{19}$ cm^2, $C=0.42$, Ref. 11) is given by the well-known formula[13]

$$C=1-\exp(-VN\sigma\Phi), \tag{3}$$

where N and σ are well-known parameters.[11] Assuming the shape of the amorphous cluster to be spherical, we find its diameter to be equal to 70 Å. Thus, the component parts of the amorphous material are of quite small size. Let us delineate the circumstances associated with this fact.

As is well known,[12] the PDA transfers energy to the CAC micro-region in the amount of several tens of keV. Since the relaxation time of the CAC is very small ($\tau\cong10^{-11}-10^{-10}$ s, Ref. 12), it may be expected that after the passage of the CAC in this region of the crystal the positional disorder will be fixed and similar to the structure of the liquid phase. However, the experimental situation does not correspond to such a simple physical scheme. In fact, types of multicomponent solids are known (and here we are not speaking about pure metals) which are in general not amorphized by fast neutrons at 80 K (these include, for example, spinels[14] and FeNiCr alloys[15]), but are only atomically disordered.

In our view, in the construction of a realistic picture of radiation effects it is necessary to take account of the fact that the CAC micro-region is small; consequently, the lattice region surrounding it should block amorphization of this region at the relaxation stage. Within the framework of our model, restoration of the atomic periodicity in the CAC region can be held up by substitutional defects and point defects,[2)] if they cause sufficiently large local deformations of the crystal and their number exceeds some critical level.[11]

Unfortunately, a correct determination of the amplitude of the atomic displacements and concentration of point defects is difficult to wring out of diffraction experiments. Therefore we will estimate these quantities from indirect data and by calculation.

A point defect may be considered as a center giving rise to atomic displacements in its vicinity. For calculational purposes, we shall assume the medium surrounding the point defect to be an isotropic, elastic continuum. In this model, a displacement of an atom located a distance r from the defect takes place in the radial direction and is equal to[16]

$$U_{PD}=c/r^2, \tag{4}$$

where c is a constant characterizing the ''strength'' of the defect. Since vacancies in an irradiated alloy exist over a wide temperature range, in what follows we will take only this type of point defect into account. In the case of vacancies the atomic displacements are directed toward the defect and the constant c has the value $0.033v$, where v is the atomic volume. We shall give the calculated values of U_{PD} for $r=2$ and 5 Å. They are respectively 0.1 and 0.01 Å. Thus, the zone of local distortions due to a given vacancy is a sphere not greater than 5 Å in radius. It is logical to assume that the atomic-substitution distortions about the defects U_{AS} follow the same scheme. Distortions in the given case arise out of the 10% difference between the atomic radii of nickel and titanium. According to our estimates, the maximum amplitude of the atomic displacements (relative to their ideal positions in a $B2$ lattice) in the micro-region damaged by the CAC does not exceed $U=U_{PD}+U_{AS}=0.2$ Å. The need for atomic disordering in the amorphization mechanism of titanium nickelide is not limited to just the considerable contribution to the total magnitude of the atomic displacements. The need for it is apparently also connected with the fact that a higher concentration of point defects can be reached in a disordered alloy than in an ordered alloy.

The critical number of vacancies n ensuring amorphization of the micro-region damaged by the CAC can be estimated by $n=v/w$, where w is the volume of the zone distorted by an individual vacancy. This formula assumes that the zones w fill up the entire micro-region. The critical value of n is found to be 150. This amounts to about 1% of the total number of atoms in the CAC.

The estimated values of U and n are, in our opinion, physically reasonable; however, more direct and reliable methods for determining them are needed.

To summarize, in this paper we have constructed a model of the structural state of amorphous titanium nickelide, prepared by fast-neutron bombardment. According to this model, the amorphization that takes place in radiation-modified $Ti_{49}Ni_{51}$ is not the classical kind, but the so-called amorphization of distortion type. Here we are speaking of distortions of the initial crystal on the scale of the unit cell.

The centers of atomic displacements in the crystal are radiation defects, specifically atomic substitution defects (the atomic radii of titanium and nickel differ by 10%) and point defects (most probably, these are vacancies). In order for an amorphization effect to exist in a metallic alloy over a wide temperature interval, a certain number of point defects must be present in the crystal, capable of causing strong distortions of the crystal lattice.

According to our estimates, the maximum amplitude of the atomic displacements in modified titanium nickelide is around 7% of the initial lattice parameter, and the critical concentration of vacancies is equal to 1%. It is entirely natural that the atomic packing and the characteristics distances in such an amorphous phase should not differ greatly from the values of these parameters in the starting crystal. It is specifically for this reason that the macroscopic structure of the single crystal is regenerated after annealing an amorphous sample of titanium nickelide.

To elucidate the universality of the proposed model of amorphization of solids by fast neutrons, it is necessary to test this model for a large number of cases. Experiments on single-crystal samples are needed. Unfortunately, of the works cited[1–4] only in Ref. 4 was an experiment conducted on a single crystal sample, specifically a sample of gallium–gadolinium garnet. That the crystal belonged to the class of amorphous structures of distortion type was demonstrated by the result of an isochronous anneal of irradiated gallium–gadolinium oxide. After the anneal of the amorphous oxide

the macroscopic structure of the single-crystal sample was regenerated.

This work was carried out with the financial support of the State Scientific–Technical Program ''Neutron Studies of Matter'' (Project No. 96-104), the Russian Fund for Fundamental Research (Projects No. 98-02-17341 and No. 98-02-16166) and the Program of State Support for Leading Scientific Schools of the Russian Federation (Project No. 96-15-96515).

[1)]The reversibility of the macroscopic structure of the titanium nickelide single crystal, in our opinion, completely resolves the question whether the diffuse diffraction pattern in Fig. 1(c) is the result of formation of a nanostructure in the irradiated alloy.

[2)]Note here that in contrast to crystalline metals, defects in an amorphous solid cannot be considered as a local deviation from an ideal structure. A defect in an amorphous metal is a region in which the atomic density deviates significantly from its mean value. For example, negative (n-type) and positive (p-type) fluctuations of the atomic density occur. These two types of defects of the amorphous structure correspond to vacancies and interstitials in crystalline solids. With all due reservations, for simplicity we will maintain the terminology of point defects of an ideal crystal in further discussion of this experiment.

[1] Yu. Chukalkin, V. Stirts, and B. Goshchitskii, Phys. Status Solidi A **79**, 361 (1983).
[2] V. Arkhipov, V. Voronin, and B. Goshchitskii, Phys. Status Solidi A **86**, K59 (1984).
[3] V. E. Arkhipov, V. Voronin, and B. Goshchitskiĭ, Fiz. Met. Metalloved. **63**, 748 (1987).
[4] Yu. Chukalkin and V. Stirts, Phys. Status Solidi A **144**, 9 (1994).
[5] S. F. Dubinin, S. G. Teploukhov, and V. D. Parkhomenko, Fiz. Met. Metalloved. **82**, 136 (1996).
[6] R. B. Schwarz, R. R. Petrich, and C. K. Saw, Non-Cryst. Solids **76**, 281 (1985).
[7] W. Grant, Nucl. Instrum. Methods **182**, 809 (1981).
[8] C. C. Koch, O. B. Cavin, C. G. McKamey and J. O. Scarbrough, Appl. Phys. Lett. **43**, 1017 (1983).
[9] S. F. Dubinin, V. D. Parkhomenko, S. G. Teploukhov, and A. E. Khar'kin, Fiz. Met. Metalloved. **83**, 125 (1997).
[10] K. Handrich and S. Kobe, *Amorphe Ferro- und Ferrimagnetika* [in German] [Physik-Verlag, Weinheim, 1980; Moscow, 1982, p. 34].
[11] S. F. Dubinin, V. D. Parkhomenko, and S. G. Teploukhov, Fiz. Met. Metalloved. **85**, 6 (1998).
[12] V. V. Kirsanov, in *Computer Experiment in Atomic Materials Science* [in Russian], Moscow (1990), p. 302.
[13] A. Benyagoub and L. Thomé, Phys. Rev. **38**, 10205 (1988).
[14] V. Parkhomenko, C. Dubinin, and B. Goshchitskii, Phys. Status Solidi A **38**, 57 (1976).
[15] S. F. Dubinin, V. G. Vologin, and E. A. Kinevv, Fiz. Met. Metalloved. **77**, 63 (1994).
[16] G. J. Dienes and G. H. Vineyard, in *Radiation Effects in Solids* (Interscience, New York, 1957), p. 126.

Translated by Paul F. Schippnick

The role of auto-ionization transitions in the formation of the extended fine structure of high-energy secondary electron spectra

V. I. Grebennikov and O. B. Sokolov

Institute of Metal Physics, Urals Branch of the Russian Academy of Sciences, 620219 Ekaterinburg, Russia

D. E. Gaĭ, D. V. Surnin, and Yu. V. Rats

Physico-technical Institute, Urals Branch of the Russian Academy of Sciences, 426001 Izhevsk, Russia
(Submitted April 13, 1998)
Fiz. Tverd. Tela (St. Petersburg) **40**, 1589–1594 (September 1998)

Extended fine structure (EFS) of secondary electron (SE) spectra has been detected beyond the high-energy ($\sim$720 and $\sim$840 eV) LVV Auger lines in iron and nickel. Two mechanisms of its formation are considered: 1) direct transitions of electrons to the final state p according to Fermi's ''golden rule'' and 2) second-order processes of auto-ionization type, passing through excitation of a core electron to an intermediate state q of the continuum with subsequent filling of the hole formed during this process by a valence electron and transition of the electron from the intermediate state q to the final state p. Interference of the direct wave with the wave reflected from neighboring atoms generates the EFS both in the final (p) and in the intermediate (q) state with two different periods determined by the wave numbers p and q. Comparison of calculated extended fine structures with the experimentally observed ones leads to the conclusion that the structure is formed by second-order auto-ionization processes.
© *1998 American Institute of Physics.*[S1063-7834(98)00409-2]

Electron, x-ray, and optical spectroscopy are based on electron transitions from initial states to final ones, which are usually described by Fermi's ''golden rule.'' In traditional spectroscopy such an approach is well recommended. However, new experimental techniques have recently appeared which do not fit into the usual theoretical schemes and require the development of new approaches for their mathematical description. These include studies of the extended fine structure (EFS) arising in the secondary-electron (SE) spectra beyond the Auger lines in a solid body. The extended fine structure consists of oscillations in the intensity of SE emission with a period on the order of tens of electron-volts (eV) and an extent of hundreds of eV, lying on the high-energy side of the CVV Auger line (transitions in which a core level C and two valence (V) electrons participate). Such a structure was first observed by Chester and Pritchard[1] and Jenkins and Chung[2] in 1971. As the mechanism of its formation, MacDonnel *et al.*[3] in 1973 proposed coherent scattering of the experimentally recorded electrons by the crystal potential of the sample. The secondary-electron emission mechanism proposed in Ref. 3 is not energetically coupled with the Auger transition. This approach was developed further by a number of authors.[4–9] The most complete results within the framework of this approach were obtained in 1992 by Aebi *et al.*[10] They calculated the secondary-electron spectrum of copper and established a relationship between the calculated and experimentally observed spectral features for kinetic energies between 150 and 250 eV. The calculated maxima turned out to be noticeably shifted toward higher energies in comparison with the observed maxima. Moreover, the calculation generally does not reproduce the last three experimental peaks.

An alternative mechanism explaining the features of the secondary-electron spectrum beyond the MVV Auger lines in transition metals was proposed by Bader *et al.*[11] in 1983 and applied in 1986 by DeCrescenzi *et al.*[12,13] to interpret the oscillations in the secondary-electron spectrum. As the mechanism forming the EFS, Bader *et al.* proposed EXAFS-like scattering of electrons in an intermediate state which participates in an auto-ionization process. The auto-ionization mechanism affords a qualitative explanation of the location of the EFS on the high-energy side of the MVV Auger line of Co, Ni, and Cu, since the given process has an energy threshold coinciding with the position of the corresponding Auger line. In 1992 Grebennikov and Sokolov[14] developed a theoretical description of this process allowing for scattering of an electron by the surrounding atoms both in the intermediate and in the final state, which leads to the appearance of two structural terms in the spectrum.

Within the context of a cluster calculation, Vedrinskiĭ *et al.*[8] in 1995 estimated the intensities of various processes in the vicinity of the MVV Auger line of copper. They concluded that the spectrum is formed mainly as a result of direct emission of electrons from the valence states, and that the intensity of the auto-ionization process amounts to 10−15%. Unfortunately, they did not calculate the copper spectrum itself, rather its so-called Fourier filtration, which contains contributions only from the first coordinate sphere if it is assumed that the signal is formed by oscillations of only one type. Their calculation reproduces the period of the os-

 © 1998 American Institute of Physics

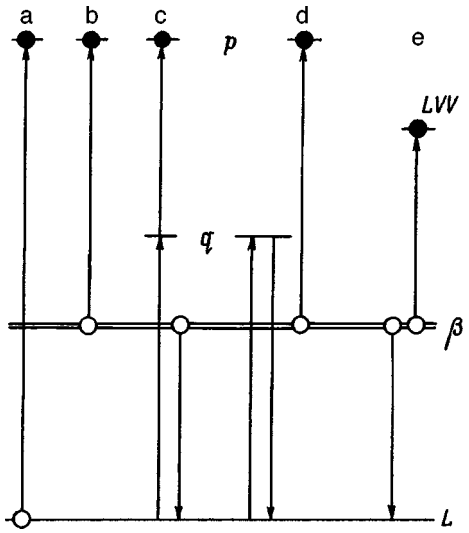

FIG. 1. Diagram of electron transitions. a, b — direct transitions from a core level L or valence band β to the final state p; c, d — second-order auto-ionization transitions through an intermediate state q to the same final state p; e — LVV Auger transition, defining the energy threshold of processes c and d.

cillations of the Fourier filtration, but differs noticeably from it in amplitude. Analytical estimates for arbitrary energies of the inner levels and kinetic energies of the contributions from the various processes forming the secondary-electron emission spectra, based on model wave functions, were made in Ref. 15, where it was shown that under certain conditions the intensity of the auto-ionization process can be comparable with the intensity of the direct transitions. We may also mention the polemics of the proponents of the two extreme views of the given problem by Woodruff[6] and De Crescenzi,[16] which is being carried on among researchers in this field[4–10,16–23] to this present day.

Summarizing the above discussion, it can definitely be said that at present there is no established set of ideas about the physical mechanism responsible for the formation of the EFS in secondary electron spectra, and that such a situation may lead to a loss of interest among experimenters in this method of spectroscopy. This is cause for regret since EFS can be a very useful tool for investigating the local atomic structure of a surface. Among its advantages are its energy selectivity, allowing one to determine the environment of atoms of specific chemical elements and, what is also important, the easy availability and simplicity of the experimental apparatus necessary for its realization: all one needs is an off-the-shelf Auger analyzer.

The aim of the present paper is to set up and carry out special experiments, which together with a theoretical interpretation of their results would make it possible to determine the physical mechanism of the EFS in secondary electron spectra.

1. THEORETICAL DESCRIPTION

Let us consider processes of secondary electron creation during inelastic scattering of high-energy electrons (3–10 keV). Figures 1(a) and 1(b) show the direct transitions of an electron from a core level (which, with a view to experiments which will be discussed presently, we denote by the symbol L) and from the valence band β to some final state p with energy varying from zero to 1 keV, which is measured by a detector. These standard transitions are described by first-order perturbation theory.

The transition in second-order theory to the same final state p is depicted by Fig. 1(c). It is realized in two steps: first, the core electron transitions to some intermediate state q, and the hole thus formed at the level L is then filled by a valence electron β, and the intermediary electron q transitions to the final state p. There also exists a corresponding exchange process [Fig. 1(d)]. The transitions shown in Figs. 1(c) and 1(d), are strongly reminiscent of the well-known auto-ionization process[24] with the difference that its first step, auto-ionization, takes place in the given case not from a localized low-energy resonance state, but from the state q, belonging to the continuum. Not forgetting this difference, we will also use the same term—auto-ionization—for the second-order transitions.

The amplitude of the second-order transition contains an integral over all possible intermediate states q. However, the well-known resonance denominator causes the contribution from the excited states to predominate. However, the energy of these states, to within their width (in our case $1-2$ eV), satisfies the energy conservation law;[25] therefore we may set $E_p - E_q \approx |E_\beta - E_L|$. Hence, it follows in particular that the auto-ionization transitions [Figs. 1(c) and 1(d)] have an energy threshold equal to the energy of the corresponding Auger line [Fig. 1(e)] while the direct transitions [Figs. 1(a) and 1(b)] begin from zero kinetic energy of the secondary electrons.

The experimental signal is equal to the sum of contributions from all processes shown in Fig. 1 (and also from transitions from other levels which are left out of the figure). Two paths are available in order to figure out which of these are the most important. The first is to carry out theoretical estimates of the probabilities of all the transitions in the solid (the EFS is formed as a result of scattering of electrons by the surrounding atoms). The second is to attempt to identify qualitative differences between the intermediate state q and final state p and, if any are found, determine the role of the second-order processes by comparing the characteristic features of the experimental signal with the theoretically predicted features.

Since both the intermediate state q and the final state p belong to the continuum, at first glance it may seem that there is no fundamental difference between them. In an atom such is indeed the case. However, in condensed matter the wave functions are distorted due to elastic scattering of waves by the immediate environment of the ionized (central) atom, which leads to the appearance of the EFS, as in EXAFS spectroscopy.[25–27] The reason for its appearance is the interference of waves. Figure 2 shows two waves: the direct wave, traveling in the direction of the detector, and a wave resulting from reflection by a neighboring atom. These waves have a phase difference which is determined by the geometrical path difference $l = R(1-\cos\theta)$ and the wave number p, where R is the distance to the atom and θ is the

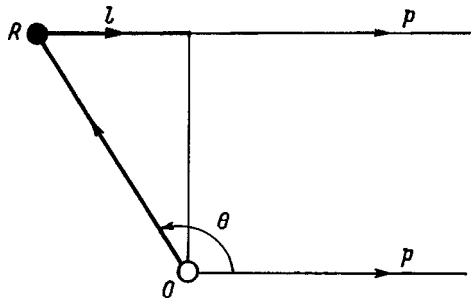

FIG. 2. Interference of the direct electron wave and the electron wave reflected from a neighboring atom, leading to the appearance of the extended fine structure (EFS).

scattering angle. The phase factor $\exp(ipl)$ leads to intensity oscillations in response to variations of the wave number p of the electron (or its energy $E_p=\hbar^2p^2/2m$). In Refs. 25 and 26 it was shown that for angular averaging (under the conditions of the experiment or, for example, in a polycrystal, amorphous material, etc.) the main contribution to the variable signal comes from backscattering ($\theta=\pi$) with the boundary value of the wave path difference $l=2R$. Wave interference takes place both in the final state p and in the intermediate state q; therefore the emission current contains two oscillating terms

$$J(p)=J_{\text{at}}(p)\left(1+\text{Re}\sum_j\left[A(p)\chi(p)+2B(p)\chi(q)\right]\right), \tag{1}$$

where

$$\chi(p)=f(p,\pi)(ipR_j^2)^{-1}W(p^2)\exp(i2(p+i\gamma)R_j). \tag{2}$$

Equation (1) contains a sum over the atoms j of the environment of the central atom. The contribution from the intermediate state q is also given by Eq. (2) with p replaced by q. The wave numbers are related by the law of conservation of energy

$$p^2/2-q^2/2=E_L. \tag{3}$$

Here E_L is the binding energy of the core level (in atomic units), $E_\beta\cong 0$, $J_{\text{at}}(p)$ is the atomic current, $f(p,\pi)$ is the backscattering amplitude of the jth atom, located a distance R_j from the center, γ is the inverse attenuation length of the wave in the material, $W(p^2)$ is the Debye–Waller factor, which depends on the temperature and the square of the momentum transfer and, finally, A and B are weighting factors, which assign the transition probabilities and also the scattering phases of the central atom.

The oscillating factors $\chi(p)$ and $\chi(q)$ have the same form as in the theory of x-ray absorption (EXAFS).[27] The quantity B is entirely determined by second-order processes while the quantity A is determined mainly by first-order transitions.[28–30]

Thus, the EFS of the secondary electron spectrum differs from the x-ray absorption (EXAFS) by an additional oscillating term $\chi(q)$, which depends on q, the wave number of the electron in the intermediate state (in the resonance approximation this term follows from conservation of energy). In the EFS beyond the low-energy MVV ($\sim$60 eV) Auger lines in $3d$ metals, which are the usual object of study here, the coefficient $A(p)$ is larger than the coefficient $B(p)$. However, because of their different energy dependence, separate spectral regions can exist, in which this relation is reversed. Taking into account the two different Debye–Waller factors $W(p^2)$ and $W(q^2)$ which govern the intensities of the terms this can lead to anomalies in the temperature behavior of the EFS spectra,[31] as are observed in iron and nickel.

Nevertheless, when low-energy levels are excited, the difference between the wave numbers in the final and intermediate states is small; therefore the periods of the oscillations $\chi(p)$ and $\chi(q)$ differ only insignificantly, which does not allow them to be clearly distinguished.

In order to make this difference apparent, we decided to look at the EFS above the high-energy and LVV Auger lines in iron and nickel.

2. EXPERIMENT

The experiment was performed on a JAMP-10S (JEOL) Auger spectrometer with a cylindrical-mirror energy analyzer ($\Delta E/E=0.35\%$) in backscattering geometry with a vacuum of 10^{-7} Pa or better. We examined a polycrystalline Fe sample (99.99) and a Ni (200) single crystal (99.99). The surfaces of the sample were pre-cleaned in an ultrasound bath of pure alcohol and acetone. In the analytic chamber of the device the surfaces of the samples were cleaned by ion etching (Ar^+, 1 kV) with a subsequent cyclic recrystallization anneal at 800 K (Ref. 32). During the course of the experiment the chemical purity of the surface was monitored by Auger electron spectroscopy, where the amount of impurity atoms, namely argon and carbon, in the investigated region did not exceed altogether one atomic percent.

The secondary electron spectra of iron and nickel were recorded in 1-eV steps. The final spectrum was obtained by summing 1000 scans, where each scan was obtained with a statistic of 1000 counts at each point of the energy scale, with the ratio of the EFS signal to noise ratio was $\sim$1/10. The EFS of the LVV spectrum of iron was obtained by integration, and the EFS of the LVV spectrum of nickel was made in the first-derivative regime (modulation amplitude $p-p$ 5 V). Both experiments were performed with the samples at room temperature. In the process of accumulating the spectra the investigated surfaces were cleaned by soft ion etching (Ar, 500 V) for 30 s after every 10 scans ($\sim$20 min). Intermediate etching of the surfaces by a soft ion beam allowed us to keep the amount of impurity atoms to a minimum during the course of the experiment. Although, for the purposes of this study, the type of surface structure has no fundamental importance (only the distance between neighboring atoms is important), it may be noted that, according to numerous studies (see, e.g., Ref. 33), ion beams of such energies leave the single-crystal character of the surface essentially untouched. The oscillating parts of the EFS were extracted from the experimental results by subtracting out the non-oscillatory component, which was approximated by a spline. The final nickel spectrum was obtained by numeri-

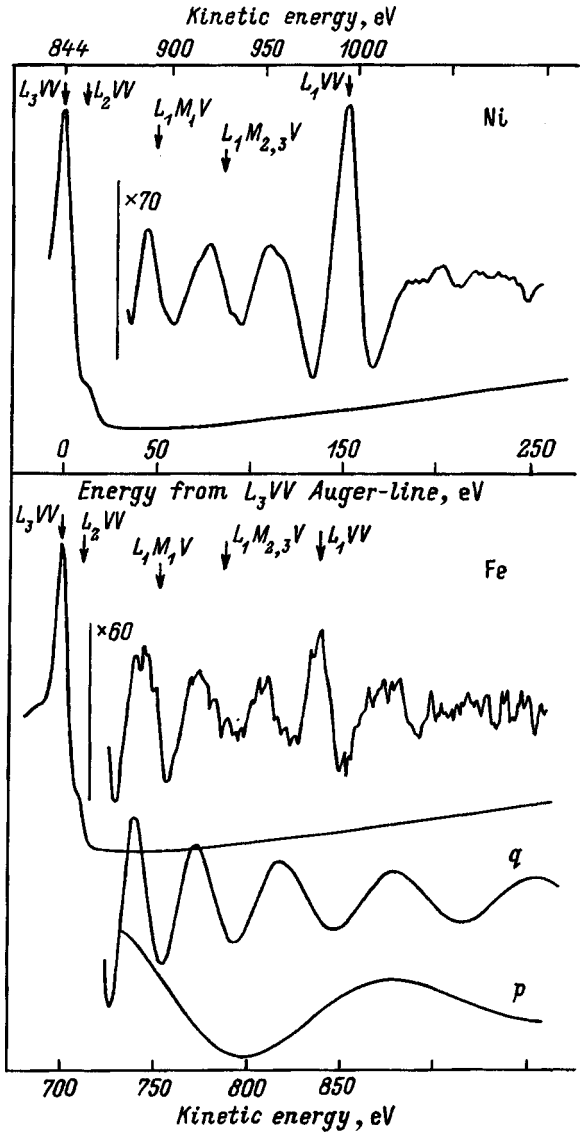

FIG. 3. Secondary electron spectrum of iron and nickel above the LVV Auger lines, and their oscillating parts. The arrows show the energies of all the Auger lines. Calculated signals from scattering in the intermediate state (q) (identical for Fe and Ni) and from scattering in the final state (p) for Fe.

cally integrating the raw spectrum obtained in the first-derivative regime.

3. RESULTS AND DISCUSSION

The EFS of the secondary electron spectra of iron and nickel are shown in Fig. 3. The kinetic energies of the secondary electrons for iron and nickel are plotted along the upper and lower horizontal axis, respectively. Both spectra are plotted against the same energy scale, with the L_3VV Auger lines of both elements lined up with the origin of this common scale. The energy measured from the L_3VV Auger peak is indicated on the middle axis (the common scale). If we take $E_\beta \approx 0$, then this is the energy of the intermediate resonance states E_q. Recall that the nickel spectrum was recorded in the first-derivative regime with subsequent integration; therefore it contains less noise than the iron spectrum.

The extent of the fine structure of the LVV spectra is not great (around 100 eV) in comparison with the MVV spectra. This is due to the small excitation cross section of the deep levels and decreased level of coherent scattering for electrons with large kinetic energy. The iron and nickel spectra contain almost the same oscillations, on which are the well-expressed L_1VV Auger lines are superimposed. Two more lines—L_1M_1V and $L_1M_{2,3}V$—are located in the given energy interval. Their contribution, along with the contribution of other Auger lines of possible impurity atoms, is discussed in detail below. We will show that their intensity is negligibly small. Therefore, let us first consider effects associated with coherent scattering in the intermediate and final states.

We base the analysis on the energy conservation law (3) establishing a connection between the observed electrons p and the intermediate resonance states q. The structural terms $\chi(q)$ and $\chi(p)$ lead to oscillations in the spectrum (1) in response to variation of the momentum p or energy E_p of the observed electrons. It is not hard to obtain a simple relationship between the periods of the oscillations originating from the intermediate state and the final state

$$T_q/T_p = q/p = \sqrt{1 - E_L/E_p}. \tag{4}$$

Since the binding energy E_L ($\sim$720 eV in Fe and $\sim$870 eV in Ni) and the kinetic energies E_p of the recorded electrons in the case of the LVV spectra are quite similar over the entire existence interval of the EFS, the periods T_q and T_p differ greatly, one from the other (by roughly a factor of three).

The interference terms $\mathrm{Re}\,\chi(p)$ and $\mathrm{Re}\,\chi(q)$ (in arbitrary units) are also plotted in Fig. 3. The functions $\chi(q)$ in nickel and iron coincide since the distance to neighboring atoms is the same in them: $R = 2.48$ Å. The functions $\chi(p)$, generally speaking, are different, but these differences are not large; therefore only one of them (for iron) is shown in the figure. Comparison of the experimental and calculated data clearly indicates that the observed extended fine structures originate in the coherent scattering in the intermediate states which take part in the auto-ionization process. Some difference between the phase of the experimental signal and that of the calculated function $\chi(q)$ in the region of the L_1VV Auger line may be due to the influence of this line and possible inaccuracies associated with it in the subtraction of the background—the non-oscillatory part of the spectrum. The almost complete coincidence of the oscillations in the iron and nickel spectra has as its origin the identical energies of the intermediate resonance states for the chosen manner of measuring the kinetic energies (for identical interatomic distances). Interference in the final states leads to periods completely different from those observed.

Note that a comparison of the periods of the two types of oscillations calculated according to Eq. (4) with the experimental results of De Crescenzi *et al.*[16] for the EFS of the $M_{4,5}VV$ lines of silver (energy $\sim$350 eV) leads to analogous results and conclusions.

The question now arises, why is the second-order perturbation theory, which one would naturally assume to be weaker, suddenly stronger than the first-order theory? Of course, we are not dealing here with atomic probabilities:

$A(p) \gg B(p)$ in Eq. (1). The reasons have to do with the physics of the solid state and consist in the significantly greater probability of coherent elastic scattering of the low-energy q electron by neighboring atoms in comparison with the high-energy electron p (Ref. 31). In Eq. (2) the amplitude $f(q, \pi) > f(p, \pi)$, but the decisive contribution comes from the Debye–Waller factor

$$W(p^2) = \exp\left(-\frac{2}{3} p^2 \langle \Delta R^2 \rangle \right) \tag{5}$$

and the analogous Debye–Waller factor $W(q^2)$, the argument of the exponential in both of which is proportional to the corresponding energy, E_p or E_q, as a result of which $W(q^2) \gg W(p^2)$. It is specifically for this reason that the oscillations formed by scattering in the intermediate states exceed the analogous oscillations due to scattering in the final states. The relative intensity of the signals from the intermediate (q) state and final (p) state is given by

$$\frac{Bp|f(q,\pi)|W(q^2)}{Aq|f(p,\pi)|W(p^2)}. \tag{6}$$

Using the electron backscattering amplitudes from the tables of Teo and Lee,[34] estimates from Ref. 31, and the Debye–Waller factors from Ref. 35, we find that the intensity of the q-type oscillations exceeds the intensity of the p-type oscillations by roughly a factor of three for Fe and a factor of 10 for Ni.

The examined fine structure of the secondary electron spectra is a very weak signal with amplitude around 1% of the constant component of the spectrum. This necessitates careful checking and analysis of possible alternative explanations of the experimental results. Let us turn now to the results of such an analysis.

In the energy interval under consideration, besides the L_1VV Auger line, two more lines appear (their energies are noted in Fig. 3) which previously went undetected due to their low intensity. The appearance of Auger lines from uncontrolled impurities atoms is also a possibility. In such a case, is it possible in the given precision experiment to reveal such Auger lines but no EXAFS-like structure? To answer this question, we recorded spectra at a raised sample temperature (500 K) under the same conditions and for the same statistics as the above-described spectra at $T = 300$ K. At $T = 500$ K the L_1VV Auger line remained, but the rest of the structure could not be extracted from the noise. In our opinion, this is evidence of the considered EXAFS-like mechanism. Auger transitions are specifically atomic processes and should not depend on thermal vibrations of the atoms. Contrary to this, the approach developed here is based on wave interference, which is governed by the interatomic distance and the Debye–Waller factors (5), which fall off rapidly with increase of temperature, $\langle \Delta R^2 \rangle \propto T$.

We performed another control experiment with the aim of checking the threshold nature of the mechanism of EFS formation. Spectra were recorded with energies less than the energy of the LMM series of Auger lines (in the interval of critical energies $400-600$ eV, where Auger peaks are absent). We were not able to detect an EFS in the spectral region. We propose the following interpretation. Coherent, elastic scattering in final states with such energy is weak (the backscattering amplitudes and the Debye–Waller factor are small) and the auto-ionization channel is practically excluded since the most probable (resonance) energy of the intermediate states $E_q \approx E_p - E_L < 0$ lies in the region of occupied states. This channel is opened when the energy of the secondary electrons exceeds the energy of the Auger line.

To summarize, we have shown theoretically and experimentally that extended fine structures in secondary electron spectra above the high-energy Auger lines (the $L_{2,3}VV$ lines of iron and nickel) are a new physical phenomenon, which is not encompassed within the framework of Fermi's standard ''golden rule.'' It has its origin in a threshold auto-ionization process, to which we must add coherent, elastic scattering of electrons of intermediate states by the immediate environment of the central atom.

[1] M. A. Chester and J. Pritchard, Surf. Sci. **28**, 460 (1971).
[2] L. H. Jenkins and M. F. Chung, Surf. Sci. **26**, 151 (1971).
[3] L. McDonnel, B. D. Powell, and D. P. Woodruff, Surf. Sci. **40**, 669 (1973).
[4] G. E. Becker and H. D. Hagstrum, J. Vac. Sci. Technol. **11**, 284 (1974).
[5] E. G. McRae, Surf. Sci. **44**, 321 (1974).
[6] D. P. Woodruff, Surf. Sci. **189/190**, 64 (1987).
[7] R. G. Agostino, A. Amoddeo, L. S. Caputi, and E. Colavito, Phys. Scr. **41**, 149 (1992).
[8] R. V. Vedrinskii, A. I. Taranukhina, A. A. Novakovich, and L. A. Bugaev, J. Phys.: Condens. Matter **7**, L181 (1995).
[9] N. K. Singh, R. G. Jones, and D. P. Woodruff, Surf. Sci. Lett. **232**, L228 (1990).
[10] P. Aebi, E. Erbudak, F. Vanini, and D. D. Vvedensky, Surf. Sci. Lett. **264**, L181 (1992).
[11] S. D. Bader, G. Zajac, and J. Zak, Phys. Rev. Lett. **50**, 1211 (1983).
[12] M. DeCrescenzi, E. Chinet, and J. Derrien, Solid State Commun. **57**, 487 (1986).
[13] E. Chainet, J. Derrien, R. C. Cinti, T. T. A. Nguyen, and M. DeCrescenzi, J. Phys. (Paris), Colloq. **47**, C8-209 (1986).
[14] V. I. Grebennikov and O. B. Sokolov, Phys. Scr. **41**, 5 (1992).
[15] V. I. Grebennikov and O. B. Sokolov, Fiz. Met. Metalloved. **78**, 113 (1994).
[16] M. DeCrescenzi, A. P. Hitchcock, and T. Tyliszczak, Phys. Rev. B **39**, 9893 (1989).
[17] T. Tyliszczak, A. P. Hitchcock, and M. DeCrescenzi, Phys. Rev. B **38**, 5768 (1988).
[18] M. DeCrenscenzi, Surf. Sci. Rep. **21**, 89 (1995).
[19] L. S. Caputi, A. Amoddeo, R. Tucci, and E. Cavalita, Surf. Sci. **251/252**, 262 (1991).
[20] I. Davoli, R. Bernardini, C. Battistoni, P. Castucci, R. Gunnella, and M. DeCrescenzi, Surf. Sci. **309**, 144 (1994).
[21] L. Lozzi, M. Passacantando, P. Picozzi, S. Suntucci, and M. DeCrescenzi, Surf. Rev. Lett. **2**, 225 (1995).
[22] M. Tomellini and M. Fanfoni, Solid State Commun. **90**, 391 (1994).
[23] M. DeCrescenzi, R. Gunnella, and I. Davoli, J. Electron Spectrosc. Relat. Phenom. **79**, 29 (1995).
[24] U. Fano and J. W. Cooper, Rev. Mod. Phys. **40**, 441 (1968).
[25] V. I. Grebennikov and O. B. Sokolov, Fiz. Tverd. Tela (St. Petersburg) **37**, 773 (1995) [Phys. Solid State **37**, 420 (1995)].
[26] V. I. Grebennikov and O. B. Sokolov, Jpn. J. Appl. Phys. **7**, 5713 (1995).
[27] P. A. Lee and J. B. Pendry, Phys. Rev. B **11**, 2728 (1975).
[28] D. E. Guy, V. I. Grebennikov, Yu. U. Ruts, S. P. Sentemov, and O. B. Sokolov, Jpn. J. Appl. Phys. **32**, *Suppl. 32-2*, 26 (1993).
[29] D. E. Guy, Yu. V. Ruts, S. P. Sentemov, V. I. Grebennikov, and O. B. Sokolov, Surf. Sci. **298**, 134 (1993).
[30] D. E. Guy, Yu. U. Ruts, D. V. Surnin, V. I. Grebennikov, and O. B. Sokolov, Physica B **208–209**, 87 (1995).
[31] D. E. Guy, Yu. U. Ruts, D. V. Surnin, V. I. Grebennikov, and O. B. Sokolov, Surf. Rev. Lett. **4**, 224 (1997).

[32] I. I. Novikov, *Theory of Heat Treatment of Metals* [in Russian], Metallurgiya, Moscow (1978), 286 pp.
[33] K. N. Eltsov, A. N. Klimov, S. L. Priadkin, V. M. Shevlyuga, and V. Yu. Yurov, Phys. Low-Dimens. Semicond. Struct. **7/8**, 115 (1996).
[34] B. K. Teo and P. A. Lee, J. Am. Chem. Soc. **101**, 2815 (1979).
[35] Landolt-Bornstein, *Phonon States of Elements* (Springer, Berlin, 1981), Vol. 13a, 458 pp.

Translated by Paul F. Schippnick

Effect of deuteration on the electronic and electron–vibrational properties of the organic conductor k-$(D_8$-BEDT–TTF$)_2$ [Hg(SCN)$_2$Br]

R. M. Vlasova, O. O. Drozdova, and V. N. Semkin

A. F. Ioffe Physicotechnical Institute, Russian Academy of Sciences, 194021 St. Petersburg, Russia

R. N. Lyubovskaya

Institute of Chemical Physics, Russian Academy of Sciences, 142432 Chernogolovka, Moscow Region, Russia

(Submitted February 25, 1998)
Fiz. Tverd. Tela (St. Petersburg) 40, 1595–1598 (September 1998)

We present here for the first time polarized reflection spectra and optical conductivity spectra of single crystals of the newly deuterated organic conductor k-$(D_8$-BEDT–TTF$)_2$[Hg(SCN)$_2$Br] at room temperature. The spectral region investigated is $700-40\,000\,\mathrm{cm}^{-1}$. We examined the effect of deuteration on electronic and electron–vibrational transitions observed in the spectra. The observed shift of the electron ''dimer'' transition in the infrared toward lower frequencies upon deuteration is linked with an increase in the interaction between neighboring, mutually perpendicular dimers in the structure of the deuterated crystal. A lowering of the symmetry of the BEDT–TTF molecule is demonstrated in crystals similar to k-(BEDT–TTF$)_2$ [Hg(SCN)$_2$Br], relative to the symmetry D_{2h} of the free molecule. We refine the assignment of the spectral features determined by the interaction of electrons with the fully-symmetric intramolecular vibrations of the C=C, C–S, and C–C–H bonds of the BEDT–TTF molecule. © *1998 American Institute of Physics.* [S1063-7834(98)00509-7]

As of the present time, a large number of highly conducting, low-dimensional organic compounds based on donor and acceptor molecules have been synthesized, manifesting a wide variety in their chemical composition, stoichiometry, crystal structure, and other properties.[1–3] Ion-radical salts based on the bis(ethylenedithio)tetrathiafulvalene (BEDT–TTF) molecule occupy a central place among these compounds since they include superconductors with the highest superconducting transition temperatures for organic compounds ($T_c > 10\,\mathrm{K}$)[1,2] and conductors that undergo transition to the insulating state at lower temperatures.[1,3] Compounds of both types often have very similar crystal structures, packing of the BEDT–TTF molecules in conducting layers, and band filling.

Recently, we carried out optical studies on the electronic structure and electron–vibrational interaction of a new group of isostructural organic conductors having metal–insulator transition, based on this molecule: k-(BEDT–TTF$)_2$ [Hg(SCN)$_2$Br], k-(BEDT–TTF$)_2$[Hg(SCN)Cl$_2$] (Ref. 4), and k-(BEDT–TTF$)_2$[Hg(SCN)$_2$Cl] (Ref. 5). These studies showed that the chemical modification of the anion taking place in this series of compounds leads to considerable quantitative differences in their optical properties. Thus, for example, a substantial difference in the oscillator strengths of the electronic and electron–vibrational transitions in the infrared is observed in the indicated series of salts, along with a corresponding difference in the effective mass of the quasi-two-dimensional valence electrons and, apparently a difference in the electron–electron interaction.

In the course of these studies we investigated the optical spectra of a bromine-containing salt in which the BEDT–TTF molecule was modified by isotopic substitution of deuterium for hydrogen: k-$(D_8$-BEDT–TTF$)_2$[Hg(SCN)$_2$Br]. The effect of isotopic substitution in the BEDT–TTF molecule on its optical properties was investigated for the superconductors k-(BEDT–TTF$)_2$[Cu(SCN)$_2$] (Refs. 6–8) and k-(BEDT–TTF$)_2$Cu[N(CN)$_2$]Br (Refs. 9 and 10). The goal of these studies was to examine the electron–vibrational interaction (EVI) characteristic of these objects and the relation between its features manifested in the infrared spectra and the shape of the vibrations. A study of the crystal structure and electrical conductivity of the deuterated conductor k-$(D_8$–BEDT–TTF$)_2$[Hg(SCN)$_2$Br] was presented in Ref. 11. The results of this study are used in part here in the discussion of the results of the present study.

1. EXPERIMENT

The crystals of k-$(D_8$–BEDT–TTF$)_2$[Hg(SCN)$_2$Br] (the D_8 salt, for short) and k-$(H_8$–BEDT–TTF$)_2$[Hg(SCN)$_2$Br] (the H_8 salt) are isostructural and belong to the monoclinic system $B2/b$, $Z=4$. The main crystallographic parameters of the D_8 salt are: $a=37.044$, $b=8.307$, $c=11.721$ Å, $\beta=89.30°$, $V=3607\,\text{Å}^3$, and of the H_8 salt are: $a=37.039$, $b=8.321$, $c=11.713$ Å, $\beta=89.66°$, $V=3610\,\text{Å}^3$ (Ref. 11) (the notation of the crystallographic parameters is that used in Ref. 12).

The crystal structure of both salts consists of two-dimensional layers of the cation–radicals BEDT–TTF parallel to the (100) plane which alternate along the a axis with layers of the polymeric anion $[\mathrm{Hg(SCN)_2Br}]^-$. The cation–

 © 1998 American Institute of Physics

radical layers consist of the dimers $(BEDT-TTF)_2^+$ packed orthogonally, one with respect to the other (the *k* phase). In the structure of the cation layer there are two shortened intermolecular contacts S...S in the dimers and six shortened intermolecular contacts between the dimers. Important differences in the structure of the cation layer are observed only in the interplanar distances between the molecules forming the dimers (3.51 Å in the H_8 salt and 3.58 Å in the D_8 salt) and in the values of the angles between the central C=C bond of the BEDT–TTF molecule and the *c* axis (87.21° in the H_8 salt and 91.05° in the D_8 salt). The anions form chains extending along the *c* axis.

The crystals are thin, black, shiny, not completely formed rhombic platelets with the most developed (100) face having typical dimensions $0.5\times0.5\times0.05$ mm. The *c* and *b* axes are directed parallel and perpendicular to the long diagonal of the rhombus, respectively. The *a* axis is perpendicular to the most developed face.

Polarized reflection spectra $R(\omega)$ for almost normal incidence of the incoming light on the various faces of the crystals were measured at room temperature on a Bruker IFS-88 infrared Fourier spectrometer constructed from an infrared microscope and a KRS-5 polarizer, in the spectral range $700-5500\,cm^{-1}$ and on a double-beam microspectroreflectometer developed at GOI (State Optical Institute), with a Glen–Thompson prism as the polarizer in the spectral range $9000-40\,000\,cm^{-1}$. The diameter of the light probes of the two instruments was 75 and 25 μm, respectively. The absolute value of the reflection coefficient *R* was determined from ratios to an aluminum mirror and two standard reference mirrors made out of SiC and quartz. The reflection spectra in the spectral range $700-5500\,cm^{-1}$ were recorded in the regime of extended accumulation of interferograms (up to 10 000 scans), which allowed us to achieve a high (>20) signal-to-noise ratio for such small crystals. The absolute measurement error in the second spectral range was 1.5%. Reflection was measured from the natural growth face of the crystals (100), where we chose the most specular segment of the surface for the measurements. The crystals were oriented in the light wave field along the long diagonal of the rhombus **c**: $\mathbf{E}\|\mathbf{c}$ and $\mathbf{E}\perp\mathbf{c}(\|\mathbf{b})$.

Optical conduction spectra $\sigma(\omega)$ were obtained from the reflection spectra by means of the Kramers–Kronig relations. The technique used in the calculations for extrapolating the reflection spectra to lower and higher frequencies, and also into the region $5500-9000\,cm^{-1}$, is described in our earlier papers.[4,5]

2. EXPERIMENTAL RESULTS AND DISCUSSION

Figures 1 and 2 display reflection spectra from the (100) face of k-$(D_8$-BEDT–TTF$)_2$[Hg(SCN)$_2$Br] in the spectral range $700-40\,000\,cm^{-1}$, the polarizations without the electric vector of the light wave **E** parallel to the *b* and *c* axes, respectively. For comparison, the corresponding reflection spectra of k-$(H_8$-BEDT–TTF$)_2$[Hg(SCN)$_2$Br] from our previous paper (Ref. 4) are also shown.

Optical conductivity spectra $\sigma(\omega)$ of the D_8 and H_8 salts in the range $800-5500\,cm^{-1}$, obtained from the reflection

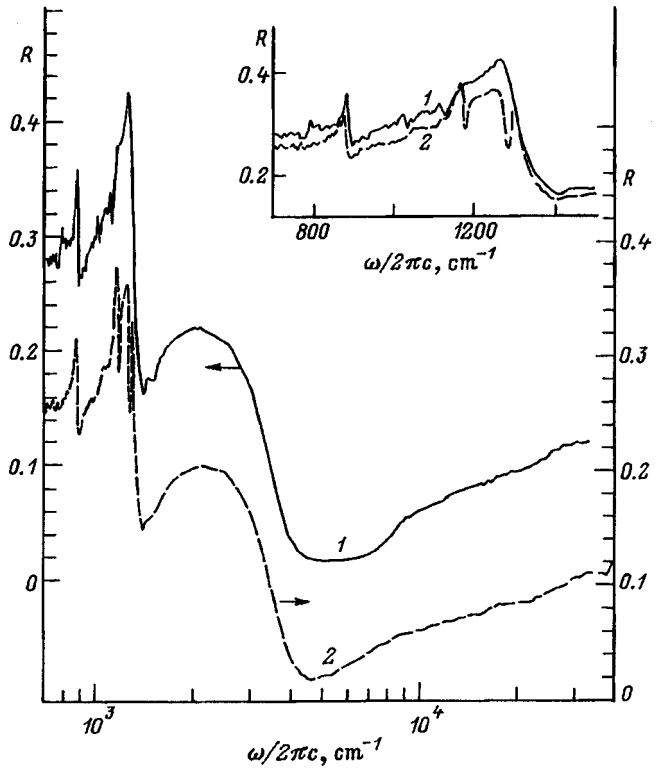

FIG. 1. Reflection spectra of k-$(D_8$-BEDT–TTF$)_2$[Hg(SCN)$_2$Br] (*1*) and k-$(H_8$-BEDT–TTF$)_2$[Hg(SCN)$_2$Br] (*2*) single crystals from the (100) face in $\mathbf{E}\|\mathbf{b}$ polarization. The inset displays the low-frequency part ($700-1500\,cm^{-1}$) of the spectrum, in which the structural features of the electron–vibrational interaction are located.

spectra for $\mathbf{E}\|\mathbf{b}$ and $\mathbf{E}\|\mathbf{c}$, are shown in Figs. 3 and 4, respectively. The general form of the spectra and their anisotropy are typical of conducting BEDT–TTF salts in the *k* phase. A wide maximum in the $\sigma(\omega)$ spectra is observed at $2100-2400\,cm^{-1}$ for $\mathbf{E}\|\mathbf{b}$ and at $2600-2800\,cm^{-1}$ for $\mathbf{E}\|\mathbf{c}$, which, according to the data of Ref. 5, is determined chiefly by charge transport between BEDT–TTF molecules in the dimer. The low-frequency side of this electronic maximum has characteristic vibrational structure, due, as is well known, to interaction of the electrons with the fully symmetric, intramolecular vibrations (A_g) of the BEDT–TTF molecule. It can be seen from Figs. 3 and 4 that upon deuteration the maximum undergoes a weak shift (of approximately $200\,cm^{-1}$) toward lower frequencies. A calculation of the $\sigma(\omega)$ spectra based on a cluster (''tetrameric'') theory of optical properties developed for *k*-phase salts in Ref. 13 showed that the shift of the electronic maximum toward lower frequencies results from taking the interaction between neighboring, mutually perpendicular dimers into account. Therefore, the observed shift of the electronic maximum in the spectra is apparently evidence of an increase in this interaction caused by deuteration. It may be conjectured that the increase in the role of the interaction between neighboring dimers in charge transport is due to the above-indicated increase in the distance between BEDT–TTF molecules in the dimer upon deuteration (without any change in the corresponding distances between dimers).

Figures 3 and 4 show that the largest change in the deu-

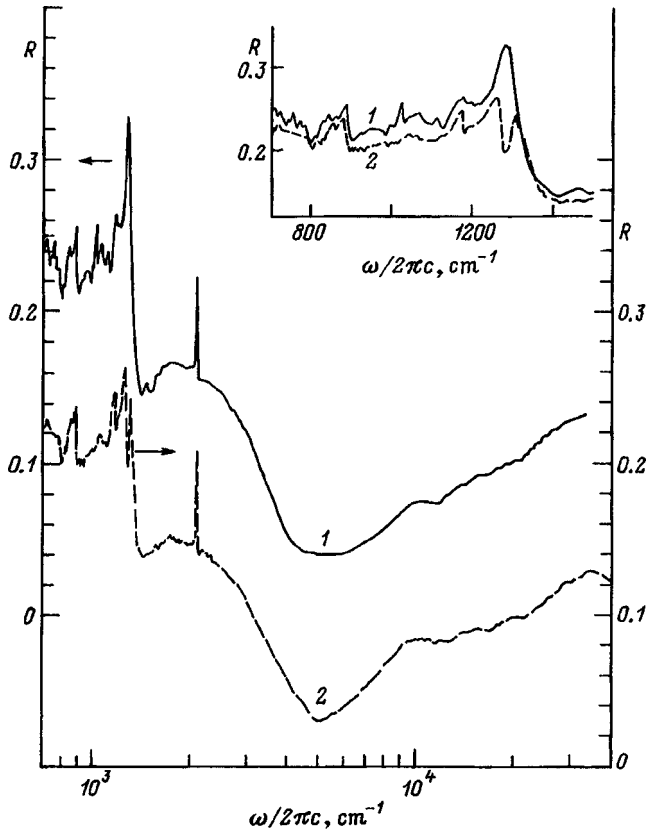

FIG. 2. Reflection spectra of k-(D_8-BEDT–TTF)$_2$[Hg(SCN)$_2$Br] (*1*) and k-(H_8-BEDT–TTF)$_2$[Hg(SCN)$_2$Br] (*2*) single crystals from the (100) face in the $\mathbf{E}\|\mathbf{c}$ polarization. The inset displays the low-frequency part (700 $-1500\,\mathrm{cm}^{-1}$) of the spectrum, in which the structural features of the electron–vibrational interaction are located.

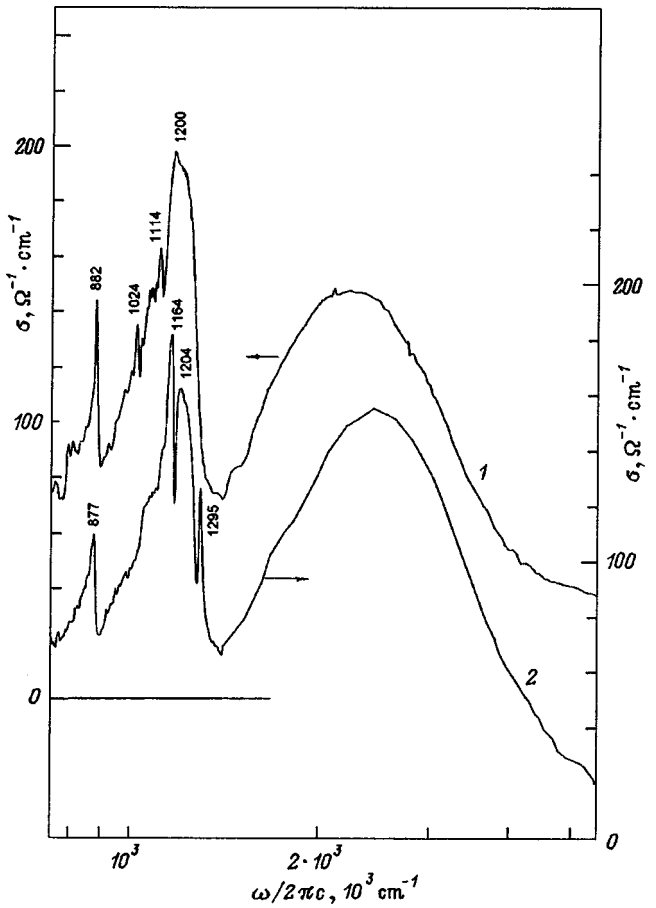

FIG. 3. Optical conductivity spectra of crystals of k-(D_8-BEDT–TTF)$_2$[Hg(SCN)$_2$Br] (*1*) and k-(H_8-BEDT–TTF)$_2$[Hg(SCN)$_2$Br] (*2*) for $\mathbf{E}\|\mathbf{b}$. The numbers next to the curves give the positions of the maxima (in cm^{-1}) of the main features of the electron–vibrational interaction.

terated $\sigma(\omega)$ spectra occurs in the region of electron–vibrational structure ($\sim 850-1350\,\mathrm{cm}^{-1}$). It can be seen that the intense electron–vibrational bands observed in the spectra of the H_8 salt at 1295 and 1164 cm^{-1} for $\mathbf{E}\|\mathbf{b}$ and at 1305 and 1174 cm^{-1} for $\mathbf{E}\|\mathbf{c}$ in the spectra of the D_8 salt are absent. In their place new, weaker bands appear at lower frequencies: 1114 and 1024 cm^{-1} ($\mathbf{E}\|\mathbf{b}$), 1115 and 1024 cm^{-1} ($\mathbf{E}\|\mathbf{c}$). The assignment of the electron–vibrational features observed in the spectra can be made assuming either D_{2h} symmetry (as in Ref. 14) or D_2 symmetry (as in Ref. 15) of the ET molecule. In the first case, there are 12 fully symmetric, intramolecular vibrations while in the second case there are 19 fully symmetric vibrations. For D_2 symmetry there are two vibrations of the isolated BEDT–TTF molecule in the indicated region which include motions of the hydrogen atoms—the deformational vibrations of the C–C–H groups $A_g\nu_6$ and $A_g\nu_7$ (observed values 1281 and 1147 cm^{-1}, calculated values 1289 and 1195 cm^{-1}, respectively, Ref. 15). For D_{2h} symmetry in this region there is only one such vibration at 1290 cm^{-1} (Ref. 14). The shift of the two vibrational features toward lower frequencies observed upon deuteration points to a lowering of the symmetry of the BEDT–TTF molecule in a crystal relative to the D_{2h} symmetry of the isolated molecule and confirms our earlier assignment[4,5] to the vibrations $A_g\nu_6$ and $A_g\nu_7$. The authors of Ref. 9, departing from the symmetry of the molecule, which is D_{2h}, assign the feature at 1174 cm^{-1} to vibrations with symmetry B_{3u} or B_{2g}.

It can be seen from Figs. 3 and 4 that the intense, wide feature at 1204 cm^{-1} ($\mathbf{E}\|\mathbf{b}$) and 1257 cm^{-1} ($\mathbf{E}\|\mathbf{c}$) in the spectrum of the H_8 salt, which, as we represented it in Ref. 4, is the $A_g\nu_4$ vibration due to an interaction of the electrons with the valence vibrations of the central C=C bond, (observed value 1494 cm^{-1}, calculated value 1549 cm^{-1}, Ref. 15) is shifted insignificantly upon deuteration. The inset to Fig. 1 shows that the features due to the interaction of the electrons with the vibrations $A_g\nu_6$ and $A_g\nu_7$ appear in the reflection spectrum for $\mathbf{E}\|\mathbf{b}$ in the form of dips in this wide band. Such a form is evidence of interference of the three indicated electron–vibrational states. In the $\mathbf{E}\|\mathbf{c}$ polarization this fact is not so clearly noticeable. It should be noted that the participation of the deformational vibrations of the H–C–H bonds ($A_g\nu_5$, 1421 cm^{-1}) in the electron–vibrational interaction (EVI) remains unclear.

We assign the sharp peak at 877 cm^{-1} ($\mathbf{E}\|\mathbf{b}$) and 881 cm^{-1} ($\mathbf{E}\|\mathbf{c}$) to valence vibrations of the C–S groups ($A_g\nu_{10}$, 876 cm^{-1}). It can be seen that this band undergoes a weak positive shift ($+5\,\mathrm{cm}^{-1}$ for $\mathbf{E}\|\mathbf{b}$ and $+7\,\mathrm{cm}^{-1}$ for $\mathbf{E}\|\mathbf{c}$) upon deuteration. A theoretical calculation of the fundamental vibrations, including the C–S bonds, for isolated

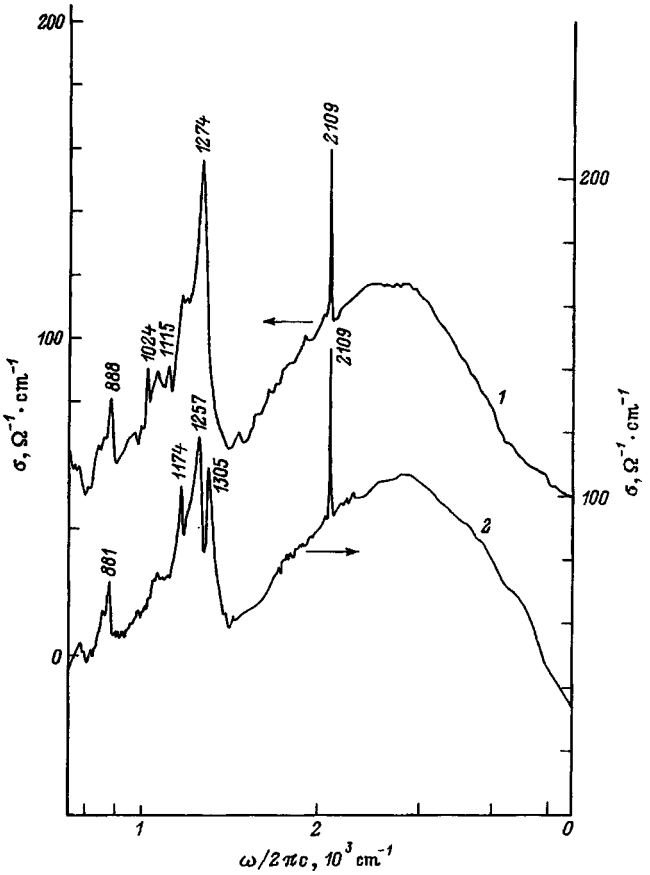

FIG. 4. Optical conductivity spectra of crystals of k-(D_8-BEDT–TTF)$_2$[$Hg(SCN)_2Br$] (*1*) and k-(H_8-BEDT–TTF)$_2$[$Hg(SCN)_2Br$] (*2*) for $\mathbf{E}\|\mathbf{c}$. The numbers next to the curves give the positions of the maxima (in cm^{-1}) of the main features of the electron–vibrational interaction.

molecules of H_8- and D_8-BEDT–TTF (Ref. 14) also indicates a small positive shift ($+15\,cm^{-1}$) upon deuteration.

It should be emphasized that strong bands at 1486, 1276, 1174, and $912\,cm^{-1}$ are observed in the Raman spectra of the related salt k-(BEDT–TTF)$_2$Cu[$N(CN)_2$]Br (Ref. 9). This fact confirms our assignment of the intense EVI features in the infrared spectra of the investigated compounds.

Besides the EVI features in the $\sigma(\omega)$ spectra of both salts for $\mathbf{E}\|\mathbf{c}$ already considered (Fig. 4), we also observed a very narrow band at $2109\,cm^{-1}$, which we assigned in Ref. 4 to optically active valence vibrations of the CN groups of the polymeric anion. It can be seen that this band is identical in shape and position for both these salts, i.e., it is insensitive to the changes in the configuration of the SCN groups observed in Ref. 11 upon deuteration.

We wish to thank B. Z. Volchok for helpful methodological consultations and assistance with the measurements of the infrared reflection spectra.

This work was performed with the financial support of the State Scientific–Technical Program ''Superconductivity'' within the scope of Project No. 94055 and partial financial support of the Russian Fund for Fundamental for Basic Research (Grant No. 98-02-18303).

[1] J. M. Williams, J. R. Ferraro, R. J. Thorn, K. D. Carlson, U. Geiser, H. H. Wang, A. M. Kini, and M.-H. Whangbo, *Organic Superconductors (Including Fullerenes): Synthesis, Structure, Properties, and Theory* (Prentice Hall, Englewood Cliffs, New Jersey, 1992), 367 pp.
[2] G. Saito, A. Otsuka, and A. A. Zakhidov, Mol. Cryst. Liq. Cryst. **284**, 3 (1996).
[3] M. Z. Aldoshina, R. N. Lyubovskaya, S. V. Konovalikhin, O. A. Dyachenko, G. V. Shilov, M. K. Makova, and R. B. Lyubovskii, **55–57**, 1905 (1993).
[4] R. M. Vlasova, O. O. Drozdova, R. N. Lyubovskaya, and V. I. Semkin, Fiz. Tverd. Tela (St. Petersburg) **37**, 703 (1995) [Phys. Solid State **37**, 382 (1995)].
[5] R. M. Vlasova, N. V. Drichko, O. O. Drozdova, and R. N. Lyubovskaya, Fiz. Tverd. Tela (St. Petersburg) **39**, 1313 (1997) [Phys. Solid State **39**, 1165 (1997)].
[6] M. Tokumoto, H. Anzai, K. Takahashi, K. Murata, N. Kinoshita, T. Ishiguro, Y. Tanaka, Y. Hayakawa, H. Nagamori, and K. Nagasaka, Synth. Met. **27**, A171 (1988).
[7] T. Sugano, H. Hayashi, M. Kinoshita, and K. Nishikida, Phys. Rev. B **39**, 11 387 (1989).
[8] K. Kornelsen, J. E. Eldridge, H. H. Wang, and J. M. Williams, Phys. Rev. B **44**, 5235 (1991).
[9] J. E. Eldridge, Y. Xie, H. H. Wang, J. M. Williams, A. M. Kini, and J. A. Schlueter, Spectrochim. Acta A **52**, 45 (1996).
[10] J. E. Eldridge, Y. Xie, H. H. Wang, J. M. Kini, and J. A. Schluener, Mol. Cryst. Liq. Cryst. **284**, 97 (1996).
[11] E. I. Yudanova, S. K. Hoffmann, A. Graja, S. V. Konovalikhin, O. A. Dyachenko, R. B. Lyubovskii, and R. N. Lyubovskaya, Synth. Met. **73**, 227 (1995).
[12] S. V. Konovalikhin, G. V. Shilov, O. A. D'yachenko, M. Z. Aldoshina, R. N. Lyubovskaya, and R. B. Lyubovskiĭ, Izv. Akad. Nauk. SSR, Ser. Khi. **10**, 2323 (1992).
[13] V. M. Yartsev, O. O. Drozdova, V. N. Semkin, and R. M. Vlasova, J. Phys. I **6**, 1673 (1996).
[14] M. E. Kozlov, K. I. Pokhodnia, and A. A. Yurchenko, Spectrochim. Acta A **43**, 323 (1987).
[15] M. Meneghetti, R. Bozio, and C. Pecile, J. Phys. (France) **47**, 1377 (1986).

Translated by Paul F. Schippnick

Influence of magnetic scattering centers in the insulator component of the composite HTSC+$Cu_{1-x}Ni_xO$ on its resistive properties

M. I. Petrov, D. A. Balaev, K. A. Shaĭkhutdinov, and S. G. Ovchinnikov

L. V. Kirenskiĭ Institute of Physics, Siberian Branch of the Russian Academy of Sciences, 660036 Krasnoyarsk, Russia

(Submitted February 2, 1998)
Fiz. Tverd. Tela (St. Petersburg) **40**, 1599–1603 (September 1998)

We present results of an experimental study of the effect of magnetic scattering centers (nickel) in the insulator component (cuprous oxide) of the composite HTSC+$Cu_{1-x}Ni_xO$ on its transport properties. A suppression of the superconducting properties of this system is observed to take place with increasing nickel content. The results are analyzed within the framework of the model of strong electron correlations. © *1998 American Institute of Physics.* [S1063-7834(98)00609-1]

Weak bonds in materials based on HTSC's are presently under intense study, both theoretically and experimentally, motivated by the fact that they display most strikingly carrier-pairing regularities.[1] A study of the transport properties of two-component composite samples, one whose components is a HTSC and the other is either an insulator (I) or semiconductor (Sm) or normal metal (N), is tantamount to a study of the transport properties of an artificially created network of weak bonds of given type ($S-I-S$, $S-Sm-S$, $S-N-S$, where S is a superconductor).[2–8] Despite the fact that the weak bonds in such composites are distributed randomly with respect to geometrical dimensions, the transport characteristics [temperature dependence of the critical current $J_c(T)$ and resistance $R(T)$, current–voltage characteristics (CVC)] reflect the primary regularities of supercurrent flow through an effective contact of the corresponding type. We prepared composites based on the classical HTSC $Y_{3/4}Lu_{1/4}Ba_2Cu_3O_7$ and CuO.[8,9] We showed that such a system is an example of a network of weak bonds of $S-I-S$ type. Current–voltage characteristics of quasitunneling type and thermally activated phase slippage (TAPS) are characteristic of such a system below T_c (Ref. 10). When CuO is transformed by lithium doping into a superconductor, composites based on it manifest the characteristics of a network of weak $S-Sm-S$ bonds — specifically, we are looking here at a transformation of the CVC from quasitunneling to metallic and the appearance of a plateau in $J_c(T)$ in the low-temperature region as a result of increased carrier concentration in the superconductor constituent.[7,11] A study of HTSC+$BaPbO_3$ composites with paramagnetic impurities introduced in the normal metal $BaPbO_3$ (Ref. 12) motivated us to examine the influence of magnetic scattering centers introduced in the insulator component of the HTSC+CuO composite. The choice of CuO is based on the experimental observation of an absence of chemical interaction between the HTSC with $1-2-3$ structure and the cuprous oxide, as was shown by electron microscopy[13] and x-ray diffraction studies.[8,13] Although CuO is a semiconductor, at temperatures below 100 K its resistivity (ρ) is 15 orders of magnitude larger than the resistivity of the HTSC;[14] for this reason CuO can be taken to be an insulator in our case. Doping of CuO by isovalent nickel should not, in our opinion, lead to the induction of valence and the appearance of impurity carriers in contrast to nonisovalent doping of CuO by Li (CuO:Li), which gives rise to a substantial growth in the conductivity and even a change in its character with increasing concentration of impurity carriers.[7,15] In Refs. 16–18 it was theoretically shown that magnetic impurities introduced into the insulting barrier also suppress the Josephson supercurrent. The present paper reports an experimental study of the influence of a nickel impurity in a CuO matrix on the resistive properties of HTSC+$Cu_{1-x}Ni_xO$ composites.

1. EXPERIMENT

Composite samples having the formula HTSC+$Cu_{1-x}Ni_xO$ were prepared in the following way. First, the initial components of the composite to be prepared were synthesized: $Y_{3/4}Lu_{1/4}Ba_2Cu_3O_7$ and $Cu_{1-x}Ni_xO$. The standard ceramic technique was used to synthesize $Y_{3/4}Lu_{1/4}Ba_2Cu_3O_7$. $Cu_{1-x}Ni_xO$ was prepared by the ceramic technique from CuO and NiO at 950 °C. The synthesis time was ~40 h with several intermediate grindings.

A Debyegram of the sample with the largest x—$Cu_{0.94}Ni_{0.06}O$ (samples with $x<0.06$ were not investigated since the standard x-ray technique does not give reliable results in this case)—revealed the presence of two crystallographic phases in which a solid solution the system $(CuO)_{1-x}(NiO)_x$ can exist. These results are in full agreement with the conclusions of Ref. 19. Magnetic measurements were performed in the components of the composite $Cu_{1-x}Ni_xO$ with $x=0$, 0.01, 0.03, 0.06 using a vibrating magnetometer.[20] Figure 1 plots the magnetization dependence on the temperature of the samples in the interval 4.2 -300 K, measured in a field $H=5$ kOe. A monotonic increase of the absolute value of the magnetization with increase of the nickel content is evident in the samples, as well as a decrease of the Néel temperature with increase of x (for

 © 1998 American Institute of Physics

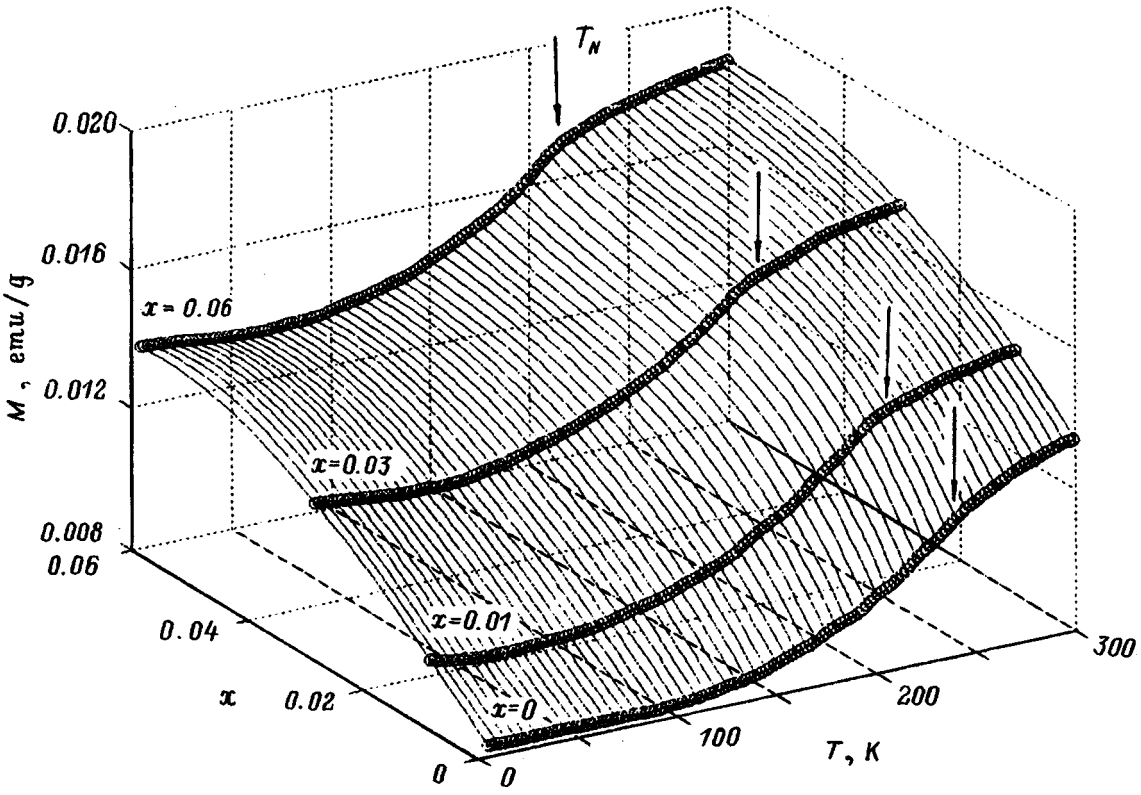

FIG. 1. Temperature dependence of the magnetization M of $Cu_{1-x}Ni_xO$ as a function of x. $x=0$, 0.01, 0.03, 0.06. Isotherms are drawn with a 5 K step. Arrows indicate the Néel temperature.

CuO T_N is $\sim$250 K, which is in qualitative agreement with the data of Refs. 14 and 21). Although this value is somewhat larger than the value measured by other authors and is probably due to impurities and a possible oxygen nonstoichiometry, what is more important in the given case is the relative variation of the Néel temperature with doping of CuO with nickel. Measurements of the magnetization $M(H)$ of the components of the composites were performed in fields up to 60 kOe at $T=4.2$ K. All of the dependences turned out to be linear, their slopes increasing monotonically with growth of x. Analysis of these measurements showed that the magnetization is additive in the nickel concentration. On the basis of magnetic measurements and x-ray diffraction studies, we can describe the $Cu_{1-x}Ni_xO$ system as an antiferromagnetic CuO matrix in which copper atoms are randomly replaced by nickel atoms. These atoms can enter as additional magnetic scattering centers for carriers of the superconducting current in a network of weak $S-I-S$ bonds with a barrier formed from such material.

The mixture of powdered components of the composite to be formed, taken in the required proportions (85 vol% HTSC and 15 vol% $Cu_{1-x}Ni_xO$), were pressed into pellets which were then loaded into the working zone of a furnace heated to 910 °C. The pellets were kept at this temperature for 2 min and then loaded into a second furnace at 350 °C, where they were kept for 3 h, after which they were allowed to cool in the furnace. All of the samples investigated in this work were prepared from a single series of initial ingredients to avoid random deviations of their physical properties associated with possible impurities and variations in their stoichiometry and particulars of their preparation.

Figure 2 plots the resistivity of samples of the composite HTSC+$Cu_{1-x}Ni_xO$ as a function of temperature and composition, normalized to ρ (93.5 K) for $x=0$, 0.01, 0.03, 0.06. The absolute values of ρ (93.5 K) of the composites were 0.055 $\Omega\cdot$cm for $x=0$, 0.069 $\Omega\cdot$cm for $x=0.01$, 0.061 $\Omega\cdot$cm for $x=0.03$, and 0.059 $\Omega\cdot$cm for $x=0.06$, i.e., within the limits of measurement error the values of the resistivity at 93.5 K [ρ (93.5 K)] for all samples of the composite HTSC+$Cu_{1-x}Ni_xO$ can be taken to be identical. Hence we conclude that nickel is not an additional scattering center for ordinary current carriers as they tunnel through the insulating interlayer. The form of the $\rho(T)$ curves is the same as for HTSC + CuO composite samples:[8] they have a quasisemiconductor character up to the superconducting transition temperature of the HTSC grains (93.5 K) (not shown in Fig. 2), which is followed by an abrupt decrease in the resistance corresponding to transition to the superconducting state of the HTSC grains (the invariance of this temperature for all x and its equality to T_c of the starting HTSC point to an absence of nickel diffusion into the HTSC), and they have a smooth ''tail'' reflecting the transition to the superconducting state of the weak bonds. This part of the dependence for $x=0$ has been attributed to thermal fluctuations (TAPS)[10] in a network of Josephson junctions.[8]

It is explicitly clear from Fig. 2 that the temperature of the transition to the state of zero resistance falls as the nickel content in the insulator component of the composite is in-

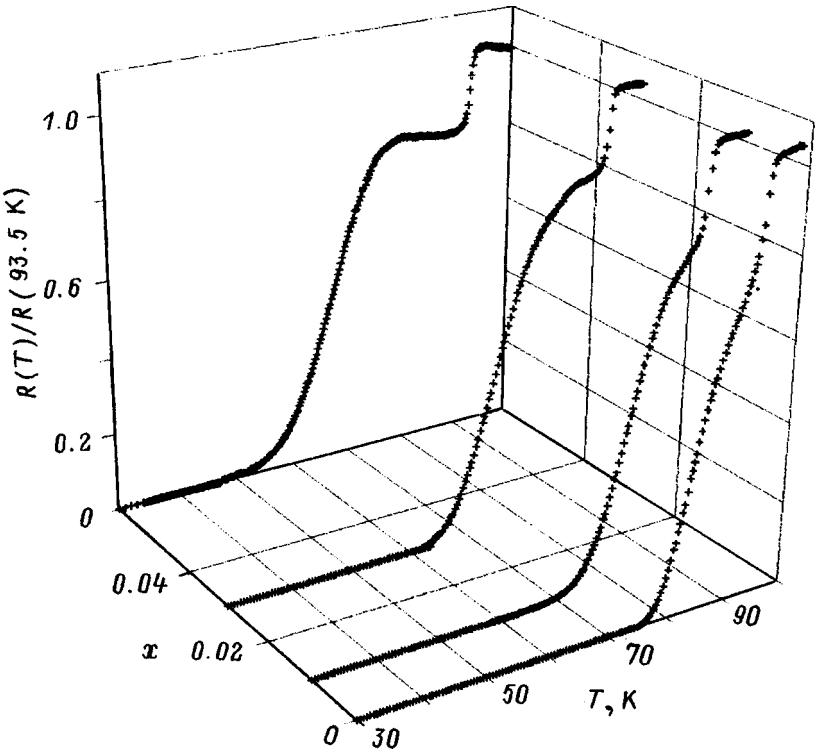

FIG. 2. Temperature dependence of the normalized electrical resistance $R(T)/R$ (93.5 K) as a function of x for composite samples 85 vol.% $Y_{3/4}Lu_{1/4}Ba_2Cu_3O_7$ + 15 vol% $Cu_{1-x}Ni_xO$. $x=0$, 0.01, 0.03, 0.06.

creased. Since the volume fraction of $Cu_{1-x}Ni_xO$ in all the composite samples was the same (15 vol%), and likewise the particulars of their preparation, the decrease in the temperature at which the resistance vanishes can be explained only by an additional (besides TAPS) magnetic scattering of the supercurrent carriers in the insulating interlayer.

2. DISCUSSION

According to the phase diagram of the system $Cu_{1-x}Ni_xO$ (Ref. 19), for $x<0.05$ a solid solution with monoclinic CuO structure exists, i.e., the substitution Cu $\rightarrow$ Ni can be considered as isostructural. Changes in the electronic structure and magnetic properties caused by such a substitution were treated for the system $La_2Cu_{1-x}Ni_xO$ in Ref. 22 with the aid of exact diagonalization of the microelectronic Hamiltonian of the $p-d$ model for CuO_4 and CuO_6 clusters. Since the immediate environment of the copper and nickel atoms in $Cu_{1-x}Ni_xO$ is almost the same, the calculated results of Ref. 22 can also be applied to this system.

According to Ref. 22, the substitution Cu$\rightarrow$Ni in oxides does not result in the formation of the bivalent configuration $Ni^{2+}(d^8)$ with spin $s=1$, which is energetically unfavored because of the strong intra-atomic electron correlations of the $3d$ electrons. It is more favorable for the two holes (relative to the filled $3d^{10}$ shell) not to be localized in the $3d^8$ state, but to be partly ''smeared'' over the nearest neighbors, that is, oxygen ions, so that the wave function of the two-hole state can be written as a superposition of the $3d^9L$ and $3d^{10}L^2$ configurations

$$|2\rangle = u_0|p^5d^{10}p^5\rangle - v_0(|p^6d^9p^5\rangle + |p^5d^9p^6\rangle)/\sqrt{2}, \qquad (1)$$

where the coefficients u_0 and v_0 are determined by such parameters of the Hamiltonian of the $p-d$ model as the charge transfer energy, the copper–oxygen Coulomb interaction, and the energies of the p and d levels in the crystal field. Thus, because of covalency effects the nickel ion is found in the diamagnetic state d^{10} with probability u_0^2 and in the state d^9 with spin $s=1/2$ with probability v_0^2. The weight of the configuration d^8 with spin $s=1$ is small ($\sim 1\%$); therefore it can be neglected. All these conclusions are valid only for low concentrations of the substituent atoms, i.e., for $x \ll 1$.

Let us apply these ideas to an analysis of the magnetic and electrical properties of the composites described above. In an antiferromagnetic CuO matrix, according to Eq. (1), the substitution Cu $\rightarrow$ Ni with probability v_0^2 conserves the $s=1/2$ spin, and with probability u_0^2 leads to diamagnetic dilution. The suppression of antiferromagnetism can be explained by diamagnetic dilution, where the falloff of T_N is proportional to the concentration of diamagnetic centers, $dT_N/dx \sim u_0^2 x$. From the data of Fig. 1, for $Cu_{1-x}Ni_xO$ we have $dT_N/dx \cong -5$ K/at. %, which is quite close to the value $dT_N/dx = -5.5$ K/at. % in the system $La_2Cu_{1-x}Ni_xO$ (Ref. 23).

The electrical properties of the system $Cu_{1-x}Ni_xO$ are configured by the fact that with the appearance of the two-hole states (1), deep impurity levels are formed in the one-electron spectrum,[24] which by virtue of their large depth (~ 1 eV) do not affect the carrier concentration (at room temperature and below), which is determined by the intrinsic defects in CuO. Therefore, the resistance for $T>T_c$ of the

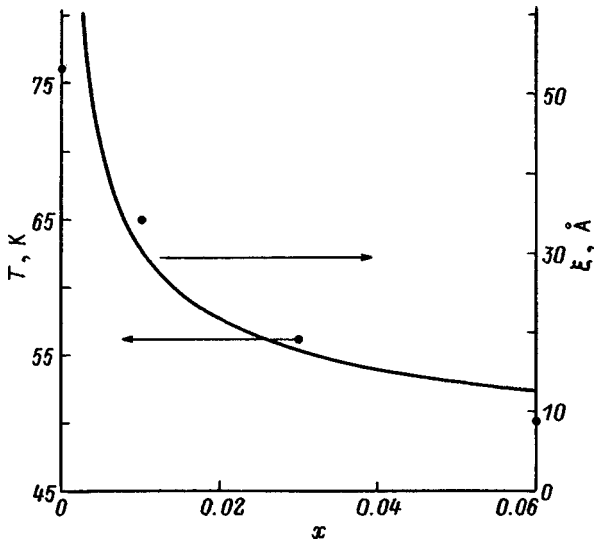

FIG. 3. Concentration dependence of the antiferromagnetic correlation length ξ_A for $Cu_{1-x}Ni_xO$ (solid line) and the temperature at which the resistance of the HTSC+$Cu_{1-x}Ni_xO$ composites goes to zero (filled circles).

HTSC, i.e., for ordinary carriers in the composite HTSC+$Cu_{1-x}Ni_xO$, is not a function of nickel doping. Nor is the onset point of the transition T_c, which is determined by the superconducting transition inside the HTSC grains, since the probability of nickel diffusion into the HTSC grains is exceedingly small in view of the short annealing time of the composite. As for the depression of the temperature of the transition to zero resistance in the sample, it is necessary to consider tunneling in a composite with antiferromagnetic insulating interlayers.

Since even in optimally doped HTSC's, antiferromagnetic correlations exist on scales ξ_A larger than the coherence length of a Cooper pair, ξ_S, motion of such a pair takes place, as it were, against a background of antiferromagnetic order. Therefore, for tunneling in the system HTSC + CuO, the presence of antiferromagnetic order in CuO will scarcely lead to additional breaking of Cooper pairs. A different situation arises in the case of $Cu_{1-x}Ni_xO$, where the antiferromagnetic structure contains $d^{10}L^2$ diamagnetic centers.

It is well known that in an antiferromagnet containing diamagnetic substitutions, because of the nonequivalency of one of the sublattices, an uncompensated moment appears in the vicinity of the diamagnetic impurity. Such moments were detected by measurements of the static magnetic susceptibility in $La_2Cu_{1-x}A_xO_4$, A=Zn, Ga, Al (Refs. 23 and 25) and from NMR data in $YBa_2(Cu_{1-x}Zn_x)_3O_7$ (Ref. 26). Scattering by such impurity magnetic moments suppresses superconductivity in the usual way according to BCS theory. Figure 3 plots the dependence of the antiferromagnetic correlation length ξ_A in $Cu_{1-x}Ni_xO$, calculated according to the formula $\xi_A = q_0/\sqrt{x}$ (Ref. 27) for $a_0 = 3.08$ Å, where a_0 is the nearest-neighbor Cu–Cu distance in CuO (right axis). Figure 3 also plots the dependence of the temperature at which the resistance of the HTSC+$Cu_{1-x}Ni_xO$ composites becomes equal to zero, as a function of x (left axis). The correlation between these two dependences is obvious.

The additional salient point in the $R(T)$ curves in Fig. 2 appearing below T_c with growth of x can be compared to an analogous salient point in the $R(T)$ curves in $YBa_2Cu_3O_7/Pr_{0.7}Sr_{0.3}MnO_3/Ag$ and $YBa_2Cu_3O_7/Pr_{0.7}Sr_{0.3}MnO_3/YBa_2Cu_3O_7$ sandwiches with a ferromagnetic barrier layer.[28] Apparently, scattering by the magnetic moments in the magnetically ordered barrier layer is responsible for the indicated salient points.

In high-temperature superconductors, phase layering is often observed,[29] where the non-conducting and superconducting phases can form ordered one-dimensional superstructures.[30,31] The composite systems HTSC+CuO that we have investigated can be considered as artificially created systems with phase layering where, in contrast to natural layering, we have the possibility of intentionally introducing magnetic impurities into the non-conducting layers and studying their effect on the tunneling of Cooper pairs.

In the system $Y_{3/4}Lu_{1/4}Ba_2Cu_3O_7+Cu_{1-x}Ni_xO$ we discovered three important experimental facts: 1) independence of the transition temperature T_c and the resistance above the transition temperature of the level of nickel doping, 2) a lowering of the temperature at which the resistance vanishes with growth in the nickel concentration, and 3) the appearance of special features in the $R(T)$ curves below T_c. All of these facts are qualitatively explained by peculiarities in the electronic structure of CuO and changes in it wrought by substitution of nickel for copper. The appearance of magnetic moments in the insulating interlayer is caused not only by the states $Ni^{2+}(3d^8)$ with spin $s=1$, which have a very high energy due to effects of strong electron correlations, but also by the diamagnetic configurations $d^{10}L^2$. The uncompensatedness of the CuO antiferromagnetic sublattices in the vicinity of the diamagnetic spin hole also gives a magnetic moment with effective spin $<1/2$ per impurity atom. The reduction of the superconducting properties of HTSC+$Cu_{1-x}Ni_xO$ composites with increasing x correlates with the decrease in the antiferromagnetic correlation length in $Cu_{1-x}Ni_xO$, where the latter fulfills the role of a tunneling interlayer in the network of $S-I-S$ bonds of these composites.

We thank A. D. Balaev for assistance in carrying out the magnetic measurements, A. D. Vasil'ev for performing x-ray diffraction studies of the samples, and K. S. Aleksandrov for useful discussions.

This work was carried out with the partial financial support of a grant for young scientists of the Siberian Branch of the Russian Academy of Sciences.

[1] D. J. Van Harlingen, Rev. Mod. Phys. **67**, 515 (1995).
[2] J. J. Calabrese, M. A. Dubson, and J. C. Garland, J. Appl. Phys. **72**, 2958 (1992).
[3] J. Jung, I. Isaae, and M. A.-K. Mohamed, Phys. Rev. B **48**, 7256 (1993).
[4] V. Yu. Tarenkov, A. I. D'yachenko, and A. V. Vasilenko, Fiz. Tverd. Tela (St. Petersburg) **36**, 2196 (1994) [Phys. Solid State **36**, 1197 (1994)].
[5] B. I. Smirnov and T. S. Orlova, Fiz. Tverd. Tela (St. Petersburg) **36**, 3542 (1994) [Phys. Solid State **36**, 1883 (1994)].
[6] M. I. Petrov, D. A. Balaev, B. P. Khrustalev, and K. S. Aleksandrov, Sverkhprovodimost': Fiz., Khim. Tekh. **8**, *1*, 53 (1995).
[7] M. I. Petrov, D. A. Balaev, K. A. Shaĭkhutdinov, B. P. Khrustalev, and K. S. Aleksandrov, Fiz. Tverd. Tela (St. Petersburg) **39**, 829 (1997) [Phys. Solid State **39**, 735 (1997)].

[8] M. I. Petrov, D. A. Balaev, K. A. Shaĭkhutdinov, and B. P. Khrustalev, Fiz. Tverd. Tela (St. Petersburg) **39**, 1956 (1997) [Phys. Solid State **39**, 1749 (1997)].
[9] M. I. Petrov, D. A. Balaev, K. A. Shaihutdinov, B. P. Khrustalev, and K. S. Aleksandrov, Physica C **282-287**, 2453 (1997).
[10] V. Ambegaokar and B. I. Halperin, Phys. Rev. Lett. **22**, 1364 (1969).
[11] M. I. Petrov, D. A. Balaev, K. A. Chaĭkhutdinov, B. P. Khrustalev, and K. S. Aleksandrov, Dokl. Akad. Nauk **346**, 616 (1996) [Phys. Dokl. **41**, 59 (1996)].
[12] M. I. Petrov, D. A. Balaev, S. V. Ospishchev, B. P. Khrustalev, K. S. Aleksandrov, Physica C **282-287**, 2447 (1997).
[13] Chan-Joong Kim, Ki-Baik Kim, Il-Hyun Kuk, and Gue-Won Hong, Physica C **255**, 95 (1995).
[14] B. A. Gizhevskiĭ, A. A. Samokhvalov, N. M. Chebotayev, S. V. Naumov, and G. K. Pokazan'eva, Sverkhprovodimost': Fiz., Khim., Tekh. **4**, 827 (1991).
[15] R. Feduzi, F. Lanza, and V. Dallacasa, Mod. Phys. Lett. **7**, *3*, 163 (1993).
[16] I. O. Kulik, Zh. Éksp. Teor. Fiz. **49**, 1211 (1965) [Sov. Phys. JETP **22**, 841 (1966)].
[17] L. N. Bulaevskii, V. V. Kuzii, and A. A. Sobyanin, Solid State Commun. **25**, *12*, 1053 (1978).
[18] S. V. Kuplevakhskiĭ and I. I. Fal'ko, Fiz. Nizk. Temp. **10**, 691 (1984) [Sov. J. Low Temp. Phys. **10**, 361 (1984).
[19] R. Zilber, E. F. Bertaut, and P. Burlet, Solid State Commun. **8**, *12*, 935 (1970).
[20] A. D. Balaev, Yu. V. Boyarshinov, M. M. Karpenko, and B. P. Khrustalev, Prib. Tekh. Éksp. **3**, 167 (1985).
[21] B. X. Yang, J. M. Tranquada, and G. Shirane, Phys. Rev. B **38**, 174 (1988).
[22] S. G. Ovchinnikov, Fiz. Tverd. Tela (St. Petersburg) **37**, 3645 (1995) [Phys. Solid State **37**, 2007 (1995)].
[23] S. T. Ting, P. Pernambuco-Wise, J. E. Crow, and E. Manousakis, Phys. Rev. B **46**, 11 772 (1992).
[24] S. G. Ovchinnikov, Zh. Éksp. Teor. Fiz. **103**, 1404 (1993) [JETP **76**, 687 (1993)].
[25] G. Xiao, M. Z. Cieplak, J. Q. Xiao, and C. L. Chien, Phys. Rev. B **42**, 8752 (1990).
[26] H. Alloul, A. Mahajan, P. Mendels, T. Riseman, Y. Yoshinari, G. Collin, and J. F. Marucco, Workshop on High-Temperature Superconductivity. Miami (1995), p. 7.
[27] W. Brenig, Phys. Rep. **251**, 153 (1995).
[28] G. C. Xiong, G. J. Lian, J. F. Kang, Y. F. Hu, Y. Zhang, and Z. Z. Gan, Physica **282–287**, 693 (1997).
[29] É. N. Nagaev, Phys. Usp. **165**, 529 (1995) [sic].
[30] A. Biankoni and M. Misori, J. Phys. I **4**, 361 (1994).
[31] O. N. Bakharev, M. V. Eremin, and M. A. Teplov, JETP Lett. **61**, 515 (1995).

Translated by Paul F. Schippnick

SEMICONDUCTORS AND INSULATORS

Characteristic features of the low-temperature thermal conductivity of highly-enriched and natural germanium

A. P. Zhernov and D. A. Zhernov

Russian Science Center ''Kurchatov Institute,'' 123182 Moscow, Russia;
Institute of Superconductivity and Solid-State Physics, Moscow, Russia
(Submitted February 10, 1998)
Fiz. Tverd. Tela (St. Petersburg) **40**, 1604–1607 (September 1998)

Experimental data on the thermal conductivity $K(T)$ of natural and highly enriched (99.99%) Ge^{70} crystals with ground and polished surfaces are analyzed in the temperature interval $\sim 2-8$ K. In all samples, the boundary scattering mechanism predominates in the interval from 2 to 4.0 K. As temperature increases, in highly enriched samples N processes start to contribute to phonon transport and the behavior of $K(T)$ corresponds to viscous Poiseuille flow of a phonon gas. The isotopic scattering mechanism plays a large role in isotopically nonideal samples. © *1998 American Institute of Physics.* [S1063-7834(98)00709-6]

Recently, V. I. Ozhogin's group synthesized chemically pure, perfect and highly enriched Ge^{70} crystals (with 99.99% enrichment). A study of different properties of these crystals was initiated. An experimental investigation of the thermal conductivity $K(T)$ both in a highly enriched sample and in Ge^{70} samples with 96% enrichment and a natural sample in wide temperature intervals has been already been performed.[1,2] Corresponding data have been obtained both for crystals with fine polishing of the surface and for crystals with a more coarsely worked (ground) surface (see details in Ref. 2). As a result, we have unique experimental data for studying in greater detail kinetic processes in regular systems and the role of isotopic disorder in kinetics.

In the present paper we analyze the experimental data of Refs. 1 and 2, obtained for the range of liquid-helium temperatures from 2 to 8 K. First, the effect of the degree of working of the sample surfaces and the possible role of strong dispersion of the acoustic phonon spectrum of germanium are studied in natural Ge samples. Second, for the case of highly enriched and perfect samples, the possibility of the manifestation of an effect predicted by R. N. Gurzhi is discussed. The essence of this effect is that quasiparticle displacements occurring in a phonon flux can be regarded under certain conditions as a random walk (similar to a Poiseuille flow of a fluid).[3,4] The point is that, at very low temperatures, for an acoustic phonon mode with frequency ω and polarization j, the relaxation rate due to anharmonic Umklapp processes (U), in which short-wavelength phonons with large momenta participate directly, is exponentially small:

$$1/\tau_U^{(j)} \sim \omega^2 T \exp(-B_j/T).$$

At the same time the relaxation rates for longitudinal l and transverse t modes on account of normal N-processes, in which any phonons can participate, including only long-wavelength phonons, are described by power-law temperature dependences

$$1/\tau_N^{(l)} \sim \omega T^4, \quad 1/\tau_N^{(t)} \sim \omega^2 T^3$$

(see, for example, Refs. 4 and 5). For this reason, for the corresponding mean-free paths there exist, as is well known, a temperature interval such that

$$l_N \ll d \ll l_U,$$

where d is the characteristic sample size. In the indicated interval, in the case of very perfect monoisotopic crystals, the effect of statistical defects and isotopic disorder on the structure of the nonequilibrium distribution function is veiled by N processes. The only resistive processes is scattering by the walls of the sample. However, because the nonresistive N processes are more frequent the phonon transport mean-free pathlength increases effectively as $\sim d^2/l_n$ (Ref. 3; see also Refs. 4–6).

L. P. Mezhov-Deglin has performed measurements of the thermal conductivity in very perfect and monoisotopic samples of solid He^4 and observed the characteristic features, predicted by R. N. Gurzhi, in the temperature behavior of $K(T)$ in the region to the left of the maximum (Ref. 7; see also Ref. 8). But, except for solid helium, as far as we know, the hydrodynamic region has not been reliably identified in other materials.

1. GENERAL RELATIONS

We shall express the thermal conductivity K of the lattice in the standard form[9]

$$K(T) = \sum_{j=1}^{3} \frac{k_B}{4\pi^2 v_j} \left(\frac{k_B T}{h}\right)^3 \int_0^{z_{D,j}} dz\, \tau_j(z) \frac{z^4 e^z}{(e^z-1)^2}. \qquad (1)$$

Here $z_{D,j} = k\Theta_j/k_B T$ and $\tau_j(z)$ are, respectively, the reduced Debye temperature and the relaxation time of the phonon mode with polarization index j and group velocity v_j.

 © 1998 American Institute of Physics

We shall consider only the boundary scattering processes (i.e., the region of very low temperatures). In this situation τ is a relaxation time determined by boundary scattering. For the case of diffuse boundary scattering and an infinitely long sample $\tau_j^{(b,c)}=l_c/\nu_j$, where l_c is the mean-free pathlength of the phonon mode (or the Casimir length[10]). For samples with cross section S the Casimir length is given by $l_c=1.12\sqrt{S}$.

The effect of fine polishing as well as grinding (the case of coarser working) of the surface on the temperature dependence of the thermal conductivity can be studied qualitatively in the Ziman–Soffer theory.[9,11] This theory contains the relaxation time

$$\tau_j^{(b)}=\frac{l_c}{v_j}\frac{1+P(k_j,\phi)}{1-P(k_j,\phi)},$$

$$P(k_j,\phi)=\exp[-(2k_j\eta\cos(\phi))^2]. \tag{2}$$

Here P is the specularity factor, which for the j-th mode depends on the phonon wave vector k_j and its orientation, i.e., the angle ϕ; η is a parameter characterizing the degree of polishing of the surface. We note that $k=\omega/\nu_j$ and $\phi=\pi/2-\Theta$, where Θ is the angle made by the phonon wave vector and a unit vector in the direction of the temperature gradient.

Let us substitute the expression (2) into Eq. (1). Taking account of what we have said above, we obtain

$$K(T)=\sum_{j=1}^{3}\frac{k_B l_c}{2\pi^2 v_j^2}\left(\frac{k_B T}{h}\right)^3 \times\int_0^{z_{D,j}}dx\,\frac{z^4e^z}{(e^z-1)^2}\int_0^1 dy\,y^2\coth Z_j(y). \tag{3}$$

The factor Z_j is defined as

$$Z_j(y)=\begin{cases}\dfrac{4k_B^2}{2\nu_j^2h^2}\eta^2z^2T^2(1-y)^2, & \coth Z_j(y)\leqslant r,\\ ry^2, & \coth Z_j(y)>r.\end{cases} \tag{4}$$

Here $y=\cos\Theta$; the parameter $r=l_{\max}/l_c$, where $l_{\max}$ is the linear size of the sample.

We call attention to the fact that Z_j is not only sensitive to the degree of polishing of the surface of the sample, i.e., the quantity η, but it also depends on the temperature T. We also note that if $y\approx 1$, i.e., the phonons ''move'' parallel to the sample axis, then the integral over y diverges. In reality, the sample length is finite. This is taken into account in the Ziman–Soffer theory. When $F(y)=\coth Z_j(y)>r$, $F(y)$ is replaced by ry^2.

2. RESULTS AND DISCUSSION

In the present work, using relations (3) and (4), we analyzed the low-temperature experimental data for the thermal conductivity of natural and isotopically highly enriched samples (with 99.99% enrichment) in the interval $T\approx 2-8$ K. As mentioned above, the data were obtained for the cases of fine polishing of the surface and for coarser working of the surface by grinding.[1,2] Thus, there are four sets of experimental curves. The isotopic disorder parameter

$$g=\frac{\Sigma c_iM_i^2-(\Sigma c_iM_i)^2}{(\Sigma c_iM_i)^2}$$

(where c_i and M_i are the concentration and mass of the isotope of the kind i) equals, respectively, 5.87×10^{-4} and 8.18×10^{-8}.

TABLE I. Geometric dimensions l_x, l_y, and l_z of the samples and the values of the parameter η in the Ziman–Soffer theory.

Sample	l_x, l_y, l_z, mm	η,A
$n(s)$	2.33×2.3×40.7	65
$n(p)$	2.4×2.35×40.8	36
$h(s)$	2.2×2.5×40.4	65–75
$h(p)$	2.44×2.13×40.4	28

Note: The isotopic disorder parameter g for natural (n) and highly enriched (h) samples equals, respectively, 5.87×10^{-4} and 8.18×10^{-8}. The symbols s and p denote ground and polished samples, respectively.

The only adjustable parameter in the theory is η. The standard values were taken for the group velocities of the transverse and longitudinal acoustic phonons: $\nu_t=3.16\times10^5$ cm/s and $\nu_l=5.21\times10^5$ cm/s. To determine the Casimir length l_c and the parameter r, the specific parameters of the samples were used (see Refs. 1 and 2). The corresponding values are presented in Table I.

The computed theoretical curves for different values of the parameter η, characterizing the degree of working of the surface, and the experimental data in the form of points for four samples are presented in Figs. 1 and 2.

We shall comment on Figs. 1 and 2. It is immediately evident that the factor η decreases considerably as the degree of working of the surface increases. In the case of fine polishing, $\eta\approx 36$ and 28 for natural and highly enriched

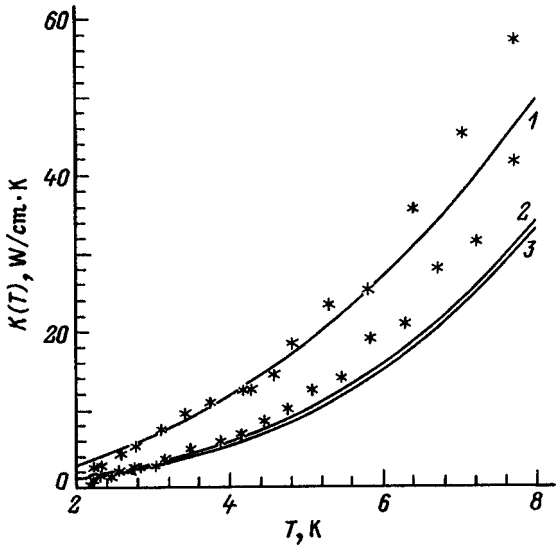

FIG. 1. K versus T. The case of highly enriched crystals. The theoretical curves correspond to samples with polished (*1*) and ground (*2*, *3*) surfaces. The specularity parameter η equals 28 (*1*), 65 (*2*), and 75 (*3*). The experimental points were taken from Ref. 2.

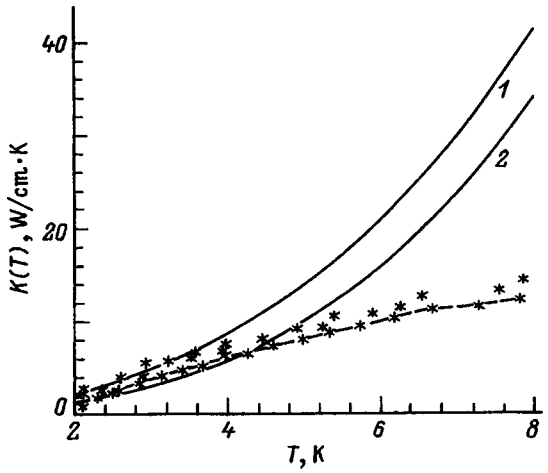

FIG. 2. K versus T. The case of natural samples. The theoretical curves correspond to samples with polished (*1*) and ground (*2*) surfaces. The specularity parameter η equals 36 (*1*) and 65 (*2*). The experimental points were taken from Ref. 2. For the ground surface they are connected by a dashed line.

samples, respectively. For samples whose surface was worked by grinding, the values of the parameter η are also close, but $\eta \approx 65$ (see Table I).

We note that the agreement between theory and experiment for natural samples is reasonable in the interval $T \approx 2-4$ K. But for $T \geqslant 4$ K the computed curves lie above the experimental points (see also Refs. 12–14). For highly enriched samples agreement between theory and experiment also obtains in the temperature interval $\sim 2-4$ K. However, as temperature increases ($T \sim 4-8$ K) the theoretical values are found to fall below the experimental values.

Let us now discuss these results. In the simplest approximation

$$K(T)=\frac{1}{3}C_v(T)v^2\tau_s, \quad \tau_s^{-1}=\sum_i (\tau^{(i)})^{-1}. \tag{5}$$

Here C_v is the phonon specific heat, v is the average phonon velocity, and τ_s is the total relaxation time.

At very low temperatures $\tau_s=\tau^{(b,c)}$ for highly enriched samples. Next, we take into consideration the fact that for germanium the effective Debye temperature $\Theta(T)$ has a pronounced minimum at 25 K (see, for example, Refs. 10 and 11) and

$$C_v(T) \sim \Theta^{-3}(T). \tag{6}$$

Then, according to Eqs. (5) and (6), the specific behavior of $K(T)$ (''positive'' deviation for $T>4$ K) can be explained qualitatively as being due to the appearance of soft transverse modes. However, specific estimates using the results of Refs. 15 and 16 do not permit describing, even roughly quantitatively, the observed deviation.

As noted above, the question of the hydrodynamic flow regime of phonons is being discussed in the literature. If this regime materializes, then it leads to a substantial increase in the thermal conductivity on the left side of the temperature maximum. At present there is one experimental observation of such a regime in solid-helium crystals.[7] Specifically, at the lowest temperatures ($T<0.6$ K) in helium the phonon mean free path determined by anharmonic collisions is found to be shorter than the diameter of the sample. Then $K(T) \sim C_v \sim T^3$. In the interval 0.6–1 K $l_N \ll d$ and $l_R l_N \gg d^2$, where l_N and l_R are the mean-free pathlengths corresponding to normal and resistive processes. Here $l_{\text{ef}}=0.1d^2/l_N$.

In this situation, according to experiment and simple theoretical estimates, to the left of the maximum $K(T) \sim C_v l_N \sim T^8$.

We also note that criteria under which the motion of a phonon gas under the action of an applied temperature gradient can be interpreted as viscous Poiseuille flow were established in Ref. 7. It is required that

$$l_R/l_N \geqslant 10^3, \quad d/l_N \geqslant 30.$$

On this basis it is possible to explain qualitatively the specific ''positive'' deviation of the experimental values of $K(T)$ from the theoretical values at temperatures $T>4$ K in Ge[70] as the result of the appearance of a hydrodynamic regime in perfect, highly enriched samples. We note that degree of surface working (not discussed in Ref. 7) influences the temperature dependence of the thermal conductivity to a certain extent. Specific estimates require knowing the mean-free pathlengths determined by normal anharmonic processes. Moreover, effects associated with the phonon focusing must also be taken into account.[17]

Next, according to Ref. 5, for crystals with the natural isotopic composition

$$K(T) \approx \frac{1}{3}C_v(T)v^2\tau^{(b)}\left(1-\frac{\tau^{(b)}}{\tau^{(is)}}\right),$$

where $\tau^{(is)}$ is the relaxation time due to isotopic disorder. Hence one can see that the ''negative'' deviation for $K(T)$ at temperatures $T \geqslant 4$ K is due to the fact that our analysis neglected the strong isotopic phonon scattering due to soft modes (see also Refs. 5 and 6).

Let us now summarize. In the temperature range 2–4 K the change in the behavior of the thermal conductivity as a function of the measure of specularity of the surface can be described qualitatively on the basis of the Ziman–Soffer theory. In perfect, highly-enriched samples at temperatures $T \geqslant 4$ K a deviation is observed from Knudsen flow of the phonons, when most collisions occur with the walls. The deviations that arise can be explained by the fact that a viscous Poiseuille regime materializes. In natural Ge samples, at temperatures $T \geqslant 4$ K, isotopic scattering starts to play a considerable role.

We note that, under conditions of Poiseuille flow, the existence of second sound—oscillations in the density of thermal excitations—becomes possible. This effect has been observed in helium (see, for example, Ref. 8). It would be interesting to investigate second sound in Ge also.

[1] V. I. Ozhogin, A. V. Inyushkin, A. N. Toldenkov, G. É. Popov, E. Haller, and K. Itoh, JETP Lett. . **63**, 490 (1996).
[2] M. Asen-Palmer, K. Bartkowsky, E. Gmelin, M. Cardona, A. P. Zhernov, A. V. Inuishkin, A. V. Taldenkov, V. I. Oghogin, K. M. Itoh, and E. E. Haller, Phys. Rev. B **56**, 9431 (1997).
[3] R. N. Gurzhi, Zh. Éksp. Teor. Fiz. **46**, 719 (1964) [Sov. Phys. JETP **19**,

490 (1964)]; Usp. Fiz. Nauk **94**, 689 (1968) [Sov. Phys. Usp. **11**, 255 (1968)].
[4] E. M. Lifshitz and L. P. Pitaevskii, *Physical Kinetics* [Pergamon Press, N. Y.; Nauka, Moscow, 1979].
[5] R. Berman, *Thermal Conduction in Solids* [Clarendon Press, Oxford, 1976; Mir, Moscow, 1979].
[6] V. L. Gurevich, *Kinetics of Phonon Systems* [in Russian], Nauka, Moscow, 1980.
[7] L. P. Mezhov-Deglin, Zh. Éksp. Teor. Fiz. **49**, 66 (1965) [Sov. Phys. JETP **22**, 47 (1966)]; Zh. Éksp. Teor. Fiz. **71**, 1453 (1976) [Sov. Phys. JETP **25**, 568 (1967)]; Fiz. Tverd. Tela (Leningrad) **22**, 1748 (1980) [Sov. Phys. Solid State **22**, 1018 (1980)].
[8] B. N. Esel'son, V. N. Grigor'ev, V. G. Ivantsov, É. Ya. Rudakovskiĭ, D. G. Sanikidze, and I. A. Serbin, *Solutions of Quantum Liquids* [in Russian], Nauka, Moscow, 1973.
[9] J. M. Zaiman, in *Electrons and Phonons*, Oxford, 1960, p. 456.
[10] H. B. Casimir, Physica **5**, 495 (1938).
[11] S. B. Soffer, J. Appl. Phys. . **38**, 1710 (1967).
[12] D. R. Frankl and G. J. Campisi, in *Proceedings of the International Conference on Phonon Scattering in Solids*, Paris, 1972, edited by H. J. Albany, La Documentation Francaise, Paris, 1972, pp. 88–93.
[13] W. S. Hust and D. R. Frankl, Phys. Rev. **186**, 801 (1969).
[14] W. S. Hust and D. R. Frankl, Phys. Rev. B **19,** 3133 (1979).
[15] A. D. Zdetsis and C. S. Wang, Phys. Rev. B **19**, 2999 (1979).
[16] Resul Eryigit and Irving P. Herman, Phys. Rev. B **53**, 7775 (1996).
[17] A. K. Mc Curdy, H. J. Maris, and C. Elbaum, Phys. Rev. B **2**, 4077 (1970).

Translated by M. E. Alferieff

Sign inversion of the rotatory power and topology of the surface of gyration of $\alpha NiSO_4 \cdot 6H_2O$

Ya. O. Dovgiĭ and I. G. Man'kovskaya

L'vov State University, 290602 L'vov, Ukraine
(Submitted February 10, 1998)
Fiz. Tverd. Tela (St. Petersburg) **40**, 1608–1609 (September 1998)

The sign inversion point of the rotatory power of the gyrotropic crystals α-$NiSO_4 \cdot 6H_2O$ ($\lambda_l = 503$ nm at 300 K) has been established. The topology of the gyration surface varies greatly in the vicinity of λ_l. We have demonstrated the possibility of using this method of spectrophotometric polarimetry for precise monitoring of the mounting of a gyrotropic crystal in the system ''polarizer–crystal–analyzer.'' © *1998 American Institute of Physics.* [S1063-7834(98)00809-0]

The phenomenon of sign inversion of the rotatory power of gyrotropic crystals has been observed so far only in individual cases[1,2] and for this reason has been insufficiently studied so far. It is of both theoretical and experimental interest.

In this paper we present results of spectropolarimetric studies of uniaxial negative crystals of nickel sulfate hexahydrate, $\alpha NiSO_4 \cdot 6H_2O$, which are tetragonal polymorphs of the corresponding compounds. The space groups of its enantiomorphic modifications are $P4_122$ (D_4^4) and $P4_322$ (D_4^8). The appearance of gyrotropy in the electronic transitions in this crystal in the wavelength range 200−2500 nm is due entirely to intracomplex interactions in the octahedral $[Ni(H_2O)_6]^{2+}$ clusters deformed by the crystal field. In a solution, $NiSO_4$ loses its rotatory power.[3]

Measurements of the dispersion of the rotatory power of $\alpha NiSO_4 \cdot 6H_2O$ were performed in the direction of the optic axis near the inversion point $\lambda = \lambda_l$. The polarimetric setup was based on the KSVU-12 automated serial spectrometer.

The light transmission function of the system ''polarizer–optically active crystal–analyzer'' (PCA) has the form

$$I = I_0 \left[\cos\varphi \cos\psi + \frac{\alpha_0}{l} \sin\varphi \left(\sin\psi - \frac{a}{p^2} \sin(2\theta + \psi) \right) \right]^2 + \left[\frac{a}{pl} \sin\varphi \cos(2\theta - \psi) \right]^2, \quad (1)$$

where $\varphi = \frac{\omega}{2c}(n_+ - n_-)d = kd\frac{n_+ - n_-}{2}$; $p = 1/n_+ + 1/n_-$; $l = |1/n_+ - 1/n_-|$; I_0 and I is the light intensity at entrance and exit from the system, respectively; d is the thickness of the sample; ψ is the angle between the directions of the vibrations in the polarizer and the analyzer; θ is the angle between the principal directions of the polarizer and of the crystal; α_0 is a scalar parameter characterizing the optical activity of the crystal; a is a parameter characterizing the linear anisotropy of the crystal; n_+ and n_- are the refractive indices for the right- and left-circular polarizations of the light waves.

The transmission spectra of the PCA system were written for $\psi_\pm = \pi/2 \pm |\beta|$ (Fig. 1)

$$T_{\pm\beta}(\lambda) = \cos^2[\varphi(\lambda) - \pi/2 \mp |\beta|] = \sin^2[\varphi(\lambda) \mp |\beta|]. \quad (2)$$

The difference spectrum

$$\Delta T(\lambda) = T_{-\beta}(\lambda) - T_{+\beta}(\lambda) = \sin[2\varphi(\lambda)]\sin|2\beta|, \quad (3)$$

hence the specific rotatory power

$$\rho(\lambda) = \frac{1}{2d} \arcsin\left[\frac{\Delta T(\lambda)}{\sin|2\beta|} \right]. \quad (4)$$

It can be seen from Eq. (4) that the sign of the rotatory power is uniquely determined by the sign of the transmission difference. The curves $T_{+\beta}(\lambda)$ and $T_{-\beta}(\lambda)$ intersect at the inversion point of the rotatory power ($\lambda = \lambda_l$) (Fig. 2). The position of the intersection point does not depend on $|\beta|$.

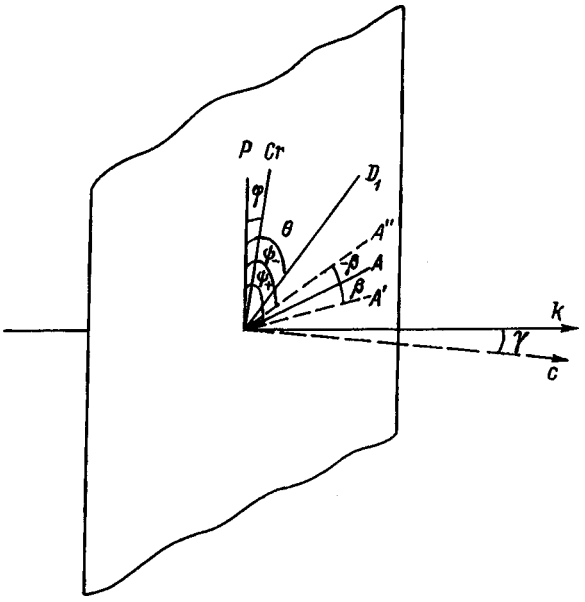

FIG. 1. Principal vectors of the PCA system.

 © 1998 American Institute of Physics

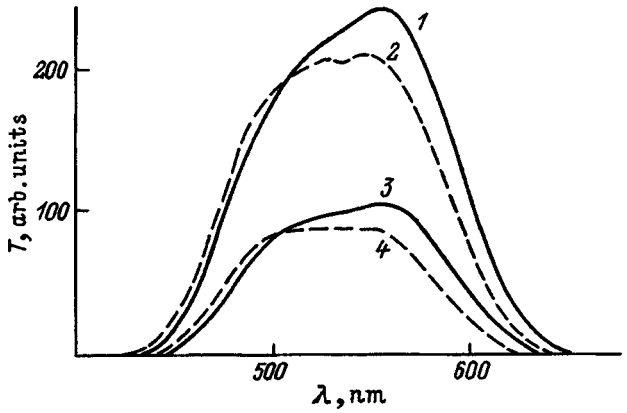

FIG. 2. Transmission spectra of an α-$NiSO_4\cdot 6H_2O$ crystal in a PCA system for $\mathbf{k}\|\mathbf{c}$, $\beta=\pm 20°$ (*1*, *2*) and $\pm 10°$ (*3*, *4*). $T=300$ K.

As can be seen from Fig. 2, at 300 K in the geometry $a=0$, $\alpha_0=l\neq 0$ ($\mathbf{k}\|\mathbf{c}$) for a crystal of $\alpha NiSO_4\cdot 6H_2O$, $\lambda_l=503$ nm.

The dependence of the dispersion of the rotatory power of nickel sulfate hexahydrate is governed by the structure of the circular dichroism spectrum and in the spectral range 400−750 nm is mainly determined by the transitions $^3A_{2g}\rightarrow{}^3T_{1g}$, which, allowing for the symmetry selection rules, become possible, thanks to the configurational interactions of the corresponding components of the spin–orbit splitting.[4]

By varying the geometry of the experiment and taking advantage of computerized spectropolarimetry, it is possible to track the qualitative variation of the shape of the gyration

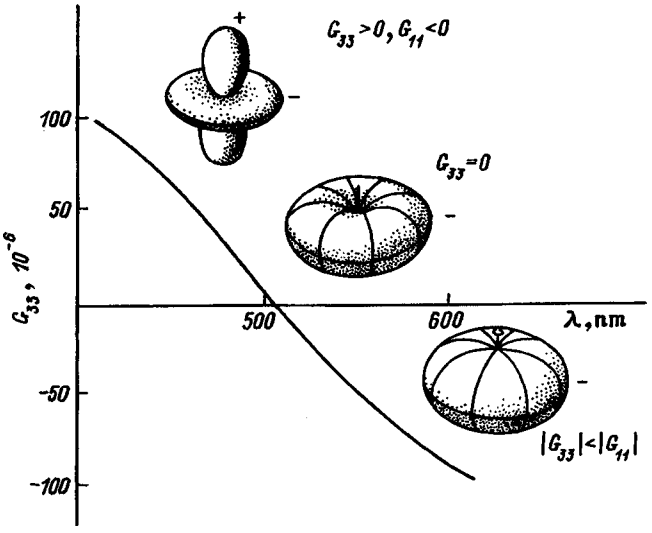

FIG. 3. Spectral dependence of the $G_{33}(\lambda)$ component and dispersion of the gyration surface of an α-$NiSO_4\cdot 6H_2O$ crystal in the vicinity of the inversion point.

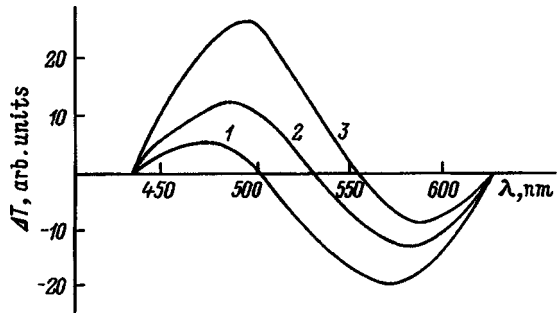

FIG. 4. Shifting of the $\Delta T(\lambda)$ curves for insignificant deviations of the crystal from the orientation $\mathbf{k}\|\mathbf{c}$, $\gamma=0'$ (*1*), $6'$ (*2*), $11'$ (*3*).

surface of $\alpha NiSO_4\cdot 6H_2O$ in the vicinities of sign inversion of the rotatory power (Fig. 3) since $G_{33}=0$ for $\lambda=\lambda_l$, $G_{33}>0$ for $\lambda<\lambda_l$, and $G_{33}<0$ for $\lambda>\lambda_l$.

In conclusion, note that the spectrophotometric polarimetery method is extremely sensitive to variations in γ (Fig. 1). Thus, for a deviation of the direction of a ray relative to the optical axis by a few angular minutes, the intersection point of the $T_{+\beta}(\lambda)$ and $T_{-\beta}(\lambda)$ curves shifts noticeably (Fig. 4). This is due to the influence of ellipticity

$$\Delta T(\lambda)=\frac{\alpha_0}{l}\sin 2\varphi\,\sin|2\beta|\left[1-\frac{a}{p^2}\cos 2\theta\right]+\frac{2a}{l^2p^2}\times\sin^2\varphi\,\sin|2\beta|\sin 2\theta\left[\left(1+\frac{\alpha_0^2}{p^2}\right)a\cos 2\theta-\alpha_0^2\right]. \tag{5}$$

It follows from the last relation that the condition $\Delta T=0$ leads to two solutions. The first is the trivial solution $\varphi=0$, which corresponds to the inversion point at $\gamma=0$. The second solution

$$\varphi=\operatorname{arccot}\left[\frac{a}{lp^2}\sin 2\theta\left(\alpha_0-\frac{a\cos 2\theta}{\alpha_0(1-a/p^2\cos 2\theta)}\right)\right] \tag{6}$$

gives the complicated dependence of the transmission difference function $\Delta T(\lambda)$ on the parameters of linear and circular birefrigence.

[1] Ya. O. Dovhyj, Phys. Status Solidi B **15**, 2, 77 (1966).
[2] S. Hirotsu, J. Phys. C: Solid State Phys. **8**, 12 (1975).
[3] V. A. Kizel' and V. I. Burkov, *Gyrotropy of Crystals* [in Russian], Nauka, Moscow, 1980.
[4] M. H. L. Pryce, G. Agnetta, T. Farofano *et al.*, Philos. Mag. **10**, 477 (1964).

Translated by Paul F. Schippnick

Study of the electronic structure of impurity mercury atoms in compounds by conversion-electron spectroscopy

V. V. Kharitonov and V. N. Gerasimov

Russian Scientific Center "Kurchatov Institute", Institute of General and Nuclear Physics, 123182 Moscow, Russia

(Submitted February 11, 1998)
Fiz. Tverd. Tela (St. Petersburg) **40**, 1610–1614 (September 1998)

First studies of the structure of the valence region in the conversion spectrum of the 1.56-keV ($M1+E2$) transition in ^{201}Hg have been carried out. Physicochemical environment has been found to affect substantially the local electron density of impurity mercury atoms. The mechanisms responsible for the electronic-structure rearrangement are discussed.
© *1998 American Institute of Physics.* [S1063-7834(98)00909-5]

Progress in experimental techniques and theoretical concepts broadens the range of nuclear phenomena being applied to investigation of the properties of matter. It was shown (see Ref. 1 and references therein) that such a classical method of nuclear physics as conversion-electron spectroscopy can be used to advantage in studies of the electronic structure of matter if a resolution of ~ 1 eV can be attained. Indeed, the electron shells of an atom participate directly in the conversion of a nuclear multipole and, therefore, rearrangement of electron shells caused by a change in the physicochemical environment of an atom should become manifest in conversion spectra. Conversion spectroscopy applied to the investigation of the electronic structure of matter is called conversion-electron (CE) spectroscopy.[1] The characteristic feature of this method consists in that conversion occurs in the immediate vicinity of the converting atom (for all transition multipolarities but $E1$, Refs. 2 and 3), so that CE spectroscopy measures the local density of electronic states near an isomeric nucleus.

The influence of the nature of surrounding atoms on the structure of valence-band conversion spectra measured with a high resolution (1–2 eV) was studied earlier for the $E3$ transition in ^{99m}Tc (transition energy about 2.2 keV),[4–6] $E3$ transition in ^{235m}U (transition energy about 0.077 keV),[7–10], as well as for the $E2$ transition in ^{73}Ge (transition energy about 13.3 keV, Ref. 11). Applying CE spectroscopy to a broad range of elements of the Periodic Table appears a topical problem.

This work reports a similar study of the 1.56-keV ($M1+E2$) transition in ^{201}Hg. Mercury was chosen from the following considerations. Investigation of high-T_c superconductors (HTSC), in particular, of those containing thallium and mercury, as offering the most promise, is attracting presently considerable interest. Our studies of the electronic structure of impurity mercury atoms in a number of simple compounds were regarded as a preliminary stage to applying CE spectroscopy to HTSC research on thallium- and mercury-containing materials.

A conversion-electron spectrum produced in the 1.56-keV ($M1+E2$) transition in ^{201}Hg and observed in the $^{201}\mathrm{Tl} \xrightarrow{\varepsilon} {}^{201}\mathrm{Hg}$ decay[12] was measured for the internal N subshells,[13] and the total conversion spectrum, in Ref. 14. The above studies dealt primarily with the nuclear characteristics of the transition. The objective of this work was to isolate and measure the signal due to the valence-band electrons against the intense Auger-electron background[14], and to estimate the nature of the changes in the structure of the valence-band conversion-electron spectrum of this transition in samples prepared by different technologies (referred to subsequently as different samples), as well as in samples both irradiated and unirradiated by an external x-ray source.

1. EXPERIMENTAL PART

The spectra were obtained on an HP 5950A x-ray photoelectron spectrometer[15] providing vacuum in the operating chamber of $\leqslant 2\times 10^{-9}$ Torr and an electron binding-energy measurement accuracy of 0.2 eV. The spectrometer resolution in the conversion-electron measurement mode deduced from the experimental linewidths is ≈ 1.1 eV for a source size of 1×5 mm^2.

The isotope used to prepare the samples was ^{201}Tl (manufactured by IZOTOP) in the form of an aqueous thallium-chloride solution. The samples were made by electrolytic deposition of ^{201}Tl from the solution on platinum substrates. The main details of the sample preparation technique (including the voltage, current, duration of electrolysis) are described elsewhere.[14]

The technique developed in this work enabled one to obtain samples in different chemical states. The chemical state was established by x-ray photoelectron spectroscopy.

Three different samples were prepared. Based on the technique used, it was expected that sample I is a Pt-Au-Hg-Tl solid solution (with possible presence of hydrogen) produced by diffusing ^{201}Tl into a specially prepared multicomponent solid solution, sample II - thallium oxide on a platinum substrate, and sample III - thallium sulfate [metallic thallium on a platinum substrate subjected to a H_2SO_4 solution (6×10^{-4} mol/l)]. The chemical shifts of the internal lines in x-ray photoelectron spectra provide supportive evi-

 © 1998 American Institute of Physics

dence for this assumption. In particular, the Tl4f-electron lines exhibit a shift of $+1.4$ eV in the oxide relative to the solid solution.

It is known that radiation can affect the state and composition of the surface of a solid. Therefore in order to study the effect of x-ray irradiation on the physicochemical state of samples the valence-band conversion spectra of samples I and III were measured twice. The first measurement was made before the irradiation (with the samples retaining their numbers, I and III), and the second, after irradiation by x rays with a photon energy of 1486.6 eV (these samples will be labeled Ia and IIIa).

The experimental method and conversion-spectrum treatment was described in Ref. 4.

The binding-energy scale of the instrument was calibrated against x-ray photoelectron lines reckoned from the Fermi level position. The conversion-electron binding energies were derived from the expression

$$\varepsilon_c = \varepsilon_x + \Delta E ,$$

where ε_c is the binding energy of conversion electrons, ε_x is the position of a conversion line on the standard x-ray photoelectron-energy scale, and $\Delta E = 78.2$ eV is the energy difference between the conversion and x-ray photoelectron lines for the same Hg$4p_{3/2}$ subshell (Ref. 14).

The spectrum processing (least-squares fitting,[16,17] peak-position determination) was performed using the SPRO program package[18].

2. RESULTS AND DISCUSSION

Figure 1a–e displays mercury valence-band conversion spectra obtained in different samples before and after irradiation with soft (1486.6 eV) x-rays. It is known[19] that outer and inner valence molecular orbitals can form in the electron binding-energy regions below 15 eV and within the 15–50-eV interval, which gives rise to a fine structure in the electron spectra. An additional fine structure in the conversion spectra can appear in connection with characteristic losses, Auger transitions, etc. Because Auger peaks in the energy range of interest to us here are actually smooth broad maxima,[14] they do not interfere with an analysis of the structure of conversion spectra, which consist of narrow lines.

The spectra in Fig. 1a, 1d, and 1e are normalized in intensity to the inner line of the Hg $5p_{3/2}$ electrons. This line was measured simultaneously with the valence-band spectrum, thus making possible this normalization. The normalization of the spectra permits estimation of the relative contributions of various electronic states to the valence-band spectrum.

As seen from Fig. 1, there is a substantial difference between the valence-band structures of different samples, as well as of a sample before and after x-ray irradiation.

Note that the conversion probabilities for a given transition [for a multipolarity ratio in the mixture $\delta^2(E2/M1) = 2.1\times10^{-4}$, Ref. 14] are of the same order of magnitude for s and p states, which sets them off in intensity in a conversion spectrum, and that the conversion probability ratios for valence subshells are related through $\omega(5d_{3/2})/\omega(5d_{5/2}) = 1.16$ and $\omega(5d_{3/2})/\omega(6s) = 0.17$.[13,20]

The electronic configuration of a free mercury atom is $\{\mathrm{Xe}\}4f^{14}5d^{10}6s^2$. Solid metallic mercury was shown[21,22] to have a broad (9.25 eV) sp band including partially the $5d_{5/2}$ subshell, which accounts for its broadening. The spreadout of the s-electron density in the broad sp region should reduce significantly the sp-band conversion amplitude to the extent where it becomes, by our estimates, of the order of the amplitude due to the Hg5d electrons. Therefore the valence conversion spectra of our samples consist primarily of the peaks due to the mercury $5d$ electrons and of a broad sp band. In contrast to the conversion spectrum, in an x-ray photoelectron spectrum the s and p states are much less pronounced (see, e.g., Fig. 1f taken from Ref. 22).

Table I lists the electron binding energies corresponding to the different valence-band maxima (Fig. 1), the binding energies of $5d$ electrons for metallic mercury,[22,23] the weighted mean of the sp-band electron energy,[22] and the binding energy of the oxygen O2p electrons[24].

An analysis of conversion spectra (Fig. 1) and of the data presented in Table I reveals a structural similarity between the spectra in Fig. 1a and 1b (samples I and Ia, respectively), except for the features associated with the clearly seen splitting of peaks K and G (Fig. 1a) into two components following x-ray irradiation. Peak M undergoes a similar, although less pronounced, change. Peaks H and I in both figures are close in position to the Hg $5d_{3/2}$ line of metallic mercury, and peak K, to the Hg $5d_{5/2}$-electron line. On the whole, the valence-band spectra of mercury in the Pt-Au-Hg-Tl solid solution exhibit a complex structure determined by a mixture of electronic states. The irradiation-induced changes in the valence-band structure associated with the splitting of the peaks into components are possibly due to a transition of the sample from the amorphous to a more ordered state. In particular, Ref. 25 discusses this point by invoking experimental spectra of silicon, germanium, and other elements. The splitting of the Hg $5d_{5/2}$-electron line of mercury by the crystal field has been studied both experimentally and theoretically.[22]

The spectrum in Fig. 1c is actually a spectrum of mercury formed by electron capture at the thallium site in sample III. X-ray irradiation of sample III produces strong changes in the valence conversion spectrum (see Fig. 1d, sample IIIa) making it similar to a certain extent to that of mercury in the Pt-Au-Hg-Tl solid solution. It may be conjectured that irradiation initiates a reducing reaction in sample III, so that the conversion spectrum in Fig. 1d is actually due to mercury surrounded by metallic thallium on the Pt substrate (sample IIIa). Peak H (Fig. 1d) is close in position to the Hg $5d_{3/2}$-electron line, and peak K approaches in binding energy the Hg $5d_{5/2}$ line. Similar to sample I, one observes peaks G and K to split into components following x-ray irradiation of sample III. Note also the remarkable feature of the spectrum in Fig. 1c (sample III) associated with the absence of any significant electron density in the Hg $5d_{3/2}$-electron region (peak H) and its presence in the Hg $5d_{5/2}$ region (peak K). This feature may be due to the

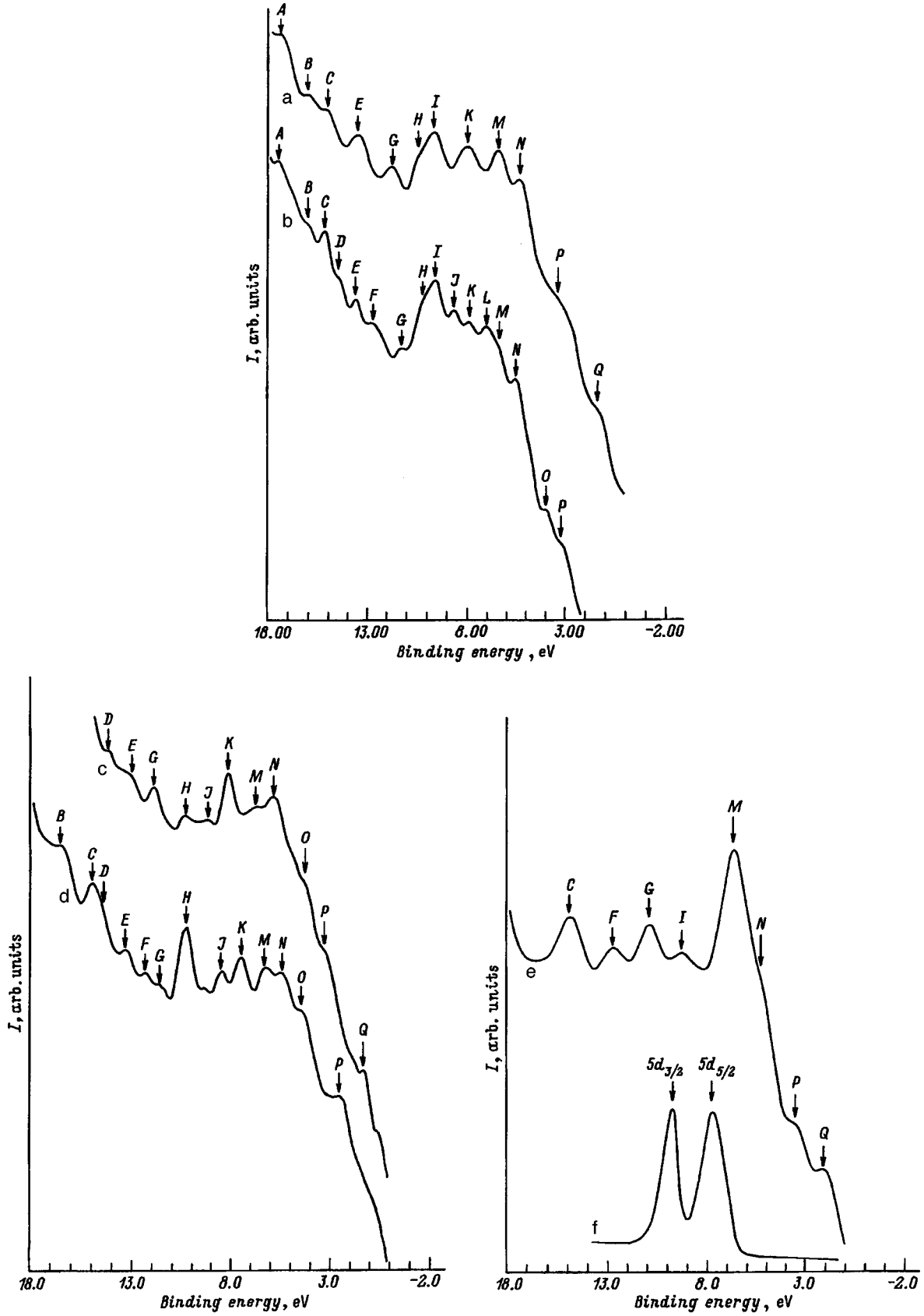

FIG. 1. (a–f) Conversion valence-electron spectra of the 1.56-keV ($M1+E2$) transition in ^{201}Hg for samples: (a) I (before x-ray irradiation), (b) I*a* (after irradiation of sample I); (c) III (before irradiation), (d) III*a* (after irradiation of sample III), (e) sample II, (f) x-ray photoelectron spectrum of metallic mercury[22] shown for comparison. Spectra *a*, *d*, and *e* are normalized in intensity against the inner Hg $5p_{3/2}$-electron line. The maxima in the figure are labeled in accordance with the notation in Table I.

TABLE I. Energy positions of maxima in the valence-band electron spectrum in eV (Fig. 1) and data of Refs. 22–24. The maxima in the Table are labeled as in Fig. 1.

	Notation of maxima																
Sample	*A*	*B*	*C*	*D*	*E*	*F*	*G*	*H*	*I*	*J*	*K*	*L*	*M*	*N*	*O*	*P*	*Q*
I	17.3	16.1	15.1		13.4		11.8	10.3	9.7		8.1		6.5	5.4		3.3	1.3
I*a**	17.5	16.0	15.2	14.4	13.6	12.7	11.4	10.2	9.7	8.7	7.9	7.1	6.5	5.5	4.0	3.1	
III				14.2	13.0		12.0	10.4		9.3	8.2		6.8	5.9	4.3	3.2	1.3
III*a***		16.5	15.0	14.5	13.3	12.3	11.7	10.3		8.5	7.5		6.3	5.4	4.4	2.5	
II			15.0			12.8	11.0		9.3				6.8	5.2		3.5	2.1
Shell																	
Hg 5*d*, 6*s****									9.8		7.8					3.7	
Hg 5*d*****									9.6		7.8						
O2*p******													7				

* After x-ray irridation of sample I.
** After x-ray irradiation of sample III.
*** Ref. 22, the value of 3.7 corresponds to the weighted mean for whole *sp* band.
**** Ref. 23.
***** Ref. 24.

formation in sample III of a molecular orbital involving the Hg $5d_{5/2}$ electrons and to their substantial delocalization. This is what causes the decrease in this line intensity in the conversion spectrum. Thus the atomic-orbital system is replaced in the spectrum of sample III by a system of newly formed molecular orbitals.

The spectrum in Fig. 1e reflects the structure of the valence band of mercury formed at the site of a thallium atom in its oxide (sample II). As seen from Table I, the difference in the electron binding energy between peaks *G* and *I* in this spectrum is close to the spin-orbit splitting of the mercury Hg $5d$ lines. It should be pointed out that in Tl_2O, for instance, the distance between the oxygen and metal atoms is 2.15 Å.[26] It is known that at such atomic distances molecular orbitals can form effectively in the valence band. The very strong peak *M* in this figure is close in binding energy to the position of the O $2p$ oxygen line (Table I). Because conversion takes place in the vicinity of the mercury atom, observation in the conversion spectrum of this molecular orbital containing the O $2p$ atomic orbital evidences the presence of O $2p$ electronic density near the ^{201}Hg atom. Similar phenomena were observed by a number of authors for uranium and technetium compounds.[5,7,8,10,27]

The specific features in the spectral structure revealed in the above analysis agree with the assumptions concerning the chemical state of the samples studied.

On the whole, the spectra clearly exhibit a dependence of the local electron-density distribution near an isomeric nucleus on the physicochemical state of the sample. The present work permits formulation of a general idea regarding the magnitude and nature of the changes in local electronic density (observed in conversion spectra) induced by changes in the chemical environment of a probe atom. The observed changes are accounted for by a rearrangement of the electronic structure and by the differences in the degree of localization of the outer electrons of mercury and of the surrounding atoms. To better understand the nature of the changes occurring in valence-band spectra one has to carry out adequate calculations which would take into account the actual chemical environment of mercury atoms, similar to the ones performed[6,28–33] for technetium and uranium compounds.

The authors express their gratitude to Yu. A. Teterin for valuable comments and to S. K. Lisin for fruitful discussions on the experimental techniques.

[1] V. N. Gerasimov and V. M. Kulakov, Izv. Akad. Nauk SSSR, Ser. Fiz **54**, 1705 (1990).
[2] I. M. Band, L. A. Sliv, and M. B. Trzhaskovskaya, Nucl. Phys. A **156**, 170 (1970).
[3] D. P. Grechukhin and A. A. Soldatov, Vopr. At. Nauki Tekh., Ser.: Yad. Konstanty **2**(56), 36 (1984).
[4] V. N. Gerasimov and V. M. Kulakov, *Effect of Chemical Environment on the Conversion Process. Conversion Electron Spectroscopy of Technetium Compounds: a Review* [in Russian], TsNII atominf., Moscow (1988), 71 pp.
[5] V. N. Gerasimov, A. G. Zelenkov, V. M. Kulakov, V. A. Pchelin, M. V. Sokolovskaya, A. A. Soldatov, and L. V. Chistyakov, Zh. Éksp. Teor. Fiz. **82**, 362 (1982) [Sov. Phys. JETP **55**, 205 (1982)].
[6] V. N. Gerasimov, A. G. Zelenkov, V. M. Kulakov, and A. A. Soldatov, Zh. Éksp. Teor. Fiz. **89**, 540 (1985) [Sov. Phys. JETP **62**, 307 (1985)].
[7] V. I. Zhudov, A. G. Zelenkov, V. M. Kulakov, B. V. Odinov, and Yu. A. Teterin, in *Abstracts of the XXX All-Union Meeting on Nuclear Spectroscopy and Nuclear Structure* (Leningrad, 1980), p. 614.
[8] D. P. Grechukhin, V. I. Zhudov, A. G. Zelenkov, V. M. Kulakov, B. V. Odinov, A. A. Soldatov, and Yu. A. Teterin, JETP Lett. **31**, 592 (1980).
[9] V. I. Zhudov, V. M. Kulakov, and A. D. Panov, Vopr. At. Nauki Tekh., Ser.: Yad. Konstanty **3**(36), 48 (1986).
[10] A. D. Panov and V. M. Kulakov, *Study of the Electronic Structure of Uranium Compounds by Conversion Spectroscopy: Review* [in Russian], TsNII atominform. (Moscow, 1988), 45 pp.
[11] J. W. Petersen, G. Weyer, E. Holzschuh, W. Kundig, and ISOLDE Collaboration, Phys. Lett. A **146**, 226 (1990).
[12] *Tables of Isotopes*, edited by C. M. Lederer and V. S. Shirley, Wiley, New York (1978), pp. 1291–1292.
[13] O. Dragoun, V. Brabes, M. Ryšavý, A. Špalek, and K. Freitag, Z. Phys. A **326**, 279 (1987).
[14] V. N. Gerasimov, D. V. Grebennikov, V. M. Kulakov, S. K. Lisin, and V. V. Kharitonov, Yadernaya Fizika **60**, 1948 (1997).
[15] M. A. Kelly and C. E. Tyler, Hewlett-Packard J. **24**, No. 11, 2 (1973).
[16] A. Savitzky and M. J. E. Golay, Anal. Chem. **36**, 1627 (1964).
[17] J. Steinier, Y. Termonia, and J. Deltour, Anal. Chem. **44**, 1906 (1972).
[18] A. D. Panov, IAÉ Preprint No. 6019/15 (Moscow, 1997), 31 pp.
[19] Yu. A. Teterin and S. G. Gagarin, Usp. Khim. **65**, 895 (1996).

[20] I. M. Band and M. B. Trzhaskovskaya, Izv. Akad. Nauk SSSR, Ser. Fiz **55**, 2121 (1991).
[21] S. C. Keeton and T. L. Loucks, Phys. Rev. **152**, 548 (1966).
[22] S. Svensson, N. Mårtensson, E. Basilier, P. Å. Malmqvist, U. Gelius, and K. Siegbahn, J. Electron Spectrosc. Relat. Phenom. **9**, 51 (1976).
[23] J. C. Fuggle and N. Mårtensson, J. Electron Spectrosc. Relat. Phenom. **21**, 275 (1980).
[24] A. S. Koster and H. Mendel, J. Phys. Chem. Solids **31**, 2511 (1970).
[25] V. V. Nemoshkalenko and V. G. Aleshin, in *Electron Spectroscopy of Crystals* (Naukova Dumka, Kiev, 1976), pp. 222–225.
[26] K. S. Krasnov, in *Molecular Constants of Inorganic Compounds: Handbook* [in Russian], Khimiya, Leningrad (1979), p. 96.
[27] D. V. Grebennikov, V. I. Zhudov, V. M. Kulakov, B. V. Odinov, and A. D. Panov, Vopr. At. Nauki Tekh., Ser.: Yad. Konstanty **5**(13), 68 (1990).
[28] C. Schober, N. E. Christensen, and P. Ziesche, Solid State Commun. **77**, 173 (1991).
[29] V. N. Gerasimov, A. G. Zelenkov, V. M. Kulakov, V. A. Pchelin, M. V. Sokolovskaya, A. A. Soldatov, and L. V. Chistyakov, Zh. Éksp. Teor. Fiz. **86**, 1169 (1984) [Sov. Phys. JETP **59**, 683 (1984)].
[30] E. Hartmann, R. Der, and M. Nagel, Z. Phys. A **290**, 349 (1979).
[31] E. Hartmann and G. Seifert, Phys. Status Solidi B **100**, 589 (1980).
[32] T. Ziegler, A. Rauk, and E. J. Baerends, Chem. Phys. **16**, 209 (1976).
[33] V. N. Gerasimov, V. Yu. Dobretsov, V. M. Kulakov, and A. A. Soldatov, Izv. RAN, Ser. Fiz. **56**, No. 7, 181 (1992).

Translated by G. Skrebtsov

Self-consistent diffusion-controlled growth of nuclei from eutectic solutions

S. A. Kukushkin and A. S. Sokolov

Institute of Problems of Mechanical Engineering, Russian Academy of Sciences, 199178 St. Petersburg, Russia

(Submitted February 17, 1998)
Fiz. Tverd. Tela (St. Petersburg) **40**, 1615–1618 (September 1998)

A study is made of the dynamics of self-consistent motion and growth of spherical new-phase nuclei from a eutectic melt. The growth rate of nuclei is shown to be proportional to supersaturation in both components. Motion of a single nucleus in a concentration-gradient field and of a pair of nuclei in a self-consistent concentration field is investigated. The velocity of motion of the nucleus as a whole has been established to depend on the key parameters of the problem, namely, supersaturation, radii of the nuclei, and their separation. The force of mutual attraction between nuclei is estimated, and it is shown to be inversely proportional to the fifth power of their separation. © *1998 American Institute of Physics.* [S1063-7834(98)01009-0]

Investigation of the early stages in crystallization of eutectic melts has recently been started.[1,2] Interest in these problems is motivated primarily by the extreme diversity of the structures produced in solidification of such melts.[3] There is still no clear understanding of the observation[3] that the final structure of the solid phase produced in solidification of melts of the same composition but under different cooling conditions may be radically different. Indeed, in some conditions these may be layered periodic structures, with layers of one component alternating with those of the other, whereas if produced under other conditions the solid phase will consist of small crystals.

The approach developed by us earlier[1,2] and continued in the present work consists essentially in calculating the interaction among grains of the new phase in eutectic melts.

It was shown[2] that in late crystallization stages of eutectic melts a peculiar interaction arises among grains of the new phase, which brings about a common universal distribution of grains of different composition by size. It was also shown,[2] on the other hand, that grains forming in early stages in eutectic melts interact with one another to form singular systems which resemble in many respects electric dipoles called in Ref. 2 ''diffusion dipoles''. It was found that a common critical size sets in in the melt.

1. SELF-CONSISTENT GROWTH RATE OF NUCLEI IN A EUTECTIC MELT

We are considering here self-consistent growth of two spherical nuclei of compositions A and B separated by a finite distance from one another, in contrast to the growth of a eutectic nucleus[2] assumed to consist of two hemispheres of different composition. It is assumed that the heat conductivity of the melt is infinite (hence that the temperature is constant throughout the volume), that components A and B have the same diffusion coefficients, and that thermodynamic equilibrium obtains between the phases on the surface of the nuclei.

Under these assumptions, the growth of the nuclei is controlled by diffusion transport of the components. Assuming the growth of the nuclei to proceed sufficiently slowly, we have to solve the Dirichlet problem in quasi-steady-state approximation for the melt:

$$\nabla^2 C_i = 0\,, \tag{1}$$

where $C_i = C_A, C_B$ are the concentrations of components A and B in the melt, respectively. The concentrations of components A and B at infinity and at the surface of the spheres can be written (Fig. 1):

$$C_{A_\infty} = C_E\,, \quad C_{B_\infty} = 1 - C_E\,,$$

$$C_{AS_A} = C_1 + \frac{2\omega_1\sigma_1}{R_1} = \hat{C}_1 < C_E\,,$$

$$C_{BS_B} = (1 - C_2) + \frac{2\omega_2\sigma_2}{R_2} = 1 - \hat{C}_2 < 1 - C_E\,. \tag{2}$$

The notation here is as follows: C_E is the concentration of component A corresponding to the eutectic composition, $R_i(t)$ are the radii of the nuclei, $2\omega_i\sigma_i/R_i$ is the excess concentration of components above the surface of spherical particles resulting from the Gibbs-Thomson effect, σ_i is the surface-tension coefficient, and ω_1 and ω_2 are, respectively, volumes per A and B atom in new-phase nuclei.

Introducing a new variable

$$\varphi = \frac{C_A - C_E}{C_E}\,, \tag{3}$$

one reduces Eq. (1) with boundary conditions for component A to the form

$$\nabla^2 \varphi = 0\,, \tag{4}$$

$$\varphi_\infty = 0, \quad \varphi_{S_A} \equiv \varphi_A < 0, \quad \varphi_{S_B} \equiv \varphi_B > 0\,. \tag{5}$$

Because the problem is linear, it can be divided into two with the following boundary conditions

$$\varphi_A^{(1)} = \varphi_A\,, \quad \varphi_B^{(1)} = 0\,, \tag{6}$$

 © 1998 American Institute of Physics

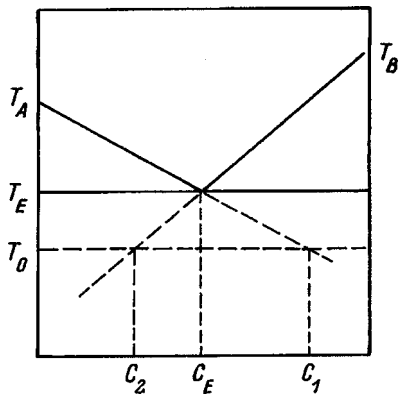

FIG. 1. Phase diagram of a eutectic system.

$$\varphi_A^{(2)}=0, \quad \varphi_B^{(2)}=\varphi_B, \tag{7}$$

where conditions (6) and (7) correspond to melt supersaturation in the corresponding component only at one of the two nuclei. The general solution can now be obtained by superposition

$$\varphi=\varphi^{(1)}+\varphi^{(2)}. \tag{8}$$

As seen from Eqs. (4) and (5), this problem suggests an intimate analogy with the problem of finding the electrostatic field of two spheres charged to potentials φ_A and φ_B, and therefore we shall use for its solution the image method and, dropping intermediate operations, write out only the main results. To do this, we first find some dimensionless fictitious charges similar to real charges in electrostatics and use the Gauss theorem to calculate the vector fluxes, from which one can subsequently derive the growth rate of grains of the A and B compositions.

Let R_A and R_B be, respectively, the radii of the nuclei of compositions A and B, and h, separation between them (Fig. 2), with $h>R_A+R_B$. Then an approximate expression yields for the growth rate of a nucleus of composition A

$$\frac{dR_A}{dt}=\frac{1}{R_A(t)}\frac{\omega_S}{\omega_l}D[(C_E-\hat{C}_1)G_1+(\hat{C}_2-C_E)G_2], \tag{9}$$

where

$$G_1=1+\frac{R_AR_B}{h^2-R_B^2}, \quad G_2=\frac{R_B}{h}\left(1+\frac{R_AR_B}{h^2-R_A^2-R_B^2}\right),$$

D is the diffusion coefficient, and ω_s and ω_l are the volumes per molecule in the solid and liquid states, respectively.

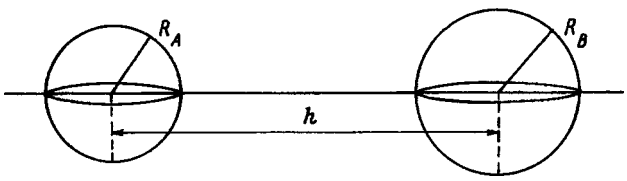

FIG. 2. Schematic position of interacting nuclei.

2. MOTION AND GROWTH OF NUCLEI IN A CONCENTRATION-GRADIENT FIELD

A. Motion of a single nucleus in a uniform concentration field

It was shown[4,5] that if the nucleus of a new phase is in a field with a uniform concentration gradient of the form

$$C_A(\mathbf{r})=C_0+\mathbf{r}\nabla C_\infty, \tag{10}$$

it can move as a whole.

For times longer than the relaxation time

$$\tau_r\sim\frac{R^2}{D}, \tag{11}$$

the growth of the nucleus and its motion as a whole in the melt reach a quasi-steady-state regime.[4] In these conditions, the concentration distribution in the melt is described by the Laplace equation

$$\Delta C=0 \tag{12}$$

subject to the following boundary conditions 1) for $r\to\infty$, condition (11), 2) at the surface of a nucleus

$$C_S=C_0\left(1+\frac{2\sigma\omega}{RkT}\right). \tag{13}$$

Similarly, a grain will move in a binary melt with a concentration gradient of such a kind. The velocity of this motion can be calculated by making a few manipulations with the equations derived in Ref. 5. For the velocity of the center-of-mass motion we obtain

$$\mathbf{V}_c=3\frac{\omega_S}{\omega_l}D\nabla C_\infty. \tag{14}$$

In eutectic melts

$$C_A(\mathbf{r})=C_0+\mathbf{r}\nabla C_\infty\approx C_E \tag{15}$$

the rate of growth of a nucleus (for $\omega_l\approx\omega_s$) will be

$$\frac{dR}{dt}\approx D\frac{C_E-C_S}{R}\equiv\frac{D\Delta C}{R}. \tag{16}$$

Equation (16) coincides with the expression for the growth rate with zero concentration gradient. The effect of ∇C_∞ on the growth of a nucleus manifests itself only in different supersaturations ΔC of component A in different parts of the melt.

B. Motion of a pair of nuclei in a self-consistent concentration field

Because the sum of component concentrations in a eutectic melt is equal to one, the growth of a nucleus of one composition, e.g., A, results in its absorbing substance A from the melt, and in the corresponding increase of the concentration of B in the melt. This, in its turn, increases the growth rate of the nucleus of composition B. Besides, a concentration gradient sets in, which should give rise to a certain ″attraction″ of nuclei to one another and, accordingly, to their

motion in a self-consistent concentration field. Let us study this process in a quantitative way. Consider a binary melt of eutectic composition containing a nucleus of composition A having radius R_A and a B nucleus of radius R_B, which are separated by a distance h (Fig. 2). Restricting ourselves to an approximate solution of the problem (1) and (2), we retain only the first three terms in the image method, which yields the following expression for the diffusion flux $\mathbf{J}_S$ to an element of area dS on the surface of nucleus A:

$$\mathbf{J}_S=\frac{D}{R_A\omega}\left[(C_\infty-C_A)+(C_B-C_\infty)\frac{R_A^2R_B}{r^3}\left(\frac{h^2}{R_A^2}-1\right)\right]\mathbf{n}. \tag{17}$$

The notation in Eq. (17) is as follows: C_∞, C_A, and C_B are the concentrations of component A far away from the nuclei and at the surface of nuclei A and B, respectively, and r is the distance from the center of nucleus B to an element dS on the A surface.

Taking into account that the velocity $\mathbf{V}_S$ of the element of surface area dS is related to $\mathbf{J}_S$ through

$$\mathbf{V}_S=-\omega\mathbf{J}_S,$$

and the velocity $\mathbf{V}_c$ of the center of mass of nucleus A relative to the melt is given by (see, e.g., Ref. 6)

$$\mathbf{V}_c=\frac{1}{V}\oint_S\mathbf{r}_S(\mathbf{V}_S,d\mathbf{S}), \tag{18}$$

where $\mathbf{r}_S$ is the position vector of a point on the surface reckoned from the center of mass, we obtain for $\mathbf{V}_c$ the following relation

$$\mathbf{V}_c=\frac{D}{V}\oint_S\mathbf{n}\left[(C_\infty-C_A)+(C_B-C_\infty)\frac{R_A^2R_B}{r^3}\left(\frac{h^2}{R_A^2}-1\right)\right]dS. \tag{19}$$

The problem being axially symmetric, the velocity of the center of mass is directed along the line connecting the nuclei and can be written

$$V_c=\frac{3}{2}\frac{\omega_S}{\omega_l}\frac{D}{h}\left(\frac{1}{\delta_1}-1\right)\delta_1\delta_2(C_B-C_\infty)\times\int_0^\pi\frac{\cos\Theta\,d\Theta}{(1-2\delta_1\cos\Theta+\delta_1^2)}, \tag{20}$$

where $\delta_1=R_A/h$ and $\delta_2=R_B/h$.

Evaluation of V_c for $\delta_1\ll1$ yields

$$V_c=\frac{9\pi}{4}\frac{\omega_S}{\omega_l}(C_B-C_\infty)\frac{DR_B}{h^2}. \tag{21}$$

A comparison of Eq. (21) with the rate of growth $\dot{R}_A(t)$ of the radius of nucleus A [see Eq. (9)] shows that

$$\frac{V_c}{\dot{R}_A}\sim\frac{9\pi}{4}\frac{R_AR_B}{h^2}\frac{C_B-C_\infty}{C_\infty-C_A}. \tag{22}$$

For

$$R_A\sim h,\ R_A\ll R_B,\quad (C_B-C_\infty)/(C_\infty-C_A)\sim1$$

we have

$$\frac{V_c}{\dot{R}_A}\sim\frac{R_B}{h}.$$

On the other hand, if the radii of the nuclei $R_A\sim R_B\sim h/3$, then $V_c/\dot{R}_A\sim\pi/4$, so that the rate of growth and the velocity of motion of a nucleus are comparable.

The expressions we have derived permit one to estimate the force of mutual attraction of nuclei. As follows from Eq. (21), for $\delta\ll1$, $V_c\sim h^{-2}$. One can readily show that the force of interaction between nuclei F is of a short-range nature and falls off inversely proportional to the fifth power of distance between them:

$$F\sim h^{-5}. \tag{23}$$

3. DISCUSSION OF RESULTS

An analysis of the dynamics of self-consistent motion and growth of spherical nuclei in a eutectic melt has shown that the growth rates of nuclei are determined by the melt supersaturation in both components. This implies, in particular, that self-consistent growth of nuclei in a binary melt occurs faster than the corresponding diffusion-controlled growth of nuclei in one-component systems. The growth rate of grains in a diffusion-dominated regime is inversely proportional to their dimensions, which is in agreement with published experimental data.

Our study has shown also that, in the course of growth, nuclei are attracted to one another, which results in their concerted motion as a whole. The attracting force falls off rapidly with distance, however, so that the motion of nuclei has to be taken into account only at later stages in the melt crystallization.

Partial support of the Russian Fund for Fundamental Research (Grant 96-03-32396) and of the Integration Program (Grant 589, leading organization this Institute) is gratefully acknowledged.

[1] S. A. Kukushkin and D. A. Grigor'ev, Fiz. Tverd. Tela (St. Petersburg) **38**, 1262 (1996) [Phys. Solid State **38**, 698 (1996)].
[2] S. A. Kukushkin and A. V. Osipov, Fiz. Tverd. Tela (St. Petersburg) **39**, 1464 (1997) [Phys. Solid State **39**, 1299 (1997)].
[3] R. Elliott, *Eutectic Solidification Processing of Crystalline and Glassy Alloys* [Butterworths, London, 1983; Metallurgiya, Moscow, 1987, 351 pp.].
[4] Ya. E. Geguzin and M. A. Krivoglaz, *Migration of Macroscopic Inclusions in Solids* [Consultants Bureau, New York, 1973; Metallurgiya, Moscow, 1971, 344 pp.].
[5] Ya. E. Geguzin, *Diffusion-Controlled Zone* [in Russian], Nauka, Moscow (1979), 343 pp.
[6] V. V. Slezov and L. V. Tanatarov, Metallofizika **10**, 4, 67 (1988).

Translated by G. Skrebtsov

Pulsed EPR spectroscopy of the V_{KA} center in CaF_2:Na

T. A. Gavasheli, D. M. Daraseliya, D. L. Dzhaparidze, R. I. Mirianashvili, and T. I. Sanadze

Tbilissi State University, 380028 Tbilissi, Georgia

(Submitted January 12, 1998; resubmitted March 3, 1998)
Fiz. Tverd. Tela (St. Petersburg) **40**, 1619–1622 (September 1998)

An EPR study of the self-trapped hole center (V_{KA} center) in Na-doped single-crystal CaF_2 is reported. A five-component hyperfine-interaction tensor was used for the first time to describe EPR spectra adequately. The parameters of the electron spin Hamiltonian of the V_{KA} center, the tensors of ligand hyperfine interaction with all nearest-neighbor nuclei, and constants of quadrupole interaction with the Na nucleus have been determined. The structure of the center has been unambiguously established from the results obtained, and the mechanisms of its formation are discussed. © *1998 American Institute of Physics.* [S1063-7834(98)01109-5]

The defects produced in single crystals by ionizing radiation at low temperatures are of considerable interest for the physics of solid state and are being studied actively by various techniques, including the magnetic-resonance method. In particular, EPR and ENDOR spectra of the hole centers involving the molecular ion F_2^- in single-crystal CaF_2 were investigated.[1,2]

Investigation of these crystals doped by univalent alkali metals could shed light on the mechanisms responsible for the formation and thermal dynamics of radiation-induced defects. Our previous publications reported some of the results obtained in a study of EPR spectra and of hyperfine interactions of the hole V_{KA} center in Na-doped CaF_2.[3,4] The present work summarizes the final results of these studies and, in particular, offers a new interpretation of the EPR spectra.

1. EXPERIMENT

The experiments were carried out on a 3-cm EPR superheterodyne spectrometer at 4.2 K. An additional pulsed saturating klystron was employed to obtain spectra of discrete saturation (DS) and rf discrete saturation (RFDS). The DS and RFDS technique, which is actually a pulsed analog of ENDOR, is described in detail elsewhere.[5] CaF_2 samples contained 0.1% Na and were irradiated by a Co^{60} gamma source to an integrated dose of 10 Mrad. A special device permitted irradiation at a controlled temperature within the 77–200 K interval. The sample was subsequently transferred without any intermediate warm-up to a cryostat and cooled to liquid-helium temperature for taking EPR and RFDS spectra.

2. EPR STUDY OF THE V_{KA} CENTER IN CaF_2:Na

We showed that samples subjected to γ irradiation at 77 K produce two identical EPR spectra shifted by approximately 2° with respect to one another (as if the crystal consisted of two blocks turned through 2°).[3] This "block" pattern disappeared after the samples were heated above 170 K leaving one EPR spectrum with a substantially lower intensity. The samples irradiated by γ rays at a high temperature (170 K) exhibited the same EPR spectrum as after the heating, and its intensity was an order of magnitude higher. We shall return to the thermal transformation of EPR spectra later.

The samples used in the study were irradiated at 170 K. The superhyperfine (SHF) interaction studies of the V_{KA} center in CaF_2:Na reported below support the model presented in Fig. 1. Using the coordinate frame of this figure, the electron spin Hamiltonian of orthorhombic symmetry describing the EPR spectrum of the molecular ion F_2^- can be written

$$H_{\mathrm{EPR}}=\beta\mathbf{S}\mathbf{g}\mathbf{B}+\mathbf{S}(T_1\mathbf{I}_1+T_2\mathbf{I}_2)-g_F\beta(\mathbf{I_1}+\mathbf{I_2})\mathbf{B}, \qquad (1)$$

where $\mathbf{B}$ is the external magnetic field, $\mathbf{S}$ is the electron spin operator ($S=1/2$), g is the electron g factor, $\mathbf{I}_1$ and $\mathbf{I}_2$ are the

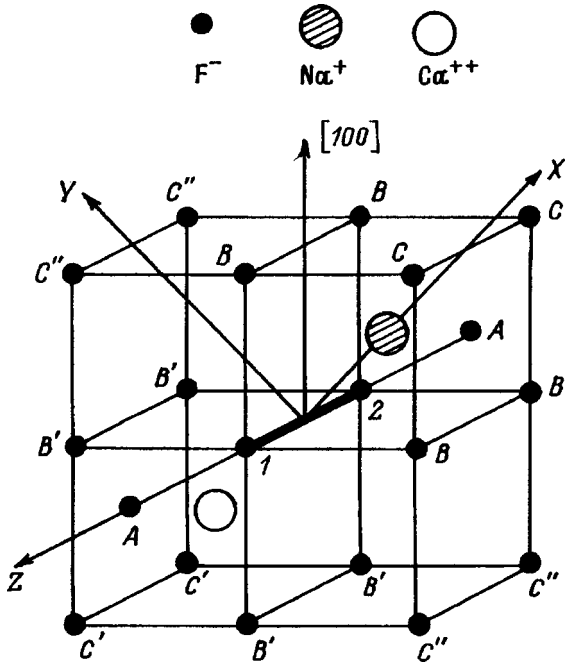

FIG. 1. Model of the V_{KA} center in CaF_2:Na.

 © 1998 American Institute of Physics

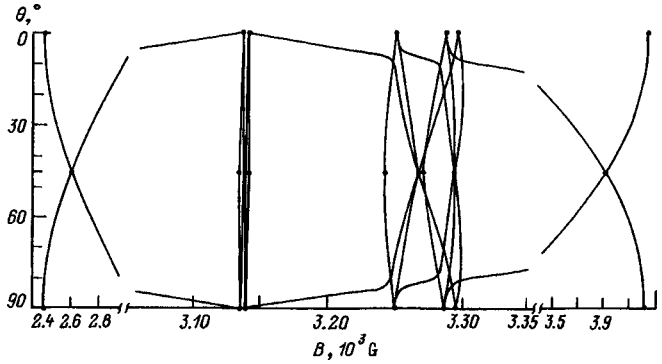

FIG. 2. Angular dependence of the EPR spectrum of six inequivalent V_{KA} centers in CaF_2:Na obtained with the magnetic field swept in the (100) plane of the crystal. The parameters of spin Hamiltonian (1) were taken from Table I.

nuclear spin operators of the fluorine nuclei 1 and 2 in the molecular ion, and T_1 and T_2 are, respectively, the corresponding hyperfine interaction tensors. From general symmetry considerations (the presence of the reflection plane XZ), tensor T_1 has the form

$$T_1 = \begin{vmatrix} T_{xx} & 0 & T_{xz} \\ 0 & T_{yy} & 0 \\ T_{zx} & 0 & T_{zz} \end{vmatrix}. \tag{2}$$

Tensor T_2 has the same form, the only difference being that the terms T_{xz} and T_{zx} are negative, because reflection in the XY plane sends nucleus 2 of the molecular ion into nucleus 1.

It should be pointed out that the description of the hyperfine (HF) structure in EPR spectra uses here for the first time a five-component HF interaction tensor. We measured the angular dependence of EPR spectra by sweeping the magnetic field in the (100) plane of the crystal. Because there are three possible mutually-perpendicular orientations of the F_2^- molecular ion and two possible positions of the Na^+ ion relative to F_2^- in each of these orientations, there must be six inequivalent types of the V_{KA} center. Each center produces a strongly anisotropic spectrum consisting of four EPR lines, hence, in a general case, there must be 24 lines altogether. With the magnetic field swept in the (100) plane, there remain in only 16 lines a general case, with some of them completely, and many lines strongly overlapping (see Fig. 2).

Adequate description of an EPR spectrum for orthorhombic symmetry requires measurements in two planes. We chose from the total angular dependence of the EPR spectrum for all six inequivalent V_{KA} centers the dependences obtained for one of the centers measured in two mutually-perpendicular planes.

The parameters of spin Hamiltonian (1) were determined by a computer code for the minimization of variance, $\Sigma(B_i^{\rm exp} - B_i^{\rm theor})^2$, where the summation is performed over all well-resolved EPR lines, and $B_i^{\rm theor}$ was calculated by precise diagonalization of the 8×8 complex matrix of Hamiltonian (1). The variance was found to be only weakly sensitive to the difference between the parameters T_{xz} and T_{zx}, and therefore in our final calculations we had to assume $T_{xz} = T_{zx}$. The calculated parameters of the electron spin Hamiltonian are presented in Table I. Figure 2 displays the total angular dependence of the EPR spectrum of V_{KA} centers derived from these parameters for the magnetic field swept in the (100) plane.

TABLE I. Calculated parameters of the molecular-ion spin Hamiltonian. The HF interaction constants are given in MHz (and in G in the parentheses).

g_x	g_y	g_z	T_{xx}	T_{yy}	T_{zz}	T_{xz}
2.0199 ±0.0002	2.0188 ±0.0004	2.0015 ±0.0002	70±3 (25±1)	43±8 (15±3)	2572±1 (918.2±0.4)	73±1 (25.8±0.4)

The difference of the parameters listed in Table I from our previous data[3] is accounted for by the fact that our earlier study made use of the traditional diagonal form of the HF interaction tensor, and, accordingly, one could not correctly identify the EPR lines.

3. SUPERHYPERFINE INTERACTIONS

The preliminary investigation[4] of SHF interaction in the V_{KA} center by the DS technique was followed by a more comprehensive RFDS study. The angular dependence of RFDS spectra was measured on an EPR line having small anisotropy. Also, for this line $I=0$, $M=0$, and there is no electronic-state mixing by strong hyperfine interaction. Therefore one can describe the SHF coupling of the F_2^- molecule to the nearest-neighbor nuclei by a spin Hamiltonian containing only nuclear interactions and set $S=1/2$. The Hamiltonians of the nuclei surrounding the molecular ion F_2^- were constructed in the coordinate frame shown in Fig. 1.

A. Interaction with sodium nuclei

The nuclear spin Hamiltonian of sodium can be written

$$H_{\rm Na} = g_{\rm Na}\beta_N \mathbf{IB} + \mathbf{SAI} + \mathbf{IPI}, \tag{3}$$

where $S=1/2$, $I=3/2$, A and P are the SHF- and quadrupole-interaction tensors, $g_{\rm Na}$ is the nuclear g factor of Na, and β_N is the nuclear magneton. The presence of two mutually perpendicular reflection planes makes these tensors diagonal, and besides $P_{xx}+P_{yy}+P_{zz}=0$.

The angular dependence of RFDS frequencies is presented in Ref. 4. The parameters of spin Hamiltonian (3) were found by the variance minimization procedure described above in connection with EPR spectra, which in-

TABLE II. Components of the SHF and quadrupole interaction for sodium nuclei (in MHz).

A_{xx}	A_{yy}	A_{zz}	P_{xx}	P_{yy}	P_{zz}
−1.801±0.003	−4.714±0.003	−4.089±0.007	−0.153±0.002	−0.149±0.003	0.004±0.004

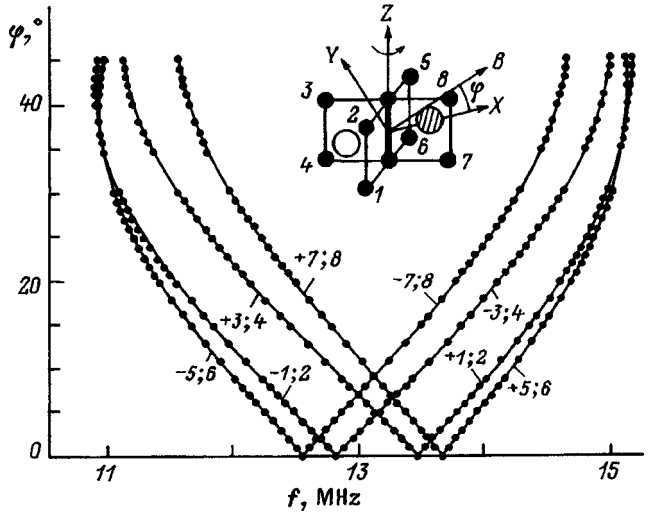

FIG. 3. Angular dependence of the RFDS spectrum of type-*B* fluorine nuclei measured in the (001) plane of the crystal. The figures at the curves and in the model label particular fluorine nuclei: *5–8* for type *B*, and *1–4* for type *B′*. The ± signs at the curves refer to the $|+1/2\rangle$ and $|-1/2\rangle$ electronic states. The solid lines are plots of Eq. (5) with the parameters taken from Table III.

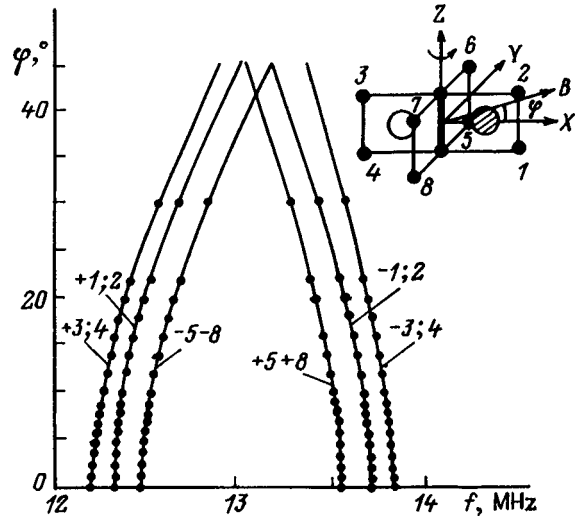

FIG. 4. Angular dependence of the RFDS spectrum of type-*C* fluorine nuclei measured in the (001) plane of the crystal. *C* refers to the *1–2* nuclei, *3–4*, to *C′* nuclei, and *5–8*, to *C″* nuclei. The *C″* lines are actually doublets with a maximum splitting of 30 kHz due to the $\pm A_{xy}$ components of the SHF interaction tensor. The solid lines are plots of Eq. (5) with the parameters taken from Table III.

cludes precise diagonalization of the complex 8×8 matrix of Hamiltonian (3). The results of the calculations are given in Table II. The mean deviation between the theoretical and experimental points is 3 kHz.

B. Interaction with fluorine nuclei

The nuclear Hamiltonian of the *n*th fluorine nucleus near a molecular ion F_2^- can be written

$$H_n = -g_F\beta_N\mathbf{I_nB}+\mathbf{SA}_n\mathbf{I}_n\,. \tag{4}$$

The fluorine nuclei surrounding the V_{KA} center can be divided into three groups denoted usually by *A*, *B*, and *C*.[2] The strongest HF interaction is observed for the *A* nuclei located along *Z*, which is the molecular-ion axis. These nuclei are responsible for the allowed HF structure in the EPR lines observed in the $B\|Z$ orientation. As follows from experiments, in contrast to the V_K center[2], nuclei *B* can be divided into two inequivalent groups, *B* and *B′*, located at Na^+ and Ca^{2+}, respectively. Similarly, in place of the two types of *C* nuclei for the V_K center, the V_{KA} center can be associated with three groups, namely, *C*, *C′*, and *C″*. The angular dependences of RFDS spectra of *B*- and *C*-type nuclei are displayed in Figs. 3 and 4.

The resonant frequencies of fluorine nuclei were determined from the expressions[5]

$$\nu_\pm = \sqrt{\nu_F^2+\frac{1}{4}\tilde{A}^2\mp\overline{A}\nu_F}\,, \tag{5}$$

where the ± sign refers to the two electronic states; $\tilde{A}^2=\alpha_{\zeta i}\alpha_{\zeta k}A_{pi}A_{pk}$; $\overline{A}=\alpha_{\zeta' i}\alpha_{\zeta k}A_{ik}$; $i,k,p=x,y,z$; $\alpha_{\zeta' x}=l_X$, $\alpha_{\zeta' y}=l_Y$, and $\alpha_{\zeta' z}=l_z$ are the direction cosines of the external magnetic field; the electron spin is quantized along the ζ axis with the direction cosines $\alpha_{\zeta k}=(g_k/g)l_k$; and ν_F is the nuclear Zeeman frequency. The calculated components of the HF interaction tensors for the nearest-neighbor nuclei are given in Table III.

4 DISCUSSION OF RESULTS

It is well known that the growth of fluorites doped by alkali metals is accompanied by the formation of the so-called impurity-vacancy dipoles.[6] In Na-doped CaF_2, it is the Na^+–fluorine-vacancy dipole. An electron knocked out from a fluorine ion by γ rays at 77 K is trapped by a vacancy to form an F_A center, and the ion which has lost the electron combines with a neighboring fluorine ion into a molecular ion F_2^-. Based on the dynamics of evolution of EPR spectra with temperature observed in our case, we believe that the vacancies occupied the sites denoted by *C* in Fig. 1. Accordingly, after the γ irradiation an F_A center forms at one of

TABLE III. Components of SHF interaction tensors for nearest-neighbor fluorine nuclei (in MHz).

Nucleus type	A_{xx}	A_{yy}	A_{zz}	A_{xy}	A_{xz}	A_{yz}
A	2.25±0.02	0.38±0.04	36.47±0.03	0	0.29±0.07	0
B	±0.63±0.01	0.22±0.02	−2.61±0.01	4.06±0.01	0.28±0.03	0.09±0.03
B′	−1.10±0.01	0.04×0.02	−2.90±0.01	3.65±0.01	0.23±0.03	0.07±0.03
C	1.60±0.01	−0.94±0.03	−0.99±0.02	0	0.56±0.05	0
C′	1.36±0.01	−1.13±0.03	−0.55±0.03	0	0.27±0.05	0
C″	−1.04±0.01	1.62±0.04	−0.68±0.02	0.04±0.01	0.06±0.06	0.55±0.10

these sites and will perturb slightly the EPR spectrum of the V_{KA} center. Heating this sample may result either in migration of the F_A center leaving in place the "pure" V_{KA} center, or in recombination, which will bring about the observed decrease in EPR intensity.

If a sample is irradiated at an elevated temperature (170 K), the recombined V_{KA} centers may appear again under irradiation, which will give rise to their build-up in the sample.

We note in conclusion that the above study of EPR and of HF interaction with nearest-neighbor nuclei provides unambiguous support for the model of the V_{KA} center presented in Fig. 1.

[1] W. Hayes and J. W. Twidell, Proc. Phys. Soc. London **79**, 1295 (1962).
[2] R. W. Marzke and R. I. Mieher, Phys. Rev. **182**, 453 (1969).
[3] T. A. Gavasheli, R. I. Mirianashvili, O. V. Romelashvili, and T. I. Sanadze, Fiz. Tverd. Tela (Leningrad) **34**, 672 (1992) [Sov. Phys. Solid State **34**, 361 (1992)].
[4] T. A. Gavasheli, D. M. Daraseliya, R. I. Mirianashvili, and T. I. Sanadze, Fiz. Tverd. Tela (St. Petersburg) **36**, 1787 (1994) [Phys. Solid State **36**, 979 (1994)].
[5] Ts. I. Sanadze and G. R. Khutsishvili, *Problems in Magnetic Resonance* [in Russian], Nauka (1978), 206 pp.
[6] Z. P. Chorniĭ, G. A. Shchur, S. I. Kachan, and S. P. Dubel't, Fiz. Élektron. **35**, 97 (1987).

Translated by G. Skrebtsov

Acoustic emission in the chalcogenide glass $Ge_{0.18}As_{0.28}Se_{0.54}$

Ya. M. Olikh

Institute of Semiconductor Physics, Ukrainian Academy of Sciences, 252650 Kiev, Ukraine
(Submitted March 10, 1998)
Fiz. Tverd. Tela (St. Petersburg) **40**, 1623–1626 (September 1998)

The effect of structural relaxations, which are caused by a temperature change as well as induced by external ultrasonic loading, on the velocity of elastic waves and on the acoustic noise spectrum in the chalcogenide glass $Ge_{0.18}As_{0.28}Se_{0.54}$ is investigated. The acoustically stimulated ''softening'' of the glass, observed for the first time, and acoustic emission signals, also observed for the first time, suggest that this method can be used to study structural changes in glass-like materials. © *1998 American Institute of Physics.* [S1063-7834(98)01209-X]

It is well known that chalcogenide glasses are promising acoustooptic materials with high radiation and beam hardness and chemical resistance. By its very nature glass, being in a supercooled state at low temperatures, is characterized by internal thermodynamic equilibrium, while it is metastable with respect to the crystalline state and, in principle, different structural configurations of the same composition can materialize.[1] The number of possible states increases substantially for multicomponent (ternary and higher order) compositions. For example, in the case of the chalcogenide glass (CG) system $Ge_xAs_ySe_{1-x-y}$, which we investigated, for most compositions, together with polymer chains, two- and three-dimensional structural groups are also realized simultaneously.[2] This means that there exists a possibility of their undergoing a phase transformation, including as a function of external factors.

In addition to the known structure-sensitive methods for investigating glass,[1] measurements of the acoustic characteristics in wide temperature and frequency intervals are also found to be effective.[3,4] Since acoustic emission (AE) signals, as far as we know, have not been previously observed in glassy materials, AE methods, being especially sensitive to structural changes in solids in general, also appear to be very promising for CGs in particular.

In this connection the objective of the present work is to determine the fundamental possibility of using the AE method to study structural relaxations in CGs in the process of varying the temperature and external ultrasonic (US) loading on a sample and to compare these data with the results of acoustic measurements.

Acoustic emission from solids in a prefracture state has been investigated quite thoroughly.[5] In solids, different external factors increase the internal stresses, which in some regions of the sample reach limiting values and result in the formation or rearrangement of defects. A portion of the energy released as a result of structural transformations goes into elastic waves, which propagate in the form of AE in the experimental sample. A local change of the specific volume and a density jumps are characteristic for all known mechanisms of AE in crystals. Hence the necessary condition for the appearance of AE is that the action of the source must be local.

It is also possible in solids that there exists acoustically stimulated AE, caused by defect formation under intense US loading.[6,7] The existence of medium-range order in glass in this sense makes glass similar to crystals. A substantial increase in the correlation length for medium-range order is observed for GaAsSe compositions with $\langle m\rangle = 2.6$.[4]

1. EXPERIMENTAL SAMPLES AND PROCEDURE

The choice of samples and composition of the CG system $Ge_xAs_ySe_{1-x-y}$ for solving the problem posed was determined by the minimal activation energy of structural transformation processes that is required for observing AE experimentally under conditions of US loading.

It has been shown[2] in an investigation of the effect of structural changes associated with variation of the chemical composition in the CG $Ge_xAs_ySe_{1-x-y}$ ($0<x<0.3$, $0.1<y<0.4$) on its elastic properties that for compositions with $\langle m\rangle=[2+2x+y]$ in the interval $2.4<\langle m\rangle<2.78$ the equilibrium physicochemical parameters studied (density, specific molecular volume, elastic moduli) stabilize and become composition-independent. However, the dynamical characteristics (thermal expansion coefficients and sound speed) increase, indicating indirectly that the degree of connectedness of the glass network decreases.[1] As a result, for these compositions more favorable conditions for structural relaxation are realized and a percolation phase transition is observed.

An important factor for choosing the composition $Ge_{0.18}As_{0.28}Se_{0.54}$ was the presence of temperature ($T=300$ K) anomalies of the acoustic characteristics (Fig. 1). These anomalies confirm that the material is predisposed to structural transformations even at room temperatures.

The samples were prepared in the form of $6\times6\times10$ mm parallelepipeds. Indium was deposited on the surface of the sample on all sides to obtain an electrical contact with the US transducers $T1$ and $T2$. A definite feature of the experiment was the possibility of measuring simultaneously the propagation velocity of US waves and AE signals accompanying a change in the temperature of the sample as well as

 © 1998 American Institute of Physics

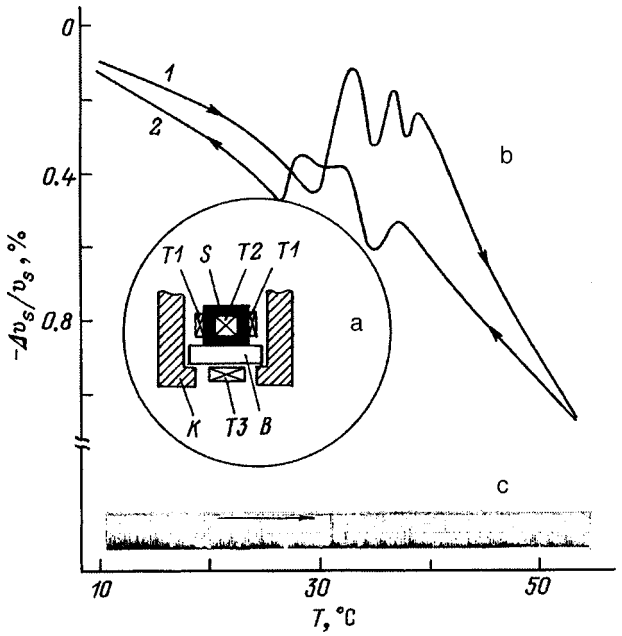

FIG. 1. a) Diagram illustrating the mounting of the sample in the cryostat (*K*). *S* — Sample, *B* — buffer plate consisting of fused quartz, *T*1 — US transducers ($F_1=13.2$ MHz) for measuring the velocity of ultrasound, *T*2 — US transducer ($F_2=0.7$ MHz) for measuring the AE signals, *T*3 — US transducer ($F_3=3.2$ MHz) for US loading. b) Temperature dependences of v_s in $Ge_{0.18}As_{0.28}Se_{0.54}$ (longitudinal waves, $F_1=13.2$ MHz). US intensity $W_s=0$. *1* — Increasing temperature, *2* — decreasing temperature. Rate of temperature change — 0.4 K/min. c) Spectrum of AE signals during heating of the sample.

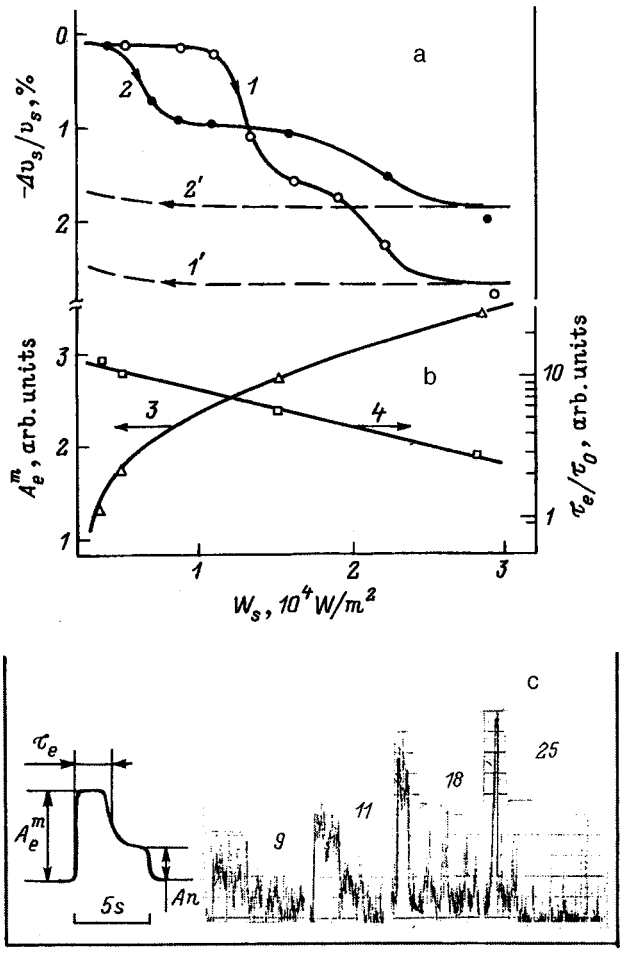

FIG. 2. Amplitude (as a function of W_s) dependences of v_s during two successive cycles of US loading (*1, 2*) and unloading (*1′,2′*) respectively (a) of the AE parameters: amplitudes A_e^m (*3*) and relaxation time τ_e (*4*) (b). c — Spectra of AE signals under US loading, the numbers in the upper right-hand corner of the oscillograms of AE are the voltage on the US transducer *T*3 (in V). Inset — AE parameters.

under US loading. The temperature of the sample was monitored with a copper-constantan thermocouple. The mounting scheme of the sample is shown in Fig. 1a.

The US velocity v_s was measured by a pulse-phase method[8] using piezoelectric transducers *T*1 ($F_1=13.5$ MHz), and the intensity of the AE signals N_e was measured with the *T*2 transducer ($F_2=0.7$ MHz) and an AF-15 apparatus. The temperature measurements of v_s and N_e were performed in a dynamic range with a constant rate of change of temperature and with automatic plotting. Ultrasonic loading of the sample was accomplished with the transducer *T*3 ($F_3=3.2$ MHz) through a buffer plate *B*, required for thermal and electrical decoupling. We note that the choice of the experimental geometry — mutual orthogonality of the arrangement of the transducers *T*1–*T*3, operating on longitudinal waves in different frequency ranges — essentially excluded direct deformational or an electromagnetic effect of one on the other. A control experiment on a neutral germanium sample confirmed this.

Since relaxation of the sound velocity (relaxation time $\tau_v=1-10$ s) was observed when a sufficiently intense US load W_s was applied, the measurements of v_s as a function of W_s were performed in a steady-state regime. The error in determining $\Delta v_s/v_s$ did not exceed 0.05%.

2. RESULTS AND DISCUSSION

Figure 1b shows the results of thermal measurements of v_s with increasing temperature (curve *1*) and decreasing temperature (curve *2*). Figure 1c shows $N_e(t)$ with $W_s=0$. One can see that 1) in the temperature interval $\Delta T=30-40\,^\circ$C a characteristic nonmonotonic section appears in the temperature dependence $v_s(T)$ in the form of a broadened multimode peak. When the sample is heated above 50 °C, the temperature coefficient $Tv_s=(1/v_s)\partial v_s/\partial T$ approximately doubles; 2) hysteresis of the shape, position, and amplitude of the peak in $v_s(T)$ with slow (hours) relaxation to the initial position is observed as a function of the direction of variation of the temperature; heat cycling results in suppression of the peak; 3) AE signals are not observed with heating or cooling of the sample, including with the heating rate varied from 0.4 to 2 K/min.

Figure 2 shows the US velocity v_s as a function of the amplitude of the US deformation (as a function of W_s) (a), the amplitudes A_e^m and relaxation times τ_e of the AE pulses (b), and the temporal AE spectra (c). Generalizing these results, we note the following: 1) A multithreshold amplitude-dependent decrease of v_s is observed, where both the value of the threshold of the US intensity $W_s^c=0.4-0.8$ W/cm^2

and the slope of the curve of v_s versus W_s depend on the past history of the sample — in subsequent cycles of US loading (curves *2* and *2′*) W_s^c, $\Delta v_s/v_s$ and the slope of $v_s(W_s)$ decrease; 2) amplitude hysteresis of $v_s(W_s)$ is observed as a function of the direction of variation of the US load on the sample, relaxation of the elastic properties to the initial state is very slow (tens of hours) and incomplete; and, 3) AE signals were detected with an increasing load $W_s > W_s^c$ The temporal process of development of AE is characterized by two stages. First, when W_s is switched on, the amplitude of the AE pulses grows rapidly ($\tau < 0.2$ s) up to a maximum value A_e^m (curve *3*) and AE develops over a prolonged period of time ($\tau_e = 0.3-0.5$ s) at constant A_e^m (curve *4*). This is followed by a slow dropoff — to the noise level A_n, which is virtually independent of both W_s and time. Subsequently, rare single bursts of AE are observed against a background of the continuous noise spectrum A_n.

Let us consider a possible mechanism for the observed structural changes in $Ge_{0.18}As_{0.28}Se_{0.54}$. Preceding investigations of this system showed that for compositions close to the composition studied in this work coexistence of planar clusters As_2Se_3 and Ge_2Se_4, ''joined'' transversely by Se bridge atoms (''soft network'') and Ge bridge atoms (''rigid network''), is characteristic. As the coordination number $\langle m \rangle$ increases in connection with an increase in the relative fraction Ge atoms, the stiffness of the framework increases and $T\nu_s$ decrease.[2–4]

On the basis of the experimental results presented above, the opposite situation can be conjectured: As a result of thermal and acoustically stimulated structural transformations, a shift in the distribution of all possible structural units in the direction of the composition of the glass of the present system with a lower value of $\langle m \rangle$ and a shift of the phase equilibrium in the direction of As and Se occur. Apparently, the effective coordination number $\langle m \rangle$ is not constant for a given composition of the glass, but rather it depends on the specific structure of the glass under definite external conditions.

Under US loading near $T = T_c$ such a shift should intensify and the contribution of As–As and/or Se–Se bonds should increase. The fact that the decrease in v_s under US loading ($> 2\%$) is greater than under temperature loading (0.8%) (compare Figs. 1 and 2) can be taken as an experimental confirmation of this conclusion. Breaking and/or formation of bonds can be accompanied by a release of energy, which goes to generation of AE signals. For example, 35 kJ/mole is released as a result of the reaction 2 Ge–Se − Ge–Ge + Se–Se.[1] The condition for the AE process to continue after the stage of acoustically stimulated exhaustion of reactions with closest bonds in a time τ_e is their preliminary diffusion. The study of the temperature and amplitude characteristics of AE should shed light on this question.

Indeed, relaxation of the structure in glass into a new state, separated from the initial state by a barrier U_b, is described by the equation[1]

$$\tau = \tau_0 \exp[(-U_b)/kT]. \quad (1)$$

Assuming that the US interaction effect leads to a formal decrease of U_b by means of acoustic deformation γ_s of the potential

$$U_b^{\text{ef}} = (U_b - \gamma_s W_s), \quad (2)$$

while $\tau = \tau_e(W_s)$, we find from Fig. 2b, taking account of relations (1) and (2), $U_b = 0.05$ eV, $\gamma_s = 2 \times 10^{-21}$ cm$^3 \cdot$ s, $\tau_0 = 0.1$ s. The value obtained, $U_b = 0.05$ eV, is an activation energy and, according to the relaxation mechanisms,[1,9–11] probably corresponds to fine-scale deformations of the network due to the segmental mobility of the structure in regions of local disordering. When the US load is removed, the glass structure relaxes very slowly into the initial state. However, under cyclic loading the system ''stabilizes'' and the dependence of v_s on the US load decreases sharply. The AE signals are observed only at the initial stages of the US loading. The absence of AE in temperature measurements (Fig. 1c), within the limits of sensitivity of the apparatus employed (10 μV), can be explained, in our view, by the diffuseness of the temperature region of phase transformations in glass ($T - 20$ K) and the definite randomness of the structural transformation events in time and space. At the same time, US deformation not only induces such transformations but it also ''synchronizes'' them over the entire volume of the sample.

In conclusion, we note that we have observed AE signals at room temperature under US loading conditions on different samples of this system with $\langle m \rangle > 2.5$, for example, in $Ge_{0.22}As_{0.32}Se_{0.46}$, as well as in a number of cases with low-temperature (100–200 K) anomalies of the acoustic characteristics.

In summary, a method of comprehensive investigation of the acoustic characteristics and AE in chalcogenide glasses, including also under US loading, has been developed.

Acoustic emission and the effect of US loading on the elastic properties of chalcogenide glasses have been observed for the first time for glassy materials. The temporal spectrum of AE was investigated. It consists of two components: a pulsed component, ''explosive'' emission, and continuous noise. It is believed that the ''explosive'' component is due to reorientation (rupture and ''joining'') of some weak molecular bonds between layered structural fragments, while the noise component is due to diffusion and healing of broken bonds. The amplitude dependence $v_s(W_s)$ and, especially, the AE observed in the chalcogenide glass $Ge_{0.18}As_{0.28}Se_{0.54}$ under US loading definitely confirm that the structure of the chalcogenide glass system investigated is highly stable even at room temperature.

A mechanism of acoustically stimulated structural transformations in glassy materials, consisting of a decrease in the potential barriers on account of configurational reorientations, was proposed. It was shown that the AE method can be used to determine the activation energy of the relaxational process. However, the available experimental data do not make it possible to determine unequivocally the mechanism and character of the relaxation processes.

This work was supported by the Fund for Fundamental Research of the Ukrainian State Committee on Science and Technology.

[1] A. Feltz, *Amorphous Inorganic Materials and Glasses* [VCH Pubs., 1993; Mir, Moscow, 1986, 556 pp.].
[2] S. D. Gapochenko, Ya. M. Olikh, V. A. Bazakutsa, V. P. Pinzenik, and V. I. Belozertseva, Fiz. Tverd. Tela (St. Petersburg) **35**, 465 (1993) [Phys. Solid State **35**, 240 (1993)].
[3] K. Tanaka, J. Non-Cryst. Solids **97/98**, 391 (1987).
[4] V. A. Bazakutsa, S. D. Gapochenko, Ya. M. Olikh, O. V. Luksha, V. P. Ivanitskiĭ, V. I. Belozertseva, and V. P. Pinzenik, Uzv. Ross. Akad. Nauk, Ser. fiz. **57**, 91 (1993).
[5] A. S. Tripalin and S. I. Buĭlo, *Acoustic Emission. Physicomechanical Aspects* [in Russian], Rostov University Press (1982), 160 pp.
[6] V. A. Kalitenko, O. A. Korotchenko, I. Ya. Kucherov, I. V. Ostorvskiĭ, and V. M. Perga, Ukr. Fiz. Zh. **30**, 1358 (1985).
[7] V. A. Kalintenko, Ya. M. Olikh, and V. M. Perga, Ukr. Fiz. Zh. **33**, 788 (1988).
[8] R. Truell, C. Elbaum, and B. Chick, *Ultrasonic Methods in Solid-State Physics* (Mir, Moscow, 1972), 307 pp.
[9] I.L. Hopkins and C. R. Kurkjian, in *Physical Acoustics*, edited by W. P. Mason [Academic Press, N. Y., 1965; Mir, Moscow, 1969, Vol. IIB, 420 pp.].
[10] G. M. Bartenev and D. S. Sanditov, *Relaxation Process in Glassy Systems* [in Russian], Novosibirsk, Nauka (1986), 235 pp.
[11] V. S. Bilanich, A. A. Gorvat, I. M. Yurkin, and V. I. Fedelash, Ukr. Fiz. Zh. **35**, 1841 (1990).

Translated by M. E. Alferieff

DEFECTS. DISLOCATIONS. PHYSICS OF STRENGTH

Spatial distribution, build-up, and annealing of radiation defects in silicon implanted by high-energy krypton and xenon ions

A. R. Chelyadinskiĭ, V. S. Varichenko, and A. M. Zaĭtsev

Belarus State University, 220050 Minsk, Belarus
(Submitted January 20, 1998)
Fiz. Tverd. Tela (St. Petersburg) **40**, 1627–1630 (September 1998)

An x-ray diffraction study of defect formation in silicon irradiated by Kr^+ (210 MeV, $8\times10^{12}-3\times10^{14}\,cm^{-2}$) and Xe^+ (5.6 BeV, $5\times10^{11}-5\times10^{13}\,cm^{-2}$) ions is reported. It has been established that irradiation produces a defect structure in the bulk of silicon, which consists of ion tracks whose density of material is lower than that of the host. The specific features of defect formation are discussed taking into account the channeling of part of the ions along the previously formed tracks and the dominant role of electron losses suffered by the high-energy ions. It is shown that the efficiency of incorporation of stable defects by irradiation with high-energy ions is lower than that reached by implanting medium-mass ions with energies of a few hundred keV. © *1998 American Institute of Physics.* [S1063-7834(98)01309-4]

The current interest in high-energy ion implantation stems from the possibility of its use in fabrication of buried layers and multi-layer structures in semiconductors. From the scientific standpoint, of major interest are the specific features of defect formation, the spatial distribution of defects, and their annealing in crystals subjected to high-energy ion irradiation. This work studies these problems using silicon implanted with Kr^+ ions having an energy of 210 MeV and Xe^+ ions of 5.6-BeV energy.

1. EXPERIMENTAL TECHNIQUES

The study was carried out on a two-crystal x-ray spectrometer using Cu $K\alpha_1$ radiation in fourth order of (111) reflection. The implantation-induced change in the silicon-lattice period was determined to within $\pm1\times10^{-6}$ nm. The defect concentration was estimated from the measured lattice-period change based on the fact that the atomic displacements in prevailing defects are about 0.01 nm.[1] The spatial distribution of distortions was studied by layer-by-layer removal of silicon with micron-grade diamond paste. The accuracy of sample thickness determination was $\pm0.5\,\mu$m. Isochronous annealing of the implanted structures was carried out in evacuated quartz ampoules. The temperature was maintained to within $\pm2\,^\circ$C. To exclude channeling in the course of implantation, the samples were mounted in the position where the angle between the surface normal and the beam axis was 5°.

2. RESULTS AND DISCUSSION

Figure 1 shows depth profiles of the lattice-period change Δa in silicon irradiated to various doses of 210-MeV Kr^+ ions. The depth distribution of distortions in Δa in silicon irradiated by 5.6-BeV Xe^+ ions to a dose of $5\times10^{13}\,cm^{-2}$ is displayed in Fig. 2. In the latter case, the method used is sensitive to defects only starting with depths of about 600 μm. For both Kr^+ and Xe^+, the positions of the maxima in the distribution of distortions agree satisfactorily with the calculations made using the TRIM-90 code. We shall dwell on this point in more detail later. As seen from Fig. 1, a buried tail appears in the distribution with increasing dose (curve *2*), and an additional maximum at a depth of $\sim31\,\mu$m forms at still higher doses (curves *3* and *4*). At a Kr^+ dose of $3\times10^{14}\,cm^{-2}$ this maximum exceeds in height the main peak.

Curve *1* in Fig. 3 shows in arbitrary units the total build-up of radiation-induced defects (the areas bounded by curves *1–4* in Fig. 1) with increasing dose of Kr^+ ions. The

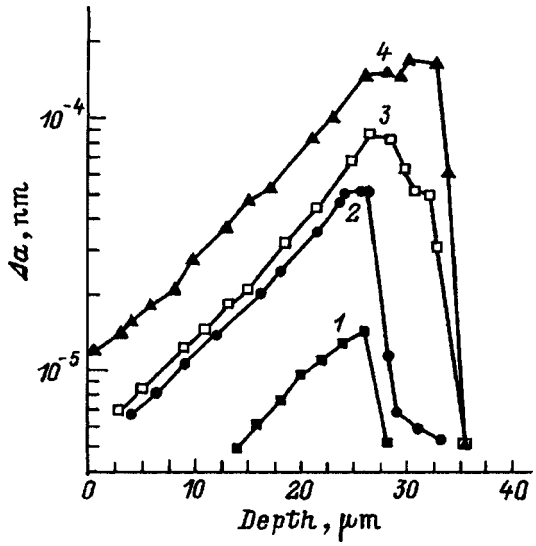

FIG. 1. Spatial distribution of the lattice-period change Δa in silicon irradiated by 210-MeV Kr^+ ions to a dose (cm^{-2}): *1* — 8×10^{12}, *2* — 4×10^{13}, *3* — 1×10^{14}, and *4* — 3×10^{14}.

 © 1998 American Institute of Physics

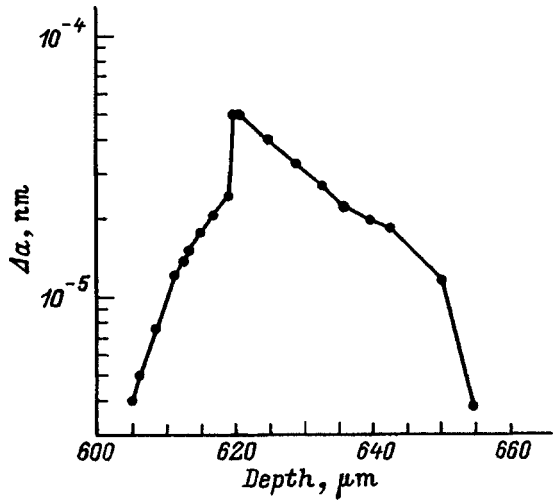

FIG. 2. Spatial distribution of the lattice-period change Δa in silicon irradiated by 5.68-BeV Xe^+ ions to a dose of $5\times10^{13}\,cm^{-2}$.

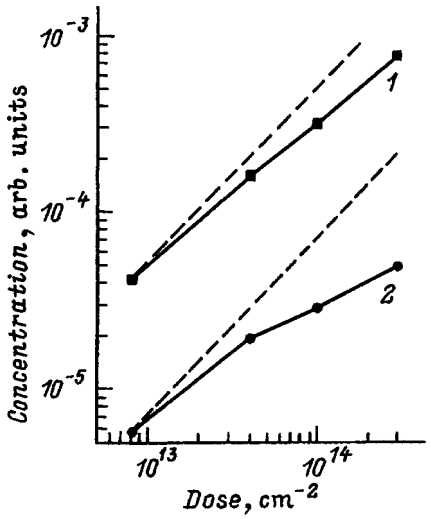

FIG. 3. Dose dependence of radiation-induced defects in silicon irradiated by 210-MeV Kr^+ ions: *1* — at sample surface, *2* — at a depth of 15 μm.

defect build-up in the same samples at the 15-μm depth is illustrated by curve *2* in Fig. 3. The deviation from linearity in the defect build-up in this case is still more pronounced.

Curve *1* in Fig. 4 displays the profile of 210-MeV Kr^+ elastic energy losses calculated by the TRIM-90 code. Curve *2* in the same figure shows the product of the elastic and inelastic loss curves. Also presented are experimental depth profiles of the implanted layer for Kr^+ ions measured for a dose of $8\times10^{12}\,cm^{-2}$, just before the formation of a buried distorted layer. The good agreement of the experimental data with curve *2* demonstrates the effect of electronic losses on defect formation. This suggests also, however, that the electronic losses do not play a major role in defect formation. If the electronic losses were an independent source of defects, the experimental curve would be dominated by the sum of the elastic and inelastic ion-energy losses. The increase in the number of displacements is most likely due to a decrease in the threshold energy required to displace an atom from a lattice site at a high level of target-atom ionization. Indeed, the ionization losses of 5.6-BeV Xe^+ ions are very high at the beginning of the ion path, but because the ion energy losses to elastic interactions here are not high, the defect concentration is too low to be detectable by the technique employed.

Under the experimental conditions used, the appearance of a buried defect maximum cannot be accounted for by crystallographic channeling. We assign the onset of the second defect-concentration maximum to the traversal by Kr^+ ions of the tracks produced by previous ions. TRIM-90 calculations show that the experimentally observed second maximum of defects at a depth of ~31 μm should appear if the density of material in the ion track or, at least, in its core is less by $\sim10\%$ than the crystal density. If N ions are incident on a unit surface area S of the crystal, the probability for n ions ($n=1,2,3,\ldots$) to strike a given surface area s can be described by the Poisson distribution

$$P(N,s,n)=\exp(-N\cdot s)\frac{(N\cdot s)^n}{n!}.$$

This area s is actually the characteristic size of the track cross section with a lower density compared to the host material. Function $P(N\cdot s)$ is shown graphically in Fig. 5 for $n=1,2,3,4,5$. The numerical values of $P(N\cdot s)$ are the relative areas occupied by nonoverlapping tracks (curve *1*), doubly overlapping tracks (curve *2*), and so on. The experimental data of Fig. 1 offer an estimate of $\sim3\times10^{13}\,cm^{-2}$ for the ion dose at which tracks start to overlap. We can now match the horizontal axis of the $P(N\cdot s)$ dependences with the ion dose axis. This permits one to estimate the dimensions of a lower-density track produced by a 210-MeV Kr^+ ion. Its diameter is of the order of 1 nm. The dimensions of the tracks of the heavier Xe^+ ions are larger, and they start to overlap at lower doses. The additional maximum is clearly seen already at a Xe^+ dose of $5\times10^{13}\,cm^{-2}$ (Fig. 2).

The deviation from linearity in the integrated build-up of defects (curve *1* in Fig. 3) results from annihilation of newly forming mobile vacancies and Si interstitials by stable defects incorporated earlier. The still more pronounced sublinearity in the defect build-up at the depth of 15 μm (curve *2*

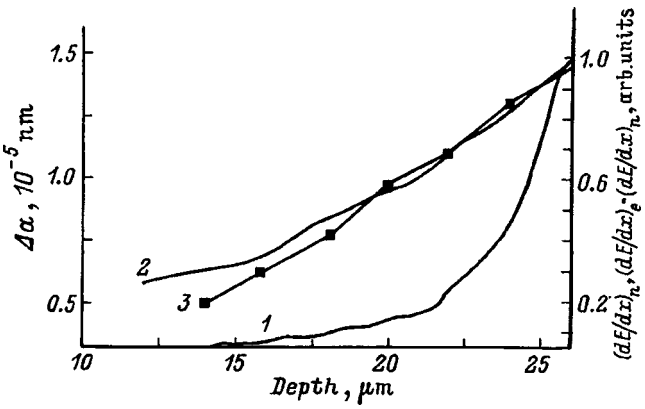

FIG. 4. Spatial distribution of (*1*) nuclear losses, (*2*) product of nuclear and electronic losses of 210-MeV Kr^+ ions, and (*3*) experimentally measured radiation-defect concentration in silicon irradiated by 210-MeV Kr^+ ions to a dose of $8\times10^{12}\,cm^{-2}$.

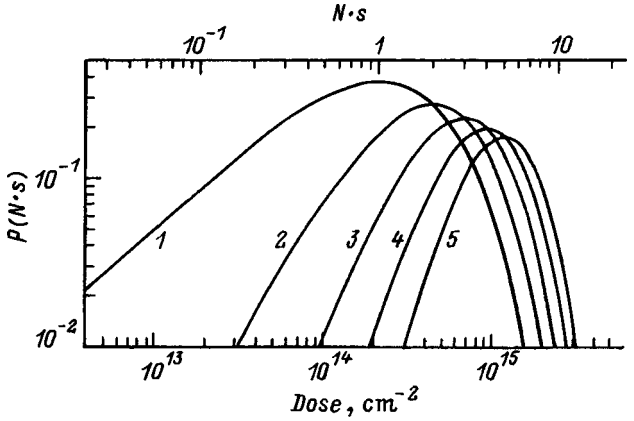

FIG. 5. Poisson distribution for (*1*) nonoverlapping and (*2–5*) *n*-fold overlapped tracks.

in Fig. 3) is caused by the decrease in the energy losses of the ions traveling along the previously formed tracks. This energy is subsequently expended in creating the buried distorted layer. At the ion dose of $3\times10^{14}\,\mathrm{cm}^{-2}$, the second maximum exceeds in height the main peak. This implies that the number of ions traveling along primary tracks at this dose is larger than that of the ions that produced them. As seen from the $P(N\cdot s)$ distributions in Fig. 5, at the Kr^+ dose of $3\times10^{14}\,\mathrm{cm}^{-2}$ the total number of doubly, triply, and quadruply overlapping tracks is larger than that of the nonoverlapped ones.

It is of interest to discover what defects are incorporated at various depths of their distribution, in particular, whether defect-cluster regions or isolated point defects dominate in the near-surface layer. This question may be conveniently answered by studying defect annealing. Figure 6 presents graphically the lattice-period recovery of Kr^+-implanted silicon in the course of isochronous annealing in the near-surface layer (curve *1*), at a depth of 15 μm (curve *2*), and at 25 μm from the surface (curve *3*). Curve *4* in the same figure plots defect annealing in Xe^+-irradiated silicon at the depth corresponding to the maximum in their distribution.

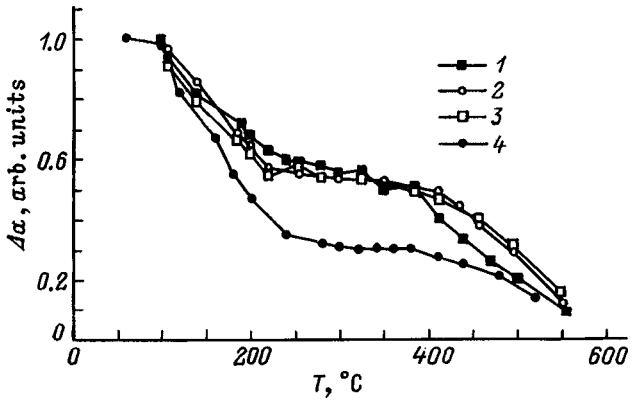

FIG. 6. Recovery of lattice period Δa in the course of isochronous anneal in silicon irradiated by 210-MeV Kr^+ ions to a dose of $1\times10^{14}\,\mathrm{cm}^{-2}$ (*1* — in near-surface layer, *2* — at a depth of 15 μm, *3* — at a depth of 25 μm), and irradiated by 5.68-BeV Xe^+ ions to a dose of $5\times10^{13}\,\mathrm{cm}^{-2}$ (*4* — at the depth of the maximum in radiation-defect distribution).

The lattice period recovers in two main stages, namely, within the 100–280 and 380–600 °C intervals. The same annealing stages are observed also for silicon irradiated by medium-mass ions of comparatively low energies (for instance, by 200-keV Si^+ ions).[2] In the first stage, it is divacancies that anneal predominantly.[3] Annealed in the second stage are more complex structures, for example, five-vacancy (Si-P1) centers and other, not yet identified complexes.[4,5] These complex defects form in the course of heat treatment of irradiated samples as a result of a structural rearrangement of the defects present in the cluster core. The defects located in the periphery of a cluster region and beyond it anneal in the first stage. It was pointed out[4,5] that formation of complex radiation-defect structures during annealing is characteristic only of irradiation by heavy particles (neutrons, ions) generating displacement cascades. The second stage is not observed in the case of light ions (including Li^+) with energies of tens and hundreds of keV.[3] Also annealed in the first stage are interstitial complexes of the type of Si-P6 (at 120 °C).[6] Type Si-B3 interstitial complexes anneal at ~560°.[7] It was established that the concentrations of interstitial complexes are comparable with those of divacancies, a vacancy-type defect stable at room temperature and prevailing in implanted silicon.[3,8]

As evident from Fig. 6, both annealing stages are observed at the surface and at the depth of the distorted layer (curves *1–3*). The fractions of the defects annealed in stages *1* and *2* are the same for different depths of the distorted layer. This implies formation of identical defect-cluster regions throughout the distribution. According to Cheng's model, defect clusters, which are assumed to be spherical, consist of a divacancy core, with the outer shell made up of interstitial defects.[9] The track produced by high-energy ions is axially symmetric, with a divacancy core and an outer shell consisting predominantly of interstitial-type defects.

One could expect the second defect maximum to broaden in depth with increasing ion dose as a result of multiple track overlapping. This is not observed, however (Fig. 1), because the overlap is not perfect, and mixing takes place in the region where the denser track shell meets the less dense core. In the case of ideal superposition of two tracks, the density of material in its core would be still lower than it is in the primary track. Under these conditions, the third ion traversing the doubly overlapped track would move a longer distance than the second one. Ideal track superposition, however, is too rare an event to be observable experimentally.

The mean free path of Kr^+ ions is 10% longer because the density of material at the track core is 10% lower than that of the host. At the same time, the second maximum for the Xe^+ ions is downshifted by about 3–4% relative to the main peak. This is not connected apparently with the higher density of the Xe^+ ion track. From the viewpoint of elastic losses, silicon is quasi-transparent in the initial part of the trajectory of a 5.6-BeV Xe^+ ion. Therefore the ion can only produce a track starting from a certain depth.

It should be pointed out that EPR studies of samples irradiated by high-energy Kr^+ and Xe^+ ions did not reveal the anisotropic line with the g factor of 2.0055.[10,11] This suggests that irradiated silicon layers do not contain amor-

phous inclusions. This seems somewhat unexpected, because at the end of the path, where the energy losses may be as high as a few hundred keV, ions should produce amorphous inclusions. It is known that at low energies (tens and hundreds of keV) the tracks of Kr^+ and Xe^+ heavy ions are amorphous.[12]

The defect concentration at the distribution maximum in silicon irradiated by Kr^+ ions at a dose of $8\times10^{12}\,cm^{-2}$, which was calculated based on Δa, is $1.6\times10^{19}\,cm^{-3}$. For the number of primary displacements determined[13] from the elastic losses with a threshold energy $E_d=12.6$ eV we obtained $1.7\times10^{21}\,cm^{-3}$. Whence it follows, even disregarding the change in the threshold displacement energy E_d, that the efficiency of defect production (the ratio of the number of stable defects to that of displacements) is 1%. For comparison, under neutron irradiation, irradiation of silicon by 46-MeV electrons which typically produce cascades, and implantation of silicon by medium-mass ions[2,14] the production efficiency of stable defects is about 5%. Apparently, on the one hand, the high ionization level observed under high-energy implantation favors an increase in the number of displaced atoms through the decrease of the displacement threshold, and this affects the defect depth profile. But on the other hand, the large amounts of energy released inelastically in the ion track produce noticeable annealing of defects, so that the resultant efficiency of defect incorporation is found to be significantly lower than that observed in implantation of low-energy medium-mass ions.

Thus the defects produced in implantation of 210-MeV Kr^+ ions and 5-GeV Xe^+ ions represent cluster regions forming a continuous track with a core having a lower density compared to the host. The density of material in the track core in silicon irradiated by Kr^+ ions is 10% less than that of the host. This core is about 1 nm in diameter. As the irradiation dose increases, the mean free paths of ions increase because of their striking the tracks produced earlier. This results in formation of an additional buried distorted layer. It has been established that the inelastic ion energy losses increase the number of displaced lattice atoms, which is assigned to the decrease of the threshold energy required to knock an atom out of its site. As for the efficiency of production of stable defects, it is lower under implantation of high-energy ions than it is with low-energy medium-mass ions.

The authors are grateful to A. Yu. Didyk and V. A. Skuratov for high-energy irradiation of samples by krypton ions, and to N. M. Kazyuchits for fruitful discussions.

Partial support of the INTAS Program (Grant 94-1982) is gratefully acknowledged.

[1] A. N. Zhevno, V. V. Sidorik, and V. D. Tkachev, Dokl. Akad. Nauk BSSR **20**, 409 (1976).
[2] O. J. Araika, A. R. Chelyadinskii, V. A. Dravin, Yu. R. Suprun-Belevich, and V. P. Tolstykh, Nucl. Instrum. Methods Phys. Res. B **73**, 503 (1993).
[3] N. I. Bereonov, V. F. Stelmakh, and A. R. Chelyadinskii, Phys. Status Solidi A **78**, K121 (1983).
[4] W. Jung and G. S. Newell, Phys. Rev. **132**, 648 (1963).
[5] V. A. Botvin, Yu. V. Gorelkinskiĭ, V. O. Sigle, and M. A. Gubisov, Fiz. Tekh. Poluprovodn. **6**, 1683 (1972) [Sov. Phys. Semicond. **6**, 1453 (1972)].
[6] Y. H. Lee, N. N. Gerasimenko, and J. W. Corbett, Phys. Rev. B **14**, 4506 (1976).
[7] K. L. Brower, Phys. Rev. B **14**, 872 (1976).
[8] M. Jadan, N. I. Berezhnov, and A. R. Chelyadinskii, Phys. Status Solidi B **189**, K1 (1995).
[9] L. J. Cheng and M. L. Swanson, J. Appl. Phys. **41**, 2627 (1970).
[10] V. A. Martinovich, A. R. Chelyadinskii, V. S. Varichenko, N. M. Penina, E. N. Drozdova, A. M. Zaitsev, and W. R. Fahrner, in *Abstracts Conference of the German Physics Society* (Regensburg, 1996), p. 1547.
[11] V. S. Varichenko, A. M. Zaitsev, N. M. Kazutchits, A. R. Chelyadinskii, N. M. Penina, V. A. Martinovich, Ya. I. Latushko, and W. R. Fahrner, Nucl. Instrum. Methods Phys. Res. B **107**, 268 (1996).
[12] J. F. Gibbons, Proc. IEEE **60**, 1062 (1972).
[13] P. Sigmund, Appl. Phys. Lett. **14**, 114 (1969).
[14] G. D. Watkins, in *Lattice Defects in Semiconductors* (Inst. of Phys., London, 1975), p. 1.

Translated by G. Skrebtsov

Kinetics of dislocation ensembles in deformable irradiated materials

N. V. Kamyshanchenko and V. V. Krasil'nikov

Belgorod State University, 308007 Belgorod, Russia

N. V. Neklyudov and A. A. Parkhomenko

Khar'kov Physicotechnical Institute, 310108 Khar'kov, Ukraine
(Submitted February 5, 1998)
Fiz. Tverd. Tela (St. Petersburg) **40**, 1631–1634 (September 1998)

The development of plastic instability in the initial deformation stages of irradiated materials is studied. The dependence of the fraction of dislocations which overcome obstacles in the dynamic regime (dislocation ''channeling'') on the degree of radiation hardening (irradiation dose) and the dislocation velocity is analyzed. It is shown that this effect plays a role in radiation embrittlement of reactor materials. © *1998 American Institute of Physics.* [S1063-7834(98)01409-9]

The investigation of radiation hardening and, as a rule, the associated embrittlement is one of the most practical issues in reactor materials science. Radiation hardening of materials appears not only as an increase in the yield stress and decrease of the rate of hardening of materials but also in the formation of a ''creep tooth'' and a creep plateau on the strain curves of the Chernov–Lüders type.[1,2] According to modern ideas, the existence of these effects indicates plastic instability in materials, which could be the cause of the sharp decrease in the plasticity.

Figure 1 shows typical strain curves for reactor steels at test temperatures below $0.3T_m$ (T_m — melting temperature). Our analysis[3] showed that strain curves of this type (curve *2*) are observed in many materials even at irradiation doses $\leqslant 10^{-2}-10^{-1}$ dpa (displacement per atom). The minimum or the plateau in the curve *2* is due to plastic instability effects — dislocation channeling: destruction of obstacles by moving dislocations and localization of glide in given volumes of the material followed by deformation.[1] For the subsequent analysis, it is especially important that the material leaves the plastic instability regime mainly as a result of the development of transverse glide of screw dislocations. At higher irradiation doses ($\geqslant 1-10$ dpa, curve *3*) the stage corresponding to the plateau in curve *2* passes directly into the fracture stage of the material.

The modern approach to plastic deformation, as a collective dislocation process, is to describe the localization and self-organization of dislocations based on a study of the evolution of dislocation ensembles in the deformed materials. In Refs. 4 –7 the kinetics of a dislocation ensemble were studied in detail theoretically in a synergetic approach and models making it possible to explain not only the evolution of the local density of dislocations in unirradiated materials but also the formation of defect-free channels and localization of deformation in irradiated materials.

There also exist models[8] that study the appearance of plastic instability and localization of plastic deformation based on a description of the behavior of single dislocations. Other models (see, for example, Ref. 9) proceed from a dislocation ensemble which is characterized by a dislocation distribution function that depends on the radius vector **r** and time t.

However, since the plastic deformation of a material is associated with mobile defects, it is natural to assume that the dislocation distribution function depends not only on the radius vector **r** and time t but also on the dislocation velocity **v** and its orientation in space. In the present paper we study the dislocation distribution functions averaged over orientations of dislocation lines in space. The dislocations in an ensemble themselves can be treated as a collection of segments of dislocation lines (see Ref. 10).

In the present work we investigated the development of plastic instability in an irradiated material taking account of the dependences of the velocity distribution function of dislocations in an ensemble.

1. MODEL

The subject of the description are mobile dislocations which interact with fixed obstacles of different nature but are not held back (do not ''hang up'') on them. For example, they move in a channeling regime.[2] This situation corresponds, for example, to the typical case of the initial stages of deformation of an irradiated material when the dislocation ensembles formed ''intersect'' obstacles, consisting of small clusters, loops, and micropores. It is obvious that such a situation can occur in the presence of both a wide spectrum of dislocation velocities (energies) and different mechanisms of interaction of dislocations with obstacles.

Two other important points should be noted concerning: a) interdislocation interaction and b) mechanisms by which dislocations leave the regime under study.

a) According to Ref. 11 , the contribution of interdislocation interaction must be estimated by comparing it with the external applied (and acting on a dislocation) stress f_{ext}. In an unirradiated material the interdislocation interaction should be taken into account by ''starting from the end of the section of strain hardening'' where the dislocation density

 © 1998 American Institute of Physics

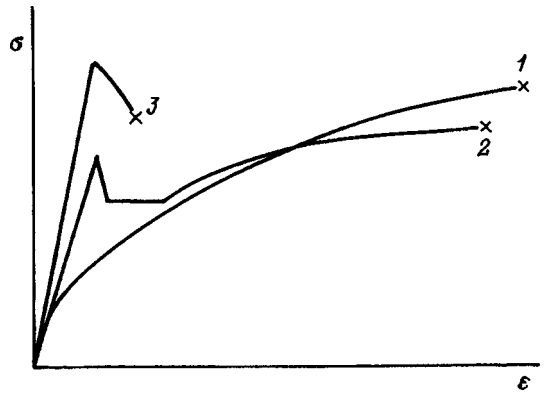

FIG. 1. Typical strain curves (σ — load, ε — deformation) for reactor steels at test temperatures below $0.3T_m$ (T_m — melting temperature). *1* — Initial (unirradiated) material, *2* — material irradiated to ''low'' doses ($10^{-2}-10^{-1}$ dpa), *3* — material irradiated to doses above 1 dpa.

$\rho(\varepsilon)$ in the material is large, the distances between dislocations ($r\approx\rho^{-1/2}$) are short, and the interdislocation interaction forces are comparable to the external applied stress.

In our case of an irradiated material conditions are realized such that the external stress acting on a dislocation is high (practically the maximum possible stress), provided that the sharp drop in the rate of strain hardening (Fig. 1) is taken into account, while the dislocation density in an ensemble (initial stages of the formation of a localized deformation) is still not so high that condition $f\geqslant f_{\text{ext}}(1/2\pi)Gb^2\rho(\varepsilon)^{1/2}$, where f is the interdislocation interaction force, G is the shear modulus, and b is Burgers vector, would be satisfied. This allows us to neglect the interdislocation interaction in the ensemble for the time being when studying the interaction with fixed obstacles — radiation defects — at the initial stages of deformation.

b) To describe the interaction of a dislocation ensemble with obstacles, we study the most likely case where some dislocations will pass through an obstacle without changing their direction of motion, while other dislocations will be ''scattered,'' changing their direction of motion, as can happen, for example, in the case of screw dislocations. As already noted above, this corresponds to the case of the deformation of an irradiated material, when the system leaves the channeling regime as a result of the motion of screw dislocations and subsequent development of multiple glide.

To characterize the dislocation structure of a crystal quantitatively it is necessary to give the distribution function $n(\mathbf{r},\mathbf{v},t)$ of the dislocations over their coordinates $\mathbf{r}$ and velocities $\mathbf{v}$ and time t so that

$$\rho_{\text{total}}=\sum_i \int d\Omega n(\mathbf{r},\mathbf{v},t) \tag{1}$$

is the total density of all dislocations with arbitrary orientations and moving with velocity $\mathbf{v}$, and $d\Omega$ is an element of solid angle in coordinate space.

In the case that the dislocations interact with certain fixed obstacles, we shall investigate the development of plastic deformation on the basis of a general kinetic equation for $n(\mathbf{r},\mathbf{v},t)$ of the following form:

$$\frac{\partial n}{\partial t}+\mathbf{v}\cdot\frac{\partial n}{\partial \mathbf{r}}+\mathbf{a}\cdot\frac{\partial n}{\partial \mathbf{v}}=\left(\frac{\hat{1}}{\tau}\right)n, \tag{2}$$

where $\mathbf{a}$ is the acceleration of a dislocation under an external load F; $(\hat{1}/\tau)$ is an operator corresponding to the reciprocal of the relaxation time, which we assume to be determined by the expression

$$\left(\frac{\hat{1}}{\tau}\right)n=\frac{|\mathbf{v}|^m}{A}\left(\frac{1}{4\pi}\int d\Omega_{\mathbf{v}'}n(\mathbf{r},\mathbf{v}',t)-n(\mathbf{r},\mathbf{v},t)\right). \tag{2a}$$

Here $d\Omega_{\mathbf{v}'}$ is an element of solid angle in velocity space. The proposed structure of the operator (2a) of the reciprocal relaxation time signifies that the frequency of collisions with obstacles for a dislocation moving with velocity $\mathbf{v}$ equals $|\mathbf{v}|^m/A$ (we assume below that $m<-1$), where A is a constant which takes account of the presence of stops of different nature and the concentration (we note that, evidently, depending on the parameter m, the dimension of A in different cases will be different). The expression (2a) presupposes, by analogy with classical mechanics, that a dislocation, treated as a quasiparticle, is scattered elastically in the potential field of an obstacle $|\mathbf{r}|^{-k}$ $(k>0)$. It is known that in this case the effective differential cross section for elastic scattering (and therefore the collision frequency also) is proportional to $|\mathbf{v}|^m$ with $m=-4/k$ (see Ref. 12). On the other hand, it is also know that moving dislocations can interact with obstacles according to the law $\sim 1/r$, where r is the distance from an obstacle to the dislocation axis,[13] as happens, for example, for an edge dislocation in the case of a Cottrell impurity atmosphere.[14] In this case, $m=-4<-1$. In what follows we shall develop this model for the general case $m<-1$.

We note that the spatiotemporal distribution function $f(\mathbf{r},t)$ of dislocations can be expressed in terms of $n(\mathbf{r},\mathbf{v},t)$ by means of the formula

$$f(\mathbf{r},t)=\frac{1}{4\pi}\int d\mathbf{v}n(\mathbf{r},\mathbf{v},t).$$

The condition of balance for $f(\mathbf{r},t)$ follows from the kinetic equation (2). In the present model (no interactions between dislocations) it has the form

$$\frac{\partial f(\mathbf{r},t)}{\partial t}+\operatorname{div}\mathbf{j}=0,$$

where $\mathbf{j}=\dfrac{1}{4\pi}\int d\mathbf{v}\,\mathbf{v}n(\mathbf{r},\mathbf{v},t)$.

We shall study the spatially uniform case

$$\frac{\partial n(\mathbf{r},\mathbf{v},t)}{\partial \mathbf{r}}=0. \tag{3}$$

The latter relation means that $\Delta=n_1-n_2\ll\alpha d$ (d — average distance between stops, α — coefficient of order 1 with dimension of length), i.e. the distribution function of a dislocation ensemble remains practically unchanged over a distance of the order of the distance between stops. Then the kinetic equation (2) will have the form

$$\frac{\partial n(\mathbf{v},t)}{\partial t}+\mathbf{a}\cdot\frac{\partial n(\mathbf{v},t)}{\partial \mathbf{v}}=\left(\frac{\hat{1}}{\tau}\right)n(\mathbf{v},t). \tag{4}$$

To Eq. (4) we add the initial condition

$$n(\mathbf{v},0;\mathbf{v}_0)=\delta(\mathbf{v}-\mathbf{v}_0), \tag{5}$$

signifying that at time $t=0$ the dislocation velocity is close to $\mathbf{v}_0$.

We now introduce the parameter $\rho^*(\mathbf{v}_0,t;m)=\rho_{\text{act}}/\rho_{\text{total}}$, where ρ_{act} is the density of dislocations which have passed ''through'' an obstacle. The parameter $\rho^*(\mathbf{v}_0,t;m)$ denotes the relative fraction of dislocations in an ensemble which have passed ''through'' an obstacle. From the physical meaning of the distribution function $n(\mathbf{v},t;\mathbf{v}_0)$ as the probability density of dislocations moving with velocity $\mathbf{v}_0$, we can establish the integral equation

$$\begin{aligned} n(\mathbf{v},t-t';\mathbf{v}_0)&=\rho^*(\mathbf{v}_0,t;m)\,\delta(\mathbf{a}t+\mathbf{v}_0-\mathbf{v})\\ &\quad-\int_0^t dt'\frac{\partial}{\partial t'}\rho^*(\mathbf{v}_0,t';m)\frac{1}{4\pi}\\ &\quad\times\int d\Omega_{\mathbf{w}}n(\mathbf{v},t-t';\mathbf{w}|\mathbf{a}t'+\mathbf{v}_0|), \end{aligned} \tag{6}$$

where $\mathbf{w}$ is a unit vector ($|\mathbf{w}|=1$) in an arbitrary direction. In Eq. (6) the first term is the fraction of dislocations which have passed through an obstacle and acquired in time t a velocity $\mathbf{a}t+\mathbf{v}_0$. The second term takes account of the fraction of dislocations whose velocity changed direction as a result of the first collisions with obstacles and acquired an arbitrary direction $\mathbf{w}$. Obviously, these directions are knocked out of the probability density $n(\mathbf{v},t;\mathbf{v}_0)$, as is indicated by the minus sign in front of the second term.

2. DISLOCATION GLIDE

Substituting the integral equation (6) into the kinetic equation (2), we obtain an equation for ρ^*

$$\frac{\partial}{\partial t}\rho^*(\mathbf{v}_0,t;m)+\frac{|\mathbf{a}t+\mathbf{v}_0|^m}{2A}\rho^*(\mathbf{v}_0,t;m)=0. \tag{7}$$

The function ρ^* must satisfy the relations

$$0\leqslant\rho^*(\mathbf{v}_0,t;m)\leqslant 1,\quad \rho^*(\mathbf{v}_0;m)=1.$$

We shall assume that the direction of the initial velocity $\mathbf{v}_0$ is the same as the vector of the applied load σ. The solution of Eq. (7) has the form

$$\rho^*(\mathbf{v}_0,t;m)=\exp\left(\frac{|\mathbf{v}_0|^{m+1}-(|\mathbf{a}|t+|\mathbf{v}_0|)^{m+1}}{2|\mathbf{a}|A(m+1)}\right), \tag{8}$$

with $m\neq -1$. For $m<-1$ the asymptotic representation of the solution (8) is expressed by the formula

$$q=\lim_{t\to\infty}\rho^*(\mathbf{v}_0,t;m+1)=\exp\left(-\frac{|\mathbf{v}_0|^{m+1}}{2|\mathbf{a}|A|m+1|}\right). \tag{9}$$

This is the fraction of dislocations which have the initial velocity and pass through an obstacle. As $|\mathbf{v}_0|\to 0$ this fraction becomes infinitesimal. As $|\mathbf{v}_0|\to\infty$ (or as $|\mathbf{a}|$ increases) this fraction tends to 1, i.e., as their velocity (energy) increases, dislocations start to ''slip past'' obstacles without stopping.

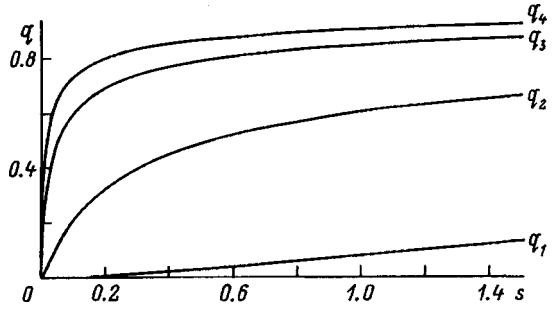

FIG. 2. Fraction of dislocations overcoming obstacles in the dynamic regime versus the initial dislocation velocity. q_1, q_2, q_3, and q_4 correspond to the following values of the density of obstacles: $p_1=10^{-4}\%$, $p_2=10^{-3}\%$, $p_3=10^{-2}\%$, and $p_4=10^{-1}\%$, increasing as a result of irradiation.

The dependence of the fraction of dislocations which overcome an obstacle in the dynamic regime on the dislocation velocity is illustrated qualitatively in Fig. 2.

For this, for example, we set $m=-3/2$, which corresponds to a dislocation–obstacle interaction law $\sim r^{-8/3}$. In order for a dislocation to acquire acceleration $a=|\mathbf{a}|$, according to Newton's second law $a=F/m^*$, a force $F>F_0/l$ (per unit length of the dislocation) must be applied, where F_0 is the maximum dislocation restraining force developed by one defect and l is the distance between defects,[15] $m^*=(db^2/4\pi)\ln(R/r_0)$ is a known expression[16] for the effective mass per unit length of a dislocation, d is the mass density of the metal, b is the magnitude of Burgers vector. Setting $l=n_i^{-1/3}$ and $|\mathbf{v}_0|=us$, where n_i is the number of defects per unit volume (specifically, irradiation produced defects) and u is the velocity of sound, we transform Eq. (9) to a form convenient for plotting

$$\begin{aligned} q&=\exp(-1/Q),\\ Q&=2A|m+1|(F_0 4\pi n^{1/3})/(db^2\ln(R/r_0))\\ &\quad\times u^{|m+1|}p^{1/3}s^{|m+1|}, \end{aligned}$$

where p is the defect density and n is the density of atoms of the main material. To obtain a clear picture, we choose the following values of the parameters: $F_0=1.6\times10^{-4}$ dynes, $u=3.3\times10^4$ cm/s, $d=8$ g/cm^3, $\ln(R/r_0)=8$, $n=8\times10^{22}$ cm^{-3}, $b=3\times10^{-8}$ cm, and $A=10^{-16}$ s$^{5/2}\cdot$cm$^{-3/2}$. For these values the function $q(s)$ has the form shown in Fig. 2. The quantity s is plotted along the abscissa. According to our data and the data of other authors,[17] a relative increase in the yield stress of a material by a factor of 4–20 is observed in most model and reactor materials even at doses $10^{-2}-10^{-1}$ dpa. Moreover, one can see that under otherwise equal conditions, the fraction of dislocations in irradiated materials which have overcome obstacles in the dynamic regime now becomes substantial (according to Ref. 8 , the criterion of the dynamic or ''pseudorelativistic'' regime is that dislocations reach velocities ~ 0.1 of the velocity of the sound).

Figure 2 also shows that the dynamic (pseudorelativistic) deformation regime is reached in irradiated materials at lower dislocation velocities.

As investigations by Popov showed,[8] for dislocation densities $\approx 10^{10}$ cm^{-2} pseudorelativistic effects must be taken into account to describe the evolution of dislocation structures, i.e., the dislocation velocities can approach the sound velocity ($\geqslant 0.1u$). In the case of, for example, irradiated nickel and vessel steel, such a dislocation density corresponds to stresses $\geqslant 100$ MPa, and hence such effects can appear even at the initial stages of deformation, which correspond to the Chernov–Lüders strain interval. As numerous experiments have shown, high dislocation densities are observed in deformation channels formed in irradiated materials even near the yield stress. This results in the appearance of the Chernov–Lüders plastic instability.[1,2]

The model presented in this work, in our opinion, may be directly related to, for example, the problem of the brittleness of irradiated materials in reactor vessels. The latest investigations[18] show that deformation and fracture processes in vessel steels are accompanied by dynamic dislocation channeling and ''destruction'' by dislocations of very small defects in the form of micropores, loops, and precipitates in vessel steels. Localized-deformation channels, encountering interfaces, could be responsible for the sharp stress concentration, proportional to the total dislocation ''charge,'' and give rise to microcracks.

In summary, in the model presented above, the development of plastic instability in an irradiated deformable material was studied taking account of the velocity dependence of the distribution function of dislocations in an ensemble. It was shown that a sharp increase in the fraction of dislocations which overcome obstacles in the dynamic regime can be observed in these materials. As the degree of hardening (concentration of defects arising under irradiation) increases, this effect can be reached at lower deformation velocities.

[1] I. M. Neklyudov and N. V. Kamyshanchenko, in *Structure of and Radiation Damage in Construction Materials* [in Russian], Metallurgiya, Moscow (1996), p. 168.
[2] A. V. Volobuev, L. S. Ozhigov, and A. A. Parkhomenko, Vop. Atom. Nauki i Tekhniki. Fizika Radiatsionnykh Povrezhdeniĭ i Radiatsionnoe Materialovedenie **1**(64), 3 (1996).
[3] I. M. Neklyudov, L. S. Ozhigov, A. A. Parkhomenko, and V. D. Zabolotnyĭ, in *Proceedings of the 2nd Scientific Conference on Physical Phenomena in Solids* [in Russian], Khar'kov University, Khar'kov (1995), p. 132.
[4] G. A. Malygin, Fiz. Tverd. Tela (Leningrad) **33**, 1069 (1991) [Sov. Phys. Solid State **33**, 606 (1991)].
[5] G. A. Malygin, Fiz. Tverd. Tela (Leningrad) **33**, 1855 (1991) [Sov. Phys. Solid State **33**, 1042 (1991)].
[6] G. A. Malygin, Fiz. Tverd. Tela (Leningrad) **34**, 3605 (1992) [Sov. Phys. Solid State **34**, 1931 (1992)].
[7] G. A. Malygin, Fiz. Tverd. Tela (St. Petersburg) **37**, 3 (1995) [Phys. Solid State **37**, 1 (1995)].
[8] L. E. Popov, L. Ya. Pudan, S. N. Kolupaeva, V. S. Kobytev, and V. A. Starenchenko, *Mathematical Modeling of Plastic Deformation* [in Russian], Tomsk University Press, Tomsk (1990), 184 pp.
[9] Sh. Kh. Khannakov, Fiz. Met. Metalloved. **78**, 31 (1994).
[10] G. A. Malygin, Fiz. Tverd. Tela (St. Petersburg) **38**, 2418 (1996) [Phys. Solid State **38**, 1329 (1996)].
[11] V. V. Rybin, *Large Plastic Deformations and Fracture of Metals* [in Russian], Metallurgiya, Moscow (1986), 268 pp.
[12] L. D. Landau and E. M. Lifshitz, *Mechanics* [Pergamon Press, N. Y.; Nauka, Moscow, 1965, 204 pp.].
[13] R. L. Fleischer, Acta Metall. **10**, 835 (1962); J. Appl. Phys. **33**, 3504 (1962).
[14] V. I. Vladimirov, *Physical Nature of Fracture of Metals* [in Russian], Metallurgiya, Moscow, 1984.
[15] O. A. Troitskiĭ and V. G. Shteĭnberg, *Radiation Physics of the Strength of Metallic Crystals* [in Russian], Atomizdat, Moscow (1969), 79 pp.
[16] J. Hirth and J. Lothe, *Theory of Dislocations* [Krieger, 1992, reprint of 1982 edition, Atomizdat, Moscow, 1972, 599 pp.].
[17] V. F. Zelenskiĭ, I. M. Neklyudov, L. S. Ozhigov, É. A. Reznichenko, V. V. Rozhkov, and T. P. Chernyaeva, *Certain Problems of the Physics of Radiation Damage in Materials* [in Russian], Naukova Dumka, Kiev (1979), 330 pp.
[18] M. Große, J. Böhmert, and H. W. Viehrig, J. Nucl. Mater. **211**, 177 (1994).

Translated by M. E. Alferieff

Activation parameters of stepped deformation of polymers

N. N. Peschanskaya and P. N. Yakushev

A. F. Ioffe Physicotechnical Institute, Russian Academy of Sciences, 194021 St. Petersburg, Russia
(Submitted February 12, 1998; resubmitted March 3, 1998)
Fiz. Tverd. Tela (St. Petersburg) **40**, 1635–1638 (September 1998)

Creep rates on short deformation base lines before and after a change in temperature and stresses were measured by interferometry to determine the activation energies and activation volumes of the process. It is shown that the activation parameters of polymer creep vary not only at a macroscopic level but also within the micron-size deformation steps. The largest potential barrier corresponds to the lowest rate in a step and plays the role of a ''physical node.'' The results confirm the supposition that micron-size jumps (steps) of polymer deformation are caused by the nonmonotonic nature of intermolecular interactions in microvolumes of this level. © *1998 American Institute of Physics.* [S1063-7834(98)01509-3]

The intent of activation analysis[1–4] is to determine the activation energy Q_0 and the activation volume α of the process leading to the transition of kinetic units through a barrier $Q=Q_0-\alpha\tau$ — the activation enthalpy (τ — tangential stress, equal to half the axial compressive of tensile stress σ applied to the sample). The quantities Q_0 and α are ordinarily determined by using probabilistic equations of the type

$$\dot{\varepsilon}=\dot{\varepsilon}_0\exp\left(-\frac{Q_0-\alpha\tau}{RT}\right), \tag{1}$$

where $\dot{\varepsilon}$ is the experimentally measured average rate of the process in the steady state, $\dot{\varepsilon}_0=10^{12}$ s^{-1} is a rate factor, T is the temperature (in K), and R is the gas constant. This relation reflects the physical nature of the deformation and corresponds to a process with one relaxation time, i.e., with constant parameters Q_0 and α with τ and T varying. The expression (1) describes a fan of straight lines converging at a single point ($\log\dot{\varepsilon}_0=12$). The conditions of applicability indicated for Eq. (1) reflect the invariability of the structural kinetics during deformation, and they can be satisfied in real polymers only within narrow temperature, stress, and strain intervals. In most cases the rate in a creep process (especially in the case of nonoriented polymers) changes continuously even with constant τ and T,[4,5] as shown in Fig. 1, displaying the variability of the parameters Q_0 and α in large deformation sections. In the conventional coordinates (inset to Fig. 1), the same creep section (from 5 to 8%) corresponds to a process with a constant strain rate.

The methodological technique of small jumps ΔT and $\Delta\tau$ with a high accuracy of rate measurements by an interferometer[4,5] makes it possible to narrow the parameter measurement section to hundreths of a percent of the deformation, i.e., to a ''point'' with a negligible change in structure, and to approach the condition of applicability of the expression (1) with constant parameters in each measurement of Q_0 and α. The parameters are measured at different points of the creep curve independently and they are assumed to be functions of the strain. The method of jumps ΔT and $\Delta\tau$ has revealed regularities in the variation of the kinetic coefficients as a function of the strain (Fig. 2) and the temperature.[4,5] As follows from what we have said above, the method of jumps makes it possible to take account of the macroscopic nonmonotonicity of the rate.

It is shown in Refs. 6 and 7 that the creep rate varies nonmonotonically on a meso level also, reflecting the stepped character of micron-size deformation in the form of oscillations of the rate about an average value. The variation of the rate over the length of a deformation step suggests that activation barriers differ within microvolumes of a deformation, and these differences are actually the cause of the stepped increments. The present work is concerned with the problem of measuring the values of the coefficients Q_0 and α in Eq. (1), corresponding to the highest and lowest rates within a single deformation step, for unoriented glassy polymers.

1. MATERIALS AND PROCEDURE

Glassy polymers having a pronounced nonmonotonic rate of micron-size deformation increments at 290 K were chosen for the experiments: styrene copolymer with methacrylic acid (PS + 16% MAA), polyvinyl chloride (PVC), and a variant of epoxy resin (ÉD-388). Polymers in the form of 3 mm in diameter and 6 mm high cylindrical samples were tested in a creep regime under uniaxial compression ($\sigma=$const). A laser interferometer was used to record the deformation per unit time.[8] The interferogram consists of a sequence of beats (Fig. 3), each of which corresponds to a deformation increment by 0.3 μm (0.005%), while the beat frequency ν determines the creep rate $\dot{\varepsilon}=\lambda\nu/2l_0$, where $\lambda=0.63$ μm is the wavelength of the laser radiation and l_0 is the initial length of the sample. The trace of the deformation (Fig. 3) makes it possible to measure the rate of the process on half a beat (0.15 μm) and to determine the changes in the rate on deformation increments of fractions of a micron.

The accuracy of the method makes it possible to estimate the parameters Q_0 and α at different ''stages'' of a single deformation jump (the period L in Fig. 3). To calculate the parameters differing most from one another, the smallest and largest values of the rate in the course of a

 © 1998 American Institute of Physics

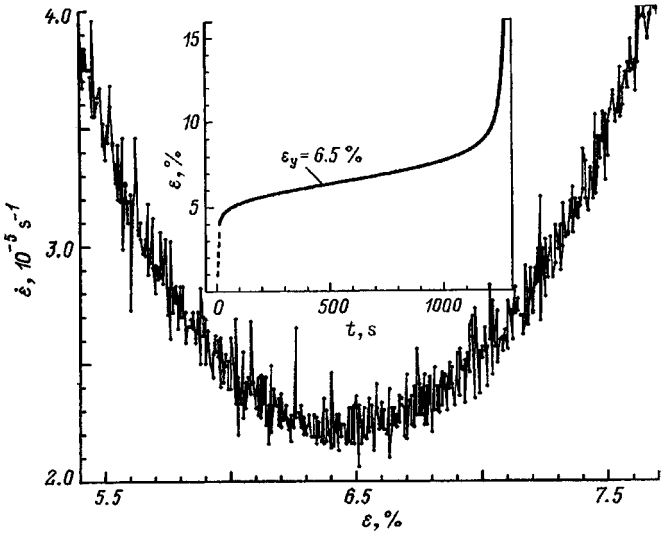

FIG. 1. Computerized measurement and construction of the dependence of the rate $\dot{\varepsilon}$ versus the strain ε near $\varepsilon_y = 6.5\%$ for polycarbonate. Each point corresponds to a deformation increment of 0.3 μm (0.005%), the variance of the rate reflects the jump-like development of deformation. Inset: Apparent stationary creep in the coordinates strain ε–time t, $\sigma = 70$ MPa, $T = 291$ K.

period L before ($\dot{\varepsilon}_1$, $\dot{\varepsilon}_1'$) and after ($\dot{\varepsilon}_2$, $\dot{\varepsilon}_2'$) a change in temperature or stress ($\Delta T = 3-5$ K, $\Delta\tau = 2$ MPa) were determined. The coefficients were determined from the formulas

$$\alpha = \frac{RT\ln(\dot{\varepsilon}_2/\dot{\varepsilon}_1)}{\Delta\tau}, \quad Q_0 = \frac{R\ln(\dot{\varepsilon}_2/\dot{\varepsilon}_1)}{1/T_1 - 1/T_2} + \alpha\tau. \tag{2}$$

It was shown in Ref. 5 that α and Q_0 are cooperative quantities, related to one another. The quantity characterizing the intermolecular interaction is the specific energy q per monomer unit

$$q = \frac{Q_0}{\alpha}V, \tag{3}$$

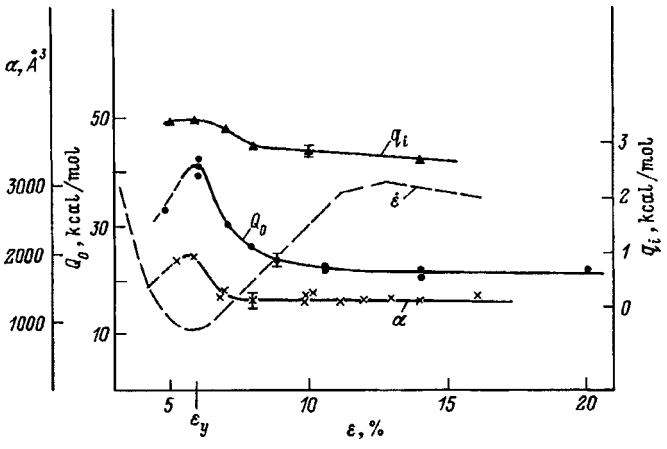

FIG. 2. Activation energy Q_0, activation volume α, and specific activation energy q_i versus strain for PS + 16% MAA. The dashed line shows the change in the creep rate $\dot{\varepsilon}$.

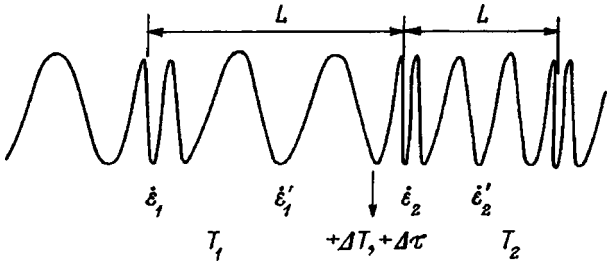

FIG. 3. Scheme of the change in rate in a deformation step ($L = 1.2$ μm) in the case of a change in stress or temperature.

where V is the volume of a monomer unit of a polymer molecule. In the present paper q is estimated for two stages of a jump L (Fig. 3).

2. RESULTS AND DISCUSSION

In previous works[7,9] regularities were obtained that led to the conclusion that deformation jumps exist on different levels and are caused by the nonuniformity of the structure and potential fields of nonchemical origin which are overcome in the process of displacement events. The stronger nonchemical interactions between molecular groups are commonly termed ''physical bonds'' which alternate with weak bonds between sections of different molecules in the slip plane. A displacement in a plane with small barriers should correspond to high rates $\dot{\varepsilon}_1$ in a deformation jump L (Fig. 3), and correspondingly the overcoming of large potential barriers (bonds) is associated with long relaxation times and slow rates $\dot{\varepsilon}_1'$. The dislocation–disclination models of deformation that were developed for polymers[10] take account of the heterogeneity of the structure and the localized character of defects, and they imply that displacements of defects are jump-like. The qualitative model of physical bonds is consistent with the specific mechanisms of the theories and is confirmed well by experiments. Table I gives the activational characteristics of deformation jumps for three polymers. It follows from this table that the high rates in a jump correspond to larger values of α and lower values of Q_0 and q compared to the values of these quantities for slow rates in a period L. The difference between the rates is most clearly reflected in the values of q. Values of q_1' that are much higher than q_1 correspond to a bond.

Therefore activational analysis has shown that potential barriers in the creep process change not only on a macrolevel[5] but also on a mesolevel, within micron-size deformations. Experiments show that the jump-like character of creep is due to the nonmonotonicity of the activation energy of the process within a single step.

Table I gives the values of q_i obtained with $\varepsilon > \varepsilon_y$ by the same method but for average rates over the length L of the jumps.[4,5] As shown earlier,[4] the values of q_i equal the activation energies of the viscous flow of a hypothetical fluid in which the kinetic unit is a monomer unit: $q_i = E_{coh}/3$, where E_{coh} is the cohesion energy for a monomer unit of a polymer. One can see from the table that q_i for a macroprocess is closest in value to the specific activation energy for the stage of easiest slip with high rates in a jump L. An analogy can be

TABLE I. Activation parameters within a single deformation step L.

Material, σ, ε_y	V, Å^3	L, μm	$\dot{\varepsilon}_1$, 10^{-5} s^{-1}	$\dot{\varepsilon}_1'$, 10^{-5} s^{-1}	α_1, Å^3	α_1', Å^3	$\frac{Q_1}{Q_{1_0}}$	$\frac{Q_1'}{Q_{1_0}'}$	ε, %	q_1	q_1'	q_i
P5+16%mAA												
σ=90 MPa ε_y=6.5%	166	1.05	0.07	0.04	2360	1730	$\frac{30}{45}$	$\frac{40}{51}$	8.0	3.2	4.8	3.0
PVC												
σ=60 MPa ε_y=5%	72.5	0.6	2.5	2.0	940	750	$\frac{11}{19}$	$\frac{15.8}{22.3}$	27	1.4	2.1	1.0
ÉD												
σ=87 MPa $\varepsilon_y \cong 5\%$	1300	3.6	5.0	4.0	2440	1400	$\frac{31}{45}$	$\frac{37}{46}$	25	25	43	20

Note: The value of q_i was calculated using Eq. (3), where Q_0 and α were determined neglecting the nonmonotonicity of the rate. The indices in the designations correspond to Fig. 3. The values of Q_0, Q, and q are given in kcal·mole^{-1}.

drawn between the change in the parameter q in a microjump of a deformation (see Table I) and in a macrojump which is observed after the deformation (Fig. 2). Indeed, a minimum of the rate in Fig. 2 corresponds to onset of destruction of the initial system of intermolecular bonds and accelerated flow of the material.[4,5] The lowest rate at the point ε_y is related to the highest value of q_i, while acceleration of deformation results in a lower value of q_i. A similar phenomenon is also observed within the microdeformation of the jumps: Acceleration of creep corresponds to a decrease in the value of q (see Table I).

The results show a similarity in the mechanism of displacement processes on different scales. Large irreversible deformations $\varepsilon > \varepsilon_y$, which change the shape of the sample, are created from microdisplacments, which probably distort the shape of ordered micron-level formations in the polymer structure. The data make it possible to associate the concept of ''levels'' not only to structure and deformation but also to activation parameters.

[1] Ya. I. Frenkel', *Introduction to the Theory of Metals* [in Russian], Moscow (1958), 368 pp.
[2] V. R. Regel', A. I. Slutsjer, and É. E. Tomashevskiĭ, *The Kinetic Nature of the Strength of Solids* [in Russian], Moscow (1974), 560 pp.
[3] A. S. Krausz and H. Eiring, *Deformation Kinetics*, N. Y. (1975), 398 pp.
[4] V. A. Stepanov, N. N. Peschanskaya, and V. V. Shpeĭzman, *Strength and Relaxation Phenomena in Solids* [in Russian], Leningrad (1984), 245 pp.
[5] N. N. Peschanskaya and V. A. Stepanov, Fiz. Tverd. Tela (Leningrad) **20**, 2005 (1978) [Sov. Phys. Solid State **20**, 1157 (1978)].
[6] N. N. Peschanskaya, Vysokomolekulyarnye Soedineniya A **31**, 1181 (1989).
[7] N. N. Peschanskaya, Fiz. Tverd. Tela (St. Petersburg) **35**, 3019 (1993) [Phys. Solid State **35**, 1484 (1993)].
[8] N. N. Peschanskaya, G. S. Pugachev, and P. N. Yakushev, Mekhanika Polimerov, No. 2, 357 (1977).
[9] N. N. Peschanskaya, P. N. Yakushev, L. P. Myasnikova, V. A. Marikhin, A. B. Sinani, and M. Yakobs, Fiz. Tverd. Tela (St. Petersburg) **38**, 2582 (1996) [Phys. Solid State **38**, 1416 (1996)].
[10] N. A. Pertsev, Prog. Colloid Polym. Sci. **92**, 52 (1993).

Translated by M. E. Alferieff

Influence of impurities on the low-temperature deformation of nanocrystalline copper

V. V. Shpeĭzman, V. I. Nikolaev, B. I. Smirnov, A. B. Lebedev, V. V. Vetrov, and S. A. Pul'nev

A. F. Ioffe Physicotechnical Institute, Russian Academy of Sciences, 194021 St. Petersburg, Russia

V. I. Kopylov

Physicotechnical Institute, Academy of Sciences of Belarus, 220730 Minsk, Belarus
(Submitted April 2, 1998)
Fiz. Tverd. Tela (St. Petersburg) **40**, 1639–1641 (September 1998)

The influence of ZrO_2 particles on the low-temperature deformation of nanocrystalline copper produced by strong plastic deformation is investigated using equichannel angular pressing. A comparison is made between the deformation characteristics in tension and compression in the temperature range 4.2–400 K, measured for copper and the composite Cu:0.3 vol. % ZrO_2. It is shown that within 4.2–200 K the yield point $\sigma_s m$ of the composite is higher than that for copper, attaining 680 MPa at 4.2 K, then the yield points are close in value up to room temperature, and diverge again as the temperature is raised. Possible causes of the dissimilar influence of an impurity on the strength and plasticity characteristics of nanocrystalline copper in various temperature intervals are discussed. © *1998 American Institute of Physics.* [S1063-7834(98)01609-8]

A factor of utmost interest in the investigation of nanocrystalline materials is the way in which their properties are affected by impurities that can improve significantly the thermal stability of the undoped structural state. It has been shown[1,2] that a small addition of ZrO_2 or HfO_2 nanoparticles preserves the high level of the yield point of ultrafine-grained copper up to a temperature ~500 °C. It is also important to study the influence of impurities with a view toward understanding the nature of the plastic deformation of nanocrystals. We have previously[3] investigated the low-temperature deformation of copper and nickel prepared by equichannel angular pressing (ECAP), the onset of deformation inhomogeneity, the temperature dependence of the flow stresses, and the sensitivity of the latter to the sign of the load. In the present study we demonstrate the influence of an ultrafine-grain stabilizing impurity on the low-temperature deformation of copper.

1. EXPERIMENTAL PROCEDURE

The experiments were performed on pure (99.98%) copper and a Cu:ZrO_2 composite. The latter was prepared from Cu–0.15 wt.% Zr solid solution by internal oxidation[4] and contained 0.3 vol. % ZrO_2 in the form of nanoparticles approximately 10 nm in diameter. An ultrafine-grained structure was obtained by repeated (up to 16 times) ECAP with 90° rotation of the bar after each cycle.[5–8] Electron microscope examinations showed that the grain size did not exceed 200 nm in either material. An x-ray examination established that the main factor contributing to line broadening for the pure copper was the smallness of the coherent scattering regions (about 50 nm); the linewidth was larger in the composite, with broadening contributions of close magnitude from the size of the coherent scattering regions (~55 nm) and from lattice distortions, where the relative variation of the lattice parameter $\Delta a/a$ due to internal stresses had a value of about 2.5×10^{-3}.

Bars approximately 50 mm in length with transverse dimensions $\sim 14\times 14$ mm were obtained after ECAP. The samples for mechanical testing were cut along the length of the bar and had the following dimensions: height 6 mm for compression, length of the working section 15 mm for tension, and a diameter of 3 mm in both cases. The samples were deformed in an Instron 1342 universal testing machine in the temperature range 4.2–400 K. The low-temperature tests were carried out in an Oxford Instruments helium cryostat. The sample was cooled to $T \geqslant 77$ K; in addition, liquid-nitrogen precooling was used for tests in the temperature interval 4.2–77 K. Liquid helium was admitted to the cryostat by means of two pumps, which created a slight rarefaction in the cryostat. The rate of deformation was 4×10^{-4} s^{-1}.

2. EXPERIMENTAL RESULTS AND DISCUSSION

As an example, Fig. 1 shows tension and compression diagrams of the Cu:ZrO_2 composite at various temperatures (the copper data are given in Ref. 3), and Tables I and II show the main characteristics of plastic deformation: the yield point σ_s at various temperatures in tension and compression; the maximum tensile stress σ_b; the total relative elongation at the instant of fracture δ; the necking down ψ for pure copper and the composite; the work-hardening coefficient in compression. It is evident that the plasticity and strength characteristics of the copper and the composite differ only slightly at room temperature. At helium temperature the strength and the yield point are higher for the composite, and the work-hardening coefficient in compression is lower

 © 1998 American Institute of Physics

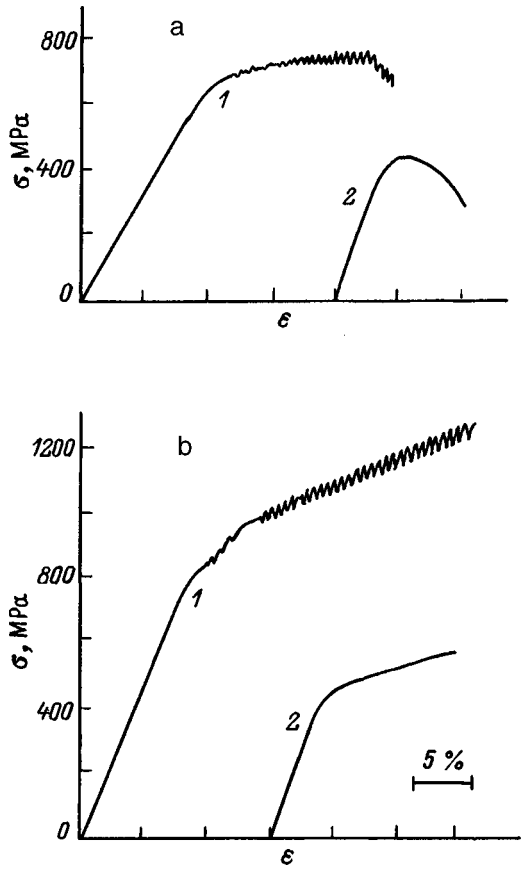

FIG. 1. Stress-strain curves of Cu:ZrO_2 nanocrystals (stress σ versus strain ε) in tension (a) and in compression (b). *1*) $T=4.2$ K; *2*) $T=290$ K.

than for the pure copper. As the temperature is lowered in tension, the uniform part of the deformation increases, while the localized deformation (necking down) decreases. The previously observed[3] anisotropy with respect to the sign of the load (the yield point being higher in compression than in tension) in nanocrystalline copper and nickel also occurs for our composite (Tables I and II). As in pure metals, the anisotropy increases as the temperature is lowered, but the disparity is smaller in the composite than in the pure copper. If this phenomenon is actually associated with strong possibilities for local relaxation during the earliest stages of deformation in tension,[3] it is not surprising that ZrO_2 should be capable of inhibiting relaxation.

The plastic deformation of the Cu:ZrO_2 composite becomes unstable at liquid helium temperature: Sudden jumps are observed, but their amplitude is not too large. No appreciable difference in the deformation jump kinetics is noted between copper and the composite. From our point of view, this result corroborates the helium-temperature deformation

TABLE I. Characteristics of the deformation of Cu and Cu:ZrO_2 nanocrystals in compression.

	Copper			Cu:ZrO_2 composite	
T, K	4.2	77	290	4.2	290
σ_s, MPa	578	570	402	680	412
$d\sigma/d\varepsilon$, MPa	3473	2737	1123	2078	1275

TABLE II. Mechanical properties of the deformation of Cu and Cu:ZrO_2 nanocrystals in tension.

	Copper		Cu:ZrO_2 composite	
T, K	4.2	290	4.2	290
σ_s, MPa	448	382	637	398
σ_b, MPa	550	435	698	431
δ, %	15	10	18	10
ψ, %	57	77	33	64

jump models based on local hot spots, because in alternative models attributing the jumps in the diagrams to avalanches of dislocations breaking away from obstructions there would have to be some evidence of dislocation pinning by ZrO_2 particles.

Figure 2 shows the temperature dependence of the yield point in compression for copper and for the composite, measured by successive loading at a constant strain rate at step-incremented temperatures. Here the increments of the flow stresses in each step have been determined and subsequently scaled to variations of the yield point. Three distinct temperature intervals are discernible from Fig. 2: below ~200 K and above ~300 K, where the yield point of the composite is higher than for copper; the intermediate interval 200–300 K, where the values of σ_s for Cu and Cu:ZrO_2 practically coincide. On the basis of this behavior we can state that the presence of ZrO_2 particles is manifested both in the high-temperature region (probably owing to their influence on recrystallization and the concomitant thermal stability of the nanocrystalline state of the composite[1]) and in the low-temperature region, where direct dislocation drag or twinning of ZrO_2 particles is possible in the initial deformation stage. However, the work-hardening coefficient of copper at 4.2 K is higher than for the composite, so that the flow stresses come closer together in further deformation. In the intermediate temperature interval the ZrO_2 nanoparticles obviously do not contribute significantly to the hardening produced by the grain boundaries in the low-deformation range

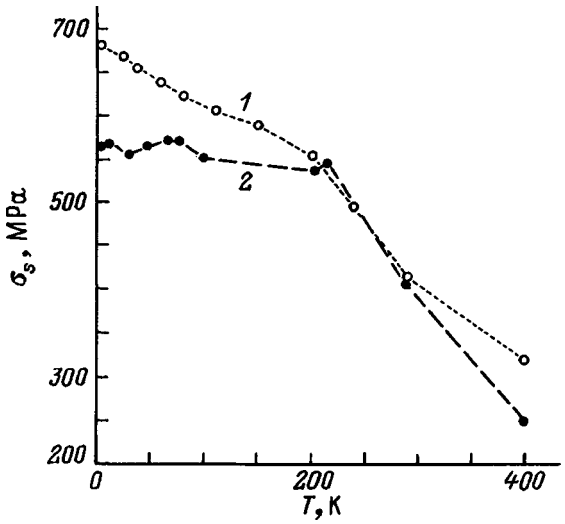

FIG. 2. Yield point versus temperature for: *1*) Cu:ZrO_2 *2*) Cu (from data in Ref. 3).

(at the level of the yield point) and are manifested only in that they slightly increase the work-hardening coefficient in the high-deformation range. Such complex behavior of the yield point and the flow stresses as a function of temperature and doping provides further evidence that the hardening of nanocrystalline materials cannot be described by a simple relation of the Hall-Petch type.[3,9–11]

Summarizing the present study, we have investigated the deformation of nanocrystalline copper containing small ZrO_2 additives. We have shown that the variation of the yield point in the low-temperature range is more pronounced for the composite than for pure copper. At 4.2 K the maximum value of σ_s is equal to 680 MPa, and the flow stresses can attain ~700 MPa in tension and more than 1 GPa in compression. These values are 1.5–2 times the known data for cold-drawn copper[12] and indicate that the nanocrystalline state of the doped material is possibly a structure having maximum resistance to plastic deformation and fracture.

The authors are grateful to I. N. Zimkin and G. D. Motovilina for doing the x-ray and electron-microscope examinations.

This work has received financial support from the Scientific Council of the Ministry of Scientific and Technical Propaganda on the Physics of Solid State Nanostructures (Project 97-3006).

[1] A. B. Lebedev, S. A. Pulnev, V. I. Kopylov, Yu. A. Burenkov, V. V. Vetrov, and O. V. Vylegzhanin, Scr. Mater. **35**, 1077 (1996).
[2] A. B. Lebedev, S. A. Pul'nev, V. V. Vetrov, Yu. A. Burenkov, V. I. Kopylov, and K. V. Betekhtin, Fiz. Tverd. Tela (St. Petersburg) **40**, 1268 (1998) [Phys. Solid State **40**, 1155 (1998)].
[3] V. V. Shpeĭzman, V. I. Nikolaev, B. I. Smirnov, V. V. Vetrov, S. A. Pul'nev, and V. I. Kopylov, Fiz. Tverd. Tela (St. Petersburg) **40**, 1264 (1998) [Phys. Solid State **40**, 1151 (1998)].
[4] I.-W. Chen and Y.-H. Chiao, Acta Metall. **31**, 1627 (1983).
[5] V. M. Segal, V. I. Reznikov, A. E. Drobyshevskiĭ, and V. I. Kopylov, Izv. Akad. Nauk. SSSR, Met. **1**, 115 (1981).
[6] N. A. Akhmadeev, R. Z. Valiev, V. I. Kopylov, and R. R. Mulyukov, Izv. Akad. Nauk. SSSR, Met. **5**, 96 (1992).
[7] V. M. Segal, V. I. Reznikov, V. I. Kopylov, D. A. Pavlik, and V. F. Malyshev, in Plastic Structuring Processes in Metals [in Russian], Nauka i Tekhnika, Minsk (1994), 232 pp.
[8] S. Ferrasse, V. M. Segal, K. T. Hartwig, and R. E. Goforth, Metall. Mater. Trans. A **28**, 1047 (1997).
[9] G. A. Malygin, Fiz. Tverd. Tela (St. Petersburg) **37**, 2281 (1995) [Phys. Solid State **37**, 1248 (1995)].
[10] J. E. Carsley, J. Ning, W. W. Milligan, S. A. Hackney, and E. S. Aifantis, Nanostruct. Mater. **5**, 441 (1995).
[11] M. Yu. Gutkin, ''Defect models and plastic deformation mechanisms in inhomogeneous mesostructured and nanostructured media,'' Author's Abstract of Doctoral Dissertation [in Russian] (Institute of Problems in Machine Construction of the Russian Academy of Sciences, St. Petersburg, 1997), 34 pp.
[12] D. A. Wigley, Mechanical Properties of Materials at Low Temperatures (Plenum Press, New York-London, 1971), 373 pp.

Translated by James S. Wood

MAGNETISM AND FERROELECTRICITY

Complex magnetic susceptibility of uniaxial superparamagnetic particles in a strong static magnetic field

Yu. P. Kalmykov and S. V. Titov

Institute of Radio Engineering and Electronics, Russian Academy of Sciences, 141120 Fryazino, Moscow Region, Russia

(Submitted October 17, 1997)
Fiz. Tverd. Tela (St. Petersburg) **40**, 1642–1649 (September 1998)

The magnetic relaxation of a system of single-domain ferromagnetic particles in the presence of a strong static magnetic field directed at an arbitrary angle relative to the particle anisotropy axis is investigated. A system of linear difference-differential equations for the moments (averaged spherical harmonics) is derived without recourse to the Fokker–Planck equation by averaging Gilbert's equations with a fluctuating field. An exact solution (in terms of matrix continuous fractions) is found for this system. The relaxation times and spectra of the complex magnetic susceptibility are calculated. © *1998 American Institute of Physics.* [S1063-7834(98)01709-2]

1. Uniaxially anisotropic, single-domain ferromagnetic particles are characterized by an internal potential having two stable equilibria separated by a potential barrier between them. If the particles are small (and, accordingly, the potential barrier is low), the magnetization vector **M** can change its orientation through the barrier as a result of thermal fluctuations.[1] The thermal instability of the magnetization produces so-called superparamagnetism,[2] because each particle behaves like a huge magnet having a magnetic moment $\sim 10^4-10^5$ Bohr magnetons. Research on the thermal fluctuations and relaxation of the magnetization of single-domain particles is of major interest these days with regard to improving the characteristics of magnetic charge carriers[3] and in relation to paleomagnetism.[4]

The dynamics of the magnetization of single-domain ferromagnetic particles is described by the Landau-Lifshitz equation.[5] Gilbert[6] has proposed a similar equation. Brown[7] has used these equations to describe the magnetization dynamics of an individual particle, relying on the Langevin equation approach from the theory of Brownian movement. In the role of the Langevin equation, Brown used Gilbert's equation with a fluctuating field to describe the thermal fluctuations of the magnetization of an individual particle. Using the method of Wang and Uhlenbeck[8] in conjunction with Stratonovich's approach[9] to the averaging of stochastic differential equations, Brown then derived a Fokker-Planck equation for the probability density function $W(\{\mathbf{M}\},t)$ of the magnetization **M**. A theory of magnetic relaxation in an ensemble of single-domain particles has been formulated[5–9] on the basis of the Fokker–Planck equation.

In the basic model used to study relaxation processes in superparamagnets, the free-energy density V of a single-domain magnetic particle (with uniaxial anisotropy) in a homogeneous external magnetic field $\mathbf{H_0}$ of arbitrary strength has the form[1,10,11]

$$V=-K\cos^2\vartheta-(\mathbf{M}\cdot\mathbf{H}_0), \tag{1}$$

where K is the anisotropy constant, and ϑ is the polar angle. This problem, formulated by Néel[1] and by Stoner and Wohlfahrt,[11] has been analyzed, for example, in Refs. 12–22. However, to simplify the mathematical calculations, in most cases (with the exception of a few papers, e.g., Refs. 23–26) it has been assumed that the field $\mathbf{H}_0$ is directed along the anisotropy axis of the particle. Previously the complex magnetic susceptibility could be calculated only under this assumption.

In the general statement of the problem, with the field $\mathbf{H}_0$ oriented in an arbitrary direction relative to the magnetization axis, the Fokker–Planck equation can be solved formally by expanding the distribution function $W(\{u\},t)$ in spherical harmonics. This operation reduces the problem to the solution of an infinite-dimensional system of linear difference-differential equations for the averaged spherical harmonics (moments) (Refs. 25 and 26)

$$\frac{d}{dt}X(t)=AX(t), \tag{2}$$

where A is the infinite-dimensional system matrix, and $X(t)$ is a column vector formed by the moments (the system for the moments (2) can also be obtained by averaging Gilbert's equation directly without using the Fokker–Planck equation[27,28]). A numerical solution of Eq. (2) (by finding the eigenvalues and eigenvectors of the system matrix) can be obtained, in principle, by successively increasing the number of equation by a finite number N until convergence is achieved. Unfortunately, it is difficult to employ this approach in practice, because the given problem requires calculations for $N\sim 10^3-10^4$, which can only be done on supercomputers.[26] However, the problem can be simplified considerably by applying the method of matrix continuous

 © 1998 American Institute of Physics

fractions[28,29] developed in Ref. 28 for the solution of infinite systems of recursion formulas for the moments. Although this approach has already been used in the investigation of analogous problems in the theory of the Kerr effect, dielectric relaxation, and magnetic relaxation,[15,30,31] it cannot be applied to our problem directly, because here the recursion formula contains two variable indices.[25,26] So far no one has proposed a simple algorithm for this case (e.g., it has been suggested[29] that infinite-dimensional matrix fractions be used in the solution of two-index recursion formulas), so that further elaboration of the method is required.

The main objective of the present study is to calculate the longitudinal component of the magnetic susceptibility $\chi_{\|}(\omega)$ of a system of noninteracting, single-domain ferromagnetic particles in a strong static magnetic field of arbitrary orientation relative to the easy axis of a particle.

2. Gilbert's equation for the magnetization **M** of a single-domain particle with allowance for thermal fluctuations has the form[5,6]

$$\frac{d}{dt}\,\mathbf{M}(t)=\gamma[\mathbf{M}(t)\times[\mathbf{H}(t)+\mathbf{h}(t)-\eta\dot{\mathbf{M}}(t)]], \tag{3}$$

where γ is the gyromagnetic ratio, and η is the friction coefficient; the total magnetic field can consist of external applied fields plus the effective magnetic anisotropy field (all denoted by **H**) and a random field $\mathbf{h}(t)$ exhibiting the properties of white noise:

$$\overline{h_i(t)}=0, \quad \overline{h_i(t_1)h_j(t_2)}=\frac{2kT\eta}{\nu}\,\delta_{ij}\delta(t_1-t_2), \tag{4}$$

where ν is the particle volume, and the overbar signifies statistical averaging over the ensemble of particles having the identical magnetization **M** at time t.

If $V(\{\mathbf{M}\},t)$ is the free energy per unit volume, expressed in terms of the components of **M**, then the field **H** is given by the equation

$$\mathbf{H}=-\frac{\partial}{\partial\mathbf{M}}\,V(\{\mathbf{M}\}),$$

where

$$\frac{\partial}{\partial\mathbf{M}}=\mathbf{i}\,\frac{\partial}{\partial M_x}+\mathbf{j}\,\frac{\partial}{\partial M_y}+\mathbf{k}\,\frac{\partial}{\partial M_z},$$

$M_x=M_s\sin\vartheta\cos\varphi=M_s u_x$, $M_y=M_s\sin\vartheta\sin\varphi=M_s u_y$, and $M_z=M_s\cos\vartheta=M_s u_z$.

Gilbert's equation (3) can be transformed to the Landau–Lifshitz equation[5,6,22]

$$\frac{d}{dt}\,\mathbf{M}(t)=M_s g'[\mathbf{M}(t)\times[\mathbf{H}(t)+\mathbf{h}(t)]] + h'[\mathbf{M}(t)\times[\mathbf{H}(t)+\mathbf{h}(t)]\times\mathbf{M}(t)], \tag{5}$$

where

$$g'=\frac{\gamma}{(1+\alpha^2)M_s}, \quad h'=\frac{\gamma\alpha}{(1+\alpha^2)M_s}=\alpha g', \tag{6}$$

and $\alpha=\gamma\eta M_s$ is a dimensionless damping factor.

Writing Eq. (5) in terms of components in laboratory Cartesian coordinates, we have

$$\begin{aligned}\frac{1}{h'M_s}\frac{d}{dt}\,u_x(t)=&[1-u_x^2(t)]h_x(t)-[\alpha^{-1}u_z(t)\\&+u_x(t)u_y(t)]h_y(t)+[\alpha^{-1}u_y(t)\\&-u_z(t)u_x(t)]h_z(t)+[1-u_x^2(t)]H_x(t)\\&-[\alpha^{-1}u_z(t)+u_x(t)u_y(t)]H_y(t)\\&+[\alpha^{-1}u_y(t)-u_z(t)u_x(t)]H_z(t),\end{aligned} \tag{7}$$

$$\begin{aligned}\frac{1}{h'M_s}\frac{d}{dt}\,u_y(t)=&[\alpha^{-1}u_z(t)-u_x(t)u_y(t)]h_x(t)\\&+[1-u_y^2(t)]h_y(t)-[\alpha^{-1}u_x(t)\\&+u_y(t)u_x(t)]h_z(t)+[\alpha^{-1}u_z(t)\\&-u_x(t)u_y(t)]H_x(t)+[1-u_y^2(t)]H_y(t)\\&-[\alpha^{-1}u_x(t)+u_y(t)u_x(t)]H_z(t),\end{aligned} \tag{8}$$

$$\begin{aligned}\frac{1}{h'M_s}\frac{d}{dt}\,u_z(t)=&-[\alpha^{-1}u_y(t)+u_x(t)u_z(t)]h_x(t)\\&+[\alpha^{-1}u_x(t)-u_y(t)u_z(t)]h_y(t)\\&+[1-u_z^2(t)]h_z(t)-[\alpha^{-1}u_y(t)\\&+u_x(t)u_z(t)]H_x(t)+[\alpha^{-1}u_x(t)\\&-u_y(t)u_z(t)]H_y(t)+[1-u_z^2(t)]H_z(t).\end{aligned} \tag{9}$$

For a single-domain particle with the magnetic anisotropy potential[5,6,8,9,24]

$$V=-Ku_z^2=-K\cos^2\vartheta, \tag{10}$$

where ϑ is the angle between the vector **M** and the z axis; in the presence of a strong static magnetic field $\mathbf{H}_0$ applied at an arbitrary angle relative to the z axis, the total field **H** has the form

$$\mathbf{H}=\gamma_1 H_0\mathbf{i}+\gamma_2 H_0\mathbf{j}+\left(\gamma_3 H_0+\frac{2K}{M_s}\,u_z\right)\mathbf{k}, \tag{11}$$

where $\gamma_1=\sin\Psi\cos\Phi$, $\gamma_2=\sin\Psi\sin\Phi$, and $\gamma_3=\cos\Psi$ are the direction cosines of the vector $\mathbf{H}_0$ (Ψ and Φ are the polar angle azimuth angles, respectively).

The stochastic nonlinear differential equations (7)–(9), which contain multiplicative noise terms $u_i u_j h_k$, need to be averaged (see, e.g., Refs. 28 and 29). We recall that stochastic differential equations of general form in N variables $\{\boldsymbol{\xi}(t)\}=\{\xi_1,\xi_2,\ldots,\xi_N\}$

$$\frac{d\xi_i(t)}{dt}=h_i(\{\boldsymbol{\xi}(t)\},t)+g_{ij}(\{\boldsymbol{\xi}(t)\},t)\Gamma_j(t) \tag{12}$$

with $\overline{\Gamma_i(t)}=0$ and $\overline{\Gamma_i(t_1)\Gamma_j(t_2)}=2D\,\delta_{ij}\delta(t_1-t_2)$, $i,j=1,\ldots,N$, averaged by Stratonovich's rule[28,29] at time t, have the form

$$\frac{dx_i}{dt}=\lim_{\tau\to 0}\frac{\overline{\xi_i(t+\tau)-x_i}}{\tau}=h_i(\{\mathbf{x}\},t)$$

$$+Dg_{kj}(\{\mathbf{x}\},t)\,\frac{\partial}{\partial x_k}\,g_{ij}(\{\mathbf{x}\},t), \tag{13}$$

where $\xi_i(t+\tau)$ $(\tau>0)$ are the solutions of Eqs. (12) subject to the initial conditions $\xi_i(t)=x_i$ [summation over the repeated indices j and k is understood in Eqs. (12) and (13)]. The second term on the right-hand side of Eq. (13) is called the noise-induced drift coefficient.[28,29] A proof of Eq. (13) is given, for example, in Ref. 29 (pp. 54–55).

In the same way it can be proved that the averaged equation for an arbitrary differentiable function $f(\{\boldsymbol{\xi}\})$ has the form[22,30]

$$\frac{df(\{\mathbf{x}\})}{dt}=h_i(\{\mathbf{x}\},t)\,\frac{\partial}{\partial x_i}\,f(\{\mathbf{x}\})+Dg_{kj}(\{\mathbf{x}\},t)$$

$$\times\frac{\partial}{\partial x_k}\left[g_{ij}(\{\mathbf{x}\},t)\,\frac{\partial}{\partial x_i}\,f(\{\mathbf{x}\})\right], \tag{14}$$

where again summation over the repeated indices, i, j, k is understood.

Stratonovich's approach[28,29] must be used in averaging the stochastic differential equations (7)–(9) because, from the physical point of view, the investigated magnetic relaxation processes are best modeled within the framework of this approach. In particular, the preliminary modification of Eqs. (7)–(9) to an equivalent form of the Itô equations is not required in this case, and ordinary methods of analysis are applicable.

For the investigation of magnetic relaxation it is convenient to use spherical harmonics X_{nm} defined as

$$X_{nm}=e^{im\varphi}P_n^m(\cos\,\vartheta),$$

$$X_{n-m}=(-1)^m\,\frac{(n-m)!}{(n+m)!}\,X_{nm}^*,\quad m\geqslant 0,$$

where $P_n^m(x)$ denotes associated Legendre functions.[17] The spherical harmonics X_{nm} are written as follows in the variables u_x, u_y, u_z:

$$X_{nm}=(u_x+iu_y)^m\,\frac{d^mP_n(u_z)}{du_z^m},$$

where $P_n(x)$ denote Legendre polynomials. Making use of the fact that

$$\frac{d}{dt}\,X_{nm}=m(u_x+iu_y)^{m-1}\,\frac{d^mP_n(u_z)}{du_z^m}\,(\dot u_x+i\dot u_y)$$

$$+(u_x+iu_y)^m\,\frac{d^{m+1}P_n(u_z)}{du_z^{m+1}}\,\dot u_z,$$

we can obtain an equation for the spherical harmonics X_{nm} if we multiply Eqs. (7)–(9) by

$$m(u_x+iu_y)^{m-1}\,\frac{d^mP_n(u_z)}{du_z^m},$$

$$im(u_x+iu_y)^{m-1}\,\frac{d^mP_n(u_z)}{du_z^m},$$

$$(u_x+iu_y)^m\,\frac{d^{m+1}P_n(u_z)}{du_z^{m+1}},$$

respectively, and then sum them. After averaging, therefore, we can obtain a system of equations for the averaged spherical harmonics (the details of the derivation are given in Refs. 22 and 27):

$$\tau_N\,\frac{d}{dt}\,c_{n,m}(t)+\left[\frac{n(n+1)}{2}+\frac{i\gamma_3\xi m}{2\alpha}\right.$$

$$\left.-\sigma\,\frac{n(n+1)-3m^2}{(2n-1)(2n+3)}\right]c_{n,m}(t)$$

$$=\sigma\left[\frac{(n+1)(n+m)(n+m-1)}{(2n-1)(2n+1)}\,c_{n-2,m}(t)\right.$$

$$\left.-\frac{n(n-m+1)(n-m+2)}{(2n+1)(2n+3)}\,c_{n+2,m}(t)\right]$$

$$+\frac{(n+m)}{2n+1}\left(\gamma_3\xi\,\frac{n+1}{2}-\frac{im\sigma}{\alpha}\right)c_{n-1,m}(t)$$

$$-\frac{(n-m+1)}{2n+1}\left(\gamma_3\xi\,\frac{n}{2}+\frac{im\sigma}{\alpha}\right)c_{n+1,m}(t)$$

$$+\frac{\xi(\gamma_1+i\gamma_2)}{4(2n+1)}\,[n(n-m+1)(n-m$$

$$+2)c_{n+1,m-1}(t)+i\alpha^{-1}(2n+1)(n-m+1)$$

$$\times(n+m)c_{n,m-1}(t)+(n+1)(n+m-1)(n$$

$$+m)c_{n-1,m-1}(t)]-\frac{\xi(\gamma_1-i\gamma_2)}{4(2n+1)}\,[nc_{n+1,m+1}(t)$$

$$-i\alpha^{-1}(2n+1)c_{n,m+1}(t)+(n+1)c_{n-1,m+1}(t)], \tag{15}$$

where

$$\sigma=\frac{\nu K}{kT},\quad \xi=\frac{\nu M_sH_0}{kT},\quad \tau_N=\frac{\nu}{2kTh'}, \tag{16}$$

$$c_{n,m}(t)=\langle X_{nm}\rangle(t)-\langle X_{nm}\rangle_0, \tag{17}$$

the angle brackets $\langle\rangle$ signify ordinary statistical averaging, $\langle\rangle_0$ denotes the equilibrium average, defined as

$$\langle A\rangle_0=\int_0^{2\pi}\int_0^{\pi}A(\vartheta,\varphi)W_0(\vartheta,\varphi)\sin\,\vartheta\,d\vartheta\,d\varphi,$$

$$W_0(\vartheta,\varphi)=\frac{1}{Z}\exp[\sigma\,\cos^2\,\vartheta+\xi(\gamma_1\,\cos\,\varphi\,\sin\,\vartheta$$

$$+\gamma_2\,\sin\,\varphi\,\sin\,\vartheta+\gamma_3\,\cos\,\vartheta)]$$

is the equilibrium distribution function, and Z is a normalization constant. The system (15) has been derived with allowance for the fact that the equilibrium averages $\langle X_{nm}\rangle_0$ satisfy the recursion formula

$$\left[2\sigma\frac{n(n+1)-3m^2}{(2n-1)(2n+1)}-n(n+1)\right]\langle X_{nm}\rangle_0$$
$$-\frac{2im\sigma}{\alpha}\left[\frac{n+m}{2n+1}\langle X_{n-1m}\rangle_0+\frac{n-m+1}{2n+1}\langle X_{n+1m}\rangle_0\right]$$
$$+2\sigma\left[\frac{(n+1)(n+m)(n+m-1)}{(2n-1)(2n+1)}\langle X_{n-2m}\rangle_0\right.$$
$$\left.-\frac{n(n-m+1)(n-m+2)}{(2n+1)(2n+3)}\langle X_{n+2m}\rangle_0\right]$$
$$+\xi\gamma_3\left[\frac{(n+1)(n+m)}{2n+1}\langle X_{n-1m}\rangle_0-i\alpha^{-1}m\langle X_{nm}\rangle_0\right.$$
$$\left.-\frac{n(n-m+1)}{2n+1}\langle X_{n+1m}\rangle_0\right]+\frac{\xi(\gamma_1+i\gamma_2)}{2(2n+1)}$$
$$\times[n(n-m+1)(n-m+2)\langle X_{n+1m-1}\rangle_0+i\alpha^{-1}$$
$$\times(2n+1)(n-m+1)(n+m)\langle X_{nm-1}\rangle_0+(n+1)$$
$$\times(n+m-1)(n+m)\langle X_{n-1m-1}\rangle_0]-\frac{\xi(\gamma_1-i\gamma_2)}{2(2n+1)}$$
$$\times[n\langle X_{n+1m+1}\rangle_0-i\alpha^{-1}(2n+1)\langle X_{nm+1}\rangle_0$$
$$+(n+1)\langle X_{n-1m+1}\rangle_0]=0. \tag{18}$$

The systems of equations (15) and (18) can also be derived from the corresponding Fokker–Planck equation[2]*x*

$$2\tau_N\frac{\partial W}{\tau}=\frac{1}{\sin\vartheta}\frac{\partial}{\partial\vartheta}\left\{\sin\vartheta\left[\frac{\nu}{kT}\left(\frac{\partial V}{\partial\vartheta}-\frac{1}{\alpha\sin\vartheta}\frac{\partial V}{\partial\phi}\right)\right.\right.$$
$$\left.\left.\times W+\frac{\partial W}{\partial\vartheta}\right]\right\}+\frac{1}{\sin\vartheta}\frac{\partial}{\partial\phi}\left[\frac{\nu}{kT}\left(\frac{1}{\alpha}\frac{\partial V}{\partial\vartheta}\right.\right.$$
$$\left.\left.+\frac{1}{\sin\vartheta}\frac{\partial V}{\partial\phi}\right)W+\frac{1}{\sin\vartheta}\frac{\partial W}{\partial\phi}\right]. \tag{19}$$

According to linear response theory,[29] the decay of the magnetization $\langle\mathbf{M}\rangle(t)$ of a system of noninteracting, single-domain ferromagnetic particles after the instantaneous application at time $t=0$ of a weak static external field $\mathbf{H}_1$ parallel to $\mathbf{H}_0$ [$\nu(\mathbf{M}\cdot\mathbf{H}_1)/kT\ll 1$ and $\mathbf{H}_0\|\mathbf{H}_1$] has the form

$$\langle M_\|\rangle(t)-\langle M_\|\rangle_0=\chi_\| H_1 C_\|(t),$$

where $C_\|(t)$ is the normalized relaxation function of the longitudinal component of the magnetization, and $\chi_\|$ is the static magnetic susceptibility. The longitudinal normalized relaxation function $C_\|(t)$ and the magnetic susceptibility $\chi_\|(\omega)$ are expressed in terms of $c_{nm}(t)$:

$$C_\|(t)=\frac{\gamma_3 c_{1,0}(t)+\mathrm{Re}\{(\gamma_1-i\gamma_2)c_{1,1}(t)\}}{\gamma_3 c_{1,0}(0)+\mathrm{Re}\{(\gamma_1-i\gamma_2)c_{1,1}(0)\}}, \tag{20}$$

$$\chi_\|(\omega)=\chi'_\|(\omega)-i\chi''_\|(\omega)=\chi_\|\{1-i\omega\tilde{C}_\|(i\omega)\}, \tag{21}$$

where

$$\tilde{C}_\|(i\omega)=\int_0^\infty C_\|(t)e^{-i\omega t}dt, \tag{22}$$

$$\chi_\|=\frac{\nu M_s N_0}{H_1}(\gamma_3 c_{1,0}(0)+\mathrm{Re}\{(\gamma_1-i\gamma_2)c_{1,1}(0)\})$$

is the static susceptibility, and N_0 is the number of particles per unit volume. Moreover, the relaxation time $\tau_\|$, defined as the area under the $C_\|(t)$ curve:

$$\tau_\|=\int_0^\infty C_\|(t)dt=\tilde{C}_\|(0), \tag{23}$$

can be measured in experiments and calculated from Eqs. (20) and (22).

Equations (21) and (23) are valid for a system of particles with their easy axes oriented at the same angle relative to the direction of the static magnetic field $\mathbf{H}_0$. If the easy axes of the particles are randomly distributed in space, Eqs. (21) and (23) must be averaged over the angles Ψ and Φ to calculate the dynamic susceptibility and the relaxation time.

3. A formal approach to the solution of recursion formulas of the type (15) with two variable indices has been proposed earlier.[29] However, it is very difficult to implement this approach in practice, because it is necessary [as in the basic equation (2)] to work with infinite-dimensional matrices. We now propose a refined method for the solution of Eq. (15), where the analytical problem can be reduced to operations involving finite-dimensional matrices.

We introduce the $8n$-element vector $C_n(t)$:

$$\mathbf{C}_n(t)=\begin{pmatrix} c_{2n,-2n}(t)\\ c_{2n,-2n+1}(t)\\ \vdots\\ c_{2n,2n}(t)\\ c_{2n-1,-2n+1}(t)\\ c_{2n-1,-2n+2}(t)\\ \vdots\\ c_{2n-1,2n-1}(t)\end{pmatrix}. \tag{24}$$

Equation (15) can then be transformed to a three-term matrix difference-differential equation of the form

$$\tau_N\frac{d}{dt}C_n(t)=Q_n^- C_{n-1}(t)+Q_n C_n(t)$$
$$+Q_n^+ C_{n+1}(t),\quad n=1,2,3,\ldots. \tag{25}$$

The matrices in this equation are defined as follows:

$$Q_n=\begin{pmatrix} X_{2n} & W_{2n}\\ Y_{2n-1} & X_{2n-1}\end{pmatrix},$$
$$Q_n^+=\begin{pmatrix} Z_{2n} & Y_{2n}\\ 0 & Z_{2n-1}\end{pmatrix},\quad Q_n^-=\begin{pmatrix} V_{2n} & 0\\ W_{2n-1} & V_{2n-1}\end{pmatrix}, \tag{26}$$

where

$$Q_1^-=\begin{pmatrix} V_2\\ W_1\end{pmatrix},\quad C_0(t)=0. \tag{27}$$

The matrices Q_n, Q_n^+, and Q_n^- have $8n\times 8n$, $8n\times 8(n+1)$, and $8n\times 8(n-1)$ dimensions, respectively. In turn, the matrices Q_n, Q_n^+, and Q_n^- consist of submatrices X_l, Y_l, Z_l, V_l, and W_l, which are given in the Appendix.

Invoking the general method for solving matrix recursion formulas of the type (25) (Ref. 28), we obtain an exact solution for the Laplace transform $\tilde{C}_1(s)$ in terms of matrix continuous fractions:

$$\tilde{C}_1(s)=\tau_N[\tau_N sI-Q_1-Q_1^+S_2(s)]^{-1}\times\left\{C_1(0)+\sum_{n=2}^{\infty}\left(\prod_{k=2}^{n}Q_{k-1}^+[\tau_N sI-Q_k-Q_k^+S_{k+1}(s)]^{-1}\right)C_n(0)\right\}, \tag{28}$$

where I is the unit matrix, and

$$S_n(s)=[\tau_N sI-Q_n-Q_n^+S_{n+1}(s)]^{-1}Q_n^- \tag{29}$$

is a matrix continuous fraction.

The vectors of initial conditions $C_n(0)$ can also be calculated with the aid of continuous fractions by Risken's method;[29] specifically, in the linear (with respect to the field $\mathbf{H}_1$) approximation the initial conditions $c_{n,m}(0)$ have the form

$$\begin{aligned}c_{n,m}(0)&=-\langle X_{nm}\rangle_0+\int_0^{2\pi}\int_0^{\pi}X_{nm}(\vartheta,\varphi)W_0(\vartheta,\varphi)\times e^{\xi_1(\gamma_1\cos\varphi\sin\vartheta+\gamma_2\sin\varphi\sin\vartheta+\gamma_3\cos\vartheta)}\sin\vartheta d\vartheta d\varphi\\&\times\left(\int_0^{2\pi}\int_0^{\pi}W_0(\vartheta,\varphi)\times e^{\xi_1(\gamma_1\cos\varphi\sin\vartheta+\gamma_2\sin\varphi\sin\vartheta+\gamma_3\cos\vartheta)}\times\sin\vartheta d\vartheta d\varphi\right)^{-1}\\&\approx\xi_1\left\{\frac{\gamma_1+i\gamma_2}{2(2n+1)}[(n+m)(n+m-1)\langle X_{n-1m-1}\rangle_0-(n-m+2)(n-m+1)\langle X_{n+1m-1}\rangle_0]\right.\\&+\frac{\gamma_1-i\gamma_2}{2(2n+1)}[\langle X_{n+1m+1}\rangle_0-\langle X_{n-1m+1}\rangle_0]\\&+\frac{\gamma_3}{2n+1}[(n+m)\langle X_{n-1m}\rangle_0+(n-m+1)\times\langle X_{n+1m}\rangle_0]-\langle X_{nm}\rangle_0[\gamma_3\langle X_{10}\rangle_0+\mathrm{Re}\{(\gamma_1-i\gamma_2)\\&\left.\times\langle X_{11}\rangle_0\}]\right\},\end{aligned} \tag{30}$$

where

$$\xi_1=\frac{\nu M_s H_1}{kT}. \tag{31}$$

Next we transform Eq. (18) to the matrix recursion formula

$$Q_n^-R_{n-1}+Q_nR_n+Q_n^+R_{n+1}=0,\quad n=1,2,3,..., \tag{32}$$

where

$$R_n=\begin{pmatrix}\langle X_{2n,-2n}\rangle_0\\ \langle X_{2n,-2n+1}\rangle_0\\ \vdots\\ \langle X_{2n,2n}\rangle_0\\ \langle X_{2n-1,-2n+1}\rangle_0\\ \langle X_{2n-1,-2n+2}\rangle_0\\ \vdots\\ \langle X_{2n-1,2n-1}\rangle_0\end{pmatrix}. \tag{33}$$

The solution of Eq. (32) has the form

$$R_n=S_n(0)R_{n-1}=S_n(0)S_{n-1}(0)\ldots S_2(0)S_1(0), \tag{34}$$

where

$$S_n(0)=[-Q_n-Q_n^+S_{n+1}(0)]^{-1}Q_n^-. \tag{35}$$

With Eqs. (30) and (34) taken into account, the initial conditions $C_n(0)$ have the form

$$C_n(0)=\xi_1[K_n^-+[K_n+K_n^+S_{n+1}(0)]\times S_n(0)]S_{n-1}(0)\ldots S_1(0),\quad n=1,2,3..., \tag{36}$$

where

$$C_1(0)=\xi_1\{K_1^-+[K_1+K_1^+S_2(0)]S_1(0)\}. \tag{37}$$

Here the matrices K_n, K_n^+, and K_n^- are defined as follows:

$$K_n=\begin{pmatrix}F_{2n} & D_{2n}\\ G_{2n-1} & F_{2n-1}\end{pmatrix},\quad K_n^+=\begin{pmatrix}0 & G_{2n}\\ 0 & 0\end{pmatrix},\quad K_n^-=\begin{pmatrix}0 & 0\\ D_{2n-1} & 0\end{pmatrix}, \tag{38}$$

where

$$K_1^-=\begin{pmatrix}0\\ D_1\end{pmatrix}.$$

The matrices K_n, K_n^+, and K_n^- consist of submatrices F_n, D_n, and G_n, which are given in the Appendix.

The exact solution in terms of matrix continuous fractions [see (28)] is well suited to numerical calculations. All the matrix continuous fractions and the series converge very rapidly, so that 10–12 ''downward'' iterations for the computation of these matrix fractions and 11–14 terms in the series (28) are sufficient for attaining accuracy to at least six significant figures in most cases. Here the maximum number of dimensions of all the matrices required for the calculations is of the order of 10^2, which falls within the capabilities of an ordinary personal computer.

4. The behavior of the relaxation time $\tau_\parallel$ as a function of the angle Ψ for $\Phi=0$, $\sigma=10$, $\alpha=100$ (strong damping), and various values of the parameter $h=\xi/2\sigma$ is shown in Fig. 1. It is evident from Fig. 1 that $\tau_\parallel$ has a deep minimum at $\Psi=\pi\|2$ (the curve is symmetrical about this line), because the alternating field $\mathbf{H}_1$ is perpendicular to the easy axis of the particle, corresponding to the condition for the observation of ferromagnetic resonance, which is determined by the transverse component of the dynamic susceptibility of the particle. Accordingly, the low-frequency (activation) mode associated with reorientation of the magnetization through

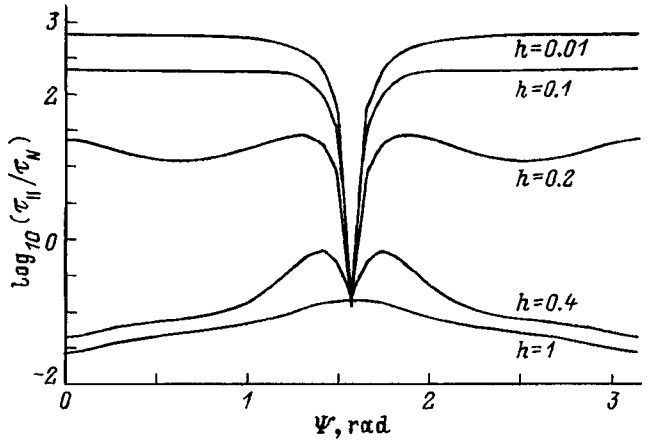

FIG. 1. $\log_{10}(\tau_{\|}/\tau_N)$ as a function of the angle Ψ for $\sigma=10$, $\alpha=100$, and various values of the parameter $h=\xi/2\sigma$.

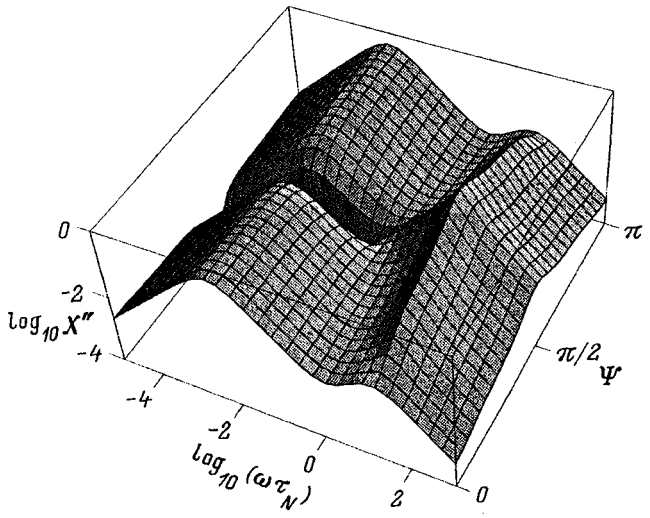

FIG. 3. $\log_{10}(\chi_{\|}'')$ as a function of $\log_{10}(\omega\tau_N)$ and the angle Ψ for $h=0.1$ and $\alpha=0.5$.

the potential barrier does not contribute to the relaxation time. As the strength of the static magnetic field $\mathbf{H}_0$ is increased, the activation process is more and more suppressed, and this process also tends to diminish the contribution of the low-frequency relaxation mode to $\tau_{\|}$. These effects are most conspicuous in the spectra of the imaginary part of the susceptibility, $\chi_{\|}''(\omega)$, which are shown in Figs. 2–4 (the calculations have been carried out for $\chi_{\|}=1$ and $\Phi=0$). In these figures two peaks are seen in the loss spectrum. The first (low-frequency) peak appears at frequencies of the order of the average frequency of reorientation of the susceptibility through the potential barrier. The characteristic frequency of this low-frequency mode is determined by the reciprocal of the lowest eigenvalue λ_1 of the Fokker–Planck equation (19). For $\Psi\approx 0$ and $\sigma\gg 1$ this quantity is given by the equation[2]

$$\lambda_1=\frac{2\tau_N\sigma^{3/2}e^{-\sigma-\xi^2/4\sigma^2}}{\pi^{1/2}}\left[1-\frac{\xi^2}{4\sigma^2}\right]\left(\cosh\,\xi-\frac{\xi}{2\sigma}\sinh\,\xi\right). \tag{39}$$

The second peak is attributable to the contribution of high-frequency modes and for ξ, $\sigma\gg 1$ occurs at a frequency $\approx(2\sigma+\xi)/\tau_N$ (Ref. 21). A ferromagnetic resonance peak is distinctly visible at $\Psi\approx\pi/2$ in Figs. 2 and 3. The relaxation behavior of the spectra $\chi_{\|}''(\omega)$ is observed for small anisotropy parameters and a weak field (ξ, $\sigma\approx 0$) or large damping. It is evident from Figs. 2–4 that the spectra depend strongly on the damping parameter α. Methods for obtaining experimental and theoretical estimates of α are discussed, for example, in Refs. 12, 17, and 32, but there do not appear to be any reliable experimental data. Theoretical estimates of α give values of the order of 0.01–0.1 (Refs. 12 and 32). Figure 4 also graphically illustrates the suppression of the low-frequency mode by the static field. This effect, first reported in Ref. 15, is attributable to depletion of the population of the upper potential well[21] and, especially, for values of the parameter h above a certain critical level ($\approx$0.166 for $\Psi\approx 0$; Ref. 21), it induces non-Arrhenius behavior on the

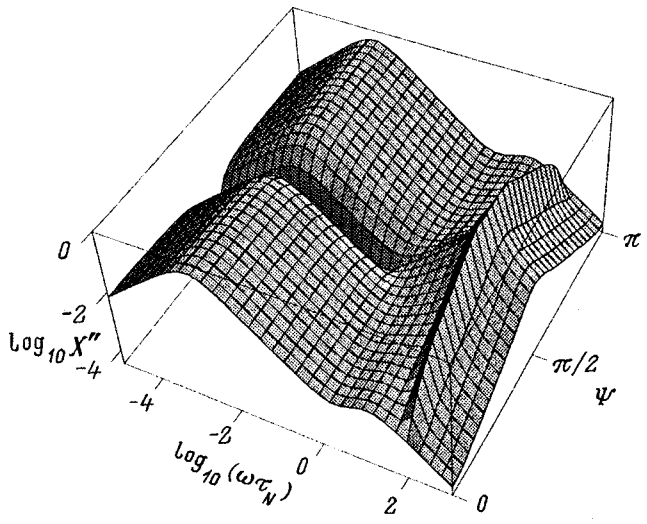

FIG. 2. $\log_{10}(\chi_{\|}'')$ as a function of $\log_{10}(\omega\tau_N)$ and the angle Ψ for $h=0.01$ and $\alpha=0.1$.

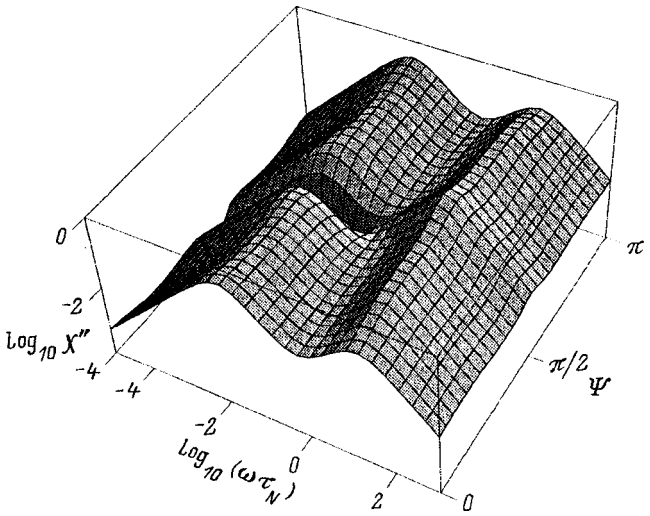

FIG. 4. $\log_{10}(\chi_{\|}'')$ as a function of $\log_{10}(\omega\tau_N)$ and the angle Ψ for $h=0.17$ and $\alpha=1$.

part of the relaxation time $\tau_{\|}$, i.e., it violates exponential growth of the relaxation time $\tau_{\|}$ as the height of the potential barrier increases.

Thus, the longitudinal component of the magnetic susceptibility of a system of noninteracting, single-domain particles can be estimated from the exact equation (28). In obtaining these results, we have assumed that all the particles are identical. To take polydispersity of the particles into account, it is also necessary to average the susceptibility over appropriate distribution functions (e.g., over the particle volumes).

This work has received support from the Russian Fund for Fundamental Research (Grant 96-02-16762-a).

APPENDIX

The submatrices X_l, Y_l, Z_l, V_l, and W_l have the form

$$X_l\left[(2l+1)\times(2l+1)\right] = \begin{pmatrix} x_{l,-l} & x^{+}_{l,-l} & 0 & \dots & 0 & 0 \\ x^{-}_{l,-l+1} & x_{l,-l+1} & x^{+}_{l,-l+1} & \dots & 0 & 0 \\ 0 & x_{l,-l+2} & x_{l,-l+2} & \dots & 0 & 0 \\ \vdots & \vdots & \vdots & & \vdots & \vdots \\ 0 & 0 & 0 & \dots & x_{l,l-1} & x^{+}_{l,l-1} \\ 0 & 0 & 0 & \dots & x^{-}_{l,l} & x_{l,l} \end{pmatrix}, \tag{A1}$$

$$Y_l\left[(2l+1)\times(2l+3)\right] = \begin{pmatrix} y^{-}_{l,-l} & y_{l,-l} & y^{+}_{l,-l} & \dots & 0 & 0 & 0 \\ 0 & y^{-}_{l,-l+1} & y_{l,-l+1} & \dots & 0 & 0 & 0 \\ 0 & 0 & y^{-}_{l,-l+2} & \dots & 0 & 0 & 0 \\ \vdots & \vdots & \vdots & & \vdots & \vdots & \vdots \\ 0 & 0 & 0 & \dots & y_{l,l-1} & y^{+}_{l,l-1} & 0 \\ 0 & 0 & 0 & \dots & y^{-}_{l,l} & y_{l,l} & y^{+}_{l,l} \end{pmatrix}, \tag{A2}$$

$$W_l\left[(2l+1)\times(2l-1)\right] = \begin{pmatrix} w^{+}_{l,-l} & 0 & 0 & \dots & 0 & 0 \\ w_{l,-l+1} & w^{+}_{l,-l+1} & 0 & \dots & 0 & 0 \\ w^{-}_{l,-l+2} & w_{l,-l+2} & w^{+}_{l,-l+2} & \dots & 0 & 0 \\ \vdots & \vdots & \vdots & & \vdots & \vdots \\ 0 & 0 & 0 & \dots & w_{l,l-2} & w^{+}_{l,l-2} \\ 0 & 0 & 0 & \dots & w^{-}_{l,l-1} & w_{l,l-1} \\ 0 & 0 & 0 & \dots & 0 & w^{-}_{l,l} \end{pmatrix}, \tag{A3}$$

$$Z_l\left[(2l+1)\times(2l+5)\right] = \begin{pmatrix} 0 & 0 & z_{l,-l} & 0 & \dots & 0 & 0 & 0 & 0 \\ 0 & 0 & 0 & z_{l,-l+1} & \dots & 0 & 0 & 0 & 0 \\ \vdots & \vdots & \vdots & \vdots & & \vdots & \vdots & \vdots & \vdots \\ 0 & 0 & 0 & 0 & \dots & z_{l,l-1} & 0 & 0 & 0 \\ 0 & 0 & 0 & 0 & \dots & 0 & z_{l,l} & 0 & 0 \end{pmatrix}, \tag{A4}$$

$$V_l\left[(2l+1)\times(2l-3)\right] = \begin{pmatrix} 0 & 0 & \dots & 0 & 0 \\ 0 & 0 & \dots & 0 & 0 \\ v_{l,-l+2} & 0 & \dots & 0 & 0 \\ 0 & v_{l,-l+1} & \dots & 0 & 0 \\ \vdots & \vdots & & \vdots & \vdots \\ 0 & 0 & \dots & v_{l,l-1} & 0 \\ 0 & 0 & \dots & 0 & v_{l,l-2} \\ 0 & 0 & \dots & 0 & 0 \\ 0 & 0 & \dots & 0 & 0 \end{pmatrix}, \quad l=2,3,\dots. \tag{A5}$$

The dimensions of the submatrices are indicated in brackets. The elements of the submatrices X_l, Y_l, Z_l, V_l, and W_l are given by the expressions

$$x^{-}_{l,m} = i\,\frac{\xi(\gamma_1+i\gamma_2)(l+m)(l-m+1)}{4\alpha},$$

$$x_{l,m} = \frac{\sigma(l(l+1)-3m^2)}{(2l-1)(2l+3)} - \frac{l(l+1)}{2} - i\,\frac{m\xi\gamma_3}{2\alpha},$$

$$x^{+}_{l,m} = i\,\frac{\xi}{4\alpha}\,(\gamma_1-i\gamma_2),$$

$$y^{-}_{l,m} = \frac{l\xi(\gamma_1+i\gamma_2)(l-m+1)(l-m+2)}{4(2l+1)},$$

$$y_{l,m} = -\,\frac{l-m+1}{2(2l+1)}\left(l\xi\gamma_3 + i\,\frac{2\sigma m}{\alpha}\right),$$

$$y^{+}_{l,m} = -\,\frac{l\xi}{4(2l+1)}\,(\gamma_1-i\gamma_2),$$

$$w^{-}_{l,m} = \frac{\xi(l+1)(\gamma_1+i\gamma_2)(l+m)(l+m-1)}{4(2l+1)},$$

$$w_{l,m} = \frac{l+m}{2(2l+1)}\left(\xi\gamma_3(l+1) - i\,\frac{2\sigma m}{\alpha}\right),$$

$$w^{+}_{l,m} = -\,\frac{\xi(l+1)}{4(2l+1)}\,(\gamma_1-i\gamma_2),$$

$$z_{l,m} = -\,\frac{\sigma l(l-m+2)(l-m+1)}{(2l+1)(2l+3)},$$

$$v_{l,m} = \frac{\sigma(l+1)(l+m)(l+m-1)}{(2l-1)(2l+1)}.$$

The submatrices F_n, D_n, and G_n in Eqs. (38) have the form

$$F_l[(2l+1)\times(2l+1)]$$
$$= -\mathrm{Re}[\gamma_3\langle X_{1,0}\rangle_0 + (\gamma_1 - i\gamma_2)\langle X_{1,1}\rangle_0]I, \quad \text{(A6)}$$

$$\boldsymbol{G}_l[(2l+1)\times(2l+3)]$$
$$= \begin{pmatrix} g^-_{l,-l} & g_{l,-l} & g^+_{l,-l} & 0 & \dots & 0 & 0 & 0 \\ 0 & g^-_{l,-l+1} & g_{l,-l+1} & g^+_{l,-l+1} & \dots & 0 & 0 & 0 \\ 0 & 0 & g^-_{l,-l+2} & g_{l,-l+2} & \dots & 0 & 0 & 0 \\ 0 & 0 & 0 & g^-_{l,-l+3} & \dots & 0 & 0 & 0 \\ \vdots & \vdots & \vdots & \vdots & & \vdots & \vdots & \vdots \\ 0 & 0 & 0 & 0 & \dots & g_{l,l-1} & g^+_{l,l-1} & 0 \\ 0 & 0 & 0 & 0 & \dots & g^-_{l,l} & g_{l,l} & g^+_{l,l} \end{pmatrix}, \quad \text{(A7)}$$

$$\boldsymbol{D}_l[(2l+1)\times(2l-1)]$$
$$= \begin{pmatrix} d^+_{l,-l} & 0 & 0 & 0 & \dots & 0 & 0 \\ d_{l,-l+1} & d^+_{l,-l+1} & 0 & 0 & \dots & 0 & 0 \\ d^-_{l,-l+2} & d_{l,-l+2} & d^+_{l,-l+2} & 0 & \dots & 0 & 0 \\ 0 & d^-_{l,-l+3} & d_{l,-l+3} & d^+_{l,-l+3} & \dots & 0 & 0 \\ \vdots & \vdots & \vdots & \vdots & & \vdots & \vdots \\ 0 & 0 & 0 & 0 & \dots & d_{l,l-2} & d^+_{l,l-2} \\ 0 & 0 & 0 & 0 & \dots & d^-_{l,l-1} & d_{l,l-1} \\ 0 & 0 & 0 & 0 & \dots & 0 & d^-_{l,l} \end{pmatrix}, \quad \text{(A8)}$$

where the elements of the submatrices are given by the expressions

$$g_{l,m} = \frac{\gamma_3(l-m+1)}{2l+1},$$

$$g^-_{l,m} = -\frac{(\gamma_1+i\gamma_2)(l-m+2)(l-m+1)}{2(2l+1)},$$

$$g^+_{l,m} = -d^+_{l,m} = \frac{(\gamma_1-i\gamma_2)}{2(2l+1)}, \quad d_{l,m} = \frac{\gamma_3(l+m)}{2l+1},$$

$$d^-_{l,m} = \frac{(\gamma_1+i\gamma_2)(l+m)(l+m-1)}{2(2l+1)}.$$

[1] L. Néel, Ann. Geophys. (C.N.R.S.) **5**, 99 (1949).
[2] W. F. Brown, Jr., IEEE Trans. Magn. **15**, 1196 (1979).
[3] H. B. Braun and H. N. Bertram, J. Appl. Phys. **75**, 4609 (1994).
[4] C. P. Bean and J. D. Livingston, J. Appl. Phys. **30**, 1205 (1959).
[5] L. D. Landau and E. M. Lifshitz, Phys. Z. Sowjetunion **8**, 153 (1935).
[6] T. L. Gilbert, Phys. Rev. **100**, 1243 (1956) [Abstract only; full report, Armour Research Foundation Project, A059, Supplementary Report, May 1, 1956].
[7] W. F. Brown, Jr., Phys. Rev. **130**, 1677 (1963); J. Appl. Phys. **30**, 130S (1959).
[8] M. C. Wang and G. E. Uhlenbeck, Rev. Mod. Phys. **17**, 323 (1945).
[9] R. L. Stratonovich, *Conditional Markov Processes and Their Application to the Theory of Optimal Control* (Elsevier, New York, 1968).
[10] A. Aharoni, Phys. Rev. **177**, 763 (1969).
[11] E. C. Stoner and E. P. Wohlfahrt, Philos. Trans. R. Soc. London, Ser. A **240**, 599 (1948).
[12] Yu. L. Raĭkher and M. I. Shliomis, Zh. Éksp. Teor. Fiz. **67**, 1060 (1974) [Sov. Phys. JETP **40**, 526 (1975)].
[13] R. S. Gekht, V. A. Ignatchenko, Yu. L. Raĭkher, and M. I. Shliomis, Zh. Éksp. Teor. Fiz. **70**, 1300 (1974) [Sov. Phys. JETP **43**, 677 (1974)].
[14] D. A. Garanin, V. V. Ishchenko, and L. V. Panina, Teor. Mat. Fiz. **82**, 242 (1990).
[15] W. T. Coffey, D. S. F. Crothers, Yu. P. Kalmykov, and J. T. Waldron, Phys. Rev. B **51**, 15 947 (1995).
[16] W. T. Coffey, P. J. Cregg, and Yu. P. Kalmykov, in *Advances in Chemical Physics*, Vol. 83, edited by I. Prigogine and S. A. Rice (Wiley, New York, 1994), pp. 263–464.
[17] Yu. L. Raikher and M. I. Shliomis, in *Advances in Chemical Physics*, Vol. 87, edited by W. T. Coffey; series edited by I. Prigogine and S. A. Rice (Wiley, New York, 1994), p. 595.
[18] Yu. L. Raĭkher and V. I. Stepanov, Zh. Éksp. Teor. Fiz. **102**, 1409 (1992) [Sov. Phys. JETP **75**, 764 (1992)].
[19] M. I. Shliomis and V. I. Stepanov, in *Advances in Chemical Physics*, Vol. 87, edited by W. T. Coffey; series edited by I. Prigogine and S. A. Rice (Wiley, New York, 1994), p. 1.
[20] É. K. Sadykov and A. G. Isavnin, Fiz. Tverd. Tela (St. Petersburg) **38**, 2104 (1996) [Phys. Solid State **38**, 1160 (1996)].
[21] D. A. Garanin, Phys. Rev. E **54**, 3250 (1996).
[22] Yu. P. Kalmykov and W. T. Coffey, Phys. Rev. B **56**, 3325 (1997).
[23] H. Pfeiffer, Phys. Status Solidi B **118**, 295 (1990).
[24] H. Pfeiffer, Phys. Status Solidi B **122**, 377 (1990).
[25] W. T. Coffey, D. S. F. Crothers, J. L. Dorman, L. J. Geoghegan, Yu. P. Kalmykov, J. T. Waldron, and W. W. Wickstead, Phys. Rev. B **52**, 15 951 (1995).
[26] W. T. Coffey, D. S. F. Crothers, J. L. Dorman, L. J. Geoghegan, and E. C. Kennedy, Phys. Rev. B (in press).
[27] Yu. P. Kalmykov, J. Mol. Liq. **69**, 117 (1996).
[28] W. T. Coffey, Yu. P. Kalmykov, and J. T. Waldron, *The Langevin Equation* (World Scientific, Singapore, 1996).
[29] H. Risken, *The Fokker-Planck Equation* (Springer-Verlag, Berlin, 1989).
[30] W. T. Coffey, J.-L. Déjardin, Yu. P. Kalmykov, and S. V. Titov, Phys. Rev. E **54**, 6462 (1996).
[31] J.-L. Déjardin, P.-M. Déjardin, and Yu. P. Kalmykov, J. Chem. Phys. **107**, 508 (1997).
[32] I. Klik and L. Gunther, J. Stat. Phys. **60**, 473 (1990).

Translated by James S. Wood

Temperature evolution of frustrated spin states in the system with competing exchange interactions $(Fe_{0.65}Ni_{0.35})_{1-x}Mn_x$ ($x=0$, 0.024, 0.034)

N. N. Delyagin, A. L. Erzinkyan, V. P. Parfenova, and S. I. Reĭman

Scientific-Research Institute of Nuclear Physics at M. V. Lomonosov Moscow State University, 119899 Moscow, Russia

G. M. Gurevich

Institute of Nuclear Research, Russian Academy of Sciences, Moscow, Russia

Ya. Dupak

Institute of Scientific Instruments, Czech Academy of Science, Brno, Czech Republic

(Submitted January 16, 1998)
Fiz. Tverd. Tela (St. Petersburg) **40**, 1650–1655 (September 1998)

The influence of temperature on the distribution function $P(B_{hf})$ of the magnetic hyperfine fields for ^{57}Fe in $(Fe_{0.65}Ni_{0.35})_{1-x}Mn_x$ alloys ($x=0$, 0.024, 0.034) are investigated by Mössbauer spectroscopy. The Mössbauer absorption spectra are measured in the temperature interval 5–300 K; in the interval 5–80 K the measurements are performed in a magnetic field of 0.2 T. Anomalies are found in the temperature curves of the intensity of the principal maximum of the functions $P(B_{hf})[B_{hf}=30-38\ \mathrm{T}]$ and the total (integrated) intensities of the low-field components $[B_{hf}=(4-13)\ \mathrm{T}]$. The detected anomalies in the behavior of the total intensities are interpreted as resulting from a change in the balance of competing exchange interactions due to the thermal annihilation of antiferromagnetic Fe–Fe exchange interaction. The emergence of strong satellite lines in the interval $B_{hf}=20-29$ T in Mn-doped alloys is attributed to reorientation of the spins of Fe atoms under the influence of strong antiferromagnetic Mn–Fe exchange interaction. © *1998 American Institute of Physics.* [S1063-7834(98)01809-7]

Iron-nickel Invar alloys having a face-centered cubic structure are an example of magnetic systems with competing exchange interactions. According to data obtained by neutron scattering,[1] Ni–Ni and Ni–Fe exchange interactions are ferromagnetic; their interaction constants are approximately equal to 600 K and 450 K. These interactions determine the ferromagnetic structure of the alloys as a whole and the nominal Curie temperatures. The Fe–Fe exchange interaction is antiferromagnetic, and the corresponding interaction constant is close to -100 K. Competing exchange interactions of opposite sign endow the effective exchange fields with a strong spatial inhomogeneity and create conditions for the onset of local instability of the ferromagnetic spin configurations. The probability of spin reorientation of the Fe atoms and spin frustration at sites having a weak resultant exchange field is very high in regions of high local iron concentration. Indications of the existence of perturbed spin configurations of these types have been obtained in experimental studies of the magnetic properties of Fe–Ni alloys (see, e.g., Refs. 2–8). The admixture of Mn in the alloy $Fe_{0.65}Ni_{0.35}$ lowers both the average magnetic moment and the Curie temperature, events that can be associated with an increase in the probability of the formation of perturbed spin configurations under the influence of antiferromagnetic Mn–Fe interaction. A detailed investigation of the dependence of the magnetic susceptibility of the system $(Fe_{0.65}Ni_{0.35})_{1-x}Mn_x$ on the temperature and the external magnetic field[9] has shown that spins having a sufficiently high manganese concentration at low temperatures goes over to the spin glass state.

Macroscopic investigations are capable of providing only indirect data on the spin configurations and the magnetic structure of the alloys. Deeper insight into the problem can be achieved by studying the spin states of Fe atoms at the microscopic level. Mössbauer spectroscopy is the only technique by which it is possible to implement such investigations of Fe–Ni–Mn alloys at various manganese concentrations and over a wide range of temperatures. This technique can be used to detect directly various types of perturbed spin configurations and to classify these states by analyzing the distribution functions of magnetic hyperfine fields $P(B_{hf})$.

In the present study Mössbauer spectroscopy is used to investigate magnetic hyperfine interaction for ^{57}Fe in $(Fe_{0.65}Ni_{0.35})_{1-x}Mn_x$ alloys ($x=0$, 0.024, 0.034). The principal objective is to obtain information about the states of Fe atoms under conditions when direct interaction between impurity Mn atoms is nonexistent or is weak, and transition to the spin-glass state is not observed. A significant consideration from the methodological standpoint is the fact that the satellite structure of the functions $P(B_{hf})$ at low manganese concentrations remains fairly well resolved, making it possible to observe small effects associated with the temperature dynamics of ''anomalous'' spin states. Special attention is

 © 1998 American Institute of Physics

given to the investigation of phenomena attributable to a difference in the temperature dependences of competing exchange interactions of opposite sign. Mössbauer spectroscopy has been used previously to investigate Fe–Ni–Mn alloys of various compositions (see Refs. 10–15, 17 and the references cited therein), but there has never been a detailed analysis of the functions $P(B_{hf})$ for $Fe_{0.65}Ni_{0.35}$ and for alloys having a small manganese impurity.

1. EXPERIMENTAL PROCEDURE

The investigated samples were prepared by alloying metals of 99.9% purity or better; the ingots were rolled into foil of thickness ≈ 10 μm and rapidly quenched. The Mössbauer absorption spectra were measured in the temperature range 5–300 K. In the interval 5–80 K, measurements were also performed in a magnetic field of 0.2 T applied in the plane of the foil. Resonance detectors were used to enhance the resonance absorption effect and the resolving power for the detection of 14.4-keV Mössbauer radiation.

The distribution functions of the magnetic hyperfine fields $P(B_{hf})$ were calculated from histograms; the details of the procedure used to process the spectra are given in Ref. 16. The widths of the histogram intervals were chosen to slightly exceed the width of instrumental distortion of the components of the initial magnetic sextets. This choice enabled us to use the direct method for minimization of the χ^2 functional (by means of the FUMILI minimization routine) and to eliminate uncertainties associated with the application of a smoothing procedure. In some cases, to analyze individual parts of the distribution functions $P(B_{hf})$, the range of B_{hf} was partitioned into intervals of unequal width. The procedure for minimizing the χ^2 functional had the following variable parameters: the components of the histogram of the function $P(B_{hf})$, the relative intensities of the second and fifth components of the magnetic sextets, the linewidths, and the isomeric shift. The average degree of alignment of the spins of the Fe Atoms in an external magnetic field was calculated by the standard technique from the relative intensities of the second and fifth components of the magnetic sextets. For the spectra measured without an external field these intensities corresponded to random orientation of the spins in the sample. Inasmuch as the parameters of weak satellite lines are determined with large errors, a procedure based on the examination of total (integrated) line intensities in selected intervals of variation of B_{hf}, rather than the intensities of individual satellites, was used in analyzing the temperature dependences of the components of the functions $P(B_{hf})$. This approach permitted statistically significant data to be obtained on the temperature dependences of the satellite intensities in the range of small values of B_{hf}, along with data on the interrelationship between these intensities and the intensity of the principal maximum of the functions $P(B_{hf})$ at various temperatures.

For all three alloys we observed in the distribution functions $P(B_{hf})$ a local maximum near the zeros of B_{hf} with approximately 3% relative intensity (Fig. 1). The position and intensity of this maximum were found to be independent of the temperature and the manganese concentration. In this light we can only assume that the onset of such a maximum is attributable, for example, to surface effects, rolling-induced defects, or other extraneous effects. We shall disregard this maximum in the discussion that follows.

2. DISTRIBUTION FUNCTIONS $P(B_{hf})$ AT 5 K

Figure 1 shows Mössbauer absorption spectra for $(Fe_{0.65}Ni_{0.35})_{1-x}Mn_x$ alloys ($x=0$, 0.024, 0.034), measured at a temperature of 5 K, and the corresponding distribution functions of the hyperfine fields $P(B_{hf})$. It is important to call attention to the strong variation in the profile of the function $P(B_{hf})$ in manganese-doped alloys, as manifested in the broadening and shift of the principal maximum of the distribution and the onset of satellites to the left of the principal maximum. The total intensities of lines situated away from the principal maximum for alloys with $x=0$, 0.024 and 0.034 are 8%, 28%, and 34%, respectively. On the other hand, the intensity increases only very slightly in the range of weak hyperfine fields. The influence of a small manganese impurity is also manifested in a decrease of the average magnetic hyperfine field $\langle B_{hf}\rangle$, which is equal to 32.6 ± 0.3 T, 28.9 ± 0.3 T, and 28.1 ± 0.3 T for $x=0$, 0.024, and 0.034, respectively. The average degrees of spin alignment of the Fe atoms at 5 K in an external magnetic field of 0.2 T are found to be 0.95 ± 0.3 T, 0.90 ± 0.3 T, and 0.85 ± 0.3 T for $x=0$, 0.024, and 0.034, respectively. These results evince a high degree of collinearity of the Fe spins, which is also preserved in manganese-doped alloys despite the emergence of strong satellite lines.

The distribution function $P(B_{hf})$ is relatively simple for the alloy $Fe_{0.65}Ni_{0.35}$ at 5 K. An intensity higher than 90% corresponds to the principal maximum, which is centered at $B_{hf}=34.5$ T. The profile of the principal maximum of the distribution $P(B_{hf})$ is interpreted on the assumption that the Fe and Ni atoms are randomly distributed among the lattice sites if the magnetic hyperfine field acting on the nucleus of an Fe atom in the given atomic configuration is described by the well-known equation

$$B_{hf}=a\mu_{Fe}+b[n_{Fe}\mu_{Fe}+(12-n_{Fe})\mu_{Ni}], \quad (1)$$

where μ_{Fe} and μ_{Ni} are the magnetic moments of the Fe and Ni ions, and n_{Fe} is the number of nearest-neighbor Fe atoms. The first term of this equation gives the contribution to B_{hf} from the intrinsic moment of the given atom, and the second term represents the total contribution to B_{hf} from nearest-neighbor atoms. The following values of the coefficients have been found for $\mu_{Fe}=2.5\mu_B$ and $\mu_{Ni}=0.6\mu_B$ by comparing the observed profile of the principal maximum with the profile calculated from Eq. (1) (taking into account the binomial distribution of the different atomic species in the nearest coordination sphere):

$$a=9.4\ \text{T}/\mu_B, \quad b=0.5\ \text{T}/\mu_B$$

(as seen in Fig. 1, the number of histogram intervals has been doubled in analyzing the profile of the principal maximum). The values obtained for the coefficients a and b are typical of ferromagnetic iron alloys (see, e.g., Ref. 12). The precise values of the atomic magnetic moments in Invar are un-

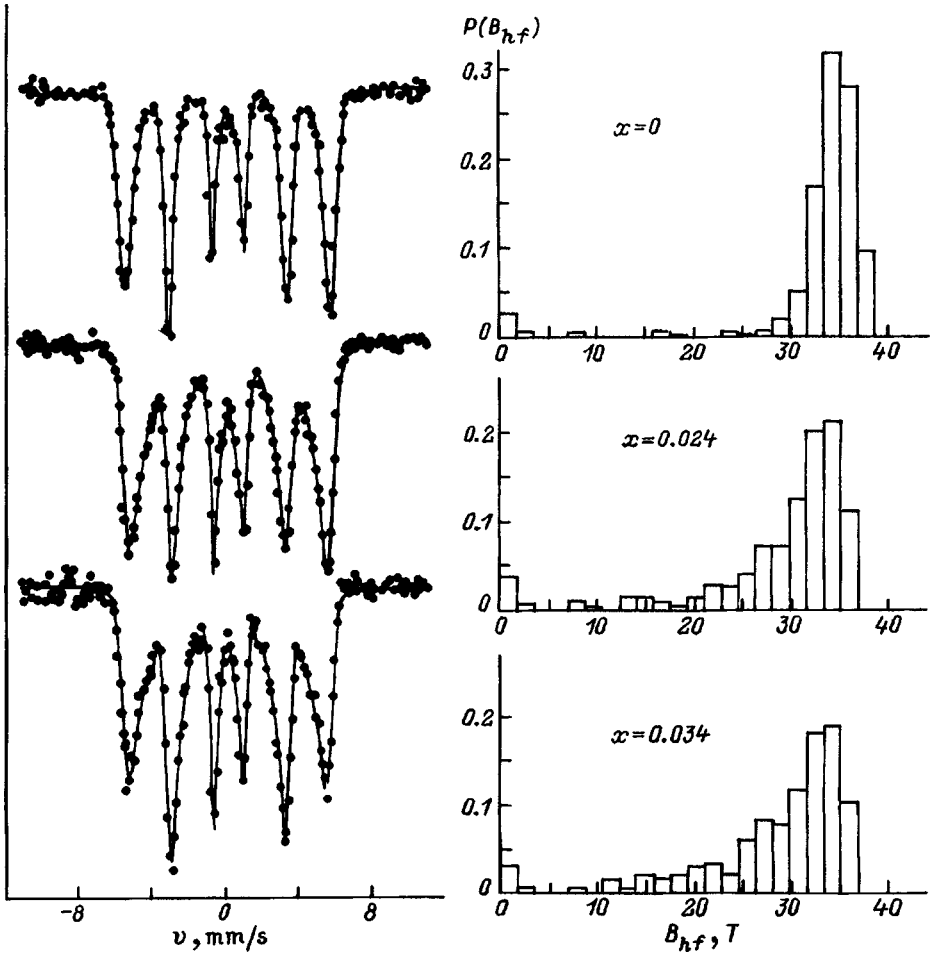

FIG. 1. Mössbauer absorption spectra measured at 5 K (left) and the corresponding distribution functions of the hyperfine fields $P(B_{\rm hf})$ (right) for alloys $(Fe_{0.65}Ni_{0.35})_{1-x}Mn_x$ ($x=0$, 0.024, 0.034). The solid curves in the graphs on the left have been calculated by the method indicated in the text.

known, but variations of $\mu_{\rm Fe}$ and $\mu_{\rm Ni}$ within the respective intervals $2.4-2.8\mu_{\rm B}$ and $0.6-0.9\mu_{\rm B}$ merely alter slightly the values of a and b, which is of minor consequence for subsequent analysis. The presence of weak satellite lines localized outside the principal maximum implies that the competing exchange interactions induce local disruptions of the ferromagnetic ordering as a result of spin reorientation. The maximum probability of the formation of perturbed spin configurations should be expected in regions having a high local iron concentration. According to the results of an analysis of the magnetic properties of the alloy $Fe_{0.65}Ni_{0.35}$ on the basis of the molecular-field model, spin reorientation and the formation of frustrated spin states take place in atomic configurations with $n_{\rm Fe}\geqslant 10$ (Ref. 2).

For the $x=0.024$ alloy at 5 K we observe two satellites with average hyperfine fields of 28 T and 22 T and intensities of 15% and 7%, respectively (Fig. 1). The onset of strong satellites with such values of $B_{\rm hf}$ implies a high probability that strong antiferromagnetic Mn–Fe interaction will induce spin reorientation of Fe atoms situated in the nearest-neighbor environment of a Mn impurity atom. In an fcc lattice every such Fe atom has four adjacent Fe atoms, which are also nearest neighbors of the Mn atom. This arrangement creates conditions for the formation of configurations in which spin reorientation occurs for several adjacent Fe atoms. According to Eq. (1), the field $B_{\rm hf}\approx 22$ T corresponds to configurations in which an Fe atom with reoriented spin has among its nearest neighbors two to four Fe atoms with like-oriented spins. The realignment of spins in the nearest-neighbor environment of the Mn atom can also influence the value of $B_{\rm hf}$ for Fe atoms that do not interact directly with Mn, but are nearest neighbors of atoms having an antiferromagnetic spin orientation. This scenario could explain the onset of a stronger satellite with average hyperfine field $B_{\rm hf}\approx 28$ T. The given estimates of $B_{\rm hf}$ have been obtained on the assumption that the perturbed spin configurations are collinear. This assumption is consistent with the observed high degree of spin alignment of the Fe atoms in an external field; however, in none of the alloys does the degree of alignment attain 100%. Not to be dismissed is the possibility of noncollinearity of the spins of Fe atoms in certain perturbed configurations, but any deviations from collinearity cannot be very large.

3. TEMPERATURE DEPENDENCE OF THE COMPETITION OF EXCHANGE INTERACTIONS IN $(Fe_{0.65}Ni_{0.35})_{1-x}Mn_x$ ALLOYS

Figure 2 shows the distribution functions $P(B_{\rm hf})$ for alloys with $x=0$ and 0.024 at various temperatures in the interval 60–220 K (because the data for alloys with $x=0.024$ and 0.034 are very similar, the results for the $x=0.034$ alloy will not be discussed below). Clearly, over a broad temperature range, the structure of the functions $P(B_{\rm hf})$ does not

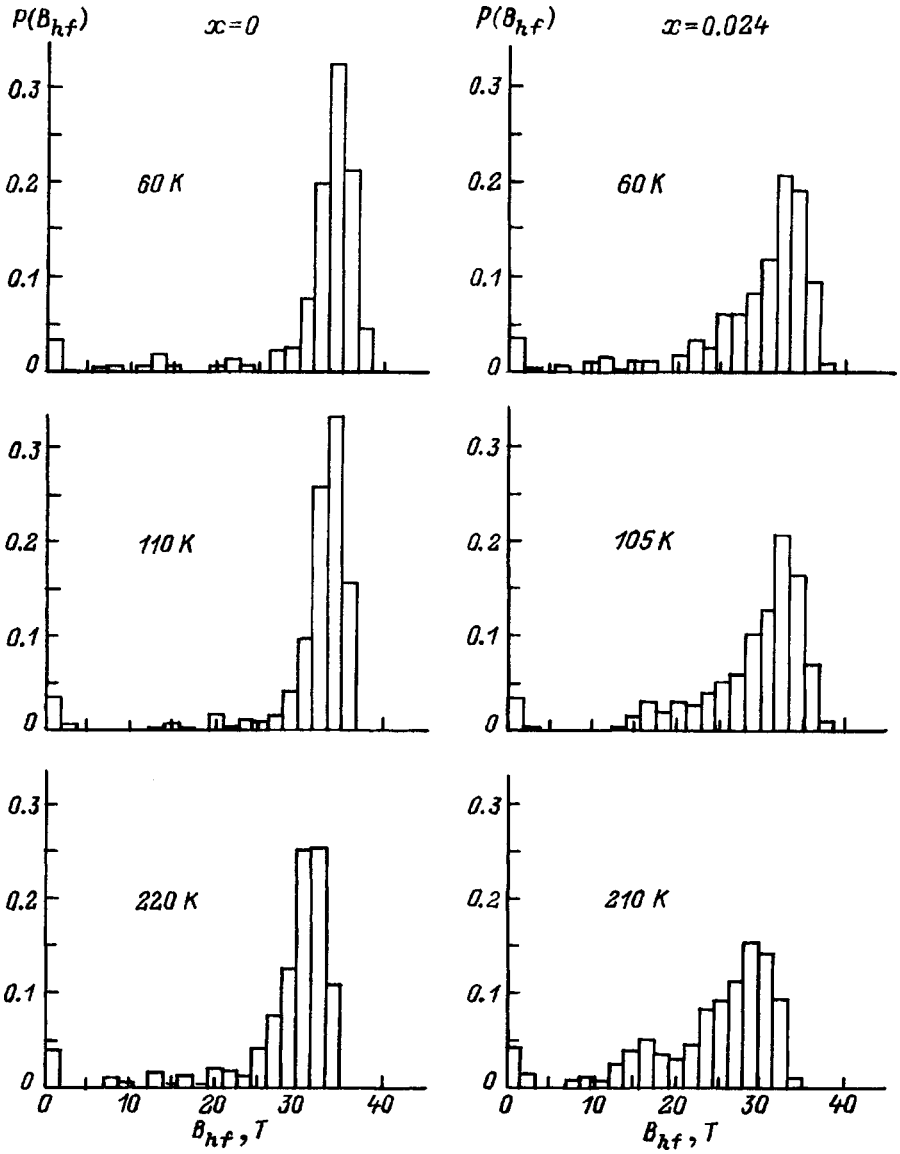

FIG. 2. Distribution of the hyperfine fields $P(B_{\rm hf})$ for $(Fe_{0.65}Ni_{0.35})_{1-x}Mn_x$ alloys ($x=0$ and 0.024) at various temperatures.

undergo any radical qualitative changes. Even at temperatures close to 200 K, only a slight increase in the intensity is observed in the range of weak hyperfine fields. This result is rather unexpected. A theoretical analysis of concentrated magnetic systems with competing exchange interactions (see, e.g., Ref. 17) predicts the onset of frustrated states having very weak exchange fields and the phenomenon of ''temperature melting'' of spins (i.e., the transition of spins into the paramagnetic state as the temperature increases). It is obvious that the spin-melting effect (which must be accompanied by an abrupt increase in the intensity in the vicinity of zeros of the hyperfine fields) is not observed in the given situation. It will be shown below that this behavior of our investigated alloys is attributable to the specific way in which temperature influences the competition of exchange interactions having opposite signs under conditions when the energy of one of these interactions is relatively low.

To observe effects associated with the formation and decay of frustrated states, we investigate the temperature curves of the total intensities of the components of the function $P(B_{\rm hf})$ in various intervals of $B_{\rm hf}$. Figure 3 shows the curves for two intervals: 30–38 T and 4–13 T. The first interval corresponds to the principal maximum of the distribution functions $P(B_{\rm hf})$. For the interval 4–13 T the total intensity at 5 K is very low, establishing favorable conditions for the reliable detection of possible intensity variations in the range of small values of $B_{\rm hf}$ as the temperature increases.

It is evident from Fig. 3 (upper graphs) that for both alloys the intensity of the principal maximum is observed to decrease rapidly (almost by a jump) in the temperature interval 50–70 K. When the temperature is further increased (to 130 K), the intensity of the principal maximum for the $x=0$ alloy remains essentially constant, while for the $x=0.024$ alloy it is even observed to increase somewhat. This behavior correlates with the temperature dependence of the total intensity in the interval $B_{\rm hf}=4-13$ T (Fig. 3, lower graphs). For the $x=0$ alloy at 50–70 K we observe a well-defined intensity maximum, and at 100–130 K the total intensity in this interval of $B_{\rm hf}$ decreases almost to zero. A similar (but flatter) maximum is also observed for the $x=0.024$ alloy.

These features of the temperature curves of the total in-

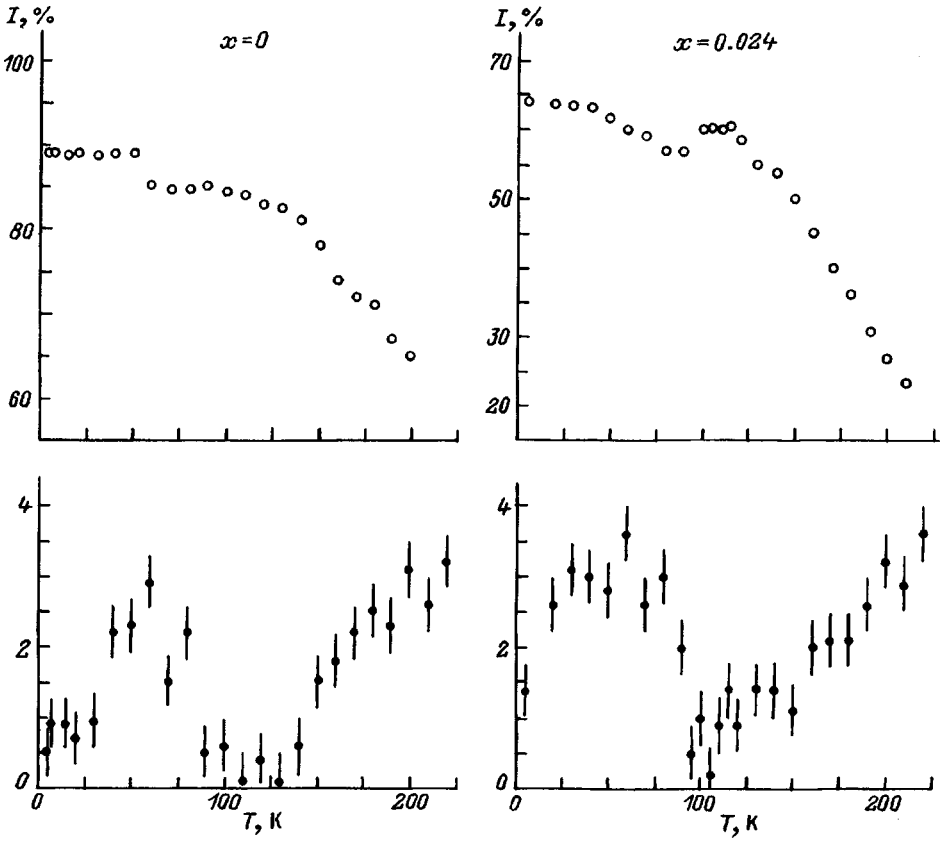

FIG. 3. Temperature curves of the total (integrated) intensities of the components of the functions $P(B_{hf})$ for $(Fe_{0.65}Ni_{0.35})_{1-x}Mn_x$ alloys with $x=0$ (left) and $x=0.024$ (right). The upper graphs refer to the vicinity of the principal maximum, $B_{hf}=(30-38)$ T, and the lower graphs to the interval $B_{hf}=(4-13)$ T.

tensities clearly indicate the existence of frustrated states with weak (but not zero) exchange fields and a very strong temperature dependence of B_{hf}. It was naturally expected that the value of B_{hf} for these states would continue to decrease with a further increase in the temperature (as observed, e.g., in the case of Fe atoms in AuFe spin glasses[16]). However, such was not the case; on the contrary, at $T>70$ K the values of B_{hf} are observed to return to the vicinity of the principal maximum (in the $x=0$ alloy this behavior cancels out the ''normal'' temperature decrease of the intensity while in the $x=0.024$ alloy it also causes the intensity of the principal maximum to increase somewhat). It follows from the latter result that the effective exchange field begins to increase at $T>(60-70)$K, and the states frustrated at low temperature are gradually transformed into states with a strong resultant exchange field.

The anomalous behavior of the frustrated states can be explained if one bears in mind the relatively low characteristic temperature of antiferromagnetic Fe–Fe exchange interaction. At low temperatures, where all exchange interactions are close to saturation, the contribution of Fe–Fe interaction to the resultant exchange fields is substantial, creating conditions conducive to the formation of Fe sites having a very weak exchange field. The contribution of Fe–Fe interaction to the resultant exchange field decreases rapidly as the temperature increases. The consequences of this behavior are gradual diminution of the competition between exchange interactions of opposite sign and eradication of the conditions for the formation of frustrated states. At $T>100$ K ferromagnetic exchange interactions dominate, and the $(Fe_{0.65}Ni_{0.35})_{1-x}Mn_x$ alloys are not really systems with competing exchange interactions.

The density of frustrated Fe sites at low temperatures can be approximately estimated from the temperature dependence of the intensity of the principal maximum (Fig. 3) if we assume that the values of B_{hf} for all such sites at 5 K are localized in the interval 30–38 T. In this approximation the density of frustrated states is ~5% in the alloy $Fe_{0.65}Ni_{0.35}$ and ~10% in the $x=0.024$ alloy. The manganese impurity raises the density of frustrated states, an effect that can be regarded as a natural consequence of a local increase in the competition of exchange interactions of opposite sign with the activation of antiferromagnetic Mn–Fe interaction. It is reasonable to expect this trend to persist in alloys having high concentrations of manganese, which enter the spin glass state at low temperatures. It is entirely probable that a high density of sites with weak exchange fields is responsible for the formation of the spin glass phase in such alloys. In this regard we call attention to the fact that the temperature interval in which anomalies of the temperature curves of the total intensities are observed (Fig. 3) coincides with the temperatures of transitions to the spin glass phase for $(Fe_{0.65}Ni_{0.35})_{1-x}Mn_x$ alloys, $x>0.1$ (Ref. 9). On the other hand, as mentioned above, the satellite structure acquired by the function $P(B_{hf})$ under the influence of the manganese impurity in the $x=0.024$ alloy is stable over a wide range of temperatures. This means that the energy of antiferromagnetic Mn–Fe interaction is high, its absolute value exceeding 200 K.

This work has received partial support from the Russian Fund for Fundamental Research (Grant No. 97-02-16479).

[1] M. Hatherly, K. Hirakawa, D. Lowder, J. F. Mallett, M. W. Stringfellow, and V. N. Torrie, Proc. Phys. Soc. London **84**, 55 (1964).
[2] J. B. Müller and J. Hesse, Z. Phys. B **54**, 35 (1987).
[3] S. Komura, T. Takeda, and M. Roth, Phys. Lett. A **62**, 365 (1977).
[4] H. Maruyama, R. Pauthenet, J. Picoche, and O. Yamada, J. Phys. Soc. Jpn. **55**, 3218 (1986).
[5] S. Hatta, M. Hayakawa, and S. Chikazumi, J. Phys. Soc. Jpn. **43**, 451 (1977).
[6] M. Shiga, T. Satake, Y. Wada, and Y. Nakamura, J. Magn. Magn. Mater. **51**, 123 (1985).
[7] T. Miyazaki, Y. Ando, and M. Takahashi, Phys. Rev. B **34**, 6334 (1986).
[8] B. Huck and J. Hesse, J. Magn. Magn. Mater. **70**, 425 (1987).
[9] J. Hesse, C. Bottger, A. Wulfes, J. Sievert, and H. Ahlers, Phys. Status Solidi A **135**, 343 (1993).
[10] B. Window, J. Phys. F **4**, 329 (1974).
[11] J. B. Müller and J. Hesse, Z. Phys. B **54**, 43 (1983).
[12] M. Shiga and Y. Nakamura, J. Magn. Magn. Mater. **40**, 319 (1984).
[13] M. M. Abd-Elmeguid, B. Schleede, and H. Micklitz, J. Magn. Magn. Mater. **72**, 253 (1988).
[14] B. Huck and J. Hesse, J. Magn. Magn. Mater. **78**, 247 (1988).
[15] M. Fricke and J. Hesse, Hyperfine Interact. **93**, 1537 (1994).
[16] N. N. Delyagin, G. M. Gurevich, A. L. Erzinkyan, V. P. Parfenova, S. I. Reĭman, S. V. Topalov, and M. Trkhlik, Zh. Eksp. Teor. Fiz. **109**, 1451 (1996) [JETP **82**, 783 (1996)].
[17] W. W. Saslov and G. Parker, Phys. Rev. Lett. **56**, 1074 (1986).

Translated by James S. Wood

Resonance retardation of a domain wall by Winter magnons in orthoferrites

M. V. Chetkin, A. P. Kuz'menko, A. V. Kaminskiĭ, and V. N. Filatov

Khabarovsk State Technical University, 680035 Khabarovsk, Russia
(Submitted January 20, 1998)
Fiz. Tverd. Tela (St. Petersburg) **40**, 1656–1660 (September 1998)

Supersonic domain-wall dynamics is investigated in wafer samples of $YFeO_3$ having thicknesses of 10 μm, 35 μm, 40 μm, 120 μm, and 125 μm, prepared by different methods, and in a $EuFeO_3$ sample of thickness 60 μm at liquid-nitrogen temperature. Relations are established for the occurrence of nonlinear segments in the form of constant-wall-velocity intervals in the dependence of the wall velocity on the pulsed magnetic field amplitude. Qualitative agreement is obtained between the experimental data and calculated values of the velocities and widths of the constant-velocity intervals, on the assumption that the mechanism of resonance retardation of the domain walls by parametrically excited Winter (wall as opposed to bulk) magnons is operative at supersonic velocities. © *1998 American Institute of Physics.*
[S1063-7834(98)01909-1]

Investigations of the dynamics of domain walls in orthoferrites[1,2] have showed the saturation rate $C=20\times10^3$ m/s theoretically interpreted to be higher than the transverse and longitudinal sound velocities, theoretically interpreted in several papers, and is equal to the minimum phase velocity of spin waves along the linear part of their dispersion law. The high fields for reversal of the magnetic sublattices in these materials (~80 kOe), the supersonic velocities of the moving domain walls, far exceeding the well-known Walker limit for ferromagnetic materials, allow examining the movement of the domain walls in terms of magnetization reversal. The field dependence of the domain-wall velocity $V(H)$ in orthoferrites exhibits a very distinct nonlinear behavior. In addition to the saturation rate, magnetic-field intervals ΔH_t and ΔH_l have been discovered on the $V(H)$ curve, characterized by constant velocities of 4.2×10^3 m/s and 7.2×10^3 m/s, respectively, which are close to the transverse and longitudinal sound velocities V_t and V_l. In theoretical studies it has been shown that these anomalies of the curve are of magnetoelastic origin.

The refinement of experimental research techniques in recent years has been conducive to a significant increase in the accuracy of velocity measurements. This advancement has been fostered by the favorable combination of magnetic and magnetooptical properties of orthoferrites and has thrust these materials to the forefront as a highly practical object for investigations of magnetization reversal processes. The high contrast of the domain structure permits the domain-wall dynamics to be investigated without the use of optical intensifiers. As a result, it has been possible to observe experimentally a whole series of anomalous intervals (ΔH_n) in the $V(H)$ curve, in addition to those mentioned above, for wall velocities in the interval from V_t to C. The formation of these anomalies has been attributed to retardation of the domain walls by optical phonons and by Lamb plane waves excited in the domain walls. The main results of studies of the supersonic nonlinear and multidimensional dynamics of domain walls in orthoferrites have been generalized in a survey[1] and in a book.[2]

However, none of the indicated mechanisms has provided a systematic and complete explanation of the sum-total of experimentally observed anomalies of the magnetic-field dependence of the wall velocity. In this paper we seek to compare the experimental and theoretical results and to explain the origin of the additional anomalies (over and above those at the velocities V_t, V_l, and C) within the framework of the model of resonance retardation of the domain walls by Winter magnons excited by the moving domain walls.[3–5] The experimental data obtained in the study are in good agreement with theoretical conclusions, attesting to the adequacy of the model proposed in Refs. 4 and 5. Our calculations of the velocities V_n and the intervals ΔH_n and the most prominent features of the behavior of a multidimensional domain wall at supersonic velocities exhibit qualitative agreement with the experimental results for orthoferrite wafers of various thicknesses and orientations grown by different methods.

1. PROCEDURE AND SAMPLES FOR THE INVESTIGATIONS

The nonlinear, supersonic domain-wall dynamics in orthoferrites impose strict requirements on the accuracy of the method chosen to measure velocity. Considerable progress in this sense occurs by switching over to pulsed methods and high-speed photomicrography. The design of stroboscopic apparatus using light pulses having a duration of the order of 6 ns has significantly enhanced the accuracy of investigations.[1,2] This achievement has made it possible for the first time to establish the multidimensional, transient character of the transition to supersonic motion. The latter consideration has created a demand for even substantially shorter light pulses (of 1-ns duration or less). Shiga *et al.*[6] have proposed a two-shot illumination technique. This was the first method to utilize spatial separation of the laser beam into two rays. A time delay between the differently polarized

 © 1998 American Institute of Physics

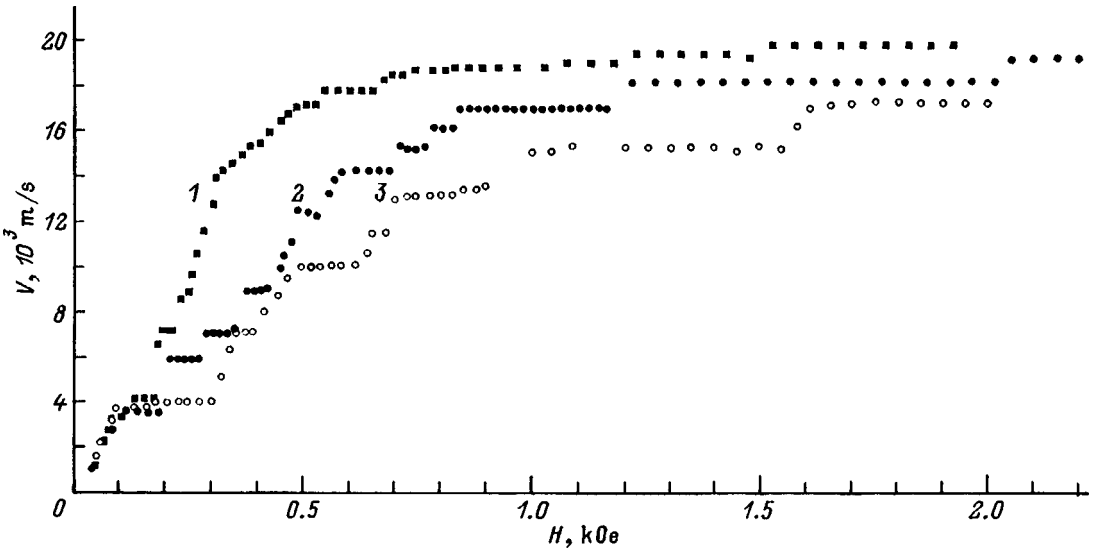

FIG. 1. Field dependence of the domain-wall velocity in yttrium orthoferrite wafers of various thicknesses. *1*) $d=10$ μm; *2*) 35 μm; *3*) 120 μm.

rays was created by a system of variable-distance mirrors and could be varied from 1 ns to 15 ns. The synchronization of the light pulses with the magnetic field pulses did not affect the accuracy of the velocity measurements. We were able to obtain high-contrast double-exposure photographs of the domain structures in real time. The distance traversed by the domain walls during the optical time delay was measured from the negatives on a UIM-23 microscope within 0.5-μm error limits. All these factors ensured minimization of the error of our wall velocity measurements in orthoferrites; the error was less than 2%, had a significant dependence only on the wall velocity, and merely tended to smear the domain walls within the duration of the light pulse.

The investigated samples were $YFeO_3$ wafers having thicknesses of 10 μm, 35 μm, 90 μm, and 120 μm and a $EuFeO_3$ wafer of thickness 60 μm, cut perpendicular to the optical axis; we investigated the dynamics of Néel walls in the samples after preliminary chemical polishing. The sample of thickness 90 μm was specially embedded in an amorphous mass of Canadian balsam between two thin plates. The wall dynamics in the $EuFeO_3$ wafer sample was investigated at $T=4.2$ K and 77 K in an optical helium cryostat. All these samples were synthesized by the floating zone method with optical heating. We also investigated wall motion in a wafer sample of thickness 125 μm grown by hydrothermal synthesis. Almost all the investigations of the wall dynamics were carried out by the two-shot illumination technique in real time. The wall velocity measurements in the sample of thickness 10 μm were performed by a stroboscopic technique.

2. DESCRIPTION AND ANALYSIS OF EXPERIMENTAL RESULTS

Figures 1 and 2 show experimental graphs obtained for

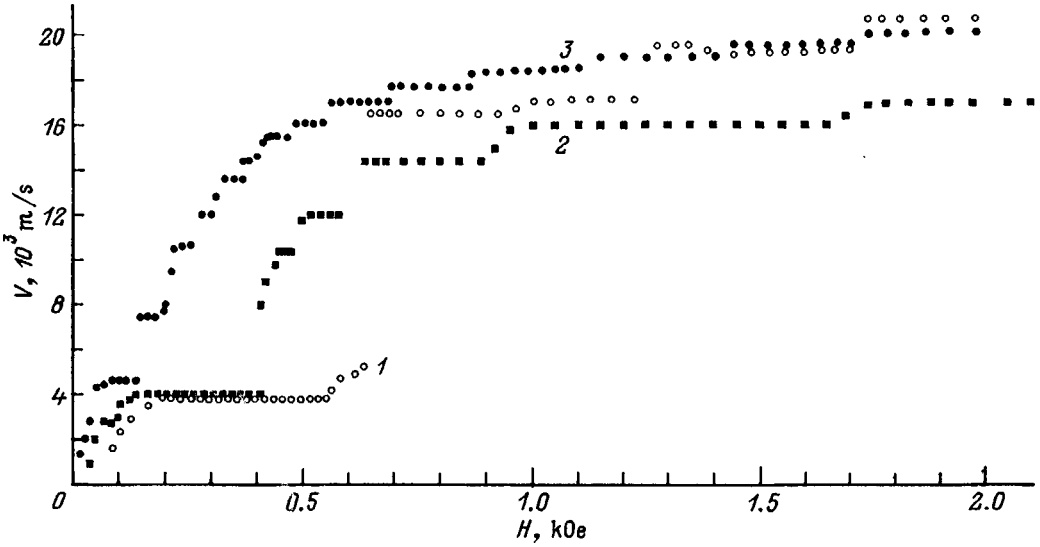

FIG. 2. Field dependence of the domain-wall velocity in yttrium and europium orthoferrites. *1*) $YFeO_3$, $d=120$ μm, [010] wall; *2*) $YFeO_3$, $d=125$ μm, grown by hydrothermal synthesis; *3*) $EuFeO_3$, $d=60$ μm at $T=77$ K.

the wall velocity as a function of the amplitude of the pulsed magnetic field, $V(H)$, in all the investigated samples. Figure 1 shows the $V(H)$ curves in wafers of various thicknesses (10 μm, 35 μm, and 120 μm), obtained at room temperature. All the investigations were carried out in fields up to 2 kOe, while the sample of thickness 35 μm was investigated in fields up to 5 kOe.

The field dependence $V(H)$ for $YFeO_3$ samples of thickness 120 μm with Néel walls exhibits a sequence of constant-velocity intervals (ΔH_n) with velocities $V_n = (10.6, 12, 13.8, 14.5, 15.5, 16.2, 17, 17.8, 18.4, 19.2, 19.8) \times 10^3$ m/s. Altogether 11 of these anomalies are observed. We note in this regard that ΔH_n for $n=6(\Delta H_6)$ has a width of 75 Oe, whereas $\Delta H_0 = 260$ Oe. As n increases, the width of ΔH_n increases, and the difference $(V_{n+1} - V_n)$ decreases. For the sample with $d = 10$ μm anomalies are observed on the $V(H)$ graph only for $V_n = 16.2 \times 10^3$ m/s and 19.2×10^3 m/s. The width of the anomaly ΔH with $V_n = 16.2 \times 10^3$ m/s for this sample is 570 Oe, in contrast with 70 Oe for the width of the same interval for the sample of thickness 120 μm. The $V(H)$ graph behaves similarly for the sample of thickness $d = 35$ μm. In this case the number of anomalies ΔH_n is reduced to seven, and they occur for $V_n = (10.4, 12, 14.5, 16.2, 17.0, 18.0, 19.0) \times 10^3$ m/s in fields up to 5 kOe. As a result of the considerable increase in the widths of the anomalies ΔH_n, the maximum wall velocity C is attained only in fields higher than 5 kOe, which are not represented in Fig. 1.

As mentioned in previous work,[1,2] in all experiments with yttrium orthoferrite wafers of small thickness, $d = 10$ μm, 35 μm, and 40 μm, it is observed that the width of the magnetoelastic anomaly tends to increase at the transverse sound velocity ΔH_t. The interval ΔH_t has widths of 370 Oe, 270 Oe, and 90 Oe for samples of thickness $d = 10$ μm, 35 μm, and 120 μm, respectively; these results were first indicated in Ref. 6. The tendency, noted for samples of various thicknesses, toward a substantial increase in the width of the interval ΔH_n as the thickness and mobility of the domain walls decrease is noted for samples of various thicknesses is preserved in this case, as is evident from the graphical dependence $V(H)$. The number of velocities V_n is again found to depend on the sample thickness. For example, we have $n=2$ for the sample of thickness $d = 10$ μm, $n=7$ for $d = 35$ μm, and $n=11$ for $d = 120$ μm. The dependences of ΔH_t and ΔH_l on the wall mobility is consistent with Maxwell's rule, whose validity has been justified in a paper by Gomonov *et al.*[7]

The field dependences $V(H)$ in Fig. 1 for $YFeO_3$ samples of various thicknesses can be used to establish the following characteristic patterns in the formation of the intervals ΔH_n: 1) The formation of a discrete series of anomalies ΔH_n is observed on the $V(H)$ graphs for the orthoferrite $YFeO_3$ at velocities $V_n < C$ distinct from V_t and V_l; 2) the number of observed anomalies depends significantly on the sample thickness and increases as the thickness of the investigated wafer increases; 3) as the wall velocity approaches the velocity limit C, the interval between the different values of V_n diminishes, and the difference $(V_{n+1} - V_n)$ tends to zero; 4) the widths of the intervals ΔH_n increases as V_n increases and as the thickness of the wafer decreases.

Figure 2 shows graphs of the field dependence $V(H)$ obtained in a $EuFeO_3$ sample and in an $YFeO_3$ sample growth by hydrothermal synthesis. The dynamics of a tilted Bloch wall, its plane perpendicular to the [010] axis in the static situation, was investigated in a sample of thickness $d = 120$ μm. The wall mobility in this sample is almost half the value for the graphs in Fig. 1. The width of the anomaly at the longitudinal sound velocity, H_l, is equal to 220 Oe, whereas for a float-zoned sample (Fig. 1) it has a width of 90 Oe. A comparison of the experimental values of ΔH_t and ΔH_l on the $V(H)$ graphs in Figs. 1 and 2 indicates agreement with the conclusions of other authors[4,7,8] on the existence of a functional relation between the wall mobility and the widths of the magnetoelastic anomalies of the velocity-field curves. On the other hand, in Ref. 7 the interval of constant wall velocity ΔH_t has been analyzed without regard for the significant influence of the thickness of the investigated wafers.

In addition to the magnetoelastic anomalies, prominent features at velocities V_n are also observed on this graph of $V(H)$. The above-mentioned patterns in the distribution of ΔH_n also occur here. However, the total number of ΔH_n is somewhat lower. The domain wall is no longer plane at supersonic velocities. Its motion deviates considerably from one-dimensional.[1,2,6] For an initially tilted domain wall in fields above 1.9 kOe it was possible to attain the velocity limit C, which is also equal to 20×10^3 m/s. Consequently, the limiting velocities of two types of domain walls become identical. It is also important to note the inference drawn from Ref. 9 that, for all types of domain walls, the plane of the wall remains perpendicular to the plane of the samples at these velocities.

We have investigated the dependence $V(H)$ for an $YFeO_3$ wafer of thickness 90 μm set in Canadian balsam. An increase in the widths of the magnetoelastic anomalies ΔH_t and ΔH_l is observed under these conditions. The transition to supersonic motion is a sudden, highly transient process and is accompanied by pronounced bending of the domain wall. The wall mobility is 3000 cm/(s·Oe), whereas in the free state the wall mobility in this sample is 4500 cm/(s·Oe). The abrupt transition to supersonic wall motion observed in this experiment can be attributed qualitatively to the instability of its motion due to disruption of the boundary conditions in the plane perpendicular to the plane of a Néel-configuration domain wall, as suggested in Ref. 10.

Figure 2 also shows the dependence $V(H)$ for a sample of thickness 125 μm grown by hydrothermal synthesis. The wall mobility in this sample has been determined to be 4500 cm/(s·Oe). The formation of magnetoelastic anomalies ΔH_t and ΔH_l is also observed on the experimental graph of $V(H)$ With a further increase in the driving field the wall velocity is observed to increase smoothly, for all practical purposes, to 15.5×10^3 m/s. Then as the magnetic field is increased, $V(H)$ exhibits the formation of anomalies ΔH_n at velocities $V_n = (17.1, 17.8, 18.8, 19.4, 19.8) \times 10^3$ m/s. The formation of these anomalies follows the previously indicated patterns.

It is evident from Fig. 2 that retardation of the domain

TABLE I. Experimental and calculated values of the velocities V_n at which domain-wall retardation by Winter magnons is observed.

Sample thickness/width of inhomogeneities, μm		Order number and value of velocity $V_n > V_l$, 10^3 m/s										
		1	2	3	4	5	6	7	8	9	10	11
10	(exp.)	16.2	19.2									
30/10	(calc.)	16.6	19.0	19.6	19.8							
120	(exp.)	10.6	12.0	13.8	14.5	15.5	16.2	17.0	17.8	18.4	19.2	19.8
30/120	(calc.)	8.9	10.6	12.0	13.2	14.1	15.0	15.6	16.2	16.6	17.0	17.4

walls is observed for the $V(H)$ graph obtained at $T=77$ K in $EuFeO_3$ at velocities of $(3.5, 5.8, 7.5, 12, 14, 15.5, 17)\times 10^3$ m/s in fields up to 4 kOe and at velocities of $(3.5, 5.8, 7.5, 14), \times 10^3$ m/s in fields up to 0.5 kOe. The transition to supersonic motion is a transient, multidimensional process.

3. DISCUSSION OF THE RESULTS

It has been mentioned above that the transition to supersonic motion is accompanied by transient behavior and departure from one-dimensionality. This behavior of the domain walls is especially conspicuous for the sample set in Canadian balsam and for the sample of thickness 10 μm. The field interval in which the transition to a velocity $V_n > V_{t,l}$ is observed has a width less than 10 Oe (Refs. 1 and 2). In this interval the investigated field dependence of the motion of a domain wall from the beginning to the end of its transit through the sample is highly unstable. This factor makes it impossible to determine accurately the wall velocity at the instant of transition to supersonic motion. As the amplitude of the magnetic field is further increased, the domain wall motion tends toward a steady-state, stable course. The departure from one-dimensional motion at the instant of transition persists in this case. It is evident from the double-exposed photographs of dynamic domain structures in Refs. 1, 2, and 9 that the multidimensional character of the wall motion remains ''self-similar'' in transit through the sample in homogeneous magnetic fields.

A theoretical study[4] of the anomalies of $V(H)$ in the form of constant-velocity intervals is based on the possibility of resonance retardation of the domain walls by Winter (wall as opposed to bulk) magnons.[3] The flexural modes of vibration in a domain wall, corresponding to wall magnons, have eigenfrequencies governed by the thickness of the investigated wafer. The formation of a system of growth bands is noted in single-crystal samples grown by the floating-zone method. In the opinion of Balbashov *et al.*[11] the emergence of these periodic inhomogeneities is associated with local temperature fluctuations under the influence of a concentration supercooling mechanism. Temperature fluctuation during the growth process produces inclusions with nonmagnetic Fe^{2+} or Fe^{4+} ions and distortions in the octahedral oxygen environment of Fe^{3+} ions. The nonmagnetic inclusions are less transparent in transmitted light. They can be visually observed therefore under a microscope as an alternating system of dark bands. The period of these inhomogeneities is 20–30 μm on the average. For samples whose planes are perpendicular to the optical axis, the growth bands of the inhomogeneities are almost parallel to the domain walls.

The dimensions of the observed inhomogeneities determine the spatial frequencies of the periodic force acting on the moving domain walls. When the natural frequency of the wall magnons coincides with this spatial frequency, resonance retardation of the walls takes place in orthoferrites. This mechanism has been proposed in Ref. 4.

To test the adequacy of the above-described physical mechanism of the wall retardation by Winter magnons, we compare the experimental data with the theoretical conclusions. The velocities V_n at which the formation of the anomalies ΔH_n is observed can be determined from the expression

$$V_n = \frac{Cn(L/2d)}{\sqrt{1+(nL/2d)^2}}. \tag{1}$$

According to Eq. (1), the set of values of V_n is determined by the ratio of the period of the inhomogeneities L to the thickness of the wafer d. Table I gives experimentally observed and theoretically calculated values of the velocities V_n obtained according to (1) under the assumption that the mechanism of resonance retardation of the domain walls by wall magnons is operative. By the proper choice of the ratio L/d we have succeeded in achieving qualitative agreement between these values of V_n. The most complete correspondence is observed when an inhomogeneity period of 30 μm is assumed, consistent with the results of our measurements of the period of these inhomogeneities. The best agreement is observed for velocities V_n observed in thin wafers. An estimation of the number of ΔH_n from Eq. (1) for an orthoferrite plate of thickness 10 μm for $L=30$ μm gives $n=2$, which agrees with the experimental data.

In the theoretical conclusions[4] an analytical expression also has been proposed for the field dependence $V(H)$, containing the experimentally observed anomalies ΔH_n at the velocities V_n. The widths of these anomalous intervals are given by the relation

$$\Delta H_n \approx \frac{(CQ\varepsilon_n(d))^2 V_n \tau}{32\gamma\omega_d\Delta_0}\left(\sqrt{1-(V_n/C)^2}+\frac{2d^2}{l^2}\right), \tag{2}$$

where $\omega_d=10^5$ is the Dzyaloshinskiĭ field, $\varepsilon_i=10^{-2}$ is the percentage modulation of the spectrum of Winter magnons by the spatial potential relief (spatial frequency), $Q=10^5$ is the Winter magnon quality factor, and Δ_0 is the width of the static domain wall. The quantity ΔH_n is found to depend

significantly on the wafer thickness. As the thickness decreases, the constant-velocity interval ΔH_n increases approximately by the factor $2/d$. The experimental results shown in Figs. 1 and 2 also exhibit the same dependence. As an example, we compare the widths of the anomalies ΔH_n at the velocity $V_n = 16.2 \times 10^3$ m/s (observed for wafers with $d = 120$ μm, 20 μm, and 10 μm): They are equal to 120 Oe, 350 Oe, and 570 Oe, respectively.

Equation (2) can be used in conjunction with the experimental data on ΔH_n to estimate the values of τ_n and to test whether conditions are satisfied for the validity of Zvezdin and Popkov's model[4] of resonance retardation of the domain walls in orthoferrites by Winter wall magnons; according to this model, $\omega_n \tau_n \gg 1$. The estimation of τ_n gives 10^{-7} s, and for the condition $\omega_n \tau_n \gg 1$ to be satisfied, it must be assumed that the Winter magnons have a lower frequency threshold of 10^8 Hz. For the final confirmation of the validity of the model it is necessary to test the stated condition for the experimentally measured relaxation times of Winter magnons.

In summary, we have confirmed experimentally the presence of a resonance mechanism of retardation of the domain walls in orthoferrites by Winter wall magnons. We have obtained qualitative agreement between the experimental values of the velocities V_n and the intervals ΔH_n in which they are constant, on the one hand, and the analytical values calculated on the basis of the model of resonance retardation of the domain walls by Winter magnons excited when the natural frequency of a wall mode coincides with the spatial frequency of the growth inhomogeneities, which for the domain walls represent the potential relief of nonmagnetic ions of the type Fe^{2+} and Fe^{4+}. We have also confirmed the possibility that a mechanism of parametric resonance amplification at certain velocities V_n is operative under these conditions when the maximum transfer of energy from a dynamic domain wall to Winter magnon modes is observed in a certain interval of velocities close to V_n, causing multidimensional flexural formations to appear at the wall. We have verified experimentally the adequacy of the given wall retardation model by determining the anomalies of the functional dependence $V(H)$ from artificially created magnetic inhomogeneities.

[1] V. G. Bar'yakhtar, B. A. Ivanov, and M. V. Chetkin, Usp. Fiz. Nauk **146**, 417 (1985) [Sov. Phys. Usp. **28**, 563 (1985)].
[2] V. G. Bar'yakhtar, M. V. Chetkin, B. A. Ivanov, and S. N. Gadetcky, *Dynamics of Topological Magnetic Solitons* (Springer-Verlag, Berlin–New York, 1994).
[3] J. M. Winter, Phys. Rev. **124**, 452 (1961).
[4] A. K. Zvezdin and A. F. Popkov, Pis'ma Zh. Tekh. Fiz. **10**, 449 (1984) [Sov. Tech. Phys. Lett. **10**, 188 (1984)].
[5] V. G. Bar'yakhtar, B. A. Ivanov, and A. L. Sukstanskiĭ, Pis'ma Zh. Tekh. Fiz. **5**, 853 (1979) [Sov. Tech. Phys. Lett. **5**, 351 (1979)].
[6] M. V. Chetkin, S. N. Gadetskiĭ, A. I. Akhutkina, and A. P. Kuz'menko, Zh. Éksp. Teor. Fiz. **86**, 1411 (1984) [Sov. Phys. JETP **59**, 825 (1982)].
[7] S. V. Gomonov, A. K. Zvezdin, and M. V. Chetkin, Zh. Éksp. Teor. Fiz. **94**(11), 133 (1988) [Sov. Phys. JETP **67**, 2250 (1988)].
[8] A. K. Zvezdin and A. A. Mukhin, Zh. Eksp. Teor. Fiz. **102**, 577 (1992) [Sov. Phys. JETP **75**, 306 (1992)].
[9] M. V. Chetkin, Yu. N. Kurbatova, and V. N. Filatov, JETP Lett. **65**, 797 (1997).
[10] N. Papanicolaou, Phys. Rev. B **55**, 12 290 (1997).
[11] A. M. Balbashov, A. Ya. Chervonenkis, A. V. Antonov, and V. E. Bakhteuzov, Izv. Akad. Nauk Ser. Fiz. **35**, 1243 (1971).

Translated by James S. Wood

Critical behavior of the specific heat of small magnetic Cr_2O_3 particles

A. K. Murtazaev, I. K. Kamilov, Kh. K. Aliev, and K. Sh. Khizriev

Institute of Physics, Dagestan Science Center, Russian Academy of Sciences, 367003 Makhachkala, Russia
(Submitted September 30, 1997; resubmitted January 23, 1998)
Fiz. Tverd. Tela (St. Petersburg) **40**, 1661–1662 (September 1998)

The critical behavior of the specific heat of small magnetic particles of the real antiferromagnet Cr_2O_3 is investigated by the Monte-Carlo method. The critical indices $\alpha=-0.17\pm0.03$ and the ratio of the critical amplitudes $A/A'=1.03\pm0.07$ are calculated for particles containing $N=286$ to 2502 spins. © *1998 American Institute of Physics.* [S1063-7834(98)02009-7]

The investigation of the phase-transition characteristics in three-dimensional systems based on microscopic Hamiltonians remains an important problem in the modern theory of phase transitions and critical phenomena.[1]

Studies of this kind are especially timely in relation to small particles,[2] where rigorous analytical calculations of the magnetic and thermal characteristics are severely hampered both by the need to correctly incorporate strong interspin interactions into the theory and by the impossibility of utilizing transition to the thermodynamic limit in calculations. Major difficulties are also encountered in the organization of laboratory experiments and the interpretation of their results.[2] In effect, all these difficulties can be surmounted in the investigation of small systems by Monte-Carlo methods.[3,4] This method has been used primarily to study simple ferromagnetic model systems involving interaction between nearest neighbors. The investigation of real antiferromagnetic systems taking into account the specific crystallographic structure and other parameters is not nearly as complete.

We consider small particles of the real antiferromagnet Cr_2O_3 having a rhombohedral lattice. Here spatial, exchange, and other quantities all conform to real Cr_2O_3 samples. The Hamiltonian of the system can be written[5]

$$H=-\frac{1}{2}\sum_{i,j} J_1(\boldsymbol{\mu}_i\boldsymbol{\mu}_j)-\frac{1}{2}\sum_{k,l} J_2(\boldsymbol{\mu}_k\boldsymbol{\mu}_l)-D_0\sum_i (\boldsymbol{\mu}_i^z)^2,$$

$$|\boldsymbol{\mu}_i|=1, \tag{1}$$

where, according to experimental data,[6] J_1 is the interaction parameter of each spin with one nearest neighbor, and J_2 is the same for interaction with the next three nearest neighbors ($J_2=0.45J_1$, $J_1<0$, $J_2<0$). Various relativistic interactions are approximated here by an effective single-ion anisotropy $D_0>0$, and the ratio between anisotropy and exchange is assumed to be equal to 0.025.

The calculations are carried out for spherical particles of diameter $d=(24.0, 28.4, 32.8, 34.8, 41.82, 46.4, 48.64)$ Å, and the number of spins in the particles are (respectively) $N=286$, 508, 760, 908, 1602, 2170, 2502. Markov chains of length ranging from 2×10^4 to 10^5 Monte-Carlo steps per spin are computer generated.

One of the distinctive characteristics of small particles is the fact that they have a relatively high fraction of surface elements, and many of their properties are attributable in large part to the very presence of the surface.[2] In our investigated particles the fraction of surface spins varied from 46.8% for the smallest particle to 22.8% for a particle with $N=2502$.

The temperature behavior of the specific heat is observed using the expression[7]

$$C=(NK^2)(\langle U^2\rangle-\langle U\rangle^2), \tag{2}$$

where $K=J_1/k_BT$, k_B is the Boltzmann constant, N is the number of particles, U is the internal energy, and the angle brackets signify averaging over the canonical ensemble. The temperature curves of the specific heat for all the investigated particles exhibit distinctly pronounced maxima in the critical region. Figure 1 shows data on the temperature dependence of the specific heat for two particles: $N=508$ and 2170. It is evident from the figure that when the number of particles in the system is increased, the specific heat maximum increases and shifts toward higher temperatures; this behavior is a characteristic feature of small particles and is consistent with the data of other authors.[3]

To approximate the critical behavior of the specific heat, we use the expression[8]

$$C=\frac{A}{\alpha}(|t|^{-\alpha}-1)+D|t|^x, \tag{3}$$

where $t=|T-T_N|/T_N$, and α, A, and D are fitting parameters for $T>T_N$. The same quantities primed refer to the case $T<T_N$. The power exponent x is set equal to 0.55, consistent with the value obtained theoretically and experimentally for the Heisenberg model.[9] Monte-Carlo processing of the data is implemented by a nonlinear least-squares method. The choice of the fitting equation (3) as one of several possible[8] is dictated by the fact that it provides the smallest mean-square deviation. The use of other fitting equations alters the parameters α, A, and D slightly, but within the error limits they still agree with those obtained on the basis of Eq. (3); however, the computational error is somewhat higher for the other equations.

For the optimal values of α, A, and D we use data that minimize the mean-square deviation. The critical temperatures are determined from the specific heat maxima; the values of T_N are varied in the calculations. The temperature

 © 1998 American Institute of Physics

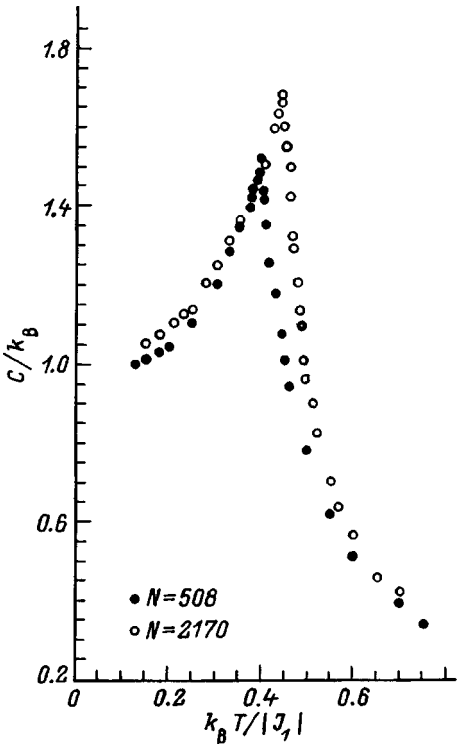

FIG. 1. Specific heat dependence of small magnetic Cr_2O_3 particles on temperature.

chosen for T_N corresponds to minimum variance. On the whole, the range of the normalized temperature t wherein α, A, and D are determined lies between the limits $t_{\min}=5\times10^{-3}$ and $t_{\max}=0.75$. In this range the effective values of the critical index α are approximately the same for all the particles, being equal to $\alpha=-0.17\pm0.03$. The theoretical values of α for the Heisenberg model and Ising models are equal to -0.126 and 0.108, respectively.[9] Results of experimental studies of the critical behavior of the specific heat with the calculated value of α are also available for macroscopic Cr_2O_3 samples. Here the critical index α varies from $\alpha=0.14$ to -0.12 for different authors and from data obtained by different measurement techniques.[10] We also note that according to our data, the index α varies only within the error limits and when the lower limit $t_{\min}$ of the range is dropped from 5×10^{-3} to 3×10^{-2}.

In processing data corresponding to the low-temperature phase on the basis of statistical scaling predictions,[1] it is assumed that $\alpha'=\alpha$, and then the quantities A' and D' are chosen accordingly. The ratio between the critical amplitudes A and A', determined by the indicated scheme for particles of all sizes, takes on the value $A/A'=1.03\pm0.07$. In the investigated temperature interval, therefore, the critical behavior of the specific heat of ultrasmall Cr_2O_3 particles containing $N=286-2502$ spins is essentially independent of the number of interacting spins and, hence, of their fraction in the surface layer.

In our investigated temperature interval we do not detect any crossover from Heisenberg to Ising critical behavior; according to the Hamiltonian data, crossover is expected at $t=t_{cr}\approx0.052$. It has been established[5] that the surface spins of small magnetic particles freely change orientation, even at temperatures well below T_N. This behavior of the spins is more consistent with the Heisenberg model, and we postulate that this fact is conducive to broadening of the temperature interval of Heisenberg critical behavior and to a shift of the crossover temperature t_{cr} to the Néel point.

[1] A. Z. Patashinskiĭ and V. L. Pokrovskiĭ, *Fluctuation Theory of Phase Transitions* [Pergamon Press, Oxford-New York, 1979; Nauka, Moscow, 1982].
[2] Yu. I. Petrov, *Physics of Small Particles* [in Russian] (Nauka, Moscow, 1982).
[3] K. Binder, *Monte Carlo Methods in Statistical Physics*, edited by K. Binder (Springer Verlag, Berlin-New York, 1979) [Mir, Moscow, 1982].
[4] K. Binder and D. W. Heermann, *Monte Carlo Simulation in Statistical Physics*, 3rd ed. [Springer Verlag, Berlin-New York, 1997; Nauka, Moscow, 1995].
[5] A. K. Murtazaev and I. A. Favorskiĭ, Fiz. Nizk. Temp. **19**, 160 (1993) [Low Temp. Phys. **19**, 113 (1993)].
[6] E. J. Samuelsen, M. T. Hutchings, and G. Shirane, Physica (Utrecht) **48**, 13 (1970).
[7] P. Peczac, A. M. Ferrenberg, and D. P. Landau, Phys. Rev. B **43**, 6087 (1991).
[8] G. Bednarz, D. J. W. Geldart, and M. A. White, Phys. Rev. B **47**, 14 247 (1993).
[9] J. C. Le Guillio and J. Zinn-Justin, Phys. Rev. Lett. **46**, L137 (1985).
[10] M. Marinelli, F. Mercuri, U. Zammit, R. Pizzoferrato, and F. Scudieri, Phys. Rev. B **49**, 9523 (1994).

Translated by James S. Wood

Thermal expansion anomalies in $TbVO_4$ due to the cooperative Jahn–Teller effect

Z. A. Kazeĭ

M. V. Lomonosov Moscow State University, 119899 Moscow, Russia

N.P. Kolmakova, A. A. Sidorenko, and L. V. Takunov

Bryansk State Technical University, 241035 Bryansk, Russia

(Submitted January 26, 1998)
Fiz. Tverd. Tela (St. Petersburg) **40**, 1663–1666 (September 1998)

The thermal expansion anomalies in $TbVO_4$ due to the cooperative Jahn–Teller effect were studied experimentally and theoretically. Characteristic magnetoelastic anomalies were observed in the curves of $\Delta a/a$ and $\Delta c/c$ of the cell parameters at $T<T_c$. Calculations of the magnetoelastic contribution to $\Delta a/a$ and $\Delta c/c$ from fully symmetric ε^{α_1} and ε^{α_2} and low-symmetry ε^{δ} modes were performed using the general crystal-field formalism, and the values of the magnetoelastic coefficient B^{δ} were obtained from spectroscopic and spontaneous-deformation data. It is shown that the thermal expansion of $TbVO_4$ in both the tetragonal and orthorhombic phases can be described well on the basis of a general model based on a single set of interaction parameters. © *1998 American Institute of Physics.* [S1063-7834(98)02109-1]

1. Rare-earth oxide compounds having the zircon structure RXO_4 (X = V, P, As; R — rare-earth (RE) ion) are known to be characterized by substantial single-ion magnetoelastic and pair quadrupole interactions, which give rise to large magnetoelastic effects and, in a number of cases ($TbVO_4$, $DyVO_4$, and $TmVO_4$), lead to spontaneous structural transitions — a cooperative Jahn–Teller effect. The parameters of the magnetoelastic and quadrupole interactions for fully symmetric and low-symmetry modes have been determined in detailed investigations of thermal expansion and magnetostriction anomalies in the tetragonal phase for RE vanadates and phosphates, taking account of all characteristic features of the crystal field.[1,2] To date, the low-symmetry phase has been described on the basis of a simplified pseudospin formalism, which though fully justified for low temperatures, makes it impossible to perform a systematic comparison with a description of the high-temperature phase. For this reason, in our view, it is certainly of interest to investigate magnetoelastic effects in the orthorhombic phase and also for the purpose of constructing a self-consistent description of the magnetoelastic beahvior of RE zircons in a wide temperature interval and fields based on real interaction parameters. For these purposes, the most suitable object, in our view, is $TbVO_4$, which has the highest transition temperature $T_c \approx 34$ K (orthorhombic deformation with B_{2g} symmetry along the [110] axis) and the strongest magnetoelastic effects.[3] The present paper is devoted to an investigation of this compound.

2. The measurements were performed on single-crystal samples grown by spontaneous crystallization from a fluxed solution. The x-ray diffraction investigations of the parameters *a* and *c* of the tetragonal unit cell were performed on a Geigerfleks diffractometer with a CF-108 flow-through helium cryostat (Oxford Instruments) on single-crystal wafers with natural (100) crystal faces using (10.00) (Cu $K\beta$, $2\theta \sim 152°$) and (008) (Cu $K\alpha_1$, $2\theta \sim 154°$) reflections. The orthorhombic deformation with B_{2g} symmetry was investigated using single-crystal $\langle 110 \rangle$ microsections (Co $K\beta$, (600), $2\theta \sim 148°$). The relative error in measuring the parameters *a* and *c* with respect to temperature was $\delta a/a \approx \delta c/c \approx \cot\theta \cdot \Delta\theta \approx 10^{-5}$ ($\Delta\theta \approx 0.003°$). The accuracy of the measurement of the orthorhombic deformation was equal to $\sim 10^{-4}$.

3. To calculate the RE contribution to the thermal expansion we shall employ the Hamiltonian $H_0 = H_{CF} + H_{QT}$, which includes the crystal-field Hamiltonian H_{CF} and the total quadrupole Hamiltonian H_{QT} written in terms of the equivalent Stevens operators O_n^m ($P_{xy} = \frac{1}{2}(J_x J_y + J_y J_x)$)

$$H_{CF} = \alpha_J B_2^0 O_2^0 + \beta_J (B_4^0 O_4^0 + B_4^4 O_4^4) + \gamma_J (B_6^0 O_6^0 + B_6^4 O_6^4), \tag{1}$$

$$H_{QT} = -\alpha_J^2 (G^{\alpha} \langle O_2^0 \rangle O_2^0 + G^{\delta} \langle P_{xy} \rangle P_{xy}). \tag{2}$$

In these expressions α_J, β_J, and γ_J are the Stevens parameters, B_n^m are the crystal-field parameters (of which there are five in the case of tetragonal symmetry), and the total quadrupole constants G^{δ} (G^{α}) contain contributions from both the single-ion magnetoelastic interaction B^{δ} (B^{α_1}, B^{α_2}) and the pair quadrupole interaction K^{δ} (K^{α}) (C_0^{δ} — elastic constant)

$$G^{\delta} = G_{ME}^{\delta} + K^{\delta} = \frac{(B^{\delta})^2}{C_0^{\delta}} + K^{\delta}. \tag{3}$$

We note that in the single-ion magnetoelastic contribution G_{ME}^{δ} RE zircons is, as a rule, the determining one, and when the interaction via acoustic phonons predominate the relation $K^{\mu}/G_{ME}^{\mu} = -1/3$ ($\mu = \alpha, \delta$) holds for each mode. The single-particle magnetoelastic Hamiltonian, which is lin-

 © 1998 American Institute of Physics

ear in the strain tensor components ε^{μ} (harmonic approximation), and the Hamiltonian of the pair quadrupole interaction for a RE ion in a site having a tetragonal environment contains, in the quadrupole approximation, each contain five invariants. In the full quadrupole Hamiltonian H_{QT} [see Eq. (2)] only the invariants which are important for the spontaneous magnetoelastic effects we are studying are written out explicitly. Terms similar to $\alpha_J^2 G^{\delta}\langle P_{xy}\rangle P_{xy}$ for the γ and ε modes are omitted, since in the absence of external actions they make no contributions in the case of $TbVO_4$. The term corresponding to deformation with δ symmetry (B_{2g} symmetry) is different from zero only in the presence of the corresponding external actions, for example, a magnetic field along the [110] axis, or in a low-symmetry phase. In the latter case a spontaneous phase transition occurs, accompanying by ordering of the quadrupole moments $\langle P_{xy}\rangle$. The necessary conditions for the existence of such a quadrupole ordering are, first of all, a sufficiently large total quadrupole constant G^{δ} and also a favorable electronic structure of the RE ion, for which the presence of low-lying ''quadrupole'' levels is characteristic. These conditions are satisfied in $TbVO_4$. This means that for the total Hamiltonian H_0 there exists a low-temperature solution with a nonzero quadrupole moment $\langle P_{xy}\rangle \neq 0$ that corresponds to the low-symmetry phase. This quadrupole ordering is accompanie by a B_{2g}-type orthorhombic distortion $\varepsilon^{\delta} = \alpha_J B^{\delta}\langle P_{xy}\rangle / C_0^{\delta}$.

The RE contribution to the thermal expansion can be found in the conventional manner by minimizing the free energy. Calculations similar to those performed in Ref. 1 show that the contribution to thermal expansion in the distorted phase along the tetragonal axis is due only to fully symmetric modes (isotropic ε^{α_1} and tetragonal ε^{α_2}), while along the [100] axis there is also a contribution that is quadratic in the orthorhombic deformation ε^{δ}:

$$\frac{\Delta c_{ME}}{c} = A_1 \Delta Q_0, \quad \frac{\Delta a_{ME}}{a} = A_2 \Delta Q_0 + \frac{3}{4}(\varepsilon^{\delta})^2, \tag{4}$$

where

$$Q_0(T) = \alpha_J \langle O_2^0 \rangle = \alpha_J \frac{1}{Z} \Sigma_i \langle i | O_2^0 | i \rangle \exp(-E_i / k_B T),$$

E_i are the energy levels of the RE ion calculated on the basis of the full Hamiltonian H_0, and Z is the partition function. The expressions for the coefficients A_1 and A_2 as functions of the magnetoelastic and elastic coefficients have the same form as in the tetragonal phase.[1]

4. The experimental temperature dependences of the parameters a and c ($\Delta a/a = a(T)/a_0 - 1$, $\Delta c/c = c(T)/c_0 - 1$, $a_0 = a(290\ \mathrm{K})$, $c_0 = c(290\ \mathrm{K})$) for the $TbVO_4$ unit cell at low temperatures are displayed in Fig. 1. We note that below T_c for the a axis in the basal plane under the experimental conditions, strictly speaking, the change in the interplanar spacing $\Delta d_{100}/d_{100}$ and not the parameter a itself is measured. One can see that characteristic anomalies are observed in both curves $\Delta a/a$ and $\Delta c/c$ at $T_c \approx 35$ K. The signs of the anomalies for these curves are opposite, and their magnitudes differ substantially — $\delta(\Delta a/a) \sim 3.5 \times 10^{-4}$ amd $\delta(\Delta c/c) \sim 0.4 \times 10^{-4}$, respectively. These anomalies are of a magnetoelastic nature and are due to the cooperative Jahn–Teller effect, since the phonon contribution to thermal expansion of the vanadate lattice below 40 K is quite small.

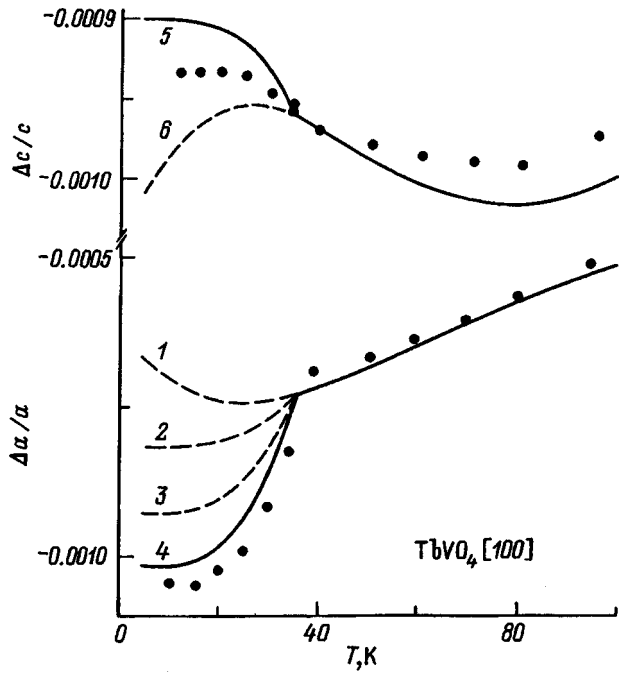

FIG. 1. Experimental (dots) and computed (curves *4*, *5*) of relative temperature variations of the parameters $\Delta a/a$ (bottom part) and $\Delta c/c$ (top part) in the $TbVO_4$ unit cell near a structural phase transition. The lines show the computed contributions to $\Delta a/a$ and $\Delta c/c$ from the orthorhombic ε^{δ} (*3*) and fully symmetric ε^{α_1} and ε^{α_3} deformations in the absence (*1*, *6*) and presence (*2*, *5*) of a structural transition.

The much larger magnitude of the anomaly along the a axis is explained by the fact that a spontaneous orthorhombic lattice deformation having B_{2g} symmetry makes a contribution to it. Indeed, though the contribution to the measured value of $\Delta a/a$ from the spontaneous orthorhombic deformation ε^{δ} is quadratic [see Eq. (4)], it is comparable to the magnetoelastic contribution on account of the large value of the spontaneous deformation ε^{δ}. Our measurements on $TbVO_4$ crystals from the same batch gave at 5 K $\varepsilon^{\delta} = (a' - b')/\sqrt{2}a_0' = 1.63 \times 10^{-2}$, where a' and b' are the parameters of the orthorhombic cell in a coordinate system rotated by 45°. Thus, the contribution of orthorhombic deformation to $\Delta a/a$ equals 1.98×10^{-4}.

5. The Hamiltonian $H_0 = H_{CF} + H_{QT}$ presented above makes it possible to describe, using a common set of interaction parameters, the characteristic features of the thermal expansion of $TbVO_4$ in both the tetragonal and orthorhombic phases in the absence of external actions. The crystal field in $TbVO_4$ has not been established at present with adequate reliability but, as our calculations show, the different sets of parameters available in the literature[4,5] lead to virtually identical results. For our calculations we employed the magnetoelastic coefficients B^{α_1} and B^{α_2} for fully symmetric modes in $TbVO_4$, determined from the thermal expansion anomalies in the tetragonal phase, and the value of the elastic modulus $C_0^{\delta} = 19.5 \times 10^4$ K for $HoVO_4$.[6] To determine the coefficient B^{δ} we used spectroscopic data given in Ref. 7 for the orthorhombic phase. The structural phase transition is accompa-

nied by a large change in the energy spectrum and the wave functions of the Tb^{3+} ion. At temperatures $T>T_c$ the Tb^{3+} ion in terbium vanadate has a singlet–doublet–singlet scheme, whose levels are separated by distances of 0.9 and 18 cm^{-1}, respectively, and all other excited states are separated by a substantial gap from the states enumerated. Below T_c the levels modify into two doublets, separated by a gap of 50 cm^{-1}.

First, the dependence of the phase-transition order parameter $\langle P_{xy}\rangle$, for which the critical temperature $T_c=36$ K, close to that observed exeprimentaly,[8] was obtained with the indicated parameters. This made it possible to calculate the change in the spectrum and in the wave functions of the Tb^{3+} ion below T_c and then the temperature dependence of the quadrupole moment $Q_0(T)$ in the experimental temperature range. The orthorhombic parameter of the crystal field $B_2^2=-\alpha_J G^{\delta}\langle P_{xy}\rangle$ equals 222 K, which, assuming that the interaction via acoustic phonons predominates, leads to a magnetoelastic constant $B^{\delta}=20.4\times10^3$ K. Using our experimental value of the orthorhombic distortion $\varepsilon^{\delta}=1.63\times10^{-2}$, we obtain for this coefficient the very close value $B^{\delta}=20.3\times10^3$ K.

The magnetoelastic contribution to the thermal expansion in the orthorhombic phase is determined by the temperature variation of the quadrupole moments of the Tb^{3+} ion $Q_0=\alpha_J\langle O_2^0\rangle$ and $Q_{xy}=\alpha_J\langle P_{xy}\rangle$ [see Eq. (4)], for both of which the computational procedure was described above. The coefficients A_1 and A_2 for $TbVO_4$ in the tetragonal phase were determined in Ref. 1 and equal $A_1=0.25\times10^{-2}$ and $A_2=-0.34\times10^{-2}$. Viewing the orthorhombic phase of $TbVO_4$, as a small ($\varepsilon^{\delta}\sim10^{-2}$) distortion of the tetragonal phase, as is ordinarily done, it is natural to use the same coefficients to calculate the magnetoelastic contribution to the thermal expansion in the orthorhombic phase. The computed contributions to the thermal expansion $\Delta a/a$, which are due to the orthorhombic mode ε^{δ} (curve *3*), the fully symmetric modes ε^{α_1} and ε^{α_2} in the absence and in the presence of a structural transition (curves *1* and *2*), as well as the total contribution (curve *4*) are shown in the figure (bottom part). One can see that the computed curve *4* describes quite well the experiment along the *a* axis. It is also evident from the figure that the temperature dependences of Q_0 differ very strongly in the tetragonal phase, which would be present in the absence of a structural transition (curve *1*), and in the orthophase (curve *2*).

To compare experiment and theory along the tetragonal axis, it is necessary to take account of the phonon contribution, which is comparable to or even larger than the magnetoelastic contribution above 40 K. In the figure (top part) the computed curves for the tetra- and orthophases along the *c* axis include the phonon contribution calculated in the Debye model with the parameters $T_D=445$ K and $\alpha_{c0}=8.42\times10^{-6}$, obtained in Ref. 1 by extracting the magnetoelastic contribution in the tetragonal phase of $TbVO_4$. One can see that the theoretical curve describes the experiment qualitatively, though the computed anomaly is much larger than the experimentally observed anomaly. Thus, a quite good description of experiment was obtained in the indicated model both along the tetragonal axis and in the basal plane. The quantitative disagreement between theory and experiment could be due, at least partially, to a misalignment of the sample and a systematic error below T_c due to the appearance of Jahn–Teller domains in the distorted phase.

6. In summary, in the present work the thermal expansion anomalies in $TbVO_4$ due to the cooperative Jahn–Teller effect were investigated experimentally and theoretically. The computed curves describe experiment quite well, both in the tetragonal and orthorhombic phases, on the basis of a single set of interaction parameters. The values of the δ-symmetry magnetoelastic coefficient obtained on the basis of two experimental methods are virtually identical and fall between the values of the this coefficient for $TbPO_4$ and $HoVO_4$ (14.4×10^3 and 24.3×10^3 K), found from comprehensive investigations of magnetoelastic effects in the tetragonal phase of the indicated zircons.[2,9] Characteristically, the coefficient B^{δ} for $TbVO_4$ is closer to its value for $HoVO_4$. This confirms the conjecture that magnetoelastic coefficients (normalized to the Stevens parameter α_J) depend to a larger degree on the matrix than on the RE ion. We emphasize that in the present work, in contrast to most works investigating the distorted phase in RE zircons, the calculations were performed in a more general crystal-field model. Previously, only the contribution of the dominant Jahn–Teller mode to the thermal expansion of RE zircons with a cooperative Jahn–Teller effect was studied, while the contribution from the fully symmetric modes was neglected. In so doing, it was assumed that the cooperative Jahn–Teller effect is accompanied only by a deformation of the crystal in the basal plane and does not give rise to volume or tetragonal deformation. Although the indicated contribution is appreciably smaller than the first contribution by virtue of the hierarchy of magnetoelastic and elastic coefficients, we found that it nonetheless gives rise to the observed magnetoelastic effects. We note that a calculation of this contribution, proportional to the change in the quadrupole moment Q_0, requires going beyond the pseudospin formalism and taking into account all features of the crystal field. In our view, it is of interest to investigate analogous magnetoelastic effects also for other RE zircons exhibiting a cooperative Jahn–Teller effect, for example, $DyVO_4$, which exhibits a deformation below T_c having B_{1g} symmetry.

This work was supported in part by the Russian Fund for Fundamental Research (Grant 96-15-96429 in support of scientific schools).

[1] Z. A. Kazeĭ and N. P. Kolmakova, Zh. Éksp. Teor. Fiz. **109**, 1687 (1996) [J. Exp. Theor. Phys. **82**, 909 (1996)].
[2] P. Morin, J. Rouchy, and Z. Kazei, Phys. Rev. B **51**, 15103 (1995).
[3] G. A. Gehring and K. A. Gehring, Rep. Prog. Phys. **38**, 1 (1975).
[4] M.-D. Guo, A. T. Aldred, and S.-K. Chan, J. Phys. Chem. Solids **48**, 229 (1987).
[5] V. R. Pekurovskiĭ and S. I. Andronenko, Fiz. Tverd. Tela (Leningrad) **26**, 3440 (1984) [Sov. Phys. Solid State **26**, 2066 (1984)].
[6] T. Goto, A. Tamaki, T. Fujimura, and H. Unoki, J. Phys. Soc. Jpn. **55**, 1613 (1986).
[7] K. A. Gehring, A. P. Malozemoff, W. Staude, and R. N. Tyte, Solid State Commun. **9**, 511 (1971).
[8] M. R. Well and R. D. Worswick, Phys. Lett. A **42**, 269 (1972).
[9] P. Morin, J. Rouchy, and Z. Kazei, Phys. Rev. B **50**, 12 625 (1994).

Translated by M. E. Alferieff

Band structure and magnetic properties of $M_3M'C$ antiperovskites (M=Mn, Fe; M'=Zn, Al, Ga, Sn)

A. L. Ivanovskiĭ, R. F. Sabiryanov, and A. N. Skazkin

Institute of Solid-State Chemistry, Ural Branch of the Russian Academy of Sciences, 620219 Ekaterinburg, Russia

(Submitted February 3, 1998)
Fiz. Tverd. Tela (St. Petersburg) **40**, 1667–1670 (September 1998)

LMTO-ASA nonempirical self-consistent method has been used to study the electron band structure of the cubic antiperovskites $M_3M'C$ (M=Mn, Fe; M'=Zn, Al, Ga, Sn) in ferromagnetic state, and to calculate the local atomic magnetic moments. The results obtained are compared with previous calculations and available experimental data. © *1998 American Institute of Physics.* [S1063-7834(98)02209-6]

The ternary carbide phases $M_3M'C$ involving d metals of the VIIa and VIIIa subgroups (M) and nontransition elements of the IIb-VIb subgroups (M') of the Periodic Table have a simple antiperovskite-type cubic structure.[1] While being Pauli paramagnets at elevated temperatures, a number of perovskite-like carbides undergo tetragonal lattice distortions at low temperatures and exhibit magnetic properties, which suggest formation of several possible types of magnetic structures.[2–7]

The electronic and magnetic properties of some representatives of these ternary carbides were studied by quantum theory. A semiquantitative model of the $M_3M'C$ electronic spectrum suggests the presence in the density-of-states (DOS) distribution of a well-pronounced resonance near EF dominated by p-symmetry functions.[8] Numerical band-structure calculations were subsequently performed for some $Mn_3M'C$ antiperovskites (M'=Zn, Ga, In, Sn),[9–13] Mn_3AlC and Fe_3AlC (Ref. 14). The spin polarization effects were also considered for a number of crystals [Mn_3GaC (Refs. 9 and 13), Mn_3InC and Mn_3SnC (Ref. 12]. A systematic investigation of the energy-band structure, charge distributions, and the nature of interatomic interactions in ternary perovskite-like carbides of manganese and iron $M_3M'C$ (M=Mn, Fe; M'=Zn, Al, Ga, Sn) has recently been made within the self-consistent linear muffin-tin-orbital method in the atomic-sphere approximation (LMTO-ASA).[15] The crystals were assumed to be in the nonmagnetic (high-temperature) state. An analysis of the composition of the near-Fermi bands within the Stoner model showed that all the above carbides (with the exception of Fe_3SnC) can be stable ferromagnets.[15]

The present communication reports band-structure calculations of the $M_3M'C$ cubic antiperovskites (M=Mn, Fe; M'=Zn, Al, Ga, Sn) in ferromagnetic state made by the LMTO-ASA method. The structural constants and atomic-sphere radii were those used by us earlier[15] in the nonmagnetic calculations.

The results are displayed in Tables I and II and Figs. 1 and 2. We shall illustrate the electron density-of-states distributions obtained in these calculations by two phases, Fe and Mn aluminocarbides (Figs. 1 and 2), and compare them with the electronic energy spectrum (EES) of these compounds calculated[15] by the LMTO-ASA method in its nonmagnetic version. The fact that the component atoms of Fe_3AlC are confined within the same density-of-states (DOS) region (Fig. 2) argues for the formation of a common valence band, whose lower edge (within the interval from -0.61 to -0.36 Ry) is dominated by the C2p states with an admixture of the Al s,p,d and Fe 3d functions. The Al 3p,3d states form a subband ~ 0.21 Ry wide, and the near-Fermi region contains predominantly contributions due to the Fe 3s,4s states. The valence states of Mn_3AlC are arranged in a similar order in energy (Fig. 1), and the differences in the extent of some hybrid subbands are caused by the interatomic spacing increasing from 3.78 Å for Fe_3AlC to 3.86 Å for Mn_3AlC, which is in accord with the pertinent results obtained[15] in the nonmagnetic calculation. The electronic energy spectra of the other antiperovskites considered by us are also in agreement with nonmagnetic LMTO-ASA calculations (see Ref. 15 which analyzes in detail the main trends in the dependence of the spectrum of ternary carbides on composition of the M and M' sublattices).

As follows from Figs. 1 and 2, taking into account ferromagnetic ordering leads to energy splitting between the two spin subsystems; it is seen most clearly in the high-energy (near-Fermi) region of delocalized transition-metal states and is also responsible for the pronounced differences between ferromagnetic spin order and nonmagnetic states exhibited by their partial density-of-states distributions at the conduction-band bottom.[15]

Local atomic magnetic moments (LMM) for Mn_3GaC are compared in Table I with available calculations and experimental data on magnetic susceptibility[3] and are seen to be in good agreement. Table II lists LMMs for the component atoms of all the ternary antiperovskites considered here.

 © 1998 American Institute of Physics

TABLE I. Magnetic moments (in μ_B) on Mn_3GaC atoms in ferromagnetic state: calculation and experiment.

Mn	Ga	C	Method	
1.36	−0.061	−0.106	LMTO-ASA	(our calculation)
1.38	−0.008	−0.12	APW*	(Ref. 10)
1.39	–	–	LMTO-ASA	(Ref. 13)
1.3±0.1	–	–	Experiment	(Ref. 3)

*Augmented plane-wave approximation.

TABLE II. Magnetic moments (in μ_B) on atoms of $M_3M'C$ antiperovskites in ferromagnetic state: LMTO-ASA calculations.

Compound	Mn	M′	C	Compound	Fe	M′	C
Mn_3ZnC	1.163	−0.051	−0.054	Fe_3ZnC	0.943	−0.001	−0.003
Mn_3AlC	0.952	−0.044	−0.085	Fe_3AlC	0.156	−0.001	−0.002
Mn_3GaC	1.361	−0.061	−0.106	Fe_3GaC		Nonmagnetic	
				Fe_3SnC		Nonmagnetic	

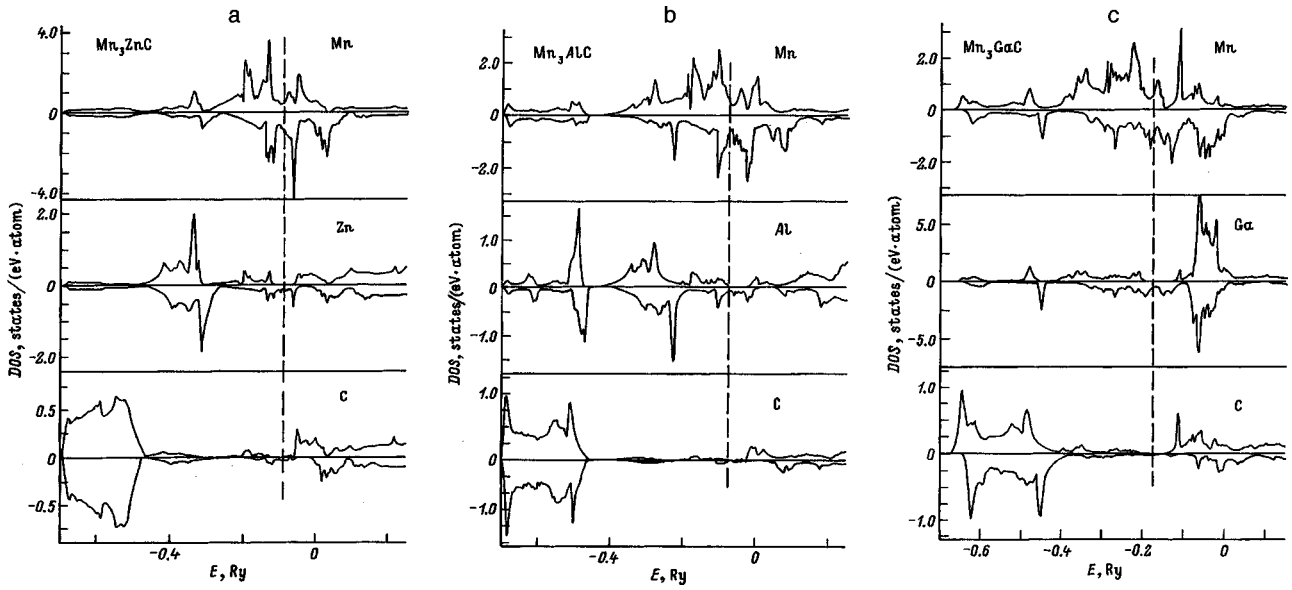

FIG. 1. Local densities of spin states of the cubic antiperovskites Mn_3ZnC, Mn_3AlC, and Mn_3GaC in ferromagnetic state.

We readily see that the LMMs vary within a broad range and cannot be interpreted in terms of the simplified rigid-band model[8] which includes only the degree of subband filling (i.e., electron concentration), and that the shape of the spin DOS distribution and the magnitude of LMMs are determined in each particular case by the actual type of outer wave-function hybridization of the centers making up the crystal.

It should be stressed that our calculations determine the ferromagnetic state of ideal cubic systems. The results obtained can be used as a basis for further nonempirical studies of possible transformations of the spin order, which can depend on the phase composition (the presence of inclusions and vacancies), crystal distortions [involved, e.g., in structural phase transitions occurring in a number of antiperovskites within certain temperature regions (see a review in Ref. 16)], be determined by competition in energy among various types of spin ordering, as well as respond to external factors (for instance, to thermal treatment or pressure).

Band-structure calculations of antiperovskite ternary carbides with various magnetic-order patterns are presently under way.

Support of the Russian Fund for Fundamental Research (Grant 96-03-32037) is gratefully acknowledged.

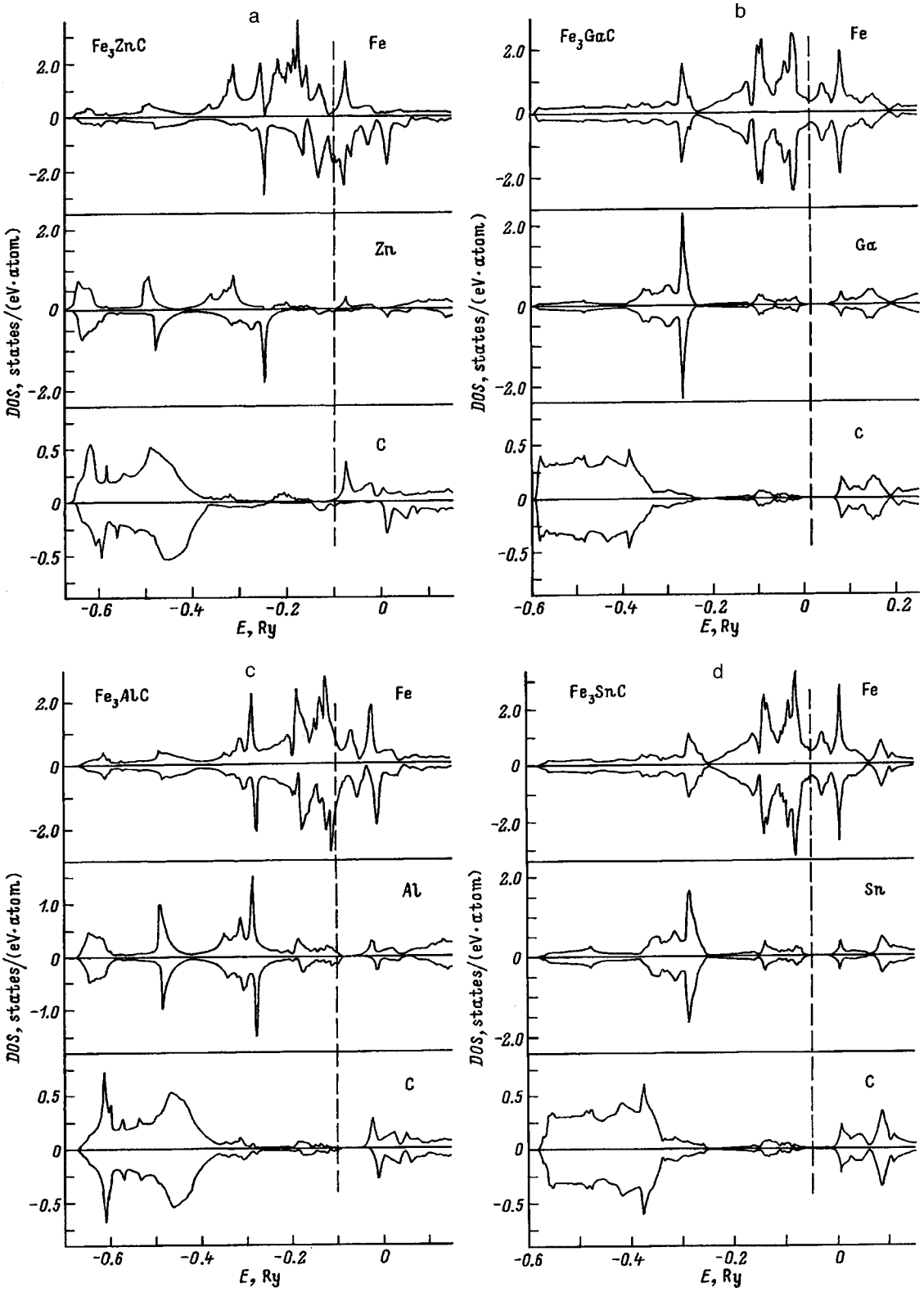

FIG. 2. Local densities of spin states of the cubic antiperovskites Fe_3ZnC, Fe_3AlC, Fe_3GaC, and Fe_3GaC, and Fe_3SnC in ferromagnetic state.

[1] H. J. Goldschmidt, in *Interstitial Alloys* [Butterworths, London, 1967; Mir, Moscow, 1971, Vol. 1, pp. 263–273].
[2] A. Kenmotsu, T. Shinohara, and H. Watanabe, J. Phys. Soc. Jpn. **32**, 377 (1972).
[3] D. Fruchart and E. F. Bertaut, J. Phys. Soc. Jpn. **44**, 781 (1978).
[4] D. Fruchart, E. F. Bertaut, F. Sayetat, M. NasrEddine, R. Fruchart, and J. Sénateur, Solid State Commun. **8**, 91 (1970).
[5] L. Khoi, E. Fruchart, and M. R. Fruchart, Solid State Commun. **8**, 49 (1972).
[6] T. Kaneko, T. Kanomata, and K. Shirakawa, J. Phys. Soc. Jpn. **56**, 4047 (1987).
[7] T. Kanomata, T. Kaneko, and Y. Nakagawa, J. Solid State Chem. **96**, 451 (1992).
[8] J. P. Jardin and J. Labbé, J. Solid State Chem. **46**, 275 (1983).

[9] K. Motizuki, H. Nagai, and T. Tanimoto, J. Phys. (Paris) **49**, C8-161 (1988).
[10] K. Motizuki and H. Nagai, J. Phys. C **21**, 5251 (1988).
[11] M. Shirai, Y. Ohata, N. Suzuki, and K. Motizuki, Jpn. J. Appl. Phys., Suppl. **32**, 32-3, 250 (1993).
[12] S. Ishida, S. Fujii, M. Maeda, and S. Asano, Jpn. J. Appl. Phys., Suppl. **32**, 32-3, 248 (1993).
[13] S. Ishida, S. Fujii, A. Swabe, and S. Asano, Jpn. J. Appl. Phys., Suppl. **32**, 32-3, 282 (1993).
[14] A. L. Ivanovskiĭ, I. S. Elfimov, A. N. Skazkin, V. M. Zhukovskiĭ, and G. P. Shveĭkin, Fiz. Tverd. Tela (St. Petersburg) **37**, 3738 (1995) [Phys. Solid State **37**, 2061 (1995)].
[15] A. L. Ivanovskiĭ, Zh. Neorg. Khim. **41**, 650 (1996).
[16] A. L. Ivanovskiĭ, A. I. Gusev, and G. P. Shveĭkin, *Quantum Chemistry in Materials Sciences: Ternary Carbides and Nitrides of Transition Metals and IIIb and IVb Elements* [in Russian], UrO RAN, Ekaterinburg (1996), 340 pp.

Translated by G. Skrebtsov

Magnetostriction of the spin–Peierls magnet $CuGeO_3$

G. A. Petrakovskiĭ and A. M. Vorotynov

L. V. Kirenskiĭ Institute of Physics, Siberian Branch of the Russian Academy of Sciences, 660036 Krasnoyarsk, Russia

H. Szymczak and L. Gladczuk

Institute of Physics, Polish Academy of Sciences, 02-668 Warsaw, Poland
(Submitted February 17, 1998)
Fiz. Tverd. Tela (St. Petersburg) **40**, 1671–1673 (September 1998)

The temperature dependence of the longitudinal magnetostriction of a $CuGeO_3$ single crystal is measured within the temperature range 4.2–20 K in a magnetic field of 10 T. As the temperature is raised above 4.2 K, the magnetostriction at first increases from vanishingly small values, attains a maximum at a temperature of approximately 12 K, and then abruptly drops as the temperature approaches the spin-Peierls transition. The results are interpreted on the basis of a simple model utilizing the real pattern of magnetic excitations in the spin system. © *1998 American Institute of Physics.* [S1063-7834(98)02309-0]

It has now been reliably established that the low-temperature decay of the magnetic susceptibility of an orthorhombic $CuGeO_3$ crystal is attributable, in large part at least, to the spin-Peierls phase transition of this magnet into a singlet dimerized state. This phenomenon essentially entails the capability of an antiferromagnetic chain of spins $S=1/2$ situated in a three-dimensional lattice to go over to the dimerized state at temperatures below a certain critical value. The transition is accompanied by doubling of the lattice period along the axis of the chain and, from the magnetic standpoint, is characterized by a singlet ground state. The spectrum of magnetic singlet-triplet excitations has a characteristic energy gap, which governs such salient features of the magnetic properties of a spin-Peierls magnet as low-temperature exponential decay of the magnetic susceptibility and the intensity of magnetic resonance, as well as the magnetization jumps at a certain critical value of the magnetic field.

These considerations spotlight the importance of investigating spin-phonon interactions in spin-Peierls systems.[1–4] The investigation of the magnetostriction of $CuGeO_3$ single crystals at various temperatures has shown that its temperature dependence is nonmonotonic and that the magnetostriction has a maximum at a temperature of approximately 10 K. We have proposed a simple model of this behavior of the magnetostriction of a spin-Peierls magnet.[4] Here we describe a more detailed measurement of the temperature dependence of the magnetostriction of a $CuGeO_3$ single crystal and submit a more correct analysis of the model for explaining the results.

1. EXPERIMENTAL RESULTS

The $CuGeO_3$ single crystals used for the measurements were grown by the technology described in Ref. 5. The samples were prepared from blue single crystals. Measurements of the magnetic susceptibility of the crystals have shown that the spin-Peierls transition temperature is $T_{sP}=14.2$ K and that a low-temperature rise of the susceptibility is not observed. The latter result attests to the high quality of the crystals.[6]

The magnetostriction was measured by a tensometric method using low-magnetoresistance strain gauges in the temperature range 4.2–25 K. The results are shown in Figs. 1 and 2. Curves *1* are plotted for cooling and subsequent heating of the sample without any external magnetic field; curves *2* are plotted for cooling and heating of the sample in an external magnetic field $H=10$ T. It follows from the data in the figures that when a magnetic field is applied, the sample increases in size, corresponding to positive longitudinal magnetostriction along the *c* and *b* axes of the crystal.

The magnetostriction-temperature curves *3* have been obtained by subtracting curve *1* from curve *2*. It is evident that the magnetostriction is small at temperatures below 5 K, increases as the temperature is raised, attains a maximum at $T=12-13$ K, and then drops to vanishingly small values at the spin-Peierls transition temperature. We note that a similar behavior of the temperature dependence of the magnetostriction of $CuGeO_3$ has been observed Ammerahl *et al.*[3]

2. DISCUSSION OF THE RESULTS

We have previously[4] proposed a simple model that can be used to explain the unusual behavior of the magnetostriction of a spin-Peierls magnet as a function of the temperature in comparison with conventional magnetic materials. This model is based on a very simple representation of the spin-Peierls state of a two-level singlet-triplet system. At $T=0$ K this kind of system is nonmagnetic, and the spin subsystem of the crystal does not influence the lattice. As the temperature is raised, the triplet states becomes populated, and the magnetic subsystem influences the equilibrium lattice strains by way of magnetostrictive coupling. It is obvious that the temperature dependence of this influence is associated with the population variation of the triplet states of

 © 1998 American Institute of Physics

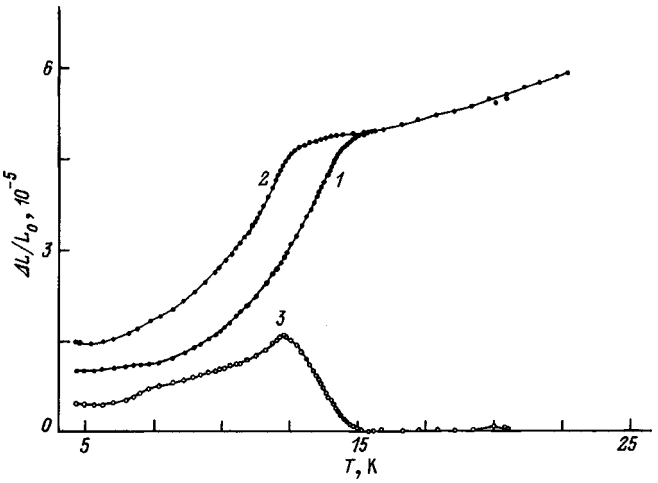

FIG. 1. Temperature dependence of the lattice strain of a $CuGeO_3$ crystal along the *b* axis. *1*) Magnetic field $H=0$; *2*) magnetic field $H=10$ T applied along the *b* axis; *3*) magnetostriction (obtained by subtracting curve *1* from curve *2*).

the system. The application of a magnetic field alters the singlet-triplet energy gap, causing the population of the triplet states and, hence, the ''magnetic'' contribution to the lattice strain to change. At high temperature, where the populations of the triplet and singlet states equalize, the influence of a magnetic field on the equilibrium lattice strains through vanishes by virtue of the decrease in the energy gap.

Neutron-diffraction examinations[7] have shown that magnetic excitations of the spin-Peierls system form a triplet band with maximum dispersion along the *c* axis of the crystal. Consequently, to analyze the spin-Peierls system more correctly, it is necessary to investigate the band of magnetic singlet excitations instead of the triplet excited level. Inasmuch as exchange interaction within the chain of spins of the Cu^{2+} ions of the $CuGeO_3$ crystal is an order of magnitude larger than exchange interactions between chains, we can consider only spin excitations along the *c* axis. The dispersion relation for such excitations can be written in the form[8]

$$w(k)^2=[\Delta^2+(w_M^2-\Delta^2)\sin^2(k)], \tag{1}$$

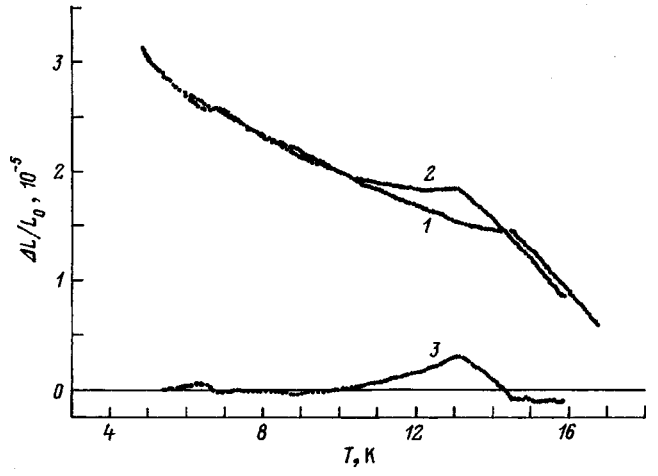

FIG. 2. The same as Fig. 1, but the strain and magnetic field are directed along the *c* axis.

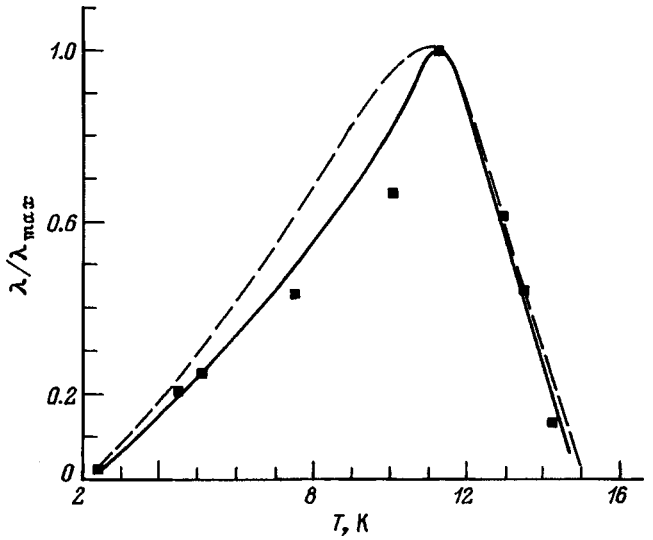

FIG. 3. Calculated and experimental graphs of the temperature dependence of the longitudinal magnetostriction. The dashed curve represents the calculated dependence, and the black squares represent the experimental results with the magnetic field along the *b* axis. The curves are normalized to the maximum values of the magnetostriction.

where Δ is the energy gap in the spectrum of singlet-triplet excitations, and w_M is the maximum value of the energy $w(k)$. The following values of the parameters were determined from the spectrum at low temperatures (1.8 K) in experiments on the inelastic scattering of neutrons by a $CuGeO_3$ crystal: $\Delta=23$ K; $w_M=180.5$ K (Ref. 8). Measurements in strong magnetic fields have shown that the energy gap Δ and the transition temperature T_{sP} of the system to the spin-Peierls state depend on the magnetic field.[9,10] The gap Δ decreases linearly as the magnetic field H increases: $\Delta=23[1-0.077H]$ (Δ in kelvins, and H in teslas). The temperature T_{sP} also decreases as the field increases and is equal to 12.5 K in a field of 10 T. It is also important to bear in mind the strong temperature and pressure dependence of Δ (Refs. 8 and 10).

We analyze the temperature dependence of the magnetostriction of the spin-Peierls magnet on the basis of an investigation of the strain dependence of the internal energy:

$$U=U_{\rm el}+U_{\rm mag}=\frac{1}{2}Eu^2+\frac{2v_0^{-1}}{(2\pi)^3}\int_0^{\pi/2}\frac{w(k)d^3k}{e^{w(k)/T}-1}, \tag{2}$$

where E is Young's modulus, u is the strain of the crystal, and $v_0=abc$. The minimization of the energy (2) with respect to the strain u gives its equilibrium value for a fixed energy gap Δ. The difference in the equilibrium strains for different values of Δ with and without an external magnetic field H determines the temperature and magnetic-field dependence of the magnetostriction. Bearing in mind the experimentally measured temperature and field dependences of Δ, we have used a numerical method to find the temperature dependence of the magnetostriction, which is represented by the dashed curve in Fig. 3. Also shown in this figure is the experimentally measured temperature dependence of the magnetostriction when the magnetic field is directed along the *b* axis. All the results are given in values normalized to

the maximum magnetostriction. In the calculations it has been assumed that the governing magnetostriction mechanism is the strain dependence of Δ. The temperature dependence of w_M is not taken into account. Satisfactory agreement is observed between the calculations and experiment. Qualitative agreement is preserved for a field directed along the c axis of the crystal but, at temperatures below the temperature of the maximum, the experimental temperature dependence of the magnetostriction is sharper.

The qualitative agreement of the magnetostriction-temperature curves calculated on the basis of the proposed model and determined experimentally indicates that the proposed magnetostriction mechanism based on a strong dependence of the energy gap Δ on the lattice strain and on the magnetic field, on the one hand, and based on the Δ dependence of population of the band of triplet states, on the other, is the principal mechanism in the region of the spin-Peierls magnetic state of a $CuGeO_3$ magnet. The root cause of magnetostriction is the strain dependence of the exchange interactions. Anisotropy of the magnetostriction is induced both by the elastic anisotropy of the crystal and by the complex influence of various strains on the exchange interactions. One possible cause of the imperfect correspondence between the calculated and experimentally measured temperature dependences of the magnetostriction is the disregard of the temperature dependence of the spectral bandwidth of magnetic singlet-triplet excitations.

The mechanism underlying the evolution of antiferromagnetic exchange interaction in the chains of Cu^{2+} spins of $CuGeO_3$ is not entirely clear at the present time. For example, Geertsma and Khomskii[11] have proposed an explanation of why the Goodenough–Kanamori rules are violated in terms of the influence of Ge^{4+}–O^{2-} side groups on 90° Cu^{2+}–O^{2-}–Cu^{2+} exchange. On the other hand, it has been shown[12] that marked distortion of the CuO_6 oxygen octahedra under certain conditions can generate an orbital superlattice and, in keeping with the Goodenough-Kanamori rules, produce antiferromagnetic exchange interaction in the chains of copper ions. There is a need for more precise calculations from first principles of exchange interactions to quantitatively account for the results of measurements of exchange and magnetoelastic interactions in $CuGeO_3$.

This work has received support from the Krasnoyarsk Regional Science Foundation (Grant No. 6F0004).

[1] K. Takehana, M. Oshikiri, G. Kido, M. Hase, and K. Uchinokura, J. Phys. Soc. Jpn. **65**, 2783 (1996).
[2] L. Gladczuk, I. Krynetskii, G. Petrakovskii, K. Sablina, H. Szymczak, and A. Vorotinov, J. Magn. Magn. Mater. **168**, 316 (1997).
[3] U. Ammerahl, T. Lorenz, B. Buchner, A. Revcolevschi, and G. Dhalenne, Z. Phys. B **102**, 71 (1997).
[4] G. Petrakovskii, K. Sablina, A. Vorotinov, I. Krynetskii, A. Bogdanov, H. Szymczak, and L. Gladczuk, Solid State Commun. **101**, 545 (1997).
[5] G. A. Petrakovskiĭ, K. A. Sablina, A. M. Vorotynov, A. I. Kruglik, A. G. Klimenko, A. D. Balaev, and S. S. Aplesnin, Zh. Éksp. Teor. Fiz. **98**, 1382 (1990) [Sov. Phys. JETP **71**, 772 (1990)].
[6] G. A. Petrakovskiĭ, A. I. Pankrats, K. A. Sablina, A. M. Vorotynov, D. A. Velikanov, A. D. Vasil'ev, H. Szymczak, and S. Kolesnik, Fiz. Tverd. Tela (St. Petersburg) **38**, 1857 (1996) [Phys. Solid State **38**, 1025 (1996)].
[7] M. Nishi, O. Fujita, and J. Akimitsu, Phys. Rev. B **50**, 6508 (1994).
[8] L. P. Regnault, M. Ain, B. Hennion, G. Dhalenne, and A. Revcolevschi, Phys. Rev. B **53**, 5579 (1996).
[9] M. Hase, I. Terasaki, and K. Ushinokura, Phys. Rev. B **48**, 9616 (1993).
[10] M. Nishi, O. Fujita, J. Akimitsu, K. Karurai, and Y. Fujii, Phys. Rev. B **52**, 6959 (1995).
[11] W. Geertsma and D. Khomskii, Phys. Rev. B **54**, 3011 (1996).
[12] O. A. Bayukov, G. A. Petrakovskiĭ, and A. F. Savitskiĭ, Fiz. Tverd. Tela (St. Petersburg) **41**, 1686 (1998) [Phys. Solid State **41**, 1530 (1998)].

Translated by James S. Wood

Quantum temperature fluctuations in the magnetization of antiferromagnetic semimetals

V. V. Val'kov and D. M. Dzebisashvili

L. V. Kirenskii Institute of Physics, Siberian Branch, Russian Academy of Sciences, 660036 Krasnoyarsk, Russia; Krasnoyarsk State University, 660036 Krasnoyarsk, Russia

(Submitted February 17, 1998)
Fiz. Tverd. Tela (St. Petersburg) **40**, 1674–1680 (September 1998)

It is shown that in semimetallic, low-temperature antiferromagnetic materials located in a quantizing magnetic field, the part of the band magnetization $M_{\sim}$ which oscillates in H can have a nonmonotonic temperature dependence. This non-Fermi liquid behavior will show up experimentally in the form of quantum temperature fluctuations of the magnetization when the decrease with rising temperature is oscillatory, rather than the usual monotonic decrease. It is shown that the magnetization from an individual spin electron (or hole) subband has the form of weakly damped periodic oscillations as a function of T^2. This result makes it possible to develop an efficient method for studying the electronic structure of antiferromagnetic semimetals based on an examination of the quantum temperature fluctuations. Calculations show that quantum temperature fluctuations can be observed, for example, in the cerium monopnictides CeP and CeAs, which are strongly correlated, antiferromagnetic, compensated semimetals with low Neel temperatures. © *1998 American Institute of Physics.* [S1063-7834(98)02409-5]

Studies of the electronic structure of strongly correlated systems have stimulated experimental studies of the de Haas-van Alphen effect in compounds with mixed valence, heavy fermions,[1–3] and high-temperature superconductors.[4,5] The class of strongly correlated systems includes compounds with a low current-carrier concentration. The cerium monopnictides CeX, with X=Sb, Bi, As, and P are striking representatives of this type of compound.[6–8] The presence of a long-range antiferromagnetic order in these compounds has led to the creation of the concept of magnetopolaron liquids and crystals[9] for describing the ground state of the electronic system. This has made it possible to explain the features of the de Haas-van Alphen effect in CeAs.[10]

In addition to the ordinary de Haas-van Alphen effect, which involves a fluctuating magnetic field dependence of the magnetization of band charge carriers, experimental studies have recently been made[11] of a new type of fluctuations in the magnetization. These involve a nonmonotonic variation in the magnetization as the temperature is changed. They have been referred to, therefore, as quantum temperature fluctuations. The degenerate magnetic semiconductor n-$HgCr_2X_4$ has been chosen for testing. A theoretical analysis[12] of quantum temperature fluctuations showed that the major factors determining the possibility of observing quantum temperature fluctuations are the existence of strong single-site correlations, magnetic ordering, and $s-d$ coupling between localized and collectivized electrons. The principal sources of the motion of the Landau levels, as the temperature is varied, were the $s-d$-exchange interaction, along with a change in the average magnetization. Since the Curie temperature is quite high ($T_c=130$ K), it was not possible to observe many spikes in the magnetization (before the fluctuations were damped out).

Quantum temperature fluctuations are evidently best observed using materials with low magnetic ordering temperatures ($T_c \sim 1-10$ K). Then the reduction in the spontaneous magnetization will be fairly strong over a small temperature interval and the number of spikes in the quantum temperature fluctuations will be large. In this regard, the cerium monopnictides are extremely promising. For them $T_N \simeq 7$ K and the de Haas-van Alphen effect shows up quite well. Since these compounds have an antiferromagnetic order, and the antiferromagnetic sublattices become tapered in strong magnetic fields, there is some interest in analyzing the quantum temperature fluctuations in the antiferromagnetic semimetals taking this tapering into account.

In this paper we examine the quantum temperature fluctuations in the magnetization of antiferromagnetic materials theoretically under conditions such that the quantizing magnetic field causes a reordering of the ground state. Taking the strong tapering of the antiferromagnetic sublattices into account in a spin-wave approximation, we study the low-temperature thermodynamics of a localized subsystem and determine the dependence of the magnetic-order parameters on the magnetic field and temperature. It is shown that, even at the low temperatures where the spin-wave approximation is justified, a change in the temperature leads to a large number of spikes in the fluctuating magnetization of the band electrons. The contributions from individual electron- and hole-spin subbands to the quantum temperature fluctuations are analyzed and it is found that these contributions are weakly damped functions periodic in T^2. This makes it possible to use Fourier analysis to study quantum temperature fluctuations and to develop an effective technique for testing the electronic structure of antiferromagnetic semimetals.

1. MODEL HAMILTONIAN AND SPECTRUM OF FERMI QUASIPARTICLES

Before considering quantum temperature fluctuations in antiferromagnetic semimetals such as CeP, CeAs, and CeSb,

 © 1998 American Institute of Physics

let us recall the general properties of their electronic structure. The cerium monopnictides have an NaCl cubic structure. Low-energy states of the conduction band lie as the X points of the Brillouin zone. The top of the valence band lies at the Γ point. A slight overlap of these bands is responsible for the semimetallic properties of these compounds. At low temperatures ($T_N=7$ and 10.5 K for CeAs and CeP, respectively), a long-range antiferromagnetic order develops in the subsystem of localized electronic states. The antiferromagnetic sublattices undergo tapering in the presence of a magnetic field H, influencing the energy spectrum of the current carriers through an interaction between the electrons in localized and collectivized states. The major features of these interactions are modelled by the following hamiltonian for an antiferromagnetic semimetal:

$$\begin{aligned}\mathscr{H}=&\sum_{\lambda ff'\sigma}\{t^{\lambda}_{ff'}-\delta_{ff'}(2\sigma\mu_{\mathrm{B}}H+\mu_{\lambda})\}c^{+}_{\lambda f\sigma}c_{\lambda f'\sigma}\\&+\sum_{\lambda gg'\sigma}\{t^{\lambda}_{gg'}-\delta_{ggf'}(2\sigma\mu_{\mathrm{B}}H+\mu_{\lambda})\}c^{+}_{\lambda g\sigma}c_{\lambda g'\sigma}\\&+\sum_{\lambda fg\sigma}f^{\lambda}_{fg}(c^{+}_{\lambda f\sigma}d_{\lambda g\sigma}+d^{+}_{\lambda g\sigma}c_{\lambda f\sigma})+\sum_{fg}K_{fg}(\mathbf{S}_f\mathbf{S}_g)\\&-\frac{1}{2}\sum_{ff'}I_{ff'}(\mathbf{S}_f\mathbf{S}_{f'})-\frac{1}{2}\sum_{gg'}I_{ggf'}(\mathbf{S}_g\mathbf{S}_{g'})\\&-\sum_{f}g\mu_{\mathrm{B}}HS^{z}_{f}-\sum_{g}g\mu_{\mathrm{B}}HS^{z}_{g}-\sum_{f\lambda}J_{\lambda}(\mathbf{S}_f\boldsymbol{\sigma}_{f\lambda})\\&-\sum_{g\lambda}J_{\lambda}(\mathbf{S}_g\boldsymbol{\sigma}_{g\lambda}).\end{aligned}\tag{1}$$

Here the first three terms describe the free-electron-hole subsystem in the Wannier representation. To describe effects associated with the antiferromagnetic order in the localized subsystem, one performs the conventional separation into two sublattices, F and G. The Fermi operator $c_{\lambda f\sigma}$ annihilates an electron for $\lambda=e$ or hole for $\lambda=h$ at site f with projection σ ($\sigma=\pm 1/2$) of the spin angular momentum. The operator $d_{\lambda g\sigma}$ corresponds to the same kind of process, but for site g from the sublattice G. For electrons $\mu_e=\mu$ and for holes $\mu_h=-\mu$. The next group of operators in Eq. (1) describes the Heisenberg interaction among the spin angular momenta of the localized electronic states, which brings about an antiferromagnetic order, as well as an interaction of the spin angular momenta with the magnetic field H. Here we have included both the interaction within the sublattices and the interaction among spin angular momenta from the F and G sublattices. Finally, the last two terms account for the $s-f$ exchange coupling among the spin angular momenta of the localized and collectivized states.

The energy spectrum of the electrons and holes in the tapered antiferromagnetic phase is conveniently found by first going to local coordinate systems for the F and G sublattices. The procedure for transforming to local coordinates and obtaining the electron and hole spectra in the noncollinear geometry of this problem has been described in detail elsewhere.[13] Thus, here we only give the final expression for the lower branches of the spectrum for the electrons ($\lambda=e$) and holes ($\lambda=h$),

$$\begin{aligned}E^{\lambda}_{\mp}(\mathbf{k})=&\varepsilon^{\lambda}+t_{\mathbf{k}}-\left\{\left[\Gamma^{\lambda}_{\mathbf{k}}\mp\left(\mu_{\mathbf{B}}H+\cos\,\theta\,\frac{J_{\lambda}R}{2}\right)\right]^2\right.\\&\left.+\sin^2\,\theta\left(\frac{J_{\lambda}R}{2}\right)^2\right\}^{1/2},\end{aligned}\tag{2}$$

where

$$\varepsilon^{\lambda}=t^{\lambda}_{\mathbf{k}}=\sum_{f'}\,t^{\lambda}_{ff'}\,\exp\{-i\mathbf{k}(\mathbf{R}_f-\mathbf{R}_{f'})\},$$

$$\Gamma^{\lambda}_{\mathbf{k}}=\sum_{g}\,t^{\lambda}_{fg}\,\exp\{-i\mathbf{k}(\mathbf{R}_f-\mathbf{R}_g)\}.$$

The angle θ defines the orientation $\mathbf{R}$ of the equilibrium magnetization of the sublattice relative to the z axis along which the external magnetic field H is directed. For $H=0$, $\theta=\pi/2$, while at the spin-flip transition point $\theta=0$. We are interested in the fairly high magnetic fields when the tapering of the antiferromagnetic sublattices is large ($\theta\geqslant\pi/4$). In this case, the lower energy states have energies given by the simpler expressions

$$\begin{aligned}E^{e}_{\mp}(\mathbf{k})=&\mp\left(\mu_{\mathrm{B}}H+\cos\,\theta\,\frac{J_eR}{2}\right)+\frac{\hbar^2\mathbf{k}^2}{2m_e},\\E^{h}_{\mp}(\mathbf{k})=&-\Delta\mp\left(\mu_{\mathrm{B}}H+\cos\,\theta\,\frac{J_hR}{2}\right)+\frac{\hbar^2\mathbf{k}^2}{2m_h},\end{aligned}\tag{3}$$

in which the effective masses are related to the jump parameters by the following equations

$$\frac{\hbar^2}{2m_{\lambda}}=-\frac{1}{6}\left\{\sum_{g}\,t^{\lambda}_{fg}(\mathbf{R}_f-\mathbf{R}_g)^2+\sum_{f'}\,t^{\lambda}_{ff'}(\mathbf{R}_f-\mathbf{R}_g)^2\right\}.\tag{4}$$

Here the cubic structure of the lattice is taken into account. In Eq. (3), the choice of reference scale for the energy is such that, in the paramagnetic phase with $H=0$, the bottom of the conduction band corresponds to zero energy. Then the degree of overlap of the valence band with the conduction band is determined by the parameter $\Delta>0$. In order to determine the temperature dependence of this energy spectrum it is necessary to study the low-temperature thermodynamics of this system and to calculate the temperature dependence of $R\cos\,\theta$ in a noncolinear geometry.

2. TEMPERATURE EVOLUTION OF THE SUBLATTICE MAGNETIZATION

The parameters which determine the magnetic structure of the localized subsystem (R and $\cos\,\theta$) can be calculated in our case using an exchange hamiltonian. In local coordinates this hamiltonian is obtained by rotation through an angle θ for the F sublattice and by an angle $-\theta$ for the G sublattice. Then (for details, see Ref. 13),

$$H_{mz}=-\frac{1}{2}\sum_{ff'} I_{ff'}(\mathbf{S}_f\mathbf{S}_{f'})-\frac{1}{2}\sum_{gg'} I_{gg'}(\mathbf{S}_g\mathbf{S}_{g'})$$
$$+\sum_{fg} K_{fg}\{\cos 2\theta(S_f^xS_g^x+S_f^zS_g^z)$$
$$+S_f^yS_g^y+\sin 2\theta(S_f^zS_g^z-S_f^xS_g^z)\}$$
$$-g\mu_{\mathrm{B}}H\cos\theta\left(\sum_f S_f^z+\sum_g S_g^z\right)$$
$$+g\mu_{\mathrm{B}}H\sin\theta\left(\sum_f S_f^x-\sum_g S_g^x\right). \quad (5)$$

For examining the low-temperature thermodynamics in the localized subsystem we use the Dyson–Maleev representation,

$$S_f^+=\sqrt{2S}(a_f-a_f^+a_fa_f),\quad S_f^-=\sqrt{2S}a_f^+,$$
$$S_f^z=S-a_f^+a_f,\quad S_g^+=\sqrt{2S}(b_g-b_g^+b_gb_g),$$
$$S_g^-=\sqrt{2S}b_g^+,\quad S_g^z=S-b_g^+b_g, \quad (6)$$

where a_f (a_f^+) are the annihilation (creation) operators for excitation at site f for sublattice F. For the G sublattice the corresponding operators are denoted by b_g (b_g^+).

Substituting Eqs. (6) in the Hamiltonian (5), taking the Fourier transform, and proceeding as usual,[14] we obtain the Hamiltonian in the second quantization representation. The quadratic form is given by

$$H_{mz}^{(2)}=\sum_{\mathbf{q}}\{\varepsilon_{\mathbf{q}}(a_{\mathbf{q}}^+a_{\mathbf{q}}+b_{\mathbf{q}}^+b_{\mathbf{q}})+\nu_q(a_{\mathbf{q}}^+b_{\mathbf{q}}+b_{\mathbf{q}}^+a_{\mathbf{q}})$$
$$+\xi_{\mathbf{q}}(a_{\mathbf{q}}^+b_{-\mathbf{q}}^++b_{-\mathbf{q}}a_{\mathbf{q}})\}, \quad (7)$$

where we have introduced the following notation;

$$\varepsilon_{\mathbf{q}}=g\mu_{\mathrm{B}}H\cos\theta-SK_0\cos 2\theta+S(I_0-I_{\mathbf{q}}),$$
$$\nu_{\mathbf{q}}=SK_{\mathbf{q}}\cos^2\theta,\quad \xi_{\mathbf{q}}=-SK_{\mathbf{q}}\sin^2\theta. \quad (8)$$

Here the Fourier transforms of the exchange integrals are given in the form

$$K_{\mathbf{q}}=\sum_g K_{fg}\exp\{-i\mathbf{q}(\mathbf{R}_f-\mathbf{R}_g)\},$$

$$I_{\mathbf{q}}=\sum_{f'} I_{ff'}\exp\{-i\mathbf{q}(\mathbf{R}_f-\mathbf{R}_{f'})\}.$$

In order to write down the Hamiltonian in the $a_{\mathbf{q}}$, $a_{\mathbf{q}}^+$, $b_{\mathbf{q}}$ and $b_{\mathbf{q}}^+$ operator representation, we equate the terms in first order in these operators to zero and obtain a condition for the equilibrium angle θ,

$$\cos\theta=q\mu_{\mathrm{B}}H/2SK_0. \quad (9)$$

To find the equilibrium magnetization

$$R=\frac{1}{N}\sum_g\langle S_g^z\rangle=S-\frac{1}{N}\sum_{\mathbf{q}}\langle b_{\mathbf{q}}^+b_{\mathbf{q}}\rangle \quad (10)$$

we use the ideology of the two-time temperature Green functions.[14,15] For this purpose, we introduce the following four functions into the discussion:

$$\langle\langle b_{\mathbf{q}}(t)|b_{\mathbf{q}}^+(t')\rangle\rangle,\quad \langle\langle a_{\mathbf{q}}(t)|b_{\mathbf{q}}^+(t')\rangle\rangle,$$
$$\langle\langle b_{-\mathbf{q}}^+(t)|b_{\mathbf{q}}^+(t')\rangle\rangle,\quad \langle\langle a_{-\mathbf{q}}^+(t)|b_{\mathbf{q}}^+(t')\rangle\rangle.$$

A closed system of equations for the Fourier transforms of these functions can be written in the form

$$(\omega-\varepsilon_{\mathbf{q}})\langle\langle b_{\mathbf{q}}|b_{\mathbf{q}}^+\rangle\rangle_\omega=1+\nu_{\mathbf{q}}\langle\langle a_{\mathbf{q}}|b_{\mathbf{q}}^+\rangle\rangle_\omega+\xi_{\mathbf{q}}\langle\langle a_{-\mathbf{q}}^+|b_{\mathbf{q}}^+\rangle\rangle_\omega,$$
$$(\omega-\varepsilon_{\mathbf{q}})\langle\langle a_{\mathbf{q}}|b_{\mathbf{q}}^+\rangle\rangle_\omega=\nu_{\mathbf{q}}\langle\langle b_{\mathbf{q}}|b_{\mathbf{q}}^+\rangle\rangle_\omega+\xi_{\mathbf{q}}\langle\langle b_{-\mathbf{q}}^+|b_{\mathbf{q}}^+\rangle\rangle_\omega,$$
$$(\omega+\varepsilon_{\mathbf{q}})\langle\langle b_{-\mathbf{q}}^+|b_{\mathbf{q}}^+\rangle\rangle_\omega=-\nu_{\mathbf{q}}\langle\langle a_{-\mathbf{q}}^+|b_{\mathbf{q}}^+\rangle\rangle_\omega-\xi_{\mathbf{q}}\langle\langle a_{\mathbf{q}}|b_{\mathbf{q}}^+\rangle\rangle_\omega,$$
$$(\omega+\varepsilon_{\mathbf{q}})\langle\langle a_{-\mathbf{q}}^+|b_{\mathbf{q}}^+\rangle\rangle_\omega=-\nu_{\mathbf{q}}\langle\langle b_{-\mathbf{q}}^+|b_{\mathbf{q}}^+\rangle\rangle_\omega-\xi_{\mathbf{q}}\langle\langle b_{\mathbf{q}}|b_{\mathbf{q}}^+\rangle\rangle_\omega. \quad (11)$$

From this system we obtain a dispersion equation for the energy spectrum of the elementary excitations,

$$\begin{vmatrix}\omega-\varepsilon_{\mathbf{q}} & -\nu_{\mathbf{q}} & -\xi_{\mathbf{q}} & 0\\ -\nu_{\mathbf{q}} & \omega-\varepsilon_{\mathbf{q}} & 0 & -\xi_{\mathbf{q}}\\ \xi_{\mathbf{q}} & 0 & \omega+\varepsilon_{\mathbf{q}} & \nu_{\mathbf{q}}\\ 0 & \xi_{\mathbf{q}} & \nu_{\mathbf{q}} & \omega+\varepsilon_{\mathbf{q}}\end{vmatrix}=0. \quad (12)$$

On solving Eq. (12), we find two branches of the energy spectrum,

$$\omega_1(\mathbf{q})=\sqrt{(\varepsilon_{\mathbf{q}}-\nu_{\mathbf{q}})^2-\xi_{\mathbf{q}}^2},$$
$$\omega_2(\mathbf{q})=\sqrt{(\varepsilon_{\mathbf{q}}+\nu_{\mathbf{q}})^2-\xi_{\mathbf{q}}^2}. \quad (13)$$

Given Eqs. (8) and (9), the expressions for the spectrum in the noncollinear phase, where $\theta>0$, can be written in the form

$$\omega_1(\mathbf{q})=S\{(I_0-I_{\mathbf{q}}+K_0-K_{\mathbf{q}})(I_0-I_{\mathbf{q}}+K_0-K_{\mathbf{q}}\cos 2\theta)\}^{1/2},$$
$$\omega_2(\mathbf{q})=S\{(I_0-I_{\mathbf{q}}+K_0+K_{\mathbf{q}})(I_0-I_q+K_0+K_{\mathbf{q}}\cos 2\theta)\}^{1/2}. \quad (14)$$

It is clear that the lower branch is gapless, consistent with the Goldstone theory. The exchange Hamiltonian is invariant with respect to rotation by an arbitrary angle about the z axis, while the ground state of the system in the tapered phase does not have this invariance. This explains the presence of the Goldstone boson in the system.

The second branch of the spectrum has an activation character. The energy gap for this branch is given by

$$\Delta=\omega_1(0)=2SK_0\cos\theta=g\mu_{\mathrm{B}}H. \quad (15)$$

In the right-hand neighborhood of the spin-flip transition, when $\theta=0$ and the subsystem of localized spins undergoes a transformation to the colinear phase, the two branches of the spectrum obey

$$\omega_{1,2}(\mathbf{q})=g\mu_{\mathrm{B}}H+S(I_0-I_{\mathbf{q}})-S(K_0\pm K_{\mathbf{q}}). \quad (16)$$

Solving the system of Eqs. (11), we find the Green function

$$\langle\langle b_{\mathbf{q}}|b_{\mathbf{q}}^+\rangle\rangle_\omega=\frac{[(\omega+\varepsilon_{\mathbf{q}})^2-\nu_{\mathbf{q}}^2](\omega-\varepsilon_{\mathbf{q}})+\xi_q^2(\omega+\varepsilon_{\mathbf{q}})}{[\omega^2-\omega_1^2(\mathbf{q})][\omega^2-\omega_2^2(\mathbf{q})]}, \quad (17)$$

which allows us to obtain the desired expression for the equilibrium magnetization,

$$R = S - \delta S(0) - \delta S(T), \tag{18}$$

where $S(0)$ is a term which reduces the magnetization owing to the zero-point quantum fluctuations, with

$$\delta S(0) = \frac{1}{2} - \frac{1}{4N} \sum_{\mathbf{q}} \left\{ \frac{\varepsilon_{\mathbf{q}} - \nu_{\mathbf{q}}}{\omega_1(\mathbf{q})} + \frac{\varepsilon_{\mathbf{q}} + \nu_{\mathbf{q}}}{\omega_2(\mathbf{q})} \right\}. \tag{19}$$

The temperature reduction in the magnetization is given by

$$\delta S(T) = \frac{1}{2N} \sum_{\mathbf{q}} \left\{ \frac{\varepsilon_{\mathbf{q}} - \nu_{\mathbf{q}}}{\omega_1(\mathbf{q})} n_{1\mathbf{q}} + \frac{\varepsilon_{\mathbf{q}} + \nu_{\mathbf{q}}}{\omega_2(\mathbf{q})} n_{2\mathbf{q}} \right\}, \tag{20}$$

where

$$n_{i\mathbf{q}} = \{\exp\{\omega_i(\mathbf{q})/T\} - 1\}^{-1}, \quad i = 1, 2.$$

These equations will be used to study the temperature dependence of the band magnetization in a quantizing magnetic field.

3. QUANTUM TEMPERATURE FLUCTUATIONS

Landau quantization takes place in a strong magnetic field.[16] In order to find the thermodynamic potential of the electrons and holes, whose spectrum is given by Eq. (3), it is sufficient to transform to the Landau representation and sum over the quantum numbers of this representation.[17,18] Then the fluctuating part of the magnetization from the collectivized electrons is given by

$$M_{\sim}^{e} = -\frac{T\sqrt{\hbar\omega_c^e}(m_e)^{3/2}}{2\pi\hbar^3 H} \sum_{\sigma} \tilde{\mu}_{e\sigma} \times \sum_{n=1}^{\infty} \frac{(-1)^n}{\sqrt{n}} \frac{\sin\{2\pi n \tilde{\mu}_{e\sigma}/\hbar\omega_c^e + \phi_{e\sigma}\}}{\sinh\{2\pi^2 nT/\hbar\omega_c^e\}}, \tag{21}$$

where

$$\phi_{e\sigma} = 2\pi\sigma m_e/m_0 - \pi/4,$$

m_0 is the free-electron mass, and $\omega_c^e = eH/m_e c$ is the cyclotron frequency for the conduction electrons. The important feature of this expression for $M_{\sim}^{e}$ is that, instead of a chemical potential that depends weakly on the temperature and magnetic field in the ordinary Fermi-liquid case, Eq. (21) includes the renormalized chemical potential

$$\tilde{\mu}_{e\sigma} = \mu + \sigma(2\mu_{\mathrm{B}}H + J_e R\cos\theta), \tag{22}$$

which, because of the term $\propto R\cos\theta$, can vary rather strongly as the temperature and magnetic field are changed, if the $s-f$-exchange interaction parameter is sizeable. The strong T dependence of $\tilde{\mu}_{e\sigma}$, therefore, lies at the basis of the quantum temperature fluctuation phenomenon in these antiferromagnetic semimetals. Before proceeding to a direct analysis of the quantum temperature fluctuations, we note that the contribution of the holes to the fluctuating part of the magnetization is given by an expression analogous to Eq. (21), with the subscript e for the electrons replaced by h. Then,

$$\tilde{\mu}_{h\sigma} = -\mu + \Delta + \sigma(2\mu_{\mathrm{B}}H + J_h R\cos\theta). \tag{23}$$

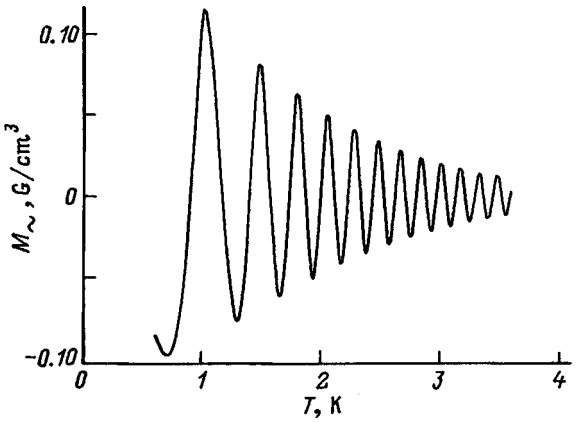

FIG. 1. Quantum temperature fluctuations of an antiferromagnetic semimetal. One electron and one hole subband are populated.

For low current-carrier concentrations and relatively large splitting of the electron- and hole-spin subbands, Fermi quasiparticles lie within the confines of spin subbands with a single spin polarization. This situation occurs when the following inequalities are satisfied:

$$n < \frac{4}{3}\frac{(m_e\Delta_e)^{3/2}}{\pi^2\hbar^3}, \quad n < \frac{4}{3}\frac{(m_h\Delta_h)^{3/2}}{\pi^2\hbar^3}, \tag{24}$$

where n is the concentration of electrons (and holes) per unit volume and

$$\Delta_e = \left| \mu_{\mathrm{B}}H + \frac{1}{2} J_e R\cos\theta \right|,$$

$$\Delta_h = \left| \mu_{\mathrm{B}}H + \frac{1}{2} J_h R\cos\theta \right|. \tag{25}$$

From the condition of electrical neutrality in the main approximation, we obtain

$$\tilde{\mu}_e = \frac{m_h}{m_e + m_h}\Delta_{eh}, \quad \tilde{\mu}_h = \frac{m_e}{m_e + m_h}\Delta_{eh},$$

$$\Delta_{eh} = \Delta + \frac{R\cos\theta}{2}(|J_e| + |J_h|) + \mu_{\mathrm{B}}H(\mathrm{sign}(J_e) + \mathrm{sign}(J_h)). \tag{26}$$

The above expressions for the Fermi energies of the electrons and holes determine their strong temperature and field dependences. Here the absolute changes in these quantities depend, in particular, on the ratio of their effective masses. Thus, for example, in the case of heavy holes, for which $m_h \gg m_e$, only the electron Fermi energy can change significantly. In this case, the quantum temperature fluctuations will be determined only by the conduction-electron subsystem.

For concrete calculations, we shall use Eqs. (9), (17)–(20), and (23). Figure 1 shows the results of a numerical calculation of the quantum temperature fluctuations for an antiferromagnetic semimetal with equivalent electron and hole bands. Here the following system parameters were used: $J_e = J_h = 0.2$ eV, $m_e = m_h = m_0$, and $T_N = 10$ K. The concentration of band carriers corresponded to the semimetal case and equalled 0.035 per lattice site. $M_{\sim}(T)$ was calculated for

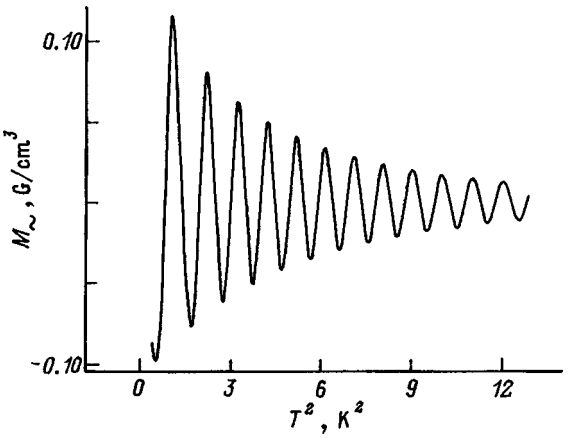

FIG. 2. Quantum temperature fluctuations of an antiferromagnetic semimetal as a function of T^2.

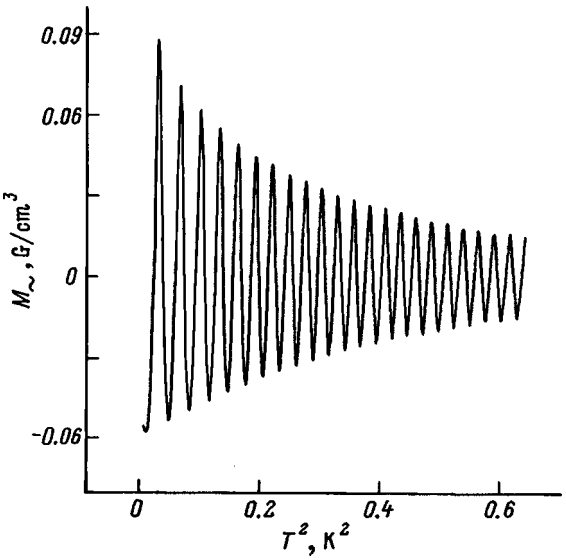

FIG. 3. Quantum temperature fluctuations of a low-temperature antiferromagnetic semimetal as a function of T^2.

temperatures $T=0.5-3.5$ K, where, as noted above, the spin-wave approximation is valid. It is quite clear from Fig. 1 that for these system parameters there are a substantial number of temperature fluctuations.

Let us analyze the results on quantum temperature fluctuations shown in Fig. 1. In the spin-wave approximation the drop in the magnetization owing to temperature is given by

$$\delta S(T)=\left(\frac{b^3}{48\alpha}\right)\left(\frac{1}{\sin\theta}\right)\left(\frac{1}{2K_0\alpha}\right)^{1/2}\left(\frac{T}{S}\right)^2, \tag{27}$$

where b is the magnetic cell parameter in the antiferromagnetic phase and the spin-wave rigidity is

$$\alpha=\frac{1}{6}\left\{\sum_f I_{0f}\mathbf{R}_f^2+\sum_g K_{0g}\mathbf{R}_g^2\right\}. \tag{28}$$

In the nearest-neighbor approximation, where $\alpha=K_0b^2/8$, we have

$$\delta S(T)=\left(\frac{1}{3\sin\theta}\right)\left(\frac{T}{K_0S}\right)^2.$$

These equations show that as the temperature changes, the phase shift in the argument of the sine in Eq. (21) is determined by

$$\frac{\delta\tilde{\mu}_e(T)}{\hbar\omega_c^e}=-\left(\frac{g}{2}\right)\left(\frac{m_{eh}}{m_0}\right)\left(\frac{|J_e|+|J_h|}{4SK_0}\right)\left(\frac{1}{3\sin\theta}\right)\left(\frac{T}{K_0S}\right)^2$$
$$=\frac{\delta\tilde{\mu}_h(T)}{\hbar\omega_c^h}, \tag{29}$$

where m_{eh} is the reduced electron-hole mass, $m_{eh}=m_em_h/(m_e+m_h)$. Equation (29) yields an important result for practical application of quantum temperature fluctuations. If we construct the part of the magnetization that oscillates with changing temperature as a function of T^2, then a plot of ''damped'' but still periodic oscillations is obtained. Figure 2 shows the results of such a construction using the same values as in Fig. 1. Clearly, in the new coordinates (neglecting the drop in amplitude of the oscillations) the curve is indeed periodic in T^2. Small deviations in this periodicity are related to the contribution of the second branch of the spin-wave perturbations and to the presence of Brillouin zone effects which were neglected in Eq. (27).

The equation for the phase shift implies that the period of the oscillations with respect to T^2 is given by

$$P=\left(\frac{2\sin\theta}{g}\right)\left(\frac{m_0}{m_{eh}}\right)\left(\frac{12SK_0}{|J_e|+|J_h|}\right)\left(\frac{K_0S}{k_B}\right)^2, \tag{30}$$

where k_B is the Boltzmann constant. This equation can be used to derive an important relationship among the parameters of the electronic structure of this antiferromagnetic semimetal from experimental data on quantum temperature fluctuations (after plotting the fluctuating part of the magnetization in the $M_\sim, T^2$ plane and measuring the period P of the oscillations).

Here we note two other features which are immediately evident from Eq. (30). First, with other conditions the same, the period of the oscillations decreases as K_0^3 when the exchange integral decreases. Given that the temperature range in which the spin-wave approximation is applicable decreases linearly (as the Neel temperature, itself) as K_0 becomes smaller, we conclude that the number of spikes in the quantum temperature fluctuations increases rapidly for antiferromagnetic semimetals with lower Neel temperatures. This feature is illustrated in Fig. 3. In calculating the quantum temperature fluctuation curve shown in this figure, the Neel temperature was taken to be 3 K (instead of 10 K, as in the earlier cases), while all the other characteristic parameters were unchanged.

The second feature is related to the dependence of the period of the quantum temperature fluctuations on the taper of the antiferromagnetic sublattices. As the spin-flip-transition point is approached, the period of the oscillations decreases $\propto\sin\theta$. Then, by measuring the periods P_1 and P_2 of the oscillations for two values of the external magnetic field $H_1<H_2<H_c$, it is possible to obtain the field for the spin-flip transition from the simple relation

$$H_c^2=\frac{(P_1H_2)^2-(P_2H_1)^2}{(P_1-P_2)(P_1+P_2)}. \tag{31}$$

A more complicated situation arises in the case where Fermi quasiparticles occupy subbands with opposite polarizations in the spin angular momentum. For example, let electrons occupy both spin subbands, while holes, as before, lie only in the lower spin subband. This occurs when the following conditions are satisfied:

$$\frac{4}{3}\frac{(m_e\Delta_e)^{3/2}}{\pi^2\hbar^3}<n<\frac{4}{3}\frac{(m_h\Delta_h)^{3/2}}{\pi^2\hbar^3}, \tag{32}$$

then it is easy to find expressions for the temperature dependences of the Fermi energies for the two electron and one hole bands by solving the equation for electrical neutrality. Calculating the temperature phase shifts in the usual way, we obtain the three periods in T^2 for the oscillations:

$$P_+^e=\left(\frac{2\sin\theta}{g}\right)\left(\frac{m_0}{m_e}\right)\left(\frac{12SK_0(g_+^e+g_-^e+g_h)}{2g_-^e|J_e|+g^h(|J_e|+|J_h|)}\right)\left(\frac{K_0S}{k_B}\right)^2,$$

$$P_-^e=\left(\frac{2\sin\theta}{g}\right)\left(\frac{m_0}{m_e}\right)\left(\frac{12SK_0(g_+^e+g_-^e+g_h)}{2g_+^e|J_e|-g^h(|J_h|-|J_e|)}\right)\left(\frac{K_0S}{k_B}\right)^2,$$

$$P^h=\left(\frac{2\sin\theta}{g}\right)\left(\frac{m_0}{m_h}\right)\left(\frac{12SK_0(g_+^e+g_-^e+g_h)}{g_+^e(|J_e|+|J_h|)+g_-^e(|J_h|-|J_e|)}\right)\times\left(\frac{K_0S}{k_B}\right)^2, \tag{33}$$

where g_+^e and g_-^e are the densities of electronic states on the Fermi surface for the two spin subbands and g^h is the density of hole states on the Fermi surface for $T=0$. When the difference in effective masses is relatively small, the amplitudes of the oscillations will be of the same order of magnitude for the electrons and holes. In this case, the resulting magnetization $M_\sim$ is obtained by adding three periodic functions and, therefore, is generally periodic in T^2. This is illustrated in Fig. 4. In these calculations the effective masses of the electrons and holes were chosen to be different, with $m_e=m_0/2$ and $m_h=m_0$. The concentration of electrons (and holes) per lattice site was chosen to be 0.06. The remaining parameters were the same as in the calculation of the quantum temperature fluctuations shown in Fig. 3. Curves *a*-*c* are quantum temperature fluctuations that are periodic with respect to T^2 and originate from the two electron- and one hole-spin subbands. The total fluctuating part of the magnetization is shown in the lowest curve of this figure. It is this form of quantum temperature fluctuations that is observed experimentally. Thus, the method proposed here for analyzing the experimental data and based on the above results, is of special importance. In fact, plotting the $M_\sim$ curve as a function of T^2 and then Fourier analyzing it makes it possible to isolate the periodic contributions from quasiparticles in the different spin subbands. After determining the periods of the oscillations for the different components and comparing them with the values obtained from Eq. (33), we obtain numerical relations for the electronic structure parameters.

Analogous results can be obtained easily even when both electrons and holes occupy both spin subbands. Then the oscillating magnetization is made up, in general, of four functions that are periodic in T^2. The proposed method for analyzing the experimental data is effective in this case, as well. We do not give concrete expressions for the four periods of the oscillations here in order to save space.

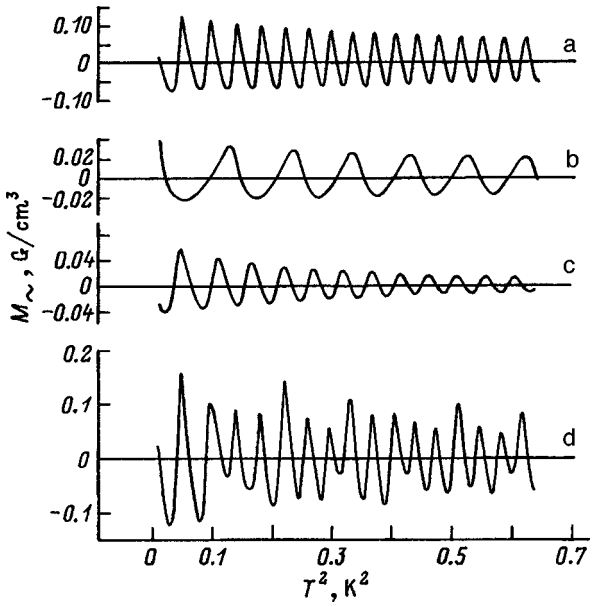

FIG. 4. Quantum temperature fluctuations of an antiferromagnetic semimetal. Two electron subbands and one hole subband are occupied. (a–c) Contributions of the electron and hole subbands; (d) total fluctuating part of the magnetization.

In conclusion, we summarize the main results of this study. The main conclusion of this work is a proof of the possible existence of a new type of oscillations, quantum temperature fluctuations, in antiferromagnetic semimetals. The conditions for a distinct experimental observation of quantum temperature fluctuations are: (a) relatively low Neel temperatures ($T_n\leqslant 1-10$ K); (b) the existence of an exchange coupling between the spin angular momenta of the current carriers and localized electrons; and, (c) samples of sufficiently good quality. At present, choosing solid-state compounds which satisfy these requirements presents no difficulties. As an example, we note the already-mentioned cerium monopnictides. These compensated semimetals have antiferromagnetic order with a Neel temperature $T_N\sim 5-7$ K. The high quality of the single crystals is confirmed, in particular, by the intense signals from the de Haas-van Alphen effect[19] in CeAs. Given that the order of magnitude of the amplitude of the quantum temperature fluctuations is the same as that of the de Haas-van Alphen effect, we may hope for good observations of quantum temperature fluctuations in these antiferromagnetic materials.

It should be noted that studies of quantum temperature fluctuations are of interest, both from the standpoint of observing the effect itself and in order to obtain additional information on the electronic structure. The predicted contributions from the individual spin subbands to the quantum temperature fluctuations periodic in T^2 provide a large information input to studies on quantum temperature fluctuations, which is, to a substantial extent, similar in its possibilities to

the usual de Haas-van Alphen effect. It is important that the period of the quantum temperature fluctuations, as opposed to the period of the de Haas-van Alphen oscillations, is easily changed by an external magnetic field. This offers additional experimental means for testing the electronic structure with the aid of quantum temperature fluctuations.

This work was supported by the Russian Fund for Fundamental Research (Grant No. 96-02-16075) and by the Krasnoyarsk Regional Science Foundation (Grant No. 6F0150).

[1] P. H. P. Reinders, M. Springford, P. T. Coleridge *et al.*, Phys. Rev. Lett. **57**, 1631 (1986).
[2] L. Taillefer and G. G. Lonzarich, Phys. Rev. Lett. **60**, 1570 (1988).
[3] M. Hunt, P. Meeson, P. A. Probst *et al.*, J. Phys.: Condens. Matter **2**, 6859 (1990).
[4] C. M. Fowler, B. L. Freeman, W. L. Hults, J. C. King, F. M. Mueller, and J. L. Smith, Phys. Rev. Lett. **68**, 534 (1992).
[5] A. I. Bykov, A. I. Golovashkin, M. I. Dolotenko *et al.*, JETP Lett. **61**, 106 (1995).
[6] H. Takahashi and T. Kasuya, J. Phys. C: Sol. State Phys. **18**, 2697 (1985).
[7] N. Mori, Y. Okayama, H. Takahashi, Y. Haga, and T. Suzuki, Jpn. J. Appl. Phys. **8**, 182 (1993).
[8] M. Date, A. Yamagishi, H. Hori, and K. Sugiyama, Jpn. J. Appl. Phys. **8**, 195 (1993).
[9] T. Kasuya, T. Suzuki, and Y. Haga, J. Phys. Soc. Jpn. **62**, 2549 (1993).
[10] T. Kasuya, J. Phys. Soc. Jpn. **64**, 1453 (1995).
[11] S. G. Ovchinnikov, V. K. Chernov, A. D. Balaev *et al.*, Pis'ma Zh. Éksp. Teor. Fiz. **64**, 620 (1995) [*sic*].
[12] V. V. Val'kov and D. M. Dzebisashvili, Zh. Éksp. Teor. Fiz. **111**, 654 (1997) [JETP **84**, 360 (1997)].
[13] V. V. Val'kov and D. M. Dzebisashvili, Fiz. Tverd. Tela (St. Petersburg) **39**, 204 (1997) [Phys. Solid State **39**, 179 (1997)].
[14] A. I. Akhiezer, V. G. Bar'yakhtar, and S. P. Peletminskii, *Spin Waves*, North-Holland, Amsterdam (1968), 368 pp.
[15] S. V. Tyablikov, *Methods in the Quantum Theory of Magnetism* [in Russian], Nauka, Moscow (1975), 528 pp.
[16] L. D. Landau and E. M. Lifshitz, *Quantum Mechanics* [in Russian], Nauka, Moscow (1989), 768 pp.
[17] L. D. Landau and E. M. Lifshitz, *Statistical Physics* [in Russian], Nauka, Moscow (1976), 584 pp.
[18] I. M. Lifshits, M. Ya. Azbel', and M. I. Kaganov, *Electron Theory of Metals*, Consultants Bureau, New York (1973), 416 pp.
[19] N. Takeda, Y. S. Kwon, Y. Haga *et al.*, Physica B **186–188**, 153 (1993).

Translated by D. H. McNeill

Magnetic properties of ultrathin Ni films

O. V. Snigirev, A. M. Tishin, and K. E. Andreev

M. V. Lomonosov Moscow State University, 119899 Moscow, Russia

S. A. Gudoshnikov

Institute of Earth Magnetism, the Ionosphere, and Radio Wave Propagation, Russian Academy of Sciences, 142092 Troitsk, Moscow Region, Russia

J. Bohr

Technical University of Denmark, DK 2800 Lyngby, Denmark
(Submitted November 20, 1997; resubmitted March 11, 1998)
Fiz. Tverd. Tela (St. Petersburg) **40**, 1681–1685 (September 1998)

The magnetic properties of Au/Ni/Si(100) films with Ni thicknesses of 8–200 Å are studied at $T=77$ K using a scanning magnetic microscope with a thin-film high-temperature dc SQUID. It is found that the Ni films, with an area of 0.6×0.6 mm, which are thicker than 26 Å have a single-domain structure with the magnetic moment oriented in the plane of the film and a saturation magnetization close to 0.17 MA/m. For films less than 26 Å thick, the magnetization of the film is found to drop sharply. © *1998 American Institute of Physics.* [S1063-7834(98)02509-X]

Studies of the properties of ultrathin magnetic films are of fundamental, as well as practical, interest. These films can be used in magnetic recording devices to enhance the memory density. From the standpoint of fundamental research, these films are interesting objects for studying magnetic ordering in two-dimensional ($2D$) magnets.[1,2]

The best known devices for measuring the magnetic properties of ultrathin films, the surfaces of $3d$ and $4f$ metals, and submicron particles of recording media can be classified into three groups: devices used to measure the integrated magnetic moment of a sample;[3–5] devices which produce an image of the structure of magnetic objects with high spatial resolution;[6–9] and, instruments using synchrotron or neutron radiation.[10–12]

Recently developed scanning SQUID-microscopes[13] make it possible to measure the absolute magnitude of the magnetization of a sample with a high sensitivity that is not accessible to other devices and to take topograms of the magnetic field of a test object with a spatial resolution down to a few micrometers.[14]

In this paper we present the results of a study of the magnetic properties of ultrathin Au/Ni/Si(100) films at a temperature of 77 K using a SQUID-microscope.

1. PROPERTIES OF THIN Ni FILMS

Thin Ni films can have two types of crystal structure [face centered (fcc) and body centered (bcc)] with substantially different magnetic properties.[15] According to theory, fcc Ni exists only in a ferromagnetic phase, while the bcc modification displays a transition from a ferromagnetic to a nonmagnetic phase[15] as the Wigner–Zeitz radius is lowered to a critical value on the order of 2.6 Å. A transition from the nonmagnetic to the ferromagnetic state has also been predicted for epitaxial bcc-Ni films subjected to a 1% stretching of the lattice caused by the substrate.[16]

The magnitude and spatial orientation of the magnetic moment of Ni films depend on the number of monolayers, the substrate, and the structure of the buffer layer.[8,16–19]

The dimensions of the magnetic domains formed in Ni films range from tens of micrometers to a few micrometers as the thickness of the Ni is changed from 20 to 140 Å.[6]

Besides the above properties, ultrathin Ni films can also manifest a spectrum of phenomena associated with the transition from two-dimensional to three-dimensional magnetic systems as the number of monolayers is increased. It has been found, for example, that the value of the critical index β in the temperature dependence of the magnetization in the neighborhood of the phase transition, $M(T)\propto(1-T/T_c)^{\beta}$, changes quite sharply from 0.125, which is characteristic of two-dimensional ''Ising'' magnets, to 0.43, which is characteristic of three-dimensional ''Heisenberg'' magnets, as the thickness of Ni films is varied from 5 to 10 monatomic layers.[7]

The Curie temperature T_c also depends on the Ni film thickness and can vary from 50 to 450 K as the thickness of Ni/Cu(001) films is increased from 1.5 to 8 monolayers.[20] Here the dependence of T_c on the film thickness can be extrapolated to $T_c=0$ for a single monolayer of Ni.[21]

2. EXPERIMENTAL TECHNIQUE

Figure 1 shows the mutual positions of the SQUID-probe[22] of the scanning magnetic microscope, the test sample of Ni film on a 0.3-mm-thick substrate of Si(100), and a thin-film calibration loop deposited on the same silicon substrate. The film samples were made[22] in the

 © 1998 American Institute of Physics

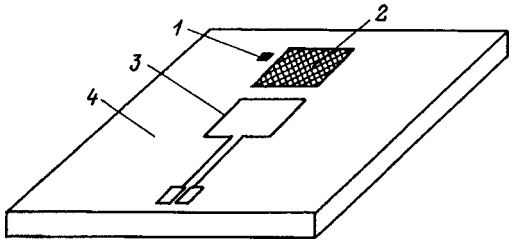

FIG. 1. Schematic illustration of the mutual positions of the SQUID (*1*), sample (*2*), and calibration loop (*3*) on the substrate (*4*) in a magnetic SQUID-microscope.

form of a square with 600 μm edges. In order to visualize the distribution of the magnetic field created by the sample, the sample was scanned with a sample-probe distance on the order of 100 μm.

A magnetizing field parallel to the sample plane was provided by a long solenoid, and a field perpendicular to the sample was created by a quasi-plane 500-turn coil. The scanning SQUID-microscope could normally operate in magnetic fields of up to 70 A/m for fields directed perpendicular to the plane of the SQUID (and the plane of the sample) and in fields up to 10^4 A/m oriented parallel to the SQUID.

Information on the crystallographic structure of the samples was obtained on thick Ni films (200 Å) without a gold coating on a Rigaku x-ray diffractometer. Only the (111) reflection was observed ($2\vartheta = 44.32°$); the full width at half maximum of the peak was 1.028°. The existence of a single reflection (111) is evidence of a textured structure for the deposited Ni film and a strongly expressed (111)-orientation. The lattice constant calculated from the position of the 2θ reflection was 3.53 Å. The observed (111) film orientation is natural, since in this case the mismatch between the lattice constant in the Si (100) plane (5.2 Å) and the Ni atoms in the plane of its film (4.99 Å) is minimal. It was not possible to check the thinner films in this manner because of the low intensity of the reflected radiation.

During the measurements, the probe of the scanning SQUID-microscope was mounted in a Dewar flask with liquid nitrogen located inside a double permalloy shield. The residual magnetic field can be measured by turning the probe around a vertical axis by 360°. Its maximum was close to 2.5 μT. An alternating current of about 300 μA was applied to the calibration coil (Fig. 1); its magnetic image could be used for mounting the sample inside the scanning field of the scanning SQUID-microscope (on the order of $8\times 8\ \text{mm}^2$). The measured magnetic field over the central portion of the coil makes it possible to determine the distance h between the sample and the SQUID, which in our experiments was varied from 100 to 400 μm and determined the spatial resolution of the apparatus.

3. RESULTS OF THE MEASUREMENTS

The properties of Ni films with thicknesses of 8–200 Å coated with a layer of Au were studied. Images were recorded after the sample had been cooled in the residual magnetic field from a temperature $T \approx 400$ K to the boiling temperature of liquid nitrogen. Scanning the 26-Å-thick film

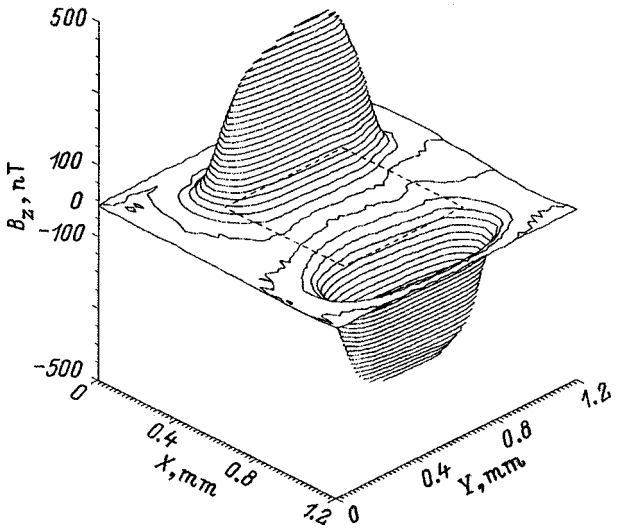

FIG. 2. Magnetic image of a 26-Å-thick, 0.6×0.6 mm Ni film in an applied magnetic field of 4000 A/m directed parallel to the *Y* axis.

yielded a weak magnetic signal corresponding to an orientation of the magnetization vector in the plane of the film. When a magnetic field of 4000 A/m was applied parallel to the plane of the film, the signal-to-noise ratio increased to over 100 and the magnetic image became distinct (Fig. 2). Sharp peaks at the maximum and minimum of the B_z component of the magnetic field lay on opposite edges of the test film which is indicated by a dotted line in Fig. 2. The symmetry of the image (the positive and negative responses are equal in size) is a result of orienting the magnetization vector in the plane of the film. The presence of only two peaks in the magnetic image of the entire film, whose dimensions greatly exceed the spatial resolution of the scanning SQUID-microscope, can be interpreted as evidence of a single-domain structure.

The change in the component $B_z(x,y)$, relative to the phonon signal $B_z(0,0)$ recorded far from the film, was calculated from the change in the output voltage ΔV_{out} of the SQUID, the known feedback coefficient $\Delta V_{\text{out}}/\Phi_0$ of the SQUID electronics (here Φ_0 is the quantum of magnetic flux), and the previously measured effective area A_{eff} of the SQUID.[22,23]

The dependence of the volume magnetization of the 26 Å Ni film on a parallel applied field is shown in Fig. 3. This hysteresis curve was obtained by successive measurements of the peak value of B_z as the magnitude of the applied field was varied from $+4000$ to -4000 A/m and back. These data show that the saturation magnetization of this film is 0.17 MA/m, which is attained at a field strength of about 2500 A/m. This value of the saturation magnetization is approximately a factor of 3 smaller than that of bulk Ni. The hysteresis loop (Fig. 3) is evidence of magnetic ordering in the sample with a phase transition temperature above 77 K. The overall shape of the $M(H)$ curve suggests that this ordering is ferromagnetic in character. The coercitive force is close to 35 A/m and the residual magnetic moment is 0.028 MA/m. When a perpendicular magnetic field with a maximum strength of 70 A/m was applied to the 26-Å-thick Ni film, the

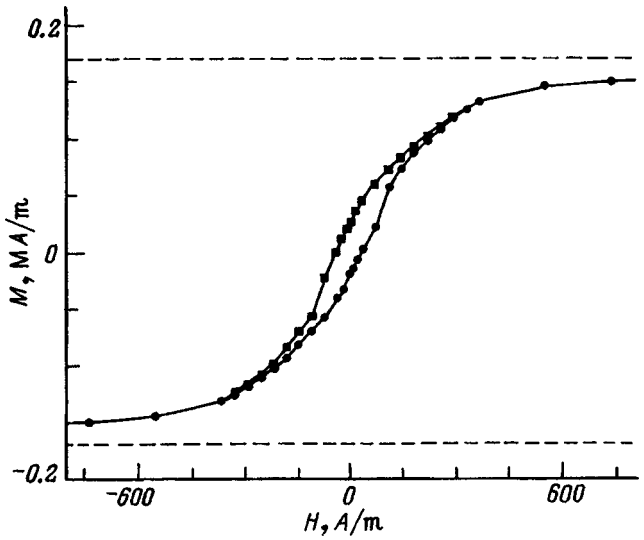

FIG. 3. Hysteresis loop of a 26-Å-thick Ni film in a parallel applied magnetic field.

signal was below the noise level of the SQUID and an image could not be obtained.

Attempts to record images of samples with thicknesses of 15 and 8 Å in parallel and perpendicular magnetic fields with distances of 100 μm between the SQUID and sample showed that their magnetizations are below the sensitivity threshold of the instrument. Thus, when the thickness of the Ni films was varied from 26 to 15 Å, the magnetization fell by more than two orders of magnitude (Fig. 4).

As opposed to the 26-Å-thick films, the images of Ni films with thicknesses of 43 and 84 Å, recorded after they were cooled in zero field, showed distinct pairs of symmetric positive and negative peaks located on opposite corners of the square film samples. These images correspond to a single-domain magnetic structure with an easy axis of magnetization lying in the plane of the film along a diagonal. When a parallel magnetizing field on the order of 4000 A/m in magnitude was applied, the magnetic moment of the film

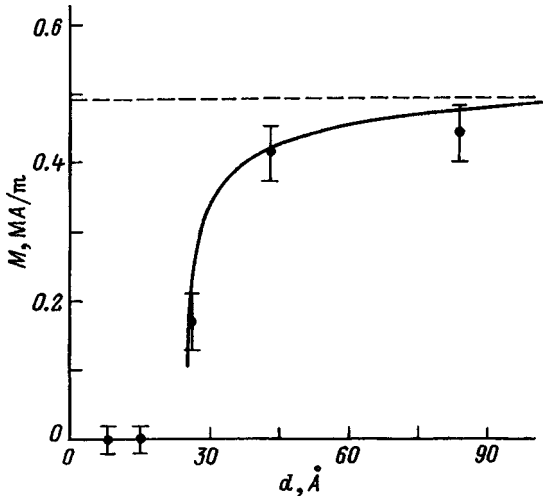

FIG. 4. Saturation magnetization as a function of Au/Ni/Si(100) film thickness.

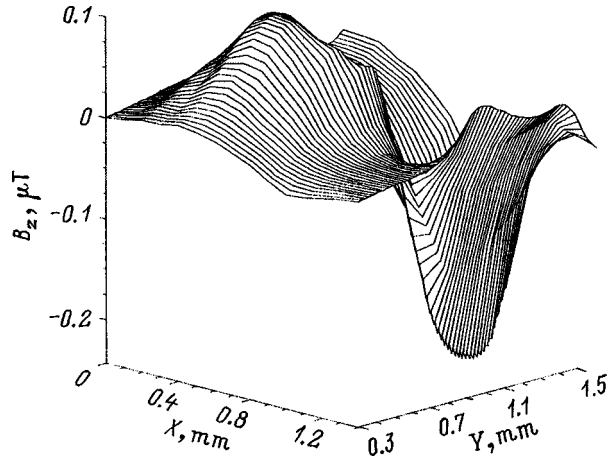

FIG. 5. Magnetic image of a 30-Å-thick Ni film deposited on a Pt buffer layer in a 4000 A/m magnetic field directed parallel to the *Y* axis.

rotated relative to the direction of the field and the peaks were shifted to the location indicated in Fig. 2a. Similar results were obtained for 200-Å-thick Ni films without a gold coating.

In order to determine the way the silicon substrate influences the orientation and magnitude of the magnetic moment of the film, we have prepared and studied samples of Au/Ni/Pt/Si(100) films with a 100-nm-thick buffer layer of Pt. The lattice parameter of the platinum, 3.9 Å, is in between those of Si and Ni, which reduces the stretching of the Ni layers in the film. An image of the distribution of the B_z component of the magnetic field is shown in Fig. 5.

4. DISCUSSION OF RESULTS

We begin the discussion with the simplest case of relatively thick Au/Ni/Si(100) films with thicknesses of 43 and 84 Å. As the measurements at $T=77$ K show, ferromagnetic ordering is observed in them. Here the saturation magnetization is close to the bulk value (Fig. 4), in agreement with theory.[15]

The observed orientation of the magnetization in the plane of the film may be the consequence of a number of factors. First, with this orientation there is almost no demagnetization field in the film; second, because of the stretching of the Ni film by the silicon substrate, the direction of easy magnetization can lie in the plane of the film; and/or, third, 77 K lies between the magnetic phase transition point and the reorientation temperature T_R for these films.[24]

The domain structure of the thick films turned out to be insensitive to the applied magnetic field, regardless of whether it was directed parallel or perpendicular to the plane of the film. (In our experiments these fields were up to 4000 and 70 A/m, respectively).

Films with intermediate thicknesses (about 25 Å) also manifested ferromagnetic ordering, but with a smaller saturation magnetization. This is most likely because the sample temperature $T=77$ K was close to the phase transition temperature for this film thickness.

An alternative reason may be an island (cluster) structure of the film, which becomes more probable as the thickness is

reduced. Ferromagnetic ordering with a magnetization oriented in the plane of the film has been observed previously with cluster radii below 30 Å, for example in rather thin (about 30 monolayers) Fe films.[24] Thus, the reduction in the magnetization of Ni films with thicknesses of 15–30 Å may be a result of cluster formation.

A magnetic moment corresponding to ferromagnetic ordering was not observed in the Ni films with thicknesses of 8 and 15 Å at the existing sensitivity of the scanning SQUID-microscope. It may be assumed that the magnetic phase transition point for these films lies below 77 K, although other mechanisms may play a role.[5,25] Perhaps, at these thicknesses the film has an island structure and is in a superparamagnetic state, as has been observed, for example, for Fe films thinner than 39 Å.[5] It has been conjectured[5] that supermagnetism is typical of magnetic films that form islands during the growth process.

The nature of the magnetic-field distribution over the surface of Au/Ni/Pt/Si films, especially the asymmetry between the positive and negative maxima, indicates the existence of a component of the magnetic moment perpendicular to the plane of the film. Thus, the presence of a buffer layer greatly changed the magnetic anisotropy energy of the film. This suggests that eliminating the stretching of the Ni monolayers leads to an orientation of the magnetic moment of a given film sample perpendicular to its plane. Besides a change in the orientation of the magnetic moment, our experimental data imply an extremely large reduction in the magnetic moment of the Ni atoms, which may indicate a substantial readjustment of the energy spectrum of films with a buffer layer.

As for the characteristics of the magnetic microscope, our results show that the sensitivity of the apparatus was sufficient to measure the hysteresis curves of films thicker than 26 Å in applied magnetic fields of magnitude ± 4000 A/m, if the field is oriented parallel to the plane of the sample and the plane of the SQUID. In the case of a perpendicular magnetizing field, it was possible to make measurements for magnetization fields no higher than 70 A/m, since in high fields the critical current of the Josephson junctions of the SQUID was suppressed. For measurements in fields higher than 100 A/m, SQUIDs with a submicron Josephson junctions must be used.

The spatial resolution in the magnetic image of the observed samples and the magnetic field resolution of the magnetic microscope used here were close to 100 μm and 10^{-15} $Am^2/Hz^{1/2}$, respectively. Both of these parameters can be improved by reducing the distance between the SQUID and the sample.[14]

In conclusion, we note that the magnetic scanning SQUID-microscopy method developed here can be used to obtain an image of the spatial distribution of one of the components of the magnetic field of ultrathin films of magnetic materials and to determine, to a high accuracy not available with other devices, their local magnetizations in regions where the acting fields are low.

We thank S. I. Krasnosvobodtsev, L. V. Matveets, A. V. Pavolotskiĭ, I. G. Prokhorova, S. N. Polyakov, N. N. Ukhanskiĭ, and I. I. Vengrus for help in various stages of this work.

This work was supported by the Russian Fund for Fundamental Research (Projects No. 96-02-19250 and 96-02-18127*a*) and INTAS (Grant No. 93-2777-ext).

[1] N. D. Mermin and H. Wagner, Phys. Rev. Lett. **17**, 1133 (1966).
[2] L. Onsager, Phys. Rev. **65**, 117 (1944).
[3] M. Sakurai, N. Imamura, K. Hirano, and T. Shinjo, J. Magn. Magn. Mater. **147**, 16 (1995).
[4] R. Bergholz and U. Gragmann, J. Magn. Magn. Mater. **45**, 389 (1984).
[5] M. Weber, R. Koch, and K. H. Rieder, Phys. Rev. Lett. **73**, 1166 (1994).
[6] G. Bochi, H. J. Hug, D. I. Paul, B. Stiefel, A. Moser, I. Parashikov, H.-J. Güntherodt, and R. C. O'Handley, Phys. Rev. Lett. **75**, 1839 (1995).
[7] F. Huang, M. T. Kief, G. J. Mankey, and R. F. Willis, Phys. Rev. B **49**, 3962 (1994).
[8] G. Bochi, C. A. Ballantine, H. E. Inglefield, C. V. Thompson, R. C. O'Handley, H. J. Hug, B. Stiefel, G. Moser, and H.-J. Güntherodt, Phys. Rev. B **52**, 7311 (1995).
[9] A. Oral, S. J. Bending, and M. Henini, J. Vac. Sci. Technol. B **14**, 1202 (1996).
[10] C. F. Majkrzak, J. Kwo, M. Hong, Y. Yafet, D. Gibbs, C. L. Chien, and J. Bohr, Adv. Phys. **40**, 99 (1991).
[11] G. H. Lander, Invited paper submitted to the 21st Rare Earth Research Conf., Duluth, MN (July 7-12, 1996), to be published in Journal of Alloys and Compounds.
[12] G. M. Watson, D. Gibbs, G. H. Lander, B. D. Gaulin, L. E. Bermann, H. Matzke, and W. Ellis, Phys. Rev. Lett. **77**, 751 (1996).
[13] L. N. Vu, M. S. Wistron, and D. J. van Harlingen, Appl. Phys. Lett. **63**, 1693 (1993).
[14] J. R. Kirtley, M. B. Ketchen, K. G. Stwaisz, J. Z. Sun, W. J. Gallagher, S. H. Blanton, and S. J. Wind, Appl. Phys. Lett. **66**, 1138 (1995).
[15] V. L. Moruzzi, P. M. Marcus, K. Schwarz, and P. Mohn, Phys. Rev. B **34**, 1784 (1986).
[16] J. I. Lee, Soon C. Hong, A. J. Freeman, and C. L. Fu, Phys. Rev. B **47**, 810 (1993).
[17] J. Vogel, G. Panaccione, and M. Sacchi, Phys. Rev. B **50**, 7157 (1994).
[18] B. Schulz and K. Baberschke, Phys. Rev. B **50**, 13467 (1994).
[19] J. Shen, J. Giergiel, and J. Kirschner, Phys. Rev. B **52**, 8454 (1995).
[20] A. Aspelmeier, M. Tischer, M. Farle, M. Russo, K. Baberschke, and D. Arvanitis, J. Magn. Magn. Mater. **146**, 256 (1995).
[21] F. Huang, G. J. Mankey, M. T. Kief, and R. F. Willis, J. Appl. Phys. **73**, 6760 (1993).
[22] O. V. Snigirev, K. E. Andreev, A. M. Tishin, S. A. Gudoshnikov, and J. Bohr, Phys. Rev. B **55**, 1429 (1997).
[23] S. A. Gudoshnikov, N. N. Ukhansky, I. I. Vergrus, K. E. Andreev, A. M. Tishin, and O. V. Snigirev, IEEE Trans. Appl. Supercond. **7**, 2542 (1997).
[24] Ar. Abanov, V. Kalatsky, V. L. Pokrovsky, and W. M. Saslov, Phys. Rev. B **51**, 1023 (1995).
[25] C. P. Flynn and M. B. Salomon, Synthesis and properties of single crystal nanostructures: *Handbook on the Physics and Chemistry of Rare Earths*, Vol. 22, edited by K. A. Gschneider and L. Eyring (North-Holland, Amsterdam, 1996), Ch. 147.

Translated by D. H. McNeill

Orbital ordering in $CuGeO_3$

O. A. Bayukov, G. A. Petrakovskiĭ, and A. F. Savitskiĭ

L. V. Kirenskii Institute of Physics, Siberian Branch, Russian Academy of Sciences, 660036 Krasnoyarsk, Russia

(Submitted November 20, 1997; resubmitted March 31, 1998)
Fiz. Tverd. Tela (St. Petersburg) **40**, 1686–1692 (September 1998)

The combined effect of the ligand crystal field and the exchange interaction on the Cu^{2+} cation in $CuGeO_3$ is examined. It is shown that, if the magnitude of the exchange interaction exceeds the splitting of the energy levels of the $d_{x^2-y^2}$ and d_{xy} orbitals, then an alternate filling of the d orbitals along a chain (orbital ordering) is possible. This effect creates an antiferromagnetic interaction between Cu^{2+} pairs in 90° exchange and a doubling of the lattice period. A Jahn-Teller pseudoeffect causes singletization of the ground state of the antiferromagnetic chain of Cu^{2+} spins. © *1998 American Institute of Physics.* [S1063-7834(98)02609-4]

In artificially synthesized single crystals of $CuGeO_3$ an anomalous reduction in the magnetic susceptibility has been observed[1] and, subsequently, an antiferromagnetic pairing of Cu^{2+} spins[2] at low temperatures, or the so-called spin-Peierls phase transition. The latter was first observed in organic compounds[3,4] and described theoretically as a consequence of the interaction of a one-dimensional antiferromagnetic chain of spins $S=1/2$ with the three-dimensional system of lattice phonons.[5] Not all features of the magnetic properties of $CuGeO_3$ can be understood at present.

The strong tetragonal crystal field of the oxygen octahedra stretched along the b_0 axis surrounding the Cu^{2+} cations leads to a doubling of the population of the d_{z^2} orbitals ($z \| b_0$ axis) by electrons, suppressing the exchange interaction along the b_0 axis of the crystal and imparting a quasi-one-dimensional exchange interaction along the c_0 axis. The observed[6] exchange interaction along the c_0 axis is antiferromagnetic, which contradicts the conventional Goodenough-Kanamori rules for 90° indirect coupling. In the neighborhood of the transition temperature $T_{sP}=14$ K, there is a doubling of the lattice period of $CuGeO_3$ along the a_0 and c_0 axes.[7] In doped $CuGeO_3$:Si crystals the coexistence of a dimerized (singlet) phase and an antiferromagnetic phase has been observed at temperatures below T_{sP}.[8] When a high pressure is applied to crystalline $CuGeO_3$, the intrachain exchange constant decreases,[9] while T_{sP} increases.[10]

An attempt[11] to explain the antiferromagnetic interaction in $CuGeO_3$ uses the concept[12] of the participation of neighboring nonmagnetic ions in indirect exchange in Cu-O-Cu dimers. In an examination of just the singly filled orbitals,[11] it was found that the deviation from quadratic symmetry and hybridization of oxygen atoms with neighboring Ge-O groups and with one another yield strong antiferromagnetic exchange of greater magnitude than the Cu-O-Cu ferromagnetic interaction. Here, unfortunately, the large potential contribution to the Cu-O-Cu interaction resulting from the interaction of filled and half-filled orbitals of neighboring Cu^{2+} was neglected.

In this paper we examine the combined effect on a Cu^{2+} cation of the ligand crystal field and the exchange interaction with nearest neighbors in the chain. It is shown that when the exchange interaction energy is sufficiently high (larger than the splitting of the energy levels of the $d_{x^2-y^2}$ and d_{xy} orbitals), ordering of the $3d$ electron orbitals of neighboring Cu^{2+} cations becomes possible and this leads to an antiferromagnetic interaction in the chain with 90° indirect coupling and a doubling of the lattice period. By changing the energy of stabilizing the Jahn–Teller pseudoeffect acting on the energy levels of the $d_{x^2-y^2}$ and d_{xy} orbitals, the energy of the spin-orbit interaction may emerge as the reason for the alternating magnitude of the exchange interaction along a Cu^{2+} chain and singletization of the ground state.

1. EXCHANGE INTERACTIONS

The model of indirect-exchange interactions developed by Anderson,[13] and subsequently by Zavadskiĭ[14] and Eremin,[15] yields an analytic expression for the Goodenough-Kanamori rules for the interaction of an arbitrary pair of $3d$ cations.[16] In this model the interaction of a pair of cations is represented by the sum of the interactions of all the $3d$ orbitals of the cations through the p orbitals of an intermediate ligand. Contributions of practical significance come from only two types of interactions: so-called kinetic and potential exchange. The kinetic exchange integral

$$I_{ij}^{1-1} = -\gamma^4 (U_i + U_j) \tag{1}$$

describes the interaction of singly occupied $3d$ orbitals of the i-th and j-th neighboring cations, while the potential exchange integral

$$I_{ij}^{1-0(2-1)} = +\gamma^4 J^{\text{int}} \tag{2}$$

describes the interaction of an empty (or doubly occupied) orbital with one that is singly occupied. The signs in Eqs. (1) and (2) denote antiferromagnetic ($-$) and ferromagnetic ($+$) interactions. γ is the bond covalency parameter, given by the mixing coefficient of the atomic wave function of the ligand with the wave function of the cation; its magnitude depends

 © 1998 American Institute of Physics

on the type of coupling (σ or π), the coupling geometry, and the ligand-cation distance. U is the energy of excitation of an electron from a ligand to a cation; its magnitude depends on the population of the $3d$ shell of the cation, the type of ligand, and the coordination. J^{int} is the intraatomic interaction integral; its value depends on the population of the $3d$ shell of the cation.

We neglect the other contributions to indirect exchange known from the literature, since they either are components of the exchange mechanisms discussed here or are associated with double excitation of the ligands. It is best to introduce extended couplings, such as Cu-O-Ge-O-Cu or Cu-O-O-Cu, only if the basic contributions indicated above are absent, since they correspond to higher orders in the small parameter for electron transport. The predictive adequacy of the contributions accounted for in Eqs. (1) and (2) has been verified[16] for different lattices and cations.

Let us consider the exchange interaction in $CuGeO_3$. The strong tetragonal distortion of the coordination octahedra around the Cu^{2+} cations along the b_0 axis makes it so that the d_{z^2} orbitals are doubly occupied, so that there is no exchange interaction along the b_0 axis. (The interaction between doubly occupied and empty orbitals equals zero.) We have neglected the interaction along the a_0 axis (Cu-O-Ge-O-Cu). Thus, as a result of the tetragonal distortion, $CuGeO_3$ becomes quasi-one-dimensional magnetically. The electron hole in the copper cations is located in the $d_{x^2-y^2}$ orbitals. The indirect exchange couplings of two Cu^{2+} cations allowed by symmetry and the populations of the individual $3d$ orbitals are shown in Fig. 1. The total indirect exchange integral for such a pair of cations,

$$J(d_{x^2-y^2},d_{x^2-y^2}) = +4bcJ^{\text{int}} \tag{3}$$

is ferromagnetic and confirms the predictions of the Goodenough-Kanamori rules for 90° coupling. Here $b=\gamma^2$ is the ligand-cation electron transport parameter with σ-coupling ($d_{x^2-y^2}-p_x$ or p_y) and c is the same parameter with π coupling ($d_{xy}-p_x$ or p_y). This means that, for sufficiently strong tetragonal distortion, the $d_{x^2-y^2}$ holes on neighboring Cu^{2+}-cations cause the ferromagnetic interaction along the chain along the c_0-axis. This is correct until the splitting of the $d_{x^2-y^2}$ and d_{xy} orbitals exceeds the energy of the exchange interaction.

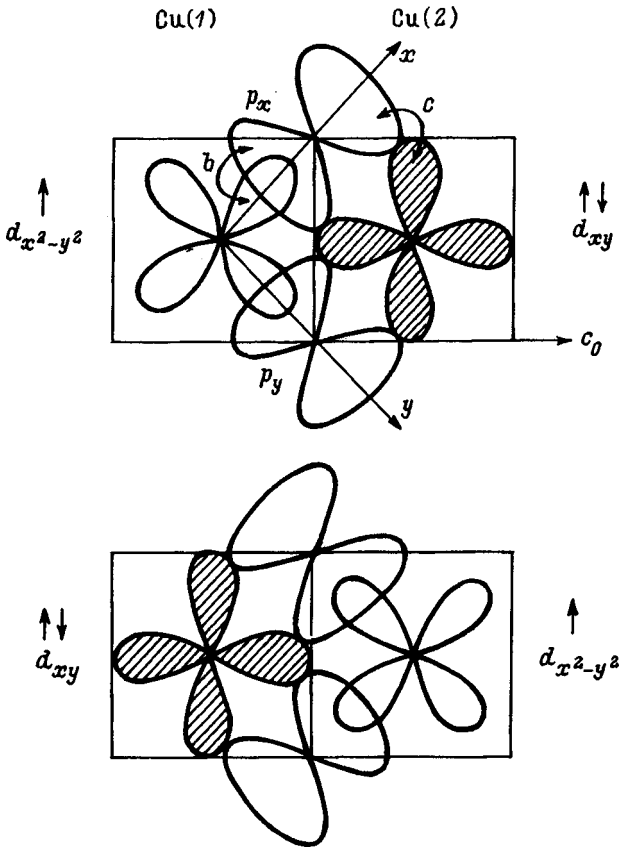

FIG. 1. A schematic representation of oblique exchange couplings of $3d$ orbitals of $Cu^{2+}(1)$ and $Cu^{2+}(2)$ cations in a $CuGeO_3$ structure with 90° exchange through intermediate p_x and p_y orbitals of the oxygens in the case where holes occupy the $d_{x^2-y^2}$ orbitals of both cations. The arrows on the d orbitals indicate their electron populations.

2. ORDERED POPULATION OF THE *d*-ORBITALS OF NEIGHBORING CATIONS

Let us consider the energy of the $3d$ electrons when the coordination octahedron of the surrounding ligands is strongly distorted. Figure 2 shows a qualitative picture of the splitting of the energy levels of the Cu^{2+} ions in crystal fields with various symmetries. The cubic component Dq' of the crystal field for a plane square is considerably smaller than the splitting in an octahedron, if it means anything at all to speak of this for such a ligand configuration.

We are interested in the magnitude of the splitting E_d between the $d_{x^2-y^2}$ and d_{xy} orbitals. This splitting is suppressed by two effects: crystal fields with symmetries lower than tetragonal and the spin-orbit interaction which develops when the ion develops an orbital angular momentum owing to mixing of the $d_{x^2-y^2}$ and d_{xy} states. Let us assume that this splitting is small and that holes on neighboring Cu^{2+} cations can be in any of these orbitals. We shall calculate the exchange integrals for the possible cases. For the case when holes are placed in the $d_{x^2-y^2}$ orbitals of neighboring Cu^{2+} ions, we have already estimated the exchange integral (see

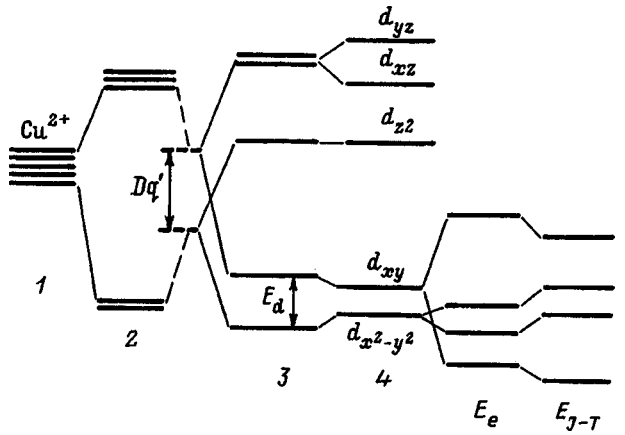

FIG. 2. A schematic diagram of the energy levels of the Cu^{2+} ion in the ligand fields of different symmetry as the octahedron is stretched tetragonally. The ion energy is determined by the $3d$ hole. (*1*) Free ion, (*2*) octahedron, (*3*) plane square, (*4*) rhombic distortion.

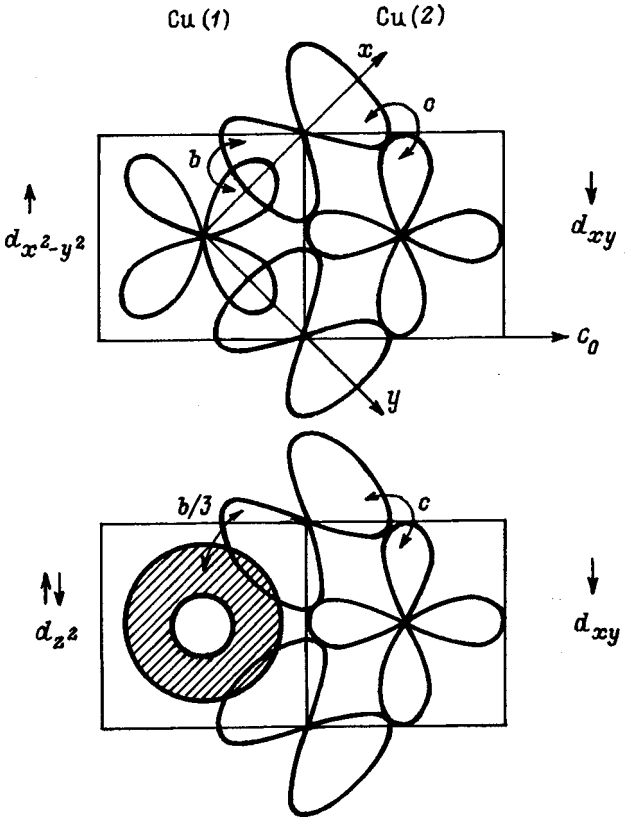

FIG. 3. A schematic representation of oblique exchange couplings of $3d$ orbitals of neighboring copper cations in a $CuGeO_3$ structure in the case where holes lie in the $d_{x^2-y^2}$ Cu(1) and d_{xy} Cu(2) orbitals (orbital ordering).

Eq. (3)) and it is positive. For the case when one hole is in the $d_{x^2-y^2}$ orbital of Cu(1) and the other, in the d_{xy} orbital of Cu(2), the oblique exchange couplings allowed by symmetry and the populations of the orbitals are shown schematically in Fig. 3. In this case, the cation-cation interaction integral is the sum of antiferromagnetic and ferromagnetic contributions,

$$J(d_{x^2-y^2},d_{xy})=-2bc\left(2U-\frac{1}{3}J^{\text{int}}\right). \tag{4}$$

For the case in which holes lie in the d_{xy} orbitals of neighboring Cu^{2+}, we have

$$J(d_{xy},d_{xy})=+\frac{16}{3}bcJ^{\text{int}}, \tag{5}$$

i.e., there is a ferromagnetic interaction.

The energy U of ligand-cation electronic excitation can be 2–6 eV for Cu^{2+}.[16] The intraatomic exchange integral for Cu^{2+}, $J^{\text{int}}\sim 1$ eV. Thus, the interaction (4) is antiferromagnetic and its absolute magnitude exceeds the exchange terms (3) and (5). The system, as it tries to minimize its energy through the exchange interaction, chooses the antiferromagnetic ordering determined by the integral (4), i.e., in those cases where the energy E_e of the exchange interaction of a pair of neighboring cations is larger than the splitting E_d of the $d_{x^2-y^2}$ and d_{xy} orbitals in the crystal field, it is to be expected that holes in neighboring Cu^{2+} will occupy different $3d$ orbitals. For a linear Cu^{2+} chain, one expects alternating $(d_{x^2-y^2}-d_{xy}-d_{x^2-y^2}-d_{xy}-\ldots)$ splitting of the holes and we shall refer to this as the orbital ordering of neighboring cations. The phenomenon of orbital ordering is not new and has been examined theoretically before[17] for the orbitally degenerate e_g level in perovskites. In the case of $CuGeO_3$, we expect pseudodegeneracy of the energy levels having $e_g(d_{x^2-y^2})$ and $t_{2g}(d_{xy})$ symmetry.

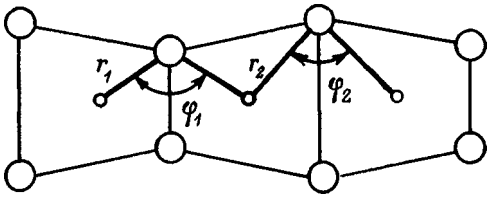

FIG. 4. A schematic representation of the distortions in the equatorial plane of the oxygen octahedra around Cu^{2+} in $CuGeO_3$ in the sP phase.

What does this imply? First, as noted above, orbital ordering leads to antiferromagnetic ordering of cation spins, with 90° oblique coupling, along chains along the c_0 axis in $CuGeO_3$, as has been observed experimentally.[6] Second, orbital ordering leads to a doubling of the lattice period, which has been observed experimentally[7] and is evident from the following reasons. The ordered placement of holes in the orbitals of neighboring cations corresponds to an alternation along the c_0 axis of $d_{x^2-y^2}$ orbitals with different populations $(d^{\uparrow}_{x^2-y^2}-d^{\uparrow\downarrow}_{x^2-y^2}-d^{\uparrow}_{x^2-y^2}-d^{\uparrow\downarrow}_{x^2-y^2}-\ldots)$. The electrons of a cation in which the $d_{x^2-y^2}$ orbital is singly populated shield the charge of the surrounding ligands less, so that the internuclear attractive forces shrink the Cu-O distance in the equatorial plane of the octahedron of this cation. The lattice period is doubled in the direction of the ordered disposition of the orbitals.

3. SINGLETIZATION OF THE GROUND STATE

When the splitting E_d is small enough, the energy levels of the $d_{x^2-y^2}$ and d_{xy} orbitals can be regarded as pseudodegenerate and the Jahn–Teller pseudoeffect must be invoked. When the stabilization energy of the Jahn–Teller pseudoeffect exceeds the spin-orbit interaction energy, it is more advantageous for the system to lower its symmetry to monoclinic. Probably these interactions manifest themselves through the distortion of the bases of the oxygen octahedra and shifts of the Cu^{2+} ions observed by neutron diffraction[18] and illustrated schematically in Fig. 4. In this case, the geometric conditions for the oblique exchange coupling of a central Cu^{2+} ion to the left and right in a chain are different owing to the differences in the bond lengths and angles $(r_1,\varphi_1$ and $r_2,\varphi_2)$. An alternation in the magnitudes of the exchange interactions sets in along the chain, leading to singletization of the ground state, as has been shown theoretically.[19]

In a system that has been stabilized by the Jahn-Teller effect, the dependence of the energy of a pair of Cu^{2+} cations on the interaction distance in an oblique Cu-O-Cu bond can be represented schematically by the curve shown in Fig. 5. For low-temperature lattice vibrations, the system is at a lo-

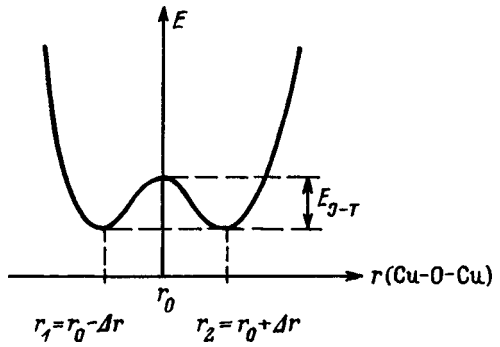

FIG. 5. The energy of a pair of Cu^{2+} cations as a function of the interaction distance in an oblique Cu-O-Cu bond in the equatorial plane of the octahedron. Δr is the change in the equilibrium distance r_0 when the lattice period is doubled. E_{J-T} is the stabilization energy for the Jahn-Teller effect.

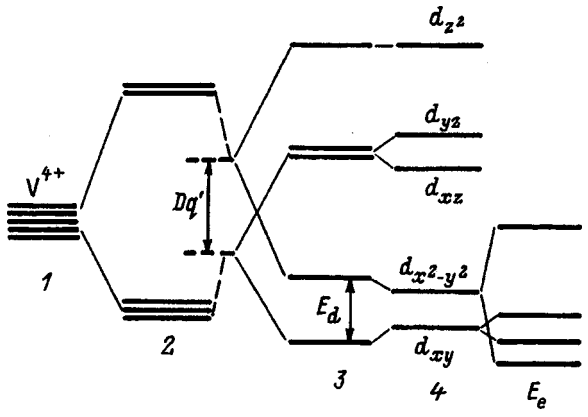

FIG. 6. A schematic diagram of the energy levels of the V^{4+} ion in fields of various symmetry as the octahedron is stretched tetragonally. The ion energy is determined by the $3d$ electron. (*1*) Free ion, (*2*) octahedron, (*3*) tetragonal compression, (*4*) rhombic distortion.

cal minimum of the dimerized state. At high temperatures ($kT > E_{J-T}$), the amplitude of the vibrations of the coordination oxygen atoms exceeds Δr, and the base of the octahedron ceases to be distorted, since now the oxygen ions of which it is composed vibrate near the equilibrium distance r_0. The lattice period is no longer doubled.

It is evident from Fig. 5 that at the temperature $kT_c = E_{J-T}$, the system undergoes a transition from an ordered dimerized state at low temperatures to a disordered state at high temperatures, i.e., the spin-Peierls transition is an order-disorder phase transition. As the phase transition temperature is reached, the chain becomes uniform and, consequently, the singlet state is destroyed.

4. EXAMPLES OF ORBITAL ORDERING

Researchers have encountered difficulties in interpreting the exchange interaction of Cu^{2+} cations with 90° oblique coupling even in studies of the properties of so-called exchange clusters, which consist of isolated copper dimers. In Cu(II) dihydroxo complexes, the oblique 90° exchange takes place through dihydroxo bridges.[20] Measurements showed that both the magnitude and sign of the exchange integral for a ground-state copper dimer vary, depending on the type of bridge. The exchange integral for the excited state of the dimer is ferromagnetic. Special exchange mechanisms have been developed to explain these results.[12]

Based on the concept of orbital ordering discussed above, however, it is possible to look at copper dimers from a new standpoint. As long as the energy of the exchange interaction is less than the splitting of the levels of the d_{xy} and $d_{x^2-y^2}$ orbitals, orbital ordering does not set in and ferromagnetic exchange (3) acts between a pair of copper cations. When the exchange energy is high enough, the dimer, minimizing its energy with respect to exchange, chooses a state of orbital ordering described by the antiferromagnetic exchange integral (4). In this case, the state corresponding to a Cu($d_{x^2-y^2}$)-Cu(d_{xy}) pair should be regarded as the ground state, while the state previously regarded as the ground state, Cu($d_{x^2-y^2}$)-Cu($d_{x^2-y^2}$), should be regarded as excited. The change in the absolute magnitudes of the exchange integrals in the hydroxo complex series is caused by a change in the ligand-cation electron-transport parameters determined by the different composition and geometry of the ligands.

Another example of orbital ordering is $(VO)_2P_2O_7$. The question of which model, dimerized or staircase chain, is better suited to describing this material has been discussed in the literature.[21,22] We shall show that the concept of orbital ordering leads us to the conclusion that $(VO)_2P_2O_7$ is best described by an ensemble of isolated dimers.

The vanadium cations in $(VO)_2P_2O_7$ lie within coordination octahedra of surrounding oxygen atoms which are compressed along the a_0 axis. Along the a_0 axis, neighboring octahedra are bound by a shared oxygen atom, which allows V1(d_{z^2})-V2(d_{z^2}) oblique coupling. Isolated V^{4+} pairs lie along the b_0 axis. The octahedra of these neighboring V^{4+} have edges in common in the (b_0c_0) plane, giving rise to 90° exchange coupling along the b_0 axis. Along the c_0 axis the octahedra of neighboring V^{4+} are separated by layers containing phosphorus. The splitting of the energy levels of a V^{4+} ion in the compressed octahedron is illustrated schematically in Fig. 6. The absence of electrons in the d_{z^2} orbitals makes it possible to neglect exchange along the a_0 axis, i.e., $(VO)_2P_2O_7$ should be regarded as an ensemble of isolated V^{4+} dimers. For sufficiently large splitting of the levels of the $d_{x^2-y^2}$ and d_{xy} orbitals, the electrons on both of the neighboring V^{4+} will lie in the d_{xy} orbitals. In this case, the 90° oblique interaction in the dimer leads to ferromagnetic exchange (5) and $(VO)_2P_2O_7$ will be an ensemble of isolated ferromagnetic dimers. If, on the other hand, $E_e > E_d$, then we should expect orbital ordering in the dimer ($d_{x^2-y^2} - d_{xy}$), which leads to an antiferromagnetic interaction (4), as observed experimentally.[21] The observed gap in the magnetic excitations[22] is natural for isolated dimers, although the rhombic distortions which occur during orbital ordering will also make some contribution to this gap. It is appropriate to interpret the temperature dependence of the magnetic susceptibility of this material in terms of a model of isolated antiferromagnetic dimers, although the forms of this dependence are similar for isolated dimers, a chain, and a single staircase.

A new material, $CaCuGe_2O_6$, that has the properties of a

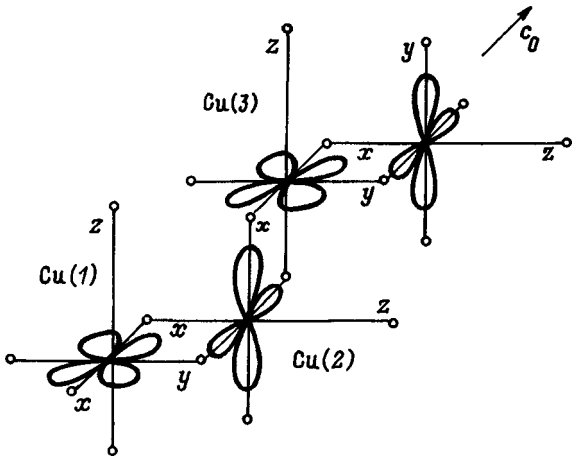

FIG. 7. Local axes of the oxygen octahedra around Cu^{2+} in $CaCuGe_2O_6$. The $3d$ orbitals, populated by holes, are shown schematically for the case of orbital ordering along a Cu^{2+} chain ($d_{xy}-d_{x^2-y^2}-d_{xy}-d_{x^2-y^2}-\ldots$), leading to a model of ferromagnetically coupled antiferromagnetic dimers.

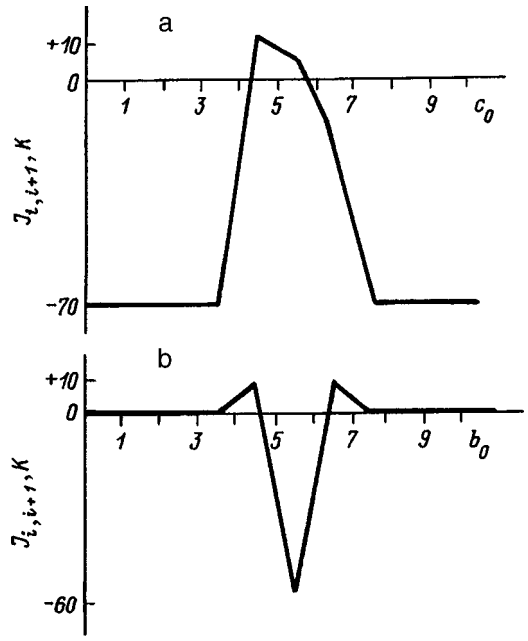

FIG. 8. Dependence of the Cu-Cu-exchange interaction on the cation number in a chain along the c_0 axis (a) and on the number of the chain along the b_0 axis (b) when the Si^{4+} dopant lies near sites 5 and 6.

spin-Peierls system with $T_{sP}\simeq 40$ K, has recently been synthesized.[23] Here the copper cations form zig-zag chains along the c_0-axis. The local symmetry around the Cu^{2+} is shown schematically in Fig. 7. The sizes of the axes of the octahedra in $CaCuGe_2O_6$ are different, with $z>y>x$. Under the action of the tetragonal distortions of the octahedra when the exchange interaction is small, the holes in all the Cu^{2+} cations lie in the $d_{x^2-y^2}$ orbitals (see Fig. 2). In this case, the oblique exchange integral of neighboring cations is given by

$$J_{12}=J_{23}=+6bcJ^{\text{int}}, \tag{6}$$

i.e., it leads to a ferromagnetic chain. When $E_e>E_d$, the exchange interaction will also determine the distribution of the electrons among the $3d$ orbitals based on the minimum energy of a cation pair. We have two possible ways of distributing the holes among the $3d$ orbitals of neighboring cations: $d_{xy}-d_{x^2-y^2}$ and $d_{xy}-d_{xy}$. In the first version,

$$J_{12}(d_{xy},d_{x^2-y^2})=-2bc\left(2U-\frac{5}{3}J^{\text{int}}\right), \tag{7}$$

and

$$J_{23}(d_{x^2-y^2},d_{xy})=+2c(2b+c)J^{\text{int}}, \tag{8}$$

i.e., the Cu(1)-Cu(2) interaction integral is antiferromagnetic, while the Cu(2)-Cu(3) integral is ferromagnetic. $3d$ orbitals of copper, occupied by holes, are shown in Fig. 7 for this version. In the second version,

$$J_{12}(d_{xy},d_{xy})=J_{23}(d_{xy},d_{xy})=+2c\left(\frac{8}{3}b+c\right)J^{\text{int}}. \tag{9}$$

In order to evaluate the exchange integrals (6)–(9), we have to know the ligand-cation electron transport parameters for a given crystal. If, on the other hand, we are interested in the relative values of these integrals, rather than their absolute values, then we can use standard estimates of these parameters for other structures. Taking the values $b=0.02$, $c=0.01$, $U(Cu^{2+})\approx 4$ eV, and $J^{\text{int}}(Cu^{2+})\approx 1$ eV for the octahedral sites of the spinel structure,[16] we obtain $+14$, -60, $+12$, and $+15$ K, respectively, for the integrals (6)–(9). The total (left+right along the chain) exchange interaction of a copper cation will be greatest for the hole distribution described by the integrals (7) and (8) and shown in Fig. 7, $|-60|+12=72$ K, compared to 28 and 30 K for the distributions (6) and (9). Thus, for an exchange interaction energy exceeding the splitting of the $d_{x^2-y^2}$ and d_{xy} orbitals, the Cu^{2+} chain in $CaCuGe_2O_6$ is a chain of antiferromagnetic dimers with a ferromagnetic interdimer interaction. Probably the intradimer interaction is ~ 5 times larger than the interdimer interaction.

The oblique coupling model is also useful for analyzing exchange interactions in crystals with different substitutions. In doped $CuGeO_3$:Si crystals, because of differences in the ionic radii of Ge^{4+} and Si^{4+}, the initial local symmetry of neighboring oxygen octahedra may be distorted through distortion of the octahedron in the base plane and a reduction in the tetragonal stretching or compression of the octahedron. In the first case, the ordered filling of the d orbitals in Cu^{2+} is disrupted and ferromagnetic pairs develop at the end of the chains. Since the Si dopant touches four neighboring chains, small degrees of doping produce a substantial number of ferromagnetic centers in the crystal, which must cause a rise in the paramagnetic susceptibility as 0 K is approached. In the second case, there is a possibility of populating the d_{z^2} orbitals of the copper cations nearest the impurity with holes, and this leads to a change in the oblique exchange interactions. The perturbation of the pairwise exchange interactions owing to the presence of the Si^{4+} impurity is shown in Fig. 8. The Si^{4+} dopant is bound to the two nearest Cu^{2+} sites along the a_0 axis and to two along the b_0 axis. In Fig. 8 these sites are indicated by the numbers 5 and 6. The change in the interaction also affects the next neighbors in the lattice. As a result, we obtain a perturbation of the pairwise interaction

along the chain, illustrated qualitatively in Fig. 8a, which leads to a change in the sign of the exchange interaction near the substituted cation. The variation in the exchange along the b_0 axis illustrates the development of interchain interactions (Fig. 8b). It is evident that the chains closest to the impurity are coupled by strong antiferromagnetic exchange. The chains after them are coupled ferromagnetically and, at large distances, the interaction is zero. Clearly, with increasing concentration of substitute Si^{4+} cations, the quasi-one-dimensional $CuGeO_3$ is converted into a quasi-two-dimensional system whose magnetic structure depends on the relationship of the antiferromagnetic and ferromagnetic bonds. It is quite possible that the appearance of an antiferromagnetic phase at low temperatures[8] is a consequence of these effects.

It has been shown therefore, that when the nature of the energy structure of the Cu^{2+} cation in the crystal field of crystalline $CuGeO_3$ is taken into account, ordered filling of the *d* orbitals along a chain of cations is possible when the exchange interaction energies of the cation pairs exceed the split in energy of the $d_{x^2-y^2}$ and d_{xy} orbitals. Orbital ordering produces an antiferromagnetic exchange interaction along a Cu^{2+} chain with 90° oblique coupling and a doubling of the lattice period.

When the Jahn-Teller stabilization energy exceeds the spin-orbit interaction energy, the reduction in symmetry of the base plane of the octahedron leads to an alternation in the angles and lengths of the exchange coupling in the Cu^{2+} chain, i.e., to alternation in the exchange interaction parameter and to a doubling of the lattice period.

$CaCuGe_2O_6$ can be represented by one-dimensional chains of antiferromagnetic dimers with a ferromagnetic interdimer coupling. The intradimer interaction is 5 times stronger than the interdimer coupling.

The entire analysis of exchange interactions in this paper has been done in terms of cubic symmetry. We assume that the nonorthogonality effects which arise with deviations from cubic symmetry are important for estimating the absolute magnitudes of the interactions, but can hardly affect the fundamental conclusions reached here.

We thank S. G. Ovchinnikov, A. I. Pankrats, K. S. Sablina, and A. M. Vorotynov for useful advice on fitting the model concepts to experimental data.

[1] G. A. Petrakovskiĭ, K. A. Sablina, A. M. Vorotynov, A. I. Kruglik, A. G. Klimenko, A. D. Balaev, and S. S. Aplesnin, Zh. Éksp. Teor. Fiz. **98**, 1382 (1990) [Sov. Phys. JETP **71**, 772 (1990)].
[2] M. Hase, I. Terasaki, and K. Uchinocura, Phys. Rev. Lett. **70**, 3651 (1993).
[3] J. W. Brag, H. R. Hart, L. V. Interrante, I. S. Jacobs, J. C. Kasper, G. D. Watkins, and S. H. Wee, Phys. Rev. Lett. **35**, 744 (1975).
[4] S. Huzinga, J. Kommander, G. A. Sawatzky, B. T. Jhole, K. Kopinga, W. J. M. DeJonge, and J. Roos, Phys. Rev. B **19**, 4723 (1979).
[5] T. Rytte, Phys. Rev. B **10**, 4637 (1974).
[6] M. Nishi, O. Fujita, and J. Akimitsu, Phys. Rev. B **50**, 6508 (1994).
[7] K. Hirota, D. T. Cox, T. E. Lorenso, G. Shirane, J. V. Tranquada, M. Hase, K. Uchinokura, H. Kojima, Y. Shibuya, and I. Tanaka, Phys. Rev. Lett. **73**, 736 (1994).
[8] L. P. Regnault, J. P. Renard, G. Dhalanne, and A. Revcolevschi, Europhys. Lett. **32**, 579 (1995).
[9] M. Nishi, O. Fujita, J. Akimitsu, K. Kakurai, and Y. Fujii, Phys. Rev. B **52**, R6959 (1995).
[10] S. Katano, O. Fujita, J. Akimutsu, and M. Nishi, Phys. Rev. B **52**, 15 364 (1995).
[11] W. Geertsma and D. Khomskii, Phys. Rev. B **54**, 3011 (1996).
[12] V. K. Voronkova, M. V. Eremin, L. V. Mosina, and Yu. V. Yablokov, Mol. Phys. **50**, 379 (1983).
[13] P. W. Anderson, Solid State Phys. **14**, 99 (1963); Phys. Rev. **115**, 2 (1959).
[14] G. A. Sawatzky, W. Geertsma, and C. Haas, J. Magn. Magn. Mater. **3**, 37 (1976).
[15] M. V. Eremin, in *Spectroscopy of Crystals* [in Russian], Nauka, Leningrad (1985), pp. 150-171; Fiz. Tverd. Tela (Leningrad) **24**, 423 (1982) [Phys. Solid State **24**, 239 (1982)].
[16] O. A. Bayukov and A. F. Savitskiĭ, Fiz. Tverd. Tela (St. Petersburg) **36**, 1923 (1994) [Phys. Solid State **36**, 1049 (1994)]; Phys. Status Solidi B **155**, 249 (1989).
[17] K. I. Kugel' and D. I. Khomskiĭ, Zh. Éksp. Teor. Fiz. **64**, 1429 (1973) [Sov. Phys. JETP **37**, 725 (1973)].
[18] M. Braden, G. Wilkendoff, J. Lorensana, M. Ain, G. J. McIntyre, M. Behruzi, G. Heger, G. Dhalenne, and A. Revcolevschi, Phys. Rev. B **54**, 1105 (1996).
[19] L. N. Bulaevskiĭ, Zh. Éksp. Teor. Fiz. **44**, 1008 (1963) [Sov. Phys. JETP **17**, 470 (1963)].
[20] Yu. V. Yablokov, V. K. Voronkova, and L. V. Mosina, *Paramagnetic Resonance of Exchange Clusters* [in Russian], Nauka, Moscow (1988), 181 pp.
[21] D. C. Johnston, J. W. Johnson, D. P. Goshorn, and A. J. Jacobson, Phys. Rev. B **35**, 219 (1987).
[22] T. Barnes and J. Riera, Phys. Rev. B **50**, 6817 (1994).
[23] Y. Susago, M. Hase, K. Uchinokura, U. Tokunaga, and N. Miura, Phys. Rev. B **52**, 3533 (1995).

Translated by D. H. McNeill

Thermodynamic parameters of diffuse phase transitions in Ag_2Te

S. A. Aliev, F. F. Aliev, and Z. S. Gasanov

Institute of Physics, Academy of Sciences of Azerbaidzhan, 370143 Baku, Azerbaidzhan
(Submitted February 28, 1998)
Fiz. Tverd. Tela (St. Petersburg) **40**, 1693–1697 (September 1998)

A differential thermal analysis in vacuum and studies of the coefficients of electrical conductivity and thermal conductivity, and of the thermal emf are made in Ag_2Te in the neighborhood of the structural phase transition. It is shown that these data can be used to calculate the switching factor $L(T)$, determine the region in which the phases coexist within the transition, and calculate the thermodynamic parameters. Prior to and after the main phase transition, additional displacement transitions are observed. It is found that the phase transition takes place roughly according to the scheme $\alpha_{385\ K}\rightarrow\alpha'_{405\ K}\rightarrow\beta'_{420\ K}\rightarrow\beta_{440\ K}$. The specific heat C_p, changes in entropy ΔS and transition enthalpy ΔH, as well as the minimum phase fluctuation volume V, and the heat Q of the phase transition are determined. It is shown that excesses of Te and Ag have almost no effect on the transition temperatures T_0, but have a substantial effect on the thermodynamic parameters. © *1998 American Institute of Physics.*
[S1063-7834(98)02709-9]

Studies of processes taking place near and in the neighborhood of phase transitions are one of the developing areas of solid-state physics. The discontinuous change in the electrical and thermal properties which occurs during a phase transition is often utilized to create various kinds of transducers. This requires reliable data on the magnitude and characteristics of the change in the effect under consideration during the phase transition, on the temperature range of the transition, and on the effect of impurities, deviations from stoichiometry, and other external influences on them. This set of data may point the way to stabilizing and controlling phenomena during the phase transition. Here information on the phase transition process itself and on its parameters is extremely important. Determining the thermodynamic and kinetic parameters of the transition and studying the various structural characteristics of the interacting modifications during the course of the phase transition aid in clarifying the mechanism for the transition. Data on the intensity of x-ray reflections from each phase in the region of the phase transition are used to determine the region in which the phases coexist and the switching factor $L(T)$, which characterizes the relative fractions of the phases.

It has been found[1] that in Ag_2Te of stoichiometric composition and with excess Te, the main $\alpha\rightarrow\beta$ transition is preceded by an $\alpha\rightarrow\alpha'$ transition, and in samples with an excess of silver, a number of other phase transitions also take place. Thus, it was necessary to make a more detailed investigation of samples from the entire series and to determine the switching function and other thermodynamic parameters for all the observed phases of Ag_2Te, as well as to study the effect on them of excess tellurium and silver. For this purpose, we propose to use data on the electrical and thermal properties in the neighborhood of the phase transition.

1. EXPERIMENTAL RESULTS

We have studied the temperature dependences of the electrical conductivity $\sigma(T)$ and thermal emf $\alpha_0(T)$, as well as the temperature drop along the sample ΔT_x, and performed differential thermal analysis (DTA) ΔT_y on a series of Ag_2Te samples, including with a stoichiometric composition, and with excess Te (up to 0.75 at. %) and Ag (up to 0.25 at. %). DTA was performed in apparatus which allowed the experiments to be made in vacuum.[2]

Figures 1 and 2 show typical plots of the temperature dependences of $\sigma(T)$ and $\alpha_0(T)$ for samples having sto-

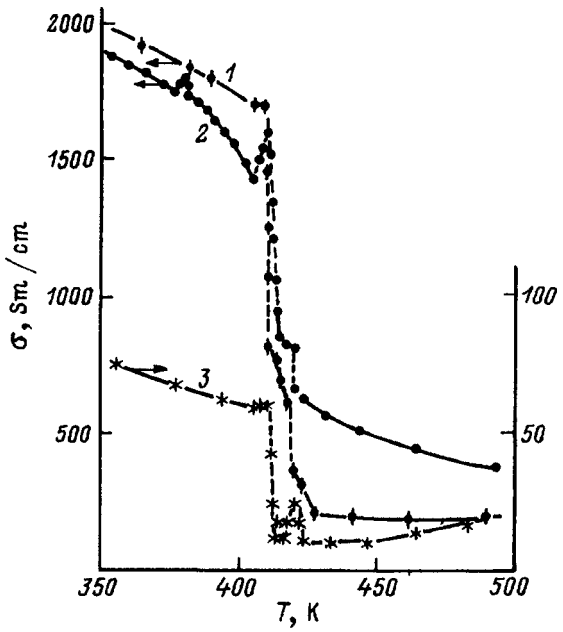

FIG. 1. Temperature dependence of the electrical conductivity $\sigma(T)$ in Ag_2Te. (*1*) Stoichiometric composition, (*2*) with excess Ag, (*3*) with excess Te.

 © 1998 American Institute of Physics

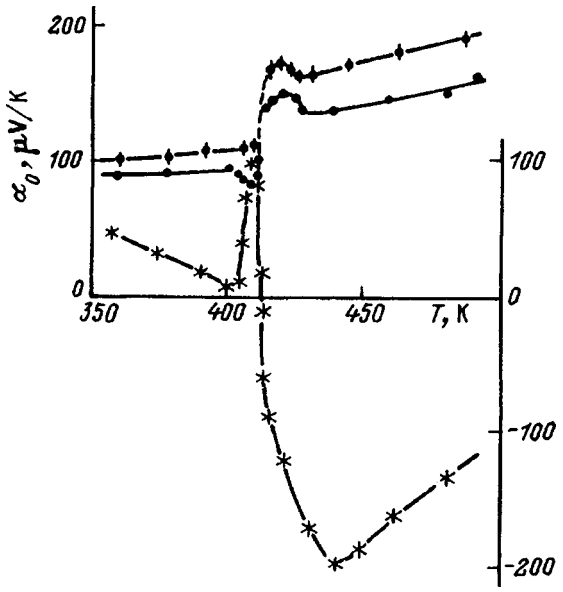

FIG. 2. Temperature dependence of the thermal emf $\alpha_0(T)$ in Ag_2Te.

ichiometric compositions and with excess Te and Ag. The $\sigma(T)$ curves for the samples with a stoichiometric composition and excess Te have a plateau before the main phase transition at temperatures of 400–410 K, drop abruptly at 410 K, and have another plateau at 414–418 K. Furthermore, in the sample with a stoichiometric composition, σ drops sharply (by 422 K), while in the sample with excess Te it passes through a slight maximum. In the sample with excess Ag, at temperatures of 400–410 K, there is a sharp rise in $\sigma(T)$ instead of a plateau, after which the temperature variation of the stoichiometric composition is repeated. This is all repeated in reverse order in the $\alpha_0(T)$ curves.

Figure 3 shows DTA plots of $\Delta T_y(T)$ for a stoichiometric composition (*1*), and compositions with excess Te (*2*) and excess Ag (*3*). It can be seen that prior to the main transition and after it, transitions occur in which heat is absorbed. In the sample with excess Ag, besides these three transitions, a transition is also observed at 364–367 K. Note that the weak transitions appear in the $\Delta T_y(T)$ curves only under adiabatic conditions, while electronic processes act on them regardless of the experimental conditions. Figure 3b shows plots of $\Delta T_x(T)$. Because of the presence of a temperature gradient along the sample, the $\Delta T_x(T)$ curves are displaced toward lower temperatures, and the weak transitions do not always show up. It is clear that ΔT_x passes through a deep minimum, which means that the coefficient of thermal conductivity is passing through a sharp maximum.

2. DISCUSSION OF RESULTS

The occurence of additional phase transitions in Ag_2Te was reported in Ref. 1, where the existence of an α' phase with trigonal structure at temperatures of 533–633 K was indicated on the basis of measurements of $\sigma(T)$. A phase transition was later observed[3] in the temperature dependence of the ionic conductivity σ at $\sim$306 K and identified as second order. It was then concluded[4] that two phase transitions (at temperatures of 150–250 K and at 307 K) occur in the low-temperature phase of Ag_2Te, which are similar in nature to first-order phase transitions. It was noted that impurity Te up to 0.75 at. % smears these phase transitions out strongly.

The physics of diffuse phase transitions has been examined elsewhere.[5,6] The question of the coexistence of each of the phases in the transition region is also analyzed there. A theory of diffuse phase transitions in condensed systems, based on introducing the switching function $L(T)$, was used for this purpose. It is assumed that if the thermodynamic potentials of the α and β phases are denoted by Φ_a and Φ_b, then the thermodynamic potential $\Phi(T)$ in the region where the phases coexist can be written in the form

$$\Phi(T)=\Phi_\alpha(T)-\Delta\Phi(T)L(T), \tag{1}$$

where $\Delta\Phi(T)=\Phi_\beta(T)-\Phi_\alpha(T)$. When the phase transition takes place over a temperature interval $\Delta T=T_2-T_1$ ($T_2>T_1$), the switching function must satisfy the conditions

$$L(T)=\begin{cases}0, & T<T_1,\\ 0<L<1, & T_1<T<T_2,\\ 1, & T>T_2.\end{cases} \tag{2}$$

The theory of diffuse transitions yields the following expression for the switching function,

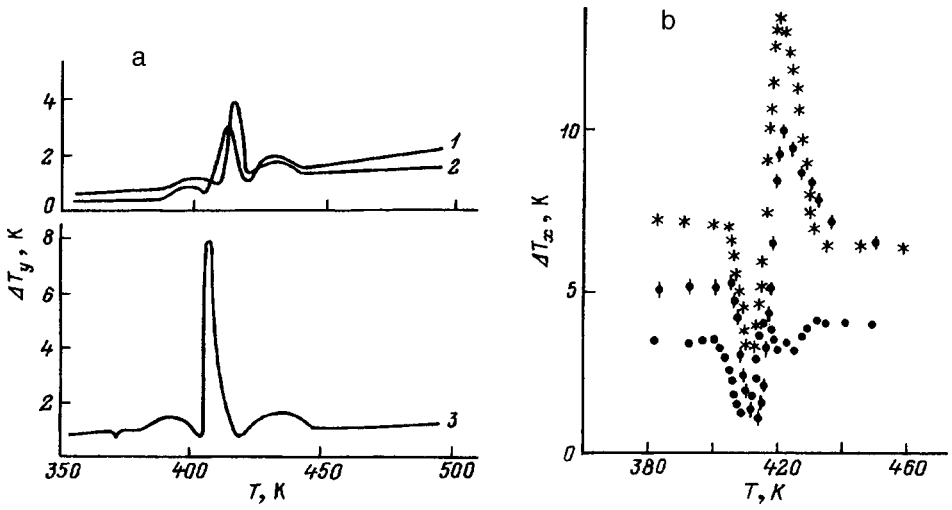

FIG. 3. Temperature dependences of the differential thermal analysis $\Delta T_y(T)$ (a) and of $\Delta T_x(T)$ (b).

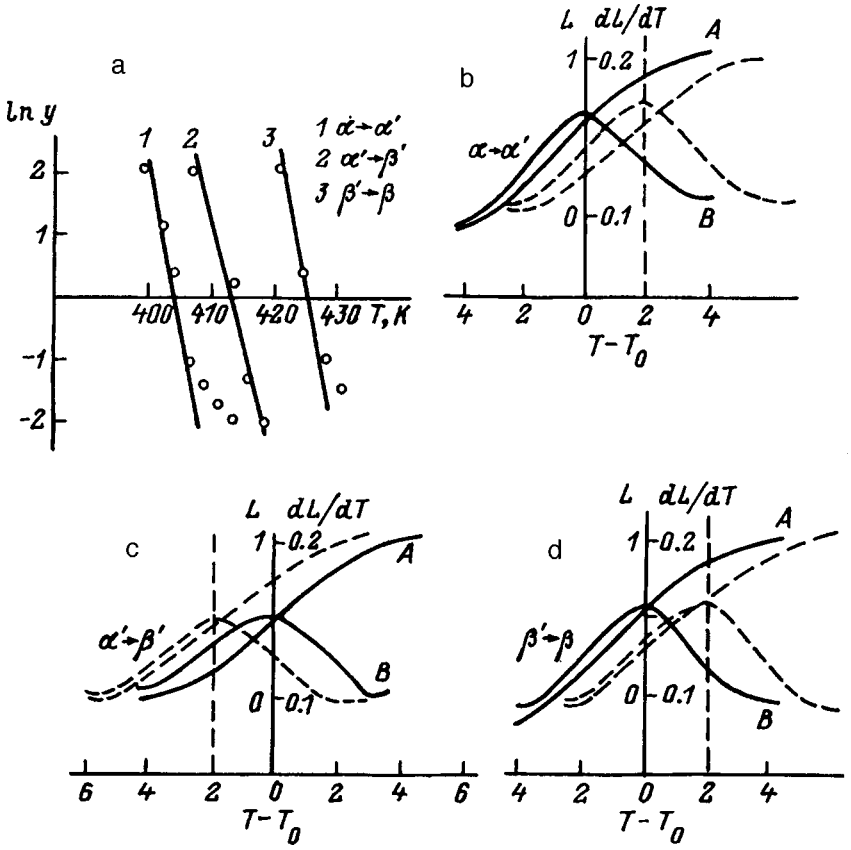

FIG. 4. Temperature dependences of the mass distribution $\ln y$ (a), switching function $L(T)$ (*A*) and its derivative dL/dT (*B*) in Ag_2Te (with excess Te) for the phase transitions $\alpha \rightarrow \alpha'$ (b), $\alpha' \rightarrow \beta'$ (c), and $\beta' \rightarrow \beta$ (d). The dashed curves (b–d) were calculated including the variation in the internal energy of the crystal during the phase transition.

$$L(T) = \{1 + \exp[-a(T - T_0)]\}^{-1}, \tag{3}$$

where the constant a, which characterizes the degree to which the phase transition is smeared out, depends on the volume of the possible phase fluctuations and the energy and temperature of the phase transition. Given that the switching function characterizes the relative fractions of the phases in the region where they coexist, it can be written in the simple form

$$L(T) = \frac{m_\beta(T)}{m_\alpha(T) + m_\beta(T)} = \left[1 + \frac{m_\alpha}{m_\beta}(T)\right]^{-1}, \tag{4}$$

where m_α and m_β are the masses of the α and β phases. From the temperature dependence of $\ln(m_\alpha/m_\beta)$, we can determine the temperature T_0 at which the masses of the two phases are equal. Comparing Eqs. (3) and (4), we obtain

$$a = \frac{1}{T_0 - T} \ln\left(\frac{m_\alpha}{m_\beta}\right). \tag{5}$$

If a is a constant, then the factor $\ln(m_\alpha/m_\beta)$ should be a linear function of the temperature difference $T_0 - T$. The possibility of determining this function from structural studies of phase transitions in solids has been demonstrated elsewhere.[4,7,8] There it was assumed that within a narrow range of coexistence of the phases, the temperature variation in the intensities of the x-ray reflections is caused by a quantitative change in the phases. If we assume that, within this region, the temperature variations in the electrical and thermal properties are also caused mainly by the quantitative change in the phases, then $L(T)$ can be determined from these data, as well. To do this, it is necessary to attain a linear temperature variation near and within the transition region. Then, form the beginning of the transition until the end, the interval ΔT can be broken up into equal steps and the corresponding values of the effects under study can be assigned to the assumed phases; for example,

$$\Delta T_y = T_{y,\alpha}\left(1 - \frac{m_\beta}{m_\alpha}\right) + \Delta T_{y,\beta}\left(\frac{m_\beta}{m_\alpha}\right).$$

Figure 4 shows typical plots of $\ln y$ ($y = m_\alpha/m_\beta$) as a function of T for samples containing excess Ag, where the corresponding masses m_α and m_β are determined from the $\Delta T_y(T)$ data (1). The nominal temperatures T_0 of the observed phase transitions are determined from the point of intersection of the line with the abscissa. The straight lines in this figure correspond to $y = \exp(-a(T - T_0))$, where the values of a, determined from the slope of the lines, are the temperature constants of the transition. As can be seen, in these coordinates the straight lines encompass almost the entire interval of the phase transition, which indicates the correctness of the method for determining $m_\alpha/m_\beta(T)$. The a and T_0 obtained from $\Delta T_y(T)$ and $\sigma(T)$ are in good agreement (see Table I), but the data from $\alpha_0(T)$ are somewhat shifted toward higher temperatures owing to the presence of a temperature drop along the sample during the measurement of $\alpha_0(T)$.

According to the theory of heterophase fluctuations,[5] $a = VQ(kT_0)^{-2}$, where V is the phase fluctuation volume, Q is the heat of the phase transition per unit volume, and T_0 is the phase transition temperature. Thus, V can be regarded as the minimum volume within which a distinct phase transition

TABLE I. Thermodynamic parameters of Ag_2Te in the region of the phase transitions

Sample	Transition	$T_{0,\sigma}$ K	$T_{0,\mathrm{DTA}}$, K	a, K^{-1}	Q, cal/g	V, 10^{20} cm^3	ΔH, cal/mol	ΔS, cal/mol·K	S, cal/mol·K	ΔC_p, cal/mol·K	C_p cal/mol·K
Ag_2Te	$\alpha\rightarrow\alpha'$	407	400	0.31	0.9	2.28	309	0.77	42.65	0.06	47.55
	$\alpha'\rightarrow\beta'$	410	416	0.42	3.8	0.82	1304	3.13	44.21	0.35	163.2
	$\beta'\rightarrow\beta$	419	432	0.30	0.83	2.90	285	0.69	44.55	0.07	45.17
Ag_2Te+0.75 at. % Te	$\alpha\rightarrow\alpha'$	408	394	0.44	1.2	1.70	412	0.52	41.93	0.12	65.17
	$\alpha'\rightarrow\beta'$	411	416	0.47	3.9	0.89	1340	3.32	44.61	0.40	167.34
	$\beta'\rightarrow\beta$	420	430	0.30	1.0	2.38	343	0.80	45.01	0.09	49.08
Ag_2Te+0.25 at. % Ag	$\alpha\rightarrow\alpha'$	407	393	0.33	1.6	1.30	549	1.40	42.97	0.14	69.37
	$\alpha'\rightarrow\beta'$	412	414	0.42	4.1	0.73	1407	3.41	44.67	0.37	176.04
	$\beta'\rightarrow\beta$	418	430	0.33	1.1	2.38	378	0.88	45.11	0.10	52.01

takes place, or as the volume of a particle of the new phase inside the old. The amount of heat (released, $+Q$, or absorbed, $-Q$) during the phase transition is determined from the $\Delta T_y(T)$ as $Q=khbM/vm$, where h and b are the height and half-width of the maximum or minimum, M is the molecular mass, v is the rate of heating, and m is the sample mass. The values of Q and V for the corresponding phase transitions are shown in the table. V is considerably smaller for the $\alpha'\rightarrow\beta'$ transition than for the $\alpha\rightarrow\alpha'$ and $\beta'\rightarrow\beta$ transitions, i.e, the phase transition $\alpha'\rightarrow\beta'$ takes place in substantially smaller volumes. The switching function $L(T)$ for each of the phases is determined from the a and T_0 data using Eq. (3). Typical $L(T)$ curves are shown in Figs. 4b–4d. These figures also show the derivatives with respect to temperature,

$$\frac{dL}{dT}=\frac{a}{2}\,\frac{1}{1+\cosh[a(T-T_0)]}, \tag{6}$$

which express the temperature rates of the phase transformations of each phase. The switching function can be used to determine the type of behavior and the magnitude of the jump in various thermodynamic quantities in the region of a diffuse phase transition. In particular, the entropy of transition and the specific heat at the nominal point T can be determined from the equations

$$S=-\frac{\partial\Phi}{\partial T}=S_1+\Delta SL, \tag{7}$$

and

$$C_p=T\,\frac{\partial S}{\partial T}=C_{p1}+\Delta C_pL+T\Delta S\,\frac{\partial L}{\partial T}, \tag{8}$$

where S_1 and C_{p1} are the entropy ad specific heat prior to the onset of the phase transition and ΔS is the entropy of transformation. Here ΔC_p is calculated from the data on Q, ΔT, and m ($\Delta C_p=Q/m\Delta T_x'$).

Note that, for these calculations, a correction must be made to ΔT_x associated with its change owing to the release or absorption of internal energy of the crystal during the phase transition: $\Delta T_x=T_{\mathrm{end}}-T_{\mathrm{beg}}+vt$. (See the dashed curves in Fig. 4.) The change in the enthalpy ΔH during the phase transition is equated to the amount of heat per mole, calculated on the basis of the differential thermal analysis in units of cal/mol. The results are shown in the table.

For a constant W driving the ΔT_x, the temperature dependence $\Delta T_x(T)$ reflects the reverse variation in the temperature dependence of the thermal conductivity $\varkappa$, which is indicative of a sharp maximum in $\varkappa$ at the phase transition point.

It is known that for a first-order phase transition the specific heat should pass through a sharp peak, breaking at the transition point. This has been observed repeatedly in experiments, including in Ag_2Te. Since $\varkappa_p\propto C$, we can assume that, in the neighborhood of the phase transition, the temperature variation in $\varkappa(T)$ is mainly caused by $C(T)$. From the set of experimental data and the thermodynamic parameters derived from them (see the table), we conclude that in Ag_2Te the phase transition from the monoclinic αT phase to the fcc β phase is accompanied by additional transitions $\alpha\rightarrow\alpha'$ and $\beta'\rightarrow\beta$, roughly according to the scheme $\alpha_{385}\rightarrow\alpha'_{405}\rightarrow\beta'_{420}\rightarrow\beta_{440}$. It has been shown that excesses of Te and Ag have no effect on the transition temperatures T_0, but they do have a substantial effect on the thermodynamic parameters. The ratio of the thermodynamic parameters of the main transition $\alpha'\rightarrow\beta'$ to the parameters of the accompanying transitions ($\alpha\rightarrow\alpha'$ and $\beta'\rightarrow\beta$) is as high as 5. This is in agreement with the general concept of a structural phase transition,[9] according to which, during a transition of a crystal with low symmetry into a crystal of higher symmetry, the main transition can be accompanied by displacement transitions (disordering of the sublattice). However, a final conclusion regarding the structure of the phases $\alpha\rightarrow\alpha'$ and $\beta'\rightarrow\beta$ will require more detailed structural studies.

[1] J. Szumi and S. Miyatani, J. Phys. Soc. Jpn. **35**, 312 (1973).
[2] S. A. Aliev, F. F. Aliev, and G. P. Pashaev, Neorg. Mater. **29**, 1073 (1993).
[3] E. S. Krupnikov, F. Yu. Aliev, and A. G. Abdullaev, Fiz. Tverd. Tela (Leningrad) **22**, 2468 (1980) [Sov. Phys. Solid State **22**, 1438 (1980)].
[4] E. S. Krupnikov, F. Yu. Aliev, and S. A. Aliev, Fiz. Tverd. Tela (Leningrad) **33**, 3408 (1991) [Sov. Phys. Solid State **33**, 1922 (1991)].
[5] B. N. Rolov, in *Diffuse Phase Transitions* [in Russian], Riga (1972), p. 311.
[6] B. N. Rolov, Izv. AN LatvSSR. Ser. Fiz. i Tekhn. nauk **4**, 33 (1983).
[7] K. P. Mamedov, M. F. Gadzhiev, and Z. D. Nurieva, DAN SSSR **231**, 94 (1976).
[8] K. P. Mamedov, M. F. Gadzhiev, and Z. D. Nurieva, Fiz. Tverd. Tela (Leningrad) **19**, 2196 (1977) [Sov. Phys. Solid State **19**, 1285 (1977)].
[9] M. J. Berger, Kristal. **16**, 1084 (1971).

Translated by D. H. McNeill

Anomalous behavior of dielectric permittivity of $Li_2Ge_7O_{15}$ crystals at a phase transition

A. Yu. Kudzin, M. D. Volnyanskiĭ, M. P. Trubitsyn, and I. A. Busoul

Dnepropetrovsk State University, 320625 Dnepropetrovsk, Ukraine
(Submitted March 16, 1998)
Fiz. Tverd. Tela (St. Petersburg) **40**, 1698–1700 (September 1998)

It is shown that the Curie-Weiss relation describes unsatisfactorily the temperature dependence of dielectric permittivity at the transition from orthorhombic paraphase to polar phase.
© *1998 American Institute of Physics.* [S1063-7834(98)02809-3]

The transition from the orthorhombic paraphase of symmetry D_{2h}^{14} to the C_{2v}^{5} polar phase in $Li_2Ge_7O_{15}$ (LHG) crystals occurs[1] at $T_c = 283.5$ K without any change in unit cell parameters and is accompanied by a weak anomaly in dielectric permittivity[2]. The physical properties of uniaxial proper ferroelectrics in the vicinity of phase transitions can be described, as a rule, in terms of the Landau theory with logarithmic corrections, which appear when fluctuations in the order parameter and the effect of long-range dipole-dipole interactions are taken into account.[3]

The temperature dependence of dielectric permittivity of LHG crystals near T_c was studied earlier.[2] An analysis of the nature of the $\varepsilon(T)$ behavior led to a conclusion that the Curie-Weiss law holds within a narrow temperature interval of ~ 3 K above T_c and yielded for the constant $C = 4.6$ K.[2] At the same time submillimeter spectroscopy data indicate an anomalously small effective charge of the soft mode in LHG.[4] This was stressed to be a key factor and, because it directly entails weakness of dipole interactions, one may expect fluctuations in the order parameter to provide a noticeable contribution to the anomalies in the physical properties of LHG near T_c.[5]

This work reports measurements of the dielectric permittivity of LHG crystals within the temperature interval of 273–315 K, which includes the ferroelectric phase-transition point. The crystals were pulled from the melt by the Czochralski method. Platinum electrodes 3 mm in diameter were deposited on sample plates measuring $7 \times 7 \times 0.5$ mm. The measurements were performed along the [001] polar axis at a frequency of 1 kHz. Figure 1 shows graphically the relation obtained under cooling at a rate of ~ 0.2 K/min. The dielectric permittivity exhibits a clearly pronounced anomaly and reaches $\varepsilon^{\max} \sim 300$ at $T^{\max} = 283.902$ K. The values of $\varepsilon^{\max}$ obtained from different samples scatter within the region of 250–350. The pattern itself of the experimental relation (Fig. 1) and the value of $\varepsilon^{\max}$, which exceeds by nearly an order of magnitude the peak value $\varepsilon^{\max} \sim 43$ quoted in Ref. 2, attest to a high quality of the crystals used in this work.

Because processes associated with domain-structure rearrangement can contribute to the dielectric permittivity below T_c, an analysis was carried out of the pattern of the experimental $\varepsilon(T)$ relation within the interval where the paraelectric phase prevails. The experimental data were treated numerically from $T^{\max} + 0.1$ K to $T^{\max} + 17$ K. The reproducibility of ε measurements degraded in the immediate vicinity of the transition point, $T - T^{\max} < 0.1$ K, and it was difficult to follow the true course of the dielectric permittivity because of errors in temperature control and of the singularity in the $\varepsilon(T)$ dependence. The interval studied was limited on the high-temperature side because, above $T^{\max} + 17$ K, the dielectric permittivity tends to saturation and, thus, varies very weakly. In this case isolation of the anomalous part of ε becomes essentially dependent on variation of the background value of ε_0 within a range in excess of experimental error.

We performed least-squares fitting of the Curie-Weiss relation including the temperature-induced drift of the background dielectric permittivity

$$\varepsilon = (\varepsilon_0 + pT) + C/(T - T_c) \tag{1}$$

to experimental data. The parameters thus found are $\varepsilon_0 = 10.632$, $p = 1.4 \times 10^{-5}\,\mathrm{K}^{-1}$, $C = 3.393$ K, and $T_c = 283.951$ K, with a mean rms error $\sigma = 9.5 \times 10^{-2}$. The Curie-Weiss constant of ~ 3.4 K obtained here differs from the value of 4.6 K quoted in Ref. 2, which may probably be

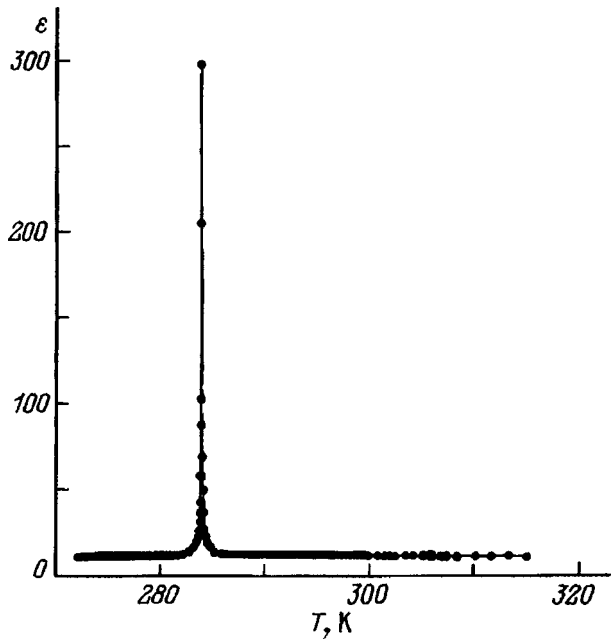

FIG. 1. Temperature dependence of $\varepsilon(T)$ of LHG crystals measured along the polar axis [001] in the vicinity of the phase transition.

 © 1998 American Institute of Physics

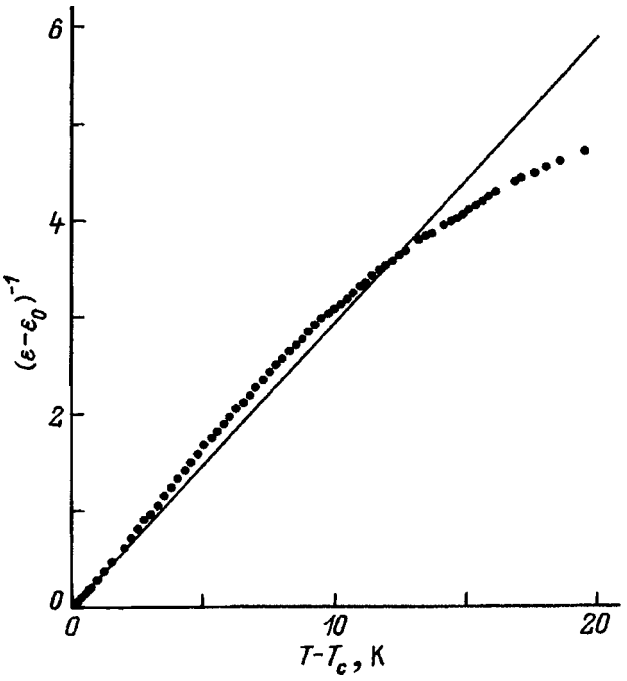

FIG. 2. $(\varepsilon-\varepsilon_0)^{-1}$ *vs* $(T-T_c)$ plot. Filled circles — experiment, solid line — a plot of Eq. (1).

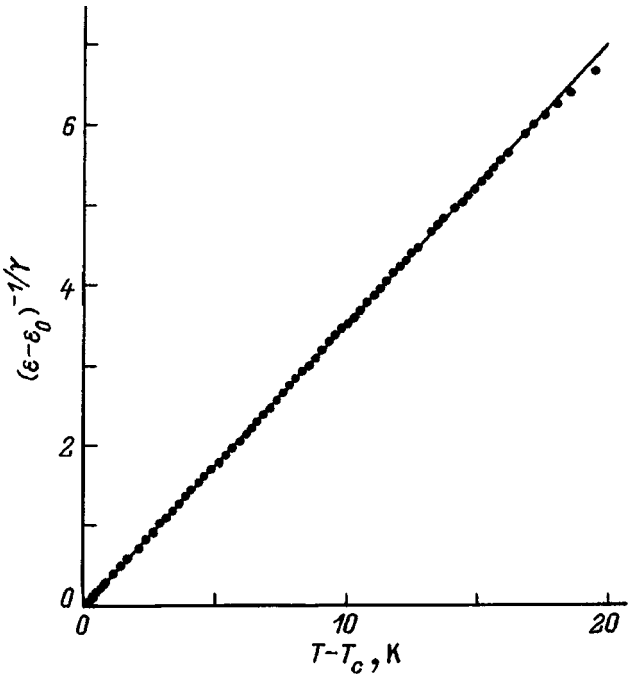

FIG. 3. $(\varepsilon-\varepsilon_0)^{-1/\gamma}$ *vs* $(T-T_c)$ plot. Filled circles — experiment, solid line — a plot of Eq. (2).

assigned to different lengths of the temperature intervals within which the behavior of $\varepsilon(T)$ was described in terms of Landau theory.

The experimental dependence was fitted within the same temperature interval by a power-law relation

$$\varepsilon=(\varepsilon_0+pT)+A/(T-T_c)^{-\gamma}. \tag{2}$$

Using Eq. (2) for the fitting, which includes as an additional parameter the critical susceptibility index γ, produced the following results: $\varepsilon_0=10.724$, $p=1.10\times10^{-4}\,\mathrm{K}^{-1}$, $A=3.779\,\mathrm{K}^{\gamma}$, $\gamma=1.261$, and $T_c=283.881\,\mathrm{K}$. The relative rms error was $\sigma=1.24\times10^{-2}$.

In this way, the use of the power-law relation (2) resulted in a decrease of the value of σ by more than a factor seven compared to approximation (1). The fits of relations (1) and (2) to the experimental $\varepsilon(T)$ dependence are shown graphically in Figs. 2 and 3, respectively.

The above results permit a conclusion that the power-law relation (2) provides a considerably better fit to the dielectric permittivity of LHG crystals near the phase transition than the classical formula (1). It should be pointed out that the dielectric permittivity obeys relation (2) over a substantially broader temperature region, $\sim20\,\mathrm{K}$ (Fig. 3), than the $\sim3\,\mathrm{K}$ interval within which the classical behavior was assumed[2].

The susceptibility index $\gamma\approx1.26$ is in agreement with studies of Raman scattering in LHG crystals[6] and coincides to within the experimental error of ±0.01 with the theoretical value predicted by Ising's three-dimensional model[7]. Remarkably, the conclusion of the critical behavior in LHG crystals being of the Ising type, which was obtained in studies of macroscopic properties, is supported by EPR measurements of local characteristics and agrees with the critical order-parameter index $\beta\approx0.32$ quoted in Ref. 8.

The specific features of the critical phenomena in LHG are obviously due to the "weakness" of the ferroelectric properties of these crystals[5], which makes the characteristics typical of ordering-type transitions dominant over a broad region around T_c.

[1] S. Haussuhl, F. Wallrafen, K. Recker, and J. Eckstein, Z. Kristallogr. **153**, 329 (1980).
[2] M. Wada and Y. Ishibashi, J. Phys. Soc. Jpn. **52**, 193 (1983).
[3] B. A. Strukov and A. P. Levanyuk, *Physics of Ferroelectric Phenomena in Crystals* [in Russian], Nauka, Moscow (1983), 240 pp.
[4] A. Volkov, G. V. Kozlov, Yu. G. Goncharov, M. Wada, A. Sawada, and Y. Ishibashi, J. Phys. Soc. Jpn. **54**, 818 (1985).
[5] A. K. Tagantsev, JETP Lett. **45**, 447 (1987).
[6] G. Y. Shitov, P. N. Timonin, V. I. Torgashev, L. T. Latush, and Y. I. Yuzyuk, Phase Transit. **46**, 143 (1994).
[7] A. E. Stanley, *Introduction to Phase Transitions and Critical Phenomena* [Clarendon Press, Oxford, 1971; Nauka, Moscow, 1973, 419 pp.].
[8] M. P. Trubitsyn, Fiz. Tverd. Tela (St. Petersburg) **40**, 114 (1998) [Phys. Solid State **40**, 101 (1998)].

Translated by G. Skrebtsov

LATTICE DYNAMICS. PHASE TRANSITIONS

Ordering of interacting subsystems. Molecular dynamics

A. É. Filippov

Donetsk Physicotechnical Institute, Academy of Sciences of Ukraine, 340114 Donetsk, Ukraine
(Submitted February 2, 1998)
Fiz. Tverd. Tela (St. Petersburg) **40**, 1701–1704 (September 1998)

The molecular dynamics method is used to examine the ordering of interacting subsystems in a two-component, two-dimensional Coulomb gas, consisting of equal amounts of positively and negatively charged particles, which simulates the behavior of a system of interacting vortices. In particular, it is found that when the system temperature is lowered from the Kosterlitz–Thouless transition point, additional ordering of the vortex chains may take place. It is noted that this process may stimulate the development of vortex chains observed in real superfluid, magnetic, and superconducting systems. Possible applications of the molecular dynamics method to phase separation and the ordering of adiabatically slowly moving subsystems in the collective field of a fast subsystem are considered. © *1998 American Institute of Physics.* [S1063-7834(98)02909-8]

The dynamics of ordering in spatially inhomogeneous systems and of phase separation recently have received special attention. Advances in computing continually are reducing the required degree of approximation in describing the processes numerically, which previously reduced to transforming from a many-particle dynamics problem to one or another form of continuum description based on collective fields (densities) and permits the direct numerical modelling of rather complex systems with long-range interactions. This makes it possible to verify the results of the continuum theory and to observe structural features of the system which are clearly lost in a crude description.

Examples of both approaches can be found in the stream of related publications.[1–12] Thus, for example, computer simulations of phase separation and spinoidal decay in simple and binary liquids[1–3] have been substantially oriented toward reproducing the results of the analytic theory,[4] while the intricate dipole chains obtained numerically[5–7] are extremely hard to find analytically. By varying the dynamic scenarios, it is possible to predict the structures, themselves, as well as ways to realize them experimentally. Here, quite realistic models are employed in the models, as, for example, in simulations of the crystallization of molecular liquids.[8,9]

These simulations have stimulated searches for analogous structures by methods based on analytic continuum fields and in experiments. As an example, the observation of orientationally ordered structures of liquids in molecular dynamics (systems of dipoles with hard spherical cores[5,6]) has aided studies of long-range ordering in dipole liquids based on the density functional.[10] Numerical experiments on quasicrystallization of vortices in two-dimensional turbulence[10,11] have been extended to natural ones, through the observation of relaxation of the random motion of magnetized electrons (which reproduce an almost ideal $2D$ liquid) in a vortex crystal.[12]

As a rule, models of long-range orientational ordering in dipole systems are based on a combination of the Lennard–Jones potential,[5–7] $w_{LJ}(r)=4\varepsilon[(\sigma/r)^{12}-(\sigma/r)^{6}]$, and the dipole potential, $w_{\mathrm{dip}}(\mathbf{r})=-3(\mu_2\cdot\mathbf{r})(\mu_1\cdot\mathbf{r})/r^5+\mu_2\mu_1/r^3$, which bears a certain imprint of the analytic tradition. It might, however, be expected that as they join to form pairs and groups, charged particles would spontaneously form a (multipole) molecular liquid with properties analogous to those used in Refs. 5–7, while retaining the degrees of freedom (rotational, vibrational, the ability to dissociate and recombine, etc.) characteristic of real molecules. This last point opens up wider possibilities than the traditional approach. Besides this, numerical solution of equations with the simplest structure for the elementary interactions can be done much faster for fairly large blocks (on the order of 10^3 particles, moving in three or two dimensions). In this paper,

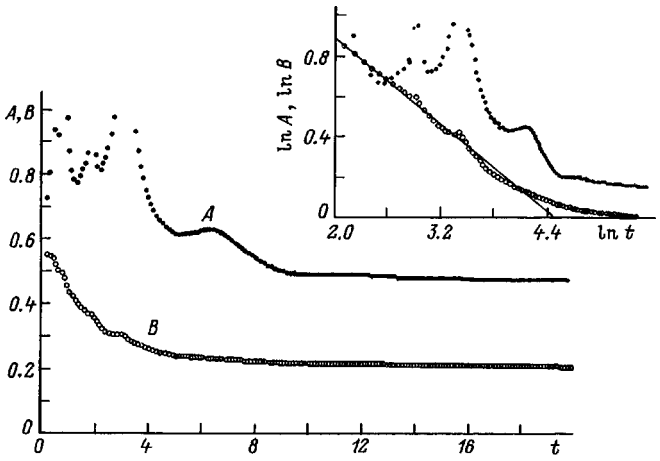

FIG. 1. Time evolution of the parameters $A=\{\Sigma_j[1/|\mathbf{r}_{jj'}|]+\Sigma_i[1/|\mathbf{r}_{ii'}|]\}/2-\Sigma_{ij}[1/|\mathbf{r}_{ij'}|]$ and $B=\Sigma_{kk'}[1/|\mathbf{r}_{kk'}|]$. The inset shows the same curves on a log-log scale.

 © 1998 American Institute of Physics

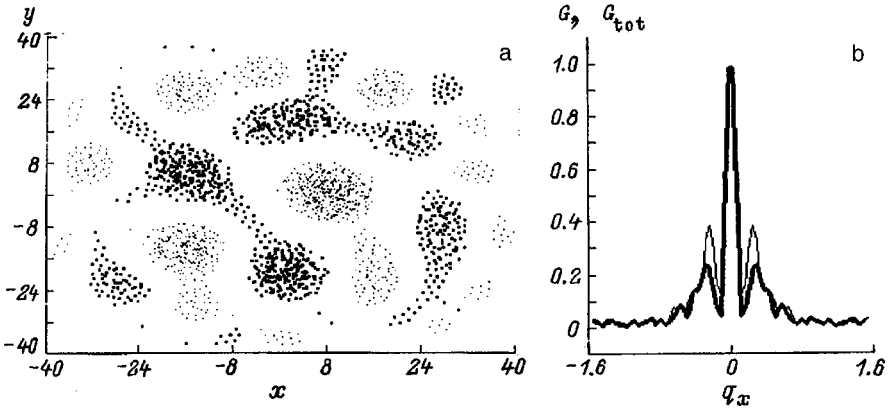

FIG. 2. (a) An intermediate stage of phase separation in molecular dynamics. The particles of different types are indicated by points of different sizes. (b) Fourier transforms of the total correlation function $G_{\text{tot}}(\mathbf{q})=\int d\mathbf{r}d\mathbf{r}'\ \exp[i\mathbf{r}\cdot\mathbf{q}]\langle\rho(\mathbf{r})\rho(\mathbf{r}+\mathbf{r}')\rangle \neq 0$, calculated by summing the discrete density over both subsystems, $\rho(\mathbf{r})=\rho_1(\mathbf{r})+\rho_2(\mathbf{r})=\Sigma_k\delta(\mathbf{r}-\mathbf{r}_k)$ (thin line), and the partial function $G_1(\mathbf{q})=\int d\mathbf{r}d\mathbf{r}'\ \exp[i\mathbf{r}\cdot\mathbf{q}]\times\langle\rho(\mathbf{r})\rho(\mathbf{r}+\mathbf{r}')\rangle$, calculated from one of them individually (thick line).

some results on the modelling of dipole chains are presented, along with some illustrations of additional possibilities offered by this approach.

1. DIPOLE CHAINS

In this section some results from a simulation of the dynamics of a two-dimensional electron gas are presented, in particular, those applying to a vortex system.[13–16] Under certain assumptions,[16] the description of superfluid liquids, crystal melting, and the two-dimensional $x-y$-model for a spin lattice can be reduced to this model. It can be used to determine the topological ordering for $2D$ systems, where ordering is impossible in the usual sense,[17,18] by identifying the phase transition with the dissociation of vortical pairs.[13–15] $H=\Sigma_{i\neq j}U(\mathbf{r}_{ij})S_iS_j$ is used as a model hamiltonian, where S_i are the Coulomb charges and the potential is given by $U(\mathbf{r}_{ij})=\int d\mathbf{r}'d\mathbf{r}''f(|\mathbf{r}'-\mathbf{r}''|)V(|\mathbf{r}'-\mathbf{r}''|)f(|\mathbf{r}''|)$. Here $U(\mathbf{r})$ is an interaction of the form $U(\mathbf{r})\propto\ln(\lambda/\zeta)$ for $\lambda/\zeta\gg1$, $U(\mathbf{r})\propto-\ln(r/\lambda)$ for $\zeta\ll r\ll\lambda$, and $U(\mathbf{r})\propto r^{-1/2}\times\exp(-r/\lambda)$ for $\lambda\ll r$, and $f(|\mathbf{r}'-\mathbf{r}''|)$ is the normalized space-charge density. The dynamic equation is derived from a description of a superfluid liquid[19,20] and for inertialess vortices has the form of a Langevin equation $d\mathbf{r}_i/dt=-\partial U(\mathbf{r}_{ij})/\partial\mathbf{r}_i+\boldsymbol{\xi}(\mathbf{r}_i,t)$ with δ-correlated noise such that $\langle\boldsymbol{\xi}(\mathbf{r},t)\rangle=0$ and $\langle\boldsymbol{\xi}(\mathbf{r},t)\boldsymbol{\xi}(\mathbf{r}',t)\rangle=D\,\delta(\mathbf{r}-\mathbf{r}')\,\delta(t-t')$. Formally, it can be regarded as the limit of the dynamic equation

$$d^2\mathbf{r}_i/dt^2=-\gamma d\mathbf{r}_i/dt-\partial U(\mathbf{r}_{ij})/\partial\mathbf{r}_i+\boldsymbol{\xi}(\mathbf{r}_i,t) \qquad (1)$$

for an infinite relaxation constant γ. For dipole molecules the repulsive core at small distances must be simulated by a short-range correction $\Delta U(\mathbf{r}_{ij})$ to the potential. At finite temperatures ($\xi\neq0$), however, because of the kinetic contribution $\Delta U(\mathbf{r}_{ij})\propto1/r_{ij}^2$ to the energy, which determines the average scale length $r_0\propto\xi$ for the energy minimum, this effect also shows up in the purely Coulomb problem with a seed potential $U(\mathbf{r})\propto-\ln(r/\lambda)$. For a given density of particles (vortices) $\rho\propto1/a^2$, the relationship between r_0 and a determines the form of the resulting structure. The model stably reproduces the well-known topological transition.[13–18] It can be verified that, with intense noise (i.e., above a temperature $T\sim\xi=T_{KT}\propto\min[U(\mathbf{r}_{ij})+\Delta U(\mathbf{r}_{ij})]$), the vortices move independently and form stable pairs below T_{KT}. We shall dwell only on the new results related to the formation of a fine structure and, therefore, absent in the approximate theory. These include the formation of chains of pairs of vortices for $r_0\ll a$, which can be observed directly during the simulation process.

Chain formation can be described by the parameter $A=\{\Sigma_j[1/|\mathbf{r}_{jj'}|]+\Sigma_i[1/|\mathbf{r}_{ii'}|]\}/2-\Sigma_{ij}[1/|\mathbf{r}_{ij'}|]$, which characterizes the difference between the average distances within subsystems of vortices ($\mathbf{r}_i\in\mathbf{R}^{(+)}$) and antivortices ($\mathbf{r}_j\in\mathbf{R}^{(-)}$) and between them $\mathbf{r}_{ij}=\mathbf{r}_i-\mathbf{r}_j$) at small scale lengths (Fig. 1). The distance $B=\Sigma_k[1/|\mathbf{r}_{kk'}|]$ between vortices of both signs, where $\mathbf{r}_k\in\mathbf{R}^{(+)}\oplus\mathbf{R}^{(-)}$, here is attracted to the equilibrium value in accordance with the power law $|B-B_0|\propto t^{1/3}$ (see the inset to Fig. 1). For $r_0\cong a$ the system forms a (quasi) crystal, whose periodic structure is reflected both in the appearance of maxima in the nonzero wave vectors $\mathbf{q}_i\neq0$ of the Fourier transform of the correlation function $G(\mathbf{q})=\int d\mathbf{r}d\mathbf{r}'\ \exp[i\mathbf{r}\cdot\mathbf{q}]\langle\rho(\mathbf{r})\rho(\mathbf{r}+\mathbf{r}')\rangle$, calculated by

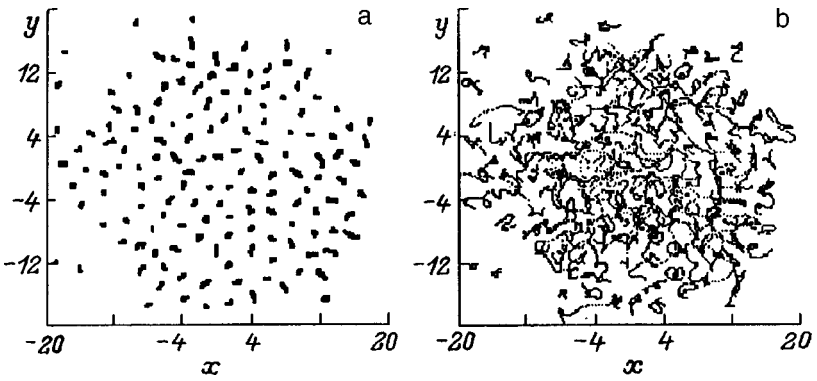

FIG. 3. A typical quasicrystalline structure obtained for a ratio of the masses of the different species on the order of 10^3. Fragments of the trajectories of (a) the heavy particles (without percolation between lattice sites) and (b) the light particles (with intense mixing) are shown to illustrate the different mobilities of the subsystems.

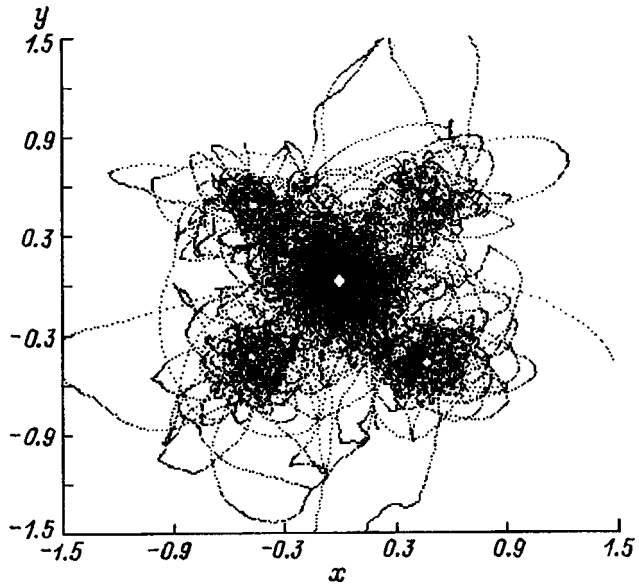

FIG. 4. Typical distribution of the electron cloud in a model BA_4 molecule. The current positions of the ions B and A stabilized by its field are indicated by the large and small white circles, respectively.

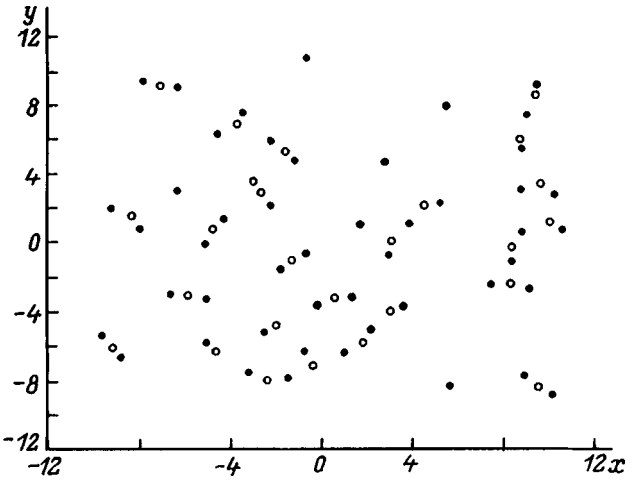

FIG. 5. An intermediate step in the generation of a chain from molecules of type A_2B. The A and B ions are indicated by dark and light circles, respectively. Here a fragment of the system is shown in which finished fragments of chains and A_2B molecules are clearly visible, as well as local groups of type A−B and A_2B−A.

summing the discrete density over both subsystems, $\rho(\mathbf{r})=\rho_1(\mathbf{r})+\rho_2(\mathbf{r})=\Sigma_k\delta(\mathbf{r}-\mathbf{r}_k)$, where $\mathbf{r}_k\in\mathbf{R}^{(+)}\oplus\mathbf{R}^{(-)}$, and in the partial form factors $S_{1,2}(\mathbf{q})=\int d\mathbf{r}d\mathbf{r}'\exp[i\mathbf{r}\cdot\mathbf{q}]\times[\langle\rho_{1,2}(\mathbf{r})\rho_{1,2}(\mathbf{r}+\mathbf{r}')\rangle-|\langle\rho_{1,2}(\mathbf{r})\rangle|^2]$, calculated from each of them separately. The distribution of vortices in the (x,y) plane is close to a sixth-order lattice. It consists of rhombohedra turned in various ways where axes of sixth, fifth, or fourth order can be observed locally.[21–23]

In free space the set of particles of one sign is stabilized by the combined field of the particles of opposite sign. The dynamic pattern is similar to an ordered structure formed in the positive column of a glow discharge in Ne,[24] where a Coulomb quasicrystal was formed by charged spherical glass particles under conditions close to those in the numerical simulations discussed here.

2. PHASE SEPARATION

A similar ordering of subsystems in their mutual self-consistent fields with formation of a crystal lattice takes place during phase separation. Figure 2a shows the intermediate stage of a separation process. (For details of the problem statement, see Refs. 1–3.) Already formed lattice fragments can be seen. Figure 2b shows the Fourier transforms of the complete correlation function, calculated over all the particles, $G_{\text{tot}}(\mathbf{q})=\int d\mathbf{r}d\mathbf{r}'\exp[i\mathbf{r}\cdot\mathbf{q}]\langle\rho(\mathbf{r})\rho(\mathbf{r}+\mathbf{r}')\rangle$, and the partial correlation function of one of the subsystems $G_1(\mathbf{q})$ (the thin and thick lines, respectively). Besides the peaks for small $q=q_{0j}\neq 0$ common to both functions, which correspond to large-scale domains in real space, in the $G_1(\mathbf{q})$ curve one can also see some additional peaks at large $q=q_{1j}\neq 0$, corresponding to a fine structure which develops inside the domains. One application of the direct simulation of phase separation may be the much discussed giant magnetoresistance in magnetic conductors. A series of data[25,26] indicate that the state of these materials, with an unsaturated spontaneous magnetic moment, is two-phase ferro-antiferromagnetic with a probable electronic mechanism for phase separation. The more favorable ferromagnetic state is possible here only after a sufficiently high carrier concentration is reached. If it is not high enough, then all the carriers can gather in localized ''ferromagnetic droplets.'' A magnetic field facilitates the transformation of the entire crystal into a ferromagnetic state. It has been suggested[25] that giant magnetoresistance is related to percolation of regions with this type of ordering.

3. ADIABATICALLY FAST MOTION OF ONE OF THE SUBSYSTEMS

The idea of this method consists of directly exploiting the balance between the noise D and relaxation γ in the framework of Eq. (1), which, essentially also reduces to a spontaneous search for energy minima by the system (and, in general, saddle kinetic trajectories[27]), in fact, ''from first principles.'' This approach to some well-known problems appears to be more convenient than numerical calculations using equations derived in the analytic tradition. These, evidently, include the adiabatic approximation. It is natural to expect that, during an interaction of subsystems with substantially different particle masses, their mutual ordering is alternated with ordering of only one of them in the average field of the other, while the motion of the fast subsystem can be characterized only by a time averaged density consistent with the structure of the slow subsystem. This effect makes it possible to demonstrate directly the ordering (of ions and electrons) in a crystal (Fig. 3) or covalent bonding in molecules (Fig. 4). Here the applicability of the method is not essentially related to the adiabatic approximation and it is still valid in the more complicated case of different masses of comparable magnitude, as occurs, for example, in the case of a ''hydrogen bond'' in molecular chains, the formation of which is illustrated in Fig. 5.

This work was partially supported by the Ukraine Fund for Fundamental Research agreement No. F4/72-97 (Project 2.4/199).

[1] E. Velasco and S. Toxyaerd, Phys. Rev. Lett. **71**, 388 (1993).
[2] F. J. Alexander, S. Chen, and D. W. Grunau, Phys. Rev. B **48**, 634 (1993).
[3] G. Leptoukh, B. Strickland, and C. Roland, Phys. Rev. Lett. **74**, 3636 (1995).
[4] S. Bastea and J. L. Lebowitz, Phys. Rev. Lett. **75**, 3776 (1995).
[5] D. Wei and G. N. Patey, Phys. Rev. Lett. **68**, 2043 (1992).
[6] J. J. Weis and A. Levesque, Phys. Rev. Lett. **71**, 2729 (1993).
[7] J. Ayton, M. I. P. Gingras, and G. N. Patey, Phys. Rev. Lett. **75**, 2360 (1995).
[8] I. M. Svishchev and P. G. Kusalik, Phys. Rev. Lett. **73**, 975 (1994).
[9] I. M. Svishchev and P. G. Kusalik, Phys. Rev. Lett. **75**, 3289 (1995).
[10] N. Kukharkin, S. A. Orszag, and V. Yakhot, Phys. Rev. Lett. **75**, 2486 (1995).
[11] L. M. Smith and V. Yakhot, Phys. Rev. Lett. **71**, 352 (1993).
[12] K. S. Fine *et al.*, Phys. Rev. Lett. **75**, 3277 (1995).
[13] V. L. Berezinskiĭ, Zh. Éksp. Teor. Fiz. **59**, 907 (1970) [Sov. Phys. JETP **32**, 493 (1970)]; Zh. Éksp. Teor. Fiz. **60**, 1144 (1971) [*sic*].
[14] J. M. Kosterlitz and D. J. Thouless, J. Phys. C: Sol. Stat. Phys. **6**, 1181 (1973).
[15] J. M. Kosterlitz, J. Phys. C: Sol. Stat. Phys. **7**, 1046 (1974).
[16] K. Holmlund and P. Minnhagen, Phys. Rev. Lett. **54**, 523 (1996).
[17] N. D. Mermin and H. Wagner, Phys. Rev. Lett. **17**, 1133 (1966).
[18] P. C. Hohenberg, Phys. Rev. **158**, 383 (1967).
[19] V. Ambegaokar *et al.*, Phys. Rev. B **19**, 1806 (1980).
[20] S. A. Trugman and S. Doniach, Phys. Rev. B **26**, 3682 (1982).
[21] D. Schechtman *et al.*, Phys. Rev. Lett. **53**, 1951 (1984).
[22] P. A. Kalugin, A. Yu. Kitaev, and L. S. Levitov, Pis'ma Zh. Éksp. Teor. Fiz. **41** (3), 119 (1985) [Sov. Phys. JETP Lett. **41**, 145 (1985)].
[23] D. V. Olenev and Yu. Kh. Vekilov, JETP Lett. **64**, 612 (1996).
[24] V. E. Fortov *et al.*, JETP Lett. **64**, 82 (1996).
[25] É. L. Nagaev, Usp. Fiz. Nauk **166**, 833 (1996).
[26] V. N. Krivoruchko, Fiz. Nizk. Temp. **22**, 1047 (1996).
[27] A. É. Filippov, Zh. Éksp. Teor. Fiz. **111**, 1775 (1997) [JETP **84**, 971 (1997)].

Translated by D. H. McNeill

Influence of neutron irradiation on the martensitic transformations and shape-memory effect in a TiNi alloy

R. F. Konopleva, I. V. Nazarkin, V. L. Soloveĭ, and V. A. Chekanov

St. Petersburg Nuclear Physics Institute, 188350 Gatchina, Leningrad District, Russia

S. P. Belyaev, A. E. Volkov, and A. I. Razov

Scientific Research Institute of Mathematics and Mechanics, St. Petersburg State University, 198904 Petrodvorets, Russia

(Submitted February 17, 1998)
Fiz. Tverd. Tela (St. Petersburg) **40**, 1705–1709 (September 1998)

The paper reports measurements of the strains and electrical resistance of a TiNi shape-memory alloy under irradiation in the low-temperature helium circuit of a nuclear reactor. Irradiation of the alloy in martensitic state at 170 K revealed that the transition temperatures from cubic to rhombohedral and from rhombohedral to monoclinic phase decrease exponentially with increasing dose. No change in the shape-memory effects and transformation plasticity was observed up to a dose of 6.7×10^{22} n/m^2. Keeping the sample at 340 K without irradiation restores (increases) partially the transition temperatures. The relations observed can be assigned to a change in the degree of long-range order in the lattice caused by neutron irradiation. © *1998 American Institute of Physics.* [S1063-7834(98)03009-3]

The temperatures of martensitic transitions in metals and alloys are very sensitive to various physical factors, which either directly shift the temperature of thermodynamic phase equilibrium (hydrostatic pressure, mechanical stresses, magnetic field) or exert indirect influence through a change of crystal structure (thermal and mechanical treatments). Neutron irradiation is an extremely powerful tool capable of producing structural changes. It was established that a flux of energetic particles affects both the kinetics of martensitic transformations with temperature and the associated deformation phenomena (shape memory, reversible change of the shape etc.).[1–5] Investigation of the effect of irradiation appears particularly important in view of the possible use of the ability of alloys with martensitic transformations to recover from large inelastic strains due to the shape-memory effect. There is an obvious potential of applying such alloys to self-contained operation of actuating mechanisms in high-radiation areas, in emergency protection systems of nuclear power plants, in coolant flow-rate controllers, and so on.

One of the most interesting objects among the large variety of materials exhibiting martensitic transformations are TiNi-based alloys, because they allow sequential initiation of various structural transformations and also display most clearly pronounced strain effects accompanying a phase transition. No martensitic transformation was reported to occur in TiNi and its alloys under cooling down to 170 K following irradiation by fast neutrons at fluences above 5×10^{23} n/m^2.[6,7] This is attributed to a decrease in the transformation temperatures induced by irradiation. This decrease is believed to be due to disordering and amorphization of the crystal lattice, which is suggested by diffraction studies of materials.[7–9] Damage of the lattice by a corpuscular flux should reduce the ability of an alloy to restore its shape, a phenomenon revealed in Refs. 3 and 6. At the same time an electron microscope study[10] demonstrated a high structural stability of the TiNi alloy against irradiation by neutrons with an average energy of 1 MeV up to fluences of 6×10^{24} n/m^2 ($E>0$). The changes in the structure observed in these conditions reduce to the appearance of a few dislocation loops.[10] A high phase stability of the TiNi alloys under irradiation was demonstrated in a study[11] which established an insignificant change in mechanical properties, as well as a retained ability of recovering from large inelastic strains after irradiation in a nuclear reactor to fluences of 2.2×10^{23} n/m^2.

On the whole, available data indicate the existence of both very strong and insignificant changes in the temperature kinetics of martensitic transformations and mechanical behavior of materials at different irradiation levels. The results obtained by different authors are contradictory. It appears that this may stem from a lack of intrareactor measurements. The available experimental data were obtained on preirradiated materials, which can reveal only the consequences of an irradiation.

This work was aimed at studying the effect of neutron irradiation on the temperatures of martensitic transformations and the transformation-plasticity and shape-memory effects in a TiNi alloy by performing measurements in the course of irradiation in the reactor low-temperature helium circuit.

1. EXPERIMENTAL TECHNIQUES

We used for the study a wire of a TiNi-based alloy containing 0.3% Cr, 0.1% Fe, 0.1% Co, and 0.02% Cu. The wire was prepared by drawing the rod through a die with a 15–20% reduction per pass. Each pass was followed by an anneal at 1100 K. The final diameter of the wire was 0.5 mm.

 © 1998 American Institute of Physics

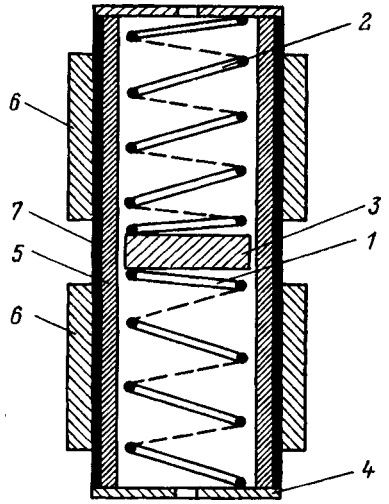

FIG. 1. Schematic of the intrachannel loading and measuring device.

The wire was wound in a coil spring by the following procedure: winding on a mandrel at room temperature, fixing the coil on the mandrel with cramps, and maintaining it at 800 K for 15 min. After cooling to room temperature, the sample had the shape of a ten-turn spring with an outer diameter of 6 mm and length of 10 mm. Next the sample was annealed at 770 K for one hour in an argon ambient. To prevent thermal cycling from affecting the properties of the material, the sample was subjected to a stabilizing treatment consisting of ten thermal cycles within the 470–77 K temperature region.

A special device permitting one to load the sample and measure the displacement of its free end was developed to study the deformation processes. This device is shown schematically in Fig. 1. Sample *1* was loaded in series with an elastic spring element *2*. The inner ends of sample *1* and of the loading spring *2* rested against slider *3* made of a magnetically soft material. The outer ends of the two springs rested against the walls of cylinder *4* so that the assembly as a whole was initially compressed. The displacement of the slider was measured with an induction-bridge circuit consisting of a modulating (*5*) and two measuring (*6*) coils. The displacement was measured to within 5 μm. The electric resistance furnace (*7*) served to heat the sample. The temperature was measured with a copper-constantan thermocouple. The displacement was measured simultaneously with the electrical resistance of the sample. The resistance was determined by the four-probe method at a current of 1 mA. All analog signals were fed into a PC through an amplifier and a CAMAC interface.

This device was placed in the low-temperature helium circuit located in one of the vertical channels available in the WWR-M research reactor at PNPI RAN.[12,13] Cryogenic equipment provided helium circulation through a closed-loop circuit in the channel. The helium flow passing through the loading and measuring device removed the heat liberated in the course of irradiation. The neutron flux density in the channel was 7×10^{17} n/(m$^2\cdot$s) for thermal, and 1×10^{17} n/(m$^2\cdot$s) for fast ($E>1$ MeV) particles. The irradiation temperature was maintained at 170 K. The dependence of the electrical resistance and displacement on temperature was studied by warming the sample periodically through the interval of martensitic transformations (up to 350 K), with its subsequent cooling back to the irradiation temperature. The sample temperature was varied in the experiments at a rate of 2–5 K/min by varying properly the helium flow rate.

The position of the slider at 170 K before irradiation was taken for reference zero (Fig. 1). When heated through the phase transition, the sample elongated and loaded simultaneously the counteracting spring (the shape-memory effect), whereas when cooled, the sample was shortened in the transition by the loading spring *2* (the transformation plasticity effect). The parameters of the loading spring were chosen such that its load remained practically constant during the slider motion.

2. RESULTS OF EXPERIMENT

The alloy chosen for the study undergoes two consecutive martensitic transformations. The high-temperature modification has a CsCl-type ordered cubic $B2$ lattice. When cooled, the lattice transforms at the temperature T_R to rhombohedral R phase. The rhombohedral structure transforms at a still lower temperature to orthorhombic $B19'$ with monoclinic distortions. The $R\rightarrow B19'$ transition begins at the temperature M_s and ends at M_f.

Figure 2a presents the temperature dependence of the electrical resistance R and of the displacement ΔL obtained before the irradiation. The arrows at the curves specify the direction of temperature variation. In accordance with the well-known data, under cooling one observes an anomalous increase of the resistance at T_R, while at M_s, its decrease. The characteristic points in the resistance curve correlate well with the bends in the displacement curve. The heating-induced transformation occurs in one stage, and starts and ends at the A_s and A_f temperatures, respectively. An analysis of the curves suggests that the martensitic reaction proceeds with increasing temperature in the order $B19'\rightarrow B2+R\rightarrow B2$, with the reverse transitions from the $B19'$ structure to $B2$ and R becoming superposed on one another because of the large difference in the width of the temperature hysteresis of the transformations.

The shape of the $R(T)$ and $\Delta L(T)$ curves changed gradually with irradiation. The character of these changes can be seen from Fig. 2b presenting data obtained at a fluence of 4.65×10^{22} n/m^2. A comparison of Fig. 2a and 2b shows that as the dose increases, the temperature region of existence of the R phase broadens considerably (from 30 to 85 K), all characteristic temperatures become lower, and the temperature hysteresis $\Delta T=A_f-M_s$ increases from 45 to 85 K. All these changes already start in the initial stage of irradiation and progress gradually with increasing dose.

At the same time the experiments revealed that the magnitude of the strain remains constant under thermal cycling up to the maximum dose of 6.7×10^{22} n/m^2. Thus the TiNi alloy retains under irradiation its ability to deform inelastically and restore the strain in the martensitic transformation.

The study envisaged a temporal shutdown of the reactor. Before the shutdown, the neutron dose was 3

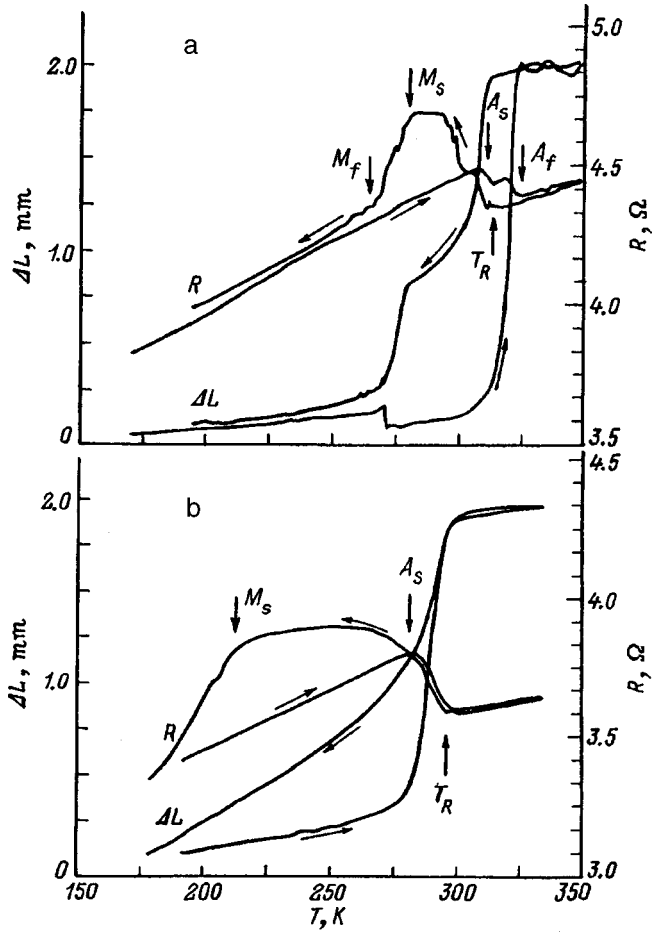

FIG. 2. Temperature dependence of electrical resistance and strain for a TiNi-alloy sample (a) before and (b) after irradiation to a dose of 4.65×10^{22} n/m^2.

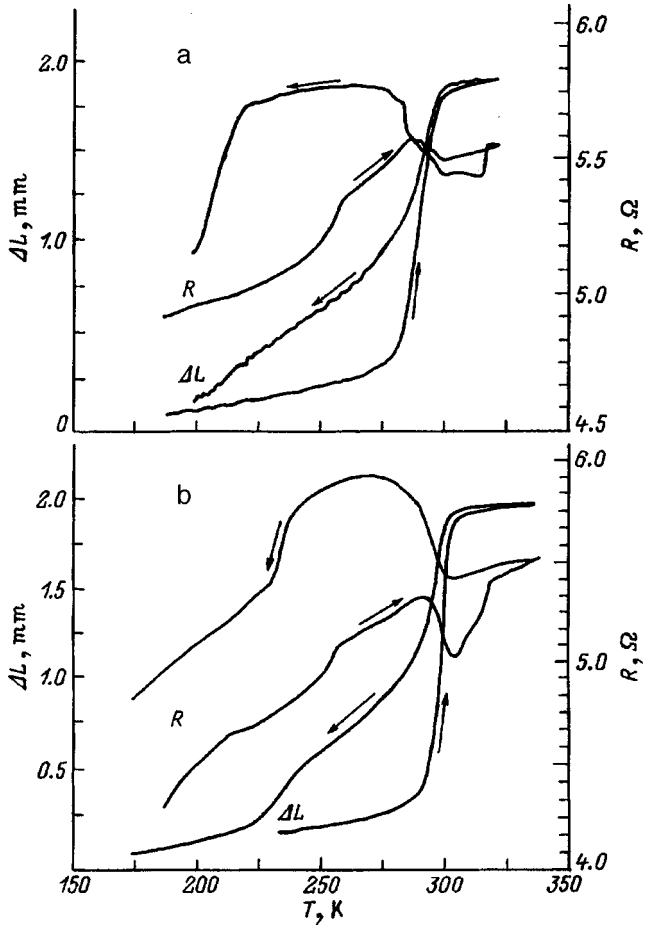

FIG. 3. Temperature dependence of electrical resistance and strain for a TiNi-alloy sample obtained (a) immediately before reactor shutdown at a dose of 3×10^{22} n/m^2 and (b) after resumption of irradiation to a dose of 3.1×10^{22} n/m^2.

$\times10^{22}$ n/m^2. After the shutdown, the sample was maintained for approximately two days at a constant temperature of 325 K with no neutrons present, after which irradiation was resumed. During the break in the irradiation the transformation temperatures were observed to partially recover their pre-irradiation levels. In the course of the recovery, the phase-transition temperatures increase, and the strain swing observed in thermal cycling again becomes constant. Figure 3 displays experimental curves measured immediately before the termination of irradiation (Fig. 3a) and after it was resumed (Fig. 3b).

A similar phenomenon was observed when the experiment was completed after accumulation of the maximum dose of 6.7×10^{22} n/m^2, and the sample was maintained for two days at $T=325$ K in the absence of radiation. Figure 4 gives an idea of the variation of the characteristic temperatures during the whole test period. Excluding from consideration the points corresponding to the intermediate and final hold-ups at $T=325$ K, the experimental data for all critical temperatures can be fitted satisfactorily by the relation

$$\Delta T_{\rm ph}=d[\exp(-\Phi/\Phi_0)-1], \tag{1}$$

where $\Delta T_{\rm ph}$ is the increment of the temperature corresponding to a change in structural state, Φ is the neutron fluence, and d and Φ_0 are constants. The corresponding empirical relations for ΔT_R, ΔM_s, ΔM_f, and ΔA_f are displayed in Fig. 4 by dashed fitting lines. Note an unusual observation. Following an isothermal delay of the material at a constant temperature, the transformation temperatures decrease rapidly during the subsequent irradiation. Already after receiving small radiation doses, all indications of the high-temperature delay vanish, and the experimental points in Fig. 4 fit again in a short time to the exponential relation displayed by the dashed line.

3. DISCUSSION OF RESULTS

As already mentioned, the TiNi alloy has an ordered crystal structure. The degree of long-range order in an annealed alloy is as high as 0.72.[7] While the order persists under martensitic transformations which do not involve diffusion, it can be destroyed by a neutron flux. It is the irradiation-induced disorder that obviously accounts for the experimentally observed decrease of the martensitic-transition temperatures. Experiments on isochronous annealing of samples subjected to a fast-neutron fluence of 8×10^{23} n/m^2 revealed a correlation between the degree of long-range order S and the phase-transition temperatures in TiNi.[7] Note that all phase-transition temperatures depend in a similar way on the annealing temperature and, hence, on pa-

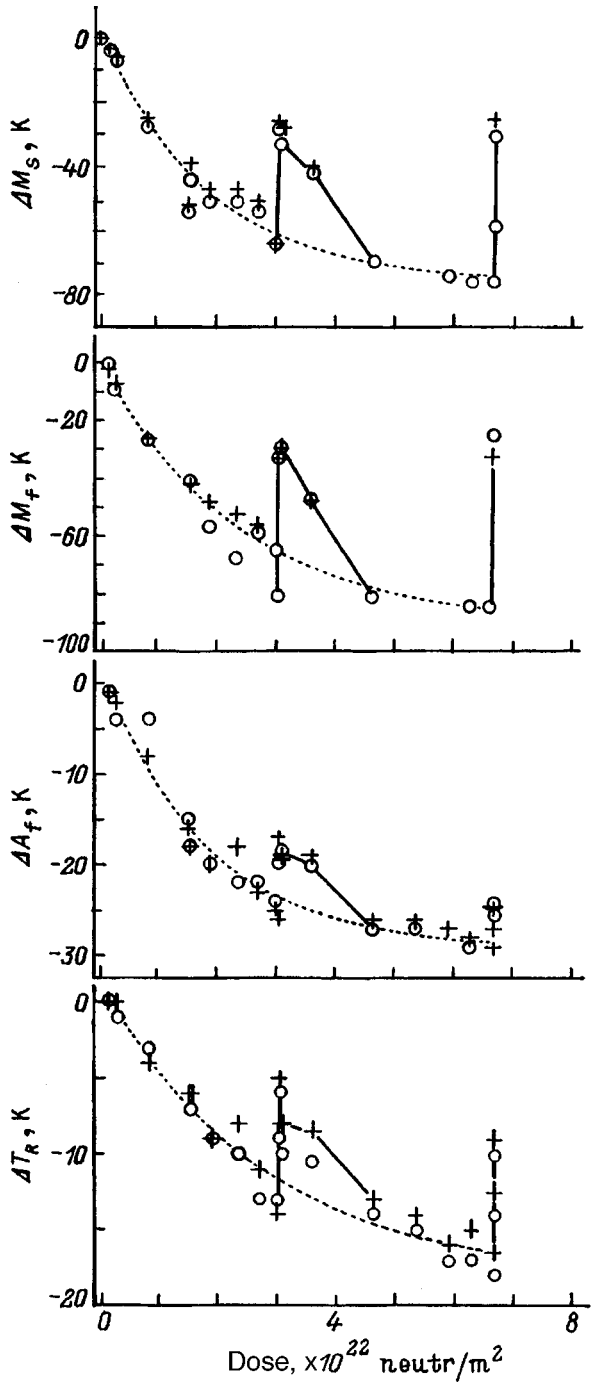

FIG. 4. Increment of the characteristic martensitic-transformation temperatures in a TiNi alloy *vs* fast-neutron dose. The transition temperatures were determined from the temperature behavior of electrical resistance (circles) and displacement (crosses).

rameter S.[7] By contrast, the present study shows that the temperatures M_s, M_f, A_s, and T_R vary differently with increasing dose (Fig. 4), and one can therefore assume that they depend differently on the degree of order. Let us assume that the relation $T_{\text{ph}}=f(S)$ established in Ref. 7 holds for the thermodynamic phase-equilibrium temperature which we define as

$$T_0=1/4(M_s+M_f+A_s+A_f)\,. \tag{2}$$

By analogy with Ref. 7, introduce a reduced temperature $T_0^*=T_0(\Phi)/T_{0S}$, where T_{0S} is the thermodynamic equilibrium temperature for an annealed unirradiated alloy. Approximating now the experimental data obtained in Ref. 7 with a linear relation

$$T_0^*=A+BS \qquad (A=-3.6; \quad B=6.4) \tag{3}$$

and taking into account that, from our data,

$$T_0^*=C+D\exp(-\Phi/\Phi_0)$$

$$(C=0.8; \quad D=0.2; \quad \Phi_0=2.2\times10^{22}\ \text{n/m}^2), \tag{4}$$

we come readily to an empirical expression relating the degree of long-range order to neutron dose

$$S=S_\infty+(S_0-S_\infty)\exp(-\Phi/\Phi_0)\,, \tag{5}$$

where $S_\infty=0.69$ is the asymptotic value of the exponential for $\Phi\to\infty$, and $\Phi_0=2.2\times10^{22}\ \text{n/m}^2$.

It should be borne in mind that the above expression describes the radiation-induced disorder in TiNi irradiated in the low-temperature martensitic state within a limited fluence range (up to $7\times10^{22}\ \text{n/m}^2$). For higher doses and high irradiation temperatures, the martensite transformation temperatures and the degree of long-range order may depend differently on the irradiation dose, because they will be determined not only by the processes occurring in the atomic-collision cascades but by other mechanisms as well, connected, for instance, with amorphization[9] or formation of pores and point-defect clusters in the crystal.

With the above reservations in mind, one can present the rate of variation of long-range order in the form of an expression in which the first term takes into account the radiation-induced disorder, and the second, the recovery of the order parameter in the course of high-temperature delay without irradiation:

$$dS/dt=a(T)(S_\infty-S)I+b(S_0-S)\exp(-U/kT)\,, \tag{6}$$

where t is the time, I is the neutron-flux density, a and b are constants, and U is the order-recovery activation energy.

That the irradiation-induced disordering is a dominant process in the evolution of the martensitic-transformation temperatures is supported by the broadening of the transformation hysteresis observed to occur with increasing dose. The inverse proportionality between the degree of long-range order and the hysteresis width was experimentally demonstrated[14] for the Fe_3Pt alloy. This alloy showed also its ability to recover completely with varying S the build-up and restoration of strain in the martensitic rearrangement of the structure. Our experiments produced a similar result for TiNi. In connection with this, description of the mechanical behavior of the alloy within the structural-analytic theory of strength developed by Likhachev–Malinin[15] does not require any additional assumptions concerning the deformation mechanisms in irradiated material. The change in the kinetics of the transformations with temperature under neutron irradiation can be taken into account in the theory by the way this was done, for example, in Ref. 16. It only should be pointed out that because of the lack of pertinent experimental data at the time of the study the authors of Ref. 16 assumed

a power-law relation for the phase-transformation temperatures as functions of dose. Our data show, however, that for correct prediction of the evolution in the temperature kinetics of strain under irradiation one should use an exponential in the form (1). No other irradiation-induced mechanical effects predicted in Ref. 16 have been observed by us. Their observation can obviously become possible in high-dose experiments (up to 10^{25} n/m^2) on a severely stressed sample, which will initiate crystallographic reorientation of the structural components in martensitic transformations.

The authors express their deep gratitude to V. A. Likhachev for stimulation of this study.

Support of the State Programs ″Neutron Studies of Matter″ and ″New Materials″ is gratefully acknowledged.

[1] Sh. Sh. Ibragimov, S. P. Pivovarov, O. V. Stakhov, and D. A. Aksenov, in *Radiation Defects in Metals* [in Russian], Nauka, Alma-Ata (1981), p. 253.
[2] I. G. Mikhaĭlov, V. M. Pan, A. V. Skripov, A. P. Stepanov, and A. D. Shevchenko, in *Radiation Defects in Metals* [in Russian], Nauka, Alma-Ata (1981), p. 224.
[3] A. M. Rogovskiĭ, E. N. Loguntsev, R. R. Ionaĭtis, and V. V. Kotov, in *Proceedings of the XXIX Seminar on Problems in Strength of Materials* (Pskov, 1993), p. 206.
[4] L. P. Sinel'nikov, E. N. Loguntsev, A. V. Kozlov, I. N. Kovalev, V. Ya. Abramov, D. F. Litvin, and R. R. Ionaĭtis, in *Proceedings of the International Conference on Radiation Mater. Sci.*, Vol. 7 [in Russian], Alushta (1990), p. 19.
[5] V. A. Bychkov, P. L. Gruzin, and Yu. V. Petrikin, in *Radiation Defects in Metals* [in Russian], Nauka, Alma-Ata (1981), p. 214.
[6] A. M. Rogovskiĭ, E. N. Loguntsev, A. N. Zankov, E. V. Serovikova, V. A. Tsygvintsev, I. N. Kovalev, and G. R. Gadaskin, Vopr. Atom. Nauki i Tekh., Ser. Fiz. Rad. Povrezhd. Rad. Mater., No. 3, 60 (1991).
[7] S. F. Dubinin, S. G. Teploukhov, and V. D. Parkhomenko, Fiz. Met. Metalloved. **78**, 2, 84 (1994).
[8] V. V. Bryk, D. G. Malykhin, Yu. I. Polyakov, S. N. Sleptsov, and T. P. Chernyaeva, in *Proceedings of the International Conference on Radiation Mater. Sci.*, Vol. 6 [in Russian], Alushta (1990), p. 190.
[9] S. F. Dubinin, S. G. Teploukhov, and V. D. Parkhomenko, Fiz. Met. Metalloved. **82**, No. 3, 136 (1996).
[10] A. M. Dvoryashin, V. D. Dmitriev, S. I. Porollo, and A. G. Portyanoĭ, Metally, 3, 88 (1993).
[11] T. Katura, K. Ara, H. Tamura, and Y. Suzuki, First Atom. Power Ind. Group **121**, 19 (1989).
[12] A. K. Pustovoĭt, B. A. Borisov, R. F. Konopleva, G. D. Porsev, V. A. Chekanov, S. O. Bokhanov, and M. V. Chudakov, PNPI Preprint No. 1749 (1991), 30 pp.
[13] R. F. Konopleva, B. L. Oksengendler, A. K. Pustovoĭt, B. A. Borisov, V. A. Chekanov, and M. V. Chudakov, Sverkhprovodimost': KIAE **6**, 568 (1993).
[14] M. Foos, C. Frantz, and M. Gantois, in *Shape-Memory Effects in Alloys*, edited by Jeff Perkins [Plenum Press, New York, 1975, p. 407; Metallurgiya, Moscow, 1993, p. 342].
[15] V. A. Likhachev and V. G. Malinin, *Structural-Analytical Theory of Strength* [in Russian], Nauka, St. Petersburg (1993), 471 pp.
[16] V. A. Likhachev and V. Yu. Sakharov, in *Proceedings of the First Russian–American Seminar on Problems in Strength of Materials*, Pt. 2 (St. Petersburg, 1995), Part. 2, p. 11.

Translated by G. Skrebtsov

LOW-DIMENSIONAL SYSTEMS AND SURFACE PHYSICS

Extraction of current carriers by photons in a quantum well

R. Ya. Rasulov, Yu. E. Salenko, T. Éski, and A. Tukhtamatov

Fergana State University, 712000 Fergana, Uzbekistan
(Submitted November 12, 1997)
Fiz. Tverd. Tela (St. Petersburg) **40**, 1710–1711 (September 1998)

The extraction of holes by photons in an infinitely deep semiconductor quantum well is studied. Both interzone and intersubzone optical transitions, which make separate contributions to this effect, are examined. In calculating the extraction current, it is assumed that the optical transition probability depends on the photon momentum only as a result of its appearance in the energy and momentum conservation laws. © *1998 American Institute of Physics.* [S1063-7834(98)03109-8]

The photon extraction effect in semiconductors is caused by a transfer of momentum from a photon to current carriers and the resulting photocurrent is described by the phenomenological relation[1–3]

$$j_\alpha = \chi_{\alpha\beta\gamma\mu} e_\beta e_\gamma \varkappa_\mu, \tag{1}$$

where $\mathbf{e}$ is the polarization vector, $\varkappa$ is the wave vector, I is the intensity of the light, $\mathbf{j}$ is the current density of the photon extraction current, and $\varkappa_{\alpha\beta\gamma\mu}$ is the photon extraction tensor $(\alpha,\beta,\gamma,\mu = x,y,z)$.

Here we consider the photon extraction effect in an infinitely deep quantum well positioned along the $z \parallel [001]$ axis in the region $(-L/2, L/2)$, where L is the width of the well. Then we can write the density of the photon extraction current in the hole representation in the relaxation time approximation can be written

$$\mathbf{j}_\perp = e \sum_{nn',k_\perp} \left[\frac{\hbar}{m_h^{(n)}} \mathbf{k}_\perp \tau_{hk_\perp} W_{hn\mathbf{k}_\perp, ln', \mathbf{k}_\perp - \varkappa} - \frac{\hbar \mathbf{k}_\perp}{m_l^{(n')}} \tau_{l\mathbf{k}_\perp} W_{hn,\mathbf{k}_\perp+\varkappa; ln'\mathbf{k}_\perp} \right]. \tag{2}$$

Here

$$W_{hn\mathbf{k}_\perp; ln', \mathbf{k}_\perp - \varkappa} = \frac{2\pi}{\hbar} |M_{hn\mathbf{k}; ln', \mathbf{k}_\perp - \varkappa}|^2 f_{hn\mathbf{k}_\perp} (1 - \exp \times(-\beta'\hbar\omega)) \delta(E_{hn\mathbf{k}_\perp} - E_{ln', \mathbf{k}_\perp - \varkappa} - \hbar\omega),$$

$$W_{hn,\mathbf{k}_\perp+\varkappa; ln', \mathbf{k}_\perp} = \frac{2\pi}{\hbar} |M_{hn,\mathbf{k}_\perp+\varkappa; ln'\mathbf{k}_\perp}|^2 f_{ln'\mathbf{k}_\perp} (e^{\beta'\hbar\omega} - 1) \times \delta(E_{hn,\mathbf{k}_\perp+\varkappa} - E_{ln'\mathbf{k}_\perp} - \hbar\omega) \tag{3}$$

are the optical transition probabilities (given for intersubband transitions; the probabilities of optical transitions within a single band are easily obtained using Eq. (3)), e is the elementary charge, $\beta' = 1/k_B T$, $E_{ln\mathbf{k}_\perp}$ is the energy spectrum of the holes in branch l, n is the number of the size quantization levels,

$$E_{ln\mathbf{k}_\perp} = \frac{\hbar^2 k_\perp^2}{2m_{lm}} + \frac{\hbar^2 \pi^2 n^2}{2L^2 m_l}, \quad l = l; l = h, \tag{4}$$

m_l (m_h) is the volume effective mass of the light (heavy) holes (expressions for m_{ln} and m_{hn} are given elsewhere[4]), $k_\perp = \{k_x, k_y\}$ is the two-dimensional wave vector, $f_{ln\mathbf{k}_\perp}$ is the equilibrium distribution function of holes in state $|ln\mathbf{k}_\perp\rangle$,[1)]

$$M_{m'\mathbf{k}', m\mathbf{k}} = \frac{eA_0}{c} F^+_{m'\mathbf{k}'} \left[\mathbf{ev} + \frac{i\hbar}{2m_0} g\mathbf{J}(\varkappa \times \mathbf{e}) \right] F_{m\mathbf{k}} \tag{5}$$

is the composite matrix element, $F_{m\mathbf{k}}$ are the eigenfunctions of the hamiltonian Γ_8,[6] $A_0\mathbf{e}$ is the vector potential of the electromagnetic wave, g is the volume g factor of the holes, $\mathbf{v}$ is the velocity operator, and J_α is the angular momentum matrix in the Luttinger basis.[6]

We write the matrix element of the optical transition between the valence band and the conduction band in the dipole approximation including the wave vector of the photon in the form

$$M_{c,\mathbf{k}-\varkappa; l\mathbf{k}} = \frac{E_{l\mathbf{k}} - E_{c,\mathbf{k}-\varkappa}}{im_0^2 \hbar c} A_0 \mathbf{eD}_{c,\mathbf{k}-\varkappa; l\mathbf{k}}. \tag{6}$$

The matrix element of the dipole moment has been calculated neglecting the photon wave vector in Ref. 7.

First let us consider dipole interband optical transitions with light incident obliquely to the well wall (xy) with a polarization vector along the x axis (s polarization). Then optical transitions between states with the same parity[2)] are allowed.[7]

The absorption coefficient for s-polarized linearly polarized light, corresponding to optical transitions between symmetric states of the conduction and valence bands, is given by

$$K_+^{(n)} = \frac{\omega |D|^2 \mu}{2m_0^4 c n_\omega \hbar^2} k_1 f_{n_1 k_1} |N|^2 (1 - e^{-\beta'\hbar\omega}) |Q_+|^2 \left(1 + \frac{\alpha_+}{3}\right), \tag{7}$$

and for transitions between antisymmetric states, by

 © 1998 American Institute of Physics

$$K_-^{(n)}=K_+^{(n)}(Q_+\to Q_-,\alpha_+\to\alpha_-), \tag{8}$$

where

$$k_1^2=\frac{2\mu}{\hbar^2}\left[\hbar\omega-E_g-\frac{\hbar^2\pi^2}{2m_c^*L^2}\left(n_c^2+\frac{m_c}{m_l^{(n_l)}}n_l^2\right)\right],$$

$$\mu^{-1}=m_l^{-1}+m_l^{(n_l-1)},$$

E_g is the band gap, m_c (m_l) is the effective mass of the electrons (holes in branch l), n_c and n_l are the size quantization quantum numbers in the conduction band and valence band of branch l. Expressions for n, $Q_\pm$, and $\alpha_\pm$ are given in Ref. 7.

In the case we are considering, the extraction current can be written in the form

$$j_x=\frac{e\hbar\varkappa}{3m_0}\frac{I}{\hbar\omega}\tau_c(k_1)(K_+^{(m)}F_++K_-^{(n)}F_-), \tag{9}$$

where

$$F_\pm=\left[\left(1+\frac{\alpha_\pm}{5}\right)\left[\frac{1}{N}\frac{\partial N}{\partial k}+\frac{1}{|Q_\pm|}\frac{\partial|Q_\pm|}{\partial k}+\frac{2W_\pm}{1+W_\pm^2}\frac{\partial W_\pm}{\partial k}+\left(\frac{\partial\ln\tau_c}{\partial\ln E_n}-\beta E_n\right)\frac{\partial\ln E_n}{\partial k}\right]+\frac{1}{15(3+\alpha_\pm)}\frac{\partial\alpha_\pm}{\partial k}\right]_{k=k_1},$$

$$E_n=E(k_\perp=k_1), \tag{10}$$

$\tau_c=\tau_c(k_\perp=k_1)$ is the volume relaxation time for the electron momenta in the conduction band. Here and in the following we neglect the contributions of induced optical transitions from the conduction band into the valence band.

The extraction current directed along the x axis and caused by optical transitions between subbands of light and heavy holes in the valence band of the semiconductor can be written in the form

$$l_x^{(l)}=\sum_{n,n'}e\tau_l(E_{ln'k_\perp^0})K_{n'n}^{(l)}\frac{\hbar\varkappa\mu_-}{m_l^{(n')}m_h^{(n)}}\frac{I}{\hbar\omega}Q_{ln'}, \tag{11}$$

where

$$K_{n'n}^{(l)}=\frac{3\alpha}{n_\omega}k_\perp^0 f_{ln'k_\perp^0}(1-e^{-\beta'\hbar\omega}),\quad \alpha=e^2/c\hbar \tag{12}$$

is the characteristic optical absorption coefficient,

$$k_\perp^0=\mu_-\hbar^{-2}\left[\hbar\omega-\frac{\hbar^2\pi^2}{2m_lL^2}\left(n'^2-\frac{m_l}{m_h}n^2\right)\right]^{1/2}, \tag{13}$$

$$\mu_-^{-1}=m_l^{(n')-1}-m_h^{(n)-1}, \tag{14}$$

and

$$Q_{ln'}=2+\left(1+\frac{\partial\ln\tau_l(E_{ln'k_\perp^0})}{\partial\ln E_{ln'k_\perp^0}}-\beta\hbar\omega\frac{\mu_-}{m_{ln'}}\right)\frac{\partial\ln E_{ln'k_\perp^0}}{\partial k_\perp^0}. \tag{15}$$

An expression for $j_x^{(h)}$ is obtained from Eq. (11) by replacing ln' by hn.

The extraction photocurrent owing to optical transitions within a single band can be determined from Eq. (11), by taking $l=h$ and summing over the subbands of the valence band, but then it is necessary to keep only the second term in Eq. (15), multiplying it by $(1+(A/B))^2$ for light holes and by $(1-(A/B))^2$ for heavy holes.

In conclusion, we note that, in calculating the photon extraction current, we have assumed that the optical transition probabilities depend on the photon momentum only because it is included in the energy and momentum conservation laws. Here we have neglected the dependence of the square of the optical transition matrix element on $\hbar\varkappa$ and have not included the contribution to the composite matrix element from the interaction of the magnetic field of the light wave with the angular momentum. These questions must be examined separately.

[1)]For simplicity, we neglect resonance saturation of single photon optical transitions.[5]

[2)]If the vector **e** is directed along the quantization axis, then in this case optical transitions between states with different parity will be allowed.

[1] E. L. Ivchenko and G. E. Pikus, in *Problems of Modern Physics* [in Russian], Nauka, Leningrad (1980), pp. 275–293.
[2] L. É. Gurevich and V. S. Pravnikov, *ibid.*, pp. 262–268.
[3] S. M. Ryvkin and I. D. Yaroshetskiĭ, *ibid.*, pp. 173–180.
[4] M. I. D'yakonov and A. V. Khaetskiĭ, Zh. Éksp. Teor. Fiz. **82**, 1584 (1982) [Sov. Phys. JETP **55**, 917 (1982)].
[5] D. Parshin and A. R. Shabaev, Zh. Éksp. Teor. Fiz. **92**, 1005 (1987) [*sic*].
[6] G. L. Bir and G. E. Pikus, *Symmetry and Strain-induced Effects in Semiconductors*, Wiley, New York (1975), 584 pp.
[7] I. A. Merkulov, V. I. Perel', and M. E. Portnoĭ, Zh. Éksp. Teor. Fiz. **99**, 1202 (1991) [Sov. Phys. JETP **72**, 669 (1991)].

Translated by D. H. McNeill

Crystal structure and electronic spectrum of SnS_2

G. B. Dubrovskiĭ

A. F. Ioffe Physicotechnical Institute, Russian Academy of Sciences, 194021 St. Petersburg, Russia
(Submitted December 26, 1997)
Fiz. Tverd. Tela (St. Petersburg) **40**, 1712–1718 (September 1998)

It is shown that layered metal dichalcogenides are quasi-one-dimensional molecular crystals and form a new class of crystal structures — molecular close packed. Since the minimum structural unit in these crystals is a monomolecular layer, using the symbols employed in atomic close packing to describe them gives a mistaken representation of their structure and symmetry. A new system of notation is proposed which provides complete and exact information about the ordering of the atomic layers in different polytype modifications and about their symmetries. It is found that in molecular close packing and, especially, in tin disulfide, there is not one (as in atomic close packing), but two, simplest structures, $1T$ and $1H$, containing one molecule each in a unit cell and, therefore, two series of superlattices constructed on their basis. An energy model is constructed for the natural superlattice in tin disulfide crystals and the electronic spectra of the $2H$, $4H$, and $9R$ polytype modifications are calculated in the Kronig–Penney approximation with rectangular potential barriers as superstructure perturbations of the simplest structures. These results make it possible to explain the observed complicated dependence of the band gaps of these crystals on polytype structure. © *1998 American Institute of Physics.* [S1063-7834(98)03209-2]

Tin disulfide belongs to an extended family of layered metal dichalcogenides MX_2 (M is a metal, X, a chalcogen) whose crystals consist of plane triple layers (sandwiches) X–M–X with strong ion-covalent bonding, weakly coupled to one another by van-der-Waals forces. These sandwiches consist of two layers of the chalcogenide with a two-dimensional hexagonal coordination of the atoms in each one and the voids between them are occupied by metal atoms, which also form plane hexagonal grids. There are two types of coordination of the metal atoms in a sandwich: trigonal prismatic, if the chalcogenide layers occupy equivalent positions, and octahedral, if the chalcogenide layers are close packed. Tin disulfide belongs to the latter type.

The representatives of this family vary greatly in their properties; they include insulators, semiconductors, and metals. But they are all united by some general properties associated with their layered structure, first of all, a strong anisotropy of these properties and polytypism owing to the infinite set of possible ordering sequences for the layers, which are distinguished by the position of the atoms of which they are formed.

Tin disulfide is a semiconducting compound and its electronic properties depend extremely strongly on the polytype structure of the crystal. Electrical measurements show[1] that the band gaps of the twelve established polytype modifications of SnS_2 vary from 0.81 eV for a $50H$ structure to 3.38 eV for an $18R$ structure, which is much wider than the range of variation in E_g for the classical polytype material SiC, which is only about 0.9 eV. The nature of this strong dependence of the electronic properties on the polytype structure in SnS_2 crystals remains unknown.

We have shown previously[2–4] that the polytype modifications of silicon carbide are natural superlattices based on the simplest $3C$-SiC structure and all the observed features of their electronic spectra, including the dependence of the band gap on the polytype structure, are the result of a superperiodic perturbation of the electronic spectrum of this simplest structure.

The polytype structures formed in SnS_2 and SiC are very similar, which suggests that the mechanisms for formation of the electronic spectra of the long-period polytype modifications of these compounds must also be similar. The purposes of this paper are to analyze the crystal structure of SnS_2, to construct a model for the natural superlattice in these crystals, and to calculate electronic spectra of the various polytype modifications on the basis of the concept that they are formed by a superstructure mechanism.

1. CRYSTAL STRUCTURE OF SnS_2

A fragment of a three-layer S–Sn–S sandwich structure is illustrated schematically in Fig. 1. The unit cell of this structure is a hexagonal prism with an Sn atom at its center. Each sulfur atom belongs simultaneously to three unit cells. All the atoms of the structure lie on the three-fold axes of symmetry, perpendicular to the plane of the layer and passing through the lateral edges and center of the hexagonal prism and customarily denoted A, B, and C. (For the metal atoms, these axes are denoted α, β, and γ.) The ordering sequence along the c axis of the atomic layers in this structure has the form $(A\gamma B)$. This kind of sandwich is nothing other than the plane monomolecular layer with saturated valence bonds that is the minimum structural unit of the SnS_2 crystal in a direction perpendicular to the layers. Crystals formed as a result of sequential placement of these monomo-

 © 1998 American Institute of Physics

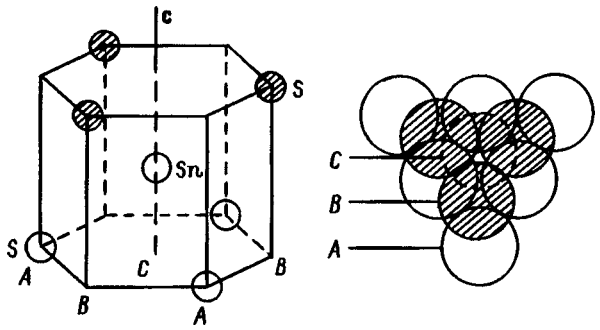

FIG. 1. Locations of atoms in a monomolecular layer of SnS_2. (Left) Unit cell, (Right) Top view.

lecular layers along the c axis without the involvement of valence bonds are molecular in one dimension, specifically in the direction which defines the polytypism. This is the fundamental difference between the SnS_2 and SiC lattices. SiC crystals consist of binary atomic close packings, made up of two volume close packings of Si and C atoms imbedded in one another with a strong ion-covalent bonding between them. Crystals such as SnS_2, however, can be referred to as molecular close packings, since they consist of monomolecular layers bound by van-der-Waals forces whose packing density is determined by the boundary layers of sulfur.

The polytype form of crystals such as SnS_2 is usually described using a system of notation for atomic close packings,[5] since, formally, they are actually volume close packings of S atoms, but every other layer of vacancies in them is occupied by Sn atoms. A description in terms of the S atoms alone does not take the molecular nature of these crystals into account and, therefore, gives an erroneous idea of their structure. Thus, a new system of notation is required for molecular close packings. In particular, the numbers in the Ramsdell symbols must reflect the number of molecular, rather than atomic, layers per unit cell length of the crystal. In the following, for describing the various SnS_2 structures we shall use just this sort of ''molecular'' Ramsdell symbols.

In order to describe superstructural perturbations, i.e., to construct a model of the natural superlattice in SnS_2 crystals, it is necessary to determine the simplest structures containing only one molecule per unit cell and to find the form of the structure defects leading to the formation of long-period modifications based on them.

It is known that in SiC there is only one simplest structure containing one atom each of Si and C in a unit cell; this is the $3C$ structure with an ordering sequence $ABCABC$ of the layers and a face-centered cubic lattice. The basis vectors of this lattice are three vectors of the same length, symmetric with respect to the z axis and forming different angles with one another, i.e, it is a special case of a trigonal lattice. It owes its high T_d symmetry to the particular value of the angles between the basis vectors, which determines an ideal tetrahedral coordination for the nearest Si and C atoms.

An analogous structure with a trigonal lattice also exists in SnS_2 crystals and is characterized by an ordering sequence $(A\gamma B)(C\beta A)(B\alpha C)$ of the layers. Here the parentheses denote the boundaries of the monomolecular layers. The symmetric unit cell of this lattice contains one molecule and is constructed on trigonal basis vectors, as is $3C$-SiC, but, since the distance between nearest molecules of the neighboring layers is much longer than within each layer, it is strongly stretched along the c axis and, therefore, has a lower symmetry, D_{3d}. The molecular Ramsdell symbol for this structure is $1T$.

Because of the molecular structure and the fact that, as noted above, the identical position of the centers of the molecules in the successive layers does not violate the principle of atomic close packing, yet another simplest structure is possible in SnS_2 with a $(A\gamma B)(A\gamma B)$ ordering sequence of the layers. This structure is characterized by a simple hexagonal lattice, whose symmetric unit cell is constructed on two basis vectors of equal length lying in the plane of the layer at 120° to one another and a single vector parallel to the c axis, also contains one molecule, and has a complete D_{6h} hexagonal symmetry. The molecular symbol for this structure is $1H$. Thus, in SnS_2 there should be two independent series of polytypes, which are superstructural perturbations of two different simplest structures, as opposed to the single series in SiC.

The main structure defects causing a superstructural perturbation of the simplest structures in SnS_2, as in SiC, are regular rotations about vertical axes which do not lead to destruction of the close packing. Thus, a 60° rotation around one of the three-fold axes (A, B, or C) leads to formation of a mirror phase. Then the $(A\gamma B)(C\beta A)(B\alpha C)$ sequence of ordering of the layers is replaced by the reverse $(C\alpha B)\times(A\beta C)(B\gamma A)$. If the intervals between the planes of rotation are the same, then a hexagonal structure with a height of two intervals is formed. Thus, rotations after each layer in a $1T$ lattice yield a $2H(A\gamma B)(A\beta C)$ structure, while rotations after every other layer yield a $4H(A\gamma B)(C\beta A)(C\alpha B)\times(A\beta C)$ structure. If, however, two different intervals follow one another, then a rhombohedral structure is formed whose unit cell height will be three times the sum of these two intervals.

It is useful to note that the $(A\gamma B)$ molecule is also converted into a mirror $(B\gamma A)$ molecule under such a rotation about a vertical axis passing through its center (Fig. 1). This makes it possible to shorten the notation for the ordering sequence of the layers in the structure considerably. If, for example, we take the sequence ABC as the forward and CBA as the reverse and denote a molecule with a reverse ordering sequence along the axis of the sulfur atoms by an additional sign, a bar over the symbol denoting the position of their center, then to obtain complete information about the structure it is sufficient to indicate the sequence in which the centers of the molecules are laid out. For example, the $2H$ structure will be denoted simply by $\gamma\overline{\beta}$ and the $4H$ structure, by $\gamma\beta\overline{\alpha\beta}$.[1)]

As for other closely packed structures, a very graphic picture of the structure of SnS_2 crystals is provided by their (110) cross-section planes. Figure 2 shows such cross sections for the forward and mirror phases of a $1T$ lattice, as well as for several superlattices based on it. The dark circles

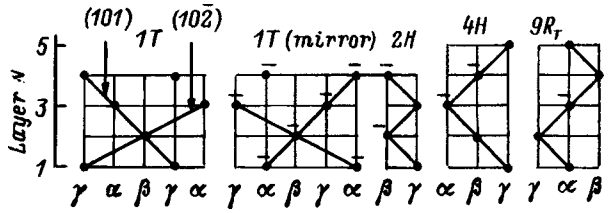

FIG. 2. Cross sections of the (110) planes of a $1T$-SnS_2 lattice and three superperiodic structures based on it.

indicate the position of the centers of the SnS_2 molecules and their orientation (a line above a circle represents the reverse ordering sequence of the sulfur layers). The inclined lines indicate the traces of the principal Bragg planes. In hexagonal axes these planes are denoted by {101} and {102}, i.e., the same as in the fcc lattice of SiC.

As can be seen from Fig. 2, the ordering of the forward and reverse phases of the $1T$ lattice leads to the appearance, on the intersecting {110} planes, of exactly the same characteristic Ramsdell zigzags as in atomic close packings. The only difference between them is that in molecular SnS_2 crystals the distances between neighboring planes of the rotations vanish, not in the atomic, but in the molecular layers. In this regard, Zhdanov symbols, as the briefest yet complete method of describing the structure, retain their significance in molecular crystals, but they must be supplemented by information on the orientation of the molecules in the layers. This is easily done by placing a bar on top (as in the notations $\alpha\beta\gamma$) of the numbers in the Zhdanov symbols corresponding to the number of the molecular layers with reverse ordering sequence of the sulfur layers. The Zhdanov symbol determined in this way for the $2H$ structure will be $(1\bar{1})$, that for $4H$, $(2\bar{2})$, and that for $9R_T$, $(2\bar{1})_3$.

Figure 3 shows cross sections of the (110) planes of a $1H$ crystal and three simplest superperiodic structures based on it. Here the situation is radically different from $1T$. The symmetric unit cell of a $1H$ lattice is a regular hexagon, whose facets determine the principal Bragg planes {100}, parts of which are isolated as thick lines in the figure. The structure defect in this lattice leading to formation of superlattices is a rotation by 120° about a vertical axis passing through the center of the triangle $\alpha\beta\gamma$. As a result of this

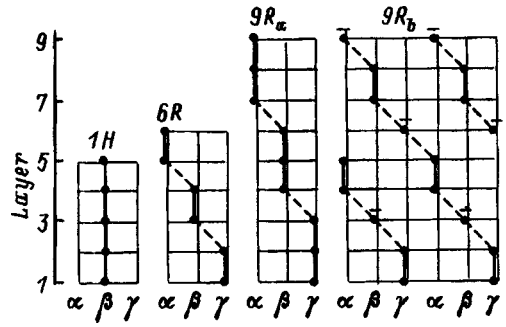

FIG. 3. Cross sections of the (110) planes of a $1H$-SnS_2 lattice and three superperiodic structures based on it.

kind of rotation, the next layer of the $1H$ lattice occupies a trigonal position relative to the previous one.

Because of the molecular structure of the SnS_2 crystals, the planes of all the rotations which create stacking faults in the $1T$ and $1H$ lattices always lie between neighboring molecular layers, i.e., pass through van-der-Waals gaps.

In order to unify the system of notation for superlattices based on $1T$ and $1H$, we denote the $1H$ lattice by the symbol ''0,'' by analogy with the Zhdanov symbol (∞) for the trigonal $1T$ lattice, and the distances between neighboring stacking faults in this lattice by numbers with a subscript 0 (e.g., 2_0, 3_0) corresponding to the number of the molecular layers. Then the analogs of the Zhdanov symbols for the structures shown in Fig. 3 will have the following form: $1H$–(0), $6R$–$(2_0)_3$, $9R_a$–$(3_0)_3$, and $9R_b$–$(2_0\bar{1})_3$.

The existence of two simplest structures and at least two forms of structure defects associated with different rotations of the lattice makes polytypism in SnS_2 crystals a considerably more complicated and diverse phenomenon than in SiC. Thus, for example, the modification with a Ramsdell symbol $18R$ for the sulfur layers can be represented by a whole set of structures. One structure with symbol $9R_T=(2\bar{1})_3$ [in terms of the sulfur layers, this structure has the Zhdanov symbol $(51)_3$] is possible based on the trigonal $1T$ lattice. However, because of the presence of a second simplest lattice, $1H$, some new variants show up: $9R_a=(3_0)_3$ constructed only from the $1H$ lattice and $9R_b=(2_0\bar{1})_3$, in which there are elements of both lattices. Note that the Ramsdell and Zhdanov symbols, which reflect the stacking order of packing of the sulfur layers, are the same for the last two structures and are $18R$ and $(1113)_3$, which indicates that they are not adequate for describing the molecular crystals. The advantages of the new notation proposed here, which is based on a molecular description of the crystals, are clearly evident from a comparison with the atomic descriptions shown in Table I.

2. SUPERLATTICE AND ELECTRON ENERGY SPECTRUM OF SnS_2

The stacking faults described in the previous section cause a shift in the phase of the electron wave function in the lattice of the basis simplest structure, which leads to formation of additional potential barriers for the electrons. The periodic arrangement of these barriers creates a superlattice, which causes splitting of the quasicontinuum electron spectrum of the original crystal within the first Brillouin zone into minibands.

The periodic field created by these additional potential barriers is particularly one dimensional and is directed along the c axis of the crystal (the z direction). Thus, when a superlattice is present, the electrons of the original simplest $1T$ or $1H$ crystal will experience a perturbation described by the one-dimensional Schrödinger equation

$$-\frac{\hbar^2}{2m_z}\frac{\partial^2\Psi}{\partial z^2}+U(z)\Psi=E_z\Psi. \qquad (1)$$

TABLE I. Comparison of the new molecular symbols and notation with those for atomic systems for ten polytype modifications of tin disulfide

Sublattice series	Ramsdell symbol	New symbol	Zhdanov symbol	New symbol	ABC notation	New $\alpha\beta\gamma$ notation	E_g, eV
$1T$	$6R$	$1T$	∞	$\underline{\infty}$	$(A\gamma B)(C\beta A)(B\alpha C)$	$\gamma\beta\alpha$	0.8
	$4H$	$2H$	(22)	$(\underline{11})$	$(A\gamma B)(A\beta C)$	$\gamma\overline{\beta}$	1.89
	$6H_b$	$3T$	(33)	$(\underline{21})$	$(A\gamma B)(C\beta A)(C\alpha B)$	$\underline{\gamma}\overline{\beta\alpha}$	1.59
	$8H_b$	$4H_b$	(44)	(22)	$(A\beta C)(B\gamma A)(C\beta A)$ $(B\alpha C)$	$\overline{\beta\gamma}\beta\alpha$	1.20
	$18R$	$9R_T$	$(51)_3$	$(\overline{21})_3$	$(B\alpha C)(A\gamma B)(C\alpha B)$ $(C\beta A)(B\alpha C)(A\beta C)$ $(A\gamma B)(C\beta A)(B\gamma A)$	$\alpha\gamma\overline{\alpha}\beta\alpha\overline{\beta}\gamma\beta\overline{\gamma}$	-
$1H$	$2H$	$1H$	(11)	$(\underline{0})$	$(A\gamma B)$	$\underline{\gamma}$	2.18
	$6H_a$	$3H_a$	(2211)	$(\underline{2_01})$	$(A\gamma B)(C\alpha B)(A\gamma B)$	$\gamma\underline{\alpha\gamma}$	-
	$8H_a$	$4H_a$	(211211)	$(\underline{2_02_0})$	$(A\gamma B)(A\gamma B)(A\beta C)$ $(A\beta C)$	$\gamma\gamma\beta\beta$	-
	$12R$	$6R$	$(31)_3$	$(2_0)_3$	$(A\gamma B)(A\gamma B)(C\beta A)$ $(C\beta A)(B\alpha C)(B\alpha C)$	$\gamma\gamma\beta\beta\alpha\alpha$	-
	$18R$	$9R_a$	$(1113)_3$	$(3_0)_3$	$(A\gamma B)(A\gamma B)(A\gamma B)$ $(C\beta A)(C\beta A)(C\beta A)$ $(B\alpha C)(B\alpha C)(B\alpha C)$	$\gamma\gamma\gamma\beta\beta\beta\alpha\alpha\alpha$	-
		$9R_b$	$(1113)_3$	$(\underline{2_01})_3$	$(A\gamma B)(A\gamma B)(A\beta C)$ $(B\alpha C)(B\alpha C)(B\gamma A)$ $(C\beta A)(C\beta A)(C\alpha B)$	$\gamma\gamma\overline{\beta}\alpha\alpha\overline{\gamma}\beta\beta\overline{\alpha}$	3.38

Here m_z is the effective electron mass in the initial crystal for the z direction, $U(z)$ is the superlattice potential, which is a periodic function of the coordinate, and E_z is the electron energy.

The top of the valence band of SnS_2 crystals lies at the center of the Brillouin zone and, because of the spherical symmetry of the wave functions at the point Γ, essentially experiences no perturbation by the superstructure potential. On the other hand, the minimum of the conduction band lies at the boundary region of the Brillouin zone and is very strongly affected by the superlattice. Thus, as a first approximation, we can assume that the change in the band gap as a function of the polytype structure is determined exclusively by the change in the energy of the electrons at the bottom of the conduction band, which obeys Eq. (1). This energy increases under the influence of the superlattice, i.e., the band gap increases. If the band gaps of the initial simplest crystal and several superstructural modifications (polytypes) based on it are known, then it is possible to determine the unknown parameters of Eq. (1), m_2 and $U(z)$, by jointly solving Eqs. (1) for $E_z(0)$, the energy at the bottom of the conduction band of these polytypes.[2] Then, however, it is important that these polytypes have the same symmetry and that their superlattices should be formed by the same structure defects and differ only in their periods. Of all the polytype modifications of SnS_2 studied in Ref. 1, only one, $9R$ ($18R$ in terms of the sulfur layers), has a band gap larger than in $1H$, i.e., is a superlattice based on it. All the others are constructed on the basis of the trigonal $1T$ lattice. Thus, we shall begin our analysis precisely with these superlattices.

The band gap of the simplest SnS_2 structure, $1T$, is unknown, since crystals with this structure have not yet been obtained. However, since E_g decreases in hexagonal structures as the period increases, approaching its value in the original unperturbed crystal, we may assume that it will be close to E_g for the longest period crystal of those described in Ref. 1, $50H$. Thus, we take E_g for the $1T$ structure to be 0.8 eV. This estimate is, certainly, very crude, since the ordering sequence of the layers in $50H$ crystals is unknown, while the location of the energy levels in a superlattice is determined, not simply by its period, but also by the sizes of the potential wells and barriers of which it consists.

Of all the structures constructed on the basis of the $1T$ lattice, the ordering sequence of the layers in the unit cell is known only for crystals with $2H$, $4H$, and $3T$ structures. The last modification has the symbol $6H$ in terms of the sulfur layers, but is actually a trigonal structure with a $\gamma\beta\overline{\alpha}$ ordering sequence of the molecular layers. Thus, there are only two modifications left with the same symmetry and the same structure defect determining the superlattice potential, $2H$ and $4H$. The band gaps of these modifications are 1.89 and 1.20 eV, respectively.[1]

For approximate calculations we use the Kronig–Penney model, which we have used successfully before to calculate the electronic spectra of SiC crystals. A plot of the potential energy in a superlattice with rectangular potential barriers is shown in Fig. 4 for the hexagonal case, when the distance between the barriers is the same throughout the entire structure. Here the zero energy corresponds to the energy of the electrons at the bottom of the conduction band of the unper-

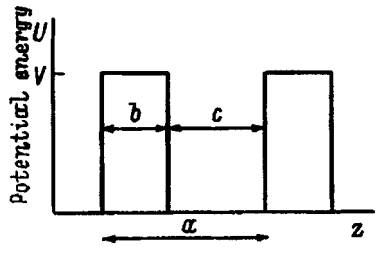

FIG. 4. A plot of the superlattice potential energy in the Kronig–Penney model.

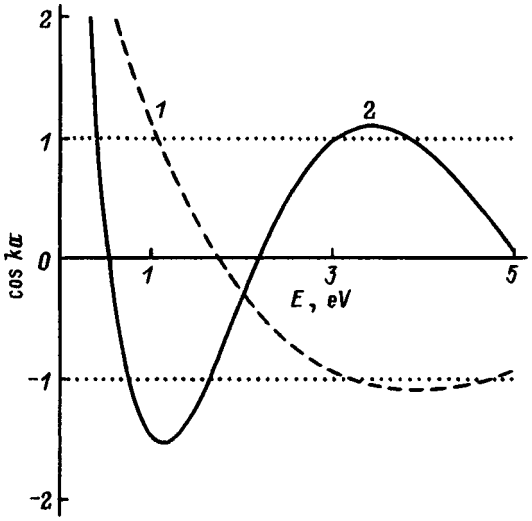

FIG. 5. The solutions of Eq. (2) for $2H$-(*1*) and $4H$-SnS_2 (*2*) crystals.

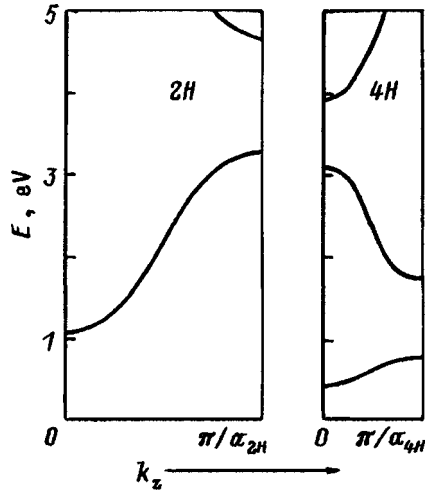

FIG. 6. Electron dispersion curves in reduced k space for $2H$- and $4H$-SnS_2 constructed from the data of Fig. 5.

turbed $1T$ crystal and all the individual barriers are characterized by width b and height V, while the potential wells between them have width c. The superlattice period $a=b+c$ is equal to half the length of a unit cell and is known from crystallography. The electron energy spectrum in a superlattice with this sort of potential energy profile is given by[6]

$$\cos ka=\cosh \beta b \cos \alpha c+\frac{\beta^2-\alpha^2}{2\alpha\beta}\sinh \beta b \sin \alpha c. \tag{2}$$

Here

$$\alpha^2=2mE/\hbar^2, \quad \beta^2=2m(V-E)/\hbar^2, \tag{3}$$

E is the electron energy, and m is the initial effective mass of an electron in the potential well. The problem involves choosing values of the parameters V, b, and m for which the minimum electron energies obtained from Eq. (2) for the $2H$ and $4H$ structures will equal 1.09 and 0.4 eV, respectively. Calculations showed that this condition is satisfied by $V=2.3$ eV, $b=3$ Å, and $m=0.4m_0$. Figure 5 shows plots of the solutions of Eq. (2) with these parameters for $2H$- (dashed curve) and $4H$-crystals (smooth curve) of SnS_2. The horizontal dotted lines, $|\cos ka|=1$, bound the region of real values of the energy, corresponding to allowed minibands. Figure 6 shows the dispersion curves of the electrons in these crystals, calculated from the data of Fig. 5.

The potential energy profile in $1H$ rhombohedral structures differs from that which we have in the $1T$ series. As can be seen from Fig. 3, the superlattice period in these structures is also 1/3 of the unit cell length, but over the length of this period there is only one potential well, i.e., the potential energy profile has a form similar to that shown in Fig. 4 for $1T$ hexagonal structures. Thus, we can use Eq. (2) for calculating the electron spectrum of the only rhombohedral structure of the $1H$ series that is currently known, $9R$-SnS_2. The band width of crystals with this structure is 3.38 eV,[1] and exceeds E_g of the $1H$ basis structure by 1.2 eV. Calculations show that this value for the energy at the bottom of the conduction band of the $9R$ crystal can be obtained by solving Eq. (2) with the following parameters: $V=3.25$ eV, $b=c=9$ Å, and $m=0.1m_0$. A plot of this solution is shown in Fig. 7 and can only correspond to a $9R_b$ structure. As can be seen from Fig. 3, in the $9R_a$ structure the barrier width b must be about 3 Å, as in the $1T$ series. However, with this low value for this parameter, the magnitude of V required to obtain a minimum energy of 1.2 eV turns out to be unrealistically high.

The electronic spectra of the polytype modifications of SnS_2 obtained here are typical for superlattices and have a distinct miniband structure. The widths of the first minibands are larger than in SiC for the same period. Thus, in the $2H$, $4H$, and $9R_b$ structures, the superlattice periods are 5.9, 11.8, and 17.7 Å, while the first minibands have widths of 2.1, 0.35, and 0.5 eV, respectively. For comparison, in $4H$- and $8H$-SiC crystals the superlattice periods are 5 and 10 Å, while the widths of the first minibands are 0.6 and 0.16 eV.[3] This is related to the circumstance that the solutions of Eq. (2) which satisfy the experimental data on E_g in SnS_2 crys-

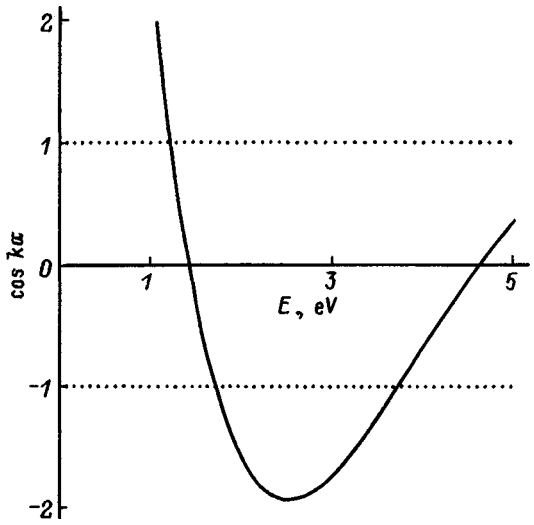

FIG. 7. The solution of Eq. (2) for a $9R_b$-SnS_2 crystal.

tals require large values of b and rather low values of m. The first obviously reflects the fact that the barrier in SnS_2 superlattices passes along a van-der-Waals gap between the molecular layers and its width cannot be less than this gap, which is 2.95 Å. As for the parameter m in this problem, matching it to the actual value of the effective electron mass in the original crystal requires further study.

The curves of Figs. 5 and 7 can be used to estimate the longitudinal effective masses of the electrons in the SnS_2 crystals studied here. When the tangent to the $\cos ka = f(E)$ curve at the point corresponding to the minimum of the conduction band ($\cos ka = 1$) is extended to its intersection with the line $\cos ka = -1$, the difference in the energies at these points will give the nominal width of the first miniband, $2\delta'$, in the approximation of a dispersion with the simple form

$$E = -\delta' \cos ka. \tag{4}$$

In this case, the effective electron mass at the minimum point is given by

$$m^* = \frac{\hbar^2}{\partial^2 E/\partial k^2} = \frac{\hbar^2}{a^2\delta'}. \tag{5}$$

The effective masses calculated using this formula are $m^*(2H) = 1.8m_0$, $m^*(4H) = 2,\ 3m_0$, and $m^*(9R_b) = 0.6m_0$.

The analysis done in this paper yields the following conclusions:

The layered metal dichalcogenides form a new class of crystal structures, molecular close packings. The generally accepted method of describing these molecular crystals using the symbols employed for atomic close packings is not up to the task and gives erroneous ideas about their structure. Here a new symbolism has been proposed for describing these crystals which takes into account their molecular structure and yields the briefest, yet exhaustive information on the ordering sequence of the layers in a unit cell. Polytypism in molecular close packings is a more diverse phenomenon than in atomic close packings because of the existence of a second simplest structure $1H$ which is forbidden in atomic close packings. Thus, in the metal dichalcogenides two, rather than one, series of polytype structures, based on the lattices of the two simplest structures, $1T$ and $1H$, should be observed.

There are, unfortunately, very few experimental data on the polytype structures of SnS_2 and electronic spectra could be calculated only for two polytypes from the $1T-2H$ and $4H$ series and one from the $1H-9R_b$ series, for which both the band gap and the ordering sequence of the layers in the unit cell are known. Kronig–Penney model calculations were done with rectangular potential barriers. The results are somewhat unexpected, first of all, in terms of the values of the model parameters which yield agreement between the calculations and the experimental data over the band gap width. Getting this agreement required very high and wide potential barriers (for similar values of V, these barriers have a width 3 times greater than in SiC in the $1T$ series and 10 times greater for the $1H$ series) and rather low effective masses. The former is explained by the fact that the barriers in SnS_2 pass along van-der-Waals gaps and their width cannot be less than the width of this gap. In addition, imbedding a molecular layer with trigonal surroundings in a $1H$ structure, as in a $9R_b$ crystal, increases the barrier width further. The discrepancy between the model values of m and the measured m^* in $1H$ crystals appears to indicate that this parameter is not an exact reflection of the effective mass in the original crystal and changes under the influence of the boundary conditions in the potential well.

It has been found that the electronic spectra of the SnS_2 crystals studied here have the miniband structure characteristic of superlattices. The first minibands, however, are relatively wide, while the energy gaps between the first and second minibands at $k = 0$ exceed the band gap. This means that the inter-miniband optical transitions typical of SiC crystals cannot be observed in these crystals, since their energies lie in the fundamental absorption region.

The author thanks the Russian Fund for Fundamental Research for support of this work (Grant No. 97-02-18300).

[1)]For crystals with a prismatic coordination of the atoms in a molecular sandwich, where the layers of sulfur occupy an identical position, as in TaS_2, we can introduce a symbol to indicate this position, such as α_B or α_C.

[1] S. Acharya and O. N. Srivastava, Phys. Status Solidi A **65**, 717 (1981).
[2] G. B. Dubrovskii, in *Silicon Carbide-1973*, edited by R. C. Marshall, J. W. Faust, and C. E. Ryan, South Carolina, p. 207.
[3] G. B. Dubrovskiĭ and A. A. Lepneva, Fiz. Tverd. Tela (Leningrad) **19**, 1252 (1977) [Sov. Phys. Solid State **19**, 729 (1977)].
[4] G. B. Dubrovskiĭ and F. G. Pikus, Fiz. Tverd. Tela (Leningrad) **31**, 19 (1989) [Sov. Phys. Solid State **31**, 10 (1989)].
[5] A. R. Verma and P. Krishna, *Polymorphism and Polytypism in Crystals*, Wiley, N.Y. (1966), 284 pp.
[6] R. A. Smith, *Wave Mechanics of Crystalline Solids*, Chapman and Hall, London (1961), 473 pp.

Translated by D. H. McNeill

System of quantum wells in a parallel magnetic field

V. I. Belyavskiĭ and S. V. Shevtsov

Voronezh State Pedagogical University, 394043 Voronezh, Russia

Yu. V. Kopaev

P. N. Lebedev Physics Institute, Russian Academy of Sciences, 117924 Moscow, Russia

(Submitted January 30, 1998)
Fiz. Tverd. Tela (St. Petersburg) **40**, 1719–1723 (September 1998)

The energy spectrum and quantum states of electrons in a system of quantum wells in a strong magnetic field parallel to the heterogeneous boundaries are studied. The combined effect of the quantizing magnetic field and the potential of the system of quantum wells leads to a radical change in the electron dispersion relation owing to the appearance of one-dimensional Landau bands. The neighborhoods of the anticrossing points of the different bands correspond to an effective redistribution of the electron envelope functions, which becomes stronger as the magnetic field is raised. The character of the electron-state density in the size-quantization subbands is examined qualitatively in connection with the change in the system of isoenergy contours when a magnetic field is applied. © *1998 American Institute of Physics.* [S1063-7834(98)03309-7]

1. Single-electron states in systems of quantum wells in a magnetic field perpendicular to the heterogeneous interfaces can be classified easily, since the magnetic field and the quantizing potential of the quantum well act independently of one another. In this case, a system of discrete Landau levels arising from the states of the given subband is associated with each two-dimensional $(2D)$ subband. On the other hand, when the magnetic field is parallel to the interfaces, size quantization and quantization in the magnetic field cannot be treated independently, so that hybrid electronic states appear which are much more difficult to classify.[1] A quantizing magnetic field parallel to the heterogeneous interfaces causes a change in the nature of the dispersion curves for the $2D$ subbands. Thus, in first-order perturbation theory the location of the quasi-wave vector corresponding to the minimum energy of a subband is shifted in proportion to the field, while the energy undergoes a diamagnetic shift that is quadratic in the field.[2] The magnitude of the shift increases with the quantum number of the subband because of the larger spatial extent of the wave functions of the higher subbands, so that the distances between the edges of neighboring subbands increase when a parallel magnetic field is applied.[3] The electron density distribution (i.e., that of the electronic envelope functions) in the quantum well system ends up depending on the magnitude of the applied magnetic field. In particular, by changing the magnetic field it is possible to make the maximum of the electron envelope shift from one quantum well into another. This sort of redistribution of the electron wave functions in a magnetic field has been examined previously[4] in terms of the simplest model of an asymmetric system of two quantum wells described by δ-function potential wells of different strengths. Each such potential well leads to the appearance of just one local level, so it is appropriate to study the effect of a magnetic field on the energy spectrum and quantum states of the electrons in a system of quantum wells, each of which is modelled as a potential well of finite width and depth. This is the type of model[5] that is usually employed to study the electronic states in structures with quantum wells.

2. Let us consider a quantum-well system with heterogeneous interfaces perpendicular to the z axis. Let a uniform magnetic field be applied parallel to the interfaces. We choose the x axis to be in the direction of the magnetic field H. As the choice of vector potential A we use a Landau gauge in order to retain the form of the solutions for quantum-well systems without a magnetic field as far as possible:[6]

$$A_x = A_z = 0, \quad A_y = -Hz. \tag{1}$$

We denote the size-quantization potential for the electrons in the quantum-well system by $U(z)$. Since the electron hamiltonian is independent of the variables x and y, the envelope function can be written in the form[6]

$$\psi(x,y,z) = \chi(z)\exp(i(k_x + k_y y)), \tag{2}$$

where k_x and k_y are quantum numbers from a complete set characterizing the electron state. For the function $\chi(z)$ we have the equation

$$\left\{ -\frac{\hbar^2}{2m}\frac{d^2}{dz^2} + U(z) + \frac{m\omega_H^2}{2}(z-z_0)^2 \right\}\chi(z) = \left\{ E - \frac{\hbar^2 k_x^2}{2m} - g^*\mu_B H\sigma \right\}\chi(z), \tag{3}$$

in which E is the electron energy, m is the effective mass, $\sigma = \pm 1/2$ is the projection of the spin along the x axis, $\omega_H = eH/mc$ is the cyclotron frequency, $\mu_B = e\hbar/2mc$ is the Bohr magneton, g^* is the effective Landé factor, and

 © 1998 American Institute of Physics

$$z_0 = -\frac{\hbar c}{eH} k_y \tag{4}$$

has the significance of the classical radius of the electron orbit in the plane perpendicular to the magnetic field. Equation (4) implies that z_0 can be used as one of the quantum numbers in place of k_y.

As can be seen from Eq. (3), the energy E and the one-dimensional ($1D$) envelope function $\chi(z)$ depend on z_0 as a parameter. Without a size-quantization potential, the energy of the electron in a magnetic field is independent of z_0, while $\chi(z)$ depends only on the difference $z-z_0$.[6] Size quantization removes a degeneracy in z_0 and for a given value of z_0, the energy, as well as the form of the $1D$-envelope function, are obviously not indifferent to the choice of origin on the z axis. It can be shown that there is always a possibility of choosing the z origin so as to fall within a region where the dependence of the energy on k_y (or z_0) is of interest.

In fact, when making a gauge transformation, besides replacing the vector potential, in Eq. (3) it is necessary to change the phase of the wave function at the same time.[6] Thus,

$$A \to A + \nabla f, \quad \psi \to \psi \exp\left(\frac{ie}{\hbar c} f\right), \tag{5}$$

where f is a, thus-far, arbitrary function of the coordinates. In order not to change the form of Eq. (3) for the $1D$-envelope function, it is necessary to retain the Landau gauge, as well, so f must depend only on y. Then, we have

$$A_x = A_z = 0, \quad A_y = -Hz + \frac{df(y)}{dy}. \tag{6}$$

In order to ensure that the condition $\nabla \cdot A = 0$ is satisfied and retain a solution in the form (2), it is necessary that f be a linear function of y, i.e. $f = \gamma y$, where γ is an arbitrary constant. (The constant term in f can be dropped.) Thus, the only nonzero component of the vector potential can be written in the form

$$A_y = -H(z - \tilde{z}), \tag{7}$$

where $\tilde{z} = \gamma/H$ just corresponds to a shift in the coordinate origin along the z axis. The phase of the wave function in Eq. (5) then changes by an amount $e\gamma y/\hbar c$, which corresponds to a change in the origin for the quantum number k_y,

$$k_y \to k_y + \frac{eH}{\hbar c} \tilde{z}. \tag{8}$$

Therefore, without any sort of restriction, we can choose the origin for z so that $k_y = 0$ would correspond, for example, to an extremum in the function $E = E(k_y)$.

3. For a qualitative investigation of the dependence of the electron energy spectrum on the quantum number k_y, it is convenient to examine the $1D$ effective potential

$$U^*(z) = U(z) + \frac{m\omega_H^2}{2} (z - z_0)^2 \tag{9}$$

as a function of z_0. Without discussing further the trivial splitting of the subbands owing to the electron spin, we limit ourselves initially to considering the simplest case of a quantum well of depth U_0 and width w. We choose the origin of the z axis as the center of the quantum well. For $k_y = 0$ (and $z_0 = 0$) the effective potential energy is symmetric with respect to the transformation $z \to -z$. A magnetic field leads to an increase in the energy of the $2D$ levels (a diamagnetic shift). Some of them will be pushed out into the continuum. For $k_y \neq 0$ the effective potential loses its symmetry with respect to the transformation $z \to -z$ and, with increasing k_y, the power of the potential well leading to the $2D$ localized states decreases. The system of discrete energy levels present in a quantum well with $E < 0$ gradually becomes a system of Landau levels $E_n = \hbar\omega_H(n + 1/2)$ as k_y increases. Thus, levels with energies below zero, which split off from the system of Landau levels owing to the presence of a potential well, do not exist (as in the absence of a magnetic field) for arbitrary k_y. Thus, the lowest of the localized quantum-well levels can only appear for

$$\frac{eH}{\hbar c} z_{01}^{(-)} < k_y < \frac{eH}{\hbar c} z_{01}^{(+)}. \tag{10}$$

The location of the points $z_{01}^{(\pm)}$ (in the case of a single symmetric quantum well or a symmetric system of quantum wells, obviously, $z_{01}^{(-)} = -z_{01}^{(+)}$ if the z origin is chosen to be the center of symmetry of the quantum well system) and the nature of the spectrum near these points can be investigated qualitatively by perturbation theory methods, treating $U(z)$ as a perturbation. Let us assume for simplicity that a $1D$-potential well $U(z)$ in the absence of a magnetic field leads to the appearance of only a single discrete level. In this case we can set $U_0 w^2 \approx 2\hbar^2/m$. Considering the case of a sufficiently strong magnetic field and using the linear oscillator wave functions as unperturbed states,[6] in first-order perturbation theory the ground-state energy is given by

$$\varepsilon_1(k_y) = \frac{1}{2}\hbar\omega_H - \frac{1}{2} U_0 \left\{ \Phi\left(\left(\frac{m\omega_H}{\hbar}\right)^{1/2}\left(z_0 + \frac{w}{2}\right)\right) + \operatorname{sgn}\left(\frac{w}{2} - z_0\right) \Phi\left(\left(\frac{m\omega_H}{\hbar}\right)^{1/2}\left(z_0 - \frac{w}{2}\right)\right)\right\}, \tag{11}$$

where $\operatorname{sgn}(x)$ is the sign function and $\Phi(x)$ is the probability integral. Setting $\varepsilon_1 = 0$ in Eq. (11), we can find $z_{01}^{(\pm)}$. Thus, for $U_0 \approx 100$ meV, $w \approx 5 \times 10^{-7}$ cm (one level in the quantum well for $H = 0$) and $H \approx 10^4$ Oe (corresponding to $\hbar\omega_H/2 \approx 0.1$ meV for the characteristic effective electron mass $m \approx 0.007 m_0$ of GaAs, where m_0 is the free electron mass), we obtain $z_{01}^{(+)} \approx 7 \times 10^{-7}$ cm. The corresponding quantum number k_y is $k_y^{(+)} \approx 10^5$ cm^{-1}. $k_y^{(+)}$ depends weakly (logarithmically) on the magnetic field strength, decreasing with rising H. Note that the difference $z_{01}^{(+)} - z_{01}^{(-)}$ is of the same order of magnitude as the quantum well width w.

We now examine the somewhat more complicated situation of a quantum-well system in a parallel magnetic field. Let there be a system of two quantum wells (widths w_1 and w_2) separated by a tunnel-transparent barrier of width b.

Size quantization causes formation of a system of $2D$ subbands of the electron energy spectrum. As in the case of an isolated quantum well, the presence of a parallel magnetic field leads to an effective potential $U^*(z)$ which depends on the quantum number k_y through the parameter z_0. Now a minimum of the potential $U^*(z)$ as z_0 varies is obviously attained at two points, $z^{(1)}$ and $z^{(2)}$, corresponding to the centers of the two quantum wells. If, for example, $w_2 < w_1$, then the power of the effective potential with a minimum in the second quantum well is less than that with a minimum in the first quantum well. Therefore, each of the discrete levels for $z_0 = z^{(2)}$ ends up being higher than the corresponding level for $z_0 = z^{(1)}$, while the dependence of the energy of an electron in the given subband on k_y is, in general, nonmonotonic.

4. Quantitative results for specific quantum-well systems can be obtained by solving Eq. (3) numerically. In the case of a quantum-well system, in each region where $U(z) = \text{const}$, the general solution of Eq. (3) can be represented by a linear combination of two linearly independent Hermitic functions. At points where $U(z)$ is discontinuous, i.e., at the heterogeneous interfaces, the solutions are matched with the aid of the boundary conditions[7] involving the continuity of the $1D$-envelope functions and of the probability densities calculated for these functions. These conditions are supplemented by the condition that the $1D$-envelope functions be finite for $z \to \pm\infty$. The system of boundary conditions, therefore, leads to a system of linear homogeneous equations for the coefficients in the Hermitic functions and the condition that this system be solvable determines the energy spectrum. It should be noted that there are values of k_y, in the neighborhood of which the energies of some pairs of subbands are extremely close to one another. Thus, the accuracy of the computational procedure should be chosen such that it is possible to compare uniquely the calculated energy levels of certain $2D$ subbands of the electron spectrum at each computational step.

As an example, let us consider a system of two quantum wells (width $w_1 = 15\bar{a}$ and $w_2 = 8\bar{a}$) separated by a barrier of width $b = 17\bar{a}$, where $\bar{a} = 5.655 \times 10^{-8}$ cm (a 15-17-8 structure). The depth of the quantum well is $U_0 = 150$ meV. Figure 1 shows several of the lowest energy levels as functions of the quantum number z_0. The numbers of the levels are indicated on the corresponding curves. The range of variation of z_0 is limited to the immediate neighborhood of the quantum-well system, which is also shown in the figure. From this it is clear that the more distant z_0 correspond to the system of Landau levels which develops from the continuum when a magnetic field is applied. The energy spectrum is shown as a function of z_0 for a magnetic induction of 10 T, as well as the evolution of the energy levels of the states localized within the confines of the quantum-well system as z_0 changes. We note the natural anticrossing of levels in the neighborhoods of certain values of z_0. (The report of crossing in Ref. 3 is the result of inadequate accuracy in the calculations for z_0 near the anticrossing points and, therefore, of a failure to number the levels correctly.) Figure 1 shows that a strong magnetic field causes a substantial change in the

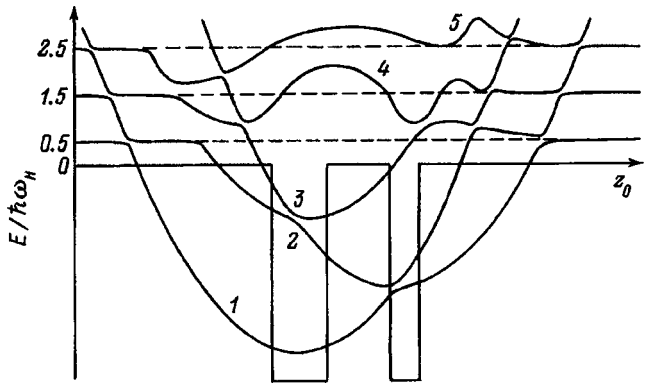

FIG. 1. The dependence of several of the lowest electron-energy levels on the parameter z_0 in a 15-17-8 structure for a magnetic induction of 10 T (schematic illustration; the scale in the neighborhoods of the anticrossing points has been enlarged somewhat). Also shown is the potential energy of the quantum-well system as a function of z_0.

electron dispersion curve for the direction along k_y, while the customary parabolic variation is retained along k_x.

The anticrossing regions are also regions with sharp changes in the character of the envelope functions, where (for states with $E<0$) they are effectively redistributed in the quantum-well system. Thus, the envelope function of the lowest $2D$ subband for the 15-17-8 structure in a 10 T magnetic field for $z_0 \leqslant 37\bar{a}$ is localized mainly within the confines of the wider potential well. Redistribution of the envelope function takes place within a rather narrow range of variation z_0 ($\Delta z_0 \approx 2\bar{a}$, which corresponds to $\Delta k_y \approx 1.7 \times 10^5$ cm^{-1} for 10 T). In weaker fields (below 10 T), redistribution of the envelopes of the lowest $2D$ subbands in this structure is essentially not observed. In structures with a narrower barrier (e.g., 10-7-8), the effective redistribution already takes place a fields in excess of 5 T and occurs more smoothly, i.e., over a wider interval of z_0.

5. Several comments must be made concerning the density of states in the $2D$ subbands. The electron-energy spectrum can be written in the form

$$E_n(k_x, k_y) = E_n^{(0)} + \frac{\hbar^2 k_x^2}{2m} + \varepsilon_n(k_y), \tag{12}$$

where $E_n^{(0)}$ is the location of the absolute minimum of the nth subband, m is the effective mass of a conduction electron, and $\varepsilon_n(k_y)$ are some functions of k_y, of which some idea can be gained from Fig. 1. This figure shows that the number of the Landau level, which is uniquely determined for large z_0, is a good quantum number which can be used to classify the electronic states, which are spatially limited (for $E<0$) along the z axis by the quantum-well system. The density of states in the nth subband

$$g_n(E) = \sum_{k_x, k_y} \delta(E - E_n(k_x, k_y)) \tag{13}$$

for $E<0$, i.e., for states corresponding to the discrete (relative to motion along the z axis) spectrum, can be reduced in standard fashion to the integral

$$g_n(E)=\frac{S}{(2\pi)^2}\sum_i\int\frac{dk_x}{|\partial\varepsilon_n(k_y^{(i)})/\partial k_y|}, \tag{14}$$

where S is the area of the structure in the xy plane and the points $k_y^{(i)}$ are determined from the equation

$$\varepsilon_n(k_y^{(i)})=E-E_n^{(0)}-\frac{\hbar^2k_x^2}{2m}. \tag{15}$$

Let us consider the density of states in the lowest ($n=1$) size quantization subband. Near its absolute minimum the dispersion as a function of k_y can be approximated by a parabola: $\varepsilon_n(k_y)\approx\hbar^2k_y^2/2m'$, where m' is a parameter with the dimensions of mass, which determines the curvature of $\varepsilon_n(k_y)$ near the minimum. (Calculations show that it differs little from the effective mass m in fields below 10 T.) In this case,

$$k_y^{(i)}=\pm\sqrt{(2m'/\hbar^2)(E-E_n^{(0)}-\hbar^2k_x^2/2m)}, \tag{16}$$

which automatically determines the limits of integration with respect to k_x in Eq. (14). An elementary integration yields the step-function dependence of the density of states near the minimum of the $2D$ subband that is customary for $2D$ systems,

$$g(E)=\frac{S(mm')^{1/2}}{2\pi\hbar}\,\vartheta(E-E_1^{(0)}). \tag{17}$$

Here $\vartheta(E)$ is the Heaviside step function. For large $|k_y|$, the electron energy approaches the energy $\hbar\omega_H/2$ of the first Landau level from below (Fig. 1). The behavior of the density of states near the Landau level can easily be studied using Eq. (11), by considering large ($\sim\pi/a$) values of k_y in this expression and using the well-known asymptotic representation for the probability integral. We have

$$\varepsilon_1(k_y)\approx\frac{\hbar\omega_H}{2}-\frac{U_0}{2\sqrt{\pi}}\frac{1}{a_Hk_y}\exp(-a_H^2k_y^2), \tag{18}$$

where $a_H^2=\hbar c/eH$. Neglecting the dependence on k_y in the preexponential factor (replacing k_y by its limit $\sim\pi/a$), we find

$$k_y^{(i)}=\pm\frac{1}{a_H^2}\sqrt{\ln\left[\frac{2\pi^{3/2}}{U_0}\frac{a_H}{a}\left(\frac{\hbar^2k_x^2}{2m}-\varepsilon\right)\right]^{-1}}, \tag{19}$$

where ε is the energy reckoned downward from the Landau level. The solutions (19) exist if the argument of the logarithm exceeds unity, which determines the limits of integration in Eq. (14). As a result of integrating as $\varepsilon\to0$ ($E\to\hbar\omega_H/2-0$), we obtain

$$g_1(\varepsilon)\approx\frac{Sa}{2\sqrt{2\pi^2}a_H^2}\frac{m^{1/2}}{\hbar}\frac{1}{\sqrt{\varepsilon}}, \tag{20}$$

i.e., the density of states near the Landau level has the form characteristic of $1D$ systems. (For $E>\hbar\omega_H/2$ the density of states evidently has the same root singularity.)

6. Between the absolute minimum of the first subband and the first Landau level, in some structures the density of states in a magnetic field can have the special behavior in the neighborhood of the level anticrossings shown schematically in Fig. 2. Near the anticrossing points the character of the dispersion relation in the first and second subbands can established using perturbation theory for two close levels. The magnitude of the perturbation is determined by the tunnel transparency of the barrier. The dispersion relation in the lower subband is one of the branches of a nonanalytic function and, depending on the structure of the quantum well system and the magnitude of the magnetic field, it can result in the three characteristic types of dependence on k_y shown in Fig. 2. In the neighborhood of the anticrossing point these dependences can be represented in the form of a simple analytic function

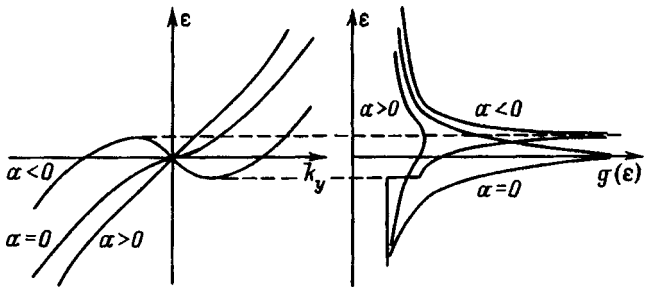

FIG. 2. The possible structure of the dispersion relation of the first subband and the behavior of the density of states (right) in the neighborhood of a crossing point.

$$\varepsilon_1(k_y)=ak_y+\frac{1}{3}bk_y^3, \tag{21}$$

where a and b are constants, and the energy and k_y in Fig. 2 are taken relative to the point 0.

For $a<0$ there are two values of the energy, $\varepsilon_1^{(m)}$ and $\varepsilon_1^{(s)}$, of which the first corresponds to the local minimum of the dispersion curve and the second, to the saddle point. Thus, at the point $\varepsilon_1^{(m)}$, where additional solutions of Eq. (15) appear, the density of states has a singularity in the form of a discontinuity of the first kind that is characteristic of $2D$ systems. In the neighborhood of the saddle point, the density of states of $2D$ systems has, as we know, a logarithmic singularity.[8]

For $a>0$ the density of states in the neighborhood of the anticrossing point has no singularities and its behavior can be understood directly from Eq. (14). As it passes through this point, the denominator under the integral sign passes through a minimum, so the density of states has a maximum in the neighborhood of the anticrossing.

The case $a=0$, where the dispersion curve as a function of k_y has an inflection point, is special. The character of the resulting singularity in the density of states can be studied using an approximation of the dispersion relation of the form (21). We denote the deviation in the energy from its value at the singular point by ε. The singular part $\delta g(\varepsilon)$ of the density of states to the right and left of the singular point $\varepsilon=0$ can be reduced to elliptic integrals; in the immediate neighborhood of the singular point, $\delta g(\varepsilon)\propto|\varepsilon|^{-1/6}$. The power-law dependence of the singularity in the density of states, $\delta g(\varepsilon)\propto|\varepsilon|^{-\lambda}$ is not related to the approximation (21); in any case, it can be stated that the exponent is bounded by the inequality $0<\lambda<1/2$. The behavior of the singularities in

the density of states in the neighborhood of the anticrossing point as the parameter a varies (which can be done by changing the magnetic field in specially selected systems of two or more quantum wells) is shown to the right in Fig. 2.

It should be noted that the limits of integration in Eq. (14) are established naturally when the range of allowable values of k_x is determined (or k_y for the obvious alternative to Eq. (14) for the density of states). The qualitative arguments used for this purpose in Ref. 1 to calculate the density of states, in the exactly soluble case of a parabolic quantum well in a parallel magnetic field, were the cause of a sharp reduction (with increasing energy) in the density of states in the size-quantization subbands and this was interpreted as a $2D \rightarrow 1D$ transition in the electronic subsystem of a quantum-well structure.

We thank S. P. Pavlov for discussing this work.

This work was supported by the Russian Fund for Fundamental Research and by the Russian Ministry of Science, Technology, and Industry through the program on Physics of Solid State Nanostructures.

[1] W. Zawadzki, in *High Magnetic Fields in Semiconductor Physics II*, edited by G. Landwehr, Springer Series in Solid State Sciences, Springer, Berlin, Heidelberg (1989), Vol. 87, pp. 220-229.
[2] F. Stern and W. E. Howard, Phys. Rev. **163**, 816 (1967).
[3] J. M. Heisz and E. Zaremba, Semicond. Sci. Technol. **8**, 575 (1993).
[4] A. A. Gorbatsevich, V. V. Kapaev, and Yu. V. Kopaev, JETP Lett. **57**, 580 (1993).
[5] G. Bastard, J. A. Brum, and R. Ferreira, Solid State Phys. **44**, 229 (1990).
[6] L. D. Landau and E. M. Lifshitz, *Quantum Mechanics* [in Russian], Nauka, Moscow (1989), 767 pp.
[7] M. Altarelli, in *Excitons in Confined Systems*, edited by R. del Sole, A. D'Andrea, and A. Lapiccirella, Springer Proceedings in Physics, Vol. 25, Springer, Berlin, N.Y. (1988), p. 170.
[8] A. M. Kosevich, *Theory of Crystal Lattices (Physical Mechanics of Crystals)* [in Russian], Kharkov (1988), 304 pp.

Translated by D. H. McNeill

Growth and optical properties of BiI_3 and PbI_2 microcrystals

V. F. Agekyan

Institute of Physics, St. Petersburg State University, 198904 Petrodvorets, Russia
(Submitted December 8, 1997; resubmitted February 24, 1998)
Fiz. Tverd. Tela (St. Petersburg) **40**, 1724–1730 (September 1998)

A study has been made of low-temperature absorption and luminescence spectra of bismuth iodate microcrystals in various hosts (layered cadmium iodate, microporous glasses and polymers), as well as of the spectra of mesoscopic domains formed in bulk bismuth iodate by mechanical strains. The structure of the spectra and the quantum shifts of the exciton levels yielded information on the dimensions and size dispersion of the microcrystals and domains, as well as on the effect of microcrystal size on the Stokes losses. The quantum exciton-line shifts in microcrystalline lead-iodate films grown in pores of the glass host have been used to calculate the film thicknesses. A photoinduced change in the mechanism of radiative recombination was observed in PbI_2 microcrystals. The spectrum of resonant Raman scattering in lead iodate microcrystals consists of broad bands corresponding to the branches of optical phonons undergoing strong angular dispersion. © *1998 American Institute of Physics.*
[S1063-7834(98)03409-1]

Investigation of quantum-confinement effects associated with excitons in microstructures is a major area of interest in the optics of semiconductors. The actual approach used in studies of microcrystals in hosts is determined not only by the average dimensions of the microcrystals and their size distribution, but also by their geometric shape, which affects considerably the properties of the system and theoretical description of the wave functions and electronic-level energies. If the host is a glass or a high-symmetry crystal, and the microcrystals form from substances with zero or small anisotropy, the potential acting on the electronic states is assumed to be spherical or cubic. In layered structures the quantum-confinement effects should be strongly anisotropic because of the different nature of the bonds acting in the plane of an elementary layered stack and between such stacks. It is to be expected that microcrystals of layered semiconductors embedded in hosts can be described as discs whose thickness is determined by a few elementary layered stacks. The weakness of interlayer coupling results in breaks in stacking order. These defects can initiate the formation of mesoscopic domains with lattice symmetry different from that of the host crystal. Of most interest are domains of small size (quantum discs), where the confined motion of the exciton center of mass gives rise to quantum-confinement effects in optical spectra.

Consider first the optical properties of BiI_3 and PbI_2 microcrystals. Because of the large carrier effective masses, excitons in bismuth iodate have a comparatively small radius $r_e \sim 0.6\,\text{nm}$,[1–3] whereas for the lead iodate estimates[4,5] give $r_e = 2.0\,\text{nm}$. Since the thickness L of the layered stacks in BiI_3 and PbI_2 is practically the same, about 0.7 nm, confinement in thin lead-iodate microcrystals should manifest itself considerably stronger. The markedly different ratios of r_e to the lattice constant (or to the molecule dimensions) for PbI_2 and BiI_3 are seen in the largest possible quantum shifts of the first excited states; indeed, the energy separations between the direct exciton of a bulk crystal and the first excited state of the molecule are 0.6 and 3.5 eV for BiI_3 and PbI_2, respectively.[6] Besides being of intrinsic interest, the knowledge of spectra of bismuth- and lead-iodate-based microcrystals may prove to be useful in studies of complex systems with perovskite symmetry, such as $(CH_3NH_3)_3Bi_2I_9$, $(C_nH_{2n+1}NH_3)PbI_4$ and others[7–10], as well as of the properties of Pb^{2+} and Bi^{2+} ions in solutions and crystals[11].

1. BISMUTH IODATE

Bismuth iodate is a model crystal for studying excitons of a relatively small radius in layered semiconductors, and its spectra are known in considerable detail. The absorption spectra of single molecules and dimers of BiI_3 are given in Ref. 6. We are considering below spectra of BiI_3 microcrystals in hosts of CdI_2 layered crystals, porous glasses, and polymers, as well as those of mesoscopic domains in bulk BiI_3 crystals.

A. Growth of BiI_3 microcrystals

Bulk crystals were prepared by sublimation in vacuum at 400–420 °C. BiI_3 microcrystals form in the host of the wide-gap crystal CdI_2 in the course of annealing of mixed CdI_2-BiI_3 crystals grown by the Bridgman-Stockbarger method. Similar to the case of Group I-VII and II-VI semiconductors in glass hosts,[12,13] the average size of the microcrystals and their size distribution depend on the time and temperature of the anneal.

The pore size distribution in alkali borosilicate glasses is narrow; indeed, electron and atomic-force microscope measurements yield for the average pore radius 6–7 nm. While the atomic-force microscope is not capable of measuring directly the pore depth, scanning of cleaved surfaces showed the pores to be distributed uniformly in depth at least within

 © 1998 American Institute of Physics

0.5 cm from the surface. The total volume of the pores can be as high as 30% of that of the host. Hosts of other porous glasses with larger pore radii (from 10 to 25 nm) were also used. The evacuated ampoules containing porous glasses and single crystals of BiI_3 were heated to 500–530 °C and cooled subsequently at various rates. Microcrystals of BiI_3 formed in glass pores by thermal sublimation of this compound.

BiI_3 microcrystals in the polymer host were prepared by drying in air the host soaked preliminarily in an iodate solution in hydrochloric acid. Because of the low solubility of BiI_3 in the acid, the filling of the polymer host pores by microcrystals is low, but it can be increased by repeating the process.

B. Optical spectra of bulk BiI_3 crystals

Bismuth iodate is an indirect-gap semiconductor, whose absorption edge begins with phonon steps of the indirect exciton.[1] The indirect and direct exciton energies are, respectively, 2.008 and 2.072 eV. The calculated total effective mass of the direct exciton in BiI_3 is $1.4\,m_0$,[14] but in order to reconcile it with experiment one has to accept a few times larger value for the direction normal to the layer plane. In single-crystal BiI_3 films one observes excited exciton states yielding for the binding energy and ground-state radius 160 meV and 0.6 nm, respectively, which is in accord with magneto-optic measurements[15]. Close to the absorption edge one sees also narrow lines of the T, S, and R excitons localized at stacking faults in BiI_3 layers (Fig. 1),[3] which are present in the luminescence spectrum as well. Lying lower in energy is a variable system of lines to be considered below.

C. Absorption and luminescence spectra of mesoscopic BiI_3 domains

In bulk BiI_3 crystals one observes a variable spectrum of W_i bands which can be enhanced by straining the crystal (Fig. 2). These bands should be interpreted as the spectrum of excitons imprisoned in mesoscopic domains.[16,17] The existence of domains in strained BiI_3 crystals was established by x-ray diffraction. These domains are initiated by stacking faults and have D_{3d} symmetry different from the symmetry of the bulk-crystal C_{3i}^2. Calculations show that the fundamental absorption edge and the exciton levels of bulk BiI_3 crystals with symmetry D_{3d} lie considerably lower in energy than those of the conventional BiI_3 crystal with symmetry C_{3i}^2. The spectrum of mesoscopic domains is redshifted with respect to that of the bulk crystal having the symmetry of the domains because of quantum confinement. This spectrum lies, however, below the exciton lines of the bulk BiI_3 crystal with symmetry C_{3i}^2, which is the host for the domains.

Figure 2 presents an exciton spectrum of mesoscopic domains. The W_i band series ($i=1,2,3$) converges toward longer wavelengths to the bulk-exciton energy of the BiI_3 crystal of symmetry D_{3d}. The position of the W_i bands is determined primarily by the thickness iL of the corresponding quantum discs (i is the number of layer stacks in a disc). The structure at the short-wavelength wing of the W_i bands is due to the quantum discs of the same thickness iL having a set of radii R_1. Domains with noninteger values of i should

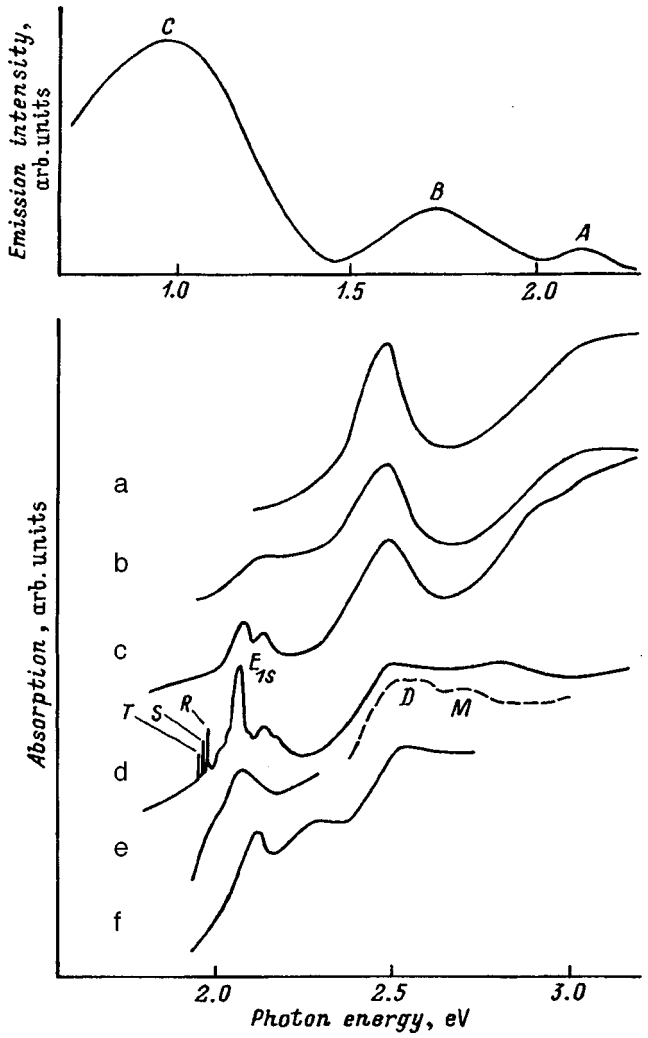

FIG. 1. Absorption spectra of BiI_3 obtained at $T=4$ K; (a) microcrystals in unannealed CdI_2 host (BiI_3 concentration 0.05 mol.%), (b) same sample after annealing, (c) microcrystals in CdI_2 host with average BiI_3 thickness in the sample of 0.5 monolayer, (d) a thin bulk single crystal, (e, f) microcrystals in glass hosts with large and small pores, respectively. E_{1s} — direct-exciton peak, T, S, and R are the lines of stacking-fault-bound excitons, the arrows identify indirect-exciton steps. Dashed line - monomer (M) and dimer (D) spectrum of BiI_3 in LTA zeolite (Ref. 6). Shown on top is a spectrum of sample c.

contribute to the spectrum too. The energies of the W_i bands measured in three differently strained BiI_3 samples agree with the spectra calculated under the following starting assumptions:

1) The model of the mesoscopic domain is a quantum disc with thickness iL and radius R_1. The exciton energies are given by the expression

$$E_{\text{nikmv}}=E_g-E_n-h^2\pi^2k^2/(2M_z i^2L^2)+h^2\pi^2 j_{mv}/(2m_{xy}R_1)\,.$$

Here i is the number of layer stacks, k is the quantum-confinement quantum number, j_{mv} is the vth solution of equation $J_m(x)=0$, where $J_m(x)$ is the Bessel function of order m, M_z and M_{xy} are the effective-mass parameters, E_g

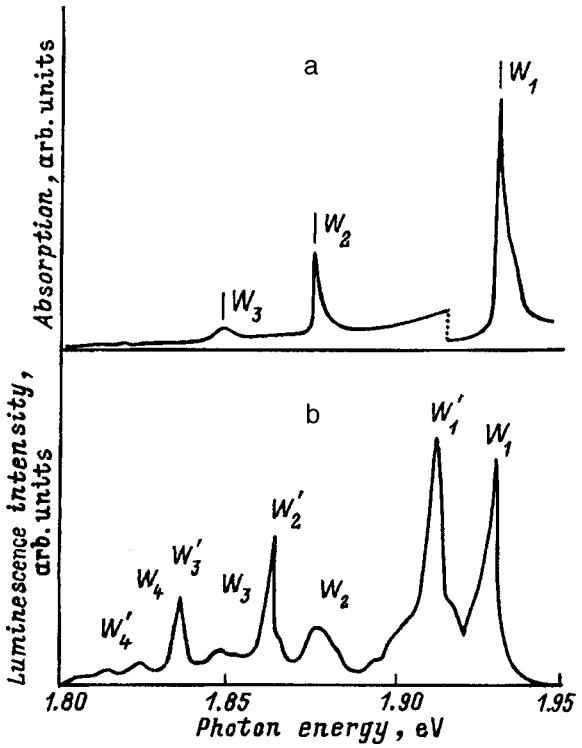

FIG. 2. (a) Absorption and (b) luminescence spectra of excitons in mesoscopic domains of a strained BiI_3 sample. $T=4$ K.

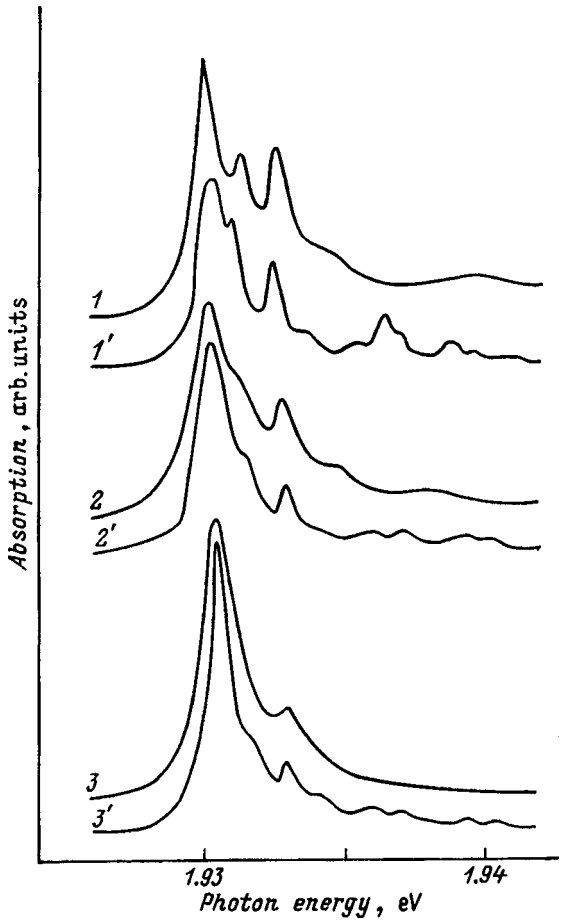

FIG. 3. Structure of the absorption band W_1 of one-layer mesoscopic domains in BiI_3 (domain crystal symmetry D_{3d}). *1–3* — experimental spectra of samples with progressively increasing bending stresses taken at $T=4$ K, *1'–3'* — calculated spectra of one-layer domains with parameters specified in text. The spectra are normalized.

is the gap width of the BiI_3 crystal with symmetry D_{3d}, and E_n is the binding energy of the exciton with quantum number n in a bulk crystal.

2) The main contribution to the optical spectrum comes from $1s$ excitons.

3) Possible values of R_1 depend on the parameters of the in-plane honeycomb structure of the BiI_3 crystal and obey Gaussian distribution

$$g(R_1)=\exp[-(R_1-\overline{R})^2/D^2]/(\pi D)^{1/2},$$

where $\overline{R}$ is the average radius, and D is the width of the distribution.

4) The absorption line of the quantum disc is a Lorentzian with a damping Γ.

5) The contribution of a single disc to the spectrum is determined by its dimensions.

The fitting parameters for simulating the structure of the W_1 band (one-layer domain) are Γ, $\overline{R}$, M_{xy}, and M_z. In these conditions, the absorption intensity at the W_1 band as a function of phonon frequency Ω can be presented by the expression

$$A(\Omega)=|\psi_{1s}(0)|^2\Sigma_v\Sigma_R(R_1/j_{mv})2(\Gamma/\pi)/\{2[\hbar\Omega-E_{1s,0,v}(R_1)]+\Gamma^2\}g(R_1),$$

where $\psi_{1s}(0)$ is the $1s$ exciton wave function.

The structure of the W_1 band and the quantum shifts of the W_i bands calculated with $\Gamma=0.3$ eV, $\overline{R}=0.7$ nm (i.e., for $\overline{R}$ equal to the radius of the ring formed by six Bi atoms in the layer plane), $M_{xy}=11.5\,m_0$, and $M_z=1.4\,m_0$ are in accord with experimental spectra. The values of D obtained for the three samples in Fig. 3 are, respectively, 27 (1), 37 (2), and 43 (3) nm.

The position of the strong long-wavelength peak in the W_1 structure corresponds to excitons in quantum discs ranging in radius from 6 to 20 nm. A study of the structure of the W_1 bands suggests that the mesoscopic domains forming at larger strains are predominantly of larger size. The luminescence spectra exhibit resonant W_i bands and their W_1' satellites corresponding to excitons trapped at defects in domains or at their edges (Fig. 2).

D. Absorption spectra of BiI_3 microcrystals in porous hosts

A study of the spectra of BiI_3 in the Na-LTA(1) zeolite host interpreted them as due to transitions to excited states of BiI_3 mono- and dimers.[6] It is of interest to compare them with the spectra of the microcrystals grown by us (Fig. 1). The absorption spectrum of mixed BiI_3-CdI_2 crystals obtained both before and after annealing, as well as of multilayer BiI_3-CdI_2 systems with an average BiI_3 content not less than one layer stack, contains a strong band near 2.5 eV, which is close in energy to the first excited states of the dimers (Fig. 1). Annealing mixed crystals gives rise to a

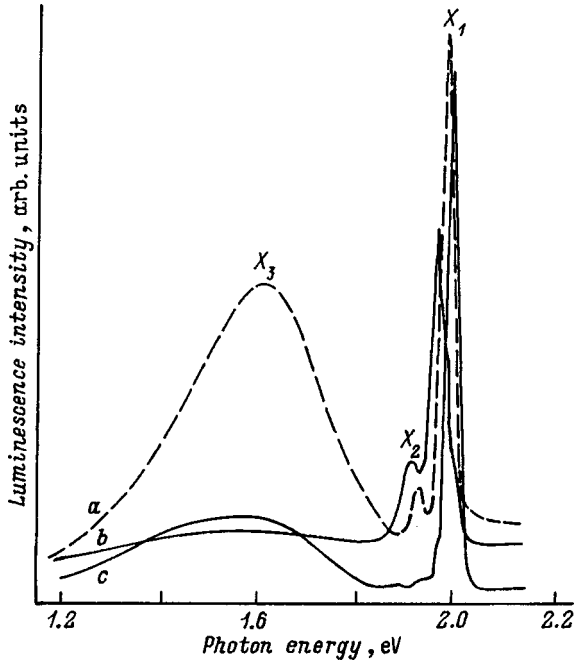

FIG. 4. Luminescence of BiI_3 microcrystals embedded in glass-host pores, $T=4$ K. Bands X_1 and X_2 — emission of excitons localized at stacking faults and in mesoscopic domains of comparatively large microcrystals, band X_3 — exciton emission from small BiI_3 microcrystals. (a) unsaturated strained sample, (b) strongly strained saturated sample, (c) weakly strained saturated sample.

long-wavelength tail extending over nearly the whole quantum-confinement region in BiI_3, from the bulk crystal to the monomer. This implies the formation and growth of BiI_3 microcrystals during the anneal. The absorption spectrum of BiI_3 microcrystals in hosts with a large pore radius is close to that of a bulk crystal. The exciton line in the spectra of hosts with smaller pores is redshifted by 20–50 meV (Fig. 1). Assuming the shift to be determined primarily by the film thickness, we obtain for it seven to two layer stacks, respectively. The absorption spectrum of porous samples with a low BiI_3 density contains also bands characteristic of small clusters. The spectra of polymer hosts with low and high BiI_3 densities are similar to those of unannealed and annealed mixed BiI_3-CdI_2 crystals, respectively.

E. Luminescence of BiI_3 in glass-host pores

Compare the luminescence spectra of large BiI_3 microcrystals, which exhibit a quantum-confined exciton-line shift of about 10 meV, with those of bulk crystals, mesoscopic domains, and small microcrystals (Figs. 1 and 2). The X_2 band in Fig. 4 peaking at 1.91–1.93 eV corresponds in energy to the structure of W_i excitons imprisoned in mesoscopic domains. The maximum of the strong X_1 band lies from 1.97 to 2.02 eV in various samples, which covers the region of the narrow T, S, and R excitons bound to stacking faults in a bulk crystal (Fig. 1). The complex X_1 band includes apparently contributions of states of the W_1 type, whereas X_2 is related to W_2 and W_3. The microcrystals must be dominated by one-layer thick domains with a stronger in-plane confinement in radius R_1 compared to domains in bulk BiI_3. Indeed, the maximum of the W_1 band in a bulk crystal corresponds to quantum discs with radii $R_1=6-20$ nm, which are larger than the host pores. This constraint accounts for the short-wavelength shift of the W_1 structure in BiI_3 microcrystals, and the predominance of one-layer stacks enhances the $i=1$ band. Quantum confinement in the BiI_3 microcrystals which host domains also provide a contribution to the W_i shift. As seen from Fig. 4, as the BiI_3 concentration in the host pores decreases, the X_1 band shifts toward shorter wavelengths because the microcrystals in unsaturated samples are smaller. Radiation of unsaturated samples exhibits a broad X_3 band (which apparently is an analog of band B observed in the spectrum of annealed BiI_3-CdI_2 crystals). Thus the spectra of BiI_3 in porous glass hosts are due to large microcrystals and their mesoscopic domains, as well as to small microcrystals (clusters).

F. Luminescence of BiI_3 microcrystals and clusters in the CdI_2 host

In contrast to the comparatively small shift of the absorption edge observed in going from the bulk BiI_3 crystal to the monomer, the shift of the luminescence spectrum is considerably larger, viz. from 2.0 eV in the bulk crystal to 1.0 eV in a small BiI_3 cluster embedded in the CdI_2 host (Fig. 1). The assignment of the broad C band peaking at 1.0 eV to small clusters is supported by the observation that, while this band is not excited near the edge in an annealed mixed BiI_3-CdI_2 crystal, its excitation spectrum lies considerably higher in energy, at about 2.52 eV, which gives 1.5 eV for the Stokes shift (see absorption spectra in Fig. 1). The shorter-wavelength B band near 1.7 eV is excited by photons of 2.2 eV or higher energy. It was established that increasing the excitation energy within the 2.2–2.4-eV interval shifts the B band maximum in the opposite direction, to lower energies. These properties of the excitation spectrum, together with the large Stokes shift, indicate that the vibronic coupling in BiI_3 microcrystals is strong and grows as they decrease in size. The luminescence decay time constant τ_0 of the B band varies over the band profile from 10 ms for 1.6 eV to 20 ms for 1.8 eV. The unusual decrease of τ_0 with decreasing energy implies an increasing lifetime of excited states with increasing microcrystal size. This can be attributed to the larger role played by surface states in smaller microcrystals. The large values of τ_0 suggest that the lowest excited state in BiI_3 microcrystals is a dipole-forbidden triplet. The luminescence band A with a small Stokes shift is due to large BiI_3 microcrystals, which are responsible for the long-wavelength absorption tail in the spectrum in Fig. 1b.

2. LEAD IODATE

The simplest lead-iodate polytype, $2H$, has a CdI_2-type structure with D_{3d}^3 symmetry; its optical properties have been studied in considerable detail, but interpretation of the nontrivial exciton spectrum meets with difficulties. We next present the results of our investigation of PbI_2 microcrystals grown in a porous host.

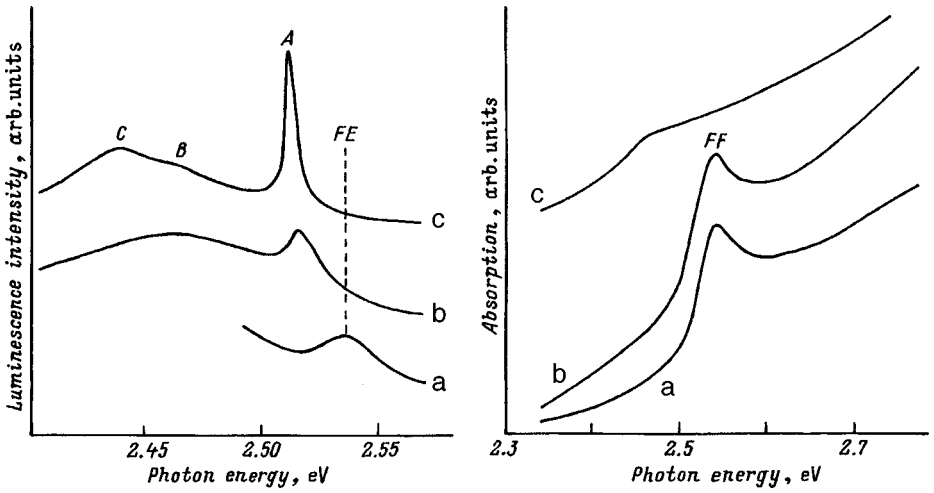

FIG. 5. Luminescence and absorption spectra of PbI_2 microcrystals in a porous glass host. Luminescence: (a) as-grown sample, $T=77$ K; (b, c) relaxed sample at $T=77$ and 4 K. Absorption: (a) 4 K, (b) 77 K, (c) 300 K.

A. Preparation of lead-iodate microcrystals

Lead iodate was grown in the porous alkali-borosilicate glass host by sublimation under conditions similar to those used to grow BiI_3 but at a lower temperature. To prepare PbI_2 microcrystals in a glass host by deposition from solution, the glass was immersed in a hot aqueous solution of PbI_2, removed from it, and dehydrated by various techniques. The optical density of samples at the fundamental absorption edge of PbI_2 was controlled by properly varying the solution temperature and concentration, as well as by repeating the above procedure. The PbI_2 solubility in water and its temperature dependence are such that one cycle of deposition of microcrystals from a saturated solution produces samples with a pore filling of about 10^{-4}.

B. Spectra of bulk lead-iodate crystals

The lattice constants of the $2H$ PbI_2 crystal are 0.70 nm normal to the layers (the layer stack thickness) and 0.46 nm in the layer plane. This crystal is a direct-gap semiconductor. The $n=1$ exciton peak lies at 2.497 eV at $T=4$ K and is produced in the $A_4^+ \rightarrow A_4^-$ interband transition.[18] The $n>1$ exciton lines have a complex structure, which complicates determination of the binding energy R_e, as well as the effective masses and their anisotropy. Magneto-optic measurements yield $R_e=63$ meV and the exciton radius $r_e=1.9$ nm.[4] The luminescence spectrum of bulk $2H$ PbI_2 single crystals grown from the same aqueous solution as the microcrystals exhibits two exciton-polariton branches and bound excitons.

C. Absorption and luminescence spectra of PbI_2 microcrystals in a glass host

We did not succeed in observing an exciton spectrum in samples produced by sublimation because of strains and a large size dispersion among the microcrystals. An exciton peak was revealed in the absorption spectrum of microcrystals grown from an aqueous solution, and the E_{1s} maximum is shifted by the quantum-confinement effect with respect to the $n=1$ exciton line of the bulk $2H$ PbI_2 crystal (Fig. 5). Depending on the actual growth regime chosen, this quantum shift varies from 30 to 70 meV, with the larger shift observed for solution-produced samples cooled at a faster rate. The exciton-band halfwidth practically does not change when a sample is cooled from 77 to 4 K, which implies that it is determined by the microcrystal size distribution in the pores. As-prepared samples exhibit free-exciton luminescence at 77 K, but it degrades rapidly, particularly under strong optical pumping. The radiation of a saturated sample with relaxed luminescence consists at $T=4$ K of a comparatively narrow A band and of broad bands B and C (Fig. 5). Band A is strongly asymmetric, and its maximum is shifted relative to the E_{1s} line by 30 meV toward lower energies. Remarkably, the short-wavelength luminescence tail measured on a saturated sample begins 20 meV above the exciton-absorption maximum. In an unsaturated sample, bands A and B are weak, and the short-wavelength tail starts at the E_{1s}-line maximum. The long-wavelength bands B and C are temperature stable and grow in intensity by an order of magnitude relative to band A in going from 4 to 77 K.

D. Discussion of absorption and luminescence spectra of PbI_2 microcrystals

Absorption spectra of small lead-iodate clusters embedded in FAU and LTA zeolites were studied in Refs. 6,19. The maximum number of molecules in a cluster is five, and the absorption edge starts at about 3.0 eV. The absorption spectra of PbI_2 microcrystals in colloids[20] are similar to those measured on a zeolite-host sample. The absorption edge of lead iodate loaded in the E-MAA copolymer host[21] lies lower in energy, and it exhibits numerous peaks believed[21] to correspond to thin PbI_2 films of different thickness. Measurements of the diamagnetic shifts of these peaks performed in magnetic fields of up to 150 T showed the electronic wave functions in microcrystals to be strongly localized.[22] The first data on the optical properties of PbI_2 microcrystals in porous glass hosts are presented in Ref. 23. Nanocrystals of lead iodate in SiO_2 films have been recently studied by optical and EPR methods.[24]

There are two thresholds (about 3.18 and 3.68 eV) in the absorption spectra of microcrystals above the first interband transition $A_4^+ \rightarrow A_4^-$, which coincide with the absorption

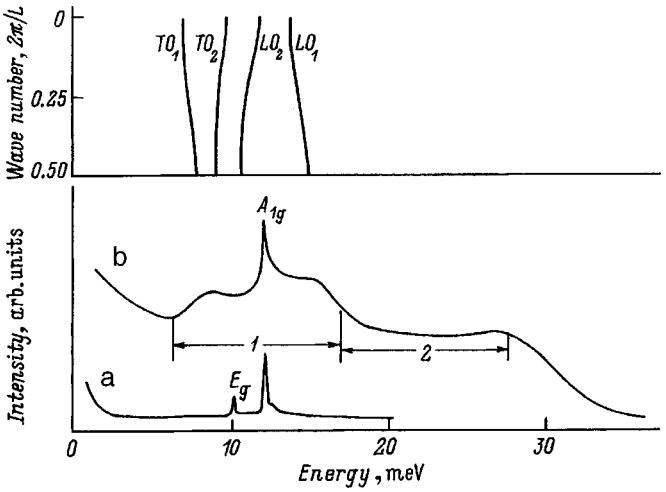

FIG. 6. Raman scattering spectra of PbI_2. (a) scattering by a bulk crystal under nonresonant excitation, (b) scattering by a system of microcrystals embedded in a glass host under excitation at the exciton absorption peak: *1* and *2* — regions of one- and two-phonon scattering in spectrum *b*, $T = 77$ K. Shown on top is the dispersion of *LO* and *TO* phonons in lead iodate in the direction normal to the layer plane obtained at 50 K (Ref. 27).

peaks of clusters consisting of four–five PbI_2 molecules; one observes in these regions also features in the reflectance spectrum of bulk PbI_2. A comparison with electron band-structure calculations made for lead iodate permits assignment of these thresholds to the $A_4^+ \rightarrow A_5^-$ and $A_4^+ \rightarrow A_6^-$ transitions.[18] The contribution of small clusters to the short-wavelength structure is a problem requiring an independent investigation.

Taking into account the strong anisotropy in the growth rate of layered lead-iodate crystals, one may assume the quantum-confinement effects to be dominated by the microcrystal thickness, despite the constraint imposed on the film radius by the glass-host pores. The exciton radius r_e is equal to the thickness of three layer stacks, and the host pore dimensions are such that the film thickness cannot exceed by far the exciton size. As follows from a theoretical estimation of the strong and weak quantum-confinement cases,[25] crystals with thickness iL of about 2.5 r_e correspond to an intermediate situation, which is difficult to consider analytically. In the case of lead iodate, the thickness of such a film is 5 nm, which is close to the average pore radius. The quantum exciton-line shift and the pore dimensions in hosts suggest that we deal here with the intermediate case. The situation is complicated because the data on the E_{1s}-line maximum is controversial. The long-wavelength bands can, however, be due to interimpurity recombination as well.

E. Raman light scattering by an ensemble of lead-iodate microcrystals

To obtain a Raman scattering spectrum, the sample was excited at the maximum of exciton absorption, so that the spectrum in Fig. 6 has a resonant character. Nonresonant scattering spectra exhibit one narrow line distant from the excitation line by 11.8 meV and corresponding to the A_{1g} phonon.[26] Resonant spectra contain, besides this line, a broad structure within the 6–16-meV region below the excitation line. A comparison with phonon dispersion branches (Fig. 6) shows this interval to include the total energy interval of the *TO-LO* phonons[27] allowed by the selection rules in resonant Raman scattering. The vibration propagating along an arbitrary direction in an anisotropic crystal is mixed and contains a longitudinal and a transverse component. The angular optical-branch dispersion and the random orientation of microcrystals give rise to broad bands in the Raman scattering spectrum. The weaker structure extending 32 meV below the pump line is due to two-phonon processes.

Thus investigation of the optical properties of BiI_3 and PbI_2 microcrystals of different size permits one to follow the transformation of the spectra of these iodates in going from a bulk crystal to a small cluster and a single molecule.

[1] Y. Kaifu and T. Komatsu, J. Phys. Soc. Jpn. **40**, 1377 (1976).
[2] Y. Kaifu, J. Lumin. **42**, 61 (1988).
[3] T. Komatsu, T. Iida, I. Akai, T. Aikami, and V. F. Agekyan, Fiz. Tverd. Tela (St. Petersburg) **37**, 2433 (1995) [Phys. Solid State **37**, 1332 (1995)].
[4] Y. Nagamune, S. Takeyama, and N. Miura, Phys. Rev. B **40**, 8099 (1989).
[5] T. Goto, J. Phys. Soc. Jpn. **51**, 3 (1982).
[6] Z. K. Tang, Y. Nozue, and T. Goto, J. Phys. Soc. Jpn. **61**, 2943 (1992).
[7] T. Kawai, A. Ishii, T. Kitamura, S. Shimanuki, M. Iwata, and Y. Ishibashi, J. Phys. Soc. Jpn. **65**, 1464 (1996).
[8] X. Hong, T. Ishihara, and A. V. Nurmikko, Phys. Rev. B **45**, 6961 (1992).
[9] E. A. Muljarov, N. A. Gippius, A. V. Kvit, G. Ya. Zueva, G. N. Mikhailova, A. M. Prokhorov, and S. G. Tikhodeev, in *Abstract of the Second International Conference on Nanostructures* (St. Petersburg, 1994), p. 127.
[10] G. S. Papavassiliou and I. B. Koutselas, Synth. Met. **71**, 1713 (1995).
[11] H. F. Folkerts, J. Zuidema, and G. Blasse, Solid State Commun. **99**, 655 (1996).
[12] A. I. Ekimov, Al. L. Efros, and A. A. Onushenko, Solid State Commun. **56**, 921 (1985).
[13] M. P. A. Müller, U. Lembke, U. Woggon, and I. Rückmann, J. Non-Cryst. Solids **144**, 240 (1992).
[14] M. Schlüter, M. L. Cohen, S. E. Kehn, and C. Y. Fong, Phys. Solid State **73**, 737 (1976).
[15] K. Watanabe, S. Takeyama, N. Miura, T. Komatsu, T. Higashimura, and T. Iida, Phys. Rev. B **49**, 7363 (1994).
[16] T. Komatsu, T. Iida, K. Murayama, M. Ishida, H. Kurisu, H. Kondo, I. Akai, and T. Karasawa, Mol. Cryst. Liq. Cryst. **37**, 218 (1992).
[17] T. Komatsu, D. Kim, T. Kobayashi, K. Watanabe, V. F. Aguekian, T. Karasawa, I. Akai, and T. Iida, Surf. Rev. Lett. **3**, 1127 (1996).
[18] E. Doni, G. Grosso, G. Harbeke, E. Meier, and E. Tosatti, Phys. Status Solidi B **68**, 569 (1975).
[19] Z. K. Tang, Y. Nozue, and T. Goto, J. Phys. Soc. Jpn. **60**, 2090 (1991).
[20] C. J. Sandroff, D. M. Hwang, and V. M. Chung, Phys. Rev. B **33**, 5953 (1986).
[21] T. Goto, S. Saito, and M. Tanaka, Solid State Commun. **80**, 331 (1991).
[22] T. Goto, M. Tanaka, M. Y. Chen, S. Sasaki, and N. Miura, Solid State Commun. **97**, 587 (1996).
[23] V. F. Agekyan and A. Yu. Serov, Fiz. Tverd. Tela (St. Petersburg) **38**, 122 (1996) [Phys. Solid State **38**, 65 (1996)].
[24] E. Lifshitz, M. Yassen, L. Bykov, and I. Dag, J. Lumin. **70**, 421 (1996).
[25] A. D'Andrea and R. Del Sole, Solid State Commun. **74**, 1121 (1990).
[26] A. Grisel and Ph. Schmid, Phys. Status Solidi B **78**, 587 (1976).
[27] W. M. Sears, M. L. Klein, and J. A. Morrison, Phys. Rev. B **19**, 2305 (1979).

Translated by G. Skrebtsov

High-frequency conductivity of an asymmetric superlattice

G. M. Shmelev, N. A. Soina, and I. I. Maglevannyĭ

Volgograd State Pedagogical University, 400013 Volgograd, Russia
(Submitted February 25, 1998)
Fiz. Tverd. Tela (St. Petersburg) **40**, 1731–1733 (September 1998)

The features of high-frequency currents in superlattices lacking a center of symmetry are established theoretically. It is assumed that the asymmetry shows up in intraband electron-scattering processes. Self-induced transparency is found to be possible. In a high-frequency field the current has a dc component with a nonmonotonic dependence on the field amplitude. © *1998 American Institute of Physics.* [S1063-7834(98)03509-6]

In this paper we present the results of a calculation of the current in a one-dimensional asymmetric superlattice located in a monochromatic high-frequency field parallel to the axis of the superlattice. Examples of crystals having asymmetric superlattices include artificially grown heterostructures,[1–3] ferroelectric materials with incommensurate phases, and polytypes of SiC. In a paper[4] on plasmons in superlattices with periodic defects, a review has been given of a number of studies of superlattices lacking inversion centers. In another paper,[5] the photogalvanic current[6,7] arising during optical transitions between minibands was calculated for the first time for superlattices lacking an inversion center.

Here we use a simple, but exactly soluble model to establish the features of the high-frequency current in an asymmetric superlattice, assuming that the superlattice has a polar axis directed along its (X) axis and that an asymmetry shows up in intraband electron-scattering processes.

In the single-miniband approximation the electron-dispersion relation has the form[2]

$$\varepsilon(\mathbf{p})=\frac{p_\perp^2}{2m}+\Delta\left(1-\cos\frac{p_x d}{\hbar}\right), \tag{1}$$

where 2Δ is the with of the miniband, m is the effective mass in the plane of the superlattice layers, d is the period of the superlattice, and p_x and $p_\perp$ are the components of the quasimomentum parallel and perpendicular to the axis of the superlattice, with $-\pi\hbar/d\leqslant p_x\leqslant\pi\hbar/d$ and $0\leqslant p_\perp^2\leqslant\infty$.

We shall calculate the current density ($\mathbf{j}(t)=\{j(t),0,0\}$) in the field $\mathbf{E}(t)=\{E\cos\omega t,0,0\}$ in the quasiclassical limit ($2\Delta\gg\hbar/\tau_0$, eEd and τ_0 is the characteristic relaxation time) and use the Boltzmann kinetic equation with a collision integral in the τ approximation,

$$\frac{\partial f(\mathbf{p},t)}{\partial t}+e\mathbf{E}(t)\,\frac{\partial f(\mathbf{p},t)}{\partial\mathbf{p}}=\frac{f_0(\mathbf{p})-f(\mathbf{p},t)}{\tau(\mathbf{p})}, \tag{2}$$

where f_0 and f are the equilibrium and nonequilibrium distribution functions, while $\tau(\mathbf{p})$ is the relaxation time, which depends on the direction of the electron momentum.[8]

Beginning with Esaki and Tsu.[9] most of the many studies of the electrical properties of superlattices have been done in the approximation $\tau(\mathbf{p})=\text{const}$.[2,10] Convincing arguments in favor of this approximation have been given by Ignatov and Romanov.[11] We note also the paper of Grahn *et al.*,[12] in which it was found experimentally that in a symmetric GaAs/AlAs superlattice at temperatures above 40 K, $\tau=\tau_0=\text{const}$. In the case of an asymmetric superlattice, we assume that $\tau^{-1}(\mathbf{p})$ depends weakly on the electron velocity $\mathbf{v}(\mathbf{p})$. Then, on expanding $\tau^{-1}(\mathbf{v})$ in a power series in $\mathbf{v}$ and limit ourselves to the linear approximation, we have

$$\frac{1}{\tau(\mathbf{p})}=\frac{1}{\tau_0}+\frac{e_x}{\lambda}\,v_x(\mathbf{p}). \tag{3}$$

Here $e_x=\pm1$, $\mathbf{e}$ is the unit vector of the polar axis, $\lambda=\text{const}$ has the dimensions of length, and $v_x=\partial\varepsilon(\mathbf{p})/\partial p_x$ is the electron velocity along the X axis.

A possible microscopic interpretation of the proposed model (3) follows. The first term in Eq. (3) corresponds to scattering of electrons by neutral impurities and the second, to scattering by acoustic phonons (in materials with a center of inversion, the frequency of collisions with acoustic phonons is $\propto|\mathbf{v}|$). Here it must be assumed that there are no charged impurities, i.e., these impurities are not ionized because of the low temperature or because they are mutually compensated.

Given Eq. (1), we rewrite Eq. (3) in the form

$$\frac{1}{\tau(\mathbf{p})}=\frac{1}{\tau_0}\left(1+b\,\sin\frac{p_x d}{\hbar}\right),\quad b=\frac{v_0\tau_0}{\lambda}. \tag{4}$$

Here $v_0=\Delta d/\hbar$ is the maximum electron velocity in the band, while λ has the significance of a characteristic mean-free path with respect to asymmetric scatterers. In this case, b serves as an asymmetry parameter (for certainty, we wrote a ''+'' sign in Eq. (4)). We assume in the following that the asymmetry is small, i.e., $b\ll1$.

The solution of Eq. (2) (with the initial condition $f(\mathbf{p},-\infty)=f_0(\mathbf{p})$) for $t\gg\tau_0$ in a linear approximation in b has the form

$$f(\mathbf{p},t)=f^{(0)}(\mathbf{p},t)+bf^{(1)}(\mathbf{p},t). \tag{5}$$

Here the function

$$f^{(0)}(\mathbf{p},t)=\int_{-\infty}^{t}\exp\left(\frac{t_1-t}{\tau_0}\right)f_0(\mathbf{p}(t,t_1))\,\frac{dt}{\tau_0}, \tag{6}$$

where

 © 1998 American Institute of Physics

$$\mathbf{p}(t,t_1)=\mathbf{p}-e\int_{t_1}^{t}\mathbf{E}(t_2)dt_2, \tag{7}$$

is a solution of the equation

$$\frac{\partial f^{(0)}(\mathbf{p},t)}{\partial t}+e\mathbf{E}(t)\,\frac{\partial f^{(0)}(\mathbf{p},t)}{\partial \mathbf{p}}=\frac{f_0(\mathbf{p})-f^{(0)}(\mathbf{p},t)}{\tau_0}, \tag{8}$$

while the function

$$f^{(1)}(\mathbf{p},t)=\int_{-\infty}^{t}\exp\left(\frac{t_1-t}{\tau_0}\right)\sin\left(\frac{p_x(t,t_1)d}{\hbar}\right)\left[f_0(\mathbf{p}(t,t_1))-\int_{-\infty}^{t_1}f_0(\mathbf{p}(t,t_3))\,\frac{dt_3}{\tau_0}\right]\frac{dt_1}{\tau_0} \tag{9}$$

satisfies the equation

$$\frac{\partial f^{(1)}(\mathbf{p},t)}{\partial t}+e\mathbf{E}(t)\,\frac{\partial f^{(1)}(\mathbf{p},t)}{\partial \mathbf{p}}=\frac{f_0(\mathbf{p})-f^{(0)}(\mathbf{p},t)}{\tau_0}\sin\frac{p_x d}{\hbar}-\frac{f^{(1)}(\mathbf{p},t)}{\tau_0}. \tag{10}$$

For $\omega\tau_0\gg 1$ this distribution function satisfies the condition

$$\sum_{\mathbf{p}} f(\mathbf{p},t)=n\left(1+bO\left(\frac{1}{\omega\tau_0}\right)\right). \tag{11}$$

Here $n=\Sigma_{\mathbf{p}}f_0(\mathbf{p})=\Sigma_{\mathbf{p}}f^{(0)}(\mathbf{p},t)$ is the carrier concentration in the band.

The current density is found by substituting Eqs. (5), (6), and (9) in the definition

$$j(t)=\sum_{\mathbf{p}} v_x(p_x)f(\mathbf{p},t). \tag{12}$$

As a result, for $\omega\tau_0\gg 1$, we have

$$j(t)=j_0J_0(a)\left[C_1\,\sin(a\sin\omega t)-\frac{bC_2}{2}\,(1-J_0(2a))\cos(a\sin\omega t)\right], \tag{13}$$

where $j_0=ev_0n$, $a=eEd/\hbar\omega$, and $J_0(a)$ is the Bessel function, while

$$C_k=\left\langle\cos\frac{kp_sd}{\hbar}\right\rangle. \tag{14}$$

Here the angle brackets denote averaging over the equilibrium charge-carrier distribution.

For $b=0$, Eq. (13) yields the result of Ignatov and Romanov[13] for a high-frequency current in a symmetric superlattice. Note that, in this approximation, $j(t)$ does not contain the dissipative component proportional to $\cos\omega t$. Here the odd harmonics are $\propto\sin(2k-1)\omega t$, while the even harmonics are $\propto\cos 2k\omega t$, where $k=1,2,3,\ldots$. It also follows from Eq. (13) that, if the parameter a coincides with the roots of the zeroth-order Bessel function, then the conduction current equals zero to within $(\omega\tau_0)^{-1}$, i.e., an asymmetric superlattice (as does a symmetric one under the same conditions) behaves as a linear dielectric. Thus, in this case, self-induced transparency occurs. The physical reason for this has been discussed in detail elsewhere.[14]

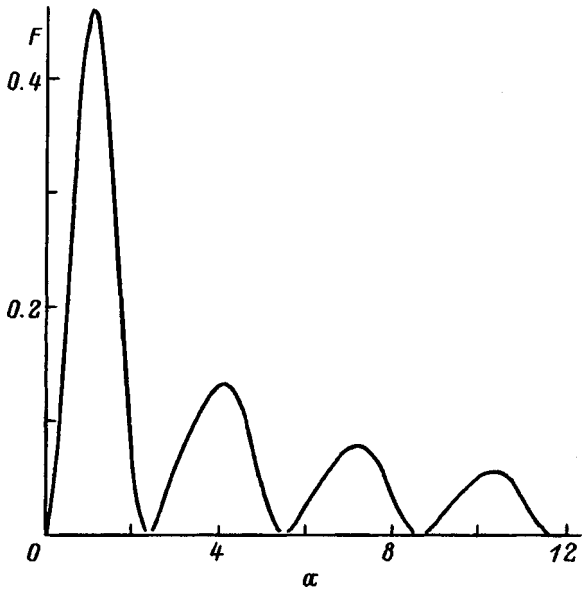

FIG. 1. F as a function of the parameter a.

The significant feature of the current $j(t)$ is that it has a dc component

$$j_c(a)=-\frac{1}{2}\,bj_0C_2F(a), \tag{15}$$

where

$$F(a)=J_0^2(a)(1-J_0(2a)). \tag{16}$$

Figure 1 shows a plot of the function $F(a)$. Note that, for $a\ll 1$, $j_c\approx -j_0C_2a^2/2$.

We emphasize that $j_c(a)$ is a nonmonotonic function of the parameter a and that $j_c(a)$ goes to zero at the points where self induced transparency occurs.

The appearance of a dc component in $j(t)$ appears to be related to the absence of a center of symmetry in the superlattice. This effect ($j_c(a)\neq 0$) must be attributed to the so-called dc-effect (optical rectification).[7]

For the optimum value $a=1$, we have $E\approx 6\times 10^3$ V/cm (for $d=10^{-6}$ cm and $\omega=10^{13}$ s^{-1}), which indicates that the conclusions drawn here are realistic and that they can be used in electronic devices.

We thank É. M. Épshteĭn for useful discussions.

This work was supported by the Russian Fund for Fundamental Research (Project No. 97-02-16321).

[1] F. Capasso, S. Luryi, W. T. Tsang, C. G. Bethea, and B. F. Levine, Phys. Rev. Lett. **51**, 2318 (1983).
[2] A. P. Silin, Usp. Fiz. Nauk **147**, 485 (1985).
[3] B. Uslu and S. Erkoc, Solid State Commun. **68**, 277 (1988).
[4] H. L. Cui and G. Gumbs, Phys. Rev. B **42**, 7015 (1990).
[5] E. L. Ivchenko and G. E. Pikus, in *Abstracts of Talks at the 12th Conference on Semiconductor Theory* [in Russian], Kiev (1985), 283 pp.
[6] V. I. Belinicher and B. I. Sturman, Usp. Fiz. Nauk **130**, 415 (1980).
[7] E. L. Ivchenko and G. E. Pikus, in *Problems of Modern Physics (A Col-*

lection of Papers in Memory of A. F. Ioffe) [in Russian], Nauka, Leningrad (1980), pp. 275–293.
[8] M. D. Blokh, L. I. Magarill, and M. V. Énтin, Fiz. Tekh. Poluprovodn. **12**, 249 (1978) [Sov. Phys. Semicond. **12**, 143 (1978)].
[9] L. Esaki and R. Tsu, IBM J. Res. Dev. **14**, 61 (1970).
[10] A. Ya. Shik, Fiz. Tekh. Poluprovodn. **8**, 1841 (1974) [Sov. Phys. Semicond. **8**, 1195 (1974)].
[11] A. A. Ignatov and Yu. A. Romanov, Izv. vuzov. Radiofizika **21**, 132 (1978).
[12] H. T. Grahn, K. von Klitzing, K. Ploog, and G. H. Döhler, Phys. Rev. B **43**, 12095 (1991).
[13] A. A. Ignatov, Yu. A. Romanov, Phys. Status Solidi B **73**, 327 (1976).
[14] F. G. Bass, A. A. Bulgakov, and A. P. Tetervov, *High Frequency Properties of Semiconductors with Superlattices* [in Russian], Nauka, Moscow (1989), 288 pp.

Translated by D. H. McNeill

Donor–acceptor recombination in type-II GaAs/AlAs superlattices

K. S. Zhuravlev, A. M. Gilinskiĭ, T. S. Shamirzaev, V. V. Preobrazhenskiĭ, B. R. Semyagin, and M. A. Putyato

Institute of Semiconductor Physics, Siberian Branch of the Russian Academy of Sciences, 630090 Novosibirsk, Russia

S. S. Chipkin

Siberian State Geodetic Academy, 630108 Novosibirsk, Russia
(Submitted January 12, 1998; resubmitted March 11, 1998)
Fiz. Tverd. Tela (St. Petersburg) **40**, 1734–1739 (September 1998)

A study is reported of steady- and nonsteady-state photoluminescence of intentionally undoped and uniformly silicon-doped type-II $(GaAs)_7(AlAs)_9$ superlattices grown by MBE simultaneously on (311)*A*- and (100)-oriented GaAs substrates. It has been established that at elevated temperatures ($160 > T > 30$ K) the superlattice spectra are dominated by the line due to the donor-acceptor recombination between donors in the AlAs layers and acceptors located in the GaAs layers. The total carrier binding energy to the donor and acceptor in a pair has been determined. © *1998 American Institute of Physics.* [S1063-7834(98)03609-0]

Considerable attention is focused presently on low-dimensional structures, which are promising for development of devices having novel electronic properties.[1–3] GaAs/AlAs superlattices are among the most actively studied low-dimensional objects, and the interest in them is due to the possibility of changing their optical and transport properties by varying properly the layer thicknesses.[2–4] The changes in the properties of GaAs/AlAs superlattices are the largest for GaAs layer thicknesses below 35 Å, i.e. at the transition from a type-I to type-II superlattice.[1,5] In type-II superlattices, the carriers are localized in different layers (the holes, in GaAs, and the electrons, in AlAs), and nonequilibrium carriers recombine in optical transitions which are indirect in real space. Most of the emphasis in the investigation of type-II GaAs/AlAs superlattices was placed on the intrinsic luminescence,[6–9] while recombination through impurity and defect levels was given only scant attention.

This work studies steady- and nonsteady-state photoluminescence (PL) of type-II GaAs/AlAs superlattices at various temperatures and excitation intensities. It is shown that at elevated temperatures ($T > 30$ K) the superlattice photoluminescence spectra are dominated by the line produced in donor-acceptor pair recombination of the donors located in AlAs layers with the acceptors in the GaAs layers.

1. SAMPLES AND EXPERIMENTAL TECHNIQUE

We studied the PL of intentionally undoped and uniformly silicon-doped type-II GaAs/AlAs superlattices grown by MBE simultaneously on (311)*A*- and (100)-oriented GaAs substrates at 600 °C, with a 0.5 μm-thick GaAs buffer layer. The superlattices consisted of 100 alternating GaAs and AlAs layers of seven and nine ML thickness, respectively. The silicon concentration in the doped superlattices was $3\times10^{16}\,\mathrm{cm}^{-3}$.

Steady-state PL was excited by an Ar^+ laser operating at 488 nm. The maximum pump-power density was $320\,\mathrm{W/cm}^2$. The nonsteady-state PL was excited by a pulsed Nd-YAG laser at a wavelength of 532 nm, the pulse duration was 0.15 μs, and the peak power density, $300\,\mathrm{kW/cm}^2$. The PL spectra were measured using a SDL-1 double-grating monochromator (focal length 600 mm, spectral resolution not worse than 0.2 meV). Photoluminescence was detected by a PM tube with an S-1 photocathode, which operated in the photon counting mode. The sample was maintained at the desired temperature by means of an UTREX-R cryostat system. The temperature in the cryostat's chamber was set to within 0.3 K and maintained within 0.1 K.

2. RESULTS OF THE EXPERIMENT

Figure 1 presents steady-state PL spectra of an intentionally undoped $(GaAs)_7(AlAs)_9$ superlattice grown on a (311)*A*-oriented substrate, which were measured at different temperatures. The PL spectrum obtained at $T = 6$ K is seen to be dominated by the *X* line due to the recombination of excitons whose electron is at the *X* point in the AlAs conduction band and the hole, at the Γ maximum of the GaAs valence band, with its two replicas, *Y1* and *Y2*, also present. The *Y1* line is separated from the *X* line by 27 meV, which corresponds to the *LA* phonon energy in GaAs and AlAs, and line *Y2* is at a distance of 49 meV from the *X* line, which is the *LO* phonon energy in AlAs.[6] While the PL spectra of $(GaAs)_7(AlAs)_9$ superlattices grown on (100)GaAs substrates do not differ from those grown on Ga(311)*A*, they are shifted as a whole toward higher energies because of the larger effective thickness of the layers in the superlattices obtained on (311)*A*-oriented substrates. As the temperature is increased, the intensity of the *X* line and of its phonon replicas decreases, until the latter become replaced at $T \sim 30$ K by line *D*, which is dominant in the PL spectra within the $30 < T < 160$ K interval. A similar PL line in GaAs/AlAs

 © 1998 American Institute of Physics

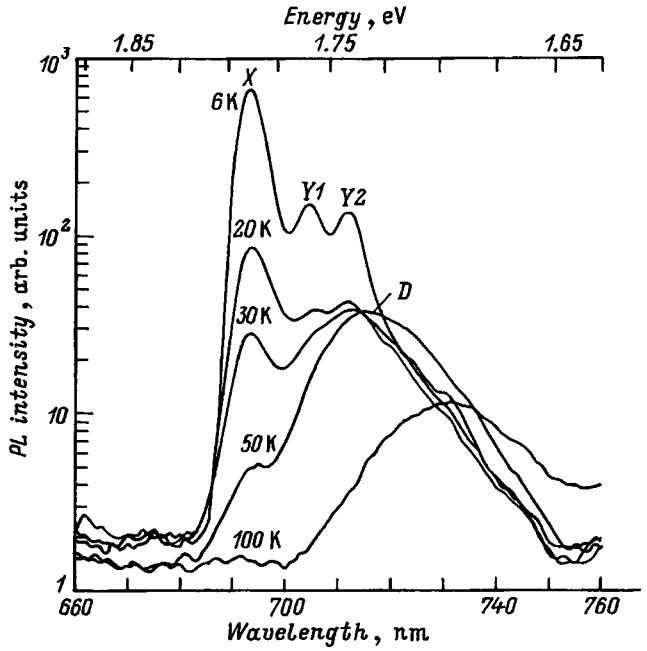

FIG. 1. PL spectra of an undoped type-II $(GaAs)_7(AlAs)_9$ superlattice grown on GaAs(311)*A* substrate, which were measured at various temperatures.

superlattices was observed earlier.[6] At higher temperatures, a high-energy $1e\text{-}hh$ line originating from recombination between quantum-confined levels in GaAs layers appears in the spectra and subsequently becomes dominant. The temperature at which this line appears depends on the gap between the electron levels in AlAs and GaAs, which, in its turn, is determined by the superlattice layer thicknesses.[5] The PL spectra of undoped superlattices grown on (100)-oriented substrates vary with temperature in a similar way. Uniform doping of superlattices with silicon does not affect the PL spectrum pattern.

Figure 2a displays characteristic temperature dependences of the integrated PL intensity of intentionally undoped $(GaAs)_7(AlAs)_9$ superlattices grown on (100) substrates. One readily sees that the PL intensity falls off exponentially with the temperature increasing from $T=6$ to 30 K, which is caused by delocalization of excitons bound to heterointerface roughness, and by their migration to nonradiative recombination centers.[10] The exciton localization energy found by fitting the relation $I=I_0/[1+A\exp\times(-E_a/kT)]$ (Ref. 10) to the experimental plot varies from one sample to another within the 1.7–4.2-meV interval, which appears not to be affected by the substrate orientation or doping. Increasing the measurement temperature from $T=30$ to 60 K does not change the PL intensity for most samples, and even increases it somewhat in some of them. The latter is probably related to the specific nature of carrier trapping by nonradiative recombination centers.[11] For $T>60$ K, the PL intensity again begins to decay exponentially.

Figure 2b displays the energy position of line *D* for intentionally undoped superlattices grown on (311)*A* and (100) substrates as a function of temperature. Also shown for comparison is the temperature dependence of the GaAs gap

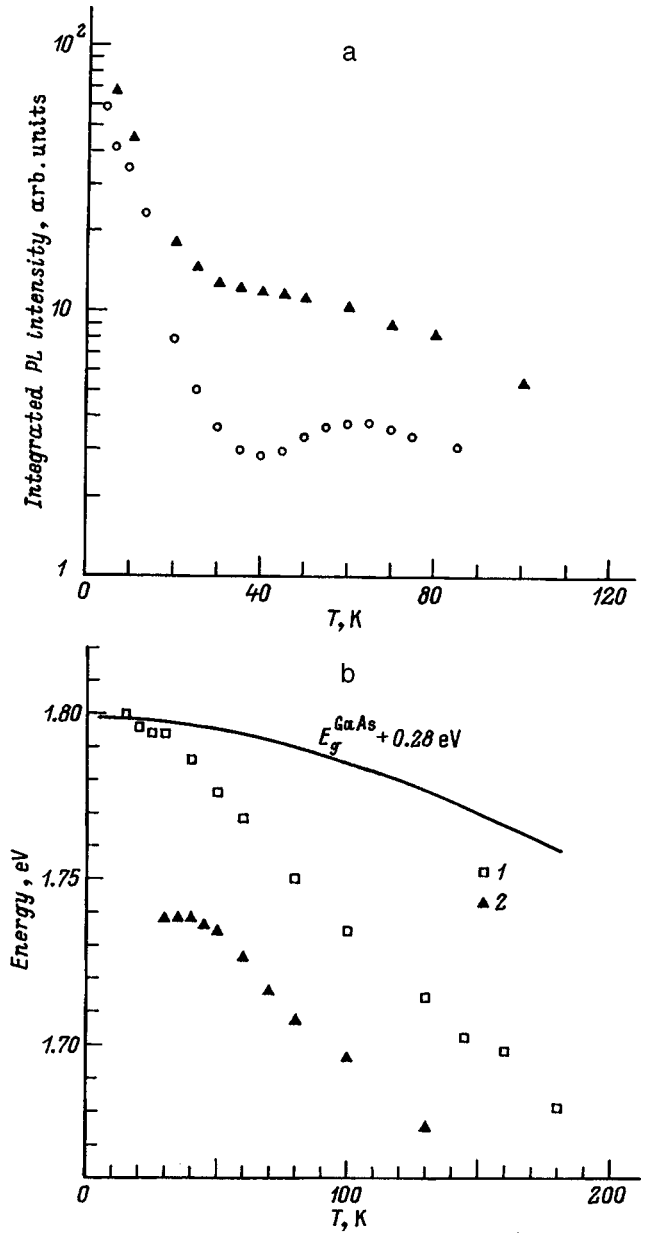

FIG. 2. (a) Integrated PL intensity of two intentionally undoped type-II $(GaAs)_7(AlAs)_9$ superlattices grown on (100)-oriented substrates vs temperature. (b) Energy position of line *D* in the PL spectra of intentionally undoped type-II $(GaAs)_7(AlAs)_9$ superlattices vs temperature. The squares and triangles relate to the superlattices grown on (100)- and (311)*A*-oriented substrates, respectively. The solid line illustrates the temperature dependence of the bulk GaAs gap width.

width (Ref. 10). As seen from the figure, line *D* shifts toward lower energies in the spectrum with increasing temperature, and the shift occurs faster than the decrease with temperature of the GaAs gap width.

Presented in Fig. 3 are dependences of the *D* line position for intentionally undoped and doped $(GaAs)_7(AlAs)_9$ superlattices grown on (311)*A* and (100) substrates on the pump light intensity, which were measured at $T=77$ K. As seen from the figure, line *D* shifts toward lower energies with decreasing excitation intensity. Note that the line width increases in the process.

Figure 4a shows nonsteady-state PL spectra of the un-

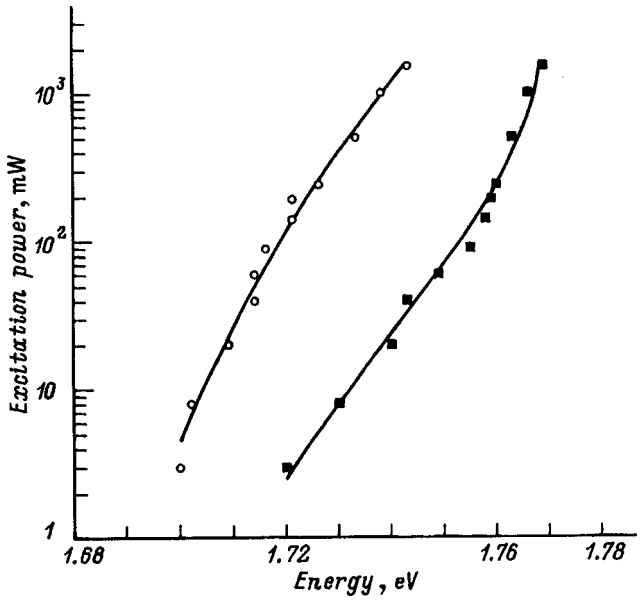

FIG. 3. Energy position of line *D* in the 77-K PL spectra of intentionally undoped and doped type-II $(GaAs)_7(AlAs)_9$ superlattices vs pump power. The squares relate to the undoped superlattice grown on a (100) substrate, and the circles, to the doped superlattice grown on a (311)*A* substrate. The solid lines show the fits.

doped superlattice grown on a (311)*A* substrate, which were taken at 45 K. It is seen that line *D* shifts toward lower energies and broadens with increasing delay after the excitation pulse. As evident from Fig. 4b, following the pulsed excitation the integrated intensity of line *D* decays rapidly during a few tens of ns. After this, the PL intensity decay rate slows down to obey the $T=(1/t)^{\gamma}$ relation. As the temperature increases, the PL intensity decay rate increases too, and the value of γ changes from 1.17 for $T=45$ K to 1.61 for $T=60$ K. The fast PL decay is probably caused by nonradiative recombination of the nonequilibrium carriers localized at quantum-confined superlattice levels, and the slow decay, to the recombination of carriers bound to the centers responsible for the *D* line.

3. DISCUSSION OF RESULTS

The above results can be interpreted by assuming that line *D* in PL spectra of type-II GaAs/AlAs superlattices is due to donor-acceptor recombination involving donors in the AlAs layers and acceptors localized in the GaAs layers.

Donor-acceptor recombination was studied in considerable detail in bulk semiconductors, and it has been established that recombination in spaced donor-acceptor pairs produces a PL line whose position and shape depend on the actual experimental conditions. This line shifts toward lower energies with increasing temperature, decreasing pump-light intensity, and increasing delay time following the excitation pulse.[11–14] The line shift depends on the carrier binding energy to impurities and grows with binding energy.[11,13] Besides, it was established that donor–acceptor recombination follows the kinetics described by the $I\sim 1/t$ law and becoming faster with increasing temperature.[15] This behavior of the donor-acceptor recombination line is explained by the dependence of the emitted photon energy $\hbar\omega$ (Refs. 11 and 13) and of the recombination probability of impurity-bound carriers W (Refs. 12,15) on the donor-acceptor separation in the pair r:

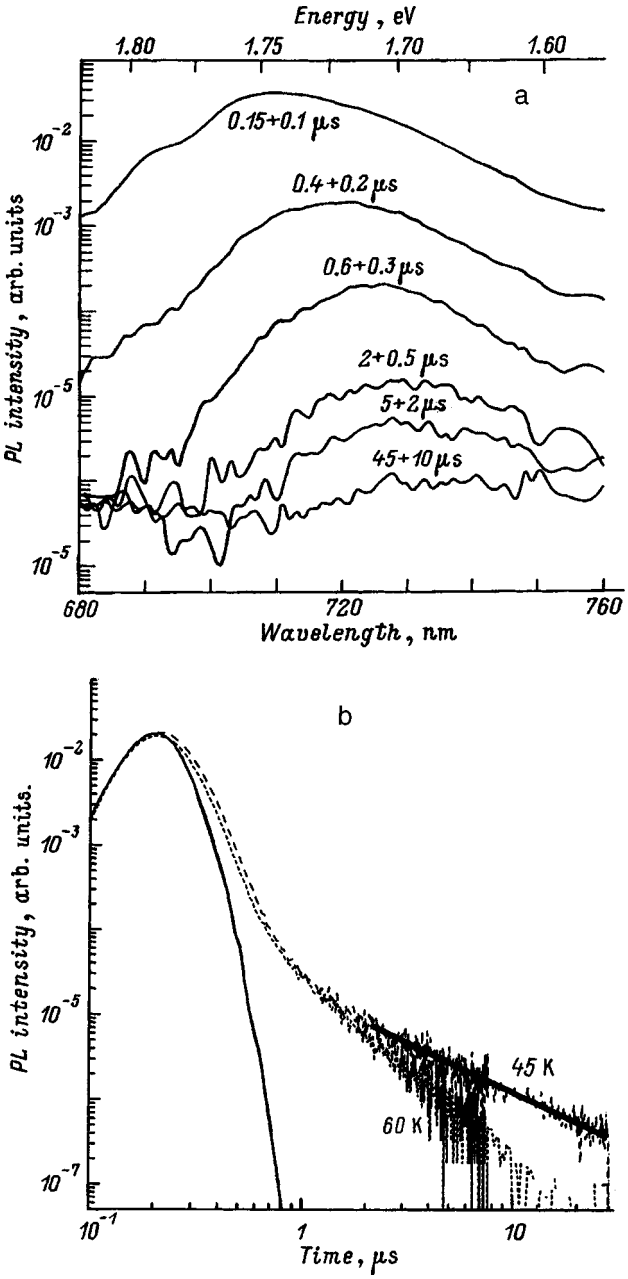

FIG. 4. (a) Nonsteady-state 45-K PL spectra of a type-II intentionally undoped $(GaAs)_7(AlAs)_9$ superlattice grown on a (311)*A*-oriented GaAs substrate. (b) Line *D* decay in a type-II intentionally undoped $(GaAs)_7(AlAs)_9$ superlattice grown on a (311)*A*-oriented GaAs substrate. The curves were measured at $T=45$ and 60 K. The thick solid line shows the fit for the experimental decay curve measured at $T=45$ K. The thin solid line shows the laser pump pulse.

$$\hbar\omega(r)=E_g-E_d-E_a+e^2/(\varepsilon r)\,, \tag{1}$$

$$W(r)=W_0\exp(-2r/R_B)\,. \tag{2}$$

Here E_g is the gap width, E_d and E_a are the binding energies of the donor- and acceptor-bound carriers, respectively, e is the electronic charge, ε is the dielectric permittivity of the medium, R_B is the Bohr radius of the carrier at the impurity

TABLE I. Total binding energies of carriers bound to paired impurities, carrier Bohr radii for the impurity with a lower binding energy, and coefficients of proportionality for intentionally undoped and uniformly silicon-doped $(GaAs)_7(AlAs)_9$ superlattices grown on (100)- and (311)*A*-oriented GaAs substrates.

Sample	GaAs substrate orientation	E_d+E_a, meV	R_B, Å	K
Undoped	(100)	198±10	5.2±0.3	$(2.8\pm0.4)\times10^4$
Undoped	(311)*A*	196±10	4.9±0.3	$(2.6\pm0.3)\times10^4$
Doped	(311)*A*	174±10	4.6±0.5	$(4.8\pm2.0)\times10^6$

with a lower binding energy, W_0 is a constant related to the probability of recombination for $r\to0$ and characteristic of donors and acceptors of a particular type in a given semiconductor.

The *D* line observed in spectra of type-II GaAs/AlAs superlattices exhibits all the features specific for donor-acceptor recombination; apart from this, we do not believe that other models (impurity-band or intracenter recombination) can account for the totality of the available experimental data.

The fairly large shift of the line induced by a change in experimental conditions compared to that of the line produced by donor-acceptor recombination in GaAs layers[14] is apparently due to the higher binding energy of the carriers localized at impurities in the superlattice layers, primarily at donors in the AlAs layers. Besides, in superlattices the line shift increases compared to the bulk material because the impurities making up the closest pairs in superlattices are located near heteroboundaries and have a lower binding energy than the more distant impurities residing in central regions of the layers.

To determine the binding energies of the carriers at the impurities making up donor-acceptor pairs, the experimental dependence of the position of line *D* at 77 K on pump intensity was fitted by a theoretical relation[16]

$$J=K\{[\hbar\omega_m-E_g+(E_d+E_a)]^3/[2(E_g-(E_d+E_a)-\hbar\omega_m)+e^2/(\varepsilon R_B)]\}\times\exp\{-2e^2/(\varepsilon R_B)/[\hbar\omega_m-E_g+(E_d+E_a)]\}, \quad (3)$$

where $\hbar\omega_m$ is the position of the maximum of the donor-acceptor recombination line, ε is the dielectric permittivity of the medium accepted equal to 11.3, and K is the coefficient of proportionality. For the gap width E_g was taken the distance between the first quantum-confined electronic level in the AlAs layer and the first heavy-hole level in the GaAs level, which is the sum of the energy of the photon emitted in the exciton annihilation at $T=6$ K and of the exciton binding energy, which was assumed[17] to be 13 meV; one took also into account the decrease of the GaAs and AlAs gap widths with temperature, which is approximately the same, 9 meV at $T=77$ K (Ref. 18).

The total carrier binding energy at the pair-component impurities are listed in Table I for intentionally undoped and uniformly silicon-doped $(GaAs)_7(AlAs)_9$ superlattices grown on (100)- and (311)*A*-oriented GaAs substrates. It should be pointed out that the values of the Bohr radius presented in Table I are nothing more than a fitting parameter, because this concept can be applied to impurity-bound carriers in superlattices only with certain reservations.

The data given in Table I can be used to derive the energy position of the donor levels in AlAs layers grown on (100)GaAs substrates. The binding energies of holes bound to shallow acceptors in single GaAs/AlAs quantum wells of various thicknesses which were grown on (100)GaAs substrates were determined experimentally and theoretically[19] to be 57 and 42 meV in a $d=21$-Å thick quantum well for acceptors located at the well center and close to the heteroboundaries, respectively. Reducing the barrier thickness between quantum wells to ≈30 Å (in the superlattices studied here the barrier thickness was set to 27 Å by the growth conditions) affects only weakly the hole-to-acceptor binding energy.[20] It should be pointed out that for a quantum well ≈20 Å thick, the binding energy of holes localized at acceptors depends strongly on its thickness; indeed, a change of the quantum-well thickness by one monolayer (≈3 Å) changes the binding energy by ±7 meV.[19] Assuming the main contribution to the donor–acceptor recombination spectrum of superlattices to be due to transitions involving acceptors in the central region of a quantum well, the binding energy of donor-bound electrons in intentionally undoped superlattices will be 140 ± 10 meV, and that for silicon-doped ones, 115 ± 10 meV.

In the AlAs layers of silicon-doped superlattices, silicon at arsenic sites acts as a donor, and, hence, the value we have obtained corresponds to the binding energy of electrons to silicon in the AlAs layer. In intentionally undoped superlattices, the donors in AlAs layers can be atoms of sulfur, selenium, tellurium, and silicon;[21] obviously enough, the above electron–donor binding energies relate to a Group VI element in the Periodic Table. The available information on the electron-donor binding energies in AlAs layers is scarce. It is known to be more than twice that calculated in the effective-mass approximation, and for silicon $E_d(\mathrm{Si})=83$ meV.[21] It is also known that the binding energies of electrons to the S, Se, and Te donors in $Al_{0.6}Ga_{0.4}As$ solid-solution layers exceed by about 20 meV that of electrons to silicon, and are $E_d(\mathrm{S})=94$ meV, $E_d(\mathrm{Se})=95$ meV, and $E_d(\mathrm{Te})=91.5$ meV (Ref. 21); the electron-sulfur binding energy in $Al_{0.75}Ga_{0.25}As$ layers was found to be $E_d(\mathrm{S})=95\pm9$ meV (Ref. 21). The binding energies of electrons to donors in AlAs layers measured by us are seen to be in excess of the available literature data, which is possibly due to the donor-bound carrier energy being influenced by the superlattice confining potential.

To conclude, we have studied PL of MBE-grown type-II

$(GaAs)_7(AlAs)_9$ superlattices. It has been established that at elevated temperatures ($160 > T > 30$ K) the superlattice spectra are dominated by the line due to the transitions between donors located in the AlAs layers and acceptors residing in the GaAs layers. The total binding energy of carriers bound to donors and acceptors in a pair has been determined. No effect of substrate orientation on the binding energy of donor- and acceptor-bound carriers in a pair has been found within experimental accuracy.

The authors express their gratitude to D. A. Petrakov for assistance in data treatment.

Support of the Russian Fund for Fundamental Research (Grant 95-02-04755) is gratefully acknowledged.

[1] M. A. Herman, *Semiconductor Superlattices* [Akademie-Verlag, Berlin, 1986; Mir, Moscow, 1989, 240 pp.].
[2] K. Ploog and G. H. Dohler, Adv. Phys. **32**, 285 (1983).
[3] A. P. Silin, Usp. Fiz. Nauk **147**, 485 (1985) [*sic*].
[4] B. A. Joyce, J. N. Neave, J. Zhang, D. D. Vvedensky, S. Clarke, K. J. Hugill, T. Shitara, and A. K. Myers-Beaghton, Semicond. Sci. Technol. **5**, 1147 (1990).
[5] D. Scalbert, J. Cernogora, C. Benoit à la Guillaume, M. Maaref, F. F. Charfi, and R. Planel, Solid State Commun. **70**, 945 (1989).
[6] I. L. Spain, M. S. Skolnick, G. W. Smith, M. K. Saker, and C. R. Whitehouse, Phys. Rev. B **43**, 14091 (1991).
[7] R. Cingolani, L. Baldassarre, M. Ferrara, M. Lugarà, and K. Ploog, Phys. Rev. B **40**, 6101 (1989).
[8] R. Cingolani, M. Holtz, R. Muralidharan, K. Ploog, K. Reimann, and K. Syassen, Surf. Sci. **228**, 217 (1990).
[9] E. Finkman, M. D. Sturge, and M. C. Tamargo, Appl. Phys. Lett. **49**, 1299 (1986).
[10] A. Chiari, M. Colocci, F. Fermi, Y. Li, R. Querzoli, A. Vinattieri, and W. Zhuang, Phys. Status Solidi B **147**, 421 (1988).
[11] G. P. Peka, V. F. Kovalenko, and V. N. Kutsenko, *Luminescent Techniques for Monitoring the Parameters of Semiconducting Materials and Devices* [in Russian], Tekhnika, Kiev, 1986.
[12] A. A. Bergh and P. J. Dean, *Lightemitting Diodes* [Oxford, 1979; Mir, Moscow, 1979, 690 pp.].
[13] J. I. Pankove, *Optical Processes in Semiconductors* (Mir, Moscow, 1973), 458 pp.
[14] P. J. Dean, in Progress in Solid-State Chemistry, Vol. 8 (Pergamon Press, New York, 1973).
[15] D. G. Thomas, J. J. Hopfield, and W. M. Augustyniak, Phys. Rev. **140**, A202 (1966).
[16] E. Zacks and A. Halperin, Phys. Rev. B **6**, 3072 (1972).
[17] K. J. Moore, G. Duggan, P. Dawson, and C. T. Foxon, Superlattices Microstruct. **5**, 481 (1989).
[18] M. Nakayama, I. Tanaka, I. Kimura, and H. Nishimura, Jpn. J. Appl. Phys. **29**, 41 (1990).
[19] W. T. Masselink, Y.-C. Chang, H. Morkoç, D. C. Reynolds, C. W. Litton, K. K. Bajaj, and P. W. Yu, Solid-State Electron. **29**, 205 (1986).
[20] G. T. Einevoll and Y.-C. Chang, Phys. Rev. B **41**, 1447 (1990).
[21] L. Pavesi and M. Guzzi, J. Appl. Phys. **75**, 4779 (1994).

Translated by G. Skrebtsov

Linear coefficients of photoelasticity in multilayer quantum well structures having a sloping bottom in exciton resonance regions

R. A. Ayukhanov and G. N. Shkerdin

Institute of Radio Technology and Electronics, Russian Academy of Sciences, 141120 Fryazino, Moscow Region, Moscow

(Submitted March 24, 1998)
Fiz. Tverd. Tela (St. Petersburg) **40**, 1740–1744 (September 1998)

An analytic expression is obtained for the linear coefficients of photoelasticity in multilayer quantum-well structures having a sloping bottom in the region of the fundamental exciton resonance. The coefficients of photoelasticity are calculated for a $GaAs/Al_{0.28}Ga_{0.72}As$ superlattice at the long-wavelength edge of the exciton ground-state resonance. It is shown that these coefficients for multilayer quantum-well structures with the sloping bottom which arises in a varizone quantum-well, are larger, and for those with a bottom slope determined by a constant electric field applied to the multilayer quantum-well structure, are lower than the same quantities for a superlattice with a rectangular quantum-well. The magnitude of the linear contribution of the piezoelectric field stimulated by the slope of the bottom of the quantum-well to the photoelasticity coefficient is calculated for piezoelectric superlattices and this is compared with the contribution introduced by the straining potential. © *1998 American Institute of Physics.* [S1063-7834(98)03709-5]

The photoelastic properties of multilayer quantum-well structures (MQWS) in the region of the exciton resonances have been studied and it has been shown that localization of electrons and holes in a quantum well (QW) leads to a substantial increase in the linear coefficients of photoelasticity in these structures compared to the bulk case.[1] Creating a slope in the bottom of a QW by one means or another can lead to an additional change in the extent of this localization owing to a displacement of the interacting electrons and holes over the width of the well because of the bottom slope.

On the other hand, the possible existence in a QW of excitons in a bound state for electric fields up to $\sim 50F_0$ (F_0 is the electric field strength required to ionize a bulk exciton)[2] suggests that a slope in the bottom of a QW can change the way the exciton energy levels are shifted in electric fields, and, in the case of piezoelectric MQWS, the way the exciton levels are modulated by sound waves.

Here we investigate the elastooptical properties of piezoelectric and nonpiezoelectric MQWS with a sloping bottom in the quantum wells near the exciton ground state resonance.

It is known that, in order to calculate the coefficients of photoelasticity, one must know the wave functions and energy levels of the excitons in the quantum well, i.e., the slope of the bottom of the QW must be taken into account. Upon solving this problem in the approximation of an infinitely deep well,[1)] we can see two cases where the coefficient of photoelasticity behaves differently: when the slopes of the bottoms of quantum wells for electrons and holes are of opposite sign and when they have the same sign (Fig. 1).

Quantum wells for electrons and holes with different bottom slopes can be created[4] by varying the composition of the layer forming the quantum wells in a MQWS. This leads to a spatial dependence of the band gap width and, in general, to different (including signs) slopes. In the particular case of a GaAs/AlGaAs system (this type of MQWS will be discussed below), when Ga atoms are replaced by Al atoms in the GaAs layer during epitaxy, the signs of the slopes will be opposite and qualitatively related to one another as follows: $A_e = -A_h \cdot 0.85/0.15$, where A_e is the slope of the bottom of an electron QW and A_h is the slope of a hole QW.[5] We shall refer to this case as a slope generated in a varizone QW.

Evidently, equal slopes ($A_e = A_h$) occur in the rather well studied case of a QW located in a constant electric field,[2,6,7] i.e., in the case of a slope at the bottom of the QW determined by the electric field. We shall analyze these two cases below.

We shall consider a linear inclination over the width of the QW (i.e., along the coordinate z perpendicular to the layers of the MQWS). The energy at the bottom of a QW of width L_z bounded by infinite barriers at $z = -L_z/2$ and $z = L_z/2$ is given by $E = A_{e,h}(z + L_z/2)$ for electron and hole wells, respectively. In the case of the incline in a varizone QW, $A_{e,h} = eF_{e,h}$, where e is the electronic charge and $F_{e,h}$ are the imbedded electric fields,[4] which are generally different for electron and hole quantum wells. In the case of an incline determined by an electric field, $F_e = F_h = F$ are the strengths of the actual electric fields which are applied equally to electron and hole quantum wells, and the problem in this case reduces to determining the exciton wave functions and energy levels when an electric field F is applied to the MQWS.[2)2,6,7] A generalization of the method to the case of an arbitrary slope at the bottom of the QW, independently of the magnitude of and reason for the slope, makes it possible to write the hamiltonian for an exciton in a quantum well with an inclined bottom in the following form:

 © 1998 American Institute of Physics

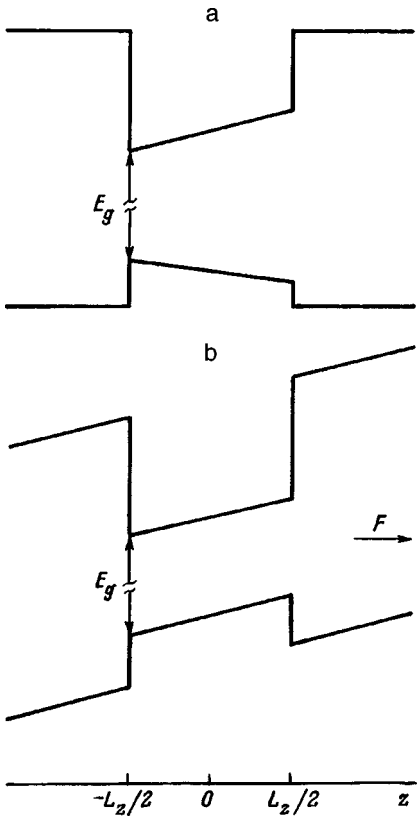

FIG. 1. The form of quantum wells with an inclined energy bottom in the case of the inclines in a varizone quantum well (a) and created by a constant electric field (b).

$$H=-\frac{\hbar^2}{2m_{e\perp}^*}\nabla_{z_e}^2+A_e\left(z_e+\frac{L_z}{2}\right)-\frac{\hbar^2}{2m_{h\perp}^*}\nabla_{z_h}^2-A_h\left(z_h+\frac{L_z}{2}\right)-\frac{\hbar^2}{2\mu_\parallel}(\nabla_x^2+\nabla_y^2)-\frac{e^2}{\varepsilon_0\sqrt{\rho^2+(z_e+z_h)^2}},\quad \rho=\sqrt{x^2+y^2}. \tag{1}$$

Here the first and second terms describe the one-dimensional state of an electron with coordinate z_e in a QW with an energy slope A_e at the bottom, the third and fourth terms, the same state for a hole with coordinate z_h and bottom slope A_h, the fifth, the kinetic energy of a noninteracting electron and hole in the XY plane, and the sixth, the potential energy of an interacting electron at $(0,0,z_e)$ and hole at (x,y,z_h), $m_{e\perp}^*$ and $m_{h\perp}^*$ are the effective electron and hole masses in a direction perpendicular to the layers of the MQWS, $\mu_\parallel$ is the reduced mass in a direction parallel to the layers, ε_0 is the stationary dielectric permittivity of the layer forming the QW (it is assumed that in the barrier layers the stationary dielectric permittivity also equals ε_0), and $\hbar$ is Planck's constant.

For the case in which the binding energy of an exciton under size-quantization conditions in a QW exceeds the same quantity in the bulk crystal (which, as the calculation shows, occurs in a GaAs/AlGaAs system for $L_z<200$ Å), a solution to the Schrödinger equation with the hamiltonian (1) is chosen in the form of the following trial function:

$$\Psi=\frac{2}{\lambda}\left[\frac{\beta_e(\beta_e^2+4\pi^2)}{2\pi^2L_z(1-e^{-\beta_e})}\right]^{1/2}\left[\frac{\beta_h(\beta_h^2+4\pi^2)}{2\pi^2L_z(1-e^{-\beta_h})}\right]^{1/2}\times\cos\frac{\pi z_e}{L_z}\cos\frac{\pi z_h}{L_z}\exp\left(-\frac{\rho}{\lambda}\right)\times\exp\left(-\frac{\beta_e}{2}\left[\frac{z_e}{\pi}+\frac{1}{2}\right]\right)\exp\left(-\frac{\beta_h}{2}\left[\pm\frac{z_h}{\pi}+\frac{1}{2}\right]\right), \tag{2}$$

where the upper sign in the second exponential corresponds to the slope in a varizone QW and the lower, to the slope created by an electric field, and β_e and β_h are variational parameters determined by solving the Schrödinger equation for a free electron and a free hole in the corresponding QW with an inclined bottom by a variational method analogous to that developed in Ref. 6, where the effect of an electric field on a free particle in a QW was examined in detail. The average values of the ground-state energy for free electrons and holes were also determined numerically by substituting β_e and β_h in the corresponding expressions for the energies E_{1e} and E_{1h} obtained by solving the Schrödinger equation including the first two and the third-fourth terms of Eq. (1), respectively. λ is a variational parameter which is determined by solving a Schrödinger equation in which the hamiltonian is the fifth and sixth terms of Eq. (1). The expression obtained for the average energy of the exciton ground state relative to the bottom of the conduction band when the slope of the bottom of the QW is taken into account can be written in the form

$$E_{\rm ex}=\frac{\hbar^2}{2\mu_\parallel\lambda^2}-\frac{e^2}{\varepsilon_0\lambda^2}\frac{\beta_e(\beta_e^2+4\pi^2)}{\pi^2(1-e^{-\beta_e})}\frac{\beta_h(\beta_h^2+4\pi^2)}{\pi^2(1-e^{-\beta_h})}\frac{1}{\pi^2}\times\int_{-\pi/2}^{\pi/2}\int_{-\pi/2}^{\pi/2}\int_0^\infty d\rho dz_e dz_h\times\frac{\rho\exp\left(-\frac{2\rho}{\lambda}\right)\cos^2 z_e\cos^2 z_h}{\sqrt{\rho^2+(L_z^2/\pi^2)(z_e-z_h)^2}}\times\exp\left(-\beta_e\left[\frac{z_e}{\pi}+\frac{1}{2}\right]\right)\exp\left(-\beta_h\left[\pm\frac{z_h}{\pi}+\frac{1}{2}\right]\right) \tag{3}$$

and is determined numerically. (The upper sign in the exponent in the integral is for the slope in a varizone QW and the lower, for the slope in an electric field.)

The calculated $E_{\rm ex}$ and λ are plotted in Fig. 2 as functions of the quantum-well width for an incline in a varizone QW $(E_{\rm ex}^v,\lambda_v)$ and for an incline determined by an electric field $(E_{\rm ex}^e,\lambda_e)$. Also shown here are more accurate data for these quantities in the case of a simple (rectangular) well $(E_{\rm ex}^p,\lambda_p)$. For a given width of the quantum well, the relationships between these quantities are $E_{\rm ex}^v>E_{\rm ex}^p>E_{\rm ex}^e$ and $\lambda_v<\lambda_p<\lambda_e$. $E_{\rm ex}^v$ is slightly greater than the energy of an exciton in a simple well, because of a shift of the peaks of the electron and hole wave functions toward one of the boundaries of the QW (toward $z=L_z/2$) and, ultimately, by their further localization. The smaller value of the exciton energy ($E_{\rm ex}^e$ relative to the energy in a simple well reflects the opposite situation: the electric field shifts the peaks of the

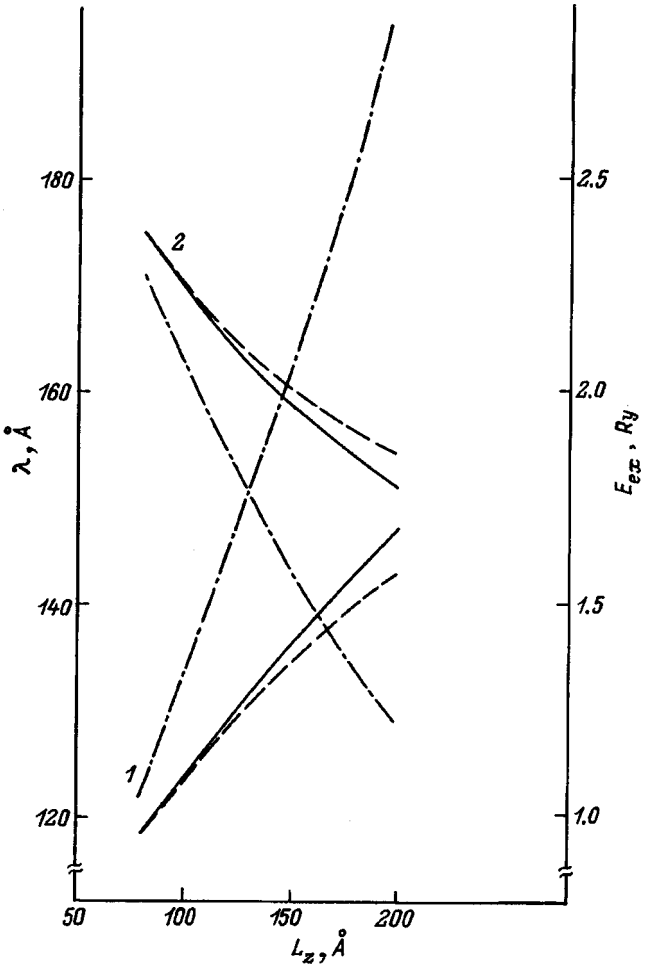

FIG. 2. The dependence of λ (the family of curves *1*) and E_{ex} (curves *2*) on the quantum-well width L_z. The dashed curves are for the incline in a varizone QW ($A_e=10^5$ eV/cm, $A_h=-1.77\cdot10^4$ eV/cm), the dot-dashed curves are for an incline created by an electric field ($A_e=A_h=10^5$ eV/cm), and the smooth curves, for a simple QW ($A_e=A_h=0$). R_y is the energy of the ground state of the bulk exciton.

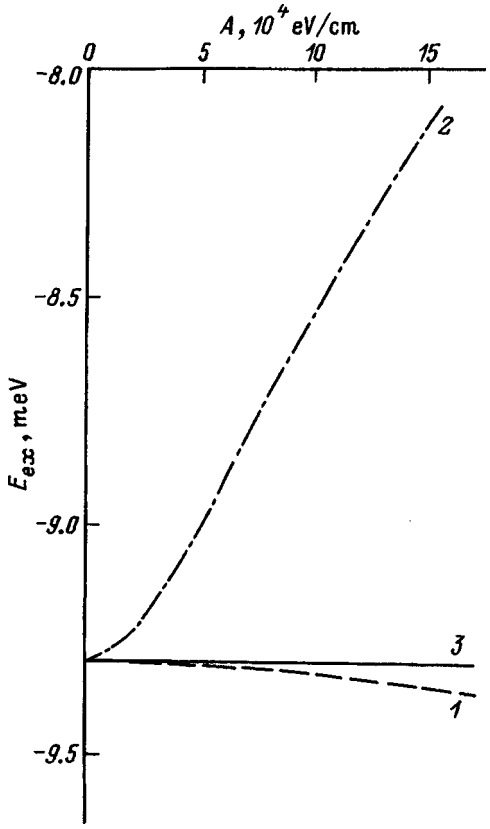

FIG. 3. The exciton ground-state energy as a function of the slope of the QW bottom ($L_z=102$ Å). (*1*) Incline in a varizone QW, (*2*) incline created by an electric field, (*3*) simple QW (shown for clarity).

electron and hole wave functions toward different boundaries (the electron toward $z=-L_z/2$ and the hole toward $z=L_z/2$), thereby weakening the effect of localizing the electron and hole in a simple QW.[7]

This sort of interpretation is also confirmed by the dependence of the exciton ground state energy on the extent of the bottom incline of the QW (Fig. 3).[3)] An increase in the slope, which enhances the degree of localization of an electron and hole along the boundary $z=-L_z/2$ for a varizone QW, raises the exciton energy. (In this case the degree of localization and, accordingly, the form of the curves for E_{ex}^{v} in Fig. 3 and for E_{ex}^{v} and λ_v in Fig. 2 depend on the relationship between A_e and A_h, which is connected to the physical and chemical properties of the varizone layer.) Increasing the incline in an electric field, on the other hand, displaces the electron and hole to opposite boundaries of the QW and, thereby, lowers it.

These major differences for the slope in a varizone QW and that determined by an electric field, which control the magnitude and behavior of the variational parameter λ in the expressions for the wave functions and exciton energies, also have an effect on the magnitude of the resonant portion of the dielectric permittivity in the presence of sound, which can be obtained, by analogy with Ref. 1, in a quasistatic, quasi-one dimensional approximation the acoustic waves,

$$\varepsilon_{ik}^{r}=-\frac{4\pi e^2 L_{ik}}{m_0^2\omega^2 L}\,\frac{2}{\pi\lambda^2}\,\frac{1}{\hbar\omega-E^r+is},$$

$$E^r=E_g^W+E_{\text{ex}},\quad E_g^W=E_g+E_{1e}-E_{1h}+(A_e-A_h)\,\frac{L_z}{2},$$

$$L_{ik}=\langle c,\mathbf{k}|e^{i\varkappa\mathbf{r}}\hat{p}_k|\nu,\mathbf{k}-\varkappa\rangle\langle\nu,\mathbf{k}-\varkappa|e^{-i\varkappa_1\mathbf{r}}\hat{p}_i|c,\mathbf{k}\rangle,$$

$$|c;v,\mathbf{k}\rangle=\frac{1}{\Omega_0}\,u_{c;v,\mathbf{k}}(r)e^{i\mathbf{kr}},\qquad(4)$$

$L=L_z+L_B$ is the superlattice period, L_B is the width of the QW layer forming the energy barrier, ω and $\varkappa$ are the frequency and wave vector of the electromagnetic wave which excites the exciton, $\varkappa_1$ is the wave vector of the current induced by the electromagnetic wave, E_g^W is the energy gap between the ground states of the electrons (E_{1e}) and holes (E_{1h}) in their own quantum wells with inclined bottoms neglecting their interaction with one another, E_g is the band gap in the three dimensional case in the layer forming the QW, $\hat{p}$ is the momentum operator, m_0 is the electron mass, Ω_0 is the volume of a unit cell of the three dimensional crystal, $u_{c;v,\mathbf{k}}(\mathbf{r})$ are the amplitudes of the Bloch functions

for the conduction band and valence band with wave vector **k**, and s is the width of the ground exciton level E^r.

Thus, it is evident that the photoelasticity coefficients calculated including the exciton effect also depend on the parameter λ. Expanding the resonant part of the dielectric permittivity (4) in a Fourier series, neglecting the nonlinear part of the modulation in the level E^r, in the form $\varepsilon_{ik} = \sum_n \varepsilon_{ik}^{nr} e^{in\alpha}$, $n=0,\pm 1,\pm 2,\ldots$, makes it possible to obtain, for the general case of a piezoelectric MQWS, an expression for the expansion coefficients which are proportional to the photoelastic coefficients of different orders of the deformation tensor u_{ik},

$$\varepsilon_{ik}^{\mathrm{r,n}} = -\frac{4\pi e^2 L_{ik}}{m_0^2\omega^2 L}\frac{2}{\pi\lambda^2}\frac{1}{\pi}\int_{-\pi}^{\pi}\frac{e^{-in\alpha}d\alpha}{a^d-(E_1+E_{\mathrm{ex}}^m)u_{ik}+is},$$

$$a^d = -E_g^{W0}+\hbar\omega-E_{\mathrm{ex}},$$

$$E_{\mathrm{ex}}^m = \frac{dE_{\mathrm{ex}}}{dF_\beta}\frac{4\pi\beta}{\varepsilon_0}, \quad \alpha=\mathbf{qr}-\Omega t, \tag{5}$$

E_g^{W0} is the size of the energy gap E_g^W unperturbed by the sound, E_1 is the deformation potential, E_{ex}^m is the shift parameter of the level E_{ex}, $E_{\mathrm{ex}}^m u_{ik}^0$ denotes the shift in the exciton level when a sound wave with a deformation tensor of amplitude u_{ik}^0 excites an electric field of strength $F_\beta = 4\pi\beta u_{ik}^0/\varepsilon_0$ in a piezoelectric crystal (β is the piezoelectric modulus), $dE_{\mathrm{ex}}/dF_\beta$ is the derivative of the exciton energy in a QW with an inclined bottom with respect to the strength of this piezoelectric field (in the case of a slope determined by an electric field, $dE_{\mathrm{ex}}^e/dF_\beta = edE_{\mathrm{ex}}^e/dA_e = edE_{\mathrm{ex}}^e/dA_h$ while in a varizone QW, where $A_e \neq A_h$, $dE_{\mathrm{ex}}^v/dF_\beta \neq edE_{\mathrm{ex}}^v/dA_e \neq edE_{\mathrm{ex}}^v/dA_h$), and Ω and **q** are the frequency and wave vector of the acoustic wave.

Estimates show that for an MQWS with an inclined bottom, as in the case of an MQWS with a simple bottom, at room temperatures the nonlinear terms in Eq. (5) are negligible for realistically attainable sound intensities. Since one of the specific features of the QW is the possibility of using exciton effects at room temperature, in the following we shall study only the linear terms ε_{ik}^{r1} of the Fourier expansion. Restricting ourselves in the integral for ε_{ik}^{r1} to the linear term with respect to u_{ik} and using a formula for the resonant photoelastic coefficient of the form $P_{1111}^{2D} = \varepsilon_{11}^{r1}/(u_{11}^0\varepsilon_0^2)$, we find an expression for the linear term of the photoelastic coefficient when the MQWS is based on a cubic crystal with piezoelectric properties,

$$P_{1111} = -\frac{4\pi e^2 L_{ik}}{m_0^2\omega^2 L}\frac{2}{\pi\lambda^2}\frac{(E_1+E_{\mathrm{ex}}^m)}{(a^d+is)^2}. \tag{6}$$

Since for equal values of a and s the linear photoelastic coefficients for an MQWS with an inclined bottom, $P_{1111}^{V,E}$, and for a simple QW, P_{1111}^{2D}, are related by

$$\frac{P_{1111}}{P_{1111}^{2D}} = \frac{\lambda_p^2}{\lambda_{v,e}^2}\frac{(E_1+E_{\mathrm{ex}}^{mv,e})}{E_1},$$

while for an incline determined by an electric field, $\lambda_e > \lambda_p$ and the level shift parameter $E_{\mathrm{ex}}^{me} < 0$, P_{1111}^E in both piezoelectric and nonpiezoelectric MQWS is always smaller than the photoelastic coefficient for a simple well, P_{1111}^{2D}. An electric field, which raises the variational parameter λ in Eq. (2), reduces the exciton wave function in the QW to a wave function which quantitatively describes the bulk crystal. Since the photoelastic coefficients for an incline determined by an electric field, P_{1111}^E, are related to the bulk photoelastic coefficients P_{1111}^{3D} by $P_{1111}^E/P_{1111}^{3D} \sim 2a_b s^{3D}/(Ls^{2D}\lambda_e^2)$ (where a_B is the Bohr radius of an atomic exciton and s^{3D} and s^{2D} are the energy spreads for the three-dimensional and quasi-two-dimensional cases), we thus have, with $L = 2a_{\mathrm{B}}$ and $s^{2D} = s^{3D}$ for the electric fields at which $\lambda_e \sim a_{\mathrm{B}}$, $P_{1111}^E \sim P_{1111}^{3D}$.

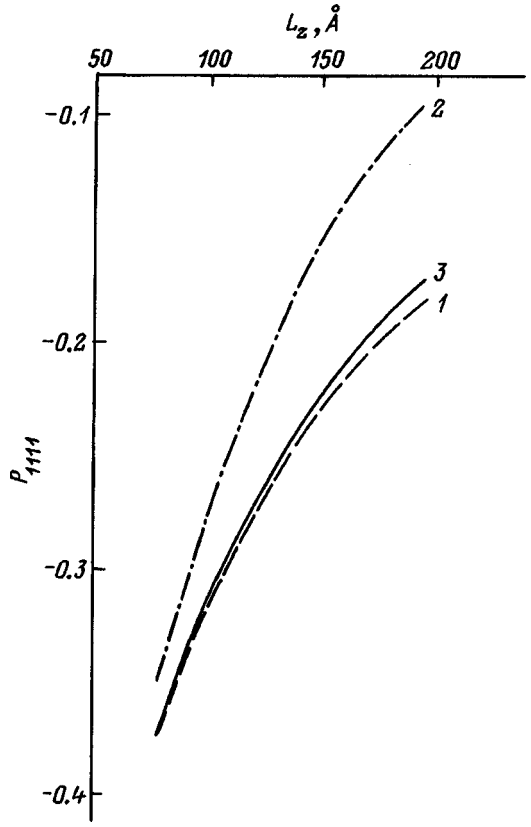

FIG. 4. The resonant part of the photoelastic coefficient P_{1111} as a function of the QW width L_z. (*1*) An incline in an MQWS with a varizone QW ($A_e = 10^5$ eV/cm, $A_h = -1.77\times 10^4$ eV/cm), (*2*) an incline created by an electric field ($A_e = A_h = 10^5$ eV/cm), and (*3*) a simple QW ($A_e = A_h = 0$).

In the case of an incline in an MQWS with a varizone QW, when $\lambda_v < \lambda_p$ and the shift parameter $E_{\mathrm{ex}}^{mv} > 0$, the additional localization of the electrons and holes effectively reduces the thickness of the QW, so that the photoelastic coefficient (P_{1111}^V) is enhanced. This is shown in Fig. 4, where Eq. (6) has been used to construct the curves for the linear resonance photoelastic coefficients for the particular superlattice $GaAs/Al_{0.28}Ga_{0.72}As$ ($L_B = 207$ Å, $L_{ik} = 1.2\times 10^{-38}$ g·erg,[8] $s^{2D} = 4$ meV) at a frequency shifted by 8 meV toward long wavelengths from the absorption peak of the exciton ground state in an MQWS with a varizone QW and for an incline imposed by an electric field applied to the MQWS, together with refined data for a simple well, as functions of the well width.

If the crystal upon which the MQWS is based has piezoelectric properties, then the magnitude and character of the modulation in the exciton ground state by the piezoelectric field (i.e., the contribution of the piezoelectric field to the photoelastic coefficients) in MQWS of this type with an inclined bottom will be different from the case of a piezoelectric MQWS with a simple QW. Since the ground state of any three-dimensional hydrogen-like system will depend quadratically on the applied electric field for electric fields much lower than the level required to ionize the system,[3] and this dependence is the same for the case of an exciton in a simple QW, the modulation of the exciton level by the piezoelectric field is also close to quadratic, is extremely small, and does not contribute to the linear photoelastic coefficients.

This situation is qualitatively different in the case of a QW with an inclined bottom. For piezoelectric fields much weaker than the applied electric field which determines the slope of the bottom of the QW or than the imbedded electric fields in the case of a varizone QW (even for good piezoelectrics, the field is less than 10^3 V/cm at medium sound intensities), the dependence of the exciton energy on the piezoelectric field is quasilinear, i.e., the creation of a slope in the bottom of the QW leads to a quasilinear modulation of the exciton ground state by the piezoelectric field and introduces a linear contribution to the photoelastic coefficients, which does not exist in the case of a simple well. The magnitude of this modulation (i.e., $E_{\rm ex}^{me}$), which depends on the derivative $dE_{\rm ex}^{e}/dF_{\beta}$, for an incline imposed by an electric field in the $GaAs/Al_{0.28}Ga_{0.72}As$ system is maximal for electric fields of $\sim 5\times 10^4 - 10^5$ V/cm, when the exciton energy as a function of the electric field created by the incline acquires a quasilinear character.

Estimates show that the magnitude of the linear contribution of the piezoelectric field to the resonant photoelasticity (as well as the magnitude of the modulation in the energy of the exciton level) is small and that the contribution of the deformation potential predominates. Thus, for the $GaAs/Al_{0.28}Ga_{0.72}As$ system, $E_{\rm ex}^{me}\sim 0.2$ eV and $E_{\rm ex}^{mv}\sim 0.04$ eV, while the deformation potential $E_1\sim 6$ eV.

Therefore, in MQWS with an inclined bottom of the QW, the photoelastic properties are substantially different from those of an MQWS with a simple well. In MQWS with a varizone QW, the slopes of the energy incline at the bottom have different signs, so that the resulting additional localization of an electron and hole in a QW increases the exciton ground state energy and, accordingly, the linear term of the resonance photoelastic coefficient. The situation is the opposite for MQWS in a constant electric field, where the slopes of the incline of the quantum wells are the same. A shift of the electron and hole to different boundaries of the quantum wells leads to a reduction in both the exciton energy and the linear resonance photoelastic coefficient. In piezoelectric MQWS the slope of the QW bottom stimulates a quasilinear modulation of the exciton energy by the piezoelectric field and a linear (in the piezoelectric field) contribution to the photoelastic coefficient, which is the distinctive feature of this case from that of a simple well or the bulk crystal. The magnitude of this contribution (and the modulation), however, is considerably smaller than the same quantities stimulated by the deformation potential.

We thank Yu. V. Gulyaev for valuable comments and E. N. Alekseev for great help in carrying out the numerical calculations.

[1)] An analysis[3] has shown that this approximation may be justified, in particular, for a QW based on GaAs when the width of the QW is close to the Bohr radius of the bulk exciton.

[2)] In order not to limit the generality of the analysis, here the zero energy, as for a varizone QW, is taken at $z=-L_z/2$. When determining the exciton energy, this does not influence the result, since for a QW in an electric field $A_e=A_h$.

[3)] Since $A_e\neq A_h$ for the incline in a varizone QW, the incline is characterized by the slope of the bottom of an electron well (A_e). The corresponding slopes for a hole well are uniquely related to A_e and are determined as noted above.

[1] R. A. Ayukhanov and G. N. Shkerdin, Fiz. Tverd. Tela (St. Petersburg) **35**, 1916 (1993) [Phys. Solid State **35**, 957 (1993)].
[2] D. A. B. Miller, D. S. Chemla, T. C. Damen, A. C. Gossard, W. Wiegmann, T. H. Wood, and C. A. Burrus, Phys. Rev. Lett. **53**, 2173 (1984).
[3] L. D. Landau and E. M. Lifshitz, *Quantum Mechanics* [in Russian], Nauka, Moscow (1963), 702 pp.
[4] G. P. Peka, V. F. Kovalenko, and A. N. Smolyar, *Varizone Semiconductors* [in Russian], Vyshcha shk., Kiev (1989), 250 pp.
[5] R. Dingle, W. Wiegmann, and C. H. Henry, Phys. Rev. Lett. **33**, 827 (1974).
[6] G. Bastard, E. E. Mendez, L. L. Chang, and L. Esaki, Phys. Rev. B **28**, 3241 (1983).
[7] J. A. Brum and G. Bastard, Phys. Rev. B **31**, 3893 (1985).
[8] *Gallium Arsenide. Production, Properties, and Applications*, edited by F. P. Kesamanly and D. N. Nasledov [in Russian], Nauka, Moscow (1973), 471 pp.

Translated by D. H. McNeill

Optical orientation of donor-bound excitons in nanosized InP/InGaP islands

R. I. Dzhioev, B. P. Zakharchenya, V. L. Korenev, P. E. Pak, D. A. Vinokurov, O. V. Kovalenkov, and I. S. Tarasov

A. F. Ioffe Physicotechnical Institute, Russian Academy of Sciences, 194021 St. Petersburg, Russia
(Submitted March 31, 1998)
Fiz. Tverd. Tela (St. Petersburg) **40**, 1745–1752 (September 1998)

Spin splitting of optically active and inactive excitons in nanosized *n*-InP/InGaP islands has been revealed. Optically inactive states become manifest in polarized-luminescence spectra as a result of excitons being bound to neutral donors (or of the formation of the trion, a negatively charged exciton) in InP islands. The exchange-splitting energies of the optically active and inactive states have been determined. © *1998 American Institute of Physics.* [S1063-7834(98)03809-X]

The fine structure of radiative exciton levels in low-dimensional systems becomes clearly apparent in the dependence of optical orientation and alignment of excitons on magnetic field in Faraday geometry. The fine structure has by now been detected for excitons localized in type-I GaAs/AlGaAs (Refs. 1 and 2) and CdTe/CdMgTe (Ref. 3) quantum wells, on one of the interfaces in type-II GaAs/AlAs superlattices,[4–6] and in InAlAs/AlGaAs quantum dots[7]. Under these conditions, polarization spectroscopy of excitons in a magnetic field permits one to measure small anisotropic-exchange splittings of levels of optically active states without their spectral resolution. Determination of the spin splitting of optically inactive exciton states, which do not directly contribute to polarized luminescence, is a more complex problem. A magnetic resonance study of this splitting in type-II GaAs/AlAs superlattices has recently been reported.[6]

The present work is based on the idea that the fine structure of optically inactive states should become directly manifest in polarized-luminescence spectra of quantum-well structures doped by shallow impurities (for instance, by donors). In this case an optically inactive exciton bound to a neutral donor forms a complex of three particles (two electrons combined into a singlet and a hole). A similar situation can occur when an electron attaches to an exciton to produce a trion in modulation-doped quantum-well structures. Recombination of such complexes gives rise to radiation, whose polarization carries information on the spin splitting of optically inactive states. This work reports detection of a fine structure of excitons (both optically active and inactive) localized in a self-organized InP-island system in strained *n*-InP/InGaP nanostructures.

1. SAMPLE PREPARATION AND EXPERIMENTAL RESULTS

The structures to be studied were prepared by low-pressure (100 mbar) MOCVD epitaxy at a growth temperature of 700 °C.[8] The starting reagents were gallium and indium trimethyls, arsine, and phosphine. The carrier gas was hydrogen purified by diffusion through palladium filters.

The structures were grown on (100)GaAs substrates oriented to within $\pm 30'$ and consisted of a 500-nm thick, lattice-matched $In_{0.5}Ga_{0.5}P$ buffer film, a layer of nanoscale InP islands with nominal thickness of three and five monolayers, and of a 50-nm thick $In_{0.5}Ga_{0.5}P$ cap layer. To produce an array of nanosized InP islands, the structure was exposed to phosphine flow immediately after the InP layer had been grown. The growth rate of the $In_{0.5}Ga_{0.5}P$ films was four and two Å/s, respectively. The impurity content in the layers was about $10^{15}\,cm^{-3}$. Figure 1 presents a TEM image of a part of the structure containing nominally three InP monolayers, which was obtained at an accelerating voltage of 120 kV. The photograph shows clearly bulk islands of about 700 Å in size, which are fairly uniform in dimensions and are distributed with a density of $\sim 3\times 10^9\,cm^{-2}$.

The samples to be studied were placed at the center of a superconducting coil (for measurements in strong fields <5 T), or of an electromagnet (for weak-field measurements, <2 kG), in a liquid-helium cryostat. A He–Ne laser beam ($h\nu = 1.96$ eV) directed along the growth axis of the structure, $z \| [001]$, produced photoexcitation. The light was focused onto the sample surface to a spot ≈ 0.5 mm in diameter. A condenser collected the recombination radiation into a parallel beam which, after passing through a polarization analyzer, was focused onto a double-grating spectrometer slit and detected with a PM tube at the spectrometer exit slit. The pump photon energy $h\nu$ was less than the InGaP barrier-material gap ($E_g \approx 2.0$ eV). At $h\nu = 1.96$ eV, the carriers are excited both in the quantum well (the wetting layer) and in the nanoislands, so that one produces here primarily nonresonant excitation of excitons in InP islands. The polarization was measured in the regime where the sign of the pump-light circular polarization was alternated at the mechanical-resonance frequency (26.61 kHz) of a quartz modulator, and the luminescence polarization was analyzed with a quarter-wave phase plate and a linear polarizer. Experiments performed in this geometry are free of the effects associated with dynamic polarization of the semiconductor nuclei.[9] We measured the effective degree of circular polarization at different points within the recombination-emission band of the nanoislands, $\rho_c = (I^{\sigma+}_{\sigma+} - I^{\sigma-}_{\sigma+})/(I^{\sigma+}_{\sigma+} + I^{\sigma-}_{\sigma+})$. Here $I^{\sigma+}_{\sigma+}$ and $I^{\sigma-}_{\sigma+}$ are the σ^+ luminescence intensities under σ^+ and σ^- pumping, respectively. In this case ρ_c may be considered as

 © 1998 American Institute of Physics

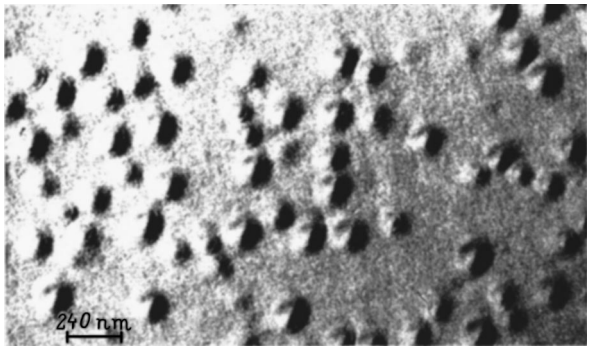

FIG. 1. TEM image of a part of a structure containing nominally three InP monolayers, obtained at an accelerating voltage of 120 kV.

the conventional Stokes parameter, which characterizes the circular polarization of luminescence due to that of the pump light.

Figure 2 shows an exciton luminescence spectrum from InP islands illuminated by σ^+ light with photon energy $h\nu = 1.96$ eV and intensity $I = 2.5$ W/cm^2. The degree of circular polarization ρ_c was measured at the line maximum. In the absence of magnetic field, $\rho_c < 0$. This means that the laser light reflected from the sample and the luminescence analyzed in reflection geometry have opposite signs of circular polarization.[1)] Magnetic field applied perpendicular to the pump beam causes depolarization of the radiation (the Hanle effect, depicted in Fig. 3). As seen from the figure, ρ_c vanishes in fields $H_\perp \approx 100$ G, reverses sign from negative to positive, and saturates at a level $\rho_c \approx +0.6\%$. Figures 4 and 5 display the results obtained on the optical orientation of excitons in a longitudinal magnetic field (Faraday geometry). We readily see that the degree of circular polarization ρ_c first slightly decreases from -0.6 to -2.1% (in fields of 0–1.3 kG), to subsequently increase from -2.1 to -0.1% (in the 1.3–50-kG range). Within the experimental accuracy, the $\rho_c(B)$ dependence is symmetrical with respect to sign reversal of the field B. In principle, ρ_c may become negative under resonant excitation of light-hole $1e-1lh$ excitons because of the change of selection rules for light absorption.[11]

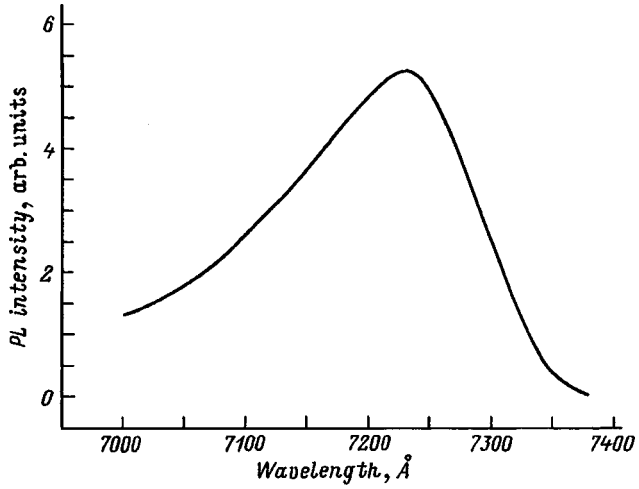

FIG. 2. Exciton luminescence spectrum from InP islands obtained under illumination with $h\nu = 1.96$-eV photons at an intensity $I = 2.5$ W/cm^2.

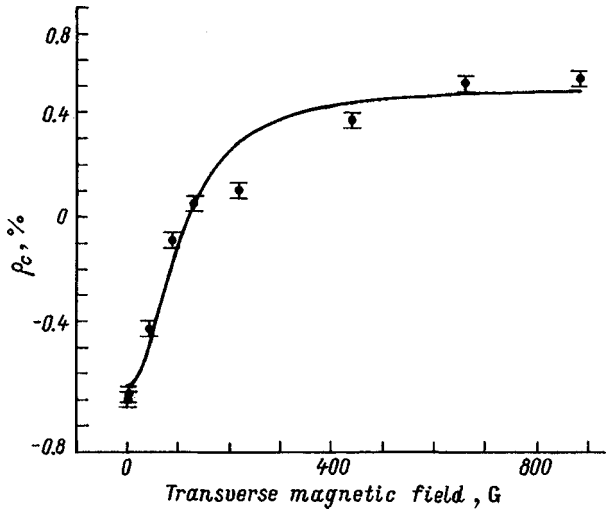

FIG. 3. Radiation depolarization in a transverse magnetic field (the Hanle effect). Excitation: σ^+ light with $h\nu = 1.96$ eV at an intensity $I = 2.5$ W/cm^2. Solid line: a Lorentzian with a halfwidth of 100 G.

This can hardly account, however, for the polarization sign reversal in the Hanle effect, as well as for the magnetic-field dependence of ρ_c in the Faraday geometry. We are going to show that the negative sign of the luminescence polarization observed in zero field, the sign reversal of polarization in the Hanle effect, and the $\rho_c(B)$ dependence in Faraday geometry can be explained through participation of an ''exciton on a neutral donor'' (or of trions, i.e., negatively charged excitons) in radiative recombination.

2. DISCUSSION OF RESULTS

We attribute both the sign reversal of the luminescence polarization and the magnetic-field dependence of ρ_c to a contribution of optically inactive excitons to the luminescence polarization, which is made possible by the formation of a bound complex of two electrons and a hole. Because the

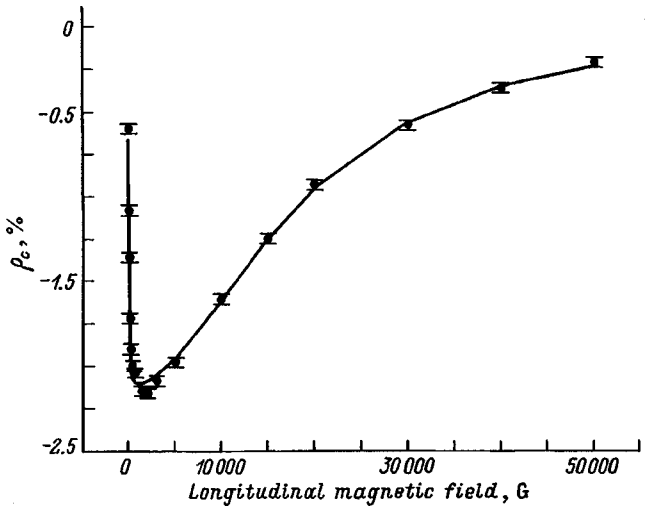

FIG. 4. Degree of circular polarization of luminescence in longitudinal magnetic field (Faraday geometry) under σ^+ excitation. Solid line is a plot of Eq. (4) with the fitting parameters $a = -0.69\%$, $b = 2.14\%$, and $c = 1.43\%$.

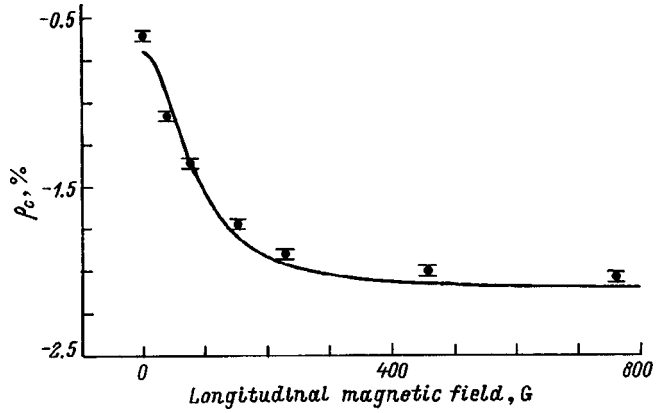

FIG. 5. Decrease of ρ_c in a longitudinal magnetic field caused by a contribution of optically inactive excitons to the polarization of the radiation. The solid curve was calculated using the parameters of Fig. 4.

samples under study contain donors not only in the InP nanosized islands but in the InGaP barrier material as well, two possibilities can be conceived in this connection. First, if there are neutral donors in the InP islands, photoexcited excitons can be trapped by them to form an exciton–neutral-donor complex (D^0X). Second, electrons can transfer from donors in the barrier material to the InP islands. This may result in the formation of the trion, a negatively charged complex of two electrons and a hole. For definiteness, we are going to consider subsequently optical orientation of D^0X complexes and bear in mind that most of the results obtained is directly applicable to the optical orientation of trions as well. We shall turn back to this point at the end of this Section.

One of the most remarkable results is the unusual magnetic-field dependence of ρ_c in the Faraday geometry (Figs. 4 and 5). We may recall that ρ_c grows monotonically, as a rule, with magnetic field, which is assigned either to suppression of carrier spin relaxation[9] or to the Zeeman splitting becoming larger than the exciton-level exchange splitting[4,12]. In our experiments, however, one observes a nonmonotonic behavior of the degree of polarization, namely, it first falls off slightly with increasing field, to eventually grow in fairly strong fields ($B>1$ kG). Moreover, as seen from Figs. 4 and 5, $\rho_c<0$, i.e., the luminescence and pump-light polarizations have opposite signs.

We shall first show how the luminescence polarization can reverse its sign in the course of exciton recombination in the D^0X complex, and then turn to a qualitative description of the $\rho_c(B)$ relation. We assume the ground state of the complex to be the state where the electron spins are antiparallel to form a singlet. We shall neglect for some time the exchange coupling between the electron and the hole in the exciton. In this case, the exciton ground state in quantum-well structures is fourfold degenerate, and the projection of the total momentum on the $z\|[001]$ direction is $M=s+j=\pm 1,\pm 2$ (here $s=\pm 1/2$ is the electron-spin projection, and $j=\pm 3/2$ is the hole momentum projection). Nonresonant excitation by circularly polarized light produces optical orientation of excitons as a result of the spin-polarized electron and hole becoming bound to form an exciton. For instance, under illumination with σ^+ light the photoelectron spin is directed predominantly antiparallel to the z axis, whereas the holes are primarily oriented along the latter. To simplify our reasoning, we assume the spins of all photoelectrons to be antiparallel to the z axis, and the holes to be unpolarized. As a result, half of the excitons will have a momentum projection $M=+1$ (optically active excitons), while for the other half $M=-2$ (optically inactive excitons). The $M=+1$ exciton recombines by emitting a σ^+ photon, which means that the sign of circular polarization of the radiation coincides with that of the pump light. Optically inactive excitons do not contribute to the radiation. The situation changes essentially if neutral donors (D^0 centers) are present in the quantum well. In this case there is a possibility for optically inactive excitons with $M=-2$ to recombine. Indeed, if an $M=-2$ exciton is bound in the exciton–neutral-donor complex (D^0X), the projection of the total momentum of the complex is determined by that of the hole momentum and is $-3/2$ (with two electrons forming a singlet). Recombination of a hole with an electron [with spin projection $(+1/2)$] is accompanied by emission of a σ^- photon, thus producing negative circular polarization of the luminescence. On the other hand, binding of optically active excitons with $M=+1$ in the D^0X complex (with total-momentum projection of $+3/2$) produces σ^+-polarized luminescence, as in the case of free-exciton recombination. We have been considering a limiting case of the spins of all photoelectrons being antiparallel to the z axis, and of unpolarized holes, which results in formation of excitons with the momentum projections $M=+1$ and $M=-2$. In a general case there are also excitons with $M=-1$ and $M=+2$ (because of carrier-spin relaxation), so that the polarization of active and inactive excitons is less than 100%. Under these conditions, however, one can also maintain that the contribution of optically inactive excitons to the resultant circular polarization of the D^0X complex is negative if the degree of their orientation $P_2=(N_2-N_{-2})/(N_2+N_{-2})<0$ (here N_2 is the number of optically inactive excitons with the momentum projection $M=+2$, and N_{-2}, that with $M=-2$). At the same time the contribution of optically active excitons is positive and is determined by the degree of orientation $P_1=(N_1-N_{-1})/(N_1+N_{-1})>0$ (N_1 and N_{-1} are the numbers of excitons with the momentum projections $M=+1$ and $M=-1$, respectively). If for some reason optically active and optically inactive excitons provide different contributions to the recombination radiation, the resultant degree of circular polarization of the luminescence ρ_c can be either positive or negative, depending on which of the contributions is dominant. This difference in the contributions may result, for instance, from the fine structure of exciton levels in low-dimensional systems. It is due to the electron–hole exchange coupling in the exciton, which has until now been neglected here. We are going to show next that the exchange splitting of the spin levels of optically active and inactive excitons can qualitatively account for the magnetic-field dependence of ρ_c (see Figs. 4 and 5).

Figure 6 shows the structure of the exciton spin sublevels.[12] The δ_2 levels of $M=\pm 1$ excitons split already in zero magnetic field into a pair of optically active states,

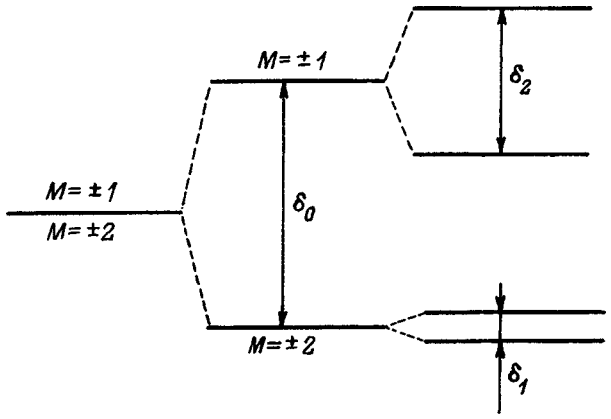

FIG. 6. Fine structure of the spin levels of the $e1-hh1$ exciton in zero magnetic field.

which are linearly polarized in two orthogonal directions. As a result of this splitting, excitation with circularly polarized light does not orient the optically active excitons, i.e., their degree of orientation $P_1=0$. In a longitudinal magnetic field, the linearly polarized states become circularly polarized, thus increasing the degree of orientation of optically active excitons. This will bring about an increase in the degree of circular polarization of the luminescence, because the contribution of optically active excitons to the radiation polarization is positive. As seen from Fig. 4, in fields $B>1$ kG the degree of circular polarization grows with increasing contribution of optically active excitons to the luminescence polarization. The characteristic field in which ρ_c begins to grow is ≈ 15 kG. The characteristic magnetic field B_2 required to restore the optical orientation of excitons can be evaluated by equating the exchange splitting δ_2 to the Zeeman splitting of optically active states, $\mu_B|g_\parallel^e-g_\parallel^h|B_2$ (here $g_\parallel^e$ and $g_\parallel^h$ are the longitudinal g factors of the electron and the hole). The values of δ_2 for excitons localized in type-I low-dimensional systems are typically $10-100\,\mu$eV.[2,12] Assuming $\delta_2=100\,\mu$eV, $g_\parallel^e=1.6$ and $g_\parallel^h=2.9$,[13] we come to an estimate $B_2=13$ kG, which is in agreement with experiment.

Let us turn now to the weak magnetic-field domain, $B<1$ kG (Figs. 4 and 5). Here ρ_c decreases with increasing magnetic field. We attribute this to an increasing contribution of optically inactive excitons to luminescence polarization. Indeed, as follows from the foregoing consideration, polarized optically inactive excitons can recombine only when bound in a D^0X complex, with the circular polarization having negative sign. It appears natural to explain the behavior of ρ_c in weak magnetic fields as due to a fine structure of the optically inactive states (see Fig. 6), similarly to the case of optically active excitons. A pair of optically inactive states represents actually a superposition of the $M=+2$ and $M=-2$ states taken with equal weights but different phases. If the time required for a donor to capture an inactive exciton, τ_2, is long enough ($\tau_2\gg\hbar/\delta_1$), then they will not be optically oriented in zero magnetic field, $P_2=0$. Application of a magnetic field transforms optically inactive states into two pure states with $M=+2$ and $M=-2$, which makes possible their orientation. Because their contribution to the polarization is negative, ρ_c should decrease with increasing magnetic field, a situation observed experimentally. The characteristic field B_1 in which ρ_c decreases is ≈ 80 G. Thence one can estimate the splitting δ_1 using the relation $\delta_1=\mu_B|g_\parallel^e+g_\parallel^h|B_1\approx 2.1\,\mu$eV, which is substantially less than the exchange splitting of optically active states. This value of the energy splitting δ_1 imposes a serious constraint on the lifetime τ_2 of optically inactive excitons against their binding in the D^0X complex. In order for the splitting of inactive states to become experimentally observable, the condition $\tau_2\gg\hbar/\delta_1\approx 0.25$ ns should be satisfied. Such long trapping times (of the order of the radiative-recombination time $\tau\geqslant 0.5$ ns in the structures under study, Ref. 14) are, in principle, conceivable, if the dimension d of the islands localizing the excitons significantly exceeds the Bohr radius of the exciton a_x and that of the donor-bound electron a_d. In this case an exciton will need a certain time to encounter a D^0 center. Besides, at low temperatures the exciton can localize at thickness fluctuations of the nanoislands, with its subsequent tunneling to a neutral donor, which likewise would require an additional time. It should be stressed that this model itself is valid only if $d\gg a_x, a_d$, i.e., when the exciton and electron at a donor may be considered as independent quasi-particles. In the samples under study $d\approx 700$ Å, and $a_x, a_d\sim 100$ Å, so that this conditions is upheld (otherwise one should consider from the very beginning spin interactions of three particles on an equal footing, without separating them into an exciton and a D^0 center).

Thus excitons appearing under nonresonant excitation form through binding of optically oriented electrons with holes. After a time $\tau_2\gtrsim 0.25$ ns, optically inactive excitons are trapped by neutral donors to form D^0X complexes. Recombination of an exciton bound in a complex is accompanied by the emission of photons, with their circular polarization being opposite in sign to the pump-light polarization. As for the optically active excitons, the time of their trapping by a neutral donor, τ_1, should not differ much from that of inactive excitons, τ_2, and therefore one can set $\tau_1\approx\tau_2>0.25$ ns. Note that optically active excitons can recombine in two ways. If their radiative-recombination time τ is much shorter than the trapping time by a donor, τ_1, optically active excitons will recombine before becoming bound in a D^0X complex. In the other limiting case ($\tau\gg\tau_1$) they recombine through the D^0X complex. The radiative-recombination time of active excitons in such structures $\tau\geqslant 0.5$ ns.[14] Therefore, both possibilities are realizable in principle. This will not change in any way a qualitative description of the behavior of ρ_c with magnetic field. Indeed, after the formation of a complex a hole will recombine only with its "own" electron, because its spin is parallel to that of the donor-bound electron. Therefore the degree of circular polarization of the luminescence of a complex formed by trapping optically active excitons will be determined by the degree of their spin polarization, similar to the case of free-exciton recombination. A quantitative consideration of the problem will, however, reveal a difference. We believe that optically active excitons in the samples under study likewise recombine through the D^0X complex, i.e., that $\tau>\tau_1$ (the lifetime of excitons is dominated by their trapping time by a donor). As a matter of

fact, optical polarization of excitons in undoped quantum dots is accompanied by optical alignment and/or conversion from optical orientation to optical alignment.[7] This is due to the electron and hole spins in the exciton being correlated. There is no such correlation, however, in the D^0X complex, and therefore there should be no linear polarization of the radiation associated with the exciton alignment. Optical alignment of excitons was observed in the samples under study neither under nonresonant excitation ($h\nu = 1.96$ eV) nor under quasi-resonant excitation ($h\nu = 1.83$ eV) of excitons. This implies that the main recombination channel for both optically active and inactive excitons involves the D^0X complex.

The model we have considered provides a qualitative explanation both for the sign reversal of the luminescence polarization and for the dependence of ρ_c on magnetic field. In zero magnetic field, excitons are not oriented because of the exchange splitting of both active and inactive states. Therefore the recombination radiation does not contain a circularly polarized component (provided the electrons at the donors are not polarized). In the magnetic field of Faraday geometry, first the splitting of optically inactive states disappears, which restores the optical orientation of these states and reduces the degree of circular polarization of the radiation [with ρ_c decreasing from $\rho_c(B=0) \approx -0.6\%$ to $\rho_c(B=500\ \text{G}) \approx -2.1\%$, see Figs. 4 and 5]. In strong magnetic fields, Zeeman splitting becomes larger than the splitting of optically active states in zero field, thus giving rise to orientation of active excitons. This accounts for the increase of ρ_c in strong magnetic fields from $\rho_c(B=500\ \text{G}) \approx -2.1\%$ to $\rho_c(B=5\ \text{T}) \approx -0.1\%$ (Fig. 4). This process can be presented schematically as follows:

$$\sigma^+\text{photon} \rightarrow e \oplus h \rightarrow M=1 \rightarrow D^0X \rightarrow \sigma^+\text{photon},$$

$$\sigma^+\text{photon} \rightarrow e \oplus h \rightarrow M=2 \rightarrow D^0X \rightarrow \sigma^-\text{photon}.$$

Absorption of σ^+ light creates electrons and holes, which subsequently combine to form excitons. After this, excitons are trapped by a neutral donor. Recombination of the complex produced by trapping of optically active excitons is accompanied by emission of a photon of the same polarization (σ^+), whereas binding of inactive excitons gives rise to emission of an oppositely polarized (σ^-) photon.

Note that, in this model, the luminescence must be unpolarized in zero magnetic field (if the electrons at donors are not polarized). As evident from Figs. 3–5, however, $\rho_c(0) \approx -0.6\%$. Besides, $\rho_c(0)$ depends on the pump light intensity, namely, under weak pumping $\rho_c(0) = +0.6\%$, then it decreases with increasing intensity, and saturates at a level of -2%. This implies that the donor-bound electrons are optically oriented. Optical orientation of electrons bound to donors in *n*-type bulk materials was studied in detail.[9] It was established that the spin polarization of donor electrons increases with the intensity of circularly polarized light, and that at high intensities the halfwidth of the luminescence magnetic-depolarization curve increases too. The same situation is observed in our case. It appears therefore reasonable to attribute the behavior of $\rho_c(0)$ as a function of pump-light intensity to polarization of donor-bound equilibrium electrons. We are going to show subsequently that the polarization of the radiation emitted by the D^0X complex should contain a contribution due to the polarization of the donor-bound electrons, P_d, even if the excitons bound in a complex are unpolarized. Two questions may arise in this connection, however. First, if in zero field the excitons are unpolarized, what process will produce spin polarization of equilibrium electrons at donors? And second, why ρ_c in a transverse field does not vanish (the excitons are unpolarized because of the electron–hole exchange interaction, and the electrons at donors are depolarized because of the Hanle effect in a transverse magnetic field) but reaches instead a level of $+0.6\%$ (Fig. 3)? Similarly, as the light intensity is reduced, ρ_c in zero magnetic field, rather than vanishing (in the weak-pumping limit the donor-bound electrons are also depolarized[9]), attains the same level of $+0.6\%$ as in the presence of a transverse magnetic field. The answer to these questions lies in the existence, besides the above, of other mechanisms of D^0X formation as well, which produce polarization of electrons at the donors and account for the presence of the ''residual'' positive polarization $\rho_c = +0.6\%$. For instance, first a photoelectron is trapped by a neutral donor to form a D^- center, after which it is joined by a photoexcited hole to produce the D^0X complex:

$$\sigma^+\text{photon} \rightarrow D^0 \oplus e \oplus h \rightarrow D^- \oplus h \rightarrow D^0X \rightarrow \sigma^+\text{photon}.$$

Because the hole is polarized along $z \| [001]$, after its capture by the D^- center the degree of circular polarization of the complex radiation will be determined only by the hole spin polarization, so that $\rho_c > 0$. The contribution of this process to total luminescence provides an explanation for the residual positive polarization and for its insensitivity to transverse magnetic field (the transverse g factor of holes is close to zero).

As for the optical pumping of donor-bound electrons, it will occur, for example, as a result of equilibrium electrons being replaced by optically oriented photoelectrons; indeed, equilibrium electrons recombine to be replaced by spin-polarized photoelectrons. If the spin relaxation of electrons at donors is not a very fast process, their polarization will persist until the creation of the next electron–hole pair, and in steady-state conditions the donor-bound electrons will be polarized, with the sign of their polarization P_d being determined by the polarization of the photoelectrons.

In principle, all the above processes may contribute to some extent to the magnetic-field dependence of the luminescence polarization. At present, however, we are not able to isolate each of them experimentally. Therefore, in the numerical calculations, we are going to restrict ourselves to the first of the above-mentioned processes, i.e., to the formation of an exciton with its subsequent trapping by a donor and its recombination. As for the spin polarization P_d of the donor-bound electrons, we shall consider it as a phenomenological parameter which does not depend on magnetic field.

We calculate first the degree of circular polarization ρ_c of the luminescence as a function of polarization of optically active, P_1, and optically inactive, P_2, excitons and of the polarization of donor-bound electrons P_d. Two cases can be conceived for optically active excitons: 1) Exciton with the

momentum projection $M=+1$ ($s=-1/2, j=+3/2$) is captured by a neutral donor whose electron spin is aligned with the z axis ($s_d=+1/2$). Recombination of such a complex is accompanied by emission of a σ^+ photon, with the intensity being proportional both to the number of $M=+1$ excitons and to the number of electrons $N_{d\uparrow}$, i.e., $I_{\sigma^+}\propto N_{+1}N_{d\uparrow}$; 2) Exciton with the momentum projection $M=-1$ ($s=+1/2, j=-3/2$) is captured by a donor whose electron spin is antiparallel to the z axis ($s_d=-1/2$). This produces σ^- luminescence with $I_{\sigma^-}\propto N_{-1}N_{d\downarrow}$. For the contribution of these processes to the luminescence polarization one readily obtains $\rho_{1c}=P_1+P_d$ (here $P_d=(N_{d\uparrow}-N_{d\downarrow})/(N_{d\uparrow}+N_{d\downarrow})$, and it is assumed that $P_1P_d\ll 1$). A similar analysis performed for the optically inactive excitons yields for their contribution to the radiation polarization $\rho_{2c}=P_2-P_d$. If the numbers of optically active and inactive excitons are in the ratio $W/(1-W)$, where $W\in[0,1]$ presents the contribution of $M=1$ excitons to the total intensity, the resultant degree of circular polarization of the luminescence will take on the form

$$\rho_c=W(P_1+P_d)+(1-W)(P_2-P_d). \tag{1}$$

Neglecting the spin relaxation, the degree of orientation P_1 of optically active excitons in a longitudinal magnetic field is given by the expression[12]

$$P_1=P_1^0\frac{1+(\Omega_1\tau_1)^2}{1+(\Omega_1\tau_1)^2+(\omega_2\tau_1)^2}. \tag{2}$$

Here $\hbar\Omega_1=\mu_B|g_\parallel^e-g_\parallel^h|B$ is the Zeeman splitting of optically active excitons, $\hbar\omega_2=\delta_2$ is the splitting of radiative states in zero magnetic field, τ_1 is the lifetime of optically active excitons, and P_1^0 is the degree of orientation at the instant of exciton creation. When independent electrons and holes produce an exciton, $P_1=P_h-P_e$ [the degree of orientation of photoelectrons $P_e=(N_\uparrow-N_\downarrow)/(N_\uparrow+N_\downarrow)$, and that of photoexcited holes $P_h=(N_{+3/2}-N_{-3/2})/(N_{+3/2}+N_{-3/2})$]. Note that under σ^+ excitation $P_h>0, P_e<0$, and $P_1^0>0$. The degree of orientation of optically inactive excitons, P_2, is determined by a similar expression

$$P_2=P_2^0\frac{1+(\Omega_2\tau_2)^2}{1+(\Omega_2\tau_2)^2+(\omega_1\tau_2)^2}, \tag{3}$$

where $\hbar\Omega_2=\mu_B|g_\parallel^e+g_\parallel^h|B$, $\hbar\omega_1=\delta_1$, $P_2^0=P_h+P_e$, and τ_2 is the lifetime of optically inactive excitons. If the exciton lifetime is long enough, i.e., if $\omega_2\tau_1, \omega_1\tau_2\gg 1$, Eqs. (2) and (3) can be simplified. Substituting under these conditions (2) and (3) into Eq. (1) yields the final equation, which we shall use in discussing the experimental data

$$\rho_c=a+b\frac{B^2}{B^2+B_2^2}-c\frac{B^2}{B^2+B_1^2} \tag{4}$$

with the parameters $a=(2W-1)P_d$, $b=W(P_h-P_e)$, $c=-(1-W)(P_h+P_e)$, $B_2=\delta_2/(\mu_B|g_\parallel^e-g_\parallel^h|)$, and $B_1=\delta_1/(\mu_B|g_\parallel^e+g_\parallel^h|)$. The first term in Eq. (4) describes the contribution of the spin relaxation of equilibrium electrons to the polarized luminescence of the D^0X complex, the second corresponds to that of optically active excitons, and the third term relates to the spin orientation of optically inactive excitons bound in the D^0X complex.

The solid lines in Figs. 4 and 5 are plots of Eq. (4) calculated with the fitting parameters $a=(-0.69\pm 0.06)\%$, $b=(2.14\pm 0.08)\%$, $c=(1.43\pm 0.06)\%$, $B_1=(82\pm 7)$ G, and $B_2=(18\pm 1)$ G. Theory is observed to agree with the experiment. Let us discuss the results obtained. Consider first parameters a, b, and c, which determine the $\rho_c(B)$ dependence in Figs. 4 and 5. The fact that parameters $b, c>0$ is in accord with the above statement that $P_h>0, P_e<0$ under σ^+ excitation. Further, because $a<0$, two possibilities are conceivable: either $W>1/2$ (i.e., optically active excitons are dominant in recombination) and $P_d<0$ (the donor-bound electrons are polarized by photoelectrons), or $W<1/2$ and $P_d>0$ (the polarizations of the donor-bound electrons and of the holes are of the same sign). We shall not analyze these cases in great detail because the model used in data treatment is too simple. A more rigorous consideration should include all the above mechanisms of D^0X complex formation. Besides, the degree of polarization of the donor-bound electrons P_d may itself depend on magnetic field, because the optical orientation of excitons is restored by magnetic field and they will affect, in their turn, the polarization P_d. Let us turn now to parameters B_1 and B_2 determining the behavior of $\rho_c(B)$ in Figs. 4 and 5. If the electron and hole g factors are known, one can find parameters δ_1 and δ_2 characterizing the exciton fine structure. Using for the g factors the values $g_\parallel^e=1.6$ and $g_\parallel^h=2.9$,[13] we come to $\delta_1\approx 2.1\ \mu$eV and $\delta_2\approx 130\ \mu$eV. Note that the simplified model used in describing our experiment does not take into account the spin relaxation of carriers in the exciton. A theory of optical orientation of excitons in the presence of spin relaxation was developed.[4] It was shown that inclusion of spin relaxation makes the characteristic magnetic field restoring the optical orientation of excitons dependent not only on δ_2 but on the ratio of the exciton optical-orientation and optical-alignment relaxation times as well. Therefore the true value of δ_2 may turn out to be smaller. Taking into account the spin relaxation can also change somewhat the value of δ_1 obtained within the simple model (see Appendix A in Ref. 4).

We have been considering the optical orientation of the exciton–neutral-donor complexes in nanosized islands, whose transverse dimension exceeds by far both the Bohr exciton radius and the radius of the donor-bound electron. The samples we studied contain donors, however, not only in the InP islands but in the InGaP barriers as well. Therefore part of the electrons from the barriers can become localized in InP layers. In such cases it would be more appropriate to speak about the optical orientation of trions, i.e., quasiparticles consisting of two electrons and a hole. The above model is applicable also to the optical orientation of trions in nanosized islands. It can be employed also in the case of optical orientation of trions in quantum wells with two-dimensional electron gas, where the mean separations among electrons exceed by far the exciton Bohr radius ($n_s a_B\ll 1$, where n_s is the surface density of the electron gas). Finally, this model can be readily generalized to the case of excitons bound to neutral acceptors in low-dimensional systems.

The authors are deeply grateful to Yu. G. Kusraev, E. L. Ivchenko, and M. N. Tkachuk for fruitful discussions.

Partial support of the work of R. I. D., B. P. Z., and V. L. K. by the Russian Fund for Fundamental Research (Grants 96-02-16887*a* and 98-02-18213) is gratefully acknowledged. The work of D. A. V., O. V. K., and I. S. T. was supported by the "Physics of Solid-State Nanostructures" Project No. 96-2005.

[1)]The phenomenon of sign reversal of the radiation in zero magnetic field was observed in bulk samples as well.[10]

[1] E. Blackwood, M. J. Snelling, R. T. Harley, S. R. Andrews, and C. T. Foxon, Phys. Rev. B **50**, 14246 (1994).
[2] D. Gammon, E. S. Snow, and B. V. Shanabrook, Phys. Rev. Lett. **76**, 3005 (1996).
[3] Yu. G. Kusraev, B. P. Zakharchenya, G. Karczewski, T. Wojtowicz, and J. Kossut, Solid State Commun. **104**, 465 (1997).
[4] R. I. Dzhioev, H. M. Gibbs, E. L. Ivchenko, G. Khitrova, V. L. Korenev, M. N. Tkachuk, and B. P. Zakharchenya, Phys. Rev. B **56**, 13405 (1997).
[5] P. G. Baranov, N. G. Romanov, I. V. Mashkov, G. B. Khitrova, H. M. Gibbs, and O. Lungnes, Fiz. Tverd. Tela (St. Petersburg) **37**, 2991 (1995) [Phys. Solid State **37**, 1648 (1995)].
[6] H. W. van Kesteren, E. C. Cosman, W. A. J. A. van der Poel, and C. T. Foxon, Phys. Rev. B **41**, 5283 (1990).
[7] R. I. Dzhioev, B. P. Zakharchenya, E. L. Ivchenko, V. L. Korenev, Yu. G. Kusraev, N. N. Ledentsov, V. M. Ustinov, A. E. Zhukov, and A. F. Tsatsul'nikov, JETP Lett. **65**, 804 (1997).
[8] O. V. Kovalenkov, D. A. Vinokurov, D. A. Lifshits, I. S. Tarasov, N. A. Bert, S. G. Konnikov, and Zh. I. Alferov, in *Abstracts of the 2nd Russian Conference ''Physics of Semiconductors''* (Zelenogorsk, Russia, 1996), Vol. 1, p. 41; O. V. Kovalenkov, D. A. Vinokurov, D. A. Lifshits, I. S. Tarasov, N. A. Bert, S. G. Konnikov, and Zh. I. Alferov, in *Proceedings of the International Symposium ''Nanostructures: Physics and Technology''* (St. Petersburg, Russia, 1996), p. 141; O. V. Kovalenkov, D. A. Vinokurov, D. A. Lifshits, I. S. Tarasov, N. A. Bert, S. G. Konnikov, and Zh. I. Alferov, in *Proceedings of the 23rd International Symposium ''Compound Semiconductors''* (St. Petersburg, Russia, 1996), p. 271.
[9] *Optical Orientation*: Modern Problems in Condensed Matter Sciences, Vol. 8, edited by F. Meier and B. Zakharchenya [North-Holland, Amsterdam, 1984; Nauka, Leningrad, 1989].
[10] A. Bonnot, R. Planel, and C. Benoit á la Guillaume, Phys. Rev. B **9**, 690 (1974); R. I. Dzhioev, B. P. Zakharchenya, Yu. G. Kusraev, and V. G. Fleisher, Izv. Akad. Nauk SSSR, Ser. Fiz **46**, 514 (1982).
[11] C. Weisbuch, R. C. Miller, R. Dingle, A. C. Gossard, and W. Wiegmann, Solid State Commun. **37**, 219 (1981).
[12] E. L. Ivchenko and G. E. Pikus, *Superlattices and Other Heterostructures. Symmetry and Optical Phenomena* (Springer, Berlin, 1995).
[13] A. A. Sirenko, T. Ruf, A. Kurtenback, and K. Eberl, in *Proceedings of the 23rd International Conference ''Physics of Semiconductors''*, Vol. 2 (Berlin, 1996), pp. 1385–1388.
[14] P. Castrillo, D. Hessman, M.-E. Pistol, C. Pryor, N. Carlsson, W. Seifert, and L. Samuelson, in *Proceedings of the 23rd International Conference ''Physics of Semiconductors''*, Vol. 2, (Berlin, 1996), pp. 1421–1424.

Translated by G. Skrebtsov

Energy spectra and quantum crystallization in two-electron quantum dots in a magnetic field

N. E. Kaputkina and Yu. E. Lozovik

Institute of Spectroscopy, Russian Academy of Sciences, 142092 Troitsk, Moscow District, Russia
(Submitted November 3, 1997; resubmitted April 7, 1998)
Fiz. Tverd. Tela (St. Petersburg) **40**, 1753–1759 (September 1998)

Quantum crystallization of electrons in a quantum dot (QD) subjected to an external magnetic field is considered. Two-electron QDs with two-dimensional ($2D$) parabolic confining potential in an external transverse magnetic field are calculated. The Hamiltonian is numerically diagonalized in the basis of one-particle functions to find the energy spectra and wave functions for the relative motion of electrons with inclusion of electron–electron interaction for a broad range of the confining-potential steepness (α) and external magnetic fields (B). The region of the external parameters (α, B) within which a gradual transition to quantum crystalline order occurs is numerically determined. In contrast to a $2D$ unbounded system, a magnetic field acts nonmonotonically on ''crystallization'' in a quantum dot with several electrons because of a competition between two effects taking place with increasing B, namely, decreasing spread of the electron wave functions and increasing effective steepness of the confining potential, which reduces the average separation between electrons. © *1998 American Institute of Physics.* [S1063-7834(98)03909-4]

Quantum dots (QD) as quasi-zero-dimensional systems are extremely interesting low-dimensional systems. They are of importance not only as a possible component base for nanoelectronics, but also as model objects for basic research, namely, as giant artificial atoms with controllable parameters, such as the type and steepness of the confining potential, the number of particles, and characteristic size of the confinement region. The type of the confining potential is determined by the actual method used to prepare the QD. Among the most commonly used are the ''rigid wall'' and the parabolic confining-potential models.[1–7] The model of the parabolic lateral confining potential was confirmed by self-consistent calculations[8] and is applicable to not very large QDs. The excitation spectra of many-electron QDs can be calculated within various approximations. It was proven, in particular,[9] that the generalized Hartree–Fock approximation is adequate to many-electron QDs in strong magnetic fields within a certain region of the confining-potential steepness.

One of the most interesting problems in the physics of two-dimensional electron systems is the crystallization of electrons predicted for three-dimensional systems by Wigner[10] and considered theoretically[11–15] for two-dimensional systems (see also reviews Refs. 16 and 17). Calculation of the two-dimensional electron-gas crystallization[15,18] yields results which agree well with numerical[19,20] and physical[21] experiments. The crystallization of electrons in quantum dots was considered[22] for the classical case by molecular-dynamics simulation (see also Ref. 23 and references therein), and for a quantum-confined region, by the quantum Monte-Carlo method[24]. As predicted in Ref. 13, a strong magnetic field expands the region of the crystal existence (see also Refs. 14, 15, and 17 and references therein). It appears of interest to consider also the effect of magnetic field on the onset of ''crystalline'' order in a quantum dot. As will be shown below, its influence on the appearance of crystalline order within a certain region of the control parameters (magnetic field and the steepness of the confining potential) is nonmonotonic because of the competition between two mechanisms, the localizing action of the magnetic field (reduced spread of the wave function) and compression of the system as a whole because of the growing *effective* steepness of the confining potential and the associated decrease of the average electron separation.

This work considers the problem of a two-dimensional QD with two electrons within a broad range of transverse magnetic fields. The model used is the parabolic confining potential $U(r)=\alpha r^2$, although the results obtained can be readily generalized to other types of the potential as well. To cover a large range of magnetic fields B and of the steepness parameters of the confining-potential α, we used in looking for the energy spectrum and wave functions numerical diagonalization of the Hamiltonian in the basis of one-particle eigenfunctions.

We are going to consider in this work quantum crystallization in a two-electron, two-dimensional QD in a transverse magnetic field.

1. ENERGY SPECTRUM AND WAVE FUNCTIONS OF THE RELATIVE MOTION OF ELECTRONS WITH INCLUSION OF ELECTRON-ELECTRON INTERACTION

Consider two electrons in an external potential well of the form $U=\alpha r^2$ (parabolic lateral potential) in a transverse magnetic field **B**.

Because of the problem being axially symmetric, we

 © 1998 American Institute of Physics

may conveniently use symmetric gauge of the vector potential $\mathbf{A}$: $\mathbf{A}=\frac{1}{2}[\mathbf{B}\times\mathbf{r}]$.

The Hamiltonian of the system can be written

$$\hat{H}=\frac{\left(\frac{-i\nabla_1-eA}{c}\right)^2}{2m^*}+\frac{\left(\frac{-i\nabla_2-eA}{c}\right)^2}{2m^*}+\frac{e^2}{(\varepsilon|\mathbf{r}_1-\mathbf{r}_2|)}+\alpha(r_1^2+r_2^2)\,, \tag{1}$$

where m^* is the effective electron mass, ε is the dielectric permittivity, and α is the steepness parameter of the confining potential.

We next make the quantities involved dimensionless by introducing the following units of distance, energy, confining-potential steepness, and magnetic field:

$$a_0=\frac{\hbar^2\varepsilon}{2m^*e^2},\quad E_0=\frac{2m^*e^4}{\hbar^2\varepsilon^2},$$

$$\alpha_0=\frac{E_0}{a_0^2},\quad B_0=\frac{(2m^*)^2e^3c}{\hbar^3\varepsilon^2}\,, \tag{2}$$

where a_0 and E_0 are the radius and binding energy of the two-dimensional exciton.

After this, the Schrödinger equation takes on the form

$$\left[\Delta_{\mathbf{r}_1}+\Delta_{\mathbf{r}_2}+\frac{i\omega_c}{4}\left(\frac{\partial}{\partial\theta_1}+\frac{\partial}{\partial\theta_2}\right)+E-\left(\alpha+\left(\frac{\omega_c}{4}\right)^2\right)\times(r_1^2+r_2^2)-\frac{1}{|\mathbf{r}_2-\mathbf{r}_1|}\right]\psi=0\,, \tag{3}$$

where ω_c is the cyclotron frequency.

The distinctive feature of an external parabolic potential is the possibility of separating the center-of-mass- from relative motion of particles. After replacing the coordinates $\mathbf{R}=\mathbf{r}_1+\mathbf{r}_2$ and $\mathbf{r}=\mathbf{r}_1-\mathbf{r}_2$, we obtain coupled equations characterizing the center-of-mass motion and relative motion:

$$\frac{\partial^2\psi_R}{\partial R^2}+\frac{1}{R}\frac{\partial\psi_R}{\partial R}+\frac{1}{R^2}\frac{\partial^2\psi_R}{\partial\theta^2}+i\frac{\omega_c}{4}\frac{\partial\psi_R}{\partial\theta_R}+\left(E_R-\frac{\beta^2}{2}R^2\right)\psi_R=0\,, \tag{4}$$

$$\frac{\partial^2\psi_r}{\partial r^2}+\frac{1}{r}\frac{\partial\psi_r}{\partial r}+\frac{1}{r^2}\frac{\partial^2\psi_r}{\partial\theta^2}+i\frac{\omega_c}{4}\frac{\partial\psi_r}{\partial\theta_r}+\left(E_r-\frac{\beta^2}{2}r^2-\frac{1}{|r|}\right)\psi_r=0\,, \tag{5}$$

$$E=E_R+E_r\,. \tag{6}$$

Here $\beta=[(\omega_c/4)^2+\alpha]^{1/2}$ is a parameter characterizing the *effective* steepness of the confining potential in a magnetic field, which grows with the field.

The total wave function should be antisymmetric with respect to electron permutation. Because the wave function characterizing the center-of-mass motion, ψ_R, is symmetric under permutation of $\mathbf{r}_1$ and $\mathbf{r}_2$, spin $S=0$ should correspond to even wave functions of the electron relative motion ψ_r, and $S=1$, to odd ones.

Equation (4) allows an analytical solution; one can thus determine the center-of-mass energies E_R (the Darwin–Fock energies) and the eigenfunctions ψ_R:

$$E_{R_{nm}}=2^{3/2}\beta\left(n+\frac{|m|+1}{2}\right)+\frac{\omega_c}{4}m\,, \tag{7}$$

$$\psi_{nm}(\mathbf{R})=\left(\frac{n!}{\pi(|m|+n)!}\left(\frac{\beta}{\sqrt{2}}\right)^{|m|+1}\right)^{1/2}R^{|m|}\times\exp(-\beta R^2/2\sqrt{2})L_n^{|m|}\left(\frac{\beta R^2}{\sqrt{2}}\right)\exp(im\theta)\,, \tag{8}$$

where $L_n^{|m|}$ is the associated Laguerre polynomial.

The equation for relative motion (5) differs from that for the center of mass only in including the electron–electron interaction. In accordance with the symmetry of the problem, the wave function of relative motion can be written as $\psi_r(\mathbf{r})=f_m(r)\exp(im\theta)$, where $m=0,\pm1,\ldots$, and the radial function $f_m(r)$ satisfies the equation

$$\frac{\partial^2 f}{\partial r^2}+\frac{1}{r}\frac{\partial f}{\partial r}+\left(E'_{rm}-\frac{\beta^2}{2}r^2-\frac{1}{|r|}-\frac{m^2}{r^2}\right)f=0\,, \tag{9}$$

where $E'_{rm}=E_r-m\omega_c/4$.

Equation (9) contains the only control parameter of the problem, namely, the effective potential steepness β, which determines the wave-function structure and the eigenvalues E'_{rm}.

Expand $f_m(r)$ in the basis of eigenfunctions of the problem without the Coulombic interaction among the electrons

$$f_{nm}=\left(\frac{n!}{\pi(|m|+n)!}\left(\frac{\beta}{\sqrt{2}}\right)^{|m|+1}\right)^{1/2}r^{|m|}\times\exp(-\beta r^2/2\sqrt{2})L_n^{|m|}\left(\frac{\beta}{\sqrt{2}}r^2\right)\,, \tag{10}$$

$$f_m=\sum_n C_{nm}f_{nm}\,. \tag{11}$$

The solution to Eq. (9) will be found by numerical diagonalization of the Hamiltonian in the basis of these functions. The eigenfunctions of energy are determined from the equation

$$\det\{V_{nm}^{n'm}+\delta_{n,n'}(\varepsilon_{nm}-E_r)\}=0\,, \tag{12}$$

where

$$V_{nm}^{n'm}=\left(\frac{n!n'!}{(n+|m|)!(n'+|m|)!}\frac{\beta}{\sqrt{2}}\right)^{1/2}\times\sum_{i=0}^{n}\sum_{j=0}^{n'}(-1)^{i+j}\binom{n+|m|}{n-i}\times\binom{n'+|m|}{n'-j}\Gamma\left(i+j+|m|+\frac{1}{2}\right)\,, \tag{13}$$

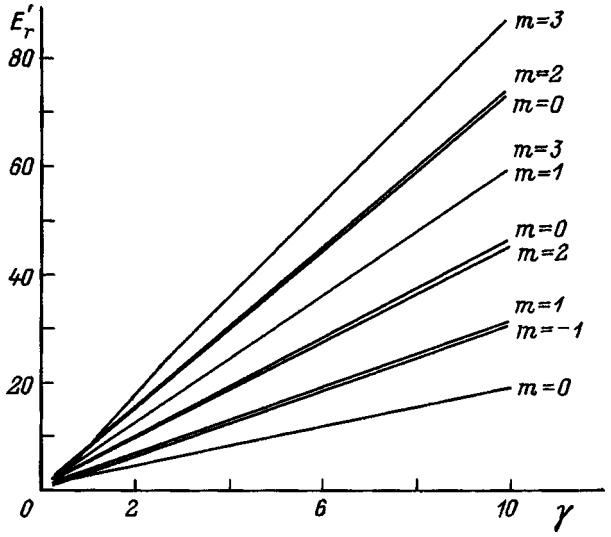

FIG. 1. Energies of the lower levels E'_r vs parameter $\gamma=\beta/\omega_c$. $\beta=[(\omega_c/4)^2+\alpha]^{1/2}$ is the effective steepness of the quantum-dot confining potential in a magnetic field, α is the confining-potential steepness parameter.

and Γ is Euler's gamma function.

The energy and length can be conveniently normalized as

$$E'=\frac{E}{\omega_c}, \quad r'=r\sqrt{\omega_c}. \tag{14}$$

Now the eigenenergies and the eigenfunctions characterizing the basis functions (in which diagonalization is done) depend on the dimensionless parameter $\gamma=\beta/\omega_c=\sqrt{\alpha/\omega_c^2+1/16}$. The center-of-mass energy can be written

$$E'_{R_{nm}}=2\sqrt{2}\,\gamma\left(n+\frac{|m|+1}{2}\right)+\frac{m}{4}. \tag{15}$$

Figure 1 presents the dependences of the lower-level energies E'_r on parameter γ derived from the solution of Eq. (12). The positions of the energy levels increase monotonically with γ (for a fixed ω_c). States with the same quantum number m exhibit quasi-crossing of energy levels. For states with different symmetry, i.e., with different quantum numbers m, one observes level crossing. These crossings and quasi-crossings are more clearly pronounced for $\gamma\sim 1$, where all factors (confining potential, magnetic field, Coulomb interaction) produce comparable effects.

If parameter γ is large enough (the case of strong magnetic fields), the electron–electron interaction is small compared to the other parameters, and therefore the relative-motion energies E_r approach asymptotically E_R (7), i.e., they are linear in γ. This is seen clearly from Fig. 1.

We considered also the dependence of the energy level positions E_r separately on the steepness of the confining potential α and on magnetic field B. The dependences of the lower energy levels on the steepness α are presented in Fig. 2a. The energies outside the level quasi-crossing region increase monotonically with α.

The level quasi-crossings are more clearly pronounced in Fig. 2b showing the dependence of the lower level energies on magnetic field B. The energies of the levels grow with B. Quasi-crossing of levels with the same symmetry is accompanied by the appearance of energy gaps. The variation of the plots in curvature reflects combined action of all factors, namely, the magnetic field B, confining potential α, and the Coulombic electron interaction. This is most pronounced for not too large α and B, i.e., in the region where all factors produce comparable effects.

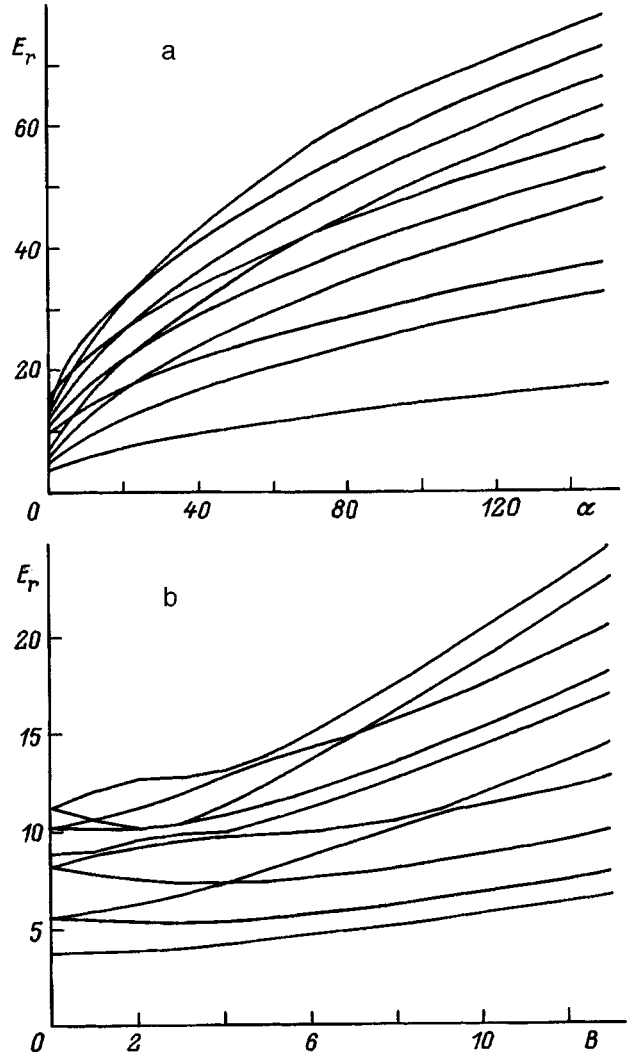

FIG. 2. Energies of the lower levels E_r vs. (a) confining- potential steepness parameter α in magnetic field $B=10$ [in units of $B_0=(2m^*)^2e^3c/\hbar^3\varepsilon^2$] and (b) magnetic field B for the confining-potential parameter $\alpha=3$ [in units of $\alpha_0=(2m^*)^3e^8/\hbar^6\varepsilon^4$].

It appears of interest to compare the energies E_r obtained by numerical diagonalization of the Hamiltonian with the results following from the perturbative theory in electron–electron interaction. It was found that perturbation theory yields fairly good results for $\gamma\gtrsim 1$ (the relative error decreases with increasing γ). This is similar to application of perturbation theory ($1/Z$ expansion) to atoms with a small number of electrons, despite the absence of an explicit small dimensionless parameter of the problem.

The applicability of perturbation theory to this case is demonstrated by Fig. 3 comparing the calculated position of

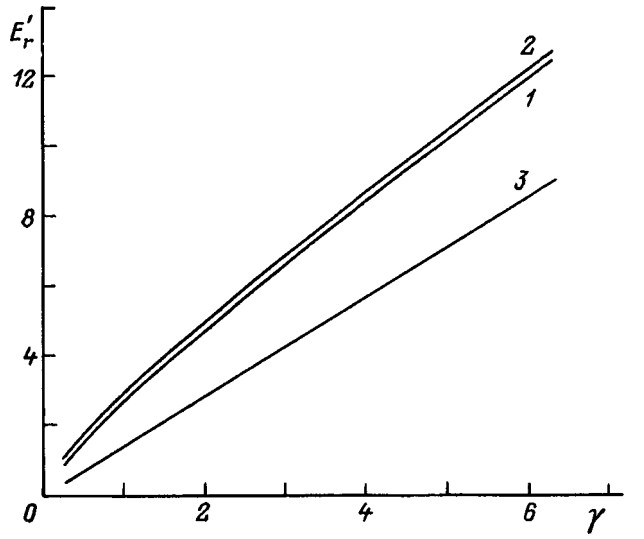

FIG. 3. Comparison of calculated dependences of the lower-level energies E'_r on parameter γ obtained by (*1*) diagonalization of Hamiltonian and (*2*) a perturbative approach. Curve *3* corresponds to the case where electron–electron interaction is neglected.

the lower energy level E_r with quantum number $m=0$ with the results obtained by perturbation theory.

To obtain the wave functions of corresponding electron motion, we find coefficients C_{nm} from the equation

$$\sum_n C_{nm}(\varepsilon_{nm}-E_r+V_{nm}^{n'm})=0\,. \tag{16}$$

In this way one determines the wave functions of corresponding motion $f_m(r)$. The squares of the wave functions $f_m(r)$ are plotted in Fig. 4 for some values of the confining-potential parameter α and magnetic field B.

The energy spectrum of QDs can be studied experimentally by spectroscopic methods. In the case of a parabolic confining potential, however, IR spectroscopy permits observation only of the excitations associated with center-of-mass motion. Nevertheless, excitations related to corresponding motion of electrons can be observed, for instance, in electronic transitions from the valence to conduction band.

2. EXPANSION IN THE BASIS OF HARMONIC-OSCILLATOR FUNCTIONS

In the region of the values of α and B where the electrons are strongly correlated their wave functions should be close not to the one-particle wave functions (10), as in the opposite case of weak correlation, but rather to the harmonic-oscillator functions localized at centers of classical electron crystallization (see Ref. 22). It appears therefore reasonable to solve Eq. (9) by expanding the solutions on the basis of harmonic-oscillator functions as well

$$f'_{nm}(x)=(a_m/2^{1/4}/(2^n n!\sqrt{\pi}))^{1/2} \times\exp(-x^2\sqrt{a_m/2}/2)H_n((a_m/2)^{1/4}x)\,, \tag{17}$$

where $x=r-r_0$, r_0 is the average distance between electrons, $a_m=\beta^2+2/r_0^3+6m^2/r_0^4$,

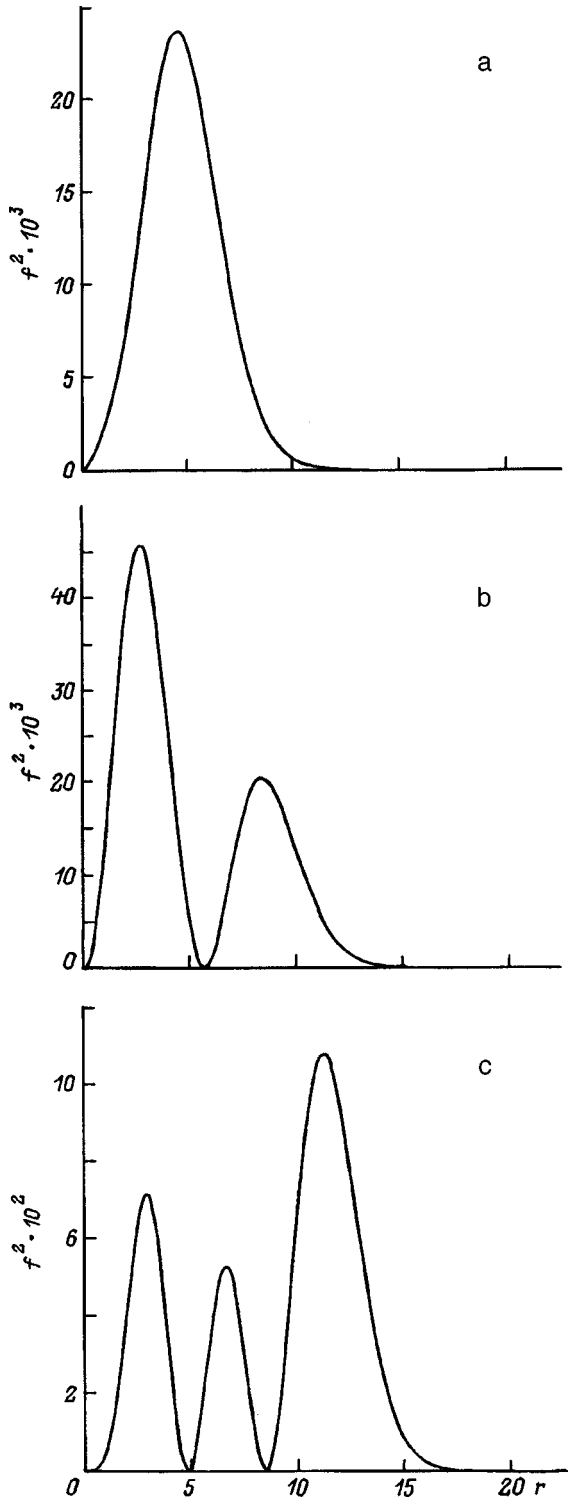

FIG. 4. Squared wave function $f^2(r)$ for $m=0$. Confining potential steepness $\alpha=0.01$, magnetic field $B=0.1$. m: (a) 0, (b) 1, and (c) 2.

$$f'_m=\sum_n C_{nm}f'_{nm}\,. \tag{18}$$

The results obtained by diagonalization on the basis of harmonic-oscillator functions differ in the region of intermediate values of α and B only by a few fractions of one percent from those obtained by numerical diagonalization of the

Hamiltonian on the basis of one-particle functions, which evidences a high accuracy of the calculations.

3. EFFECT OF MAGNETIC FIELD AND THE STEEPNESS PARAMETER OF THE CONFINING POTENTIAL ON QUANTUM CRYSTALLIZATION OF AN ELECTRONIC CLUSTER

The electron localization induced by Coulomb repulsion will be estimated from the halfwidth of the peak of the square of the wave function calculated by us (the probability regarding). This will permit a conclusion regarding the region of the external parameters (confining-potential steepness α and magnetic field B) within which quantum ''crystallization'' of electrons takes place. Thus we shall obtain a kind of phase diagram of electron states in the (α, B) plane.

In the case of a two-electron QD we can deal naturally only with formation of a two-electron cluster involving the onset of short-range order. The appearance of short-range order in an extended system can be judged from the presence of a maximum in the structure form factor $S(k)$.[19] An extended electron system can be characterized by a dimensionless parameter Γ corresponding to the ratio of characteristic potential to kinetic energies. In the classical case, $\Gamma = e^2/(ak_BT)$, $a=(\pi n)^{-1/2}$, where n is the two-dimensional density, and k_B is the Boltzmann constant. Melting of two-dimensional crystals in a classical system was studied by molecular dynamics simulation.[20] For a Coulombic system one obtained the critical value of parameter $\Gamma_{\rm cr}^{\rm cl} \sim 140$ at which long-range order sets in in the system. At the same time the calculations[20] showed that clearly pronounced clusters, i.e. regions with short-range order, exist within a fairly broad interval of Γ, even after the melting. The peak in $S(k)$ associated with short-range order persists up to $\Gamma_{so} \sim 10$ [in this region, the dielectric function $\varepsilon(\mathbf{k})<0$]. The characteristic value of Γ for a quantum system is

$$\Gamma = [e^2/(\varepsilon r)][\hbar^2/(m^* r^2)]^{-1} = r/a_B = r_s$$

[where $a_B = \hbar^2\varepsilon/(m^* e^2)$ is the effective Bohr radius ($a_B = 2a_0$), $r=(\pi n)^{-1/2}$ is the average radius of the circle occupied by one electron].

The value of parameter Γ^q at which quantum crystallization of extended systems occurs is smaller than the classical value of Γ (the critical values $\Gamma_{\rm cr}^q$ derived from theoretical calculations[22] and simulation[23] range from 10^2 to 30). For the purpose of estimation one can accept that the region of the values of Γ_{so}^q at which a region with short-range order appears in a quantum system by crossover is also $\Gamma_{so}^q \sim 10$, which corresponds to $r_s^* \sim 10$. For $T=0$, the Lindemann parameter $\gamma = \sqrt{\langle r^2\rangle}/\overline{r} \sim r_s^{-3/4}$, where $\langle r^2\rangle$ is the rms deviation of the electron from the center of the wave-function localization (compare with Ref. 15). In the region where short-range order sets in ($\Gamma_{so}^q \sim 10$) we have $\gamma_{so} \sim 10^{-3/4} \sim 0.2$ [in place of the critical value $\gamma_c \sim 0.1$ for the onset of long-range order in an extended system (cf., e.g., Refs. 15 and 20)]. Therefore as a criterion for the onset of short-range order one can use the following rule: the ratio of the halfwidth of the wave function of electron relative motion to the average distance between electrons should be 1/2, so that $\gamma_{so}=1/4$ (which agrees fairly well with the above value of γ_{so}).

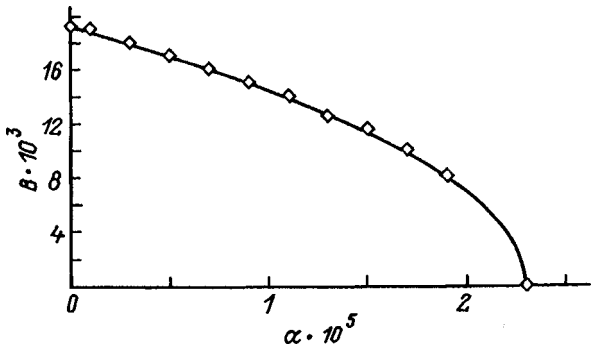

FIG. 5. Conventional boundary of the electron quantum-crystallization region.

The parameter determining quantum crystallization of electrons (i.e. the control parameter of the problem) is β, which characterizes the effective steepness of the confining potential in a magnetic field. For $\gamma=1/4$ calculations yield for the critical value of this parameter, at which crystallization takes place in a two-electron quantum dot, $\beta_{\rm cr}=0.005$. Figure 5 shows a conventional boundary of the electron quantum-crystallization region for the ground state ($m=0$) in the plane of the control parameters (α, B) determined in accordance with the above criterion. An increase of either the steepness of the confining potential or of the magnetic field gives rise to an increase of the effective steepness of the potential in a magnetic field and, accordingly, to a decrease

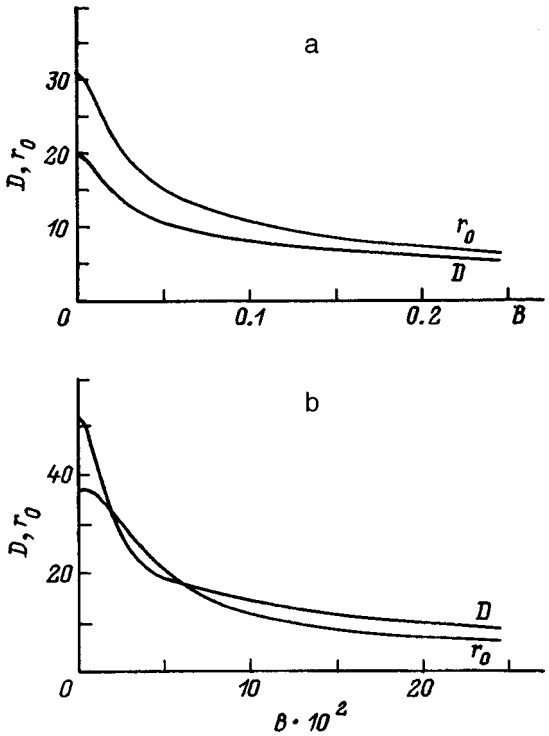

FIG. 6. Halfwidth of the peak of the squared radial wave function D and average distance between electrons r_0 vs magnetic field B plotted for a constant confining-potential steepness parameter $\alpha=10^{-5}$. $m=0$ (a), $m=1$ (b).

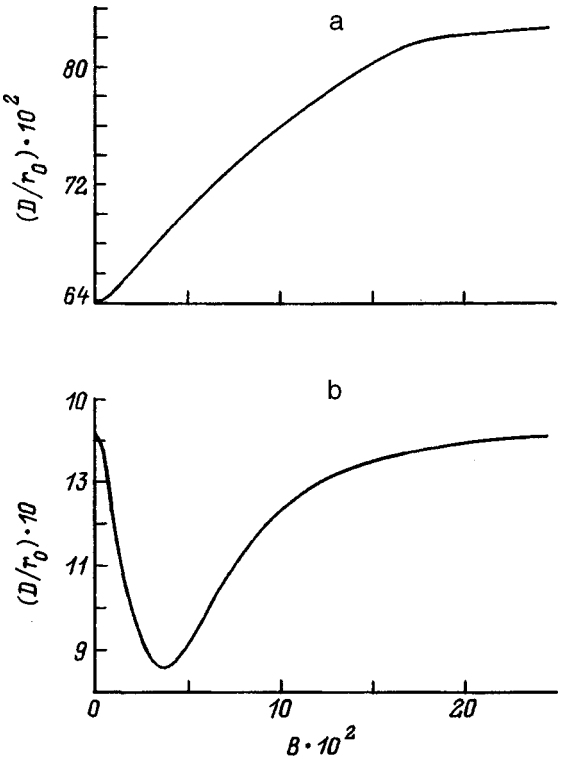

FIG. 7. Ratio of D to the average distance between electrons r_0 vs magnetic field B plotted for a constant confining-potential steepness parameter $\alpha=10^{-5}$. $m=0$ (a), $m=1$ (b).

of the average separation among electrons and to their relative delocalization. It should be stressed that magnetic field acts in two ways in a quantum dot, namely, it reduces the spread of the electron wave functions while at the same time reducing the average characteristic electron–electron distance, which increases the wave-function overlap. Figure 6 plots the halfwidth of the peak of the squared wave function D and the average separation between electrons, r_0, vs magnetic field B. Shown graphically in Fig. 7 are the ratios of the halfwidth of the peak of the squared wave function to the average distance between electrons, D/r_0, as functions of magnetic field B calculated for states with $m=0$ and 1 at a constant α. One readily sees that in the $m=0$ case the magnetic field initially favors relative localization of electrons, although the wave-function overlap is too large to speak with confidence about quantum crystallization here. At the same time strong magnetic field favors relative delocalization. Thus a magnetic field can act nonmonotonically on quantum crystallization because of the competition between two effects with increasing magnetic field, namely, the decrease not only of the wave-function spread but of the electron–electron separation as well.

The authors are grateful for fruitful discussions by the participants of the ''New Physics of Low-Dimensional Systems'' meeting (Dresden, 1997).

Support of the Russian Fund for Fundamental Research, INTAS Foundation, and of the ''Physics of Nanostructures'' program is gratefully acknowledged.

[1] F. Geerinckx, F. M. Peeters, and J. T. Devreese, J. Appl. Phys. **68**, 3435 (1990).
[2] W. Hansen, M. Horst, J. P. Kotthaus, U. Merkt, Ch. Sikorski, and K. Ploog, Phys. Rev. Lett. **58**, 2586 (1987).
[3] Ch. Sikorski and U. Merkt, Phys. Rev. Lett. **62**, 2164 (1989).
[4] C. T. Liu, K. Nakamura, D. C. Tsui, K. Ismail, D. A. Antoniadis, and H. I. Smith, Appl. Phys. Lett. **55**, 168 (1989).
[5] T. Demel, D. Heitmann, P. Grambow, and K. Ploog, Phys. Rev. Lett. **64**, 788 (1990).
[6] J. Dempsey, N. F. Johnson, L. Brey, and B. I. Halperin, Phys. Rev. B **42**, 11708 (1990).
[7] P. Hawrylak, Phys. Rev. Lett. **71**, 3347 (1993).
[8] A. Kumar, S. E. Laux, and F. Stern, Phys. Rev. B **42**, 5166 (1990).
[9] Al. A. Andreev, Ya. M. Blanter, and Yu. E. Lozovik, Solid State Commun. **91**, 581 (1994); Int. J. Mod. Phys. B **9**, 1843 (1995).
[10] E. P. Wigner, Phys. Rev. **46**, 1002 (1934); Trans. Faraday Soc. **34**, 678 (1938).
[11] R. S. Crandall and R. Williams, Phys. Lett. A **7**, 678 (1971).
[12] A. V. Chaplik, Zh. Éksp. Teor. Fiz. **62**, 746 (1972) [JETP **35**, 395 (1972)].
[13] Yu. E. Lozovik and V. I. Yudson, JETP Lett. **22**, 11 (1975); Yu. E. Lozovik and D. R. Musin, Fiz. Tverd. Tela (Leningrad) **21**, 1974 (1979) [Sov. Phys. Solid State **21**, 1132 (1979)]; B. Abdullaev and Yu. E. Lozovik, *ibid.* **24**, 2663 (1982) [Sov. Phys. Solid State **24**, 1510 (1982)].
[14] H. Fukuyama, Solid State Commun. **19**, 551 (1976).
[15] Yu. E. Lozovik and V. M. Farztdinov, Solid State Commun. **54**, 725 (1985); Yu. E. Lozovik, V. M. Farztdinov, and B. Abdullaev, J. Phys. C **18**, L807 (1985).
[16] T. Ando, A. B. Fowler, and F. Stern, Rev. Mod. Phys. **54**, 1 (1982).
[17] V. B. Shikin and Yu. P. Monarkha, *Two-Dimensional Charged Systems in Helium* [in Russian], Nauka, Moscow, 1989.
[18] M. Shaegan, *Perspectives in Quantum Hall Effects*, edited by S. Das Sarma and A. Pinchuk (John Wiley Publ., New York, 1997).
[19] R. H. Morf, Phys. Rev. Lett. **43**, 931 (1979).
[20] V. M. Bedanov, G. V. Gagiyak, and Yu. E. Lozovik, Zh. Éksp. Teor. Fiz. **88**, 1622 (1985) [JETP **61**, 967 (1985)].
[21] C. G. Crimes and G. Adams, Phys. Rev. Lett. **42**, 795 (1979).
[22] Yu. E. Lozovik, Usp. Fiz. Nauk **153**, 356 (1987) [Sov. Phys. Usp. **30**, 912 (1987)]; Yu. E. Lozovik and V. A. Mandelshtam, Phys. Lett. A **145**, 269 (1990).
[23] Yu. E. Lozovik and V. A. Mandelshtam, Phys. Lett. A **165**, 469 (1992).
[24] Yu. E. Lozovik and E. A. Rakoch, JETP Lett. **65**, 282 (1997); Phys. Lett. A **235**, 55 (1997).

Translated by G. Skrebtsov

POLYMERS. LIQUID CRYSTALS

Electric field dependence of the magnetic spin effect in the photoproduction of charge carriers in polydiacetylene

M. K. Kerimov A. É. Nabiev, and É. Z. Aliev

Radiation Research Section of Azerbaidzhan, 370143 Baku, Azerbaidzhan
(Submitted December 9, 1997)
Fiz. Tverd. Tela (St. Petersburg) **40**, 1760–1762 (September 1998)

It is shown that the external-electric-field dependence of the magnitude of the magnetic spin effect in the photoproduction of charge carriers in polydiacetylene films external-electric-field is attributable to a distribution of weakly bound electron-hole pairs with respect to the initial pair separations, within which the pair lifetimes compete with the characteristic times of evolution and relaxation of the spins of the paired partners. © *1998 American Institute of Physics.* [S1063-7834(98)04009-X]

Magnetic spin effects in the photoproduction of nonequilibrium charge carries are caused by the dependence of the recombination efficiency of light-induced, weakly bound electron-hole pairs on the spin state of these pairs.[1,2] On the other hand, the photoproduction of carriers in molecular crystals and polymers containing conjugate multiple bonds is described by the Onsager mechanism of dissociation of a bound pair.[3] This process establishes favorable conditions for extracting additional information about the photoconduction mechanism of such metals by investigating the influence of the electric field, temperature, and energy of the stimulating light on the magnitude of the magnetic effect.

As a rule, the photocurrent has served as the measured quantity in previous studies of magnetic spin effects in the photoconduction of several polymers.[4–6] Photocurrent measurements may be warranted under certain conditions, but this practice can often give rise to an erroneous interpretation of experimental data bearing on the carrier production mechanism. The problem is, as shown in Ref. 7, that the carrier mobility is also governed by spin-dependent transport, which can be controlled by an external magnetic field.

In this light we have investigated the influence of an external magnetic field on the quantum efficiency of carrier photoproduction in polydiacetylene-polydiphenyldiacetylene (PDPDA) films as determined by an electrophotographic method. This method permits the quantum efficiency of carrier production to be determined directly from the decay kinetics of the potential of an illuminated ionic contact formed on the surface of the polymer.

We have investigated samples of PDPDA prepared by the thermal polymerization of diphenyldiacetylene at a temperature of 400 K in a vacuum of 10^{-1} Pa with subsequent solution in benzene and precipitation in methanol. PDPDA films of thickness 3–4 μm were obtained by precipitating the polymer from solution in CCl_4 onto a copper substrate with subsequent evacuation and 4-h drying at a pressure of 0.1 Pa. The ion contact was formed by means of a corona discharge at a potential up to 80–100 V. The films were illuminated by a DKsSH-500 xenon lamp using light filters.

The optical absorption spectra and quantum efficiency of photoproduction η in a PDPDA film reveal coincidence of the absorption and production thresholds around 650 nm. The electric field dependence of η in the interval 10^4–10^7 V/m conforms to the Onsager pair recombination mechanism and is described by the equation[3]

$$\eta = \eta_0\left(1+\frac{e^3E}{8\pi\varepsilon\varepsilon_0k^2T^2}\right)\exp(-r_c/r_0), \tag{1}$$

where η_0 is the initial quantum efficiency, $r_c = e^2/4\pi\varepsilon\varepsilon_0kT$ is the Coulomb radius, which has a value $\simeq$200 Å for PDPDA, and r_0 is the radius of initial separation in the pairs.

The initial spin state of the light-induced bound ion pair is a singlet state, and its subsequent separation or reverse recombination will no longer depend only on the temperature and the electric field, but also on the external magnetic field, which produces mixing of singlet (S) and triplet (T) states of the pairs:

$$[M]\overset{h\nu}{\rightarrow}{}^1[M^+e^-]\rightarrow{}^{1,3}[M^+\ldots e^-].$$

The dependence of the relative variation of the quantum efficiency of photoproduction, defined as $\delta=[\eta(H)-\eta(0)]/\eta(0)$, on the magnetic field at various stimulating light wavelengths, is characteristic of a mixing mechanism based on hyperfine interaction[8] (Fig. 1).

The positive sign of the magnetic spin effect indicates that the main contribution to carrier photoproduction is from the dissociation of pairs existing in the singlet state. Figure 2 shows the dependence of δ on the electric field applied to the sample at various light wavelengths. Clearly, at $\lambda=600$ nm the magnitude of the effect increases monotonically as the electric field is increased, whereas at $\lambda=390$ nm the $\delta(E)$ curve has a maximum at 8×10^6 V/m.

 © 1998 American Institute of Physics

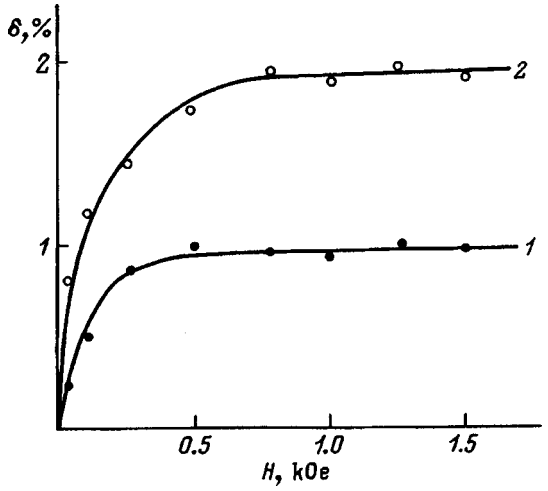

FIG. 1. Dependence of relative variation in the quantum efficiency of photoproduction in PDPDA on the external magnetic field at different light wavelengths. *1*) $\lambda = 600$ nm; *2*) $\lambda = 390$ nm.

This nature of the electric field dependence of the magnetic effect can be explained by competition of the lifetime of an ion pair with the characteristic spin evolution time $\tau_e = \hbar/g\beta a$ (a is the hyperfine interaction constant, and β is the Bohr magnetron) and the spin-relaxation time of particles in the pair.[2,8] The problem is that a necessary condition for carrier photoproduction to be magnetically sensitive is the requirement that the pair lifetime τ be long enough to allow for the $S-T$ evolution of spins in the magnetic field; on the other hand, τ must be shorter than the spin-lattice relaxation time, so that the spin states of the partners will not have time to relax. For the investigated polymers these two conditions correspond to the interval $10^{-8} < \tau < 10^{-6}$ s.

Obviously, the stated condition actually reduces to the interval of values of the initial separation in the pairs $\langle r_0 \rangle$ such as to ensure the given range of pair lifetimes. The distance $\langle r_0 \rangle$ can be estimated from the following considerations.

The initial pair separation $\langle r_0 \rangle$ is determined by the relation between the average rate of separation v_1 of the pairs at the distance $\langle r_0 \rangle$ and the electron velocity v between elastic collisions[9]:

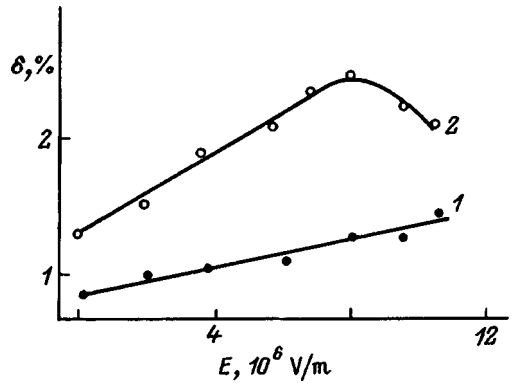

FIG. 2. Dependence of the magnetic spin-effect magnitude in PDPDA on the external electric field at different light wavelengths. *1*) $\lambda = 600$ nm; *2*) $\lambda = 390$ nm.

$$\langle r_0 \rangle = \frac{3}{2}\frac{v_1}{v} r_c . \tag{2}$$

Inasmuch as v_1 depends on the electron drift, $v_1 = \mu E$, and the electron velocity between collisions is $v = \langle r_0 \rangle / \tau$, Eq. (2) can be rewritten in the form

$$\langle r_0 \rangle = \left(\frac{3}{2} \mu E \tau r_c \right)^{1/2} . \tag{3}$$

Making use of the fact that for PDPDA with the electric fields used in our work, $10^6 - 10^7$ V/m, $\mu = 3 \times 10^{-9}$ m^2/V·s, we find that carrier photoproduction will be magnetically sensitive for pairs having an initial separation in the interval 9.5–300 Å. This means that for values $\langle r_0 \rangle < 9.5$ Å, owing to the high probability of reverse recombination, an ion pair has a low probability of $S-T$ evolution, whereas for $\langle r_0 \rangle 300$ Å the pair dissociates into states with uncorrelated spins. In reality, the interval of initial separation of radii is much narrower, because extreme values of E and τ have been chosen for the estimation of $\langle r_0 \rangle$. The values of $\langle r_0 \rangle$ calculated from Eq. (1) lie in the interval 15–120 Å, depending on the wavelength, the temperature, and the electric field.

Based on these considerations, the plots of the electric field as a function of the magnetic effect of photoproduction at various stimulation wavelengths can be substantiated by the fact that the probability of avoiding reverse recombination in pairs having a small separation $\langle r_0 \rangle$ ($\lambda = 600$ nm) recombination increases as the electric field is increased, but the condition for complete dissociation is never attained in the indicated interval of electric fields. However, when stimulation takes place in the short-wavelength range, so that pairs having a large separation are formed, the probability of avoiding recombination increases as E is increased, but the probability of pair dissociation into a state with uncorrelated spins increases at the same time, imparting the observed extremal behavior to the electric field dependence of the magnetic spin effect in the carrier photoproduction in PDPDA.

[1] E. L. Frankevich, in *Electronic Processes in Organic Molecular Crystals: Transport, Capture, and Spin Effects* [in Russian], edited by É. A. Silin'sh (Riga, 1992), 363 pp.
[2] Ya. B. Zel'dovich, A. L. Buchachenko, and E. L. Frankevich, Usp. Fiz. Nauk **155**, 3 (1988) [Sov. Phys. Usp. **31**, 385 (1992)].
[3] M. Pope and C. E. Swenberg, *Electronic Processes in Organic Crystals*, Vol. 12 [Oxford Univ. Press, New York, 1982; Mir, Moscow, 1985], 462 pp.
[4] K. Okamoto, A. Itaya, and Sh. Kusabayashi, Chem. Phys. Lett. **35**, 483 (1975).
[5] E. L. Frankevich, A. A. Lymarev, and I. A. Sokolik, Khim. Fiz. **9**, 1361 (1990).
[6] N. A. Davidenko and N. G. Kuvshinskiĭ, Fiz. Tverd. Tela (St. Petersburg) **39**, 1020 (1997) [Phys. Solid State **39**, 916 (1997)].
[7] E. L. Frankevich, I. A. Sokolik, D. I. Kadyrov, and V. M. Kobryanskiĭ, JETP Lett. **36**, 486 (1982).
[8] K. M. Salikhov, Yu. N. Molin, R. Z. Sagdeev, and A. L. Buchachenko, *Spin Polarization and Magnetic Effects in Radical Reactions* [Elsevier, Amsterdam, 1984; Russ. original, Nauka, Novosibirsk, 1978], 296 pp.
[9] A. Rose, *Concepts in Photoconductivity and Allied Problems* [Interscience, New York, 1963; Mir, Moscow, 1966], 192 pp.

Translated by James S. Wood